REPUBLIQUE DU CAMEROUN
Paix – Travail – Patrie
****
UNIVERSITE DE YAOUNDE I
FACULTE DES SCIENCES
DEPARTEMENT DE CHIMIE INORGANIQUE
****
LABORATOIRE DE CHIMIE INORGANIQUE APPLIQUEE

REPUBLIC OF CAMEROUN
Peace – Work – Fatherland
****
UNIVERSITY OF YAOUNDE I
FACULTY OF SCIENCE
DEPARTMENT OF INORGANIC CHEMISTRY
****
APPLIED INORGANIC CHEMISTRY LABORATORY

SYNTHESIS, CHARACTERIZATION AND APPLICATIONS OF SOME BISMUTH(III) AND ANTIMONY(III) SULFIDE NANOMATERIALS

Thesis submitted to the Department of Inorganic Chemistry in partial fulfilment of the requirements for the award of Doctorat/PhD degree in Chemistry

Par : **Kun Walter NDAMUKONG**
MSc Inorganic Chemistry (UY1)

Sous la direction de
NDIFON Peter Teke
Professor, University of Yaounde I
Neerish REVAPRASADU
Professor, University of Zululand ,
South Africa

Année Académique : 2020

ATTESTATION OF THESIS CORRECTION

We the undersigned LAMBI John NGOLUI (Professor, examiner), NDIFON Peter TEKE (Professor, supervisor), GHOGOMU Paul MINGO (Professor, president) attest that this Ph.D thesis defended on the 21st of February 2020 in the pedagogic block room S01/02 of the Faculty of Science, University of Yaoundé I, by KUN Walter NDAMUKONG on the theme ***Synthesis, characterization and applications of some bismuth(III) and antimony(III) sulfide nanomaterials''***, for the award of a Ph.D. in Inorganic Chemistry, has been corrected in conformity with the recommendations of the defense jury.

In this testimony whereof, this attestation is issued.

Yaoundé, 04 May 2020

Lambi John Ngolui
Ph.D (Ife), CChem, MRSC
Professor of Chemistry

Supervisor

NDIFON Peter TEKE

Professor

Examiner

LAMBI John NGOLUI

Professor

President

GHOGOMU Paul MINGO

Professor

DEDICATION

In loving memory of my late Dad, Srg Ngongha Ndamukong Michael

and

late Professor Paul O'Brien, a great mentor and role model.

ACKNOWLEDGEMENTS

My Profound gratitude goes to my home supervisor Pr NDIFON Peter Teke for the support, interest commitment, and patience in supervising this work .

I am most indebted to my host supervisor Pr Neerish REVAPRASADU of the University of Zululand, South Africa for providing the initial financial assistance that lead to a smooth start of this project.

I am equally indebted to the entire academic staff of the Inorganic Chemistry Department of the University of Yaoundé I, for the knowledge I acquired during this course.

I wish to thank the National Research Foundation (NRF), South Africa for providing financial assistance in the first year of this project.

I am particularly grateful to the Royal Society /DFID grantt for capacity building in sub saharan Africa for the finantial assistance which I benefited from including travel grants, bench fee and bursary, which permitted me to complete this project.

Special thanks go to Dr Sixberth Mlowe of the University of Zululand, Dr Nyamen Linda of the University of Yaounde I, Dr Paul Mcnaughter of the University of Manchester for their assistance in data processing during the entire project.

I wish to thank Matt Smith of the electron microscopy unit of the University of Manchester for his assistance in acquiring TEM/HRTEM data, Dr. Inigo Vitorica-yrezaba, Dr. George Whiteheard (University of Manchester), Pr. Ordre Monro (University of Witwatersrand, SA) and Dr. Matthew P. Akerman (University of KwaZulu-Natal , SA) for the single crystal X-ray analysis, Dr Ben F. Spencer (University of Manchester) for XPS analysis.

I appreciate every assistance given to me by my fellow mates of the Laboratory of coordination Chemistry of the University of Yaounde I, the nano research group of the University of Zululand SA, and the PhD students of the POB research group of the University of Manchester

Many thanks to the Dynamic Self Help group, through their secretary, Dr ALOTA John for their prompt financial assistance through out this project.

I am most grateful to my mother, Mrs NGONGHA Margerette whose love, kindness and affection have been a source of strength. To my beloved wife Mrs Nadege Ndamukong for being so understanding, patient and encouraging throughout these years. To my lovely daughters Ndahse Xola Praise Ndamukong, Aziseh Chloey Ndamukong and my son Akonui Akim Ndamukong. To my uncle and wife Mr and Mrs NGONGHA Fon for their love and support. To my Mother and father inlaw Mr/Mrs Ndikefor Joseph for their support and care especially towards my family each time I was out of the country. To my cousin Talambe Helen, for assisting me throughout these years. To my siblings Sis Ben, Gorden, Oliver, Elvis, Paddy and Elian for their love, encouragements, prayers, financial and material support. To All my nieces and nephews.

I also wish to thank all the members of RCCG throne of Grace Parish Bamenda for their endless prayers, especially during my numerous trips.

To God be all the glory.

TABLE OF CONTENTS

LIST OF ABBREVIATIONS

AACVD:	Aerosol Assisted Chemical Vapour Deposition
ALD:	Atomic Layer Deposition
ASU:	Assymetric Unit
CBD:	Chemical Bath Deposition
CHN:	Elemental analysis
CNT:	Carbon Nanotubes
CO:	Castor oil
CSD:	Cambridge Structural Database
CCDC:	Cambridge Crystallographic Data Centre
CV:	Cyclic Voltammetry
CVD:	Chemical Vapour Deposition
DA:	Decylamine
DDA:	Dodecylamine
DT:	1-Dodecanethiol
DOS:	Density of States
DSP:	Dual Source Precursor
EDX:	Energy Dispersive X-ray Spectroscopy
EIS:	Electrochemical Impedance Spectroscopy
FET:	Field Effect Transistor
GCD:	Galvanostatic Charge/Discharge
HDA:	Hexadecylamine
HER :	Hydrogen Evolution Reaction
HOMO:	Highest Occupied Molecular Orbital
ICDD:	International Centre for Diffraction Data
JCPDS:	Joint Committee on Powder Diffraction Standard

LED:	Light Emitting Diode
LPCVD:	Low Pressure Chemical Vapour Deposition
LSV:	Linear Sweep Voltammetry
LUMO:	Lowest Un-occupied Molecular Orbital
NMP:	N-methyl pyrrolidinone
Nps:	Nanoparticles
OLA:	Oleylamine
OO:	Olive oil
OER:	Oxygen Evolution Reaction
PECVD:	Plasma Enhanced Chemical Vapour Deposition
PL:	Photoluminescence
p-XRD:	powder X-ray Diffraction
QD:	Quantum dot
QDs :	Quantum dots
RA:	Ricinoleic acid
RHE:	Reversible Hydrogen Electrode
SA :	South Africa
SAED:	Selected Area Electron Diffraction
SCE:	Saturated Calomel Electrode
SEM:	Scanning Electron Microscopy
SSP:	Single Source Precursor
STM:	Scanning Tunneling Microscope
SWCNT:	Single-walled Carbon Nanotubes
TEM:	Transmission Electron Microscopy
TGA:	Thermogravimetric Analysis
TOP:	Tri-n-octylphospine

TOPO:	Tri-n-octylphospine oxide
TUM:	The University of Manchester
UK:	United Kingdom
UZ:	University of Zululand
XPS:	X-ray photoelectron spectroscopy

LIST OF FIGURES AND SCHEMES

LIST OF TABLES

ABSTRACT

Heterocyclic piperidine[($Na(S_2CPip)$] $2H_2O$), tetrahydroquinoline ([$Na(S_2CThq)$] $\cdot 4H_2O$) and morpholine ([$Na(S_2CThq)$]$4H_2O$) dithiocarbamate ligands were synthesized with yields ranging between 66.00 % to 84.04 %. The ligands were used to prepare seven (07) Sb(III) and Bi(III) complexes. Reaction yields ranging from 62.00 % to 92.00 % were obtained. X-ray crystal structures of four (04) novel Bi(III) complexes were elucidated: [$Bi(S_2CPip)_2NO_3$], [$Bi(S_2CPip)_3$], [$Bi(S_2CThq)_3$] and [$Bi(S_2CPip)_3$]$2CHCl_3$. The X-ray crystal structures of the three (03) Sb(III) complexes, [$Sb(S_2CMor)_3$], [$Sb(S_2CDed)_3$] and [$Sb(S_2CPip)_3$] were also determined but had been reported in the literature at higher temperatures.

The ligands and complexes were characterised by analytical techniques such as melting point determination, elemental analysis, Fourier transform infrared spectroscopy (FT-IR), ^1H and ^{13}C Nuclear Magnetic Resonance spectroscopy and thermogravimetric analysis (TGA). All the compounds melted sharply at temperatures ranging from 295 ℃ to 299 ℃ for the ligands and 230 ℃ to 279 ℃ for the complexes. FT-IR analysis revealed the ligand was coordinated to the central metal in a bidentate manner. Elemental analysis results were in good agreement with calculated values for the compounds. TGA analysis showed decomposition patterns at temperatures between 230 ℃ to 450 ℃ with residues corresponding to antimony sulfide and bismuth sulfide.

The complexes [$Bi(S_2CPip)_2NO_3$], [$Bi(S_2CThq)_2NO_3$], [$Bi(S_2CPip)_3$] and [$Bi(S_2CThq)_3$] were used to synthesize Bi_2S_3 nanoparticles at 190 ^oC, 230 ^oC and 270 ^oC respectively using non green and green capping agents.

UV/Vis spectral results showed a general blue shift in the absorption band edge of Bi_2S_3 nanorods synthesized at all temperatures for both green and non-green capping agents; characteristic of quantum confinement effect. TEM images showed high-quality, crystalline, elongated and short Bi_2S_3 nanorods from non-green capping agents. A general trend of increasing particle width with increasing reaction temperature for both green and non-green capped nanoparticles and increasing width with the length of the carbon chain of the amine for non-green capped nanoparticles were observed. p-XRD patterns revealed the orthorhombic crystal structure of Bi_2S_3.

A solventless synthetic route was used to produce Bi_2S_3 nanoparticles by pyrolysing [$Bi(S_2CPip)_2NO_3$] and [$Bi(S_2CThq)_2NO_3$] complexes in an inert (N_2) atmosphere at 350 ^oC, 400 ^oC and 450 ^oC. Irregularly shaped Bi_2S_3 rods out of the nanometer range were obtained at all the three temperatures from [$Bi(S_2CPip)_2NO_3$]. When [$Bi(S_2CThq)_2NO_3$] was used, irregularly

shaped particles were obtained at 350 ^{o}C and 400 ^{o}C, while at 450 ^{o}C irregularly shaped particles and elongated rod were formed.

Antimony sulfide microstructured particles were synthesized in oleylamine with and without dodecanethiol (DT) at 230 °C using [$Sb(S_2CPip)_3$], [$Sb(S_2CMor)_3$] and [$Sb(S_2CDed)_3$] by the hot injection thermolysis route. Micro peg bundles of aspect ratio 4.53, 4.12 and 3.99 were obtained without dodecanethiol. More elongated isolated rods of aspect ratio between 7.31, 7.44 and 7.92 were obtained when DT was added. p-XRD diffraction patterns obtained showed the formation of a pure orthorhombic stibnite phase.

The complete range of $(Bi_{1-x}Sb_x)_2S_3$ solid solutions, where $0 \leq x \leq 1$, were synthesized by varying the mole ratio of bismuth and antimony in [$Bi(S_2CPip)_3$] and [$Sb(S_2CPip)_3$] complexes by hot injection thermolysis in oleylamine at 230 °C. There was a near linear expansion of a and c lattice parameters as the mole ratio of the Sb precursor was increased. The composition of the particles directionally followed the amount of precursor ratio used. A slight deviation from Vegard's law was observed with a corresponding contraction of the b parameter and an approximate 3.5 % reduction of lattice volume. The nanorods obtained were Bi and Sb rich and showed aspect ratios that depend on the composition of the material.

Bismuth sulfide thin films were deposited by the aerosol assisted chemical vapour deposition (AACVD) and spin coating deposition techniques using [$Bi(S_2CPip)_3$] and [$Bi(S_2CThq)_3$] complexes at 350 °C, 400 °C and 450 °C. Both methods, gave sulfur deficient polycrystalline films of bismuthinite as revealed by energy dispersive X-ray spectroscopy (EDX). Scanning electron microscopy (SEM) images of the films showed that their morphology was dependent on the solvent mixture, temperature, precursor type and deposition method. AACVD gave films with hexagonal nanoplatelets, leaf-like platelet, ribbon-like fibre, needle-like fibre morphologies. Films in the form of rods and interwoven nanowires were obtained from spin coating. Antimony sulfide nanorods were tested for oxygen and hydrogen evolution reactions and for supercapacitance performance. It was observed the use of small quantity of DT enhanced the electrochemical and electrocatalytic performances of the nanorods.

Keywords: Bismuth sulfide, antimony sulfide, Single source precursors,

RESUME

Des ligands dithiocarbamates heterocycliques piperidine([Na(S_2CPip] $2H_2O$), tetrahydroquinoline ([Na(S_2CThq] $4H_2O$) et morpholine ([Na(S_2CThq]$4H_2O$) ont été synthetisés avec des rendements variant entre 66.00 et 84.04 %. Les ligands synthétisés ont été utilisés pour la préparation de sept (07) complexes de Sb(III) et Bi(III). Des rendements de réaction variant entre 62.00 et 92.00 % ont été obtenus. Quatre (04) nouvelles structures cristallines du complexe de Bi(III) ont été élucidées: [Bi(S_2CPip)$_2NO_3$], [Bi(S_2CPip)$_3$], [Bi(S_2CThq)$_3$] et [Bi(S_2CPip)$_3$]$2CHCl_3$. Les structures cristallines de trois (03) complexes de Sb(III), [Sb(S_2CMor)$_3$], [Sb(S_2CDed)$_3$] et [Sb(S_2CPip)$_3$] ont aussi été déterminées mais ont déjà été reportées dans la litérature à hautes températures.

Les composés synthétisés ont été caractérisés par des méthodes analytiques connues telles que la mesure du point de fusion, l'analyse microélémentaire, la spectroscopie Infra-rouge par transformé de fourrier (FT-IR), les spectroscopies RMN ^{1}H et RMN ^{13}C et l'analyse thermogravimetrique (ATG). Tous les composés fondent à une température comprise entre 295 °C et 299 °C pour les ligands et de 230 °C et 279 °C pour les complexes. L'analyse infra-rouge a revélé la nature bidentée des ligands. Les résultats de l'analyse microélementaire sont en accord avec les formules proposées pour les composés synthétisés. L'analyse thermogravimétrique a revélé des pertes de masses à des températures comprises entre 230 °C et 450 °C, les résidus correspondants au bismuth sulfure et à l'antimoine sulfure.

Les complexes [Bi(S_2CPip)$_2NO_3$], [Bi(S_2CThq)$_2NO_3$], [Bi(S_2CPip)$_3$] et [Bi(S_2CThq)$_3$] ont été utilisés pour la synthèse des nanoparticules de Bi_2S_3 à des températures de 190 °C, 230 °C et 270 °C, utilisant les surfactants conventionnels et les surfactants "verts". Les spectres UV/Vis des nanotiges montrent un "blue shift" genéral dans les bandes d'absorption des nanotiges de synthétiséés à toutes les temprératures tant dans les surfactants conventionnels que dans les surfactant « verts » ; ceci étant une caractéristique de l'effet confinement quantique. Les images MET ont montré dans les surfactants conventionnels la formation de longues et courtes nanotiges de Bi_2S_3 de haute qualité, cristalline et température dépendante. Une augmentation de la largeur des particules avec la variation de la température de la réaction pour les nanoparticules obtenues en utilisant les surfactants conventionnels et les surfactants "verts" a été observée. L'augmentation de la largeur avec la longueur de la chaîne carbonée de l'amine pour les nanoparticules obtenues en utilisant les surfactants conventionnels a été egalement observées. La DRX en poudre a révélé une structure cristalline orthorhombique des nanoparticules de Bi_2S_3. Une methode de synthèse sans solvant a été utilisée pour produire des Nps de Bi_2S_3 à 350 °C, 400 °C et 450 °C par pyrolyse des complexes de [Bi(S_2CPip)$_2NO_3$] et [Bi(S_2CThq)$_2$]NO_3 sous atmosphère inerte de N_2. Des tiges de Bi_2S_3 de forme irrégulière hors du nanomètre ont été obtenues à partir de [Bi(S_2CPip)$_2NO_3$]. Des particules de forme irrégulière ont été obtenues à 350 °C et 400 °C, tandis qu'à 450 °C, un mélange

de particules de forme irrégulière et de tiges allongées ont été formées à partir de $[Bi(S_2CThq)_2NO_3]$.

Des particules microstructurées de sulfure d'antimoine ont été synthétisées par la méthode de thermolyse à chaud dans l'oléylamine avec et sans le 1-dodécanethiol (DT) à 230 °C en utilisant des complexes $[Sb(S_2CPip)_3]$, $[Sb(S_2CMor)_3]$ et $[Sb(S_2CDed)_3]$ comme précurseurs. Des micro-pinces avec des ratio 4,53, 4,12 et 3,99 sans le DT ont été obtenus. Des tiges isolées plus allongées ayant un rapport de longueur compris entre 7,31, 7,44 et 7,92 ont été obtenues en ajoutant le DT. La DRX a montrée la formation d'une phase stibnite orthorhombique pure.

La gamme complète des solutions solides $(Bi_{1-x}Sb_x)_2S_3$, où $0 \leq x \leq 1$, a été synthétisée par thermolyse à chaud dans l'oléylamine à 230 °C en faisant varier le ratio molaire du Bi et de Sb dans les complexes $[Bi(S_2CPip)_3]$ et $[Sb(S_2CPip)_3]$. Une expansion presque linéaire des paramètres de réseau *a* et *c* a été observée lorsque le ratio molaire du précurseur de Sb augmente. La composition des particules suive de manière directionnelle le ratio de la quantité de précurseur utilisé. Un léger écart par rapport à la loi de Vegard a été observé avec une contraction du paramètre *b* et une réduction d'environ 3,5 % du volume du réseau. Les nanotiges obtenues sont riches en Bi et en Sb et, ont montré des ratio dépendant de la composition du matériau.

Les complexes $[Bi(S_2CPip)_3]$ et $[Bi(S_2CThq)_3]$ ont été utilisés pour la déposition des couches minces de Bi_2S_3 à 350 °C, 400 °C et 450 °C en utilisant la technique de déposition de vapeur chimique assistée par aérosol (DVCAA) et de dépôt par centrifugation. Les images de la MEB ont montrée des morphologies qui dépendent du mélange de solvants, de la température, du type de précurseur et de la méthode de dépôt. DVCAA a donné des films sous forme de disques hexagonaux, des plaquettes en forme de feuilles, des fibres en forme de ruban et d'aiguilles. Des films sous forme de bâtonnets et de nanofils entrelacés ont été obtenus à partir de la méthode par centrifugation. Des nanotiges de sulfure d'antimoine ont été testées pour les réactions de dégagement d'oxygène et d'hydrogène et pour les performances super condensatrice. Il a été observé que l'utilisation d'une petite quantité de DT améliorait les performances électrochimiques et électrocatalytiques des nanotiges.

Mots-clés: Précurseurs à source unique, Nanoparticules, Thermolyse par injection à chaud, Couches minces, Déposition chimique en phase vapeur assistée par aérosol.

GENERAL INTRODUCTION

Nanotechnology, as a multidisciplinary area of research, has grown exponentially during the past few years such that today, microtechnology which was the key technology during the twentieth century is slowly being replaced[1]. Moreover, the rapid growth of nanotechnology is based on the realization that new materials and devices created from nanoscale building blocks can provide access to new and improved properties and functionalities thus the novel performance of materials at the nanoscale[2]. Nanotechnology is therefore related to the manipulation of materials at the nanoscopic level, whereby the integration of materials can be manipulated to create a desired range of properties through controlled size, selective syntheses and the assembly of nanoscale building blocks[3]. Nanoscale materials are materials with at least one dimension being less than 100 nanometers (nm)[4]. A nanometer is one millionth of a millimetre, approximately 100,000 times smaller than the diameter of a human hair.

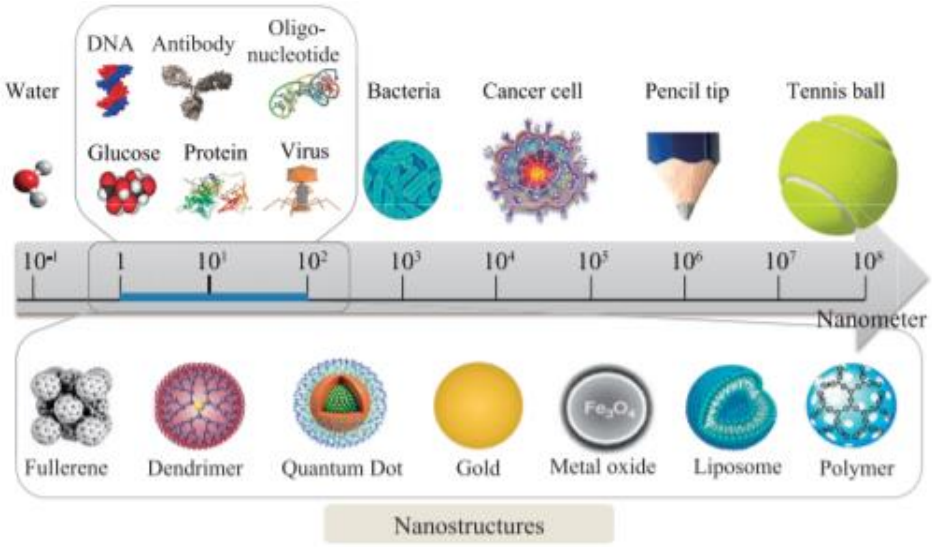

*Figure 1. Relative dimensions compared to the nanoscale (*Saallah *et al, 2018).*

Nanoscience is the study of phenomena and manipulation of materials at atomic, and molecular scales while nanotechnology is the design, production, characterization, and application of structures, devices and systems by controlling shape and size at the nanometer scale. Although the idea of producing and manipulating objects in the nanoscale has been around for quite some time, the birth of the concept is usually linked to a speech by Richard Feynman at the December 1959 meeting of the American Physical Society entitled "*There is Plenty of Room at the Bottom*" where he asked the question "*what would happen if we*

could arrange the atoms one by one the way we want them?"[5]. It was only later in the 1980s that nanotechnology and nano-science started with the birth of cluster science and the invention of the scanning tunnelling microscope (STM)[6]. Nanoscience is a multi-disciplinary field that bridges all the major areas of science like chemistry, physics, engineering, material and biological sciences. The small dimensions of nanoparticles (NPs) result in properties which differ considerably from those encountered in the corresponding bulk microcrystalline material. These unique physical properties give rise to many potential applications in a wide range of fields, from medical applications to environmental sciences.

A key to the successful application of nanomaterials is the ability to tailor their morphology, composition and structure as well as to control size-dispersion and surface functionality[7]. Size control of nanoparticles is very essential due to the fact that the fundamental factors responsible for their unique properties are related to the size of individual nanocrystals[8]. The first factor is the surface effect which causes smooth properties scaling due to the fraction of atoms at the surface. Nanomaterials have large surface to volume ratio. As particles become smaller the fraction of atoms at the surface increases compared to the bulk material. For example, carbon microparticles of mass 0.3 µg and a diameter of 60 µm has a surface area of 0.01 mm^2 while the same mass of carbon with each particle 60 nm in diameter has a surface area of 11.3 mm^2. The atoms situated at the surface have fewer neighbours than bulk atoms, resulting in lower binding energy per atom with decreasing particle size[9]. This leads to the surface playing a key role in the properties of the material. The second factor is the size effect of the particles which brings about discontinuous behaviour due to quantum confinement effects in semiconductor materials with delocalized electrons, and surface Plasmon resonance effect in metallic nanoparticles. Semiconductor nanoparticles experience changes in the electronic properties of the materials as the size of the particles become smaller. The energy band gap gradually becomes larger because of quantum confinement effect. This effect results from the confinement of an "electron in a box" leading to quantization of the energy levels, rather than formation of a continuous band as in the corresponding bulk material. For semiconductors, size effect becomes important when the particle diameter is close to the Bohr diameter of excitons in the bulk phase, the Coulombic interaction between the electron/hole pair cannot be neglected, giving them higher kinetic energy than in the bulk material. Consequently, the first excitonic transition (band gap) increases in energy with decreasing particle diameter. The consequence of quantum confinement is the existence of magnetic moments in nanoparticles of materials that show nonmagnetic property in their bulk phase, like in gold, palladium and platinum[10].

Controlling the shape of nanoparticles is an important aspect in nanotechnology, due to the effects that structural anisotropy has on many of the material's properties and consequently in their uses in several emerging technologies[11]. For example, nanoparticle catalyst has clearly demonstrated size as well as shape selectivity, and the optical activity and surface plasmon resonance have been shown to be shape dependent[12,13,14]. Due to this size and shape dependent properties, much effort has been expended in controlling the morphology and assembly of nanoparticles. The most common shapes of these nanocrystals range from spherical to highly faceted particles, such as cubic and octahedral. One - dimensional (1 - D) anisotropic nanoparticles include uniform rods and wires, whereas two - dimensional (2-D) nanoparticles consists of nanodiscs, plates and other advanced shapes such as rod - based multipods and nanostars[2]. Synthetic protocols for nanoparticles are designed in such a way as to control the size and shape of the desired particles. However, shapes or morphologies sometimes arise spontaneously as an effect of a templating or directing agent during synthesis for example during micellar emulsions or anodized alumina pores, or from the innate crystallographic growth patterns of the materials themselves.

There is a wide range of techniques used to synthesize and grow nanostructures differing in complexity, quality, speed and cost. A good synthetic method should produce monodispersed nanoparticles in high yield, with reproducibility of the synthetic method and good control over the final size and shape at the same time ensuring purity and crystallinity of the final product[2,15]. Techniques such as solvothermal (hydrothermal) route[16–19], microwave assisted route[20], polyol method[21], solvent-less (dry) synthesis[22,23], colloidal synthesis route with the use of molecular precursors[24–27] for the synthesis of particles, Chemical Vapour Deposition (CVD) based processes[28–30], such as Chemical Bath Deposition (CBD)[31,32], spray and flame pyrolysis[33], spin coating techniques[34] have been employed to deposit nanostructured materials as thin films on substrates which could be glass or silicon wafer. Other routes involve purely physical methods such as lithography[35], ball milling[36,37], and arch discharge[38,39]. Colloidal Chemistry has proven to be very efficient in fabricating metal-chalcogenide nanoparticles with well-defined structures. The colloidal access to nanoparticles is achieved by carrying out a precipitation reaction in a homogenous solution in the presence of stabilizers (surfactants), whose role is to prevent agglomeration and further growth. Synthesis of highly monodispersed colloids could be achieved if the seeds (nuclei) could be made to grow into larger particles. If the nucleation and growth processes were properly controlled, particles with nanosized dimensions could be reproducibly synthesized. In this process known as Ostwald ripening, small crystals, which are less stable, dissolve and then recrystallize on larger and more stable crystals[40].

Surfactants play an important role in directing particle growth and restricting particle size by interacting with particle surfaces during the early stage of the reaction (nucleation)[41]. Thus, as the binding affinity of a surfactant varies from one crystal facet to another, preferential binding to particular facet results in hindering the growth of the facet which is attached to the surfactant[41]. A common problem of crystallinity of the material associated with the low-temperature colloidal route could be overcome by injecting precursors that undergo pyrolysis at high temperature into a high boiling point coordinating solvent[40]. There are many kinds of precursors which can be used in these synthesis, ranging from dual molecular (source) precursors (DSP) to single molecular source precursors (SSP). Metal complexes of alkylxanthates[42,43], dichalcogenoimidophosphinate[44,45], thiosemicarbazide[46–48], alkyl/aryl thiourea[49–51], and dithiocarbamate[52–55] as single source precursors have been found to provide additional advantages as they contain the metal-chalcogenide bond necessary for the formation of the desired nanostructure. Dithiocarbamates are organic compounds obtained from the reaction between carbon disulfide and primary or secondary amines. They form very stable complexes with most transition metals and have been effective in the synthesis of many nanostructured systems[56]. Previous works on these compounds were focused on the aliphatic system until recently when the Revaprasadu research group reported the use of heterocyclic dithiocarbamate in synthesis of nanoparticles and thin films[57].

Statement of research purpose

Despite the numerous routes employed in synthesizing nanoparticles and nanomaterials, controlling the shape is still a challenge since a full understanding of the mechanism of decomposition of precursors is still to be established. Some common problems are the too many variable parameters involved during syntheses, ranging from reaction time, temperature, heating rate, capping agent, monomer concentration, and precursor type[58].

The injection of a precursor into hot coordinating solvents remains a novel method to achieve good size-control, good dispersity and reproducibility in nanoparticle syntheses. The solvents used as dispersion media and capping groups play a significant role in the final morphology of the nanomaterial obtained. Commonly used dispersion solvent like trioctylphospine (TOP) and capping agents like tributylphosphine, trioctylphosphine oxide (TOPO), oleylamine (OLA) and other long chain amines give good results with some materials, but with other materials they seem to react chemically giving unexpected products. Moreover, many of these solvents are considered toxic and with recent emphasis on environmental control and safety, alternative synthetic protocols using greener solvents need to be developed. The development of an environmentally safe route for the synthesis of organically soluble nanoparticles is the focus of most research. Nowadays less toxic coordinating solvents such as octadecene, ricinoleic (RA) acid and oleic acid (OA) with less hazardous impacts are utilized for nanocrystal syntheses. Despite an exhaustive work on the use of aliphatic dithiocarbamate as single source precursors for the syntheses of nanocrystalline materials, their heterocyclic counterparts have n until ot been given much attention untill recently when the Revaprasadu group reported on the use of Cadmium piperidine and tertrahydroquinoline dithiocarbamates to synthesize CdS nanoparticles[57].

This work seeks to use heterocyclic dithiocarbamates metal complexes in synthesizing anisotropic semiconductor nanocrystalline materials. It focuses on the synthesis of nanocrystalline Bi_2S_3, Sb_2S_3 and solid solutions of both using non-green solvents like oleyelamine (OLA), hexadecylamine (had), duodecylamine (DDA), decylamine (DA) and tri-n-octylamine oxide (TOPO) and green solvents like castor oil (CO), olive oil (OO), ricinoleic acid (RA), and oleic acid (OA). Bi and Sb are both relatively non-toxic elements whose compounds have found lots of application in cosmetics, medicine and electronics. Bi_2S_3 and Sb_2S_3 are semiconductors having interesting optoelectronic properties and energy band gaps which make them interesting candidates for many applications. They have been applied in photodiode array and photovoltaic converters. Nanostructured Bi_2S_3 and Sb_2S_3 should portray enhanced properties appropriate for energy harvesting in solar devices. Since the basic properties and application of materials depend on their composition, incorporating

a foreign atom or ion into a host crystal lattice can introduce new functional properties to the material and improve device efficiency. Solid solutions of Bi and Sb should have added properties compared to the pure materials. The Bi_2S_3 nanoparticles will be applied in the syntheseis and characterization of thin films, while Sb_2S_3 nanoparticles will be evaluated for water splitting reactions and supercapacitance studeis. Different synthetic procedures like hot injection thermolysis, AACVD, spin coating and solvent-free synthesis (melt) are used and a comparative study on the properties of the material from the different synthetic approaches is made.

Aims and objectives

The aim of this research work is to use heterocyclic metal dithiocarbamate complexes as SSPs for the syntheses of metal sulfide nanoparticles, thin films and to explore the use of green solvents as potential capping agents and dispersing solvents in nanoparticle syntheses.

The specific objectives of the project include:

• To synthesize piperidine, tetrahydroquinoline, and morpholine dithiocarbamate as well as their Bi and Sb complexes. These compounds are characterized by known analytical methods like FT-IR, elemental analyses, TGA, ^{1}HNMR, ^{13}CNMR, Melting point and single crystal analysis for the complexes.

• To use the complexes as single source precursors to syntheses and characterize Bi and Sb sulfide nanoparticles by hot injection thermolysis in green solvents such as OO, CO, RA, and OA and in non-green solvents such as OLA, HDA, DDA, DA and TOPO.

• To deposit Bi and Sb sulfide thin films by AACVD and spin coating from the synthesized SSPs

• To prepare Bi_2S_3 nanoparticles by solvent-free synthesis (melt reactions)

• To prepare $(BiSb)_2S_3$ solid solutions by hot injection thermolysis of the SSPs.

• To characterize the nanoparticles and thin films using p-XRD, in order to identify the crystalline phases present in the material, TEM, HRTEM, and SEM were used to determine their micro structure, UV/Visible, and PL analysis were used to study their electronic properties, Raman spectroscopy and XPS analysis were used to determine their composition and EDX analysis for a quantitative identification of the particles.

Scope of the study

This work focuses on the preparation of Bi_2S_3 thin films, Bi_2S_3 and Sb_2S_3 nanoparticles as well as solid solutions of $(BiSb)_2S_3$. Proper characterization of the particles, films and solid solutions were carried out to clearly establish their morphology and opticlal properties. The potential use of one of the as-synthesized materials in the area of water splitting/hydrogen evolution and supercapacitance was evaluated. The single source precursors route was used to synthesize the target materials. The single source precursors chosen are heterocyclic dithiocarbamate complexes of Bi and Sb, precisely from piperidine, tetrahydroquinoline and morpholine. These complexes are not available commecially so, they were synthesized using the dithiocarbamate ligands. The complexes were characterized in order to acertain the structure of the starting materials for our study. However, the complexes were not a central focus of the study and hence much attention was not given to them. The syntheses of the ligands, and the complexes were done in the University of Zululand in South Africa and the University of Yaounde I, Camerooon, while their characterizations were carried out in the University of Zululand, University of Witwaterstrand SA, the Center for Scientific and Inovative Research (CSIR) SA, and the University of Manchester, UK. The syntheses and characterization of the nanoparticles, thin films and the solid solutions were done in the University of Zululand and the Univnersity of Manchester. Apllications of the materials synthesized was carried out in the University of Zululand.

This work is divided into three chapters . Chapter 1 gives a general introduction to nanoscale for synthesis and discusses the influence of size and shape on the properties of semiconductor materials. Different methods and parameters enabling the production of semiconductor nanoparticles materials including precursor requirement are presented. Chapter 2 presents the various synthetic methods and characterization techniques used for both the precursors and the nanomaterials, as well as the various instrumentation techniques employed during the work. Chapter 3 presents the results obtained and the discussion of these results to bring out the significance of the work. This is followed by a conclusion and perspective.

CHAPTER 1. LITERATURE SURVEY

1.1. Introduction

An emerging areas of nanotechnology that is at the interface of chemistry, biology, physics, materials science and engineering is the field of semiconductor nanocrystals, whose unique properties have attracted much attention in the last decades. Semiconductor nanocrystals are referred to as II-VI, III-V or IV-VI semiconductor nanocrystals, based on the periodic table groups of the constituent elements. For example, silicon and germanium are group IV, GaN, GaP, GaAs, InP and InAs are III-V, while those of ZnO, ZnS, CdS, CdSe and CdTe are II-VI semiconductors[59]. Much interest was devoted to the area of semiconductor nanocrystals in the 1980s with the formulation of the concept of size quantization. Since then many advances have been in this field of studies[60–62]. This progress was stimulated by the possibilities of using semiconductor nanomaterials in field effect transistors (FET), photocatalysis, light emitting diodes (LEDs), biological labels, sensors, and solar cells. An additional advantage was the possibilities of modifying the properties of the material and consequently device performance by simply tuning the size and shape of the nanoparticles[63].

Several types of semiconductor nanocrystals have been synthesized over the past few decades with emphasis on size control. Lately, the development of semiconductor nanocrystals has extended from the pure adjustment of particle sizes to the more thorough control of its unique properties with the hope of opening new scope of applications.

1.2. Quantum confinement

In extended semiconductors, the overlap of atomic orbitals leads to the formation of valence and conduction bands separated by an energy band gap. Upon excitation of a semiconductor, an electron is promoted from the filled valence band to the largely empty conduction band[62]. This creates a positive vacancy "hole" in the valence band. When the spatial separation (the average distance between the electron in the conduction band and the hole it leaves behind in the valence band) of this electron-hole pair ("exciton") is of the order of 1– 10 nm for semiconductors, quantum confinement arises when one of the dimensions of the object becomes of the order of the exciton Bohr radius[59]. In QDs, the excitons are confined in a way like a particle-in-the-box problem leading to a finite band gap and discretization of energy levels. Theoretically, the regimes of quantum confinement differ in their main electron-hole interaction energy. Weak confinement regime is observed when the radius R of a crystallite is greater than the bulk exciton Bohr radius a_B. In this region of weak confinement, the dominant energy is the Coulomb term and there occurs a size quantization

of the exciton motion. The exciton energy states are shifted to higher energies by confinement and the shift in energy ΔE is proportional to $1/R^2$. The shift 'ΔE' of the exciton ground state is given approximately by equation 1;

$$\Delta E = \frac{\hbar^2 \pi^2}{2MR^2} \quad (1)$$

where, M is the mass of the exciton and it is given by $M = m_e^* + m_h^*$ with m_e^* and m_h^* being the effective masses of the electron and hole respectively.

In moderate confinement regime, $R \approx a_B$ and $a_h < R < a_e$, where, a_h and a_e are the hole and electron Bohr radii, respectively. In II-VI semiconductors, this region is well observable in small QDs. Its characteristic feature is the well restricted motion of a photoexcited hole. Strong Confinement Regime is attained when the size of a QD can be decreased in such a way that $R << a_B$ and $R << a_h$ and a_e. The Coulomb term of electron-hole interaction is now small and can be ignored or treated as a perturbation. The electrons and holes can now be thought of as independent confinement particles. Quantum effects would be much prominent, and the dot will act more like an atom. Excitons are not formed, and the separate size quantization of an electron and hole is the dominant factor. The optical spectra consist also of a series of lines due to the transition between sub-bands[59,64–67].

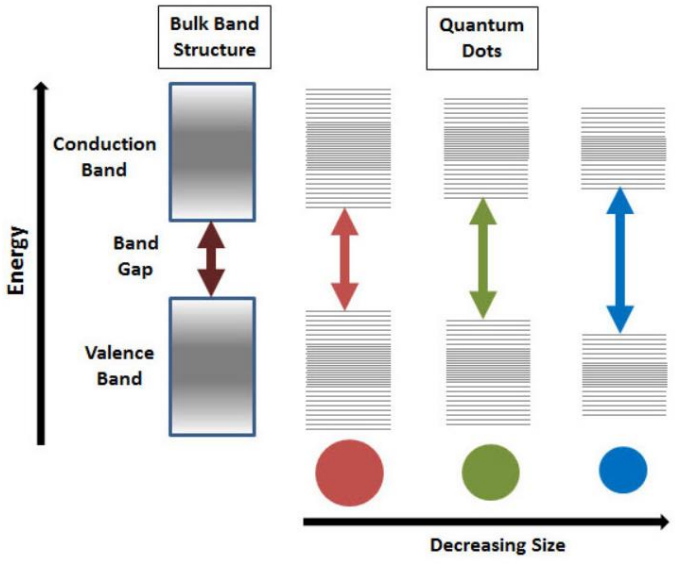

*Figure 2. Splitting of energy levels in quantum dots due to the quantum confinement effect, semiconductor band gap increases with decrease in size of the nanocrystal (*Mckitrtrick *et al, 2014).*

When several atoms are brought together, the repulsive forces experienced by their electrons cause their energy levels, which were sharply defined in an isolated atom to broaden into energy bands. Generally, two bands result, namely valance band and conduction band. In metals, the conduction and valence band overlap making them conduct at all

temperatures. Insulators have very large band gap meaning at ordinary temperature, no electron can reach the conduction band[68].

Semiconductor band gap lies midway between that of a metal and an insulator. Thermal or other excitations can promote an electron from the valence to the conduction band. The presence of small amounts of impurity material can greatly improve the conductivity of semiconductors in a process known as doping. The top of the available electron energy levels at low temperature is known as the Fermi level. The position of the Fermi level in relation to the conduction band is a crucial factor in determining electrical properties[69]. For a semiconductor that has many surface states, the Fermi level is said to be pinned at almost the midgap of the semiconductor[70]. Fermi-level pinning and its removal in semiconductor surfaces and interfaces have been a long-standing problem in semiconductor technology since it creates an energy barrier for electrons and holes by bending the bands at the interface. Fermi level pinning has the disadvantage in practical terms of limiting photovoltage in optical energy transistors[71,72]. This degrades performance radically in devices like solar cells and conversion applications.

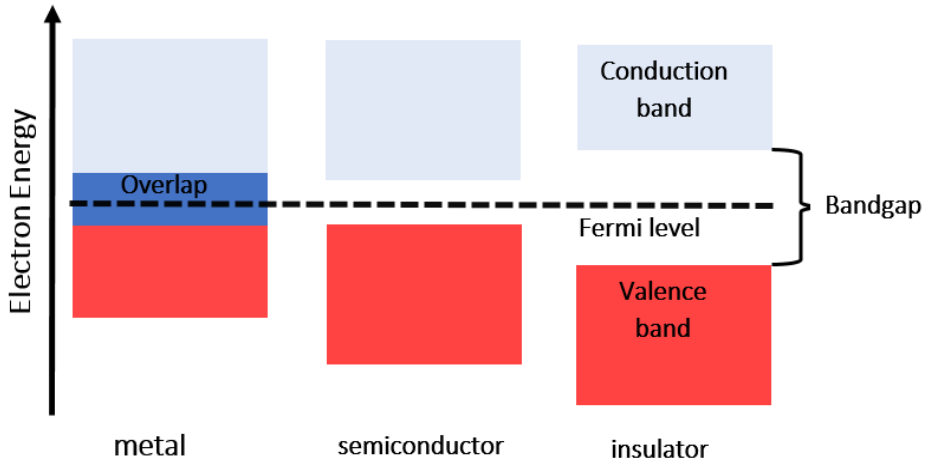

*Figure 3. Electronic band structure of metal, insulator and a semiconductor (*Schirripa *et al, 2019).*

The band gap represents the minimum energy difference between the top of the valence band and the bottom of the conduction band[73]. However, the top of the valence band and the bottom of the conduction band are not generally at the same value of the electron momentum. This difference gives rise to two types of energy band gap semiconductors: Direct and indirect band gap semiconductors. In a direct band gap semiconductor, the top of the valence band and the bottom of the conduction band occur at the same value of momentum. In an indirect band gap semiconductor, the maximum energy of the valence

band occurs at a different value of momentum to the minimum in the conduction band energy. [74].

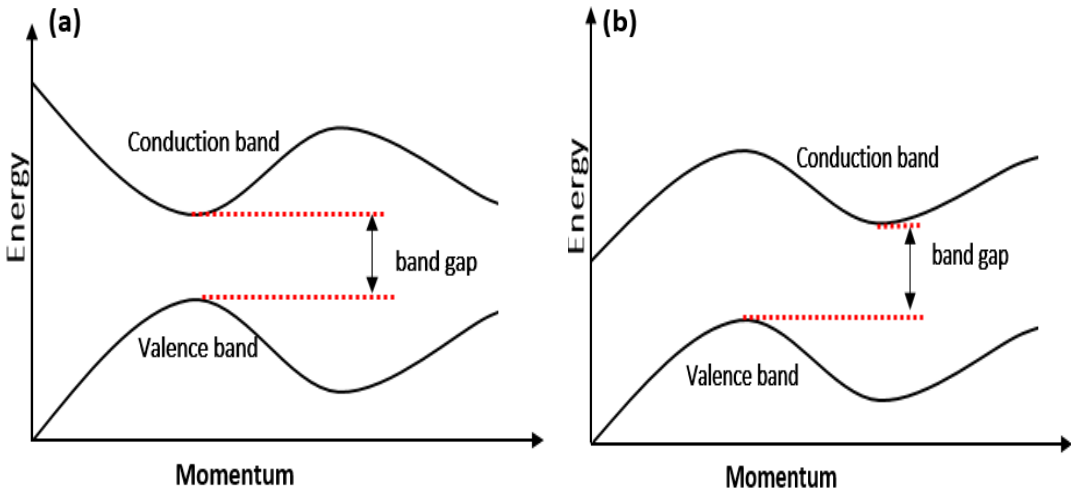

Figure 4. (a) Direct and (b) Indirect band gap semiconductors (Brus, 1984).

The difference between the two is most important in optical devices. A photon of energy *Eg*, where *Eg* is the band gap energy, can produce an electron-hole pair in a direct band gap semiconductor quite easily because the electron does not need to be given much momentum[74]. Relaxation of the excited electron back to the valence band annihilates the exciton and may be accompanied by the emission of a photon, a process known as radiative recombination. Direct band gap semiconductors are used to make optical devices such as light emitting diodes (LED) and semiconductor lasers. In an indirect band gap semiconductor, an electron must also undergo a notable change in its momentum for a photon of energy *Eg* to produce an electron-hole pair. This is possible, but it requires such an electron to interact not only with the photon to gain energy but also with a lattice vibration called a phonon to either gain or lose momentum. Transitions in indirect band semiconductors are always non-radiative and the energy is lost as heat.

1.3. Classification of nanomaterials

Nanoparticles can be classified under several categories. Some include structure, dimensionality, morphology, composition, uniformity, and agglomeration. It is also important to distinguish between nanostructured thin films or other fixed nanometer scale objects such as the circuits within computer microprocessors which are immobilized from

free nanoparticles. Immobilized or firmly attached nanostructured materials pose little health risk while the motion of free nanoparticles if released into the environment may lead to human exposure that may pose a serious health risk[5].

1.3.1. Structural classification of nanomaterials

Based on their structural configurations, nanomaterials could be classified as carbon-based, metal-based, dendrimers and composite nanomaterials. Carbon-based nanomaterials are typically spherical and ellipsoidal configured fullerenes, cylindrical carbon nanotubes (CNT) and sheets of graphene.

Metal-based nanomaterials have metals as their main components. These include nanogold, nanosilver, metal oxides, such as titanium dioxide, and closely packed semiconductors like quantum dots.

Dendrimers are nano-sized, radially symmetric molecules with a well-defined, homogeneous, and monodisperse structure consisting of tree-like arms or branches. The surface of a dendrimer possesses numerous chain which can be modified to perform specific chemical functions[75].

Nanocomposite can be described as a multiphase solid material where at least one of the phases has one, two or three dimensions in nanoscale. The most common examples of these materials are colloids, gels and copolymers[76].

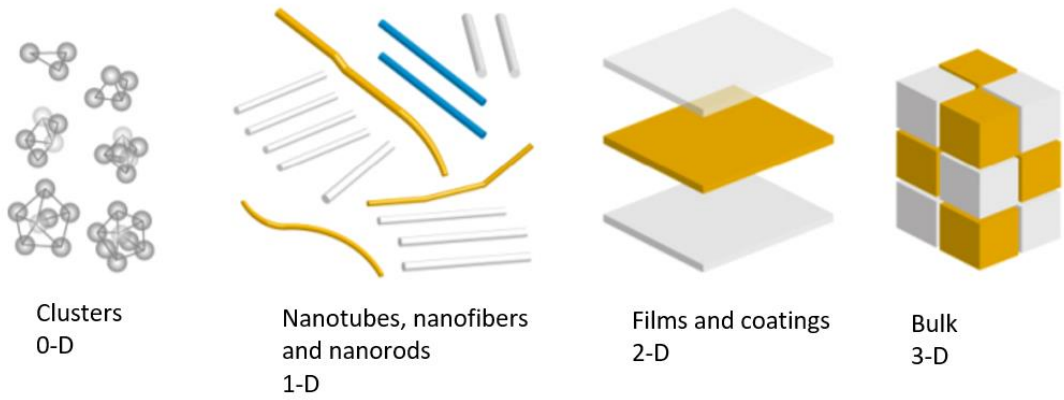

*Figure 5. Schematic of nanomaterials classified by dimensionality (*Pokropivny *et al, 2007).*

1.3.2. Dimensionality of nanomaterials

A major feature that discriminates distinct types of nanostructures is their dimensionality. Nanomaterials are entities having one or more dimensions not larger than 100 nm. They can be classified, as a function of the number of directions in which the charge carriers are confined. Based on the Pokropivny scheme, the nanostructured materials can be classified

as 0-D, 1-D, 2-D and 3-D. This dimensionality denotes the number of degrees of freedom in the particle momentum[77,78].

In *Zero-dimensional(0-D)* system, the electrons are confined in their motion in all three directions. Metallic nanoparticles including gold and silver nanoparticles and semiconductor such as quantum dots are the perfect example of this kind of nanoparticles. Most of these nanoparticles are spherical in size and the diameter of these particles will be in the 1-50 nm range. In *One-dimensional(1-D)* system (quantum wire), the electrons are free to move in one direction and confined in the other two directions. one dimension of the nanostructure will be outside the nanometer range. These include nanowires, nanorods, and nanotubes. These materials are several micrometres in length, but with a diameter of only a few nanometers. In *Two-dimensional (2-D)* system (quantum well), the electrons can easily move in two directions and are confined in one direction. These include Nanofilms, nanoplates, and nano sheets. The area of the nano films can be several square micrometres, but the thickness is always in nano scale range. In *Three-Dimensional (3-D)* system (bulk), the electrons are free to move in all three directions and there are no confinement and limitations. Example: powders, multilayer, fibrous and poly crystalline materials wherein nanostructural elements of 0-D, 1-D and 2-D are closely related to each other and form interfaces[77,78].

1.4. Properties of Semiconductor Nanomaterials

A major interest in studying semiconductor nanocrystals is to understand what happens when the semiconductor becomes small in size. This is a question that is imperative to ask, not only for the sake of understanding but also for the practical uses that emerge from this understanding. Because of the drive to miniaturize electronic and optoelectronic devices, it therefore becomes important to understand the properties of nanocrystalline semiconductors.

1.4.1. Electronic properties

The electronic wave functions of conduction electrons in semiconductors are delocalized over the entire particle. Electrons can therefore be described as ‘particles in a box’ and the densities of state (DOS) and the energies of the particles depend crucially on the size of the box which, at the onset, leads to a smooth size dependence. The HOMO– LUMO band gap of semiconductor particles and, therefore, their absorption and fluorescence wavelengths become size dependent[9]. This is what is termed “the quantum size effect”. Unlike bulk absorption spectrum which portrays a continuum in the absorption spectrum, the spectrum

of semiconductor nanocrystals exhibits a series of discrete electronic transitions between the quantized energy levels. There is a considerable blue shift in the onset of absorption in the optical spectra of nanocrystalline compounds as the size of the nanocrystal decreases, compared to that of the bulk. These size-dependent optical properties are as a result of the size quantization effect which occurs when the size to the nanoparticles is smaller than the bulk Bohr radius[79]. Based on effective mass approximation, the size dependence on the energy of the first electronic transition of the exciton or the band gap shift with respect to the typical bulk value can be approximated using equation 1 in page 6. The equation shows that the exciton energy states are shifted to higher energies by confinement and the shift in energy ΔE is proportional to $1/R^2$ (R is the radius of the particle). Consequently, the smaller the particle, the higher the energy.

At the nanoscale, the normally collective electronic properties become distorted. Reducing a bulk metal to the size of a few atoms has the effect of decreasing the DOS in the valence and conduction band leading to drastic changes in the electronic properties such as magnetism and conductivity. The quasi-continuous DOS is replaced by the quantized levels with a size-dependent spacing[80]. The increase in band gap with a decrease in diameter of nanoparticles is the most identifiable manifestation of the quantum confinement effect. The consequences of this is a blue shift in the absorption spectrum of nanomaterials compared to the bulk.

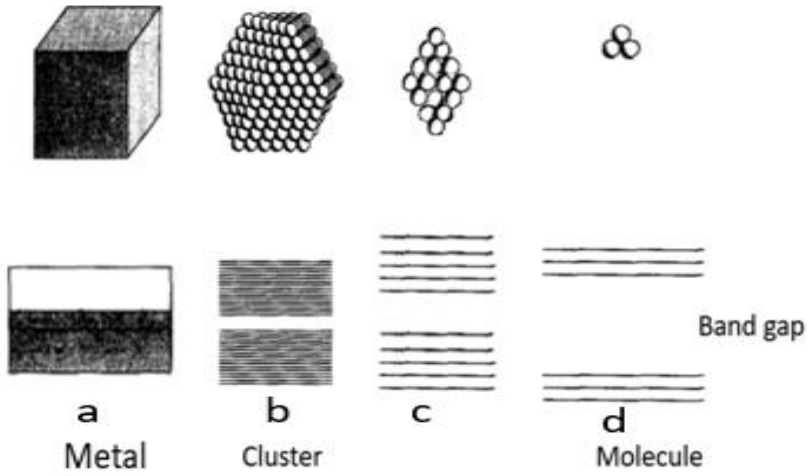

Figure 6. Illustration of the electronic states in a) a bulk metal with typical band structure, b, c) a larger close- packed cluster already with a small band gap, and d) a triatomic photoluminescence property (Bard et al, 1980).

1.4.2. Optical properties

Nanocrystals absorb electromagnetic radiation if the photon energy exceeds the band gap. Due to quantum confinement, the onset of absorption is often blue shifted and the extent of

the shift increases with a decrease in particle size. A comparatively sharp absorption feature near the absorption onset corresponds to the lowest excited state exhibiting large oscillator strength (excitonic peak). The position of this sharp absorption depends on the band-gap and, consequently, on the size of the nanoparticles, while its form and width are strongly influenced by the size distribution, as well as the type and stoichiometry of the nanocrystals. Polydisperse samples typically exhibit only a shoulder in the absorption spectrum at the position of the excitonic transition. Less pronounced absorption features in the shorter wavelength range correspond to excited states of higher energy. As a rule of thumb, it can be asserted that the larger the number of such spectral features and the more distinctly they are resolved in the absorption spectrum, the smaller is the size dispersion of the sample[81].

1.4.3. Photoluminescence properties

Photoluminescence signals of semiconductor materials result from the recombination of photo-induced charge carriers. After the excitation process, the recombination of the electron-hole pair in the solid results in the emission of photons (hν) of lower energy than that found in the absorbed photons. Optical excitation of semiconductor nanoparticles often leads to both band-edge and deep trap luminescence. The luminescence process in semiconductor nanoparticles is very complex and most nanoparticles exhibit broad and Stokes-shifted luminescence arising from the deep traps of surface states[82]. Photoluminescence is classified into two types, depending upon the nature of the ground and the excited states. In a singlet excited state, the electron in the higher energy orbital and the second electron in the lower orbital have paired spins. In a triplet state these electrons are unpaired, that is, their spins have the same orientation. Returning to the ground state from an excited singlet state does not require an electron to change its spin orientation. A change of spin orientation is needed for a triplet state to return to the singlet ground state. Fluorescence is the emission which results from the return to the lower orbital of the paired

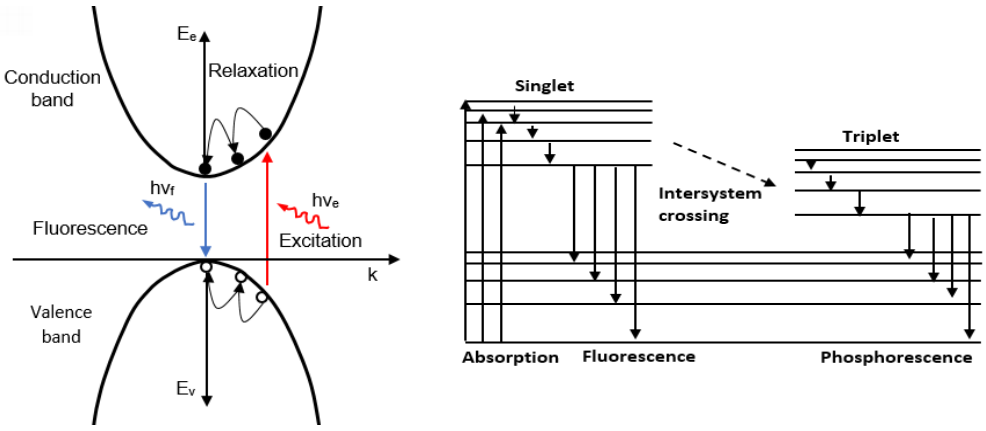

Figure 7. (a) Fluorescence in bulk semiconductor (b) Mechanism of fluorescence and phosphorescence (Brus, 1984).

electron. Such transitions are quantum mechanically "allowed" and the emissive rates are typically near 10^8 s^{-1}. These high emissive rates result in fluorescence lifetimes near 10^{-8} s or 10 ns. The lifetime is the average period a fluorophore remains in the excited state. Phosphorescence is the emission which results from the transition between states of different multiplicity, generally a triplet excited state returning to a singlet ground state. Such transitions are not allowed, and the emissive rates are slow. Typical phosphorescent lifetimes range from milliseconds to seconds[83].

The emitted photons in fluorescence have an energy corresponding to the band gap of the nanocrystals and for this reason, the emission colour can be tuned by changing the particle size. Efficient room temperature band-edge emission is only observed for nanocrystals with proper surface passivation[81]. If a semiconductor surface has defects such as vacancies for example from improper passivation, dangling bonds are created due to unsatisfied valance.

These vacancies form energy levels in the middle of the band gap called trap states which enhances non-radiative recombination of electron and hole. Loss of carriers by non-radiative recombination at surfaces and interfaces not only reduces operating efficiencies of semiconductor solar cells, lasers, and detectors but it can also reduce device lifetimes by promoting oxidation, defect formation, and the possible migration of such defects through the active region of the device. The lifetime of the injected carriers in the semiconductor is a structure-sensitive property of the material[84,85]. The many dangling bonds on the semiconductor surface can be cleaned by chemical treatment, a process known as surface passivation.

In the last few years, photoluminescence has been widely used to investigate the structure and properties of the active site on the surface of metal oxides and zeolites, because of its high sensitivity and non-destructive character. It is also an effective way to study the electronic structure, optical and photochemical properties of semiconductor materials by which information such as surface oxygen vacancies and defects, as well as the efficiency of charge carrier trapping, immigration and transfer can be obtained[86]. Photoluminescence is of strategic importance for the technological development of optical devices, such as light-emitting diodes, lasers, sensors, scintillators, medical diagnostics, displays, electronic panels, and so forth. Only clusters with good surface passivation may show high band-edge emission. The absence of band edge emission has been previously attributed to a large nonradiative decay rate of the free electrons to the deep-trapped states. As the particles become smaller, the surface/volume ratio and the surface states increase rapidly, thus, reducing the excitonic emission via nonradiative surface recombination[87,88].

1.4.4. Surface Passivation

The surface properties have significant effects on their electronic/optical properties because a substantial portion of atoms is located at or near the surface of the nanoparticles. Surface atoms usually have an unsaturated or unsatisfied valence (dangling bonds), and the heterostructural interfaces also contain strain-induced defects which potentially quench the photoluminescence (PL) and charge transport. In addition, hydroxyl quenching due to the presence of some adsorbates during the synthesis of nanoparticles degrades photovoltaic and photoluminescence efficiency[89]. Also, agglomeration of particle results during synthesis, drying, handling, or subsequent processing because of attractive van der Waals forces and the tendency of the system to minimize the total surface or interfacial energy[90]. Therefore, control of the nanocrystal surface has been a critical issue if we intend to obtain highly luminescent and enhance photovoltaic properties as well as direct growth of particles. Several methods have been used to passivate semiconductor nanomaterial surfaces.

A useful approach is to use surfactants to control the dispersion of the particles during chemical synthesis. A surfactant is a surface-active agent usually an organic molecule not necessarily completely soluble, capable of decreasing the surface or interfacial tension of the medium in which it dissolves by spreading over the surface. It has an amphipathic or lyophobic structure in that solvent and lyophilic group. Surfactants are classified as anionic, cationic, zwitterionic, or non-ionic. A surfactant is efficient if it offers maximum reduction in surface or interfacial tension. When the major component is apolar (oil), the dispersion is one in which the water (polar) phase forms droplets or reverse micelles. The polar head group of the surfactant is pointing inward toward the water phase while the hydrocarbon tail is pointing outward into the oil phase[91].

Stabilization mechanism is based on the steric repulsion between molecules or ions adsorbed on neighbouring particles. Due to geometric constraints around nanoparticles, large, bulky

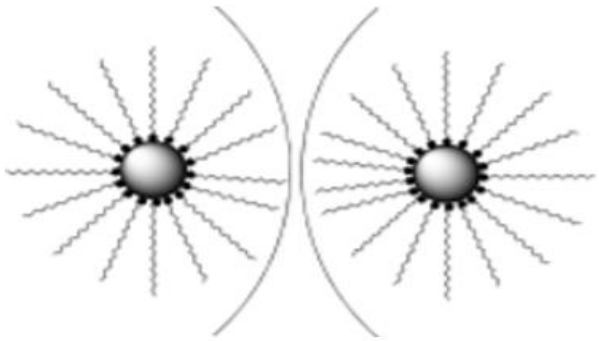

Figure 8. Stearic stabilization. Elongated or conical molecules absorb through anchoring centre hinders nanoparticles from close contact (Kitchens et al, 2003).

molecules provide a particularly effective stabilization and an elongated or conical geometry is advantageous to keep the approaching nanoparticles apart. When the length of the stabilizer is significantly longer than the characteristic size of the nanoparticles, a sphere can be formed encapsulating the nanoparticle. Another important requirement is that the stabilizer must be adsorbed strongly enough on the surface of the nanoparticles to provide long residence time and to prevent its spontaneous desorption. Metals with more valence orbitals than valence electrons have an "electron deficient" surface. Thus, molecules readily "donating" electron density (i.e. molecules with chemical groups associated with free electron lone pairs, such as divalent sulfur, trivalent phosphorus and trivalent nitrogen moieties or molecules with π-electrons,) often adsorb very strongly on metal surfaces. Strongly adsorbing, large molecules are prime candidates for stabilization of nanoparticles. The concept of steric stabilization plays a very important role in the successful synthesis of nanoparticles[92].

When the stabilizing molecules are attached to the surface of the nanocrystals as a monolayer through covalent, dative, or ionic bonds, they are referred to as capping groups. This surface capping is analogous to the binding of ligands in more traditional

coordination chemistry. Synthetic organic techniques allow the tail and head groups to be independently tailored through well-established chemical substitutions[93].

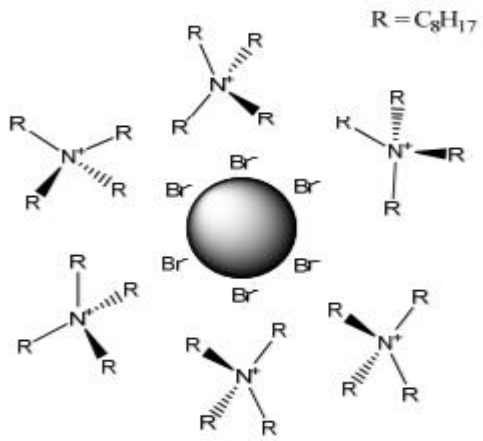

Figure 9. Schematic illustration of the electric double layer around a tetrahexylammonium bromide stabilized metal nanoparticle as an example of electrosteric (combined electrostatic and steric) stabilization (Stark and Seddon, 2007).

Another method commonly used to disperse the particles results from repulsive electrostatic force which nanoparticles experience due to interactions between the electric double layers surrounding the particles. This method known as electrostatic stabilization may be achieved by adjusting the pH of the solution or adsorbing charged surfactant molecules on the particle surfaces. This interaction leads to a thermodynamically unfavourable decrease of the entropy

of the system, thus, the particles will be prevented from approaching each other by this entropic repulsion. This electrostatic stabilization method employs bulky and highly charged adsorbent in stabilizing nanoparticles. These stabilizers known as ionic liquids consist of cations and anions only and provide huge excess of ions favouring coordination also of less strongly coordinating ions[94]. An example is the use of tetrahexyl-, tetrabutyl- and tetraoctylaminium halides in stabilizing metal nanoparticles[95].

A large step towards the preparation of robust highly luminescent nanocrystals was the passivation of their surface with an inorganic shell of a semiconductor with a wider band gap. A more efficient surface passivation can be achieved through the formation of a secondary material shell: a core/shell structure. Passivation by an inorganic shell provides both effective elimination of any surface related defect states and the confinement of charge carriers in the core material due to the band-offset potential[96]. The lattice mismatch between CdSe core and ZnS or CdS shell is small enough to allow epitaxial growth. In CdSe/ZnS and CdSe/CdS core-shell nanocrystals, the large band-gap semiconductor forms a closed outer shell and the band edges of the core material lie inside the band gap of the outer material (Figure 9). The outer inorganic shell provides high luminescence efficiency due to

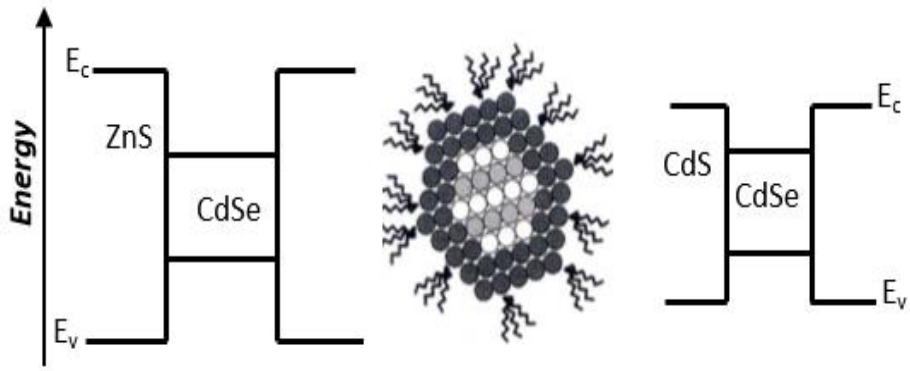

Figure 10. Schematic representation of the band structure of the core shell CdSe/ZnS and CdSe/CdS (Boles et al, 2016).

efficient passivation of the core surface states and considerably improves the chemical stability and photostability of the nanocrystal properties. Chemical stability implies negligible changes of properties like particle size, solubility, luminescence efficiency, after exposing the nanocrystals to various surroundings, e.g . to the ambient atmosphere, whereas photo-stability means stability of the nanoparticle properties under illumination[97]. The inorganic-shell growth onto the core nanocrystals may not eliminate surface dangling bonds and may also generate a nanocrystal system with different optical/electronic properties. However, proper passivation of the core material by an inorganic material of a different

bandgap can also provide both effective elimination of any surface-related defect states and the confinement of charge carriers in the core material due to the band-offset potential[89].

1.5. Methods of syntheses of nanomaterials

The development of new synthetic strategies for advanced materials with enhanced properties and affording an effective control at the nanometer level has been driven by the desire for miniaturization of machines and components using fewer resources and energy.

1.5.1. Theories

The preparation of nanoparticles can be achieved through different chemical or physical approaches, including gaseous, liquid and solid media. Physical methods employ the top-down approach, which approaches the synthesis of nanostructures by decreasing the size of the constituents of the bulk material. It employs processes such as crushing, milling or grinding. Usually, this route is not suitable for preparing uniformly shaped materials, and it is very difficult to realize very small particles even with high energy consumption. The biggest problem with the top-down approach is the imperfection of the surface structure. Such imperfection would have a significant impact on physical properties and surface chemistry of nanostructures and nanomaterials. Chemical methods which use the bottom-up approach, attempt to control the clustering of atoms/molecules at the nanoscale range. It refers to the build-up of material from the bottom: atom-by-atom, molecule-by-molecule or cluster-by-cluster. This route is more often used for preparing most of the nano-scale materials with the ability to generate a uniform size, shape and size distribution. It effectively covers chemical synthesis and precisely controlled reaction to inhibit further particle growth. Irrespective of the approach used, the aim is to obtain particles which are monodisperse in terms of size, shape, internal structure and surface chemistry. Nanoparticles are considered monodisperse when 90 % of the population lies within ± 5 % of the mean particle size.

Formation of nanocrystals takes place when the Gibbs free energy (ΔG) of the system is negative, and the solution becomes supersaturated. Monomer units break interactions with surrounding solvents molecules and assemble into a lattice. Nucleation takes place when the energy required to remove the coordinated solvent molecules is compensated by the formation of the lattice. This will lead to the formation of dangling bonds on the surface of the new particles. The free energy of nucleus formation can be expressed as in equation (2). The expression contains two competing terms: one negative, for the favourable formation of bonds in the nucleus, and one positive, for the unfavourable creation of an interface between the nucleus in its new phase and the medium of the old phase[98].

$$\Delta G = -\frac{4}{3}\pi r^3 \Delta G_v + 4\pi r^2 \gamma \quad (2)$$

Where r is the particle radius, ΔGv is the change in energy per unit volume of removing solvent molecules and assembling monomer into a lattice and Υ is the surface energy per unit area.

During nucleation, precursor monomer approaches the interfacial layer about the particles and can add to the surface, while monomer in the particle can also re-dissolve back into the solution. Whether particle formation is favourable is partly governed by the radius of the particle. If the radius of the particle is greater or equal to a critical radius r^* then the negative term of Equation (2) is dominant, ΔG is negative and the particle grows, If the radius r is below the critical radius (r^*), the γ term of Equation (2) dominates and ΔG is positive so particle formation is disfavoured and the particle re-dissolves[99].

LaMer Model for particle formation: Several models now exist for the formation of nanoparticles, however, most are based on the model proposed by LaMer in 1950, to explain the formation of colloidal sulfur [100,101]. The model is divided into three phases: In phase I, the monomer is generated, and its concentration increases until it reaches a critical supersaturation level at which point, nucleation of the particle occurs in a rapid bust. In phase II, the monomer is consumed rapidly by the burst of nucleation and its concentration

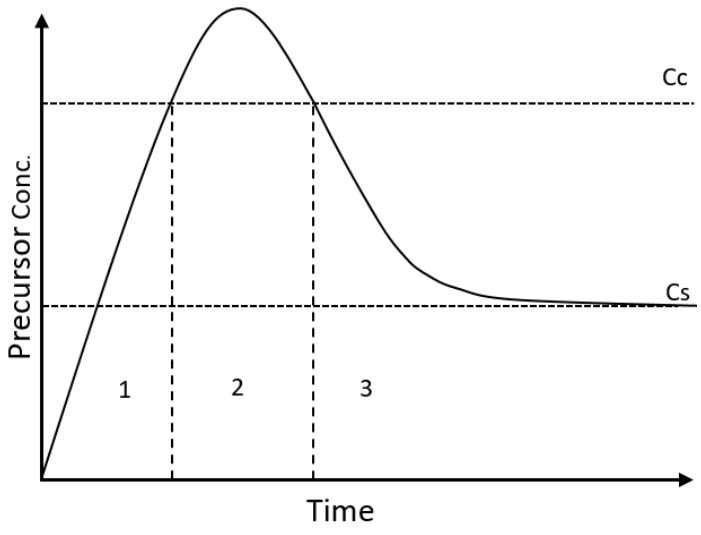

Figure 11. LaMer plot showing the three states of particle formation. Cs is supersaturation concentration and Cc is the critical concentration for nucleation (Kwon et al, 2011).

drops below the critical nucleation level. There is still monomer in the solution, however, and in phase III the particles continue to grow by diffusion of the remaining precursor monomer onto the surface of the particles.

Ostwald Ripening: After particle growth, particle ripening occurs. This has the effect of either focusing or defocusing the particle size distribution as there is an exchange of monomers between particles in solution. During this process, it is thermodynamically more favourable for small particles to lose monomer while large particles to grow at the expense of small particles. This thermodynamically-driven spontaneous process occurs because larger particles are more energetically stable than smaller particles. This stems from the fact that molecules on the surface of a particle are energetically less stable than the ones already well ordered and packed in the interior. Large particles, with their lower surface to volume ratio, results in a lower energy state. As the system tries to lower its overall energy, molecules on the surface of a small particle will tend to detach and diffuse through the solution and then attach to the surface of larger particle[102].

1.5.2. Wet chemical (colloidal) route

The first reported routes to such small particles involved the controlled precipitation of dilute colloidal solutions and the cessation of growth soon after nucleation. If seeds (nuclei) could be made to grow and concert into larger particles, monodispersed sols could be formed. If nucleation and growth are properly controlled, particles with nanometres dimensions can be reproducibly synthesized. Small crystals, which are less stable, dissolve and then re-crystallize on larger more stable crystals; a process known as Ostwald ripening. For such methods to be effective, the seeds formed also known as quantum dots must have low solubility, which can be achieved by the correct choice of solvent, pH, temperature and passivating agent. Highly monodispersed samples are obtained if the processes of nucleation and growth are distinctly separated, i.e. fast nucleation and slow growth. The colloidal stability of these crystals is improved by using solvents with low dielectric constants or by using stabilizers such as a styrene/maleic acid copolymer[40]

Although these methods can be efficient, some important semiconductors cannot easily be synthesized, e.g. CdSe, GaAs, InP and InAs[103]. There is also a problem with reproducibility and instability. Colloidal methods use low temperatures and in general, the crystallinity of the materials is poor. However, for certain materials, especially soft ones, this approach may be advantageous. Reactions in confined spaces, for example within zeolites, micelles, or biological materials, might be an interesting extension of this method[104].

1.5.2.1. Sol-Gel

The term sol-gel was first coined in the late 1800s. It generally refers to a low temperature method using inorganic precursors, that can produce ceramics and glasses with better purity and homogeneity than through high temperature conventional processes[105]. A ‘sol’ is a

dispersed system where the dispersed phase consists either of solids or discrete “globules” or oligomers in the form of chains in a dispersion medium. The medium can be water or any other liquid. A gel is a stiff mass of a continuous phase, more like a viscous liquid. The sol can be prepared by controlled hydrolysis and poly-condensation reactions of alkoxides, which then form the network of the resultant glasses[59].

The sol-gel process has two main attractive features. Firstly, it can produce compositions that cannot be created with conventional methods and secondly the mixing level of the solution is retained in the final product, often up to the molecular scale[106]. Sol-gel materials have a wide range of applications such as environmental protection, solar cells, energy storage, ceramics, sensors, magnetic devices. The sol-gel process is undoubtedly very simple, cheap, versatile with the possibility of obtaining high purity materials, whose composition is perfectly controlled[59].

1.5.2.2. Polyol method

Polyol method is a versatile liquid-phase method utilizing high boiling and multivalent alcohols to produce the nanoparticles. Polyols played a dual role as a reducing agent and solvent, also they can control the particle growth. The polyol synthetic route was first introduced in 1989 by Fievets group where they used the term polyol for metal nanoparticles synthesis[107]. Several kinds of polyols that include, ethylene glycol, propylene glycol, butylene glycol, diethylene glycol, triethylene glycol, tetraethylene glycol, and so on up to polyethylene glycol have been utilized in this process[108]. The polyols provide excellent advantages in terms of various aspects. The high boiling point of polyols can allow the synthesis in the temperature range of 473–593 K without high pressure and autoclave. The good capabilities of polyols to solubilize the starting materials allow the use of simple and cheap metal precursors as starting compounds. The chelating ability of polyol is a beneficial factor to control key features, such as nucleation, growth, and agglomeration of the particles. Another important advantage of polyols is that the reductive ability at elevated temperatures can reduce the metal solution readily to form metal nanoparticles. The selection of polyol for the preparation of NPs is highly dependent on two aspects, namely boiling point and reduction potential of the polyol[109].

1.5.2.3. Solvothermal/Hydrothermal method

Solvothermal synthesis involves a solvent that is held under pressure at a temperature above its critical point, which increases its ability to dissolve solids and thus speeds up reactions between solid species. In a typical procedure, a precursor and a reagent capable of regulating or templating the crystal growth are added into a solvent in appropriate ratios. The mixture

is then placed in an autoclave; the reaction and subsequent nanocrystal growth take place at elevated temperatures and pressures. Using this method, cadmium chalcogenide nanoparticles of various morphologies were synthesized[98]. When water is used as solvent, the process is termed hydrothermal technique. It was studied and developed a long time ago with different objectives such as mineral extraction (as for leaching ores), synthesis of geological materials, synthesis of novel materials, deposition of a thin film and the elaboration of fine particles which are well defined in size and morphology[110]. The solvothermal technique finds increasing use in nanotechnology and offers a unique means of making highly functionalized materials, for applications such as sensors, separation and catalysis, molecular devices and spintronics[59]. The hydrothermal process, due to the chemical composition of water as the solvent is appropriate for the preparation of hydroxides, oxihydroxide or oxides[111].

1.5.3. Hot Injection route

The problem associated with low-temperature colloidal synthesis can be overcome by the hot injection route. Hot-injection synthesis provides a versatile methodology for the preparation of highly luminescent colloidal nanocrystals with tunable size, shape, and surface passivation. The reason for the success of this approach lies in the use of non-ionic precursors in high-boiling organic solvents. This makes it possible to grow the nanoparticles relatively slowly at a high temperature, which yields defect-free, well-passivated nanocrystals. The second important aspect of this type of synthesis is the separation of the nucleation and growth stages by the rapid injection of a cold solution of precursors into a hot solvent followed by growth at a lower temperature[112].

This route was reported for the first time by Murray *et al* in 1993 when they synthesized monodispersed CdX (X being S, Se, or Te) nanocrystallites in molten tri-n-octylphosphine oxide (TOPO)[87]. The resultant nanoparticles were of high quality and had a spherical morphology. Further pioneering work was by Alivisatos who induced anisotropy in CdSe nanoparticles by slightly modifying the previous approach of Murray and co-workers[113]. The hot injection method consists of injecting a room temperature solution of precursor molecules into a hot solvent in the presence of surfactants[112]. The use of surfactants, generally consisting of a coordinating head group and a long alkyl chain, offers several advantages. The coating of the nanoparticles prevents agglomeration during synthesis and results in good colloidal stability of the final product in organic solvents. Dynamic adsorption and desorption of surfactant molecules at high temperature onto particle surfaces during particle growth, sometimes combined with selectivity toward specific crystal faces, enables control over particle size, size distribution, and morphology[98]. Moreover, the

surfactants can be exchanged against other ones in a post-synthetic step, allowing the chemical modification of the surface properties of the nanoparticles.

1.5.3.1. Dual precursor source

The lyothermal synthesis (hot-injection), has been widely exploited as a major route for nanoparticles synthesis. It allows for the easy manipulation of the capping ligands, ligand–solvent pair, reactant concentration and reaction temperature to control particle growth and morphology. Capping ligands preferentially bind on specific facets of the crystal through chemisorption thereby making it thermodynamically more favourable by reducing its interfacial free energy[114]. Kruszynska *et al* showed that the use of small quantity of thiols mixed with non-coordinating solvents favoured the formation of nanorods of Cu_2S by increasing the reactivity of the starting materials[115]. Thermal decomposition of multiple precursors has yielded metal sulfide nanoparticles with different morphologies such as spherical nanoparticles, nanorods, nanodiscs, and other unique shapes[116–121]. The main inconveniencies here are the toxicity of some the precursors and the possibilities of side reactions occurring[121]. This method, in general, produces high quality particles, possessing small number of defects per particle. However, the reaction conditions are harsh and often, hazardous, toxic, and in the case of metal-alkyls, pyrophoric material is used. Precursors like dimethylcadmium and dimethylzinc are volatile, toxic and pyrophoric compounds having relatively low boiling points. These precursors are injected into hot solutions (up to 350°C), which would be undesirable for commercial exploitation[104]. Also, in several cases such as for metal–sulfide semiconductors, the dual precursor approach has failed to produce highly crystalline, size-controlled nanocrystals[122].

The pioneering work on hot injection thermolysis by Murray *et al* used dual precursors of volatile metal alkyl(dimethylcadmium) and a chalcogenide source in synthesizing CdX (X is S, Se, Te) in TOPO. Dual source precursor (DSP) uses separated metallic element and nonmetallic-element precursors, such as metal carboxylates (M(OOCR)n, M = Zn, Cd, Pb, Cu, In) and phosphine chalcogenides such as EPHR2 (where E = S, Se, Te)[123]. Bendt *et al* showed that synthesis of Bi_2Te_3 from $Te(SiEt_3)_2$ and $Bi(NMe_2)_3$ yielded multiple Bi-Te phases including Bi_2Te_3 while the use of the single source precursor $(Et_2Bi)_2Te$ and $Et_2BiTeEt$ was unsuitable for the preparation of Bi_2Te_3 as tellurium poor phases were obtained upon thermolysis. This was attributed to the comparable low Te-Bi binding energy and complex decomposition mechanism of the single source precursors[124].

1.5.3.2. Single source precursors

A "one-pot" synthesis is employed for the preparation of nanocrystals using single-molecular precursors (SSP). The use of single-source precursors with preformed metal-chalcogenide bonds provides a convenient reactive intermediate for growth under lyothermal conditions, allowing for the preparation of large quantities of materials from relatively innocuous reagents[125]. The synthesis involves dispersing the precursor in an appropriate solvent e.g. TOP. The dispersed precursor is then injected into hot capping agent e.g. TOPO/TOP. The temperature of the reaction mixture is maintained for a specified period of time, after which the resulting solution is cooled followed by the addition of excess methanol or ethanol to produce a precipitate of the particles[104]. The morphology of the resulting particles depends on the reaction time, temperature, nature of capping agent and ratio of capping agent to precursor used.

There are several potential advantages of using single-molecular precursors over other existing methods[104,126]:

- Control over stoichiometry. The existence of preformed bonds can lead to the synthesis of a material with fewer defects and/or better stoichiometry[104].
- Limited pre-reactions. The main reaction is the controlled decomposition of the precursor to form the final product.
- Easy to handle.
- Reduced toxicity and potential to reduce the environmental impact of material processing. Single source precursor routes eliminate the need for volatile, sometimes toxic and/or pyrophoric precursors.
- Easy purification as there is only one precursor involved, hence there is less chance of the incorporation of impurities into the nanoparticles.
- Appreciable volatility and stability to air and moisture
- Low temperature deposition routes are possible.

This approach has been shown to be efficient in synthesizing metal chalcogenide nanocrystals with shape and size tunability by varying reaction parameters such as temperature, precursor concentration, mass of capping group and reaction time.

1.5.4. Green syntheses routes to nanomaterials

The capping agent is a key parameter when preparing nanomaterials by organometallic precursors route. The capping agent is a stabilizing agent which provides colloidal stability

and stops uncontrolled growth and agglomeration[127]. However, the inherent problem associated with the use of volatile, highly reactive and toxic compounds led to the urgent need to develope cost effective and environmentally friendly, non-toxic and safer reagent for nanoparticle synthetic process.

Green synthesis of nanomaterial respect a set of principles extracted from the twelve fundamental principles of green chemistry which were originally defined by Anastas and

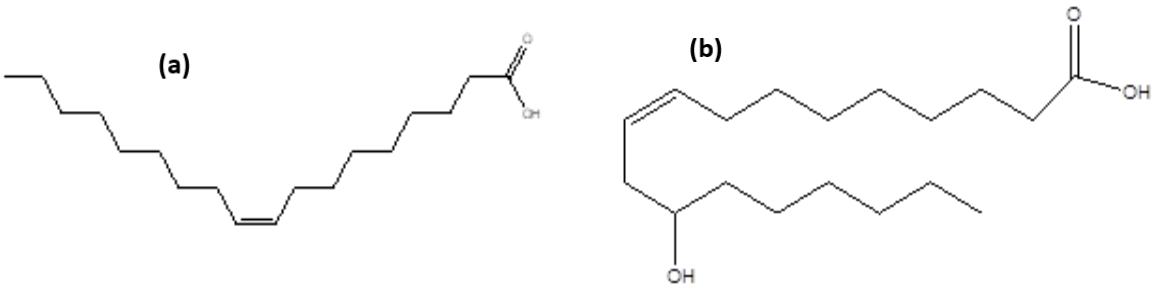

Figure 12. Structure of (a)oleic acid and (b) ricinoleic acid.

warner[128]. Green approach to synthesis can be summarized into three categories. Firstly, safety considerations requiring the use of materials and processes such as less hazardous chemicals and solvents. Secondly, the environmental concern aimed at reducing the amount of waste ejected into the environment and the use of less hazardous chemicals to minimize health and environmental pollution. Finally, process efficiency which involves both material and energy efficiency. Material efficiency looks into the atom economy and process control while energy efficiency involves the use of alternative solvents such as ionic liquids and energy sources such as sonochemical, laser ablation and microwave[129]. Plant extracts have been used for the metal ions bio-reduction to form nanoparticles. It has been demonstrated that plant metabolites like sugars, terpenoids, polyphenols, alkaloids, phenolic acids, and proteins play an important role in metal ions reduction into nanoparticles and in supporting their subsequent stability[130]. Ahmed *et al* synthesized silver nanoparticles from aqueous leaf extracts of *Azadirachta indica*[131]. Fatty acids like castor oil and olive oil contain green and low-cost biomolecules derived from plant seeds. Castor oil is non-volatile and contains about 90 % of ricinoleic acid. Olive oil is made up of about 72 % oleic acid. The double bond and associated "kink" in its alkyl chain are found to be essential features for imparting colloidal stability[132]. Fatty acids can significantly influence the assembly and morphology of inorganic structures due to complexation of their polar carboxylic groups with metal ions. Bin Xue *et al*. reported the synthesis of Bi_2S_3 nanorods with average breadths of 60-80 nm in gelatin under microwave irradiation[133]. They concluded that gelatin biomolecule played an important role in the formation of the Bi_2S_3 nanorods. Shombe *et al*. synthesized nanorods and spherical shaped CdS with size ranging from 10-22 nm in castor oil and ricinoleic acid

using heterocyclic dithiocarbamate complexes as single source precursors[134]. They suggested that the particles were bounded at the surface through the carbonyl group and OH group present in both castor oil and ricinoleic acid. Nyamen *et al*. prepared high quality Pbs and CdS nanoparticles in olive oil at low temperature by thermolysing heterocyclic dithiocarbamate complexes[135]

1.5.5. Dithiocarbamates as single source precursors

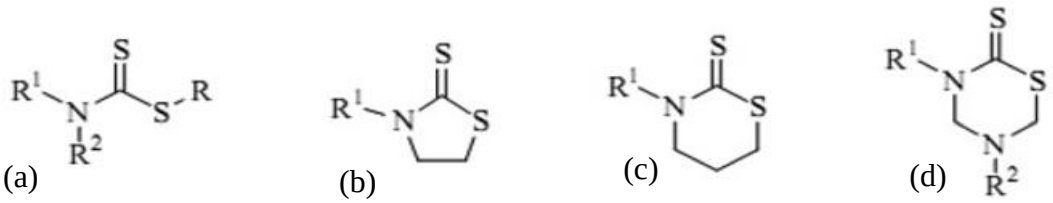

Figure 13. Structures of dithiocarbamate: (a) alkyl dialkyldithiocarbamate (b) 3-alkylthiazolidine-2-thione (c) 3-alkyl-1,3-thiazamine-2-thione and (d) 3,5-dialkyl-1,3,5-thiadiazinane-2-thione (Hassan et al, 2014).

Dithiocarbamates are organosulfur compounds bearing robust synthetic and chemical properties, with strong chelating ability and hence can easily form complexes with almost all elements. Dithiocarbamates of the general structure (a) and the cyclic derivatives (b)–(d) (Figure 15) show antibacterial, anthelmintic, fungicidal, herbicidal, growth depressant, and algicidal activity[136]. They are also effective catalysts for photopolymerization and vulcanization[136]. They have been commercialized as NO trapping agents, lubricants, vulcanizing accelerator, photovoltaic materials, in holographic recording systems and solar control devices. They are also used for the removal of heavy metals. Dithiocarbamate derivatives of tin are consi dered as promising species in the treatment of carcinoma[137].

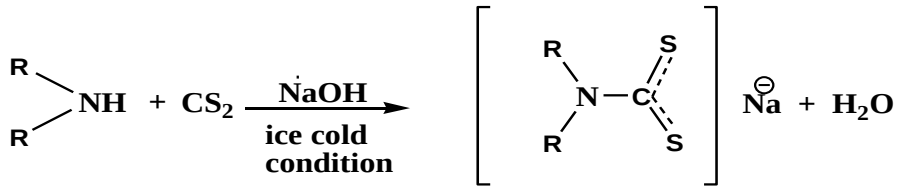

Scheme 1. Scheme for dithiocarbamates syntheses.

Dithiocarbamates are formed by the exothermic reaction between carbon disulfide and either ammonia or a primary or secondary amine in the presence of a base such as sodium hydroxide or excess of the amine. Monoalkyldithiocarbamates are formed from the exothermic reaction between carbon disulfide and a monoalkylamine. They decompose,

however, on long standing in alkali, while dialkyldithioearbamates do not experience such difficulty in their preparation. The sodium salts are extremely soluble in water and quite soluble in ethanol, but relatively insoluble in nonpolar solvents such as ether and chloroform. Most of the sodium salts are hydrated[138].

The complexes of dithiocarbamates with heavy metals are prepared by adding a solution of the metal to a solution of ammonium or alkali metal dithiocarbamate. These complexes are generally sparingly soluble in water but are more soluble in non-polar organic solvents such as chloroform, carbon tetrachloride and ether. The lead(II), zinc(II) and mercury(II) salts are colourless, but the copper(II), nickel(II), cobalt(III), iron(III) antimony(III) and bismuth(III) complexes are intensely coloured.

Dithiocarbamate complexes of formula $(R_1R_2NCS_2)_2M$ where M is a bivalent metal and $(R_1R_2NCS_2)_3M$ where M is a trivalent metal have been reported[139,140]. Crystal structure analyses of dithiocarbamates showed that the coordination environments around the central atom range from tetrahedral to distorted octahedral with the dithiocarbamate groups acting as either unidentate or bidentate[52,136].

The FT-IR spectra of dithiocarbamates show two strong absorption bands in the infrared which have received special attention. These are a band around 1500 cm^{-1}, known as the "thioureide" band (ν(C=N)) and a band in the region 1030-950 cm^{-1} attributed to ν(C=S)[141].

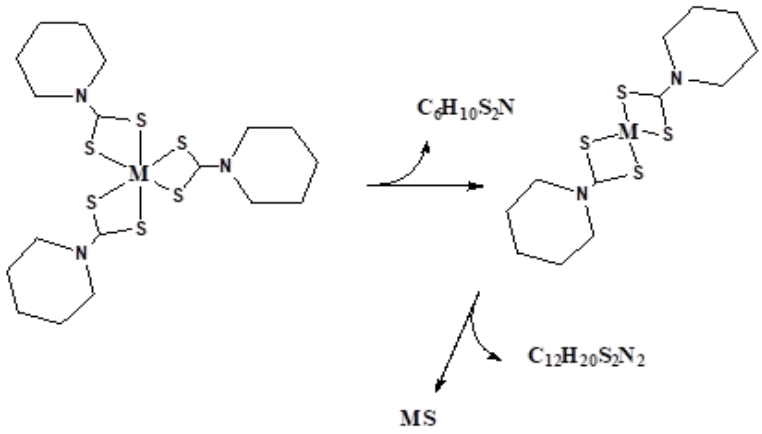

Scheme 2. Proposed thermal decomposition mechanism of Tris-(piperidinedithiocarbamato)M(III) complex (M= Fe)(Mlowe et al., 2016).

Despite exhaustive work on the use of dithiocarbamate complexes as precursors for nanomaterials, heterocyclic dithiocarbamate complexes were only recently investigated for their use as precursor for nanoparticles synthesis[53,57].

Mlowe *et al*[142] investigated the decomposition mechanism of Tris-(piperidinedithiocarbamato)iron (III) and tris-(tetrahydroquinolinedithiocarbamato)iron (III) using thermogravimetric analysis (TGA), gas chromatography/mass spectroscopy

(GC/MS) and powder X-ray diffraction (p-XRD). Thermal studies show that the decomposition proceeded through detachment of one of the three dithiocarbamate ligands in the six-coordinated complex, and lastly the final decomposition/elimination of four coordinated dithiocarbamato complex with the formation of a final M-S residue.

1.5.6. Solvent free syntheses of nanomaterials

Solvent-free synthesis, requiring only heating a precursor is one of the easiest methods to synthesize nanomaterials[22,23]. The synthesis of small, monodisperse nanoparticles is highly dependent on the type of solvent used and the concentrations of the precursors[143–145]. Therefore, in order to obtain high yields of nanoparticles, large quantities of solvent are needed. This large use of solvent translates into a more expensive and slower process. Moreover, by-products are frequently not eliminated [146], and their presence may result in inconsistencies and poor device performance when nanoparticles are used especially in devices in which purity is of prime importance.

Solvent-free synthesis of nanoparticles can be achieved through mechano-chemical process and thermal treatment. The mechanical approach uses pressure and grinding, most commonly ball milling and mortar and pestle[147,148]. Thermal treatment involves decomposition/ thermolysis[149] by conventional and microwave (MW) heating[150]. It is important to emphasise that the use of solvent-free synthetic method is advantageous, as large amount of samples are achieved in fewer steps and with the employment of fewer reactants (only the precursor required) [45,]. Likewise, the developed solvent-free method allowed a purification step to be implemented. This aspect could be very important in further catalytic applications, as it was shown that byproducts are a significant source of discrepancies[145,146].

1.5.7. Syntheses of V-VI anisotropic semiconductor nanomaterials

Semiconductor materials of type V–VI have recently attracted attention due to their earth abundance and environmentally friendly nature and their photoconductive, photosensitive, thermoelectric and fluorescence properties[151–154]. Among these materials, bismuth sulfide (Bi_2S_3), owing to its high figure of merit (ZT value) with a large absorption coefficient and high energy conversion efficiency, is widely used as a thermoelectric-cooling material. It has a direct energy bandgap between 1.3 and 1.7 eV and finds applications in photovoltaic converters[155] and photodiode arrays[156]. Many approaches have been proposed for fabricating one-dimensional Bi_2S_3 nanomaterials, including microwave irradiation, polyol method, solvo(hydro)thermal route[16–18] and single source precursor route [19,24–28]. Antimony sulfide, Sb_2S_3 is an important V-VI binary chalcogenide with a layered structure and an energy band

gap between 1.78 and 2.50 eV, which covers the visible and near infrared region of the electromagnetic spectrum properties[22,167,168]. It has attracted recent interest owing to its good photovoltaic properties, high photosensitivity and high thermoelectric power, with applications in solar energy conversion, write once and read many (WORM) optical storage devices, optoelectronic devices like IR region television cameras, infrared spectroscopy and in lithium/sodium ion batteries [159–165]. Crystalline antimony sulfide appears as a dark-grey solid with a metallic appearance or a greyish-black crystal with acicular morphology. Zhang *et al* prepared different morphologies of Sb_2S_3 by mixing $SbCl_3$ and thiourea in polyols with and without polyvinyl pyrrolidone as surfactant at 120, 160 and 180 °C, and obtained aggregates of seeds, uniform rods and microtubes, bow-tie-like nanofibers, flowerlike nanorods and straw-bundle-like nanorods at the different reaction parameters[166]. Park *et al* [167] synthesized nanowires, nanoribons, nanotubes nanobundles by separately dispersing $SbCl_3$ and elemental sulfur in oleylamine at room temperature, and slowly increased the temperature to 150, 175 and 200 °C over 90 min. The morphology of the particles was tailored by changing the concentration of sulfur. Biswal *et al* [168] synthesized antimony sulfide nanorods by solvothermal decomposition of single source dithiolatoantimony(III) precursors in ethylene glycol. In a related experiment, they isolated agglomerates of spherical Sb_2S_3 nanoparticles with average diameters of 27 nm from the pyrolysis of single source antimony thiosemicarbazone precursors in a furnace at 350 °C, and rod-like morphology having width of 135 nm and length of few microns from solvothermal treatment in ethylene glycol[27]. Lou *et al* prepared Sb_2S_3 nanorods 45 nm x 1 um in size by heating a mixture of antimony di-n-octyl-dithiophosphates ($Sb[S_2P(OC_8H_{17})_2]_3$) and oleyamine at 160 °C[169].

Anisotropic semiconductor nanomaterials possess unique and fine-tunable physical and chemical properties which make them ideal candidates for contriving new applications. Anisotropic one-dimensional Bi_2S_3 and Sb_2S_3 nanostructures especially are considered to be the best candidates for these applications due to quantum confinement effects[24].

Under thermal conditions, the morphology, size and phase of nanocrystals are influenced by many parameters, including the capping agent, the monomer concentration, the reaction temperature and the precursor used. Such basic properties and applications highly depend on the composition of the material, which motivates many researchers to modulate and optimize material performance by means of tuning chemical compositions [170–180].

1.5.8. Syntheses of ternary nanomaterials

A solid solution series is a compositional range between end-member minerals that share the same basic chemical formula but experience substitution of elements in one or more atomic sites. This substitution occurs when an element in a mineral formula can be replaced by another of similar size and charge. The formation of semiconductor solid solutions (semiconductor alloys) is essential in the engineering of many heterojunction devices such as transistors and diodes as heterojunction performance is low with pure semiconductors[181]. They are designed to effectively tune optical and electronic properties of materials by judicious control of the energy band gap which is essential for communication devices like optical fibres which require very specific wavelengths for minimum absorption coefficient in the fibre[181]. Chemical composition, size, shape, and surface engineering play key roles in the performance of electronic, optoelectronic, and energy devices[170]. Incorporating a foreign atom or ion into a host crystal lattice of semiconductor materials can introduce into the material, new functional properties such as inducing new emission, generating surface-enhanced plasmon resonance, creating magnetism, widening the absorption window,

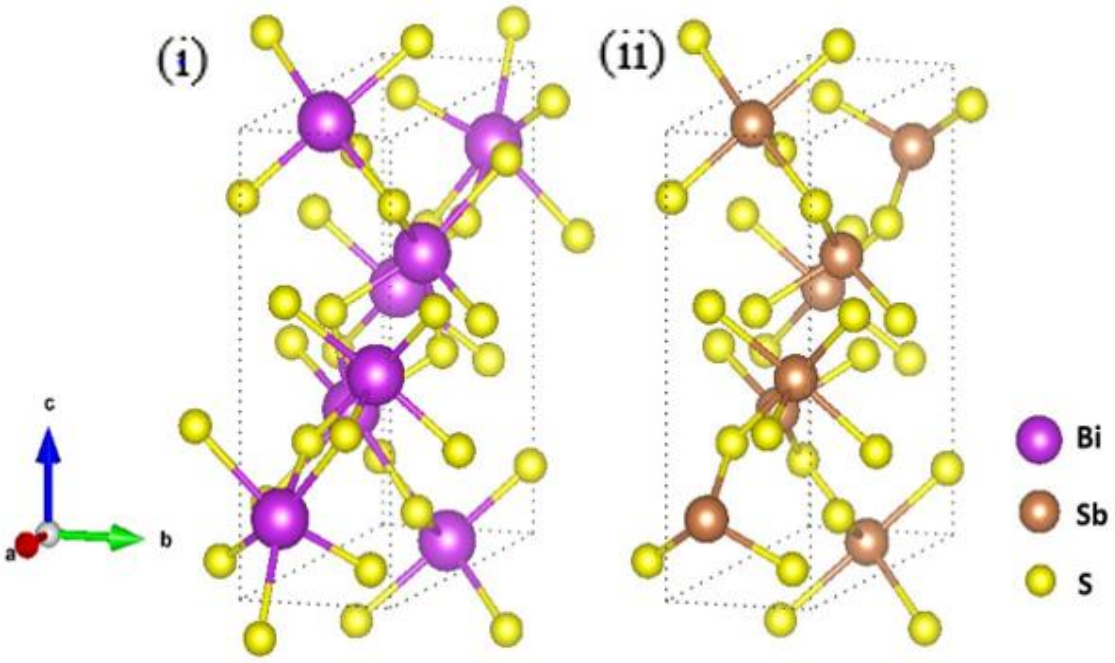

Figure 14. Crystal structure with the orthorhombic unit cell marked of (i) Bi_2S_3 (a = 11.269 Å, b = 3.971 Å, c = 11.129 Å with α= β= γ= 90°) and (ii) Sb_2S_3 (a = 11.299 Å, b = 3.831 Å, c = 11.227 Å with α= β= γ= 90°).

enhancing the carrier density and increasing the device efficiency[179,182,183].

As a contrast to the formation of solid solutions in other materials which is aimed at a controlled production of a second phases or microstructures, semiconductor alloys must be

single phase to be useful. semiconductor alloying is limited to materials which form single phase with nearly perfect mixing[181].

Ternary solid solutions are mixtures of two compound semiconductors where only one component element is changed, keeping the remaining elements in common[181]. A typical example is GaAs-AlAs, where both constituent compounds are arsenides.

Despite the significant difference in their sizes, Bi and Sb form full range solid solution series between stibnite and bismuthinite[184,185]. The Formation of solid solution between the two compounds is facilitated by the fact that they both have the same charge, crystalize in the same orthorhombic lattice with space group *P*nma having typical lattice parameters of a= 11.2690 Å, b = 3.9717 Å and c = 11.1290 Å for bismuthinite and a= 11.299 0Å, b = 3.8313 Å and c = 11.2270 Å for stibnite[186,187](Figure 16) . Their orthorhombic unit cell volume differs by 3.5 %[188–191].

Kyono *et al* synthesized a full range $(BiSb)_2S_3$ solid solution series with a nearly statistical substitution of Sb for bismuth by heating Bi_2S_3 and Sb_2S_3 at 800 to 1000 °C[189]. However, their method provided no control over stoichiometry as four samples with the same composition range were obtained from a starting mixture with the same Bi_2S_3: Sb_2S_3 molar ratio. This observation of the large deviations from linear trends on the lattice constants was in contradiction to earlier work by Nayak *et al* that showed a good agreement with Vegard's law on the entire solid solution range by depositing thin films of the solid solution by a dip-dry method[155]. Colloidal synthesis of nanostructures in surface passivating agents has proven to be an efficient route as it provides easy control over size and shape[32,47]. Wang *et al* used a dual precursor source route to synthesize a full range solid solution of $(Bi_{1-x}Sb_x)_2S_3$ with aspect ratios that depended on their compositions[170]. Patra *et al* did similar work using single source precursor diethyldithiocarbamate complexes in oleylamine and thiol[179]. However, no work has been reported on the influence of the Sb substitution on the lattice constant even though it is a basic parameter to consider when characterizing every crystal system[192].

1.6. Deposition of thin films

Thin film can be defined as a thin layer of material, whose thickness varies from several nanometers to few micrometres. Like all materials, the structure of thin films is divided into amorphous and polycrystalline depending on the preparation method and the substrate on which the films are deposited [193].

The demand for the development of smaller devices with higher speed especially in new generation of integrated circuits requires advanced materials and new processing techniques

suitable for future Giga scale integration technology. In this regard, physics and technology of thin films can play a key role to achieve this goal. Thin films as a two-dimensional system are of great importance to many real-world problems. Their material costs are very small as compared to the corresponding bulk material and they perform the same function when it comes to surface processes. The usefulness of the optical properties of metal films and scientific curiosity about the behaviour of two-dimensional solids has been responsible for the immense interest in the study, science and technology of the thin films[194]. Thin film studies have directly or indirectly advanced many new areas of research in solid state physics and chemistry which are based on phenomena uniquely characteristic of the thickness, geometry and structure of the film[195]. Thin film materials have already been used in semiconductor devices, wireless communications, telecommunications, integrated circuits, rectifiers, transistors, solar cells, light-emitting diodes, photoconductors, light crystal displays, magneto-optic memories, audio and video systems, compact discs, electro-optic coatings, memories, multilayer capacitors, flat-panel displays, smart windows, computer chips, magneto-optic discs, lithography, microelectromechanical systems (MEMS), and multifunctional emerging coatings, as well as other emerging cutting technologies[196]. Thin film technology has been developed primarily for the need of the integrated circuit industry[197]. The crucial issue for all applications of thin films depends on their morphology and their stability. The morphology of the thin films strongly depends on the deposition techniques[193]. A variety of methods have been employed to deposit these films including chemical vapour deposition (CVD), atomic layer deposition (ALD), spin coating and sol–gel methods. The most common method to thin films is CVD, which can be used to deposit on small scale coatings, such as microelectronics and larger areas such as glass/steel coatings. Due to a large number of variables and diverse types of CVD, the properties of the thin films can be fine-tuned, by controlling the uniformity and compositional control.

1.6.1. Chemical vapour deposition

Chemical vapour deposition (CVD) is a process where one or more volatile precursors are transported via the vapour phase to the reaction chamber, where they decompose on a heated substrate, resulting in the deposition of a thin film on the surface of the substrate. The decomposition of the precursor is accompanied by the production of gaseous chemical by-products that are exhausted out of the chamber along with unreacted precursor gases. As would be expected with the large variety of materials deposited and the wide range of applications, there are many types of CVD techniques which include Metal organic chemical vapour deposition (MOCVD), Low pressure chemical vapour deposition (LPCVD) plasma enhanced chemical vapour deposition (PECVD). Limitations to CVD process rest on the

fact that Conventional CVD techniques require the use of specialized equipment which is often very expensive, and the precursor requirements are always difficult to meet. Conventional CVD processes require liquid precursors that must be volatile, having good thermal stability in the delivery system, decompose cleanly and controllably on the substrate without incorporation, nontoxic and non-pyrophoric and the formation of stable by-product which is readily removed from the reaction zone [126,127].

Aerosol-assisted chemical vapour deposition (AACVD) offers improved versatility and flexibility as compared to conventional CVD processes. AACVD involves solution-based precursor delivery using solvents from which an aerosol can be generated [26,199,200]. The aerosol is generated from the precursor solution using an ultrasonic humidifier to cause the formation of a 'mist'. The aerosol is then transported to the reaction chamber where the solvent evaporates, and actual deposition process can occur either by a reaction in the gas

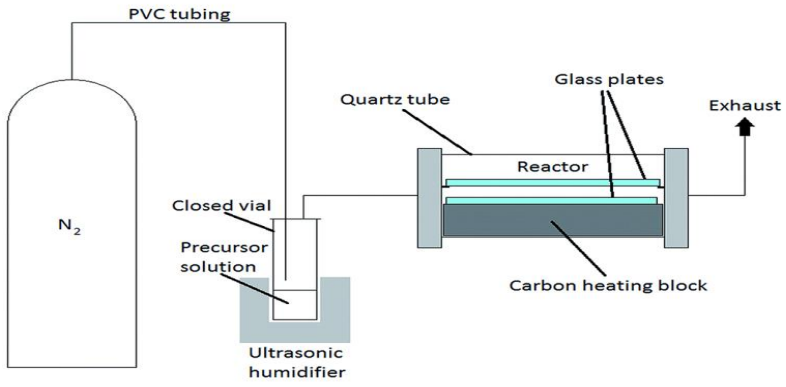

Figure 15. Schematic set-up of AACVD apparatus (Dixon et al, 2016).

phase near the heated substrate or on the surface of the substrate itself, allowing weak physisorption of precursors onto the surface and the formation of films. The method often involves the use of environmentally friendly and less expensive chemicals as precursors, which is important for mass production[161,201].

High quality thin films can be obtained as the homogeneity of the aerosol is easily controlled by the size of the aerosol droplets. The morphology of the films can be controlled by varying experimental parameters such as solution concentration, solvent, deposition time, carrier gas flow rate, and substrate temperature[26,202]. The process is easy, allowing the formation of a multicomponent material using a single source precursor with high reproducibility, while the simplification of the delivery stage reduces the cost of the deposition process. Being a solution based technique, AACVD offers several ways through which film growth can be controlled which are unavailable with alternative techniques[203].

1.6.2. Spin coating technique

Spin coating is a straightforward process for rapidly depositing thin films onto relatively flat substrates. The substrate to be covered is held by some rotating fixture often using a vacuum to clamp the substrate in place and the coating solution is dispensed onto the surface. The action of spinning causes the solution to spread out and leave behind a very uniform coating of the chosen material on the surface of the substrate[204]. Final film thickness and other properties will depend on the nature of the resin (viscosity, drying rate, solid content, surface tension) and the parameters chosen for the spinning process. After spinning, the substrate is slowed down at a given rate to a stationary state and cured either by UV, electron-beam, or thermal treatment[205]. The parameters that control the coating process include; dispense amount and location, spin speed during dispensing, acceleration rate, spin speed, spin time, slowed down speed, and multiple or complex spin profiles[205].

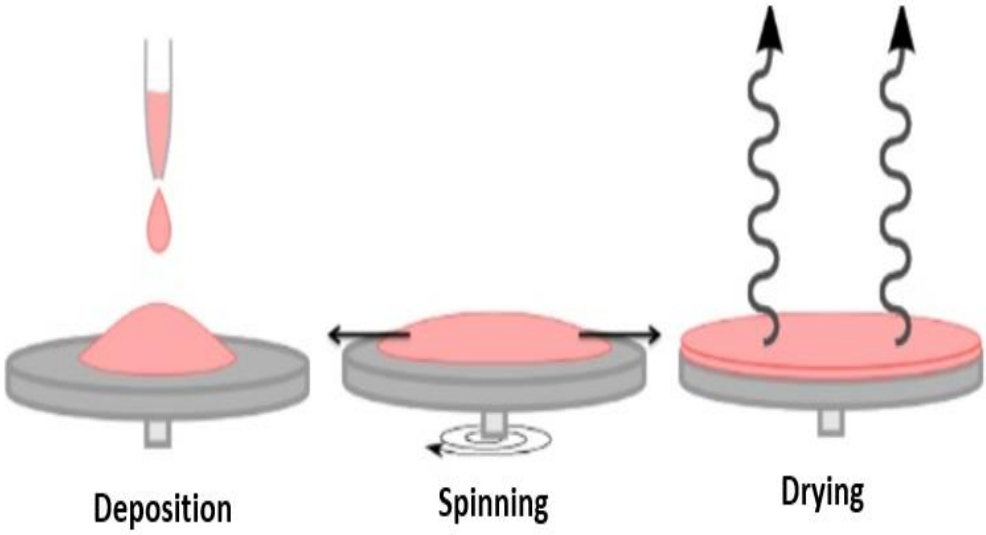

Figure 16. Schematic representation of the spin coating process (Taylor, 2001).

1.7. H2/O2 evolution and supercapacitance

Hydrogen is one of the promising green energy carriers due to its renewable nature[206]. Consequently, electrocatalytic production of hydrogen through water splitting has gained attention as a clean, sustainable and environmentally friendly source of energy[207]. However, very corrosive conditions (strong acids) are used in hydrogen evolution reactions (HER) which increases the cost and safety concerns of the overall precess[206], presenting a challenge in carrying HER in the presence of appropriate reaction medium and catalyst to achieve the future energy demands[208]. Recent studies have suggested HER in alkaline medium could be a promising and attractive alternative[209]. Platinum is one of the ideal choices in HER due to

its lowest overpotential and highest exchange current density. However, its choice is limited by its elevated cost[210]. This has led to the need for a search of alternative non-platinum group metal catalyst materials such as single atoms, metal sulfide like MoS2, WS2, Fe-Ni Sulfide, cobalt sulfide, metal selenides etc[211,212].

Electrochemical supercacitor is a type of energy sotrage device with promising properties such as low cost, high energy density, high power density and long cycle life[213]. Electochemical capacitors are considdred as favourable candidates for energy storage due to functional ability to link the perfomance gap between batteries and dieelectric capacitors with better power and energy density[214]. Naostructored electrodes are best choice with satisfactory requirements if we intend to comercialing surpercapasitor technology for large scale application. On going research involves preparing novel materials and hybrid structures to lift the specific capacitence desnsiy, power and long term stability of active materials[215].

Recently an amtimony based composit has exhivited excellent capacity, which could inspire a lot of research on energy storage devices. Antimony chalcogenide is a well-known, commonly used, and promising electrode material for batteries owing to its high theoretical capacity and suitable working voltage[213]. Antimony has immense alloying/dealloying potential and remarkable high capacity (660 mA.h.g-1). However, metallic Sb in a sodium-ion battery or lithium-ion battery demonstrase a large volume expansion during sodiation/desodiation or lithiation/delithiation in each battery system, which results in a deterioration in the long-term cycle performance of the device[216].

In semiconductor materials, the stoichiometric variation can significantly affect the characteristics of materials and their electrochemical properties.

1.8. Applications of nanomaterials

Nanomaterials possess unique beneficial chemical, physical, and mechanical properties. consequently, they can be used for a wide variety of applications.

1.8.1. Microelectronics

Microelectronics is the technology that deals with the miniaturization of electronic circuits and components. The prime objective of microelectronics fabrication is to reduce electronic circuit elements to the nanoscale. During the last four decades, the smallest feature of a transistor shrunk from 10 μm down to 30 nm[217]. A significant size reduction will make the microprocessors, which contain these components to run much faster, thereby enabling

computations at far greater speeds. Nanomaterials provide the manufacturers with nanocrystalline starting materials of ultra-high purity with better thermal conductivity, and long-lasting, durable interconnections[218]. The recent development of carbon nanotubes (CNTs) provides an exciting alternative to conventional doped semiconductor crystals due to their varied electronic properties, ranging from metallic, to semiconducting, to superconducting[217].

1.8.2. Displays

The use of nanocrystalline materials significantly reduce cost, and greatly enhance resolution of television monitors since resolution improves with reduction in pixel size. Also, flat-panel displays constructed with nanomaterials are of much higher brightness and contrast than conventional displays owing to the enhanced electrical and optical properties of the new materials. CNTs are being investigated for low voltage field-emission displays. The combination of mechanical and electrical properties makes them potentially very attractive for long-life emitters[219].

1.8.3. Renewable energy and high energy density batteries

The development of nanotechnology has the potential to revolutionize the approach to energy production. Some of the promising new areas are the use of nanomaterials to extract hydrogen from water, to harvest energy from the sun and biomass, and to store energy as hydrogen fuel cells, batteries and capacitors[220].

New nanomaterials show promising properties as anode and cathode materials in lithium-ion batteries, having higher capacity and better life span than their larger-particle equivalents[221,222]. Among them are aerogel intercalation electrode materials, nanocrystalline alloys, nanosized composite materials, carbon nanotubes, and nanosized transition metal oxides [222].

1.8.4. Imaging

Imaging is the process of creating visual representations of objects. Due to their very small diameter, high aspect ratio and stiffness, single wall carbon nanotubes (SWCNTs) have been used as probe tips for atomic-force microscopy imaging of antibodies, DNA, offering maximum resolution. SWCNTs with attached biomolecules are attached to AFM tips, and used for “molecular-recognition” to study chemical forces between molecules[223].

1.8.5. Drug delivery

Nanoparticles can target and penetrate specific organs and cells. This ability is exploited in nanomedicine by using nanoparticles to deliver drugs to specific organs of the body. Drugs can be incorporated into nanospheres composed of biodegradable polymers and administered to the body where they are carried by the body fluids. When they reach infected areas where there is a difference in the pH of the microenvironment, the polymer degrades, for example around an acid microenvironment, such as tumour cells or around inflammation sites allowing the timely release of the drug as the polymer degrades. This allows site-specific or targeted drug delivery[224].

1.8.6. Medical imaging

A variety of techniques currently called "non-invasive" have been used for more than a quarter of a century in medical imaging, for example, superparamagnetic magnetite particles coated with dextran are used as image-enhancement agents in magnetic resonance imaging. Intracellular imaging is also possible through attachment of quantum dots to selected molecules, which allows intracellular processes to be observed directly[225].

1.8.7. Elimination of pollutants

The chemical activities of nanoparticles increase with the increase in their surface area. Nanosized materials can be used as catalysts due to their enhanced chemical activity. They react with toxic gases (such as carbon monoxide and nitrogen oxide) in automobile catalytic converters and power generation equipment. This prevents gaseous environmental pollution arising from burning gasoline and coal[226]. Paints containing 30 nm spherical nanoparticles of titanium oxide and calcium carbonate mixed in a silicon-based polymer, polysiloxane, absorb nitrogen oxide gases from vehicle exhausts. The porous polysiloxane lets the nitrogen oxide gases diffuse and adheres to the titanium dioxide particles. UV radiation from sunlight converts the nitrogen oxide to nitric acid, which is then neutralized by the calcium carbonate. The paint is said to last up to 5 years[227].

1.8.8. Cosmetics

Nanogold and nanosilver particles have antibacterial and antifungal characteristics. Silver particles of size less than 10 nm dispersed in soaps impart the double advantage of killing germs and increasing effectiveness in removing dirt particles from the skin. Nanosized Titanium dioxide and zinc oxide absorb and reflect UV light, as such are being currently used in sunscreens. They are transparent to visible light and so are more appealing to the consumer[220].

1.8.9. Coatings

Nanomaterials have been used in very thin coatings for decades, if not centuries. Today thin coatings are used in a vast range of applications, including architectural glass, microelectronics, anticounterfeit devices, optoelectronic devices, and catalytically active surfaces. Structured coatings with nanometer-scale features in more than one dimension promise to be an important foundational technology for the future.

Certain nanopowders, possess antimicrobial properties. When these powders contact cells of *Escherichia coli*, or other bacteria species and viruses, over 90 % are killed within a few minutes. Due to their antimicrobial effect, nanoparticle of silver and titanium dioxide (<100nm) are assessed as coatings for surgical masks [228].

Nanoparticles have already been used in coating textiles such as nylon, to provide antimicrobial characteristics, Also the control of porosity at the nanoscale and surface roughness in a variety of polymers and inorganic materials led to ultrahydrophobic - waterproof and stain resistant fabrics[226].

Self-cleaning windows are coated in highly hydrophobic titanium dioxide nanoparticles. The titanium dioxide nanoparticles speed up the breakdown of dirt and bacteria in the presence of water and sunlight, that can then be washed off the glass more easily[5].

1.8.10. Mechanical engineering

Cutting tools made of nanocrystalline materials (such as tungsten carbide, WC) are much harder than their conventional counterparts, since the microhardness of nanosized composites is increased compared to that of microsized composites[229].

1.9. Toxicity of nanomaterials

Human skin, lungs, and the gastrointestinal tract are in constant contact with the environment. While the skin is generally an effective barrier to foreign substances, the lungs and gastrointestinal tract are more vulnerable. These three ways are the most likely points of entry for natural or anthropogenic nanoparticles. Due to their small size and chemical composition (including surface charge), nanoparticles can translocate from these entry portals into the circulatory and lymphatic systems, and ultimately to body tissues and cross the various biological barriers including the blood brain barrier and the placenta, and may reach the most sensitive organs, where they can produce irreversible damage to cells by oxidative stress and/or organelle injury[219].

Although there are very few studies examining the mechanism of nanomaterials cytotoxic effects, we can somewhat predict these mechanisms from experiences with non-

manufactured (ultrafine) particles such as the minerals quartz and asbestos, and the particles associated with atmospheric pollution. The understanding derived from studies on atmospheric pollution, mineral dust and pharmaceuticals and some data on manufactured nanomaterials has led to the general conclusion that the principal determinants of nanomaterials toxicity include[230]:

- Chemical composition (including any surface components such as transition metals and coatings and particularly its ability to take part in reactions that release free radicals,
- Particle size,
- Surface area and reactivity,
- Surface treatments on particles, particularly for engineered nanoparticulates,
- The degree to which engineered nanoparticles aggregate/agglomerate,
- Particle shape and/or electrostatic attraction potential.

NPs are more toxic to human health in comparison to large-sized particles of the same chemical substance, and it is usually suggested that toxicities are inversely proportional to the size of the NPs. For example, Titanium oxide is chemically an inert compound, but studies have shown that NPs of titanium dioxide possess some toxic health effects in experimental animals, including DNA damage as well as genotoxicity and lung inflammation[231]. Titanium dioxide NPs (<100 nm) induces oxidative stress and form DNA adducts. All the health effects of nanoparticles used in consumer products are not yet known, though nanotoxicology has revealed adverse health effects of materials previously considered safe. For example, silver, widely used as an antibacterial agent, proves to be toxic to humans or animal cells when in nanoparticle form, its cytotoxicity being higher than that of asbestos[232]. Scientists have suggested that NPs of size less than 10 nm act like gas and can enter human tissues easily and may disrupt the cell normal biochemical environment. Studies on animals and human have shown that after inhalation and through oral exposure, NPs are distributed to the liver, heart, spleen, and brain in addition to the lungs and gastrointestinal tract. The estimated half-life of NPs in human lungs is about 700 days posing a consistent threat to the respiratory system. During metabolism, some of the NPs are congregated in the liver tissues. Due to their characteristic physicochemical properties in different biological systems, unpredictable health outcomes of NPs were eminent to scientists.

Nanostructured materials firmly attached to a substrate do not pose a health risk as long as they do not detach from the substrate. However, materials in which the nanostructures are free can become airborne, consequently posing a potential health risk[233]. Surface coating is

an important parameter that can modify particle toxicity. Derfus *et al* showed that cadmium selenide (CdSe) quantum dots are cytotoxic to primary hepatocytes under certain conditions. However, when appropriately coated, CdSe-core quantum dots were rendered nontoxic and used to track cell migration and reorganization *in vitro*[230].

It is also very important to recognize that not all nanoparticles are toxic; toxicity depends on the chemical composition, shape, in addition to size. In fact, many types of nanoparticles seem to be nontoxic, others can be rendered nontoxic, while others appear to have beneficial health effects.

CHAPTER 2. EXPERIMENTAL: MATERIALS AND METHODS

The different synthetic procedures and characterization techniques are described in this chapter.

2.1. Reagents

Hexadecylamine (HDA), dodecylamine (DDA), oleylamine (OLA), tri-octylphosphine oxide (TOPO), acetonitrile, tetrahydroquinoline (98 %), piperidine (99 %), bismuth nitrate tetrahydrate, bismuth trichloride (98 %), antimony trichloride (99 %), carbon disulfide (99.9 %), morpholine (99.5 %), chloroform-d (99.8 %), ethanol (99.8 %) deuterium oxide (99.9 %), and 1-dodecanethiol (98 %), were all obtained from Sigma-Aldrich. Olive oil was purchased from Fluka, castor oil, oleic acid, tetrahydroquinoline 98 %, petroleum ether, methanol, (99.5 %), dichloromethane, chloroform, sodium hydroxide (98 %), and acetone (analar) were purchased from Merck. Hexane (97 %) was obtained from Honeywell. All the chemicals were used as purchased without further purification. Ricinoleic acid was isolated from castor oil.

2.2. Syntheses of precursors

2.2.1. Syntheses of the dithiocarbamate ligands

The dithiocarbamates were prepared using the method reported by Nyamen *et al* [55] with slight modifications as described.

Carbon disulfide (0.1 mol, 6.0 mL) was added in small portions to an equimolar mixture of sodium hydroxide (0.1 mol, 4.0 g) and the corresponding amine (piperidine, tetrahydroquinoline, morpholine, 0.1 mol) in 15 mL of ethanol cooled in an ice bath. After 15 min, the white precipitate formed was washed with chloroform and suction dried. The resulting white powder was recrystallized from acetone/petroleum ether and white crystalline powder of sodium dithiocarbamate was obtained.

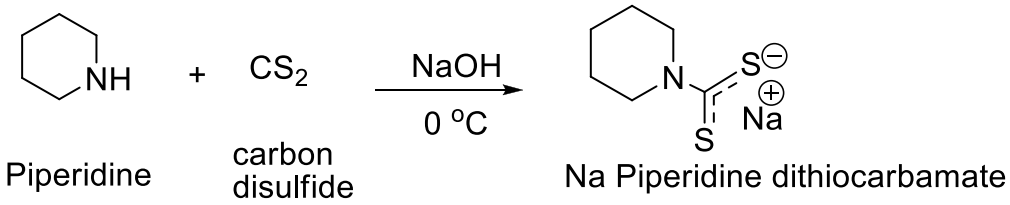

Scheme 3. Reaction scheme for the synthesis of sodium piperidine dithiocarbamate.

2.2.2. Syntheses of the complexes

MX_3 (5 mmol, M = Bi, Sb, X = NO_3, Cl) was suspended in ethanol (15 mL) and added dropwise to a solution of the piperidine dithiocarbamate ligand (15 mmol) in ethanol (25 mL). The mixture was stirred at room temperature for 1 h. The yellow precipitate formed was collected by filtration and recrystallized from chloroform/ethanol to obtain single crystals of M dithiocarbamate complexe.

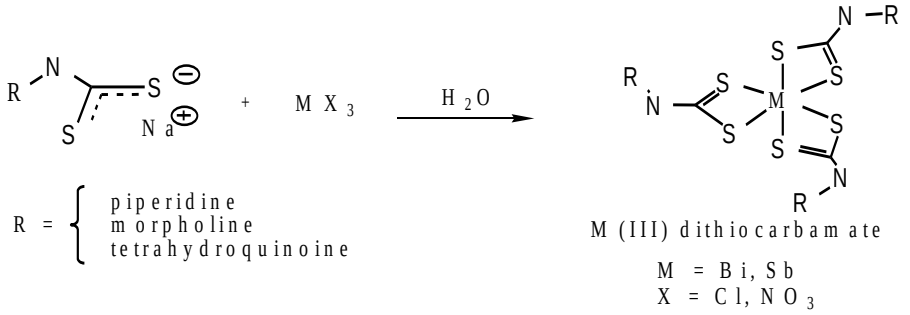

Scheme 4. Reaction scheme for the synthesis of dithiocarbamate complexes.

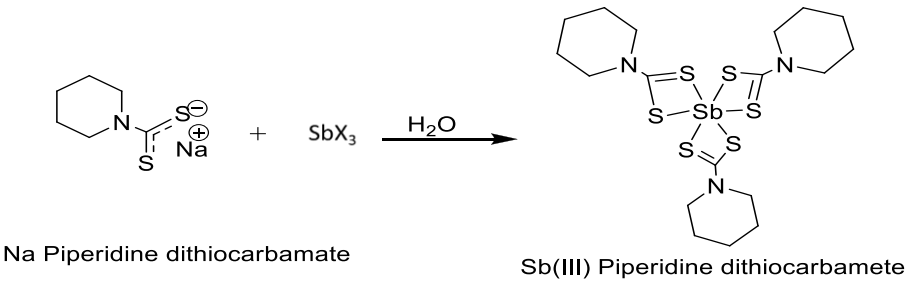

Scheme 5. Reaction scheme for the syntheses of precursors.

2.2.3. Syntheses of antimony complexes

$SbCl_3$ (1.14 g, 5 mmol) was dissolved in 10 mL of ethanol and the resulting mixtuere was added to a 30 mL solution of sodium piperidinedithiocarbamate (2.73 g, 15 mmol) and refluxed at 60 ^oC for 5 hrs. The pale yellow precipitate formed was filtered, washed with ethanol and recrystallized in dichlorometFigure xdfasfaggggfghane/ethanol 3:1 to obtain the Sb dithiocarbamate complexe.

The same procedure was carried out using morpholine and diethyldithiocarbamate ligands to obtain antimony morpholine and antimony diethyldithiocarbamate complexes.

2.3. Syntheses of nanomaterials

Nanoparticles were prepared from the single source precursors using hot injection routes in non-green and green solvents and thin films werer prepared by AACVD and spin coating. Melt reaction route was used for solvent-free syntheses.

$$[Bi(S_2Cpip)_2NO_3] \xrightarrow[HDA/DT,\ 190\ ^oC]{OLA} Bi_2S_3$$

Scheme 6. Synthesis of Bi_2S_3 nanorods from hot injection thermolysis.

2.3.1. Syntheses of Bi_2S_3 nanoparticles from non-green capping agents

0.3 g of $[Bi(S_2CPip)_2NO_3]$ or $[Bi(S_2CThq)_2NO_3]$ was dissolved in OLA (3.0 mL) and the solution injected into 3.0 g of hot HDA and 0.2 mL DT in a three-necked flask at 190 °C (Scheme 6). Immediately after injection, the mixture turned black and a drop in temperature of 25–30 °C was observed. The reaction was allowed to stabilize at 190 °C. After 2 h of reaction, heating was stopped and ethanol added resulting in the formation of a flocculent precipitate. The precipitate was separated by centrifugation, washed several times with ethanol (12 mL) and dispersed in toluene to give dark gray HDA-capped Bi_2S_3 nanoparticles.

The reaction was repeated at 230 °C and 270 °C. The above reaction procedure was repeated with DDA, OLA and TOPO as capping agents.

Table 1. Synthetic parameters for Bi_2S_3 Nps from non-green capping agents

Precursor	Capping agent	Temperature (°C)	**Time**
$[Bi(S_2CPip)_2NO_3]$	OLA	190	5 min, 10 min, 15 min, 30 min, 1 hr, 2hr
		230	2 hr
		270	2 hr
	HDA	190	2 hr
		230	2 hr
		270	2 hr
	DDA	190	2 hr
		230	2 hr
		270	2 hr
	TOPO	190	2 hr
		230	2 hr
		270	2 hr
$Bi(S_2CThq)_2NO_3]$	OLA	190	2 hr
		230	2 hr
		270	2 hr
	HDA	190	2 hr
		230	2 hr
		270	2 hr
	DDA	190	2 hr
		230	2 hr
		270	2 hr
	TOPO	190	2 hr
		230	2 hr
		270	2 hr

2.3.2. Syntheses of Bi_2S_3 nanoparticles from green capping agents

Fatty acids like castor oil and olive oil are green and low-cost biomolecules derived from plant seeds Castor oil is non-volatile and contains about 90 % of ricinoleic acid. Olive oil is made up of about 72 % oleic acid. The double bond and associated "kink" in the alkyl chain of olive oil is found to be an essential features for imparting colloidal stability[132] Fatty acids can significantly influence the assembly and morphology of inorganic structures due to complexation of their polar carboxylic groups with metal ions[133]. This section reports on the use of olive oil, castor oil, ricinoleic acid and oleic acid as green dispersion solvents and capping agents for the syntheses of Bi_2S_3 nanorods, using heterocyclic piperidine and tetrahydroquinoline complexes as single source precursors. The structures of oleic acid and ricinoleic acid are presented in Figure 12 in page 24.

2.3.2.1. Extraction of castor oil

Castor oil was extracted from castor seed, using hexane in a Soxhlet apparatus as reported by Akpan *et al*. [234] 300 mL of hexane was poured into round bottom flask. 10 g of ground dry castor bean cake was placed in the thimble and was inserted in the center of the extractor of a Soxhlet apparatus. The system was heated at 60 ^oC. When the solvent was boiling, the vapour rises through the vertical tube into the condenser at the top. The liquid condensate drips into the filter paper thimble in the center, which contains the solid sample to be extracted. The extract seeps through the pores of the thimble and fills the syphon tube, where it flows back down into the round bottom flask. This was allowed to continue for 30 minutes. The extract was then removed from the tube, dried in the oven, cooled in the desiccator and weighed[234].

2.3.2.2. Isolation of ricinoleic acid

Ricinoleic acid was isolated from the extracted castor oil by a method reported by Vaisman *et al*. [235] In a typical process, 60 g of KOH in 500 ml of ethanol was added to 250 g of castor oil and refluxed. After 3 hours, 1.5 L of 1.84 M H_2SO_4 was added. Two layers were formed from which the organic layer was collected, washed with warm distilled water and dried over $MgSO_4$ and filtered to obtain ricinoleic acid[235].

$$[Bi(S_2Cpip)_2NO_3] \xrightarrow[OO,\ 190\ ^oC]{OO} Bi_2S_3$$

Scheme 7. Synthesis of Bi_2S_3 nanorods from green capping agents.

2.3.2.3. Syntheses of Castor oil capped Bi_2S_3 nanoparticles

0.2 g of $[Bi(S_2CPip)_2NO_3]$ or $[Bi(S_2CThq)_2NO_3]$ was dispersed in 4.0 mL of castor oil and injected into 4.0 mL of hot castor oil in a three-necked flask at 190 ^oC. The mixture turned to a dark liquid and a drop in temperature of 25-30 ^oC was observed. The reaction was allowed to stabilize at 190 ^oC. After 2 hours of reaction, heating was stopped, and ethanol was added resulting in the formation of a flocculent precipitate. The precipitate was separated by centrifugation, washed several times with portions of ethanol (12 mL) and dispersed in hexane to give dark grey castor oil-capped Bi_2S_3 nanoparticles. The reaction was repeated at 230 ^oC and 270 ^oC.

The above reaction procedure was repeated with ricinoleic acid, olive oil and oleic acid as dispersing solvents and capping groups respectively.

Table 2. Synthetic parameters for Bi_2S_3 Nps from green capping agents

Precursor	**Capping agent**	**Temperature (^oC)**	**Time (hr)**
$[Bi(S_2CPip)_2NO_3]$	CO	190	2 hrs
		230	2 hrs
		270	2 hrs
	OO	190	2 hrs
		230	2 hrs
		270	2 hrs
	RA	190	2 hrs
		230	2 hrs
		270	2 hrs
	OA	190	2 hrs
		230	2 hrs
		270	2 hrs
$[Bi(S_2CThq)_2NO_3]$	CO	190	2 hrs
		230	2 hrs
		270	2 hrs
	OO	190	2 hrs
		230	2 hrs
		270	2 hrs
	RA	190	2 hrs
		230	2 hrs
		270	2 hrs
	OA	190	2 hrs
		230	2 hrs
		270	2 hrs

2.3.3. Solvent-free syntheses of Bi_2S_3 Particles

The solvent-free synthesis of Bi_2S_3 nanorods relies on the thermal degradation of dithiocarbamate precursors in inert atmosphere conditions. The rods were prepared by placing a sample of the precursor in a porcelain boat, placed in a glass tube, and purged with N_2 gas for 10 min. The tube was then placed in a carbolite tube furnace at 350 ^oC and heated for 25 min with continuous passage of N_2 gas. The tube was removed and allowed to cool under a current of N_2 gas for 10 min.The reaction was repeated with the same mass of precursor at 400 and 450 ^oC. The samples were washed several times with small portions of ethanol (12 mL) and centrifuged.

2.3.4. Syntheses of Sb_2S_3 sub-micrometer rods

Sb_2S_3 rods where synthesized by dispersing 0.3 mmols of $Sb(S_2CPip)_3$ in 3 mL of OLA and injecting into a mixture of 4 mL of OLA with and without 0.2 mL of DT at 230 ^oC. After injection, the pale-yellow solution turned brown with a rapid drop in temperature of about 30 ^oC and 8 min later the solution changed to black. The solution was left to react for 1 hr after which it was quenched by adding ethanol with the formation of a colloidal precipitate. The precipitate was washed several times with ethanol and separated by centrifugation.

The same reaction was carried out using $Sb(S_2CMor)_3$ and $Sb(S_2CDed)_3$ as shown in Table 3.

Table 3. Synthetic parameters for Sb_2S_3 Nps

Precursor	Capping Agent	Temp (^oC)	Time
$Sb(S_2CPip)_3.3H_2O$	OLA/DT	230	1hr
	OLA	230	1hr
$Sb(S_2CMor)_3$	OLA/DT	230	1hr
	OLA	230	1hr
$Sb(S_2CDed)_3$	OLA/DT	230	1hr
	OLA	230	1hr

2.3.5. Syntheses of antimony-bismuth sulfide solid solution $(Bi_{1-x}Sb_x)_2S_3$

The solid solution of $(Bi_{1-x}Sb_x)_2S_3$ $(0 \leq x \leq 1)$ was prepared by variation of the mole ratio of the two single source precursors (bismuth and antimony piperidinedithiocarbamates) as shown in Table 6. A mixture of bismuth and antimony piperidinedithiocarbamates totalling 0.29 mmol was dispersed in a mixture of oleylamine (4 mL) and 1-dodecanethiol (0.2 mL). This was injected into 8 mL of hot oleylamine (230 ^oC) under N_2 gas. After 30 min, the reaction was quenched, and the ensuing black precipitate washed three times with ethanol

(12 mL), centrifuged at 11000 rpm and dispersed in toluene. The reaction was repeated using different mole ratios of the precursors as shown in Table 6.

Table 4. Synthetic parameters for $(Bi_{1-}Sb_x)_2S_3$ solid solutions

$XBi(S_2CPip)_3$	$XSb(S_2CPip)_3$	$mBi(S_2CPip)_3$	$mSb(S_2CPip)_3$	Capping Agent	Temp. (°C)	Time (min)
1.000	0.000	0.200	0	OLA/DT	230	30
0.937	0.063	0.188	0.011	OLA/DT	230	30
0.875	0.125	0.175	0.022	OLA/DT	230	30
0.813	0.187	0.163	0.033	OLA/DT	230	30
0.750	0.250	0.150	0.044	OLA/DT	230	30
0.687	0.323	0.138	0.056	OLA/DT	230	30
0.625	0.375	0.125	0.066	OLA/DT	230	30
0.563	0.437	0.113	0.076	OLA/DT	230	30
0.500	0.500	0.100	0.087	OLA/DT	230	30
0.437	0.563	0.088	0.098	OLA/DT	230	30
0.375	0.625	0.075	0.109	OLA/DT	230	30
0.323	0.687	0.065	0.120	OLA/DT	230	30
0.250	0.750	0.050	0.131	OLA/DT	230	30
0.187	0.813	0.038	0.142	OLA/DT	230	30
0.125	0.875	0.025	0.153	OLA/DT	230	30
0.063	0.937	0.013	0.164	OLA/DT	230	30
0.000	1.000	0	0.175	OLA/DT	230	30

2.3.6. Deposition of Bi_2S_3 thin films by AACVD

Bi_2S_3 thin films were grown on bare glass substrate in a hot-walled reactor (R) containing quartz (2 cm diameter) tube (T), by a gas phase reaction in an argon environment using a self-designed aerosol-assisted chemical vapour deposition (AACVD) assembly. The glass

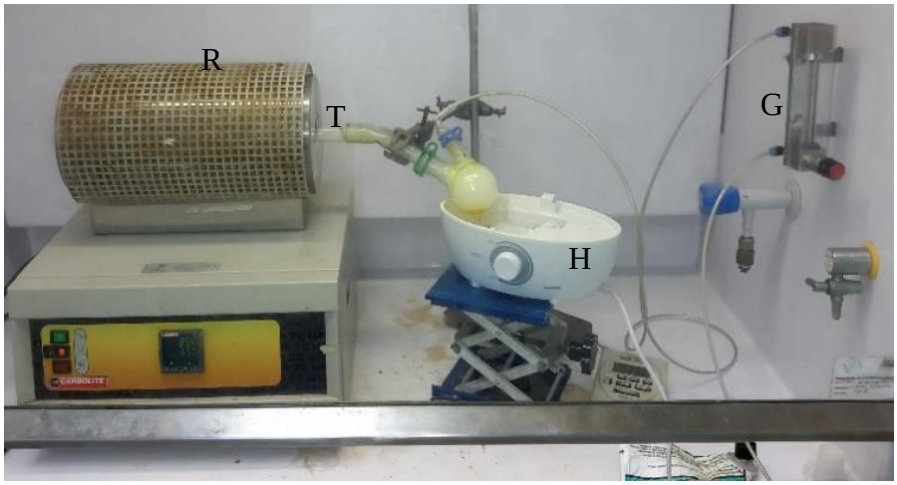

Figure 17. Simple setup for AACVD (UZ, SA): G = Gas flow meter, H = Ultrasonic humidifier, R = Furnace, T= glass tube.

substrates, 1 cm^2 were ultrasonically cleaned with distilled water, acetone, isopropyl alcohol and finally ethanol and dried in air. In a typical experiment, 0.30 mmol of the precursor was dissolved in 25.0 mL of the appropriate solvent mixture in a 100 mL two-neck flask, connected through one neck to a gas inlet. The carrier gas (argon) passed into the solution and to the reactor through the other neck. The carrier gas flow rate was controlled by a Teckfluid E08950 gauge meter (G). The precursor solution in the round bottom flask was mounted on a piezo-electric modulator of a Salton SUH 20 ultrasonic humidifier (H). The aerosol droplets generated were transported by the carrier gas into the reactor tube lined with glass substrates of 1 cm^2 each in a Carbolite tube furnace. Both solvent and precursor were transported into the reactor where thermally induced reactions and film deposition took place. Deposition took place at 350 ^oC, 400 ^oC and 450 ^oC at a constant argon flow rate. The influence of solvents and reaction temperature on the morphology of the films were investigated. Solutions of the complexes prepared by dissolving 0.30 mmol of the complex in 25.0 mL of $CHCl_3/CH_3OH$ 3:1 and $CHCl_3/CH_3CN$ 3:1 were used to generate aerosol which was transported by argon into a tube furnace fitted with a glass tube lined by 1 cm^2 glass substrates at 350 °C, 400 °C and 450 °C respectively. The complexes decomposed and a thin film of Bi_2S_3 was deposited on the glass substrates.

Table 5. Synthetic parameters for Bi_2S_3 thin films by AACVD

Precursor	**Solvent**	**Substrate Temp. (^oC)**	**Gas Flow rate (vol %)**
$Bi((S_2CPip)_3$	$CHCl_3/CH_3OH$ 3:1	350	60
		400	60
		450	60
	$CHCl_3/CH_3CN$ 3:1	350	60
		400	60
		450	60
$Bi(S_2CThq)_3$	$CHCl_3/CH_3OH$ 3:1	350	60
		400	60
		450	60
	$CHCl_3/CH_3CN$ 3:1	350	60
		400	60
		450	60

2.3.7. Deposition of Bi_2S_3 thin films by spin coating

Films were prepared by dropwise coating of 1 cm^2 glass substrates with 100 µL of a solution of the complexe (0.15 mmol in 10.0 mL of chloroform) using an Ossila E441 Spin coater at 1420 RPM for 25 s under atmospheric pressure. The films were dried in air for 5 min at 70 ^oC on a preheated hot plate, then placed in a reactor tube and purged with argon gas for 10 min before inserting in a tube furnace set at 350 ^oC. The films were annealed at this temperature for 20 min, after which heating was stopped and the furnace allowed to cool with continuous passage of argon gas. The reaction was repeated at 400 ^oC and 450 ^oC.

Figure 18. Ossilla Spin Caoter (UZ, SA).

Table 6. Synthetic parameters for Bi_2S_3 thin films by spin coating

Precursor	**Solvent**	**Substrate Temp. (^oC)**	**Spin Speed (rpm)**
$Bi((S_2CPip)_3$	$CHCl_3/CH_3OH$ 3:1	350	1420
		400	1420
		450	1420
$Bi(S_2CThq)_3$	$CHCl_3/CH_3OH$ 3:1	350	1420
		400	1420
		450	1420

2.4. Hydrogen/oxygen evolution and supercapacitance studies

Electrochemical characterizations of the samples were performed using the three-electrode system. Working electrodes were prepared by coating mixture of Sb_2S_3 (80 wt.%), acetylene black (10 wt.%), and polyvinylidene difluoride (10 wt.%) in N-methyl pyrrolidinone (NMP) on to a nickel foam. A platinum wire and saturated calomel electrode were used as a counter and a reference electrode in 3M KOH as an electrolyte. A supercapacitor device was fabricated using two working electrodes separated by ion transporting layer. The size of the device was 0.25 cm2. Before assembling the device, both working electrodes and ion-transporting layer were soaked in the 3 M KOH for 1 hr. Versa STAT 4-500 electrochemical workstation (Princeton Applied Research, USA) was used to perform cyclic voltammetry, galvanostatic charge-discharge, and electrochemical impedance spectroscopy (EIS) measurements. EIS measurements were carried out by applying an AC voltage with 10 mV amplitude in a frequency range from 0.05 Hz to 10 kHz at open circuit potential.

Electrocatalytic behavior of the Sb_2S_3 samples, for catalytic activities for oxygen and hydrogen evolution studies, was also examined using standard three electrode system consisting of samples on nickel foam as a working electrode, platinum wire as a counter electrode and saturated calomel electrode (SCE) as a reference in 1M KOH electrolyte. Electrocatalytic testing includes linear sweep voltammetry (LSV), cyclic voltammetry (CV), chronoamperometry and EIS. LSV was performed at a scan rate of 1 mV/s in both OER and HER region. The potential was converted to reversible hydrogen electrode (Eref = 0.00 V, RHE) using the Nernst equation.

2.5. Characterization of the precursors

The ligands and complexes were characterized using analytical techniques such as melting point determination, infra-red spectrometry, CHNS microanalysis, thermogravimetric analysis (TGA), Proton and Carbon-13 spectroscopy.

2.5.1. Fourier transform infrared spectroscopy (FT-IR)

Infrared (IR) spectroscopy is one of the most common and widely used spectroscopic techniques employed mainly by inorganic and organic chemists due to its usefulness in the identification and structural analyses of a variety of substances, including organic and inorganic compounds. Infrared spectroscopy takes advantage of the vibrational transitions of a molecule. An infrared spectrum is obtained by passing infrared light through a sample and by measuring the absorption or transmittance of light at each frequency, peaks which correspond to the frequency of absorbed radiation are obtained. Since different molecules

with a different combination of atoms produce their unique spectra, infrared spectroscopy can be used to qualitatively identify substances. In addition, the intensity of the peaks in the spectrum is proportional to the amount of substance present, enabling its application for quantitative analysis. Fourier transformed infrared spectroscopy has several prominent advantages over previous generation infrared spectrometers since it can handle all frequencies simultaneously with high throughput, reducing the time required for analysis[236,237].

IR spectra of the ligand and complexes were recorded directly on small samples of the compounds with a Bruker FT-IR Tensor 27 spectrophotometer in the range 200–4000 cm^{-1} and a Perkin-Elmer Spectrum Two UATR FT-IR spectrophotometer directly on small samples of the compounds in the 500-4250 cm^{-1} range, at the University of Zululand (SA), and on a Thermo Scientific Nicolet iS5 instrument (400– 4000 cm^{-1}, resolution 4 cm^{-1}) at the University of Manchester (UK).

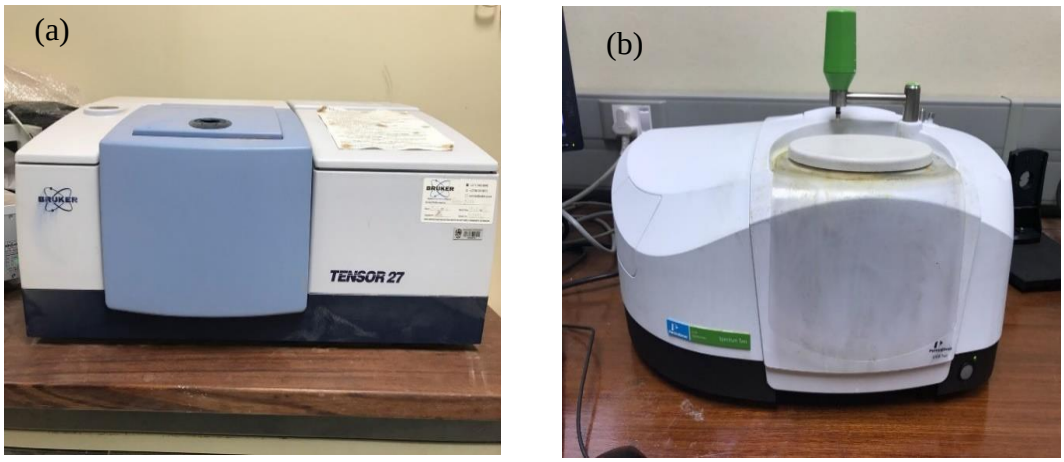

Figure 19. (a) Bruker Tensor 27 and (b) Perkin Elmer Spectrum Two UATR FT-IR spectrometers (UZ, SA).

2.5.2. CHNS microanalyses

CHNS elemental analyzers provide a means for the rapid determination of carbon, hydrogen, nitrogen, and sulfur in organic matrices and other types of materials. They can handle a wide variety of sample types, including solids, liquids, volatile and viscous samples. The sample is weighed in mg in a tin capsule and dropped into the reactor for a complete combustion process (furnace at ca. 1000^{o} C), where carbon is converted to carbon dioxide; hydrogen to water; nitrogen to nitrogen gas/ oxides of nitrogen and sulfur to sulfur dioxide. The combustion products are swept out of the combustion chamber by an inert carrier gas such as helium and passed over heated high purity copper which removes any oxygen not consumed in the initial combustion and to convert any oxides of nitrogen to nitrogen gas.

The amount of each element in the sample is determined by gas chromatography. Quantification of the elements requires calibration for each element by using high purity 'micro-analytical standard' compounds such as acetanilide and benzoic acid[238]. CHNS microanalysis was performed on the ligands and complexes with a PerkinElmer automated model 2400 series II CHNS/O analyzer and a Thermo Flash 2000 and Carlo Erba EA 1108 elemental analyzers at the Universities of Zululand (SA) and Manchester (UK) respectively.

2.5.3. Thermogravimetric analysis (TGA)

Thermogravimetric analysis (TGA) is a method of thermal analysis in which the mass of a sample is measured over time as the temperature changes. Changes in the mass of a sample due to chemical events such as desorption, absorption, sublimation, vaporization, oxidation, reduction and decomposition are studied while the sample is subjected to a program of change in temperature [239–241]. The plot of the mass change in percentage versus temperature or time known as TGA curves is the typical result of TGA analysis. TGA is used to study the thermal stability and compositional analysis of materials up to 1000 ^{o}C. TGA on the complexes was carried out by weighing 5-12 mg of the samples and heating at a rate of 20 ^{o}C min^{-1} with a PerkinElmer Pyris 6 instrument up to 600 ^{o}C in a closed perforated aluminum pan under N_2 gas flow at the University of Zululand (SA) and on a Thermo Flash 2000 elemental analysers at the University of Manchester (UK)

2.5.4. ^{1}H and ^{13}C Nuclear magnetic resonance spectroscopy

NMR spectroscopy is an important versatile analytical technique that is used to provide information about the structure and chemical bonding of molecular systems. ^{1}H and ^{13}C have nuclear spins of ½. Hence, they would behave in a similar fashion to a simple, tiny bar magnet. When subjected to an external magnetic field of a particular frequency, they absorb and re-emit electromagnetic radiation. This energy is at a particular resonance frequency which depends on the strength of the magnetic field and magnetic properties of the isotope of the atoms[242]. NMR spectrum is a plot of the ratio of the frequency applied against absorption. The precise resonant frequency of the energy transition is dependent on the effective magnetic field at the nucleus. This field is affected by electron shielding which is in turn dependent on the chemical environment[243]. The ^{1}H NMR and ^{13}C NMR spectra for both ligands and complexes were recorded on a Bruker AVIII400 NMR spectrometer at the University of Manchester (UK). The samples were prepared by completely dissolving 0.01 g of sample in 8 mL of $CDCl_3$, $(CD_3)_2CO$ or D_2O, and transfer into an NMR capillary tube. The tube was then placed in the spectrometer for analysis.

2.5.5. Single crystal X-ray diffraction

Single-crystal X-ray structure determination was performed using a Bruker Apex II Duo CCD diffractometer at the University of Witwatersrand and the University of KwaZulu Natal (SA) and on *a* Rigaku Oxford Diffractometer at the University of Manchester (UK). Single-crystal X-ray Diffraction is a non-destructive analytical technique which provides detailed information about the internal lattice of crystalline substances, including unit cell dimensions, bond-lengths, bond-angles, and details of site-ordering. In single-crystal refinement, the data generated from the X-ray analysis was interpreted and refined to obtain the crystal structure. X-ray diffraction is based on constructive interference of monochromatic X-rays and a crystalline sample. These X-rays were generated by a cathode ray tube, filtered to produce monochromatic radiation(Mo, Cu), collimated to concentrate, and directed toward the sample. The interaction of the incident rays with the sample produced constructive interference (and a diffracted ray) when conditions satisfy Bragg's Law ($n\lambda=2d\sin\theta$). These diffracted X-rays were then detected, processed and counted. By changing the geometry of the incident rays, the orientation of the centered crystal and the detector, all possible diffraction directions of the lattice were attained[244]. Samples needed to be unfractured and optically clear single crystals. Their size should be between 0.1 and 0.2 mm in the three directions of space. They were normally selected using an optical microscope (x40) equipped with a polarizing attachment and observing if light extinguishes regularly every 90º when turning the stage of the microscope. The selected crystal was fixed on the tip of a thin glass fibre using epoxy resin or cement, or in a loop including specific oil, which fits into the goniometer head in the diffractometer. The crystal was then aligned along the beam direction. Once the crystal was mounted on the diffractometer, the appropriate parameters for each measurement such as the distance to the detector and the space of the Ewald sphere were selected, and the intensity data collected. Data are typically obtained between 3 ° and 30 ° 2θ when using molybdenum radiation. Generally, a complete data collection requires between 3 to 12 hours, depending on the specimen and the diffractometer. Some of the measured intensities enabled the calculation of the unit cell parameters. All the intensities were indexed and a list of observed hkl reflections was obtained. The data were combined computationally with complementary information to produce an electron density map. The crystal structures were obtained from the diffraction pattern if the electron density function was calculated at every point in a single unit cell. Atoms were fitted to the electron density map, and after repetition of phase refinement and model fitting, the final refined atomic models were obtained, called a crystal structures[245].

2.6. Characterization of nanocrystals and thin films

The physical and chemical properties of matter change with size, and as the nanometer scale is reached new behaviours start to appear. Characterization of nanomaterials poses lots of challenges to scientists and engineers despite the growing number of research in this area. Several sophisticated nano characterization techniques have emerged to allow a better understanding of the control of morphology, size and dimensions of materials in the nano range.

2.6.1. Ultraviolet/Visible spectroscopy

UV/Vis spectroscopy offers a relatively straight forward and effective way for quantitatively characterizing both organic and inorganic nanomaterials. It is an ideal technique for determining the electronic properties of nanomaterials since it operates on the principle of absorption of photons that promote the molecule to an excited state. A sample is irradiated with electromagnetic waves in the ultraviolet and visible ranges and the absorbed light is analyzed through the resulting spectrum. It can be employed to identify the constituents of a substance, determine their concentrations, and to identify functional groups in molecules. Different sized materials can be characterized, including, nano-particles and bulk materials. Size-dependent properties can also be observed in a UV/Visible spectrum, particularly in

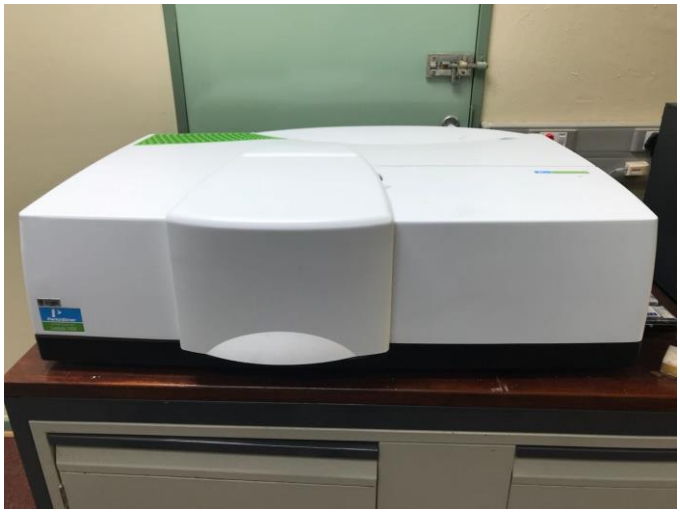

Figure 20. Perkin Elmer Lambda 1050 Near IR UV/Visible spectrometer (UZ, SA).

the nano and atomic scales. These include peak broadening and shifts in the absorption wavelength. Many electronic properties, such as the band gap of a material, can also be determined by this technique.

In the spectrum of nanoparticles, the absorption peak's width strongly depends on the chemical composition and the particle size. As a result, their spectra is different from those

of their bulk counterparts. For instance, for semiconductor nanocrystals, the absorption spectrum is broadened owing to quantum confinement effects, and as their size reduces, there is no longer a distinct peak, rather there is a band. Furthermore, semiconductor nanoparticles' absorption peaks shift towards smaller wavelengths (higher energies) as their crystal size decreases. An important consequence of using the UV/Vis spectroscopy is that the band gap of nanosized materials can be determined[246]. The UV/Vis spectra of the nanoparticles and films were recorded at room temperature using a Perkin Elmer Lambda 1050 UV/Visible spectrometer, operating in a double beam mode from 250-1500 nm region at the University of Zululand (SA) and on a Shimadzu UV-1800 spectrophotometer at the University of Manchester (UK). The samples were placed in silica cuvettes (1 cm path length), and hexane was used as reference solvent. For the films, an empty silicon glass substrate was placed in the path of the reference beam, consequently, in both cases, the spectra recorded were due to the samples only.

2.6.2. Photoluminescence (PL) spectroscopy

Photoluminescence (PL) is a process in which crystalline solids absorb higher energy photons and re-emit less energy of the electromagnetic spectra. It is a two-step process. In the first step electrons are excited from a lower energy state to higher energy state as a result

Figure 21. Perkin Elmer LS 55 photoluminescence spectrometer (UZ, SA).

of absorption of energy, and in the second step, the electrons fall back to lower energy state with the emission of photo radiation. The PL spectroscopy is suitable for the characterization of both organic and inorganic photoluminescent materials of virtually any size and the samples can be in solid, liquid or gaseous forms[236].

As dimensions are reduced to the nanoscale, PL emission properties can change, in particular a size-dependent shift in the emission wavelength can be observed. Additionally, because the released photon corresponds to the energy difference between the states, PL spectroscopy can be utilized to study material properties such as band gap, recombination mechanisms, and impurity levels. A solution containing the sample is placed in a quartz cuvette with a known path length. Double beam optics is generally employed[247]. The first beam passes through an excitation filter or monochromator, then through the sample and onto a detector. This impinging light causes photoluminescence, which is emitted in all directions. A small portion of the emitted light arrives at the detector after passing through an optional emission filter or monochromator. A second reference beam is attenuated and compared with the beam from the sample. Solid samples can also be analyzed, with the incident beam impinging on the material (thin film, powder). Generally, an emission spectrum is recorded where the sample is irradiated with a single wavelength and the intensity of the luminescence emission is recorded as a function of wavelength[246]. The PL spectra of the nanoparticles and films were recorded at room temperature using a Perkin Elmer LS 55 photoluminescence spectrometer at the University of Zululand (SA)

2.6.3. Scanning electron microscopy (SEM)

Scanning electron microscope (SEM) is an instrument that helps in forming an image of a sample surface by scanning the surface to generate signals that shed valuable information about the sample such as composition, topography, morphology, and crystallographic information. Electron microscopes were developed due to the limitations of Light Microscopes as a result of the physics of light. Scanning electron microscopy (SEM) can

Figure 22. Zeiss Sigma VP-03-67 field emission gun scanning electron microscopy (FEGSEM) (UZ, SA).

provide a highly magnified image of the surface and the composition information of near-surface regions of a material. The resolution of SEM can approach a few nanometers and the magnifications of SEM can be easily adjusted from about 10 times to 300,000 times. In a vacuum, the electron beam, which typically has energy ranging from 0.5 to 40 keV, is focused by one or two condenser lenses to a spot about 0.4 to 5 nm in diameter[248,249]. The beam passes through pairs of scanning coils or pairs of deflector plates in the electron column, typically in the final lens, which deflects the beam in the x and y-axes so that it scans in a raster fashion over a rectangular area of the sample surface. As the electrons penetrate the surface, a number of interactions occur that can result in the emission of electrons from the surface. A detector collects a fraction of the electrons emitted and an image is produced. The image may be captured by photography from a high-resolution cathode ray tube, but in modern machines is digitally captured and displayed on a computer monitor and saved to a computer's hard disk. Also emitted are characteristic X-ray photon and Auger electrons, which allows one to analyse the composition of the specimen. There are three types of images produced in SEM: secondary electron images, backscattered electron images, and elemental X-ray maps[249]. The use of SEM requires very little sample preparation, especially if the specimen is conducting and vacuum compatible. If the specimen is an insulator, it can be coated with a thin (10nm) conducting film of platinum, gold or other metals to prevent charging effects that would distort the electric fields in the electron microscope. Scanning electron micrographs (SEM) of the samples were determined using a Zeiss Sigma VP-03-67 field emission gun scanning electron microscopy (FEGSEM) at the University of Zululand (SA). The samples were coated with gold or silver.

2.6.4. Transmission electron microscopy

Transmission electron microscopy (TEM) is a technique where a beam of electrons is transmitted through an ultra-thin specimen, interacting with the specimen as it passes through. In TEM, electrons are accelerated to ~100 KeV or higher (up to 1 MeV), projected onto a thin specimen (less than 200nm) by means of the condenser lens system, and penetrate the sample thickness either undeflected or deflected. An image is formed from the interaction of the electrons transmitted through the specimen. The image is magnified and focused onto an imaging device, such as a fluorescent screen, on a layer of photographic film, or to be detected by a sensor such as a CCD camera. The greatest advantages TEM offer are the high magnification ranging from 50 to 10^6 and its ability to provide both image and diffraction information from a single sample. The scattering processes experienced by electrons during their passage through the specimen determine the kind of information

Figure 23. FEI Talos F200A HRTEM microscope (TUM, UK).

obtained. Elastic scattering involves no energy loss and gives rise to diffraction patterns. Inelastic interactions between primary electrons and sample electrons at heterogeneities such as grain boundaries, dislocations, second-phase particles, defects, density variations, etc., cause complex absorption and scattering effects, leading to a spatial variation in the intensity of the transmitted electrons[250,251]. In TEM one can switch between imaging the sample and viewing its diffraction pattern by changing the strength of the intermediate lens

TEMs are capable of imaging at a significantly higher resolution than light microscopes, owing to the small de Broglie wavelength of electrons. This enables the instrument's user to examine fine detail- even as small as a single column of atoms, which is tens of thousands of times smaller than the smallest resolvable object in a light microscope. TEM forms a major analysis method in a range of scientific fields, in both physical and biological sciences. TEM find application in a wide range of fields including materials science and semiconductor research[252]. Transmission electron microscope (TEM) images, high resolution transmission electron microscope (HRTEM) images, selected area electron diffraction (SAED) patterns and energy dispersive X-ray spectroscopy (EDX) spectra were obtained using a JEOL 1010 TEM and JEOL 2100 HRTEM microscope at the University of KwaZulu Natal and the Council for Scientific and Industrial Research (CSIR, SA) respectively, and on an FEI Talos F200A HRTEM microscope equipped with an X-FEG electron source and Super-X SDD EDX detectors at the Photon Science Institute (PSI), University of Manchester (UK).

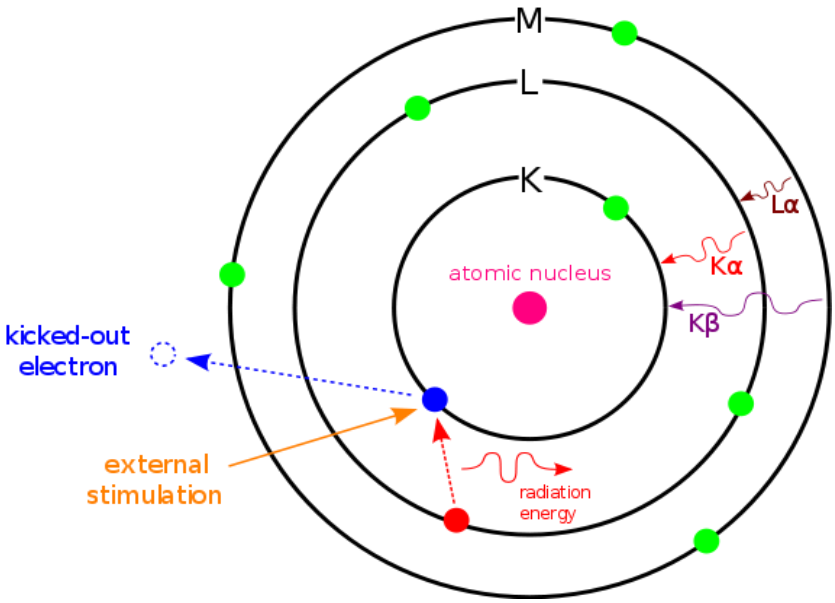

Figure 24. Schematic of the principle of EDX.

2.6.5. Energy dispersive X-ray (EDX) analysis

Energy dispersive X-ray spectroscopy is a technique used for identifying the elemental composition on an area of interest of a specimen. During EDX analyses, the specimen is bombarded with an electron beam inside the electron microscope (SEM or TEM). The bombarding electrons collide with the specimen atom's own electrons, knocking some of them off in the process. A position vacated by an ejected inner shell electron is eventually occupied by a higher-energy electron from an outer shell. To be able to do so, however, the transferring outer electron must give up some of its energy by emitting an X-ray. The amount of energy released by the transferring electron depends on which shell it is transferring from, as well as which shell it is transferring to. Furthermore, the atom of every element releases X-rays with unique amounts of energy during the transferring process. Thus, by measuring the energy of the X-rays emitted by a specimen during electron beam bombardment, the identity of the atom from which the X-ray was emitted can be established[250,253]. The output of an EDX analysis is an EDX spectrum, which is a plot of how frequently an X-ray is received for each energy level. An EDX spectrum normally displays peaks corresponding to the energy levels for which the most X-rays had been received. Each of these peaks is unique to an atom, and therefore corresponds to a single element. The higher a peak in a spectrum, the more concentrated the element is in the specimen. An EDX spectrum plot not only identifies the element corresponding to each of its peaks but the type of X-ray to which it corresponds as well. For example, a peak corresponding to the amount of energy possessed by X-rays emitted by an electron in the L-shell going down to the K-shell is identified as a

Kα peak. The peak corresponding to X-rays emitted by M-shell electrons going to the K-shell is identified as a Kβ peak as shown in Figure 24.

2.6.6. X-ray photoelectron spectroscopy

In XPS, relatively low energy X-rays are used to eject the electrons from an atom via the photoelectric effect. XPS is typically accomplished by exciting the surface of a sample with mono-energetic Al Kα X-rays causing photoelectrons to be emitted from the sample surface. An electron energy analyser is used to measure the energy of the emitted photoelectrons. From the binding energy and intensity of a photoelectron peak, the elemental identity, chemical state, and quantity of a detected element can be determined. Each surface atom possesses core level electrons that are not directly involved with chemical bonding but are influenced slightly by the chemical environment of the atom. The binding energy of each core-level electron (approximately its ionization energy) is characteristic of the atom and specific orbital to which it belongs. Since the energy of the incident X-rays is known, the measured kinetic energy of a core-level photoelectron peak can be related directly to its characteristic binding energy[254]. The binding energies of the various photoelectron peaks (1s, 2s, 2p, etc.) are well tabulated and XPS therefore provides a means of elemental identification which can also be quantified via measurement of integrated photoelectron peak intensities and the use of a standard set of sensitivity factors to give a surface atomic composition[255]. The low binding energy region of the XPS spectrum is usually excited with a separate ultraviolet photon source, such as a helium lamp, (ultraviolet photoelectron spectroscopy, UPS) and provides data on the valence band electronic structure of the surface. XPS data were collected on a Kratos Axis Ultra Hybrid and analyzed using CasaSAXPS at the University of Manchester (UK). The binding energy scales were calibrated using the principle C *1s* peak associated with hydrocarbon at 284.8 eV, Shirley backgrounds were fitted where appropriate, and atomic concentrations were calculated using relative sensitivity factors incorporating the photoionization cross section for each core electron orbital, as well as the transmission function of the electron energy analyzer. Peak fitting using Voigt-approximation Gaussian-Lorentzian products was performed to obtain binding energy positions for chemical species determination.

2.6.7. Raman Spectroscopy

Raman spectroscopy is an important tool for the elucidation of molecular structure for locating various functional groups or chemical bonds in molecules and for the quantitative analysis of mixtures. Raman spectroscopy is a form of vibrational spectroscopy, much like infrared (IR) spectroscopy. However, IR bands arise from a change in the dipole moment of

a molecule. Raman bands arise from a change in the polarizability of the molecule. In many cases, transitions that are allowed in Raman are forbidden in IR, so these techniques are often complementary. Different materials have different vibrational modes which make Raman spectroscopy to become a very sensitive and accurate technique for material identification. lasers are used as a photon source due to their highly monochromatic nature, and high beam fluxes. The most commonly used lasers are continuous-wave gas lasers like argon, krypton and helium-neon. Typical laser powers used range from milli watts to several watts, generally focused to increase the power density. However, for absorbing samples, this can result in significant heating of the sample. The scattered light is collected with an objective onto the entrance silt of a monochromator equipped with holographically ruled gratings. The dispersed light from exit silt of monochromator is usually detected by a cooled photomultiplier and photon counting system. Recent Raman spectrometers are equipped with cooled charge-coupled-Device (CCD) detectors which reduce the spectrum acquisition time and improve the signal to noise ratio[256,257]. Raman spectroscopy was performed at the University of Manchester (UK), using a Renishaw 1000 micro Raman spectrometer (Model-INVIA) in the wavenumber range 30-3000 cm^{-1} with a resolution of 1 cm^{-1}, and in a back-scattering geometry using Argon ion laser (λ= 514 nm, max power 50 mW) as excitation source focused on the alloy anode to a spot diameter of about 0.1 mm.

2.6.8. Powder X-ray diffraction

X-ray scattering techniques are a family of non-destructive analytical techniques which disclose the information about the crystallographic structure, and physical properties of materials and thin films. These techniques are based on observing the scattered intensity of an X-ray beam hitting a sample as a function of incident and scattered angle, polarization and wavelength or energy. X-ray diffraction has been in use in two main areas: for the fingerprint characterization of crystalline materials and the determination of their structure. Each crystalline solid has its unique characteristic X-ray powder pattern which may be used as a "fingerprint" for its identification. Once the material has been identified, X-ray crystallography may be used to determine its structure. X-ray diffraction is one of the most important characterization tools used in solid state chemistry and materials science[258]. Further, X-ray diffraction method can be used to distinguish crystalline materials from nanocrystalline (amorphous) materials. The structure identification is made from the X-ray diffraction pattern analysis and comparing it with the standard powder diffraction files published by the International Centre for Diffraction Data (ICDD). When a monochromatic X-ray impinges upon the atoms in a crystal lattice, each atom acts as a source of scattering the radiations of the same wavelength. The intensity of the reflected beam at a certain angle

will be maximum, when the path difference between two reflected waves from two different planes is an integral multiple of the wavelength. Reflections only occur under conditions which satisfy the equation $n\lambda = 2dsin\theta$ as shown in Figure 25.

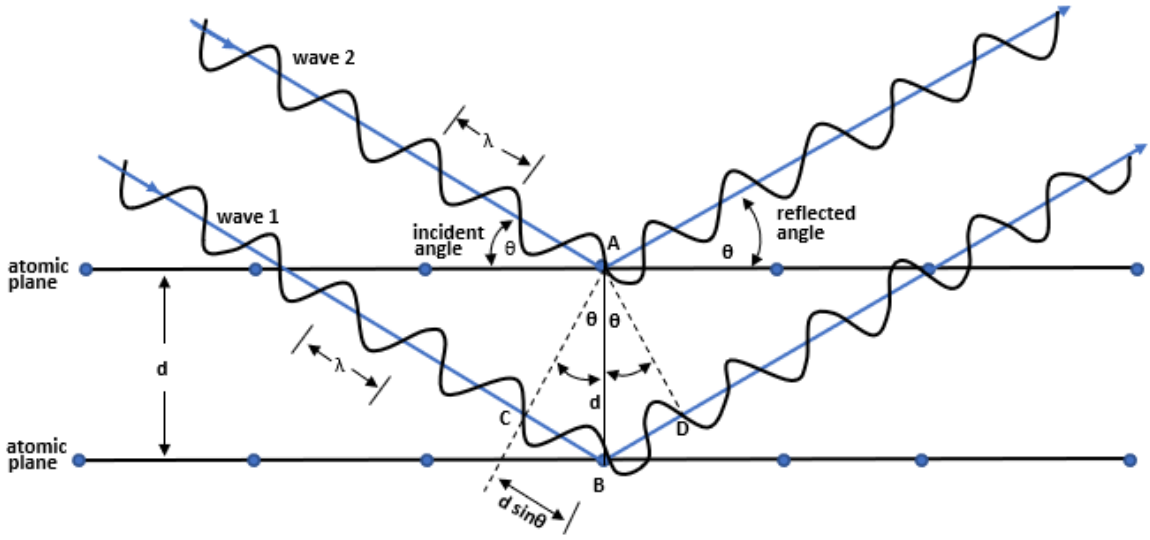

Figure 25. Visualization of the Bragg equation.

Wave 1 and wave 2 are two monochromatic X-ray beams of wavelength λ being incident on the crystalline substance. The spacing between the atomic planes in the crystal occurs over the distance, d. Wave 2 reflects off at the upper atomic plane at an angle θ equal to its angle of incidence. Similarly, wave 1 reflects off at the lower atomic plane at the same angle θ. wave 1 travels a distance of 2d farther than wave 2. Hence the path difference between waves 1 and 2 is 2d. If this distance 2d is equal to an integral number of wavelengths nλ, then waves 1 and 2 will be in phase on their exit from the crystal and constructive interference will occur, otherwise, destructive interference will occur, and the waves will not be as strong as when they entered the crystal.

$$BC = d \sin \theta$$

$$BD = d \sin \theta$$

$$\text{The path difference} = BC + BD = 2d \sin \theta$$

$$\text{Thus } n\lambda = 2d \sin \theta \qquad (3)$$

This is known as Bragg's Law for X-ray diffraction. On the basis of Bragg's Law, by measuring the angle θ, the wavelength λ, the chemical elements can be determined, if the lattice plane distance 'd' is known, or, if the wavelength λ is known, the lattice plane distance 'd' and thus the crystalline structure can be determined.

Figure 26. Bruker AXS D8 Advanced X-ray diffractometer (UZ, SA).

The sample and detector rotate through their respective angles, and the intensity of diffracted X-rays is continuously recorded. A peak intensity occurs when the mineral contains lattice planes with d-spacings appropriate to diffract X-rays at that value of θ[259].

X-ray diffraction pattern can provide the following information about the sample;

- Estimation of unit cell structure, lattice parameters and Miller indices.
- Identification of phases present in the material
- Determination of the purity of the phase of the material
- Estimation of crystalline/amorphous content in the sample.
- Evaluation of the average crystallite size from the width of the peak in a particular phase pattern. Large grain size gives rise to sharp peaks, while the peak width increases with decreasing grain/particle size.
- Analysis of structural distortion arising as a result of variation in d-spacing caused by the strain, thermal distortion.

The X-ray diffraction analysis has been the most popular method for the estimation of crystallite size in nanomaterials. Paul Scherrer, developed an equation, known as the Scherrer equation which can be used to estimate the crystallite size in a nanocrystalline powdered material. "Crystallite size" is not synonymous with "particle or grain size",. Crystallite size is the smallest - most likely single crystal in powder form. The crystallite size is commonly determined by XRD. Grain is either a single crystalline or polycrystalline

material, and is present either in bulk or thin film form. X-Ray diffraction is sensitive to the crystallite size inside the particles[260,261].

From the well-known Scherrer formula the average crystallite size, L, is:

$$L = \frac{k\lambda}{\beta cos\theta}$$

(4) where λ is the X-ray wavelength in nanometer (nm), β is the peak width of the diffraction peak profile at half maximum height resulting from small crystallite size in radians and K is a constant related to crystallite shape, normally taken as 0.9. The value of β in 2θ axis of diffraction profile must be in radians. The θ can be in degrees or radians, since the cosθ corresponds to the same number.

P-XRD patterns of the nanoparticles and films were recorded at room temperature in the high-angle 2θ range of 10–70° by using a Bruker AXS D8 Advance X-Ray diffractometer, equipped with nickel-filtered CuKa radiation (λ=1.5406 Å) at 40 kV, 40 Ma at the University of Zululand (SA), and on a PANalytical X'Pert PRO powder diffractometer with a Cu Kα radiation source (λ = 1.5406Å). The samples were mounted flat and scanned over the 2Θ range of 10° - 70° in a step size of 0.05 at the University of Manchester (UK).

CHAPTER 3. RESULTS AND DISCUSSION

3.1. Synthesis and characterization of the dithiocarbamate ligands and complexes

The heterocyclic piperidine, tetrahydroquinoline and morpholine dithiocarbamates and their Bi and Sb complexes were synthesized as shown in Scheme 3. Diethyldithiocarbamate was obtained commercially and used to syntheses complexes in a similar manner. Piperidine, tetrahydroquinoline and morpholine dithiocarbamates were isolated as white crystalline powders with very good yield (Figure 27). The four bismuth complexes were obtained as yellow precipitates while their antimony counterparts were pale yellow. All Bi and Sb complexes were air stable and of appreciable yields. The ligands and complexes were characterized by simple analytical methods including melting point, Fourier transforms infrared spectroscopy, thermogravimetric analysis, elemental analysis, ^{1}H and ^{13}C nuclear magnetic resonance spectroscopy. The ligands and complexes all melted at vary narrow temperature ranges indicating that they were pure. The purity was further elucidated by the Elemental analysis which revealed a close agreement between the expected and actual elemental compositions as shown in Table 7.

Figure 27. Synthesized ligands and complexes(a) Na pipridinedithiocarbamate (b) (i) Na morpholinedithiocarbamate, (ii) Na piperidinedithiocarbamate and (c) Bi piperidinedithiocarbamate complex.

Table 7. Summary of physico-chemical properties of ligands and synthesized complexes. Theoretical values are given in brackets

Complex	Percentage Yield (%)	Melting point (^oC)	Elemental Composition (%) Found (Calc)				
			C	H	N	S	M
$[NaS_2CPip]\,2H_2O$	76.26	295	33.05 (32.86)	6.34 (6.43)	6.33 (6.39)	28.88 (29.24)	10.66 (10.48)
$[NaS_2CMor]\,2H_2O$	84.05	299	27.15 (27.14)	5.40 (5.47)	6.19 (6.33)	28.26 (28.98)	11.39 (10.39)
$[NaS_2CThq]4H_2O$	66.00	-	40.00 (39.59)	5.38 (5.98)	4.38 (4.62)	-	-
$[Bi(S_2CPip)_2NO_3]\,2H_2O$	62.00	279	24.37 (24.36)	3.24 (3.41)	7.10 (6.95)	-	-
$[Bi(S_2CThq)_2NO_3]$	68.00	270	34.80 (34.93)	2.86 (2.93)	6.06 (6.11)	-	-
$[Bi(S_2CPip)_3]$	92.00	230	44.01 (43.21)	3.78 (3.63)	5.13 (5.04)	-	-
$[Bi(S_2CThq)_3]$	66.00	-	30.28 (31.34)	4.01 (4.38)	5.81 (6.09)	-	-
$[Bi(S_2CMor)_3]$		269*					
$[Sb(S_2CPip)_3]3H_2O$	80.90	239	32.72 (32.92)	5.84 (5.53)	6.47 (6.40)	30.14 (29.30)	19.15 (18.54)
$[Sb(S_2CMorD)_3]$	85.86	265	30.12 (29.61)	3.63 (3.98)	6.95 (6.91)	30.92 (31.62)	21.30 (20.01)
$[Sb(S_2CDed)_3]$	76.55	-	32.28 (31.80)	5.84 (5.34)	7.39 (7.42)	33.93 (33.95)	21.75 (21.49)

*decomposed

3.1.1. Infrared spectroscopy

The dithiocarbamate ligands show two characteristic bands in the infrared region (Figure 28). The band due to ν(C-N) thiouride vibration which is observed in the region 1468–1485 cm^{-1} are intermediate to those reported for C-N single bonds (1250-1360 cm^{-1}) and C=N double bonds 1640-1690 cm^{-1}), suggesting partial double bond character and, therefore, partial delocalization of π −electron density within the dithiocarbamate functions[262].

The second single band which appears in the region 950–1000 cm^{-1} corresponds to ν(C–S) and indicates that the dithiocarbamate coordinates the metal ions through the sulfur atoms. It is used

to distinguish between monodentate and bidentate behaviour. In the case of monodentate dithiocarbamate, a doublet occurs around 1000 cm^{-1} separated by ≥20 cm^{-1} due to non-equivalence of two ν(C–S) stretching vibrations. For bidentate dithiocarbamate, a strong singlet is observed around 1000 cm^{-1} indicative of symmetrically bound dithiocarbamate moiety. This band in the spectra of the complexes is unsplit, which is an indication of the bidentate bonding nature of the ligand[141]. The M-S bond stretching vibrations appeared in the range 325-384 cm^{-1} [263]. This band was observed in the spectra of the bismuth piperidine and bismuth tetrahydroquinoline complexes analyzed on the Bruker Tensor 27 spectrophotometer at 365 and 388 cm^{-1}. However, due to the limitations of the other FT-IR instruments used to analyse the other complexes, the band was not observed. The bonding of sulfur to metal ion is expected to increase the contribution of the highly polar structure to

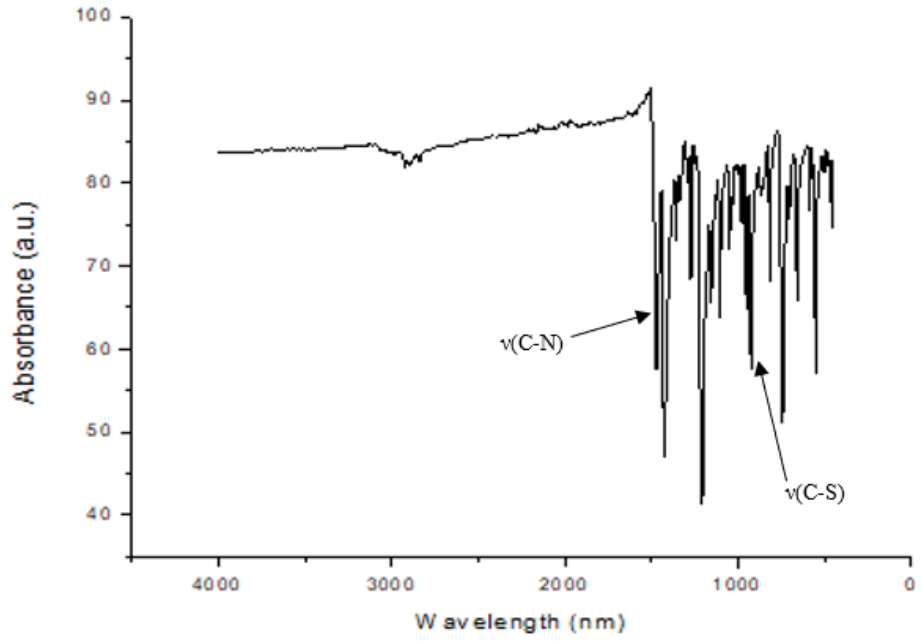

Figure 28. FT-IR spectrum of $[Bi(S_2CThq)_2]NO_3$.

the dithiocarbamates, resulting in a greater double bond character for the nitrogen to carbon bond and a greater single bond character for the carbon to sulfur bond. The ν(C=S) observed at 733-738 cm^{-1} was shifted to lower frequency in the complex. This behaviour signifies a decrease in the double bond character of the C=S bond which confirms the metal ions are

coordinated to sulfur[264]. The ligands showed broad bands around the 3300-3500 cm^{-1} indicating the presence of water molecules that is absent in the spectra of most of the complexes.

Table 8. Selected FT-IR adsorption frequencies for ligands and their respective complexes

Precursor	Wavelength (cm^{-1})			
	ν(C-N)	ν(C-S)	ν(O-H)	ν(M-S)
$[NaS_2CPip]\ 2H_2O$	1468	967	3377	-
$[Na(S_2CThq]\ 4H_2O$	1485	967	3324	-
$[NaS_2CMor]\ 2H_2O$	1463	976	3362	-
$[Na(S_2CDed]\ 3H_2O$	1476	996	3350	-
$[Bi(S_2CPip)_2NO_3]2H_2O$	1473	964	-	365
$[Bi(S_2CThq)_2NO_3]$	1475	960	-	388
$[Bi(S_2CPip)_3]$	1468	965	-	365
$[Bi(S_2CThq)_3]$	1485	952	-	-
$[Sb(S_2CPip)_3]\ 3H_2O$	1476	967	3437	-
$[Sb(S_2CMor)_3]$	1471	989	-	-
$[Sb(S_2CDed\ )_3]$	1490	987	-	-

3.1.2. ^{1}H and ^{13}C NMR spectroscopy

The ^{1}H and ^{13}C NMR spectra of the ligands and complexes were analyzed in deuterated acetone and water for the ligands and deuterated chloroform for the complexes. The resonance frequencies for the protons showed higher peaks attributed to the protons ortho to the carbon of the thioureide group. These protons are most deshielded due to the electronegativity of the nitrogen atom and the proximity to CS_2 group, while the lower resonance frequencies are due to meta and para carbons. The ^{13}C spectra of the ligand and complexes exhibit the N-CS_2 carbon signals at 197-205 ppm range, associated with the backbone carbon of dithiocarbamates. All the ^{1}H and ^{13}C resonance, as expected from the molecular structures were observed and assigned. The δ values are presented in Table 9 for ^{1}H and Table 10 for ^{13}C NMR respectively.

Table 9. ^{1}H NMR spectral data for dithiocarbamate ligands and complexes

Compound	Solvent	Chemical shift, δ(ppm)
$Na(S_2CMor)$	Acetone-d	4.31(t, J=4.9, 4H), 2-CH2, 3.55(t, J=4.9, 4H), 2-CH2
$Na(S_2CPip)$	D2O	4.27 (m, 4H),2-CH2, 1.65(dp, J=34.0, 6.1, 6H), 3-CH2
$Na(S_2CDed)$	D2O	4.02 (q, J=7.1, 4H), 2-CH2, 1.23 (t, J=7.1, 6H), 2-CH3
$[Sb(S_2CMor)_3]$	CDCl3	4.14(t, J=4.7, 12H), 6-CH2, 3.77(t, J=4.8, 12H), 6-CH2
$[Sb(S_2CDed)_3]$	CDCl3	3.87 (q, J=7.2, 12H), 6CH2, 1.29 (t, 18H)
$[Bi(S_2CPip)_3]3H_2O$	CDCl3	4.03 (t, J5.5, 12H) 1.79-1.66 (dp, 18H)
$[Bi(S_2CMor)_3]$	CDCl3	4.14(t, J=4.9, 12H), 6CH2, 3.77(t, J=4.9, 12H), 6CH2

Table 10. ^{13}C NMR spectral data for dithiocarbamate ligands and complexes

Compound	Solvent	Chemical shift, δ(ppm)
$Na(S_2CMor)$	Acetone-d	201.57 (NCS2), 66.26(CH2 ortho), 50.10 (CH2 meta)
$Na(S_2CPip)$	D2O	201.33 (NCS2), 50.03(CH2 ortho), 25.26 (CH2 meta), 24.25 (CH2 para)
$Na(S_2CDed)$	D2O	205 (NCS2), 48.75 (CH2) 11.30(CH3)
$[Sb(S_2CMor)_3]$	CDCl3	200.57 (NCS2), 66.28(CH2 ortho), 50.70 (CH2 meta)
$[Sb(S_2CDed)_3]$	CDCl3	199.02(NCS2), 48.19 (CH2), 12.18 (CH3)
$[Bi(S_2CPip)_3]3H_2O$	CDCl3	198.37 (NCS2), 52.03(CH2 ortho), 25.87 (CH2 meta), 23.95 (CH2 para)

3.1.3. Thermogravimetric analysis

The thermogram of $[Bi(S_2CPip)_2NO_3]$ showed a two-step weight loss pattern. The first step with weight losses of 57.5 % (calc: 55.6 %) at 248.4 ^{o}C corresponds to the loss of the organic moiety and sulfur atom. The second weight loss step at 436.9 ^{o}C corresponds to the loss of more sulfur atoms with mass losses of 7.5 % (calc: 7.3 %). The final residues of 35.0 % were close to the calculated values of 37.1% for Bi_2S_3. A similar decomposition pattern was recorded for $Bi(S_2CThq)_2.NO_3$, with the first weight loss of 65.0% (63.5 % calc) at 221.68 ^{o}C which was attributed to the loss of the organic moiety and a sulfur atom. The second decomposition step at 438.48 ^{o}C corresponding to loss of more sulfur occurred at a weight loss of 6.0 % (5.8 % calc). The final residue of 29.0% (30.7 % calc.) corresponded to Bi_2S_3 residue.

$[Bi(S_2CPip)_3]$ shows a two steps decomposition with the first step occurring at 184.24 °C corresponding to a loss of 5.02 % of the total mass. The second decomposition step at 322.24 °C accounts for 63.07 % of the total mass of the complex corresponded to the calculated value of 62.73 % for Bi_2S_3. The decomposition of $[Bi(S_2CThq)_3]$ proceeded through a single step, with a mass loss at 300.24 °C accounting for 69.17 % of the total mass of the complex.

This corresponded to a calculated 69.74 % Bi_2S_3 residue from the complex. These complexes are more thermally stable compared to the those prepared from $Bi(NO_3)_3.4H_2O$.

The thermogram of $Sb(S_2CPip)_3$ shows a two-step decomposition pattern. The first mass loss of 8.23 % (7.04 % calculated) at 105 °C corresponds to the loss of three H_2O molecules. The second mass loss of 76.47 % (73.40.13 % calculated) at 278 °C corresponds to the loss of the organic moiety and two S-atoms with the formation of Sb_2S_3 residue. $[Sb(S_2CMor)_3]$

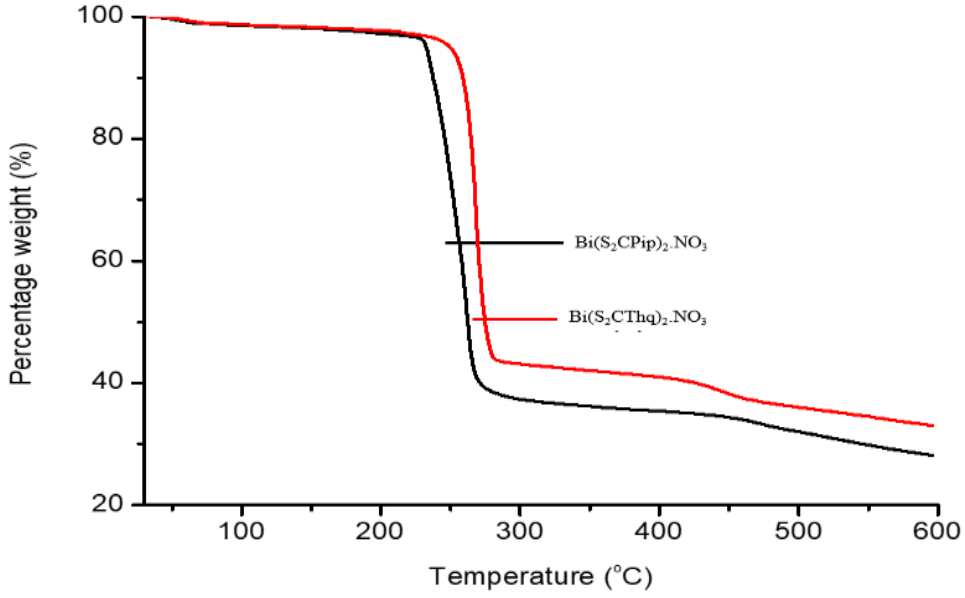

Figure 29. TGA plot of $[Bi(S_2CPip)_2]NO_3$ and $[Bi(S_2CThq)_2.]NO_3$.

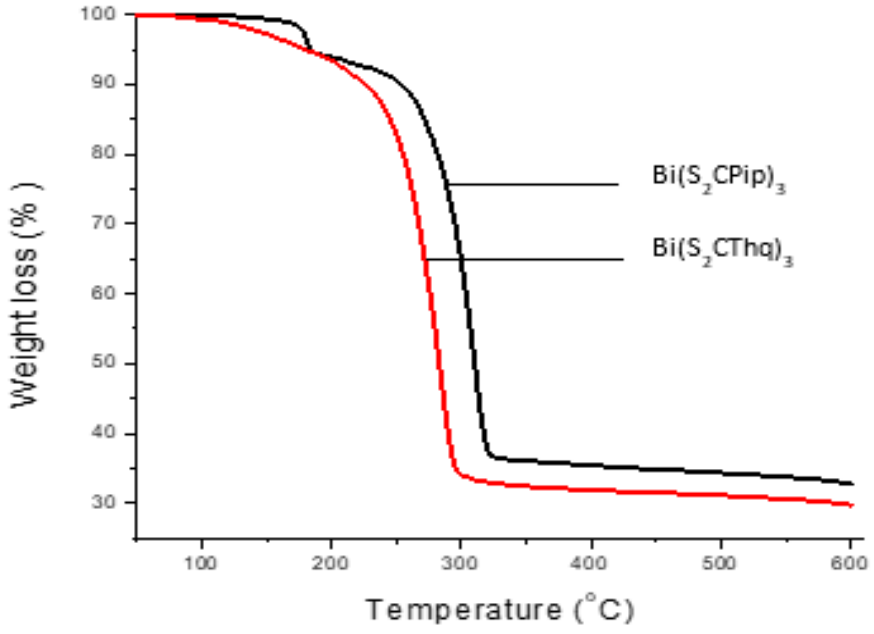

Figure 30. TGA plots of $[Bi(S_2CPip)_3]$ and $[Bi(S_2CThq)_3]$.

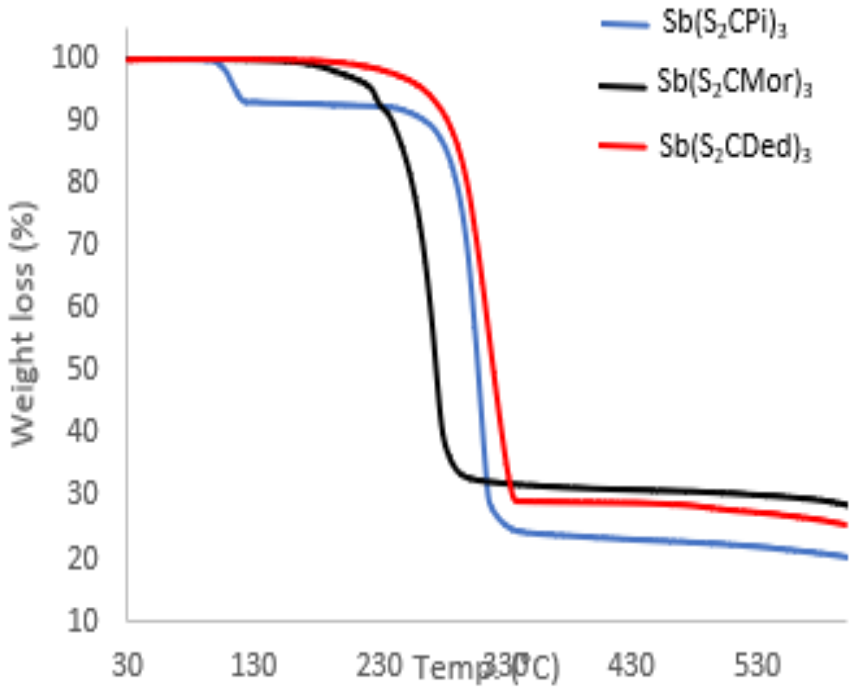

Figure 31. TGA plots of [Sb(S₂CPip)₃], [Bi(S₂CMor)₃] and [Bi(S₂CDed)₃].

and [Sb(S_2CDed)$_3$] show similar decomposition patterns, both undergoing a single step decomposition, with mass losses of 70.60 % (70.07 % calculated) at 268 °C and 72.17 % (72.09 % calculated) at 236 °C respectively attributed to the loss of organic moiety and forming residues of 29.40 % (29.93 % calculated) and 27.83 % (27.91 % calculated) both which corresponds to Sb_2S_3.

3.1.4. Single crystal X-ray structure determination

Flat, yellow, needle-like single crystals measuring about 0.35 x 0.20 x 0.15 mm for [Bi(S_2CPip)$_2$$NO_3$], 0.40 x 0.16 x 0.12 mm for [Bi(S_2CThq)$_2$$NO_3$] , 0.14 x 0.11 x 0.05 mm for [Bi(S_2CPip)$_3$]2$CHCl_3$ and 0.15 × 0.11 × 0.07 for [Bi(S_2CPip)$_3$] were mounted on the goniometer of a Bruker Apex II Duo CCD diffractometer by using a 500 mm-long needle mount and a 200 mm-diameter cryo-loop (MiTeGen), respectively, after initial suspension and selection in Paratone oil. Intensity data were collected with Mo_{Ka} radiation from an Incoatec microsource (IuS, Quazar mirror optics) at 100 K for [Bi(S_2CPip)$_2$$NO_3$] and 296 K for [Bi($S_2$CThq)$_2$$NO_3$]. The structures were solved by direct methods with SHELXS[running in Olex2. The structures were refined by least-squares methods (SHELXL). All non-H atoms were refined anisotropically ; H atoms were included in calculated positions, assigned isotropic thermal parameters (U_{iso} for atoms =1.2 U_{iso} for the attached C atom) and allowed to ride on their parent carbon atoms by using the standard HFIX parameters.

Table 11. Crystal data and structural refinement parameters for $[Bi(S_2CPip)_2NO_3]$

Compound	$[Bi(S_2CPip)_2NO_3]$
Empirical formula	$C_{12}H_{20}BiN_3O_3S_4$ (**1**)
Formula weight	591.53
Temperature (K)	100
Crystal system	Monoclinic
Space group	*P2₁/c*
Unit cell dimensions a, b, c (Å)	13.712 (7), 6.172 (3), c22.415 (11),
β (°)	102.351 (7)
Volume ($Å^3$)	1853.0 (16)
Z	4
Density calculated (g/cm^3)	2.120
Abs. coefficient (mm^{-1})	9.98
Crystal size (mm^3)	0.35 × 0.2 × 0.15
Theta range for data collection (°)	3.04 to 61.256
Reflections collected	67445
Independent reflections	5396 [R(int) = 0.0403]
Max. and min. transmission	0.746 and 0.421
Final R indices [I>2sigma(I)]	R1 = 0.0331
R indices (all data)	wR2 = 0.0725
Largest diff. peak and hole (e. $Å^{-3}$)	3.10 and -2

3.1.4.1. Structure of $[Bi(S_2CPip)_2NO_3]$

The low-temperature X-ray structure of catena-(m2-nitrato-O,O')bis(piperidinedithiocarbamato)bismuth(III) $[Bi(S_2CPip)_2NO_3]$ (Figure 32) is novel and reveals that the complex forms a 1D coordination polymer in the crystalline solid state. The asymmetric unit (ASU) which is also the polymer repeat unit, comprises a bismuth(III) ion, the two chelating dithiocarbamate ions, and the bridging nitrate ion. The mean Bi-S coordination bond length is 2.71(8) Å(Table 12) and compares favourably with the mean distance of 2.75(10) Å for the eight known X-ray structures of Bi(III) coordinated to dithiocarbamate ions of a similar structure[265–270]. The Bi-O bond lengths average 2.79(7) Å and are longer than those reported for the monodentate nitrato ligands (η^1-NO_3^-), for example, bis(nitrato)(methanol){N-phenylN'-[1-(pyrazin-2-yl)ethylidene]carbamohydrazonothioato}bismuth(III), which are distinctly non-bridging (Bi-O, 2.45(6) Å)[271].

Table 12. Selected bond lengths (Å) and angles (deg) for [Bi (S_2CPip)$_2NO_3$]

Bond	Length (Å)	Bond	Angle (°)
`Bi(1)-S(1)	2.6480 (14)	S(1)—Bi(1)—S(2)	66.25 (5)
Bi(1)—S(2)	2.7937 (16)	S(1)—Bi(1)—S(3)	78.32 (5)
Bi(1)—S(3)	2.7980 (14)	S(1)—Bi(1)—O(1)	137.69 (9)
Bi(1)—S(4)	2.6169 (14)	S(2)—Bi(1)—S(3)	134.65 (4)
Bi(1)—O(1)	2.723 (4)	S(4)—Bi(1)—S(1)	94.64 (5)
S(1)—C(1)	1.744 (5)	S(4)—Bi(1)—S(2)	88.27 (5)
S(2)—C(1)	1.727 (5)	S(4)—Bi(1)—S(3)	66.63 (4)
S(3)—C(7)	1.736 (5)	S(4)—Bi(1)—O(1)	72.54 (8)

The intrachelate S-Bi-S bond angles average 66.4(2)°, consistent with the mean of 65(2)° for related structures in the literature[265–270]. The coordination group of each BiS4 unit is completed by one O atom of a nitrate ion (Bi-O1 2.723(4) Å). However, the coordination geometry around Bi^{III} in [Bi(S_2CPip)$_2NO_3$] is distinctly irregular and defies typical classification. Each nitrate ion functions as a bridging ligand in the 1D chain by virtue of coordination of its second oxygen atom to the adjacent Bi^{III} ion in the lattice (Figure 32). The extended structure may thus be described as a 1D coordination polymer comprising alternating BiS4 repeat units and bridging nitrate ions. Interestingly, the inversion-related 1D polymer chain interacts significantly with its counterpart through weaker (longer) Bi···S interactions (3.31 Å). Note that the sum of the van der Waals radii[272] of Bi (2.54 Å) and S (1.89 Å) far exceeds the Bi···S interaction distance in [Bi(S_2CPip)$_2NO_3$], consistent with the interaction being effectively a dative covalent bond. This results in the formation of columns comprising symmetry-related pairs of 1D chains whose axes run parallel to one another but in opposite directions. The obtuse $O1^{i}$-Bi-$O3^{ii}$ bond angle of 125.2° (Figure 33) suggests,

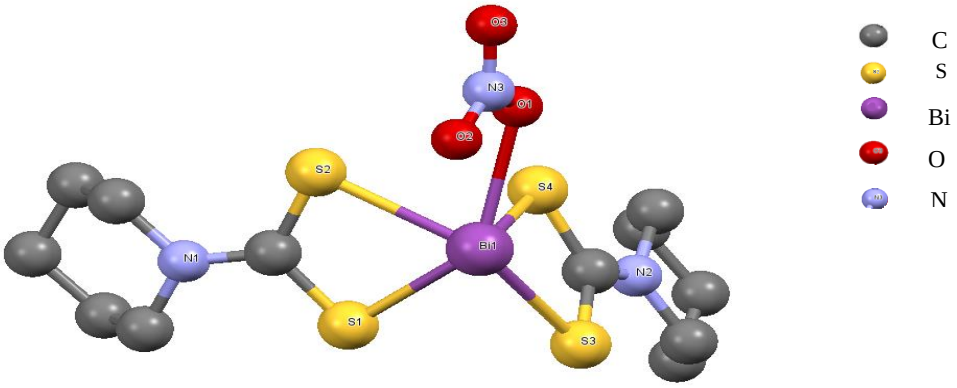

Figure 32. Thermal ellipsoid plot (50% probability surfaces) of the ASU of the single-crystal X-ray structure of catena-(μ2-nitrato-O,O')bis(piperidinedithiocarbamato)bismuth(III [Bi(S_2CPip)$_2NO_3$], determined at 100 K. Labels for all non-H atoms are shown.

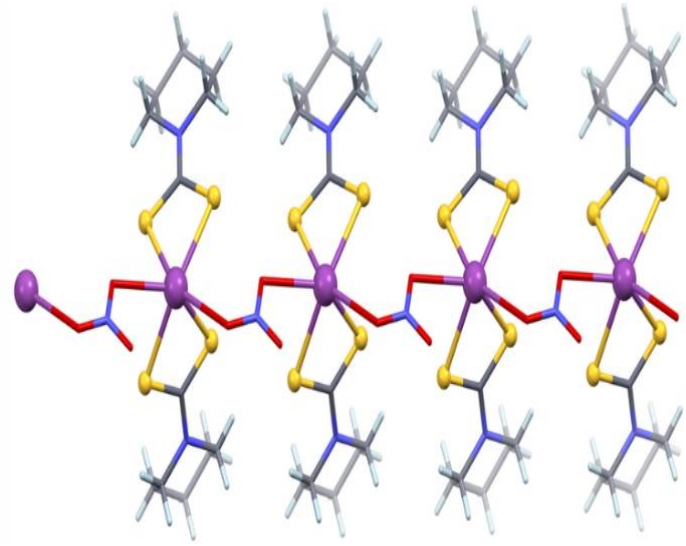

Figure 33. Illustration of the 1D coordination polymer formed by [Bi(S_2CPip)$_2$]NO_3). Heavy atoms are rendered as spheres; all other atoms are rendered as cylinders.

furthermore, that the Bi^{III} valence lone pair ($6s^2$) may be stereochemically active in [Bi(S_2CPip)$_2NO_3$], as in soft scorpionate[273] and tetraphenylimidodiphosphinate[274] chelates of Bi^{III}, and is most likely positioned midway between the two nitrate ion O donors (projecting approximately out of the plane of Figure 33 towards the reader). It is common to count the lone pair as occupying one coordination site at the metal centre for Bi^{III} coordination compounds[275]. Applying this principle here suggests that the Bi^{III} ions of [Bi(S_2CPip)$_2NO_3$] are in fact eight-coordinate. Interestingly, there are some well-characterised Bi^{III} coordination complexes in the literature with geometries that clearly indicate the presence of the stereochemically active $6s^2$ lone pair of Bi^{III}; however, its contribution to the irregular coordination geometry around the metal ion apparently not always recognised[276].

3.1.4.2. Structure of [Bi(S_2CThq)$_2NO_3$]

tetrakis(m-nitrato)tetrakis[bis(tetrahydroquinolinedithiocarbamato)bismuth(III)], [Bi(S_2CThq)$_2$]NO_3 is a centrosymmetric tetranuclear Bi^{III} cluster with bridging nitrate groups ($\mu_{1,}\eta_1$-NO_3, Figure 34). Because the geometry about the centre of gravity of the cluster is opened out by the bridging nitrate ions, no acutely short Bi···S intramolecular interactions are evident. The shortest of these, Bi1···$S1^i$ (3.650(1) Å, symmetry code i: -x, -y, -z), is probably too long to be considered even a weak dative covalent bond, despite the contact distance lying within the sum of the van der Waals radii of the bonded elements. Consistent with [Bi (S_2CPip)$_2NO_3$], the obtuse O1-Bi1-O4 bond angle of 133.7(1)° probably signals the presence of the stereochemically active nominally $6s^2$ lone pair of the Bi^{III} ion, which evidently projects in a direction that roughly bisects the O1-Bi1-O4 bond angle (inset

to Figure 34). If the $6s^2$ lone pair is treated as occupying one coordination site, each symmetry-unique Bi^{III} ion labelled Bi1 in $[Bi(S_2CThq)_2NO_3]$ should be regarded as seven-coordinate with the remaining coordination sites occupied by the four sulfur atoms of the bidentate 3,4-dihydroisoquinoline-2(1H)-carbodithioate ions and the two nitrate ion oxygen atoms O1 and O4.

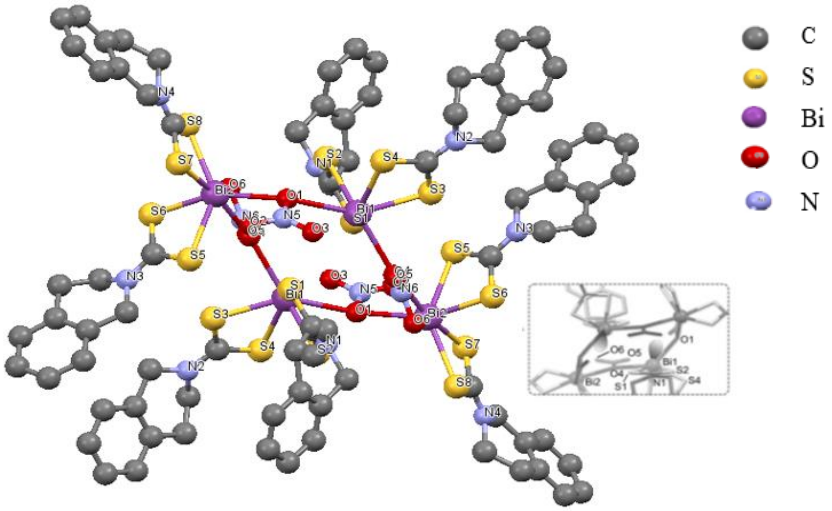

Figure 34. Partially labelled thermal ellipsoid plot (35% probability surfaces) and cylinder model of the X-ray structure of $[Bi(S_2CThq)_2NO_3]$. The inset depicts the possible orientations of the stereochemically active 6s2 lone pairs on two of the symmetry-related Bi^{III} ions.

Table 13. Crystal data and structural refinement parameters for $[Bi(S_2CThq)_2NO_3]$

Compound	$[Bi(S_2CThq)_2NO_3]$
Empirical formula	$2(C_{40}H_{40}Bi_2N_6O_6S_8)$
Formula weight	2750.44
Temperature (K)	296
Crystal system	Monoclinic
Space group	$P2_1/c$
Unit cell dimensions a, b, c (Å)	14.1529(16), 12.8531(15),
β (°)	26.270(3), 90.773(2)
Volume ($Å^3$)	4778.3 (9)
Z	2
Density calculated (g/cm^3)	1.912
Abs. coefficient (mm^{-1})	7.76
Crystal size (mm^3)	0.4 × 0.16 × 0.12
Theta range for data collection (°)	2.88 to 59.41
Reflections collected	114395
Independent reflections	12667 [R(int) = 0.0435]
Max. and min. transmission	0.746 and 0.226
Final R indices [I>2sigma(I)]	R1 = 0.0348
R indices (all data)	wR2 = 0.0955
Largest diff. peak and hole (e. $Å^{-3}$)	1.69 and -1.24

Table 14. Selected bond lengths (Å) and angles (deg) for [Bi(S_2CThq)$_2$$NO_3$]

Bond		Bond	
Bi(1)—S(1)	2.7734 (14)	Bi(1)—O(1)	2.694 (5)
Bi(1)—S(3)	2.6343 (15)	Bi(2)—S(5)	2.7313 (14)
Bi(1)—S(4)	2.7745 (16)	Bi(2)—S(7)	2.6174 (16)
Bi(1)—S(2)	2.6456 (14)	Bi(2)—S(6)	2.6026 (15)
Bi(1)—O(4)	2.725 (4)	Bi(2)—S(8)	2.8105 (15)
S(1)—Bi(1)—S(4)	137.35 (5)	O(1)—Bi(1)—S(1)	112.28 (11)
S(3)—Bi(1)—S(1)	86.28 (4)	O(1)—Bi(1)—S(4)	83.23 (12)
S(3)—Bi(1)—S(4)	66.27 (5)	S(5)—Bi(2)—O(4)	81.50 (9)
S(3)—Bi(1)—S(2)	95.02 (6)	S(7)—Bi(2)—O(4)	170.49 (9)
S(3)—Bi(1)—O(4)	76.40 (9)	O(4)—Bi(1)—S(1)	69.31 (9)
S(2)—Bi(1)—O(4)	134.67 (9)	O(4)—Bi(1)—S(4)	128.64 (9)
S(2)—Bi(1)—O(1)	71.53 (11)	Bi(1)—O(4)—Bi(2)	150.95 (15)

The coordination geometry around the second symmetryunique Bi^{III} ion, Bi2, is markedly different to that of Bi1. For example, the O1-Bi2-O4^{i} bond angle is 85.8(1)^{o} and the structural distortion around Bi2 appears to be less severe. The Bi-S bond lengths for [Bi(S_2CThq)$_2$$NO_3$]range from 2.603(1) to 2.810(2) Å (av 2.70(8) Å), in agreement with those of [Bi(S_2CPip)$_2$$NO_3$] and other similar Bi^{III} chelate complexes in the literature[265–270]. The Bi-O bond lengths average 2.74(4) Å, consistent with the bridging nature of the NO_3^- ions in the structure, as noted for [Bi(S_2CPip)$_2$$NO_3$]. The S-Bi-S bond angles for [Bi(S_2CThq)$_2$$NO_3$] average 66.3(5)^{o}, are similar to those of [Bi(S_2CPip)$_2$$NO_3$] and in close agreement with S-Bi-S intrachelate angles observed for related compounds in the CSD[265–270,277]. For both [Bi(S_2CPip)$_2$$NO_3$] and [Bi($S_2$CThq)$_2$$NO_3$], the C-S bond lengths are statistically equivalent, averaging 1.74(1) and 1.72(1) Å, respectively, consistent with the expected resonance-delocalized electronic structure of the dithiocarbamate ions in both compounds. The crystal packing in [Bi(S_2CThq)$_2$$NO_3$] is somewhat loose, presumably because of the inherent difficulty of efficiently packing the large tetranuclear cluster.

The total solvent-accessible volume per unit cell is 227.5 Å^3 (4.8%), and the total electron count within the void space is 19.9 electrons; this equates to two water molecules per unit cell. Due to their disorder, the water molecules occupying the two larger void spaces (2x25.7 Å^3, Appendix 4) were not discretely modelled during structure refinement. The smaller void spaces (2x25.7 Å^3, 4x10.1 Å^3, and 4x 8.2 Å^3) are vacant.

3.1.4.3. Structure of $[Bi(S_2CPip)_3]2CHCl_3$

The reaction between $Bi(Cl_3)_34H_2O$ and piperidinedithiocarbamate in water followed by recrystallisation from chloroform/ethanol afforded bis-chloroform solvate of tris(piperidinedithiocarbamato)bismuth(III) $[Bi(S_2CPip)_3]2CHCl_3$, space group *P*21/c). A thermal ellipsoid view of the crystal structure is shown in Figure 35. Table 15 page 80 shows the crystal data, data collection and structure refinement details for $[Bi(S_2CPip)_3]2CHCl_3$. The independent Bi^{III} ions are bound to six sulfur donor atoms, each from three chelating dithiocarbamate ligands. The coordination geometry about each Bi^{III} ion reflects an uneven distribution of the three chelate rings due to formation of a dimer comprising the two crystallographically independent molecules in the lattice (Figure 36). The dimer is stabilized by intramolecular Bi···S interactions with distances of 3.367(1) Å (Bi2···S4) and 3.402(1) Å (Bi1···S8); the B1-S4···Bi2-S8 and S4Bi1···S8-Bi2, dihedral angles of 45.53(3) and 45.46(3)Å, respectively, reflecting considerable twisting of the Bi_2S_2 core of the dimer. This leaves substantial room in the morpholinodithiocarbamate complex for a stereochemically active, nominally $6s^2$,

lone pair, which clearly culminates in a coordination number of eight for this complex. The twisted B i_2S_2 dimer core of $[Bi(S_2CPip)_3]2CHCl_3$, in contrast, appears to exclude space for t he $6s^2$ lone pair, such that the Bi^{III} ions are seven-coordinate. The Bi-S and S - Bi -S bond lengths and angles of $[Bi(S_2CPip)_3]2CHCl_3$ average 2.81(12) Å and 63.9(7) Å, respectively, which are normal for this class of com pounds (as discussed above).

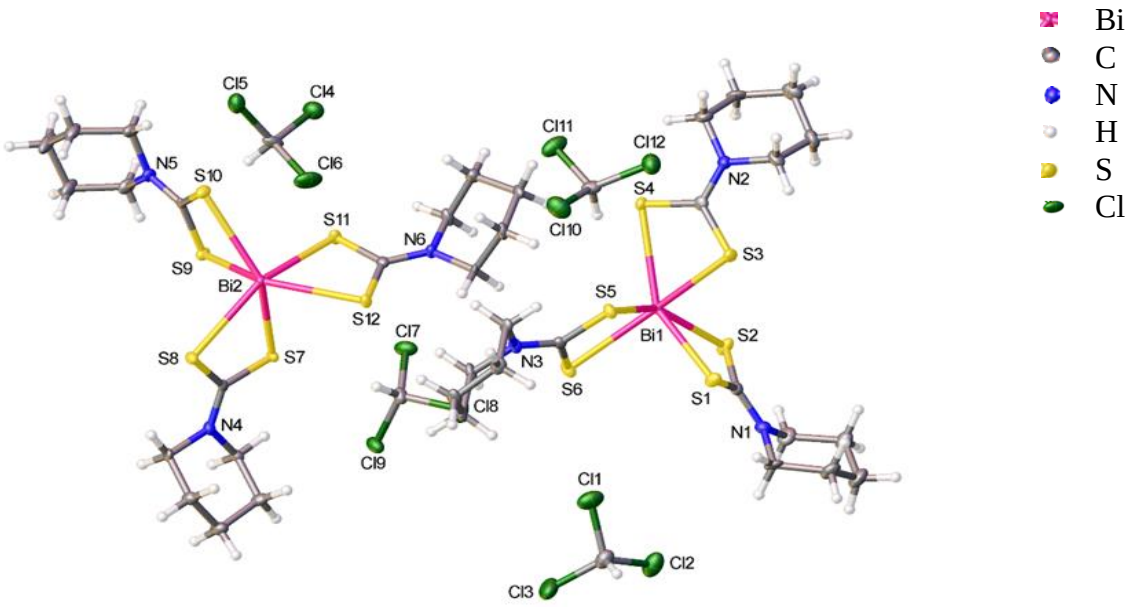

Figure 35. Thermal ellipsoid view (50% probability surfaces, OLEX2) of the low-temperature X-ray structure of $[Bi(S_2CPip)_3]2CHCl_3$. The asymmetric unit comprises two independent Bi(III) complexes with two chloroform solvate molecules per complex.

Table 15. Crystal data and structural refinement parameters for $[Bi(S_2CPip)_3]2CHCl_3$

Compound	$[Bi(S_2CPip)_3]2CHCl_3$
Empirical formula	$C_{20}\ H_{32}\ Bi\ Cl_6\ N_3\ S_6$ (3)
Formula weight	928.53
Temperature (K)	100(2)
Crystal system	Monoclinic
Space group	$P2_1/c$
Unit cell dimensions a, b, c (Å)	11.0038(3), 21.5260(5), 28.1836(79),
β (°)	4.047(2)
Volume ($Å^3$)	6659.1(3)
Z	8
Density calculated (g/cm^3)	1.852
Abs. coefficient (mm^{-1})	18.489
Crystal size (mm^3)	0.14 x 0.11 x 0.05
Theta range for data collection (°)	2.59 to 72.17
Reflections collected	39017
Independent reflections	12577 [R(int) = 0.0580]
Max. and min. transmission	0.4583 and 0.344759
Final R indices [I>2sigma(I)]	R1 = 0.0306
R indices (all data)	wR2 = 0.0662
Largest diff. peak and hole (e. $Å^{-3}$)	0.773 and -0.807

Table 16. Selected bond lengths (Å) and angles (deg) for $[Bi(S_2CPip)_3]2CHCl_3$

Bi1—S1	2.6666 (12)	S2—Bi1—S6	108.31 (3)
Bi1—S3	2.7024 (11)	S1—Bi1—S4	146.82 (3)
Bi1—S5	2.7160 (11)	S3—Bi1—S4	62.78 (3)
Bi1—S2	2.8671 (11)	S5—Bi1—S4	88.51 (3)
Bi1—S6	2.8960 (11)	S2—Bi1—S4	117.51 (3)
Bi1—S4	2.9966 (12)	S6—Bi1—S4	119.33 (3)
Bi2—S11	2.6715 (11)	S11—Bi2—S9	83.54 (3)
Bi2—S9	2.6743 (11)	S11—Bi2—S7	89.61 (3)
Bi2—S7	2.7083 (11)	S9—Bi2—S7	80.42 (3)
Bi2—S8	2.9010 (11)	S11—Bi2—S8	153.54 (3)
Bi2—S12	2.9366 (10)	S9—Bi2—S8	89.82 (3)
Bi2—S10	2.9703 (11)	S7—Bi2—S8	64.00 (3)
S1—Bi1—S3	84.23 (4)	S11—Bi2—S12	64.10 (3)
S1—Bi1—S5	86.50 (3)	S9—Bi2—S12	144.51 (3)
S3—Bi1—S5	87.59 (3)	S7—Bi2—S12	84.95 (3)
S1—Bi1—S2	64.88 (3)	S8—Bi2—S12	112.38 (3)
S3—Bi1—S2	93.30 (3)	S11—Bi2—S10	91.43 (3)
S5—Bi1—S2	151.08 (4)	S9—Bi2—S10	63.33 (3)
S1—Bi1—S6	87.50 (4)	S7—Bi2—S10	143.35 (3)

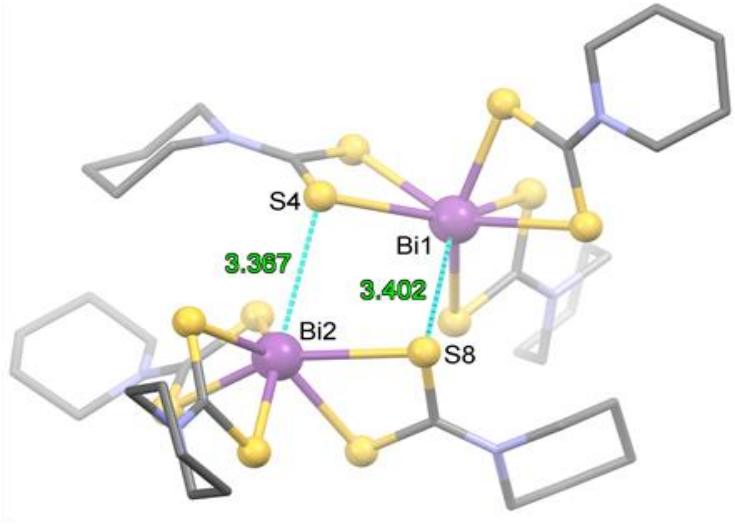

Figure 36. Illustration of the structure of the dimer formed by the two crystallographically independent molecules of complex [Bi(S_2CPip)$_3$]2CHCl$_3$. H atoms are omitted for clarity; selected atom labels and bond distances (Å) are given.

3.1.4.4. Structure of [Bi(S_2CPip)$_3$]

The complex tris-(piperidinyldithiocarbamato) bismuth(III) [Bi(S_2CPip)$_3$] not apparently been reported (Cambridge Structural Database (CSD)[278], though it is polymorphic with [Bi(S_2CPip)$_3$]2CHCl$_3$. The structure is orthorhombic, (*P*bca) with two enantiomorph molecules in the asymmetric unit and Z = 16 (Figure 37). Table 17 shows the crystal data and structural refinement parameters while key bond parameters describing its coordination sphere are summarized in Table 18 page 83. The data in Table 18 shows a few interesting trends. Firstly, for each coordinating ligand one bond is extended and the other is

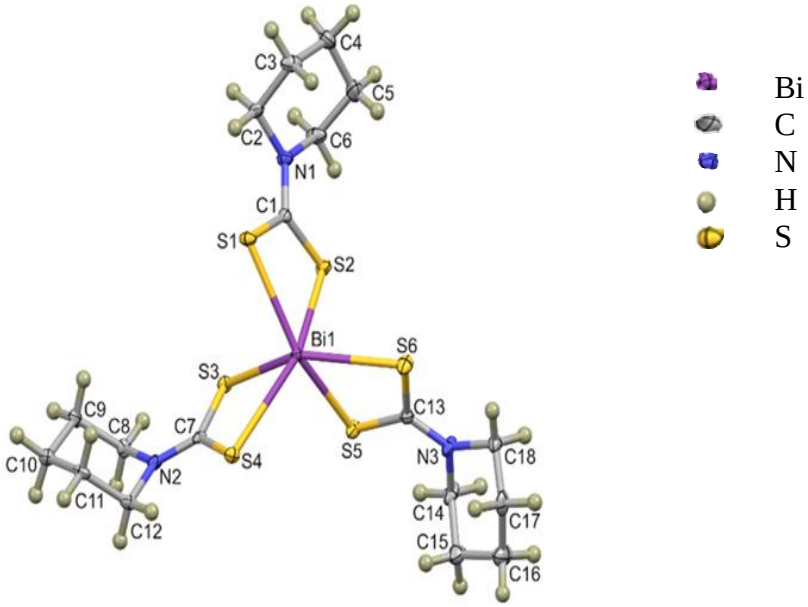

Figure 37. Thermal ellipsoid plot of a single molecule from the asymmetric unit of [Bi(S_2CPip)$_3$] showing the distorted octahedral coordination geometry.

compressed. This is surprising as measurement of the C–S bonds show they are all approximately equal ranging from 1.709 to 1.745 Å with a median of 1.727 Å. It would therefore be expected that the two coordinative bonds would be similar in length. A similar result is noted for related structures in the CSD[270,279]. The intraligand S–Bi–S bond angles are notably acute measuring ca. 63°. This is a consequence of the small ligand bite and the resulting four-atom coordination sphere. These bond lengths and bond angles are

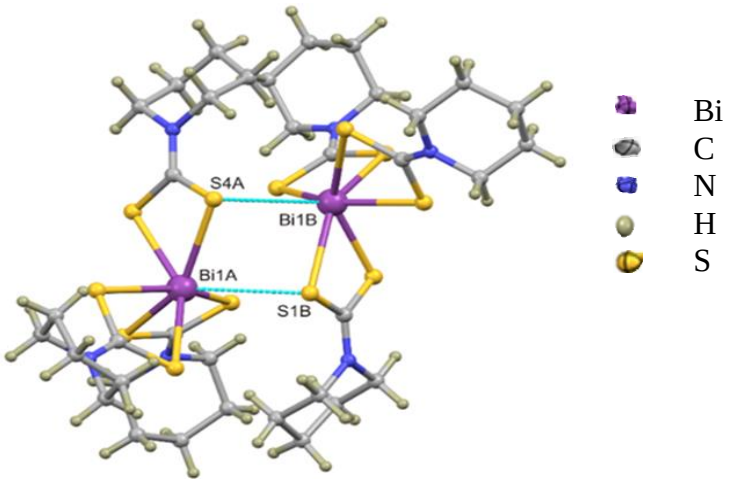

Figure 38. Dimeric nature of the asymmetric unit showing molecules linked by short (3.323(2) Å) intermolecular Bi···S interactions. Interactions are shown as dashed blue tubes, the interacting atoms are labelled.

comparable to that of $[Bi(S_2CPip)_3]2CHCl_3$ described above, and other related structures[270,279]. Although the molecule is formally six-coordinate with three bidentate ligands forming the coordination sphere, it does not show octahedral symmetry. The *trans* S1-Bi-S5 bond angles measure 150.87(4) and 148.66(4)° for molecules A and B of the asymmetric unit(Figure 38), respectively (indeed all of the trans S–Bi–S bond lengths measure <150°). This deviation from an ideal octahedral geometry is conventionally attributed to a stereochemically active lone pair on the Bi(III) ion. A similar coordination geometry is noted in $[Bi(S_2CPip)_3]2CHCl_3$ and related structures[270,279]. The two molecules in the asymmetric unit form a dimeric motif (Figure 38). These dimers are stabilised by Bi··S interactions. The mean Bi···S distance for the dimer is 3.323(2) Å, this is approximately 0.48 Å shorter than the sum of the van der Waals radii of the interacting atoms. Although the length of an interaction does not necessarily correlate with strength (due to packing constraints in the lattice), this separation is notably shorter than the sum of the van der Waals radii, suggesting an interaction. This notion is further supported by the widespread observation of such interactions in $[Bi(S_2CPip)_3]2CHCl_3$ and related structures [270,279].

Table 17. Crystal data and structure refinement details for [Bi(S$_2$CPip)$_3$]

Chemical formula	$C_{18}H_{30}BiN_3S_6$
Molar mass (g mol^{-1})	689.79
Crystal system, space group	Orthorhombic, *P*bca
Temperature (K)	100(2)
a, *b*, *c* (Å)	11.011(5), 27.789(5), 35.120(5)
α, β, γ (°)	90, 90, 90
V (Å^3)	10746(5)
Z	16
Radiation type	Mo Kα
μ (mm^{-1})	7.04
Crystal size (mm)	0.45 × 0.02 × 0.02
Absorption correction	Multi-scan, SADABS
T_{min}, T_{max}	0.546, 0.745
No. of measured, Independent and observed [$I > 2\sigma(I)$] reflections	134585, 10638, 9262
R_{int}	0.046
Refinement	
$R[F^2 > 2\sigma(F^2)]$, $wR(F^2)$, S	0.024, 0.074, 0.84
No. of reflections	10638
No. of parameters	505
H-atom treatment	H-atom parameters constrained
$\Delta\rho_{max}$, $\Delta\rho_{min}$ (e Å^{-3})	1.30, –0.83

Table 18. Selected bond lengths (Å) and angles (deg) for [Bi(S$_2$CPip)$_3$]

Bond	Length (Å)	Bond	Angle (°)
Bi1A–S1A	2.673(1)	S1A–Bi1A–S2A	63.77(3)
Bi1A–S2A	2.946(1)	S3A–Bi1A–S4A	63.37(3)
Bi1A–S3A	2.707(1)	S5A–Bi1A–S6A	64.12(3)
Bi1A–S4A	2.937(1)	S1A–Bi1A–S5A	150.87(4)
Bi1A–S5A	2.921(1)	S2A–Bi1A–S3A	146.53(4)
Bi1A–S6A	2.680(1)	S4A–Bi1A–S6A	149.80(4)
Bi1B–S1B	2.951(1)	S1B–Bi1B–S2B	63.69(3)
Bi1B–S2B	2.674(1)	S3B–Bi1B–S4B	63.16(3)
Bi1B–S3B	2.657(1)	S5B–Bi1B–S6B	63.35(3)
Bi1B–S4B	2.986(1)	S1B–Bi1B–S5B	148.66(4)
Bi1B–S5B	2.664(1)	S2B–Bi1B–S4B	147.76(4)
Bi1B–S6B	2.984(1)	S3B–Bi1B–S6B	147.79(4)

3.1.4.5. Structure of $[Sb(S_2CPip)_3]$

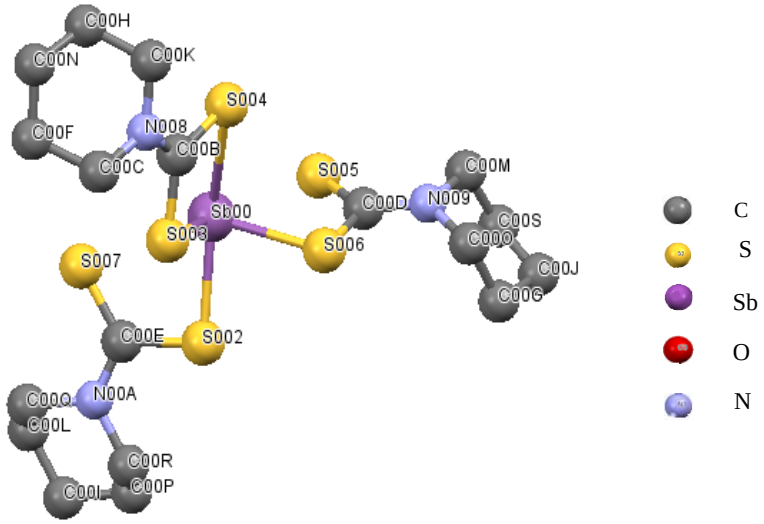

Figure 39. Single X-ray crystal structure of tris(piperidinedithiocarbamato)antimony (III) complex $[Sb(S_2CPip)_3]$.

Yellow rhomboidal crystals of $[Sb(S_2CPip)_3]$ complexes were grown in chloroform and suitable crystals of dimensions 0.15 × 0.11 × 0.07 mm was selected. X-ray data was collected on a dual source Rigaku FR-X rotating anode diffractometer using CuK_α wavelength at 150K and reduced using CrysAlisPro 171.39.30c. Absorption correction was performed using empirical methods (SCALE3 ABSPACK) based upon symmetry-equivalent reflections combined with measurements at different azimuthal angles. The structure was solved and refined using Shelx-2016 implemented through Olex2 v1.2.9. The low temperature structure of tris(piperidinedithiocarbamato)antimony(III) $[Sb(S_2CPip)_3]$(Figure 39), crystalizes into a four coordinate Sb complex surrounded by three piperidinedithiocarbate groups. One group is coordinated to the central Sb in a bidentate manner while the other two are coordinated through single s-atoms forming a distorted octahedral structure of a monoclinic crystal system and space group $P2_1/c$. A similar structure was reported by Lui and Tiekink[280] at a much higher temperature of 223 K. The mean Sb-S coordination bond length is 2.62(17) Å (Table 20 page 85) which favourably compares with the mean distance of 2.61(16) Å for the reported structure. The mean interchealate S-Sb-S bond angles is 93.60(29) compared to 92.32(29) of the reported structure.

Table 19. Crystal data and structure refinement details for [Sb(S_2CPip)$_3$]

Compound	[Sb(S_2CPip)$_3$]
Empirical formula	$C_{18}H_{30}BiN_3S_6Sb$
Formula weight (g mol^{-1})	602.56
Temperature (K)	150
Crystal system	Monoclinic
Space group	*P2$_1$/c*
Unit cell dimensions a, b, c (Å)	17.6331 (3), 11.84939 (19), 12.12535 (19),
β (°)	107.4771 (17)
Volume (Å^3)	2416.54 (17)
Z	4
Density calculated (Mg/cm^3)	1.656
Abs. coefficient (mm^{-1})	13.98
Crystal size (mm^3)	0.15 × 0.11 × 0.07
Theta range for data collection (˚)	2.6 to 68.2
Reflections collected	16485
Independent reflections	4406 [R(int) = 0.019]
Max. and min. transmission	1.000 and 0.705
Final R indices [I>2sigma(I)]	R1 = 0.043
R indices (all data)	wR2 = 1.06
Largest diff. peak and hole (e. Å^{-3})	0.31 and -0.30

Table 20. Selected bond lengths (Å) and angles (deg) for [Sb(S_2CPip)$_3$]

Bond	Length (Å)	Bond	Angle (°)
Sb00—S002	2.5330 (4)	S002—Sb00—S003	88.093 (14)
Sb00—S003	2.5358 (4)	S002—Sb00—S004	150.697 (13)
Sb00—S004	2.8918 (5)	S002—Sb00—S006	82.089 (14)
Sb00—S006	2.5337 (4)	S003—Sb00—S004	65.889 (12)
S002—C00E	1.7584 (17)	S006—Sb00—S003	90.215 (14)
S003—C00B	1.7549 (16)	S006—Sb00—S004	84.658 (14)
S004—C00B	1.7027 (16)	S005—C00D—S006	119.59 (10)
S005—C00D	1.6955 (16)	S007—C00E—S002	119.05 (10)
S006—C00D	1.7535 (17)	S004—C00B—S003	118.19 (10)
S007—C00E	1.7007 (17)		

3.1.4.6. Structure of [Sb(S_2CDed)$_3$]

Yellow crystals of [Sb(S_2CDed)$_3$] complexes were grown in chloroform and suitable crystals of dimensions 0.22 × 0.2 × 0.2 mm was selected. X-ray data for the complex was collected at a temperature of 150 K using a using Mo-Kα radiation on a RIgaku-Oxford FR-

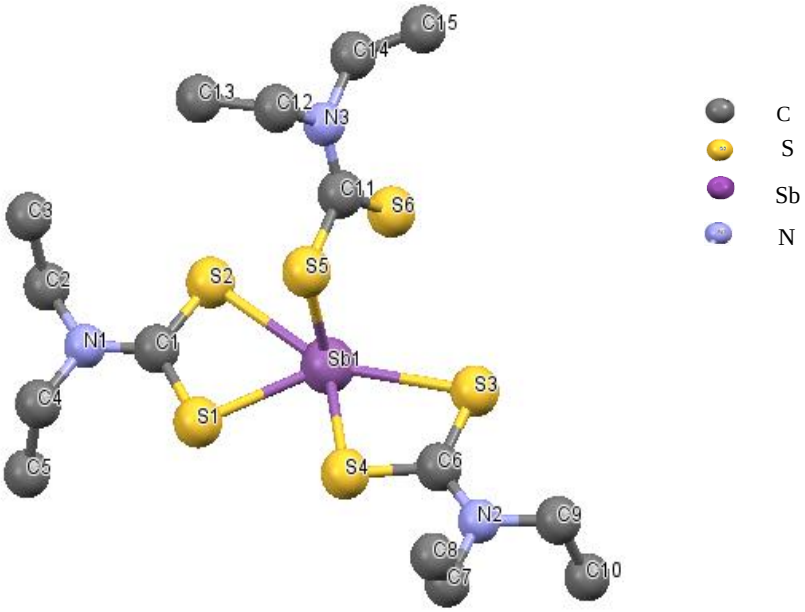

Figure 40. Single X-ray crystal structure of (tris(N,N-diethyldithiocarbamato)antimony(III))) complex [Sb(S_2CDed)$_3$].

X diffractometer, equipped with HP6000HE detector and an Oxford Cryosystems Cobra nitrogen flow gas system. Data were measured processed and reduced using CrysAlisPro suite of programs. Absorption correction was performed using empirical methods with spherical harmonics, implemented in the SCALE3 ABSPACK scaling algorithm.Crystal structures were solved and refined against all F2 values using the SHELX and Olex 2 suite of programs.All the atoms were refined anisotropically. Hydrogen atoms were placed in calculated positions, refined using idealized geometries (riding model) and assigned fixed isotropic displacement parametersTris(N,N-diethyldithiocarbamato)antimony(III)) [Sb(S_2CDed)$_3$] complex have been reported[281]. The structure is a five coordinate complex in which the Sb atom is coordinated to five S-atoms of three diethyldithiocarbamato groups (Figure 40). Two groups in an almost planar fashion are coordinated in a bidentate manner, and the third group is perpendicular to the plane and coordinated only through 1 S atom, forming a five coordinate structure of a monoclinic crystal system of space group $P2_1/c$. For the bidentate coordinated ligands, one of the Sb-S bonds is long, averaging 28.78(4) Å while the other is shorter, averaging 26.25(9) Å (Table 22). The five coordinated C-S bonds are approaximately equal in length, ranging from 1.7007 to 1.7566 Å. The uncoordinated Sb-S and C-S bonds are relatively shorter compared to others (2.4835 (Å and 1.6920 Å respectively). Similar trend in results is seen in the reported structure[281].

Table 21. Crystal data and structure refinement details for [Sb(S$_2$CDed)$_3$]

Chemical formula	$C_{15}H_{30}N_3S_6Sb$
M_r (g mol^{-1})	566.53
Crystal system, space group	Monoclinic, $P2_1/c$
Temperature (K)	150
a, b, c (Å)	12.4427 (2), 13.5147 (2), 14.6373
β (°)	(2)
V (Å$_3$)	99.915 (1)
Z	2424.64 (6)
	4
Radiation type	Mo $K\alpha$
μ (mm^{-1})	1.66
Crystal size (mm)	0.22 × 0.2 × 0.2
T_{min}, T_{max}	0.638, 1.000
No. of measured, independent and observed [$I > 2\sigma(I)$] reflections	25360, 5750, 5316
R_{int}	0.018
(sin θ/λ)$_{max}$ (Å^{-1})	0.674
$R[F_2 > 2\sigma(F_2)]$, $wR(F_2)$,	S 0.015, 0.036, 1.04
No. of reflections	5750
No. of parameters	232

Table 22. Selected bond lengths (Å) and angles (deg) for [Sb(S$_2$CDed)$_3$]

Bond	Length (Å)	Bond	Angle (°)
Sb1—S5	2.4835 (3)	S5—Sb1—S1	88.735 (11)
Sb1—S1	2.6321 (3)	S5—Sb1—S2	82.463 (10)
Sb1—S2	2.8783 (3)	S5—Sb1—S3	92.048 (11)
Sb1—S3	2.8777 (3)	S5—Sb1—S4	89.174 (11)
Sb1—S4	2.6183 (3)	S1—Sb1—S2	64.732 (10)
S5—C11	1.7566 (13)	S1—Sb1—S3	138.821 (10)
S1—C1	1.7354 (13)	S3—Sb1—S2	155.972 (10)
S2—C1	1.7092 (13)	S4—Sb1—S1	74.129 (10)
S3—C6	1.7007 (14)	S4—Sb1—S2	138.086 (10)
S4—C6	1.7398 (13)	S4—Sb1—S3	64.720 (10)
S6—C11	1.6920 (13)	S3—C6—S4	118.04 (7)

3.1.4.7. Structure of [Sb(S_2CMor)$_3$]

Yellow crystals of [Sb(S_2CMor)$_3$] complexes were grown in chloroform and suitable crystals of dimensions 0.15 × 0.06 × 0.06 mm was selected. Data were measured processed and reduced using CrysAlisPro suite of programs. Absorption correction was performed using empirical methods with spherical harmonics, implemented in the SCALE3 ABSPACK scaling algorithm. Crystal structures were solved and refined against all F^2 values using the SHELX and Olex 2 suite of programs.All the atoms were refined anisotropically. Hydrogen atoms were placed in calculated positions, refined using idealized geometries (riding model) and assigned fixed isotropic displacement parameters

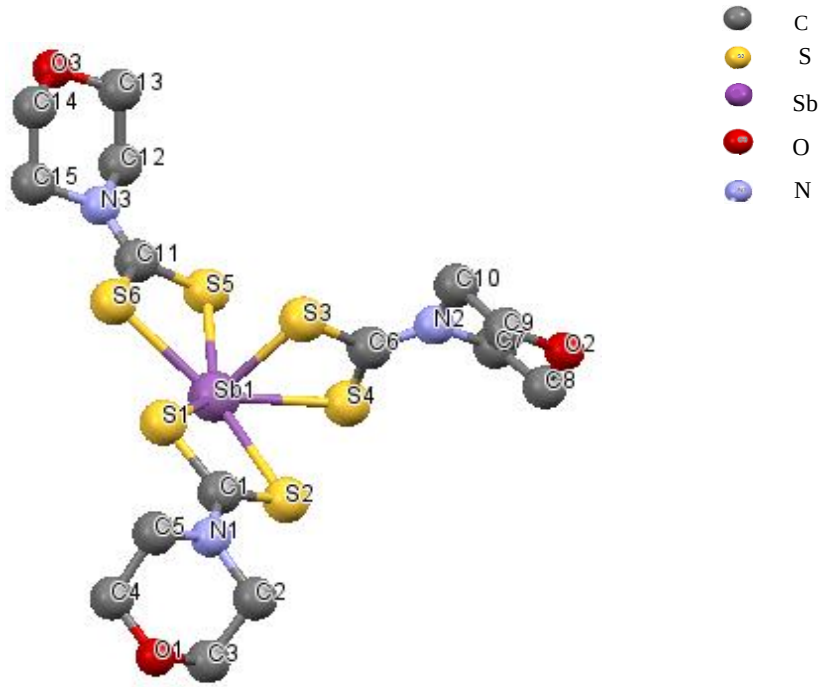

Figure 41. Single X-ray crystal structure of tris(morpholinedithiocarbamato)antimony(III) complex [Sb(S_2CMor)$_3$].

Tris(morpholinedithiocarbamato)antimony(III) [Sb(S_2CMor)$_3$] crystalizes into a monoclinic crystal system of space group $P2_1/c$. The Sb^{III} ion is coordinated by the six S atoms belonging to three morpholinedithiocarboxylate ligands (Figure 41). The resulting SbS6 coordination polyhedron approximates to a distorted pentagonal pyramid due to the stereochemical activity of the lone pair of electron on Sb^{III}, with atoms Sb1, S1, S2—S6 at the base of the pyramid and S3 in the apical position. A similar structure was reported by Zhai *et al* [282] at 298 K. The mean Sb-S bond length 2.71(13) (Table 24) is similar to that obtained by Zhai *et al*. however, [Sb(S_2CMor)$_3$] was obtained at a lower temperatur of 150 K.

Table 23. Crystal data and structure refinement details for [Sb(S$_2$CMor)$_3$]

Chemical formula	C15H24N3O3S6Sb
Mr (g mol^{-1})	608.48
Crystal system, space Group	Monoclinic, P21/c
Temperature (K)	150
a, b, c (Å)	12.7679 (3), 19.9695 (5), 8.9439 (2)
β (°)	93.858 (2)
V (Å^3)	2275.27 (10)
Z	4
Radiation type	Mo Kα
μ (mm^{-1})	1.79
Crystal size (mm)	0.15 × 0.06 × 0.06
Tmin, Tmax	0.739, 0.748
No. of measured, independent and observed [I > 2σ(I)] reflections	13617, 5265, 4372
Rint	0.035
(sin θ/λ)max (Å^{-1})	0.682
Refinement	
R[F2 > 2σ(F2)], wR(F^2),	S 0.027, 0.063, 1.02
No. of reflections	5265
No. of parameters	253
Δρmax, Δρmin (e Å^{-3})	0.75, −0.95

Table 24. Selected bond parameters describing the coordination sphere of [Sb(S$_2$CMor)$_3$]

Bond	Length (Å)	Bond	Angle (°)
Sb1—S1	2.6868 (6)	S1—Sb1—S2	64.544 (17)
Sb1—S3	2.4746 (6)	S1—Sb1—S5	137.675 (18)
Sb1—S2	2.8307 (6)	S1—Sb1—S4	136.310 (18)
Sb1—S5	2.7962 (6)	S1—Sb1—S6	73.566 (17)
Sb1—S4	2.8195 (6)	S3—Sb1—S1	88.47 (2)
Sb1—S6	2.6937 (6)	S3—Sb1—S2	83.797 (19)
S1—C1	1.734 (2)	S3—Sb1—S5	82.82 (2)
S3—C6	1.747 (2)	S3—Sb1—S4	67.554 (19)
S2—C1	1.713 (2)	S3—Sb1—S6	89.45 (2)
S5—C11	1.706 (2)	S5—Sb1—S2	153.399 (18)
S4—C6	1.695 (3)	S5—Sb1—S4	77.118 (17)
S6—C11	1.728 (2)	S4—Sb1—S2	76.542 (17)
		S6—Sb1—S2	137.668 (18)
		S6—Sb1—S5	65.048 (17)
		S6—Sb1—S4	137.991 (18)

3.2. Syntheses and characterization of Bi_2S_3 nanoparticles

Bi_2S_3, is a semiconductor material with a direct energy band gap between 1.3 and 1.7 eV. [156]. It has a high figure of merit (ZT) value, with a large absorption coefficient and high energy conversion efficiency. It is widely used as a thermo electronic-cooling material and has applications in photodiode array and photovoltaic converters. The structure of

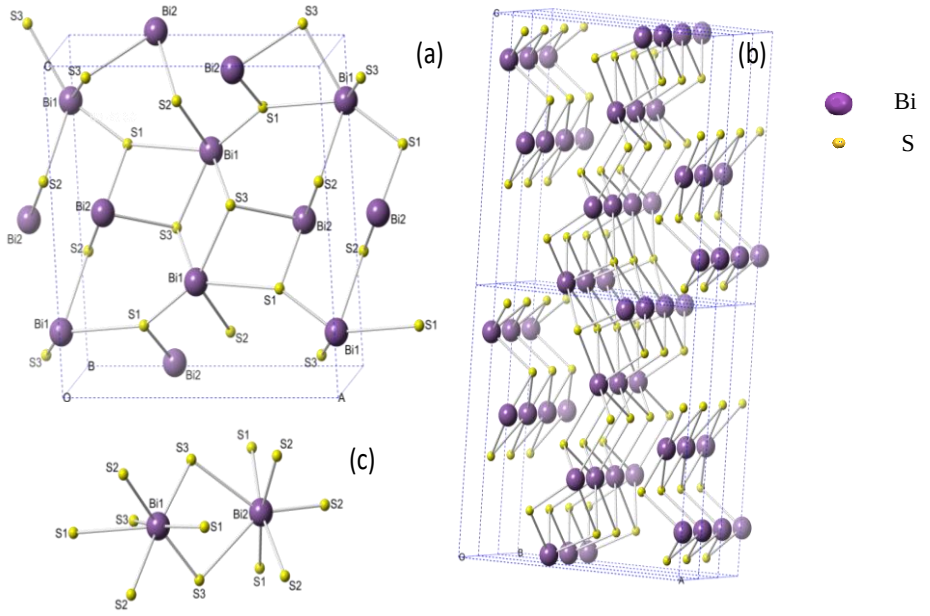

Figure 42. (a) Bismuthinite unit cell with Bi-S separations up to 4 Å, (b) with shorter Bi-S contacts to emphasise layers and (c) coordination sphere at Bi(1) and Bi(2).

bismuthinite (Figure 42) is quite complex involving two different bismuth centres with differing coordination numbers, in which Bi_2S_3 units form infinite chains parallel to the *c* axis connected via weaker van der Waals interactions between the unit cells[21]. Conventionally these structures of bismuth have been described in terms of a stereochemically active lone pair based on a VSEPR approach. It is orthorhombic with a *P*nma lattice.

3.2.1. Syntheses and characterization of Bi_2S_3 nanoparticles from non-green capping agents

Thermal decomposition using single source precursors (SSP) has been widely used as a simple, easy controlled, low cost and effective heating method for the synthesis of high quality nanomaterials[52–55,142]

Solvents such as ethylene glycol, diethylene glycol, thioglycolic acid have been favourable for the formation of Bi_2S_3 nanorods and were acting as the oriented growth reactant[16,18,20,27]. Stavila *et al*. [46] reported the decomposition of bismuth (III) thiourea and thiosemicarbazide complexes in different solvents at 120 ^oC. The addition of a small amount of dodecanethiol

or octadecanethiol resulted in the formation of Bi_2S_3 nanorods up to several nanometers in length, with better crystallinity.

3.2.1.1. DDA capped Bi_2S_3

The bismuth dithiocarbamato complexes used in this work are easily synthesized with cost-effective starting materials and reaction protocols; they are stable to air and moisture. The

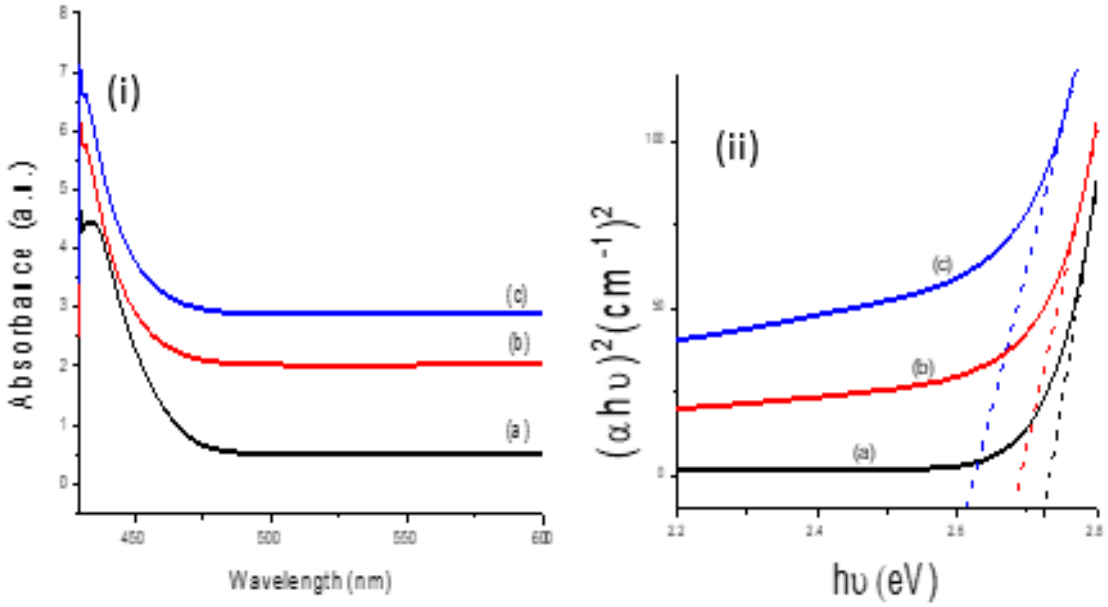

Figure 43. (i)UV visible absorption spectra of DDA capped Bi_2S_3 nanorods from $[Bi(S_2CPip)_2NO_3]$ at (a) 190 °C (b) 230 °C and (c) 270 °C (ii) Tauc plot.

ligands and the complexes were obtained in good yields, and microanalysis confirmed their purity. The complexes are yellow microcrystalline powders soluble in most organic solvents.

The absorption spectra of the DDA capped Bi_2S_3 particles synthesized from $[Bi(S_2CPip)_2NO_3]$ in 3.0 g of OLA at 190, 230, and 270 °C are shown in Figure 43 (i). The subtle differences observed on the band profiles of the optical spectra is associated with different particle size distributions for the Bi_2S_3 particles, depending on the temperature used in their preparation. The energy band edge of the synthesized nanorods is blue shifted compared to the bulk. Figure 43(ii) shows the corresponding *tauc* plot for the absorption. Bands edges with corresponding values of 2.72, 2.69 and 2.61 eV were observed for particles synthesized at 190, 230 and 270 °C, respectively, compared to that of 1.3 eV (950 nm) for bulk Bi_2S_3, characteristic of quantum confinement. The slight red shift in the optical absorption associated with increasing reaction temperature indicates an increase in mean particle size with increasing temperature, suggesting a growth process driven by the reduction of the total surface energy of the particulates (Ostwald ripening).

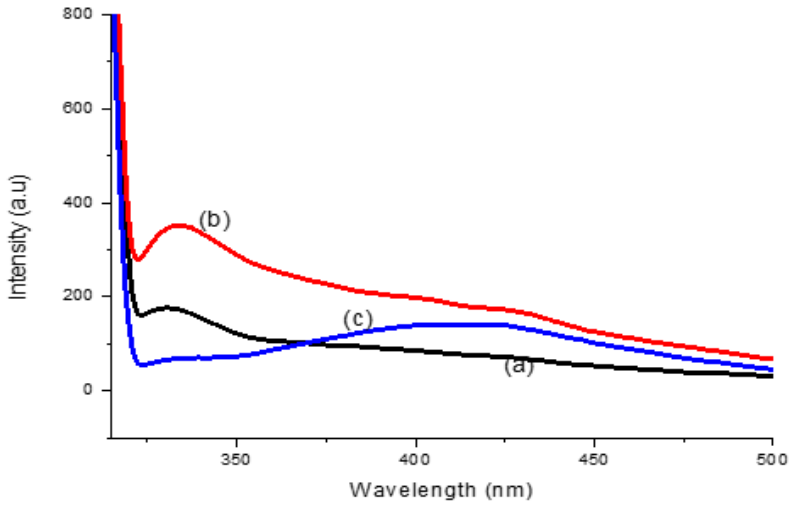

Figure 44. Photoluminescence spectra of DDA capped Bi_2S_3 nanorods from [Bi $(S_2CPip)_2NO_3$] at (a) 190 °C (b) 230 °C and (c) 270 °C.

The photoluminescence spectra of the nanoparticles show emission peaks at 330, 335 and 415 nm for samples prepared at 190, 230, and 270 ^oC respectively (Figure 44).

The morphology of the Bi_2S_3 nanostructures was determined by TEM. Figure 45a–c shows the images of Bi_2S_3 nanocrystals prepared from [$Bi(S_2CPip)_2NO_3$] in DDA (C10) at 190, 230 and 270 ^oC. Bi_2S_3 nanorods were obtained at the three different reaction temperatures using DDA as capping agent. Similar results were obtained by Xie *et al*. by thermolysing bismuth tris(diethyldithiocarbamate) complexes at temperatures ranging from 115 to 170 ^oC[19]. The formation of nanorods at all the temperatures could be attributed to the preferential

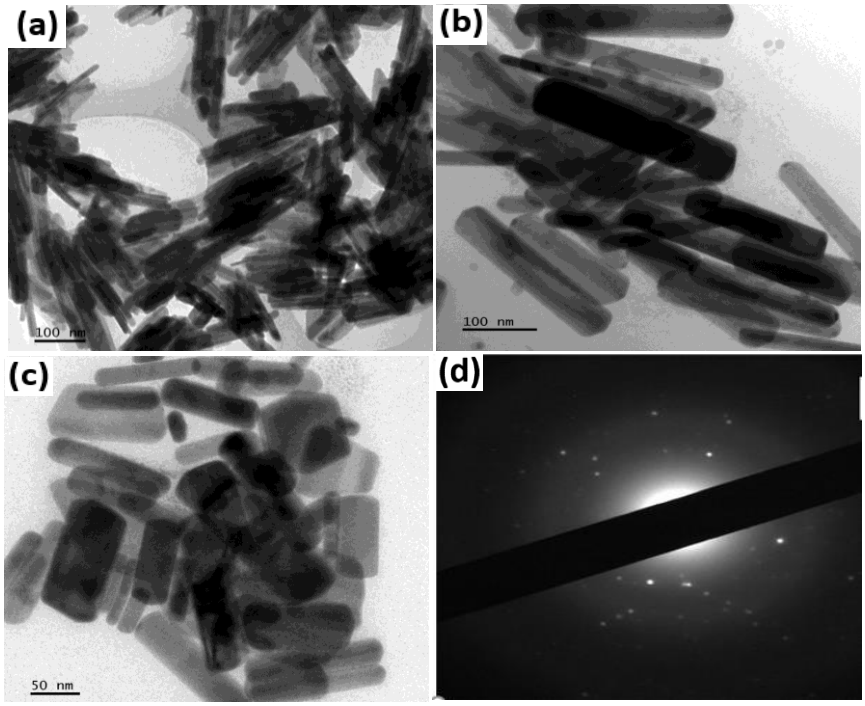

Figure 45. TEM images of Bi_2S_3 nanoparticles synthesized from [$Bi(S_2CPip)_2NO_3$]) in DDA at (a) 190 °C (b) 230 °C and (c) 270 °C, (d) corresponding SAED pattern.

bonding of the surfactant to the surface of the nanocrystals. Preferential adsorption to the (100) rather than the (111) crystal planes allows an ordered anisotropic growth to produce nanorods[283]. Another reason for anisotropic growth is the intrinsic anisotropy of the crystal system. Bi_2S_3 has the tendency to grow in the [100] direction, along the c-axis forming 1-dimensional structures. For the DDA capped Bi_2S_3 nanostructures at 190 °C, rods with average lengths of 161.9±0.3 nm and average breadth of 16.5±0.1 nm were obtained (Figure 45). When the temperature was raised to 230 °C, a slight increase in the breadth and decrease in the length of the rods was observed as nanorods with lengths of 154.7±0.4 nm and breadths of 22.7±0.1 nm was formed. At 270 °C, the aspect ratio of the rods decreased further. Table 25 summarizes the length and breadth of the nanorods prepared from $[Bi(S_2CPip)_2NO_3]$ in the different capping agents. It has been reported that at elevated temperatures the influence of the surface ligands is minimized through the dynamic bonding nature of the ligands, and as a result particle revert to thermodynamically stable morphologies such as spheres. Low-temperature routes offer more flexibility in shape control, and anisotropic-shaped particles such as rods are formed through judicious use of surfactants. The darker opaque regions of the rods observed in the TEM images indicate an overlap or stacking of rods[53]. The selected-area electron diffraction (SAED) pattern confirmed the formation of a highly crystalline single Bi_2S_3 nanorod (Figure. 45d).

Table 25. Lengths and breadths of the Bi_2S_3 nanorods synthesized from $[Bi(S_2CPip)_2NO_3]$ at various reaction parameters.

Capping group	Temp (°C)	Length (nm)	Breadth (nm)	Aspect ratio (±0.1), (L/B)
DDA	190	161.9±0.3	16.5±0.1	9.8
DDA	230	154.7±0.4	22.7±0.1	6.8
DDA	270	76.1±0.5	23.9±0.1	3.2
HDA	190	236.9±0.2	20.3±0.1	11.7
HDA	230	217.2±0.1	24.4±0.1	8.9
HDA	270	193.5±0.	49.9±0.2	3.9
OLA	190	252.6±0.2	31.2±0.1	8.1
OLA	230	221.5±0.2	36.4±0.2	6.1
OLA	270	194.2±0.4	38.3±0.2	5.1
TOPO	190	182.3±0.2	29.2±0.2	6.2
TOPO	230	106.6±0.1	42.8±0.2	2.4
TOPO	270	95.4±0.3	44.1±0.2	2.1

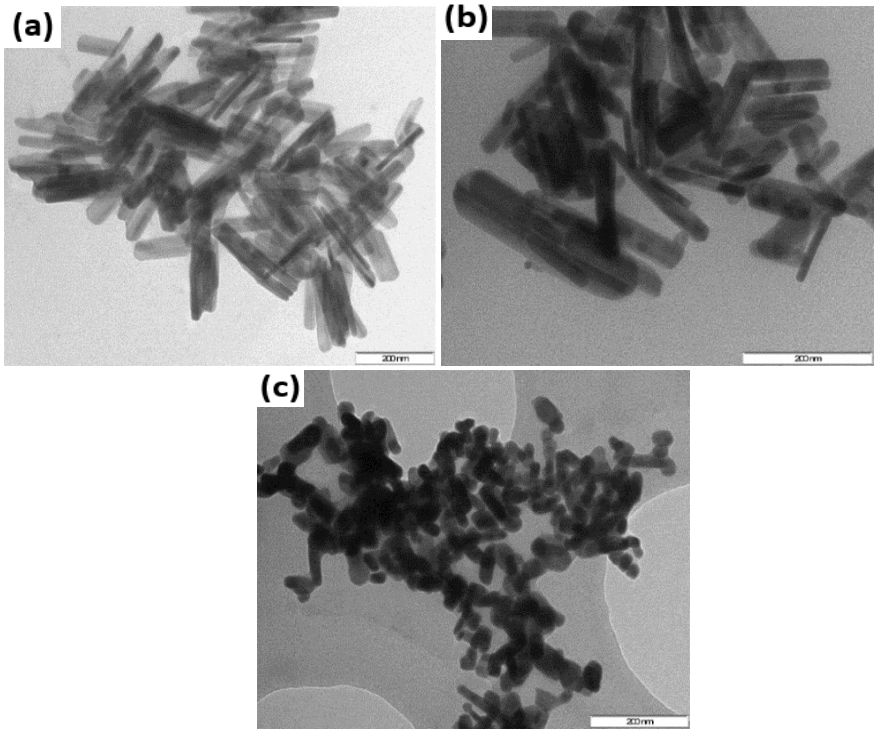

Figure 46. TEM images of Bi_2S_3 nanoparticles synthesized from $[Bi(S_2CThq)_2NO_3]$ in DDA at (a) 190 °C (b) 230 °C and (c) 270 °C, (d) corresponding SAED pattern.

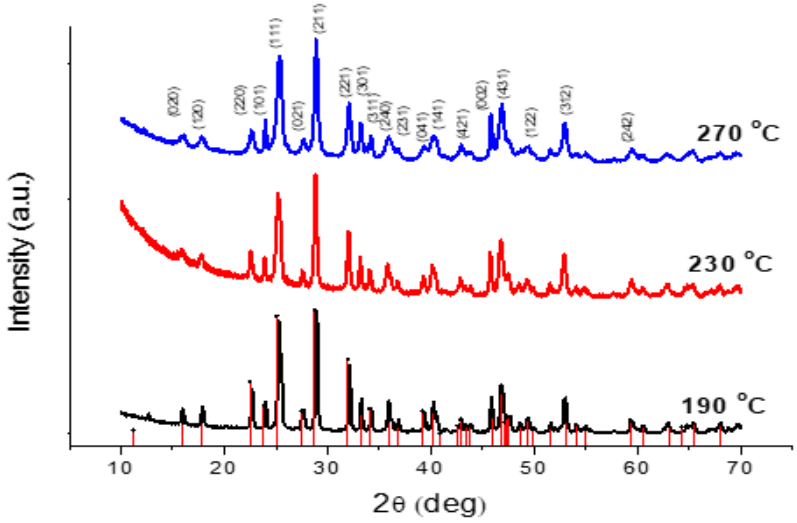

Figure 47. Powder X-ray patterns of Bi_2S_3 nanorods synthesized in DDA from $[Bi(S_2CThq)_2NO_3]$ at 190°C, 230 °C and 270 °C.

When $[Bi(S_2CThq)_2NO_3]$ was thermolyzed in DDA a similar trend in results were obtained. 1-dimensional nanorods with aspect ratios which decrease with increase in temperature were produced as shown in Figure 46. However, there was a greater reduction in aspect ratios as nanorods of length 151.2±31.5 nm and breadth of 32.6±7.5 nm was obtained at 190 °C ,

and at 230 °C rods of length 100.4±31.0 nm and breadth of 9. 6±3.7 nm, and at 270 °C rods of length 38.2±15.3 nm and breadth of 5.6±1.7 nm was obtained. This difference in aspect ratio shows that the nature of the precursor has an influence on the morphology of the synthesized particles.

Powder X-ray diffraction studies performed on the materials obtained from $[Bi(S_2CThq)_2NO_3]$ in DDA at 190 °C, 230 °C and 270 °C are shown in Figure 47. The (020), (120), (220), (101), (111), (021), (211), (002), (240) planes correspond to the pure orthorhombic phase of Bi_2S_3 (ICCD # 03-065-2435). The strong and sharp reflection peaks in the XRD patterns is an indication that the Bi_2S_3 nanorods were crystalline. No unindexed peak was present in the spectra, which was an indication of pure bismuthinite phase under synthetic condition. The XRD results are in agreement with reported data for Bi_2S_3 nanostructures synthesized from dithiocarbamate precursors using other methods of synthesis[13, 14,16].

3.2.1.2. HDA capped Bi_2S_3

The carbon chain length of the amine was increased from C10 (DDA) to C16 (HDA). Figures 48 and 49 show Bi_2S_3 nanorods prepared from $[Bi(S_2CPip)_2NO_3]$ and

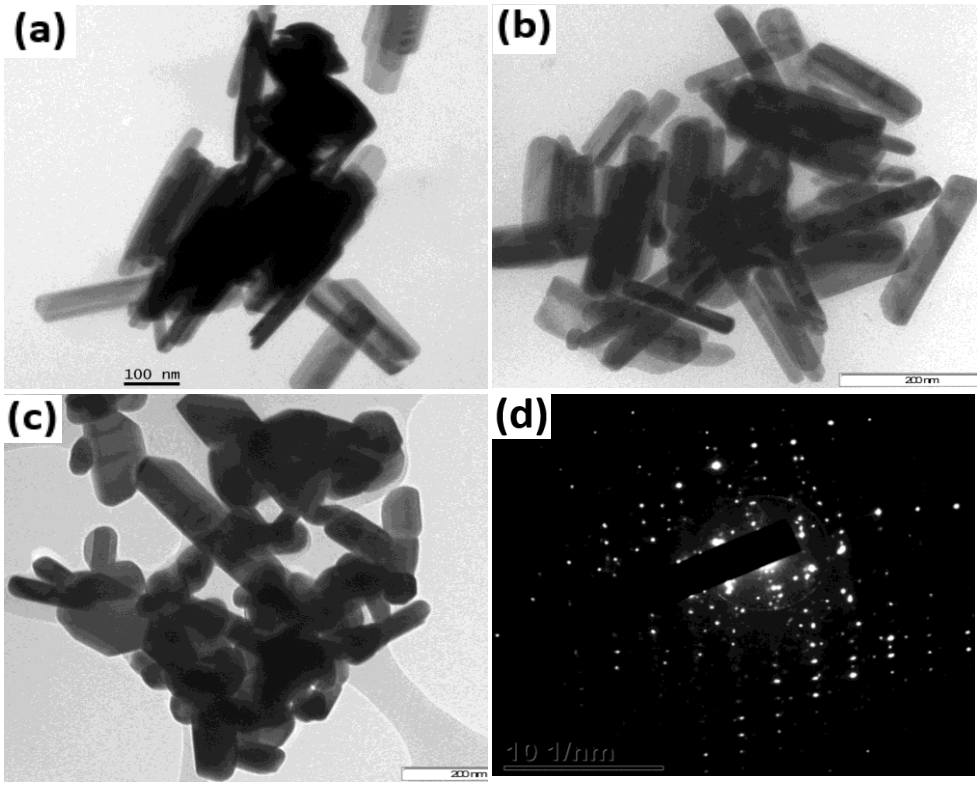

Figure 48. TEM images Bi_2S_3 synthesized from $[Bi(S_2CPip)_2NO_3]$ complex in HDA for 2hrs at (a) 190, (b) 230 and (c) 270 °C and d) SAED pattern.

[$Bi(S_2CThq)_2NO_3$] respectively in HDA at the same reaction temperatures (190, 230 and 270 ^oC). A similar trend in the Bi_2S_3 morphology was observed. There was a reduction in the aspect ratio of the rods with increase in reaction temperature as revealed by TEM. Table 25 on page 93 shows that the rods synthesized from HDA are longer than those synthesized from DDA under the same reaction conditions. The HDA-capped Bi_2S_3 nanorods obtained at 190 ^oC appeared to be agglomerated, and stacked. At 230 ^oC there was formation of distinct nanorods of equal lengths with some degree of alignment in the nanorods prepared from [$Bi(S_2CThq)_2NO_3$] (Figure 49b). Larger and more irregularly shaped particles were obtained at 270 ^oC (Figure 48c and 49c). The surface morphology of the rods synthesized from [$Bi(S_2CThq)_2NO_3$] at 270 ^oC was studied using scanning electron microscopy (SEM). The SEM image (Figure 49d) shows the irregularly shaped nanorods with a wide particle size distribution, similar to the result obtained from TEM. The energy dispersive x-ray (EDX) analysis of the rods reveals a 38.7 % Bi and 61.3 % S, giving atomic ratio of 1.89 : 3.00 close to the 2.00 : 3.00 atomic ratio of Bi_2S_3. The HRTEM image of a single nanorod synthesized at 230 ^oC from [$Bi(S_2CThq)_2NO_3$] (Figure 49e) showed distinct lattice fringes with a calculated lattice spacing of 3.60 Å, close to the 3.55 Å d-spacing of the (111) lattice plane. The corresponding Specific area electron diffraction (SAED) patterns (Figure 48 (d) and 49(f)) reveal the typical crystalline nature of the as prepared samples. This highly crystalline nature of the samples was confirmed by the strong and sharp reflection peaks in the XRD patterns (Figure 50). These peaks were indexed to the pure bismuthnite (ICCD # 03-065-2435) as no unindexed peak was present in the spectra.

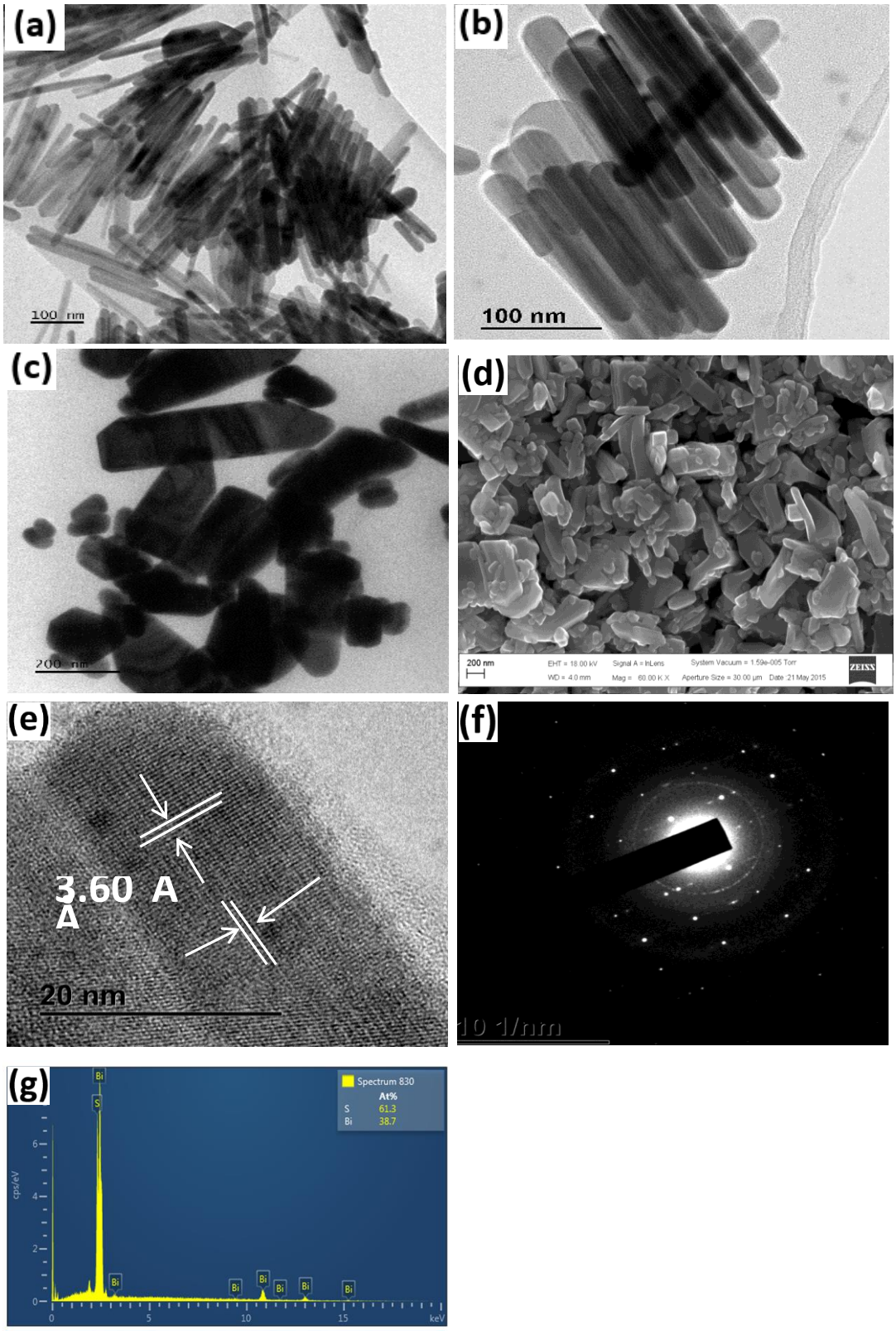

Figure 49. TEM images of Bi_2S_3 nanoparticles synthesized from $[Bi(S_2CThq)_2NO_3]$ complex in HDA for 2 hrs at (a) 190 °C, (b) 230 °C and (c) 270 °C. And its HRTEM and SAED images (d) SEM micrograph of the rods synthesized at 270 °C (e) HRTEM of single rod synthesized at 270 °C (f) corresponding SAED pattern (g) EDX spectrum of rods synthesized at 270 °C.

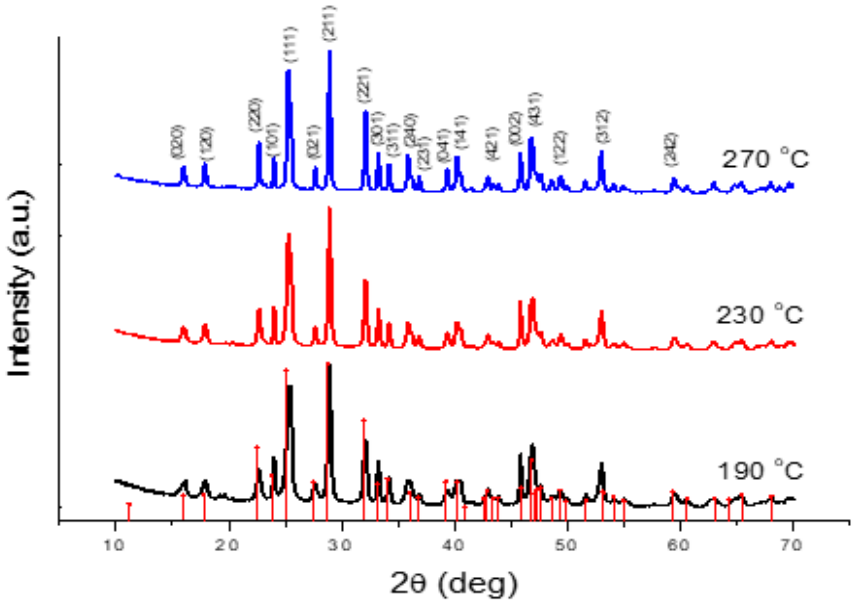

Figure 50. Powder X-ray patterns of Bi_2S_3 nanorods synthesized in HDA from $[Bi(S_2CPip)_2NO_3]$ at 190°C, 230 °C and 270 °C.

3.2.1.3. OLA capped Bi_2S_3

The absorption spectra of the OLA capped Bi_2S_3 particles synthesized from $[Bi(S_2CPip)_2NO_3]$ in 3.0 g of OLA at 190, 230, and 270 °C shows a strong blueshift in the adsorption band edge compared to the bulk Bi_2S_3. Figure 51(i) shows the UV/Visible spectra, and Figure 51(ii) the corresponding tauc plot for the absorption. Bands edges with corresponding values of 3.1, 3.09 and 2.9 eV were observed for particles synthesized at 190, 230 and 270 °C, respectively. This blue shift in band edge compared to the 1.7 eV for the bulk Bi_2S_3 is a characteristic of quantum confinement in the nanocrystals. The slight red shift in the optical absorption associated with increasing reaction temperature indicates an increase in mean particle size with increasing temperature. The photoluminescence spectra of the nanorod show emission peaks at 325 nm for the nanorods synthesized at all three temperatures. Powder x-ray diffraction shows the formation of pure orthorhombic Bi_2S_3 lattice (Figure 51(iii)).

The OLA-capped Bi_2S_3 nanostructures obtained from $[Bi(S_2CPip)_2NO_3]$ at 190 °C are rods of equal sizes and shape(Figure 52), with average length of 252.6±0.2 nm and average breadth of 31.2±0.1 nm (Table 25 page 93). When the temperature was raised to 230 °C, a slight diversity in the dispersity of the rods is observed, with an increase in breadth of

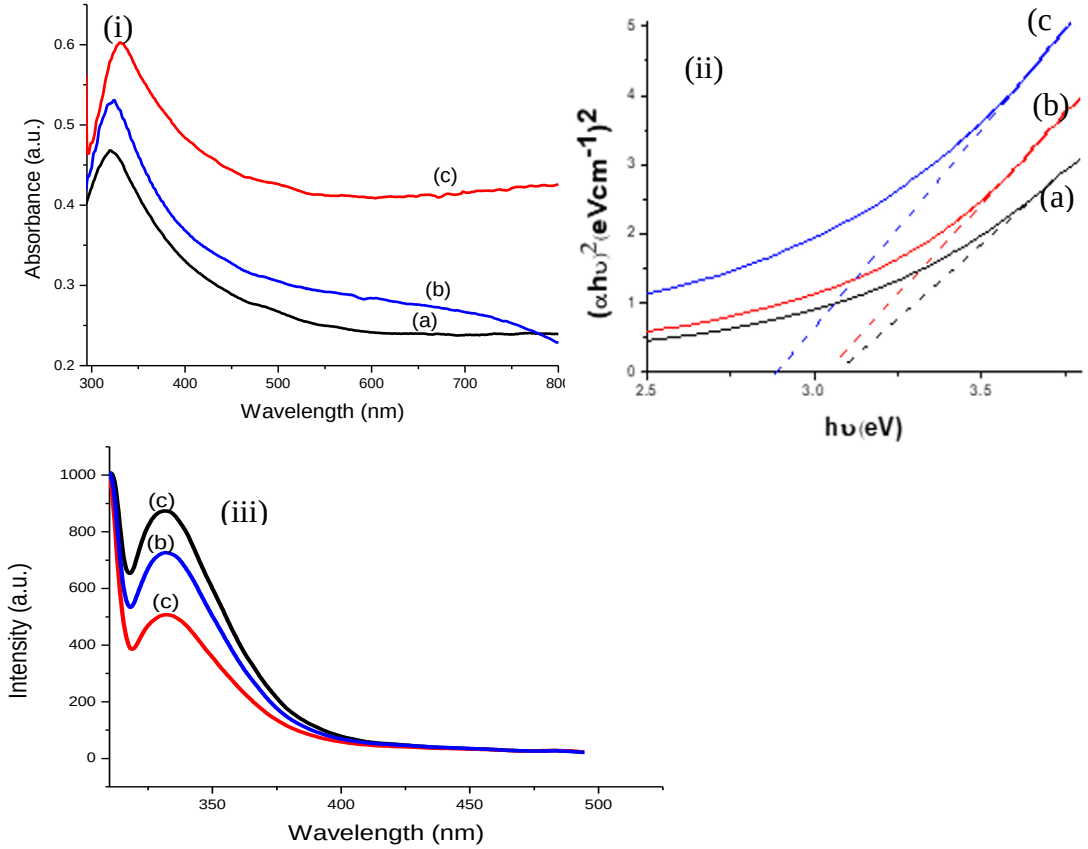

Figure 51. (i)UV/visible absorption spectra of OLA capped Bi_2S_3 nanorods from $[Bi(S_2CPip)_2NO_3]$ at (a) 190 °C (b) 230 °C and (c) 270 °C (ii) Tauc plot (iii) Photoluminescence spectra.

36.4±0.2 nm and decrease in the length 221.5±0.2 nm. At 270 °C, agglomerated polydisperse rods with further decrease in length of 194.2±0.4 nm and an increase in breath of 38.3±0.2 nm are obtained. The darker, opaque regions of the rods observed in the TEM images indicate overlap or stacking of rods (Figure 52). The polydispersity of the rods synthesized at 270 °C was further elucidated by the Surface morphological evaluation using SEM (Figure 52(d)). The nature of the rods were confirmed by p-XRD analysis. Figure 53 shows peaks indexed to the pure bismuthinite (ICCD # 03-065-2435) in all three temperatures. No unindexed peak was present, indicating that the samples were pure Bi_2S_3. A close similarity in morphology is observed in the nanorods synthesized from $[Bi(S_2CPip)_2NO_3]$ to those obtained from $[Bi(S_2CThq)_2NO_3]$. However, more polydisperse rods were obtained at all three temperatures when $[Bi(S_2CThq)_2NO_3]$ was thermolized (Figure 54 a-c). The energy dispersive X-ray (EDX) analysis of the rods synthesized at 270 °C showed peaks for Bi and S, with a 39.2 % Bi and 60.8 % S, giving an atomic ratio of 1.93: 3.00 close to the 2 : 3 Bi:S atomic ratio in Bi_2S_3 (Figure 54 e).

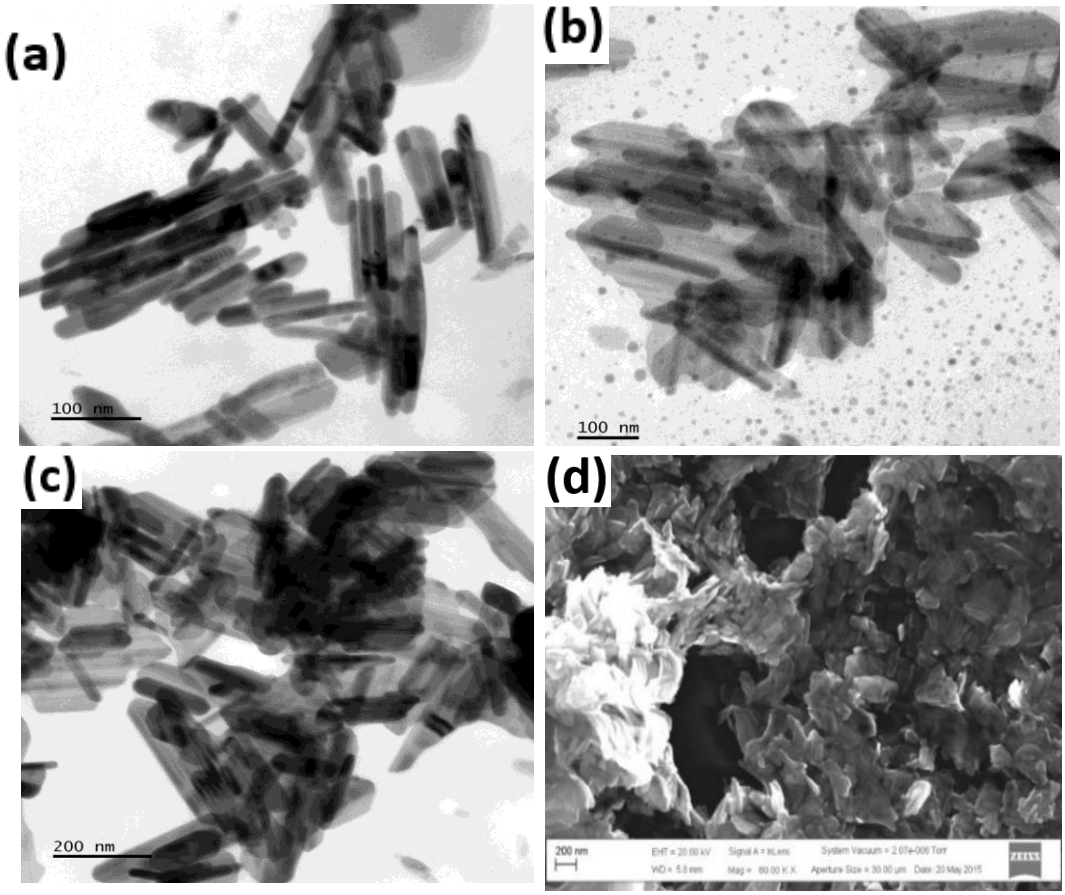

Figure 52. TEM images of Bi_2S_3 nanoparticles synthesized from $Bi[(S_2CPip)_2NO_3]$ complex in OLA for 2hrs at (a) 190 °C (b) 230 °C and (c) 270 °C. (d) SEM micrograph of rods synthesized at 270 °C.

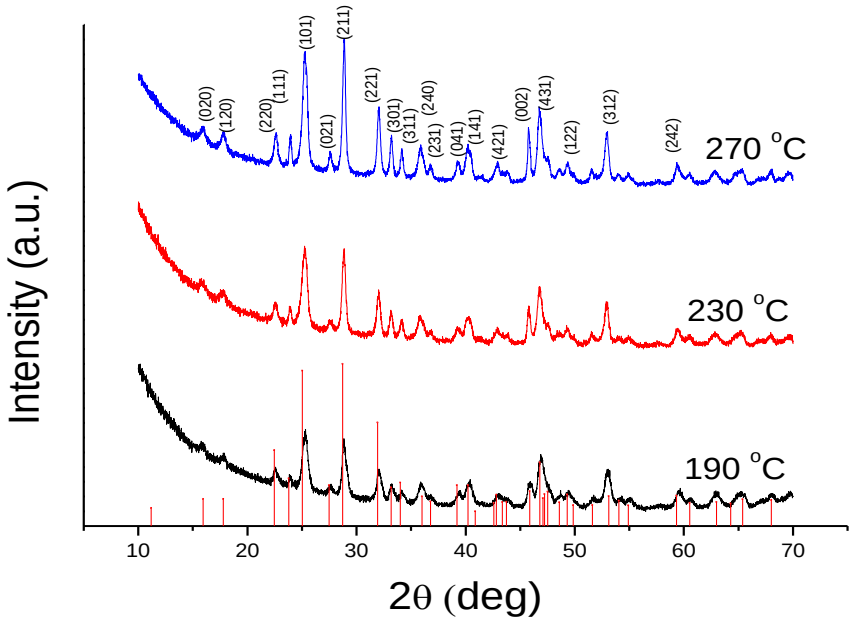

Figure 53. p-XRD pattern of OLA capped Bi_2S_3 nanorods from $Bi[(S_2CPip)_2NO_3]$ at (a) 190 °C (b) 230 °C and (c) 270 °.

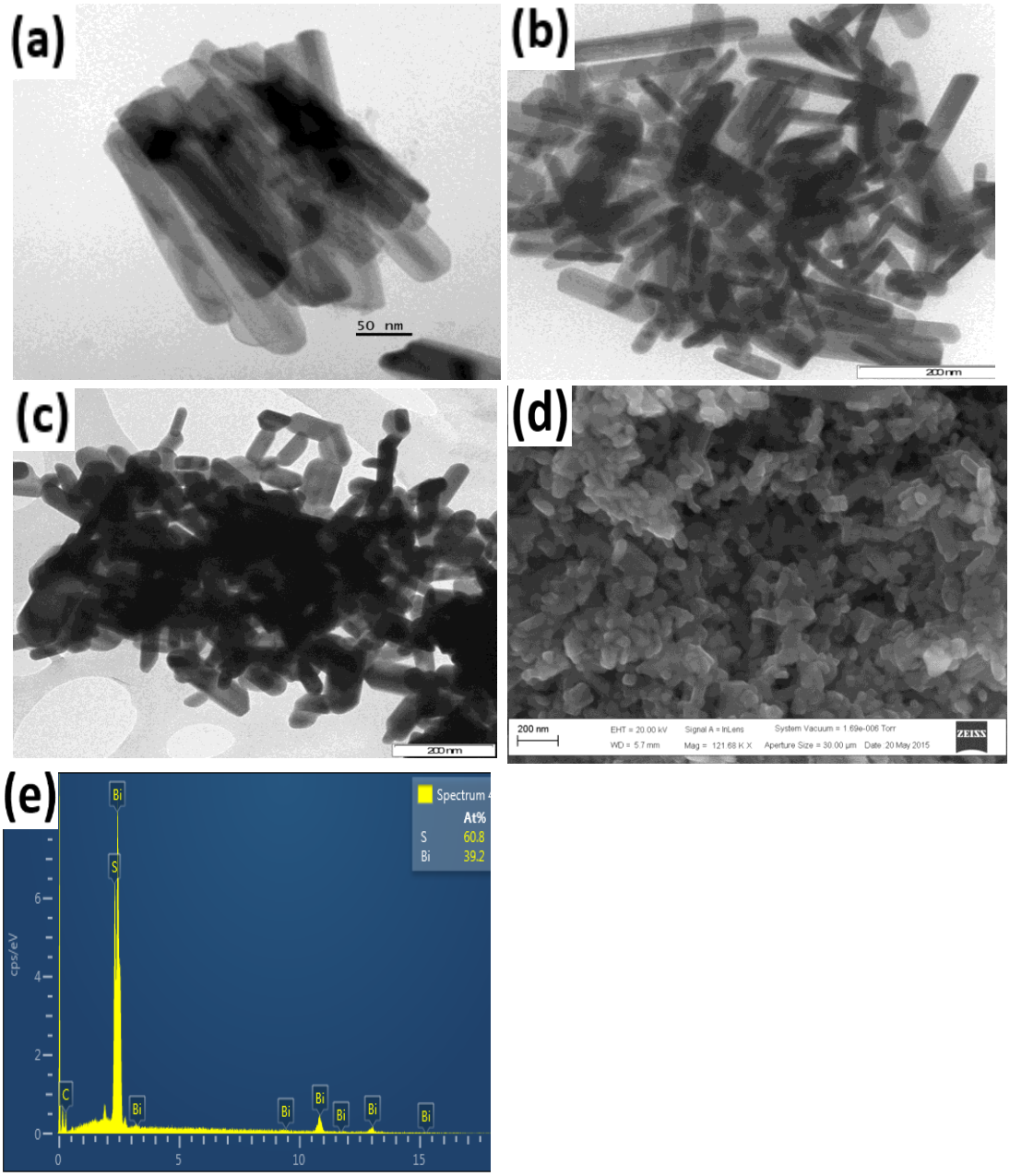

Figure 54. TEM images of Bi_2S_3 nanoparticles synthesized from $[Bi(S_2CThq)_2NO_3]$ complex in OLA for 2 hrs at (a) 190 °C (b) 230 °C and (c) 270 °C, (d) SEM micrograph of rods synthesized at 270 °C (e) EDX spectrum of rods synthesized at 270 °C.

3.2.1.4. TOPO capped Bi_2S_3

When precursor $[Bi(S_2CPip)_2NO_3]$ was thermolysed in TOPO, spherical-shaped Bi_2S_3 particles were expected at high temperature according to the thermodynamic growth regime[19] proposed by Monteiro *et al*. in the synthesis of spherical shaped- Bi_2S_3 from bismuth tris(alkyldithiocarbamate) complex in TOPO at 150 °C. However, in this work, rod-like morphologies were obtained at 190 and 230 °C and higher temperature of 270 °C gave less anisotropic morphologies with higher degree of agglomeration (Figure 55 a-c). As the temperature was varied from 190 to 270 °C there was a decrease in length of the rods

obtained with a corresponding increase in breadth leading to a decrease in aspect ratio (Table 25 page 93). Thermolysis of $[Bi(S_2CThq)_2NO_3]$ in TOPO gave less anisotropic morphologies in all three temperatures (Figure 56) with high degree of stacking at 230 and 270 °C. The SEM micrograph of the samples prepared from both complexes at 270 °C shows the rod-like morphology of the nanocrystals (Figure 55d and 56d).

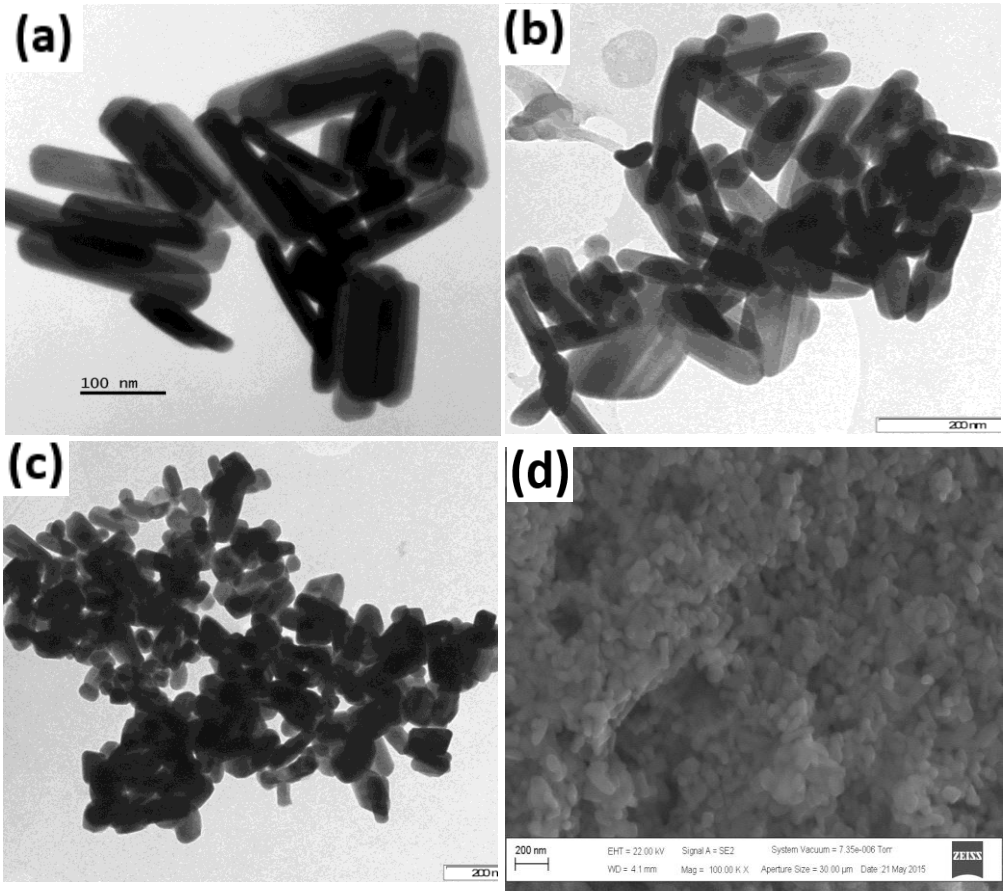

Figure 55. TEM and SEM images of Bi_2S_3 nanoparticles synthesized from $[Bi(S_2CPip)_2NO_3]$ complex in TOPO for 2 hr: TEM at (a) 190 °C (b) 230 °C and (c) 270 °C d) SEM micrograph of the rods synthesized at 270 °C.

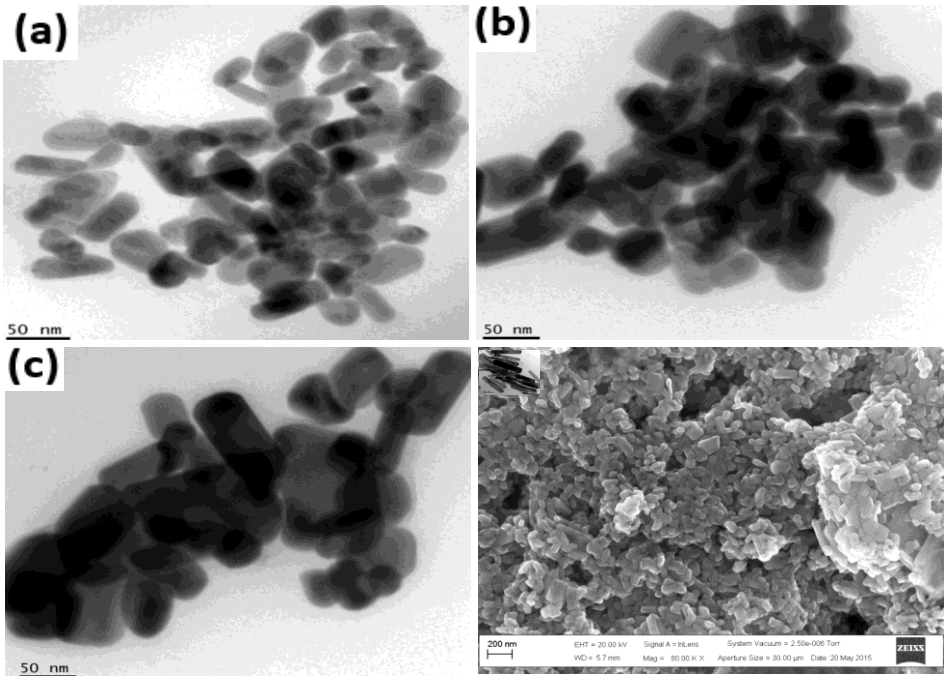

Figure 56. TEM and SEM images of Bi_2S_3 nanoparticles synthesized from $[Bi(S_2CThq)_2NO_3]$ complex in TOPO for 2 hr: TEM at (a) 190 °C (b) 230 °C and (c) 270 °C. d) SEM micrograph of the rods synthesized at 270 °C.

3.2.1.5. Solvent effect on the growth of Bi_2S_3 Nps

The dispersion medium and solvent used as capping agent play an important role in both the chemical composition and morphology of the NPs formed. We compared *p*-XRD patterns of the Bi_2S_3 particles prepared by dispersing $[Bi(S_2CPip)_2NO_3]$ in OLA and injecting in

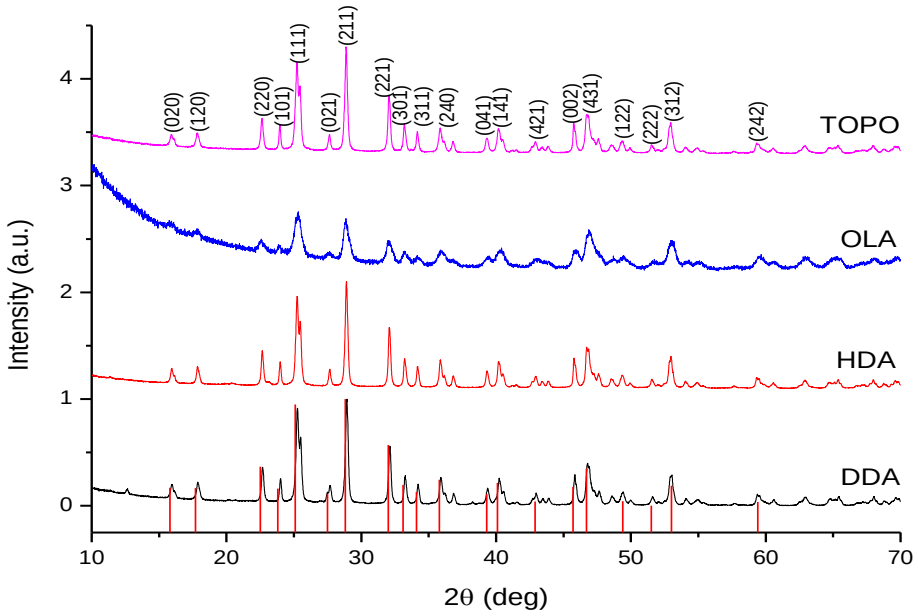

Figure 57. Powder X-ray patterns of Bi_2S_3 nanorods synthesized from $[Bi(S_2CThq)_2NO_3]$ at (a) 190 °C (b) 230 °C and (c) 270 °C.

DDA, HDA, OLA and TOPO with small portions of DT at 270 °C as shown in Figure 57. All the particles were crystalline orthorhombic Bi_2S_3 as shown by the sharp nature of the peaks. However, OLA capped Bi_2S_3 displayed broad peaks, indicating a less crystalline nature of the particles. The broadening of the peaks in Figure 57 also implies a smaller grain size of the Bi_2S_3 crystals prepared in OLA compared to the other capping groups. This was confirmed by their average crystallite sizes estimated from the Debye-Scherrer formula using the (111) plane which was 15.7 nm (OLA); 21.5 nm (TOPO); 21.9 (HDA) and 21.5 nm (DDA). Figure 58 shows the variation of the aspect ratios of the rods with temperature. At lower temperature the aspect ratios of the rods decrease from HDA with 17 C through DDA with 12 C to OLA with 18 C and a double bond and finally highly hindered TOPO. However, at 270 °C, the OLA capped rods have the highest aspect ratio. The lowest aspect ratio was observed with TOPO compared to the other capping agents, due to the low anisotropy in the particles. Monteiro *et al* obtained low anisotropic Bi_2S_3 particles when they thermolysed bismuth tris(alkyldithiocarbamate) complex in TOPO at 150 °C[24].

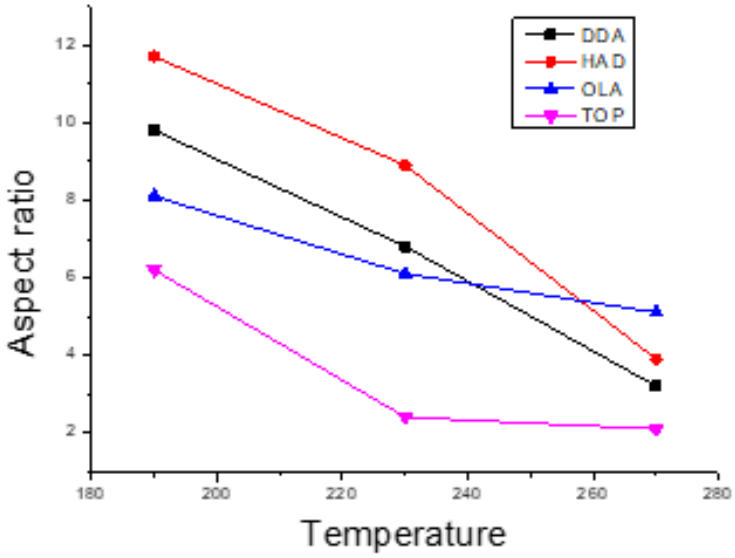

Figure 58. Variation of aspect ratio with temperature for capped Bi_2S_3 nanoparticles.

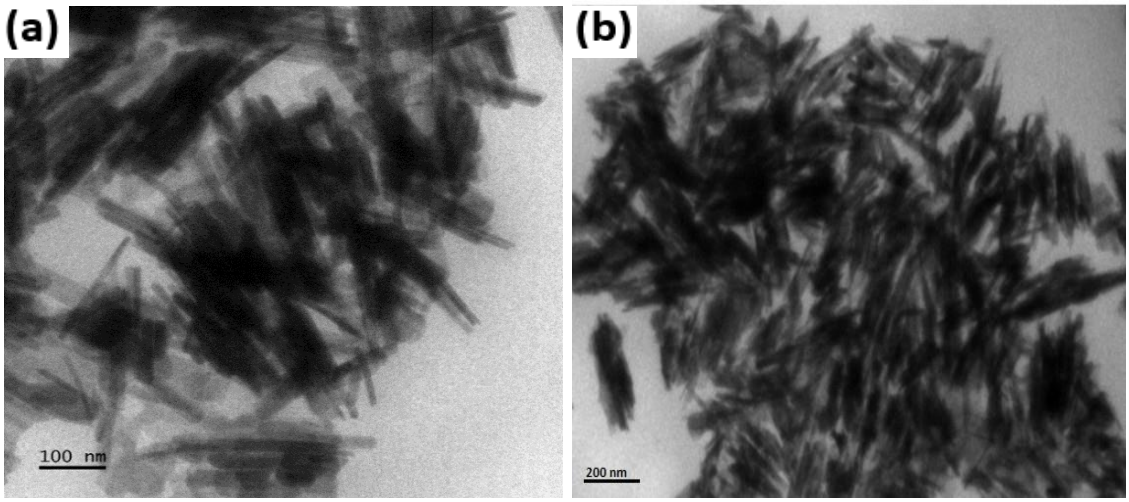

Figure 59. TEM images of HDA capped Bi_2S_3 nanoparticles synthesized at 230 °C from (a) $[Bi(S_2CPip)_2NO_3]$ and (b) $[Bi(S_2CThq)_2NO_3]$ in the absence of dodecanethiol.

The role of dodecanethiol (DT) in the formation of rod-shaped nanostructures has been reported previously for Bi_2S_3 and $Cu_{2-x}S$[46,115,284]. At high temperatures Bismuth complexes decomposed allowing sulfur from DT to react with the Bi^{3+} ions. This coordination of sulfur with the metal can control the reactivity and consequently chemical potential of the solution. High chemical potentials form thermodynamically less stable elongated structures. Both complexes were thermolysed in HDA at 230 °C without the addition of DT. The absence of DT resulted in the formation of poorly crystalline bismuth sulfide nanoparticles, as observed by TEM images in Figure 59. The p-XRD pattern also shows poorly formed nanorods (Figure 60).

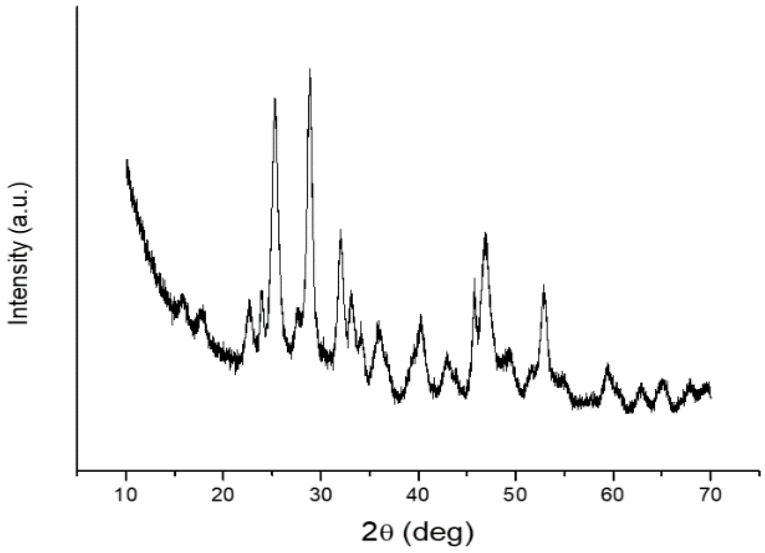

Figure 60. p-XRD pattern of nanoparticles synthesized from $[Bi(S_2CThq)_2NO_3]$ in HDA without DT.

When we dispersed the complexes in TOP and thermolyzed in the various capping agents,

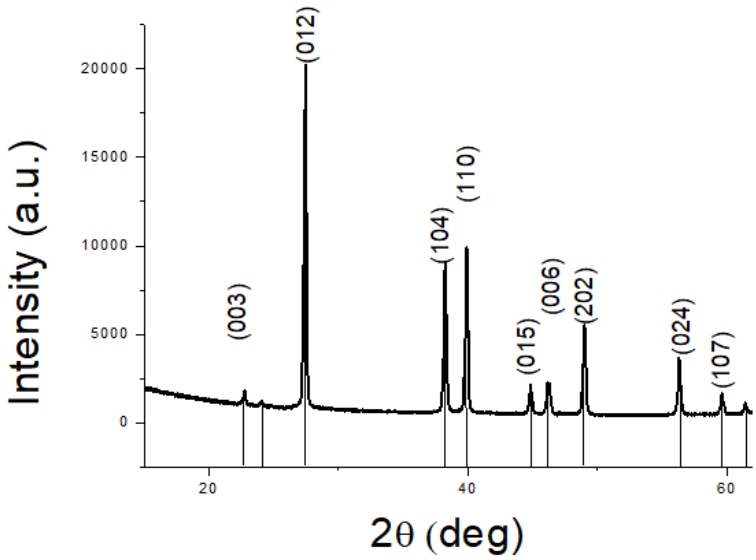

Figure 61. p-XRD pattern of metallic Bi NP Synthesized from [Bi(S_2CPip)$_2$$NO_3$] in TOP/HDA at 190 °C for 1 hr.

we did not obtain Bi_2S_3 NPs, though Monteiro *et al* reported a mixture of metallic Bismuth and Bi_2S_3 Nps when they thermolysed bismuth tris(alkyldithiocarbamate) complex in TOP/TOPO at 150 °C[24]. In this work, the presence of TOP reduced the complexes to metallic bismuth NPs at 190 and 230 °C (Figure). At 270 °C, metallic Bi pellets measuring about 3 mm were formed. The mechanism of the formation of metallic bismuth is not yet known, Figure 61 shows the TEM image of metallic bismuth Np, and the inset in the Figure shows a picture of metallic Bi pellets prepared from [Bi(S_2CPip)$_2$$NO_3$] at 270 °C . The p-XRD

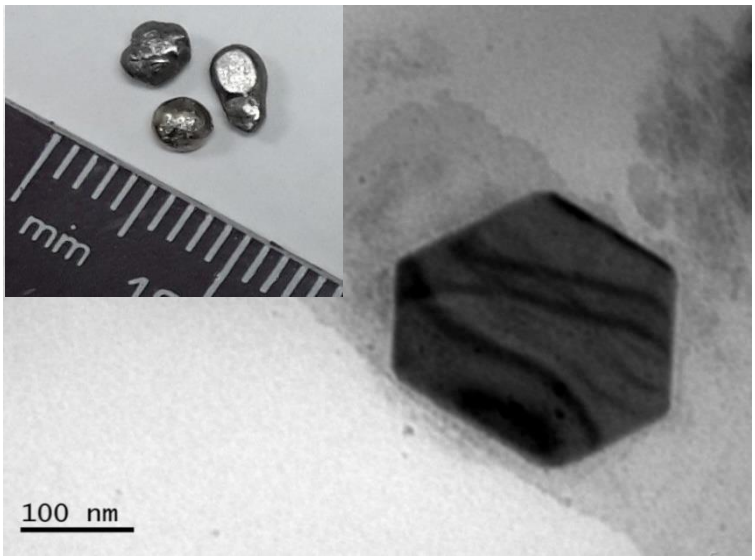

Figure 62. TEM image of Metallic Bi NP Synthesized from [Bi(S_2CPip)$_2$$NO_3$] in TOP/HDA at 190 °C for 1 hr. Inset is a picture of metallic bismuth obtained from thermolyzing [Bi(S_2CPip)$_2$$NO_3$] in TOP/HDA at 270 °C for 1 hr.

analysis on the powder formed at 190 ^{o}C shows the formation of metallic Bi phase(Figure 61).

3.2.1.6. Growth kinetics of Bi_2S_3 nanorods

Particle growth from solution by coarsening involves the growth of larger crystals at the expense of smaller crystals[285]. Since the chemical potential of a particle increases with decreasing particle size, the equilibrium solute concentration for a small particle is much higher than for a large particle, as described by the Gibbs-Thompson equation[286], the equilibrium solute concentration at the surface of larger particles is

lower than that of smaller ones and the resulting concentration gradients lead to solute ions flowing from small particles to larger ones. The coarsening mechanism is often controlled by the diffusion and particle growth *via* addition of ions to the particle surface from solution. To determine the growth kinetics in Bi_2S_3 nanoparticles, a time-dependent synthetic study was conducted in the reaction system by collecting aliquots after 1 min, 2min, 5 min, 10 min, 15 min and 30 min and quenched in ethanol. The precipitate formed was separated from the capping agent by centrifuge and dispersed in toluene for analysis. Immediately after injection of the precursor, there is a rapid formation of tiny Bi_2S_3 nuclei followed by growth. 1 min after injection, Bi_2S_3 nanorods starts forming (Figure 63). The initial growth rate is fast due to high monomer concentration[287,288]. After 5 min of reaction growth becomes slow and longer reaction time may not lead to further growth of the rods. A plot of the average length of the particles against time gives a parabola (Figure 64), in

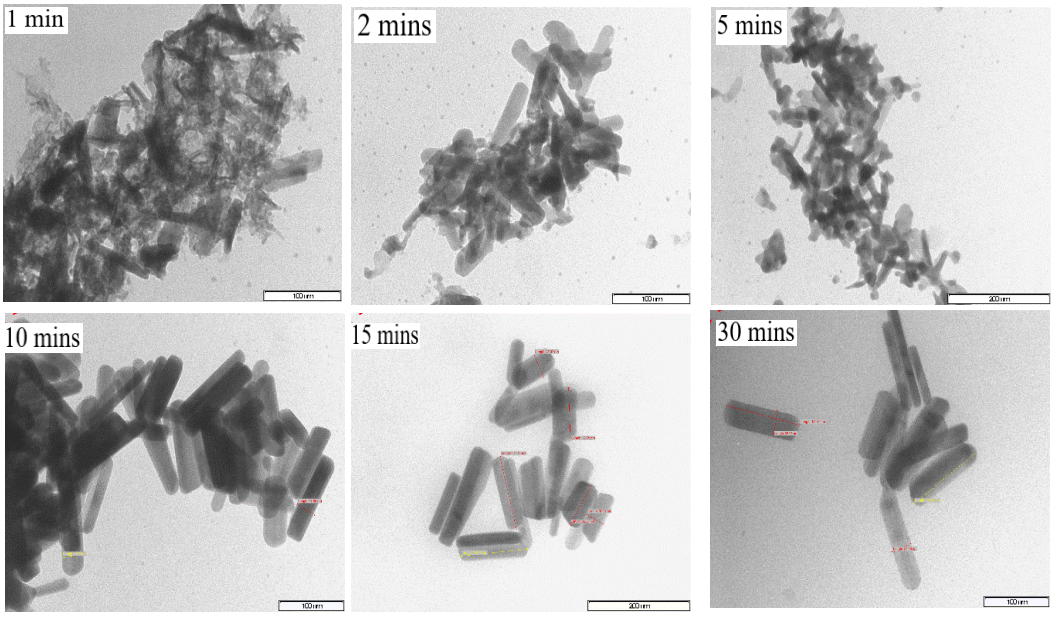

Figure 63. TEM images of aliquots of Bi_2S_3 Nps synthesised from $[Bi(S_2CPip)_2NO_3]$ at 1 min, 2min, 5 min, 10 min, 15 min and 30 min.

agreement with the Lifshitz-Slyozov-Wagner kinetic coarsening theory given in equation (4)

$$\overline{D}^n - \overline{D}^n_0 = k(t - t_0) \quad (4)$$

where $\overline{D}$ and $\overline{D}_0$ are the mean particle sizes at time t and t_0. k is a temperature-dependent material constant, and n is an exponent relevant to the coarsening mechanism.

3.3. Syntheses and characterization of Bi_2S_3 Nanoparticles from green Capping agents

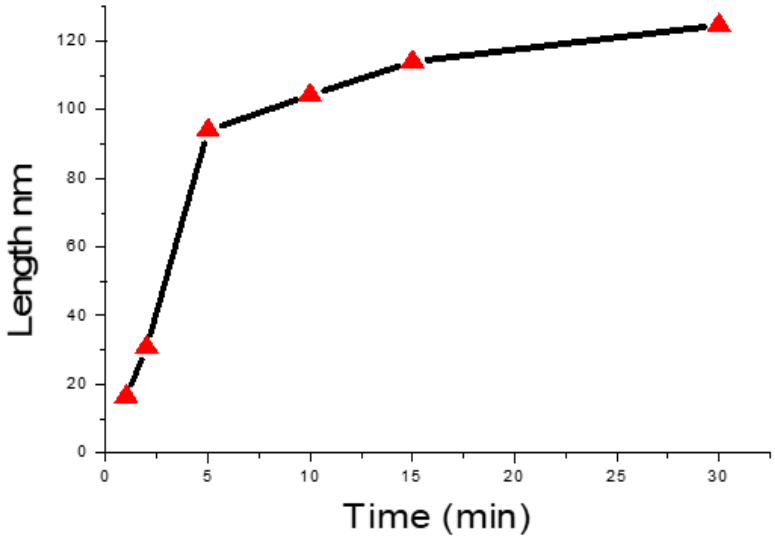

Figure 64. Average length of Bi_2S_3 Nps as a function of time.

3.3.1. Olive oil (OO) capped Bi_2S_3 nanoparticles

The optoelectronic properties of semiconducting materials are crucial for a large number of applications since unique electronic properties result from tunnelling of energy band gap. The complex $[Bi(S_2CThq)_2NO_3]$ was thermolyzed in OO at 190, 230 and 270 ^oC and the UV/Visible spectra of the particles obtained presented in Figure 65i. Compared with the bulk Bi_2S_3, which has a direct band gap of 1.3 eV (953 nm), the absorption edge of nanostructures obtained at all the three temperatures exhibit blue shift (ca. 0.8-0.3 eV) which is attributed to the quantum confinement of charge carriers in the nanoparticles[289]. At 190 ^oC, the band gap estimated from the Tauc plots (Figure 65ii) is 2.1 eV. When the temperature was raised to 230 and 270 ^oC, a red shift (1.9 eV and 1.6 eV respectively) was observed in the spectra suggesting an increase in the size of the particles as the reaction temperature increases.

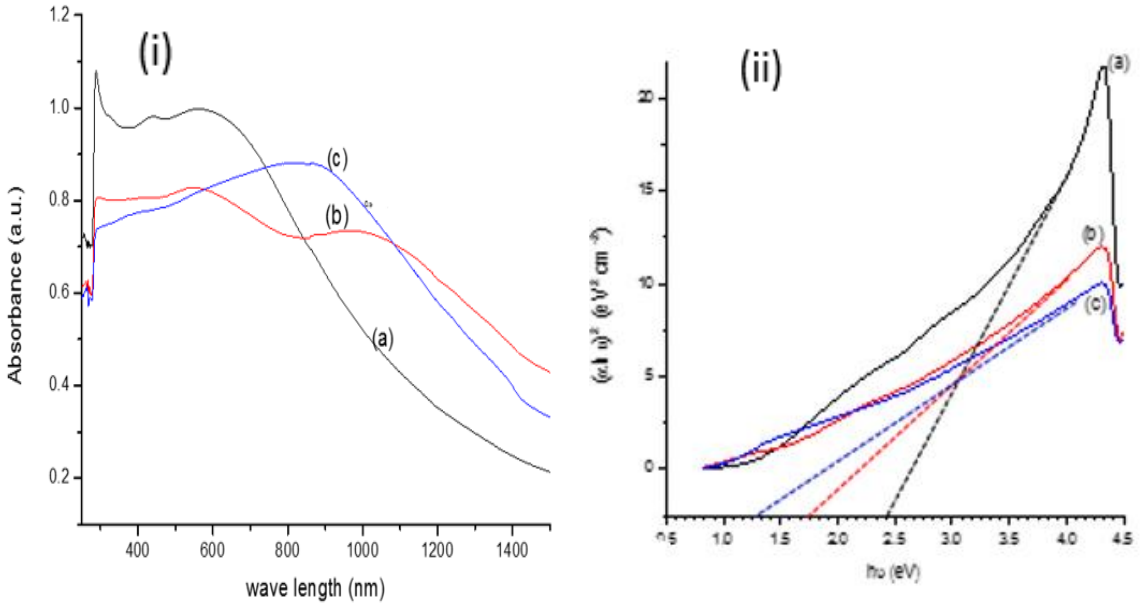

Figure 65. (i)UV/Vis absorption spectra of olive oil capped Bi_2S_3 nanorods from $[Bi(S_2CThq)_2NO_3]$ at (a): 190 °C, (b): 230 °C and (c): 270 °C. ii) plot of $(\alpha h\upsilon)^2$ vs hυ (Tauc Plot).

When $[Bi(S_2CThq)_2NO_3]$ was thermolyzed in olive oil, highly crystalline and less agglomerated Bi_2S_3 nanorods with aspect ratios which decrease with increase in temperature were formed (Figure 66). At 190 ^oC, nanorods with average breadths of 15.5 ± 3.2 nm and lengths of 316.8 ±17.5 nm were formed. At 230 ^oC the rods had average breadths 298.1 ±9.3 nm and length of 298.1 ±9.3 nm at elevated temperatures of 270 ^oC , the rods are shorter and thicker, with average breadths of 25.7 ±3.7 and lengths of 267.6 ±3.5 (Table 26 page 111).

When $[Bi(S_2CPip)_2NO_3]$ thermolyzed in olive oil agglomerated bundles of Bi_2S_3 nanorods were obtained at 190 ^oC, while at 230 more defined nanorods with some degree of alignment were obtained, and at 270 ^oC, randomly oriented well defined nanorods were obtained (Figure 67).

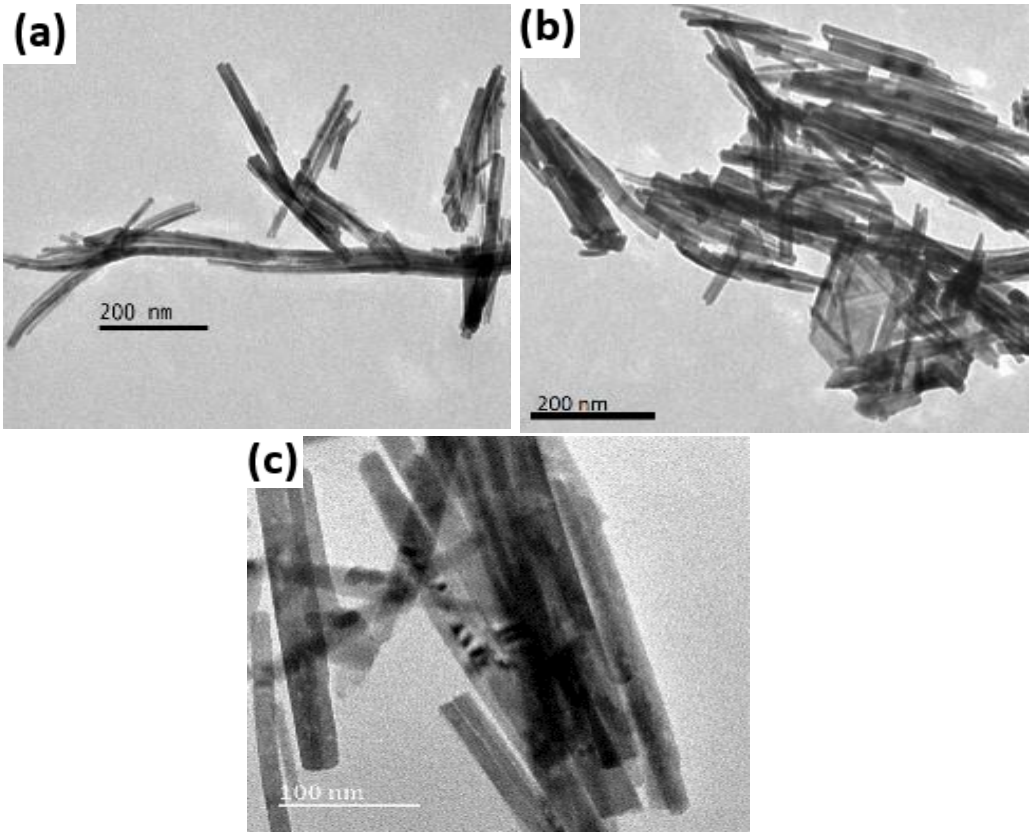

Figure 66. TEM images of Bi_2S_3 nanorods synthesized from $[Bi(S_2CThq)_2NO_3]$ in olive oil at (a) 190 °C (b) 230 °C and (c) 270 °C .

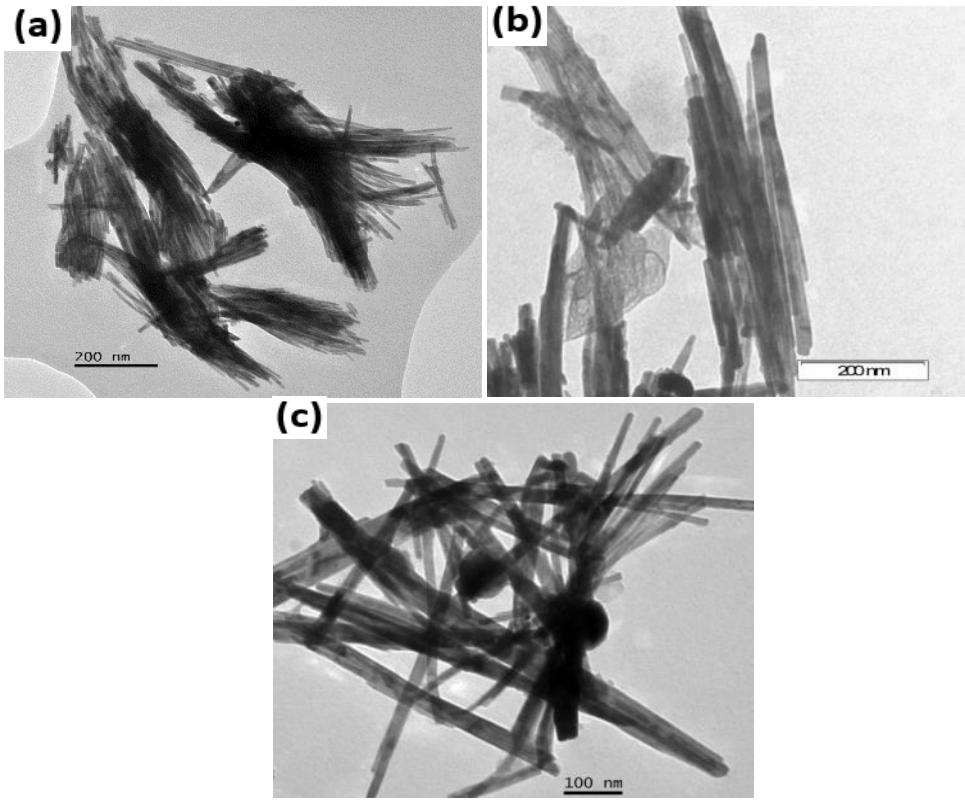

Figure 67. TEM images of Bi_2S_3 nanorods synthesized from $[Bi(S_2CPip)_2NO_3]$ in olive oil at (a) 190 °C (b) 230 °C and (c) 270 °C.

Table 26. Dimension analysis of Bi_2S_3 nanorods synthesized from $[Bi(S_2CThq)_2NO_3]$ under different capping agents and temperature.

Capping agent	Temperature (°C)	Length (nm)	Breadth (nm)	Aspect ratio (L/B)
OO	190	316.8 ±17.5	15.5 ±3.2	20.4
OO	230	298.1 ±9.3	23.6 ±3.1	12.6
OO	270	267.6 ±3.5	25.7 ±3.7	10.4
OA	190	290.9 ±7.8	11.4 ±3.4	25.5
OA	230	279.2 ±13.2	17.5 ±3.1	15.9
OA	270	255.7 ±17.4	19.2 ±3.6	13.3
CO	190	333.9 ±19.2	16.5 ±3.3	20.2
CO	230	300.1 ±21.2	25.1 ±3.5	11.9
CO	270	224.5 ±23.6	31.4 ±3.1	7.1
RA	190	383.6 ±20.5	14.6 ±3.6	26.3
RA	230	340.4 ±25.4	20.2 ±3.3	16.9
RA	270	200.2 ±25.5	31.6 ±3.8	6.3

The p-XRD patterns of the Bi_2S_3 particles obtained in olive oil at 190 °C, 230 °C and 270 °C using $[Bi(S_2CPip)_2NO_3]$ are shown in Figure 68i. The reflection from the (020), (120), (220), (101), (111), (021), (211), (002), (240) planes correspond to the orthorhombic crystal structure of Bi_2S_3 and are indexed according to JCPDS file number 03-065-2435 with lattice parameters a =1.1115, b = 1.1250 and c = 0.3970 nm. No unindexed peaks are noticed in the diffractogram. This shows that the Bi_2S_3 nanocrystals obtained are pure. The difference in peak intensity and broadening is an indication of different crystallite sizes obtained at the different temperatures). It was shown by UV/Vis. analysis that the particle sizes increase with increase in the temperature. This result was confirmed by estimating the average crystallite sizes (T) from the Debye-Scherer equation using the (211) plane and the values presented in Figure 68ii, which gave 15.9 nm, 21.0 nm and 30.5 nm, for the OO capped Bi_2S_3 particles synthesized from $[Bi(S_2CPip)_2NO_3]$ at 190, 230 and 270 °C. The calculated lattice spacing for the (211) plane was 3.09 Å for the samples prepared at all three temperatures.

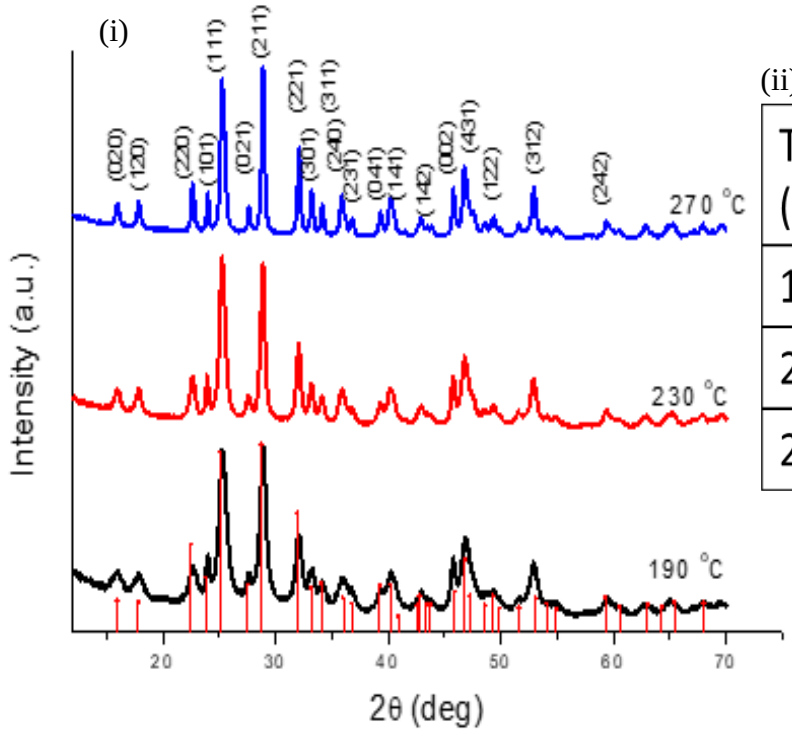

(ii)

Temp (°C)	T (nm)	$d_{(211)}$ (Å)
190	15.9	3.09
230	21.0	3.09
270	30.5	3.09

Figure 68. (i) Powder X-ray patterns of Bi_2S_3 nanocrystals synthesized in olive oil using $[Bi(S_2CPip)_2NO_3]$ at 190 °C., 230 °C. and 270 °C. ii) crystallite sizes calculated from Debye-Scherrer equation and the corresponding calculated d-spacing for the (211) plane.

3.3.2. Oleic acid (OA) capped Bi_2S_3 nanoparticles

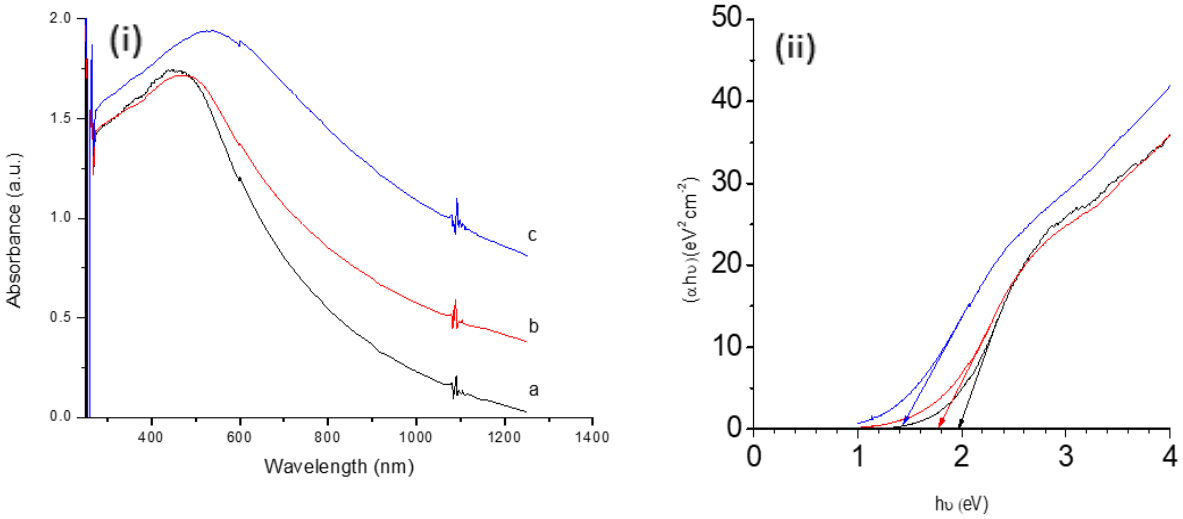

Figure 69. (i) UV/Vis absorption spectra of OA capped Bi_2S_3 nanorods using $[Bi(S_2CThq)_2NO_3]$ at (a) 190 °C, (b) 230 °C and (c) 270 °C. (ii) the plot of (αhυ)2 vs hυ.

Olive oil contains some acids such as linoleic acid, stearic acid and oleic acid (OA). The UV/Visible spectra of OA capped Bi_2S_3 prepared from $[Bi(S_2CThq)_2NO_3]$ has Similar trend to that prepared in OO. Figure 69 i shows the UV/Vis absorption spectra and Figure 70 (ii) the plot of $(\alpha h\upsilon)^2$ vs $h\upsilon$. The calculated energy band gaps are 2.0, 1.8 and 1.4 eV, respectively at 190, 230 and 270 ^oC. These band gaps are blue shifted compared to the 1.3 eV energy band gap for the bulk Bi_2S_3. The slight red shift on increase in temperature is due to increase in mean particle size.

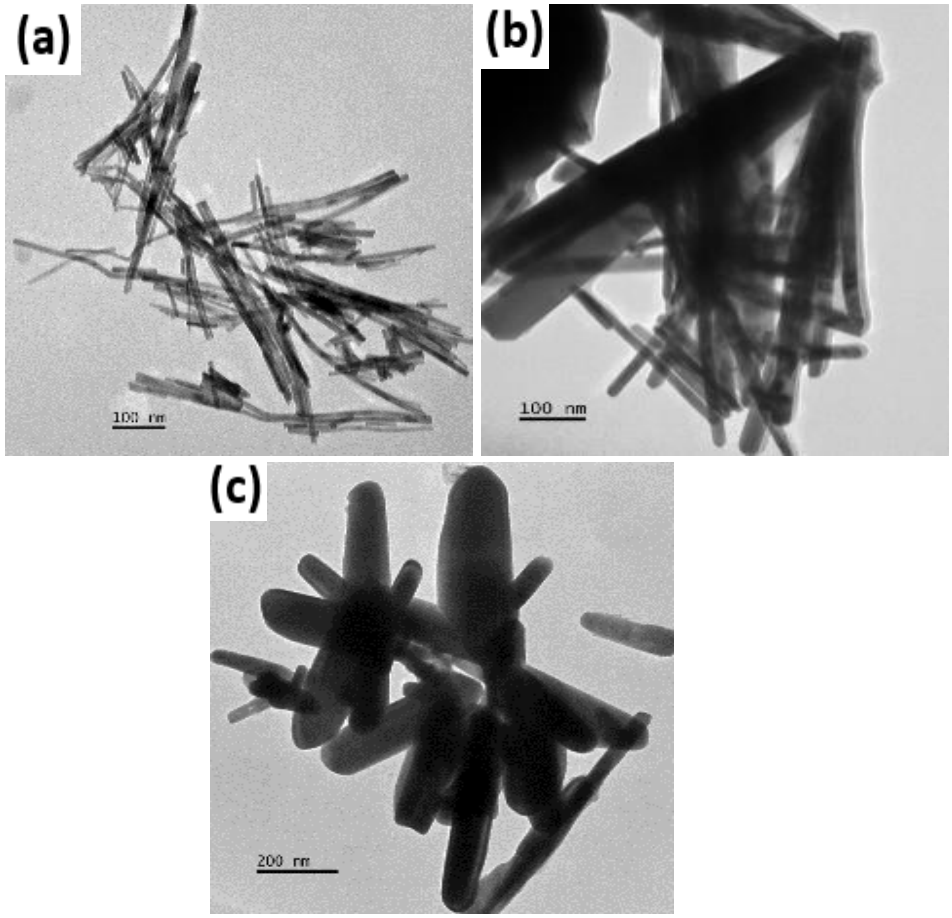

Figure 70. TEM images of Bi_2S_3 nanorods synthesized from $[Bi(S_2CThq)_2NO_3]$ in OA at (a) 190 ^oC (b) 230 ^oC and (c) 270 ^oC.

The thermolysis of $[Bi(S_2CThq)_2NO_3]$ in OA resulted in the formation of Bi_2S_3 nanorods with smaller size compared with those prepared in OO (Table 26 page 111). TEM show randomly oriented rods at all three temperatures (Figure 70). At 190 °C the rods were more isolated and appear more agglomerated at 230 °C and 270 °C .

A similar trend in TEM images are obtained when $[Bi(S_2CPip)_2NO_3]$ is thermolyzed in OA at 190 °C, 230 °C and 270 °C (Figure 71). However, the rods formed have more uniform morphology compared to those synthesized from $[Bi(S_2CThq)_2NO_3]$.

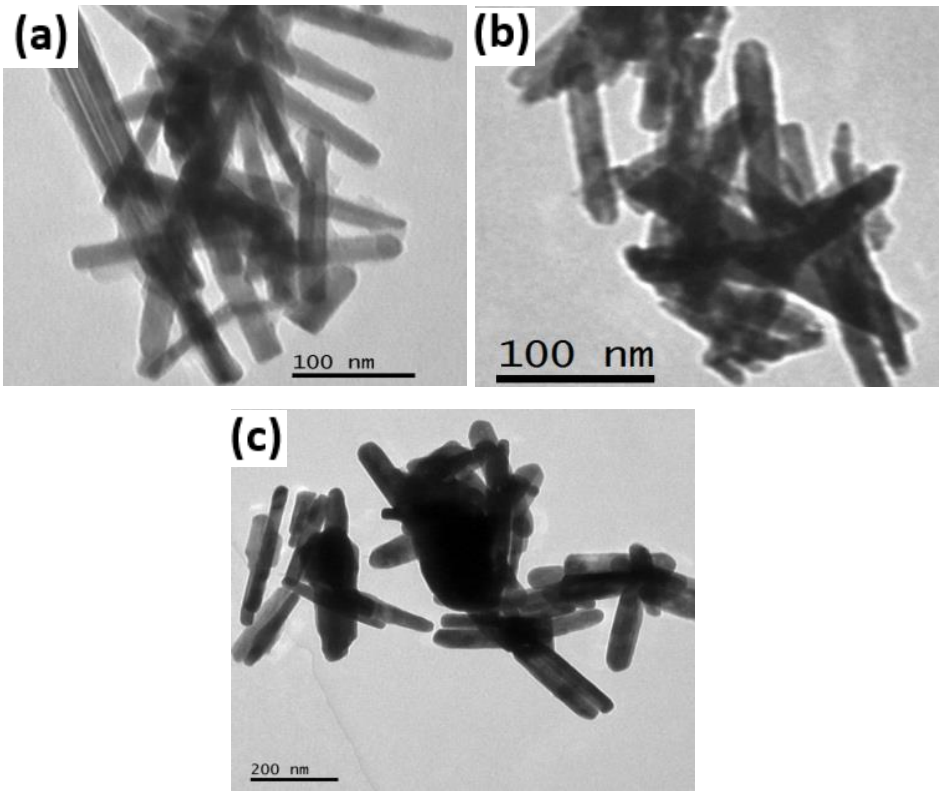

Figure 71. TEM images of Bi_2S_3 nanorods synthesized from $[Bi(S_2CPip)_2NO_3]$ in OA at (a) 190 °C (b) 230 °C and (c) 270 °C.

3.3.3. Castor Oil (CO) capped Bi_2S_3 nanoparticles

The UV/Vis spectra CO-capped Bi_2S_3 nanorods synthesized from $[Bi(S_2CThq)_2NO_3]$ are presented in Figure 72. The plot of $(\alpha h\upsilon)^2$ against $h\upsilon$ shows a similar trend to the OO and OA capped particles (Figure 72 ii). There is a slight blue shift in the observed energy band edge of 1.6, and 1.4 at 190, 230 °C respectively compared to that of bulk Bi_2S_3. However, the 1.3 eV energy band edge of the rods prepared at 270 °C do not experience any shift. The general red shift observed with increase in temperature is attributed to increase in mean particle size.

Figure 73 shows the TEM images of samples prepared by thermolyzing $[Bi(S_2CThq)_2NO_3]$ in castor oil at 190 °C, 230 °C and 270 °C. At 190 °C, elongated agglomerated nanorods with some degree of alignment are formed with average breadth and length of 16.5 ± 3.3 nm and 333.9 ±19.2 nm respectively and aspect ratio of about 20.2 (Table 26 page 111). When the

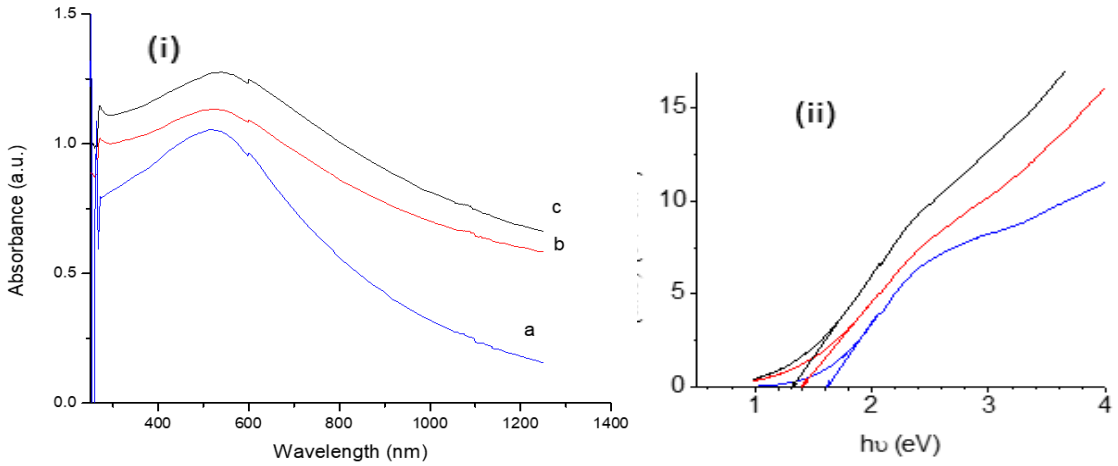

Figure 72. i) UV/Vis absorption spectra of CO capped Bi_2S_3 nanorods from $[Bi(S_2CThq)_2NO_3]$ at (a) 190 °C, (b) 230 °C and (c) 270 °C. ii) the plot of $(\alpha h\upsilon)^2$ vs hυ.

reaction temperature was raised to 230 °C, randomly oriented agglomerated Bi_2S_3 nanorods are formed, with an increase in breadth and a decrease in the length of 25.1 ± 3.5 nm and 300.1 ± 21.2 nm respectively. A decrease in the aspect ratio from 20.2 to 11.9 was also observed. At 270 °C, shorter, un-agglomerated and randomly oriented nanorods with average lengths of 224.5 ± 23.6 nm are obtained with an aspect ratio of 7.1 as shown in Figure 73c. Figure 743 shows an HRTEM image of a single rod synthesized at 270 °C. The lattices fringes are clearly visible indicating the crystalline nature of the particles.

The calculated d-spacing of 3.13 Å corresponds to the d-spacing of the (211) plane of orthorhombic Bi_2S_3 lattice.

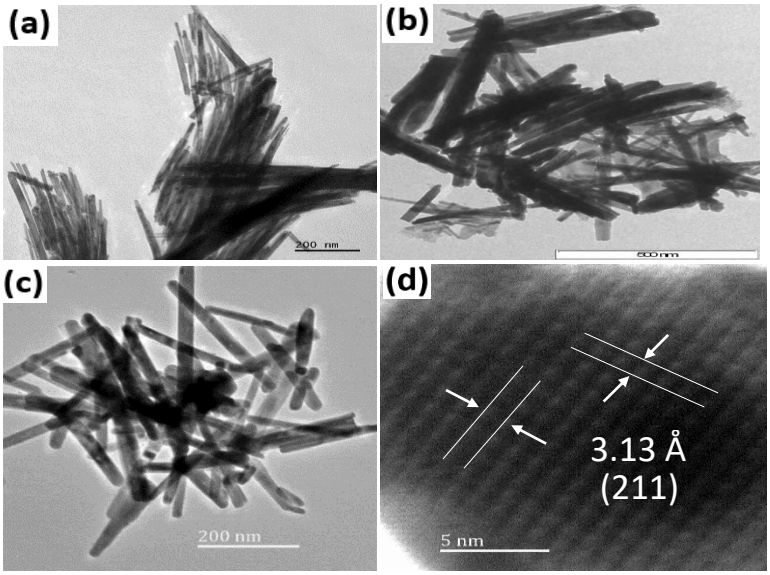

Figure 73. TEM images of Bi_2S_3 nanorods synthesized from $[Bi(S_2CThq)_2NO_3]$ in castor oil at (a) 190 °C, (b) 230 °C, (c) 270 °C and (d) corresponding HRTEM image of single rod prepared at 270 °C.

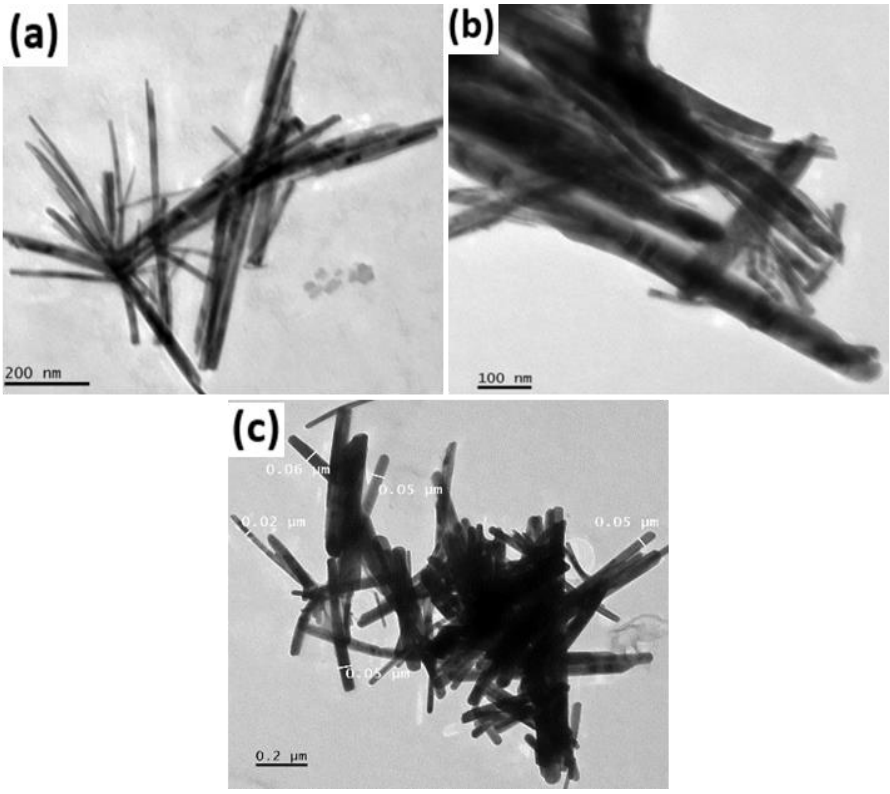

Figure 74. TEM images of Bi_2S_3 nanorods synthesized from [$Bi(S_2CPip)_2NO_3$] in castor oil at (a) 190 °C, (b) 230 °C and (c) 270 °C.

When [$Bi(S_2CPip)_2NO_3$] was thermolyzed in CO less agglomerated elongated rods were obtained at 190 °C and more agglomerated rods were obtained at 230 °C and 270 °C (Figure 74). This is opposite to the observed trend when [$Bi(S_2CThq)_2NO_3$] was thermolyzed in CO.

The p-XRD patterns of the Bi_2S_3 particles obtained in castor oil at 190 °C, 230 °C and 270 °C using [$Bi(S_2CThq)_2NO_3$] are shown in Figure 75i. The (020), (120), (220), (101), (111), (021), (211), (002), (240) planes correspond to the orthorhombic crystal structure of Bi_2S_3 and are indexed according to JCPDS file number 03-065-2435 with lattice parameters *a* =1.1115, *b* = 1.1250 and *c* = 0.3970 nm. No unindexed peaks are noticed in the diffractogram, indicative of pure Bi_2S_3 nanocrystals obtained under the explicated synthetic conditions. The diffractogram shows a difference in peak intensity and broadening due to the difference in grain sizes and crystallinity of the particles synthesized at the various temperatures. The sharp peaks at 270 °C indicate the crystalline nature of the particles. Nanorods synthesized at 190 °C show broader and less intense peaks while at higher temperatures, an increase in intensity of the peaks was observed at the expense of the breadth of the nanorods. This result was confirmed by estimating the average crystallite sizes from the Debye-Scherer equation using the (211) plane (Figure 75ii), which gave 15.3 nm, 28.6 nm and 36.7 nm, for the castor oil capped Bi_2S_3 particles synthesized at 190 °C, 230 °C and

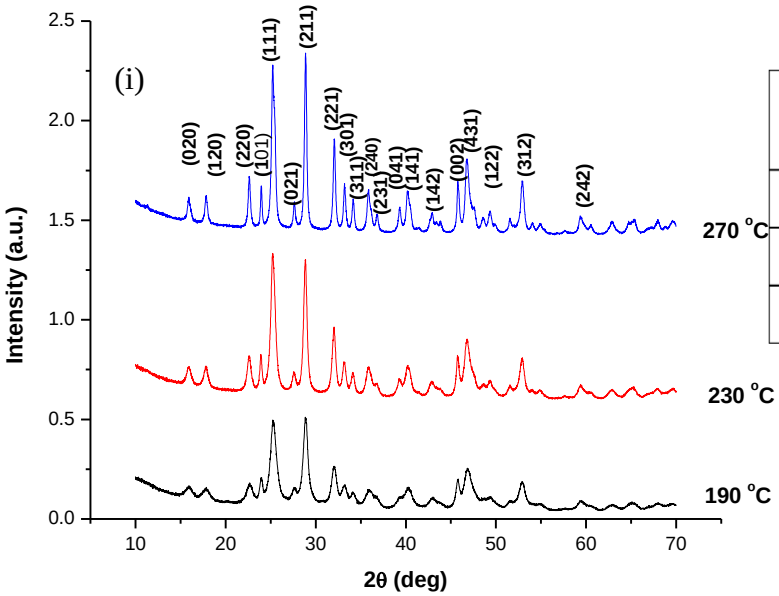

(ii)

Temp (°C)	T (nm)	$d_{(211)}$ (Å)
190	15.3	3.09
230	28.6	3.07
270	36.7	3.09

Figure 75. (i)Powder X-ray patterns of Bi_2S_3 nanocrystals synthesized in castor oil using [$Bi(S_2CThq)2NO_3$] at 190 °C, 230 °C and 270 °C. Ii) crystallite size calculated from Debye-Scherrer equation and the corresponding calculated d-spacing for the (211).

270 °C. The inset in Figure 70 show the estimated crystallite size from Debye- Scherrer equation and the calculated d-spacing for the (211) plane.

3.3.4. Ricinoleic acid (RA) capped Bi_2S_3 nanoparticles

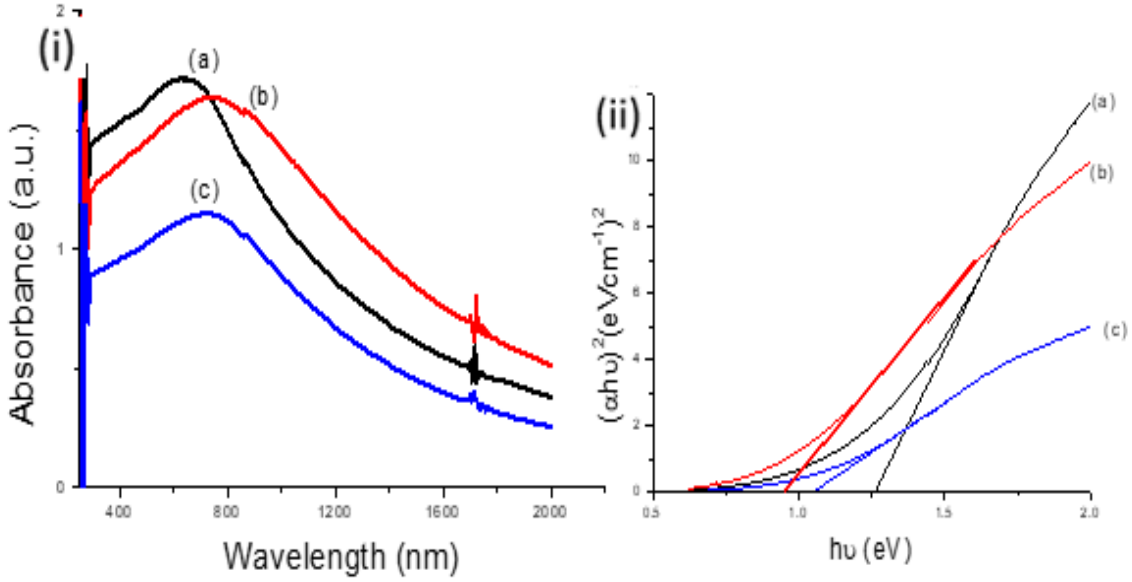

Figure 76. (i) UV/Vis absorption spectra of RA capped Bi_2S_3 nanorods using [$Bi(S_2CThq)_2NO_3$] at (a) 190 °C, (b) 230 °C and (c) 270 °C. (ii) the plot of $(\alpha h\upsilon)^2$ vs hυ.

Castor oil contains about 90 % of ricinoleic acid. $[Bi(S_2CThq)_2NO_3]$ was thermolyzed in ricinoleic acid at 190 ^oC, 230 ^oC and 270 ^oC in order to evaluate the influence of the other constituents of castor oil on the shape and size of the particles. Unlike the energy band gap of the OO, OA and CO capped nanorods prepared from $[Bi(S_2CThq)_2NO_3]$ which are blue shifted compared to that of the bulk Bi_2S_3, the RA capped nanorods experience a marked red shift in their energy band edge of 1.2, 1.1 and 0.9 eV for the particles synthesized at 190, 230 and 270 $^{\circ}C$ respectively as shown in the plot of $(\alpha h\upsilon)^2$ vs $h\upsilon$ (Figure 76ii).

The TEM images of the RA capped nanoparticles prepared from $[Bi(S_2CThq)_2NO_3]$ are presented in Figure 77. A reduction of particle agglomeration and an increase in particle

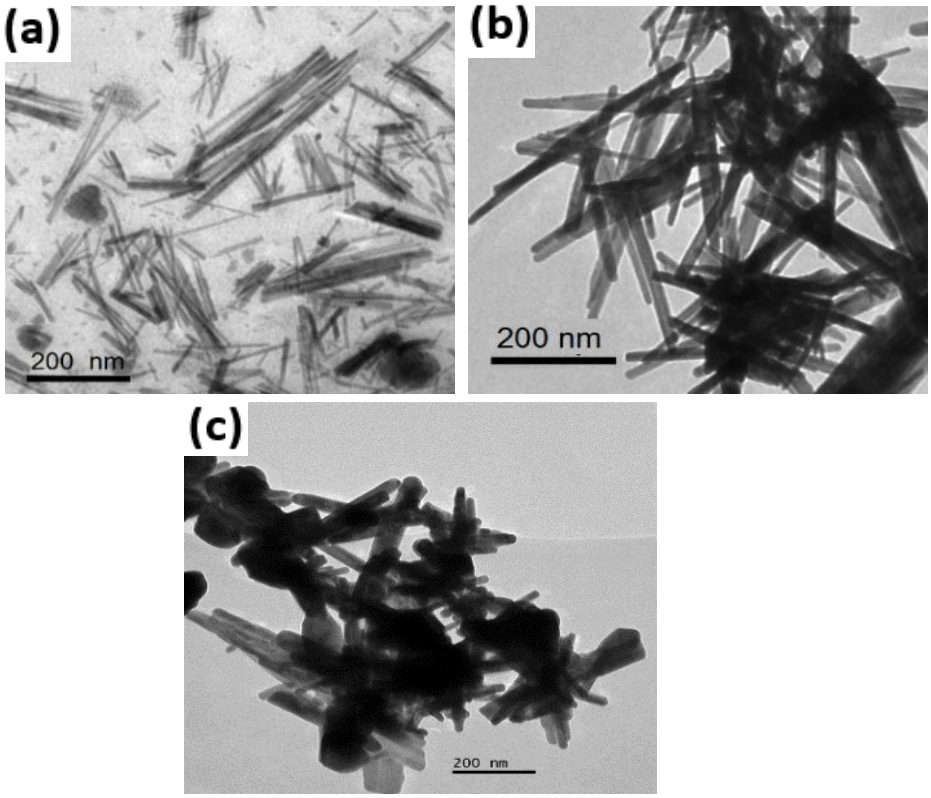

Figure 77. TEM images of Bi_2S_3 nanorods synthesized from $[Bi(S_2CThq)_2NO_3]$ in ricinoleic acid at (a) 190 ^oC, (b) 230 ^oC and (c) 270 ^oC.

lengths with a decrease in breath, as well as an increase of the aspect ratio of the particles was observed compared to particles prepared in castor oil. At 190 ^oC, more elongated nanorods were obtained with average breadths and lengths of 14.6 ± 3.6 nm and 383.6 ±20.5 nm respectively. The particles were about 50 nm longer than particles prepared in castor oil (see Figure 73 page 115). As the reaction temperature was increased, the breadth of the rods increased while their length decreased (see Table 26 page 111). At a higher temperature of 270 ^oC, highly stacked and poorly formed nanorods were obtained (Figure 77c).

When $[Bi(S_2CPip)_2NO_3]$ was thermolized, uniform agglomerated rods were obtained at 190 ^oC and 230 ^oC (Figure 78 a and b), and at 270 ^oC short agglomerated polydisperse and poorly formed rods similar to those from $[Bi(S_2CThq)_2NO_3]$ were obtained Figure 78c).

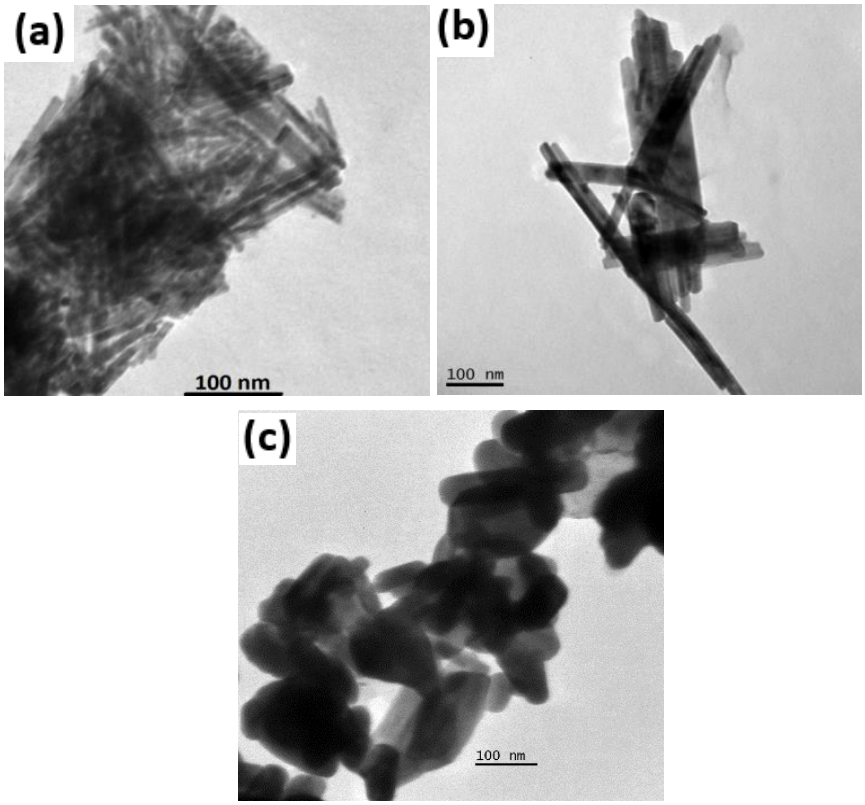

Figure 78. TEM images of Bi_2S_3 nanorods synthesized from $[Bi(S_2CPip)_2NO_3]$ in ricinoleic acid at (a) 190 ^oC, (b) 230 ^oC and (c) 270 ^oC.

No significant differences were observed in the optical spectra of Bi_2S_3 nanoparticles prepared using $[Bi(S_2CPip)_2NO_3]$ suggesting that the nature of the alkyl chain of the precursors reported here does not have a strong influence on the optical properties of the Bi_2S_3 nanoparticles resulting from the thermolysis. However, there is a clear red shift (absorption to high wavelengths) with an increase in the temperature of thermolysis, suggesting a growth process driven by the reduction of the total surface energy of the particulates (Ostwald ripening)[98].

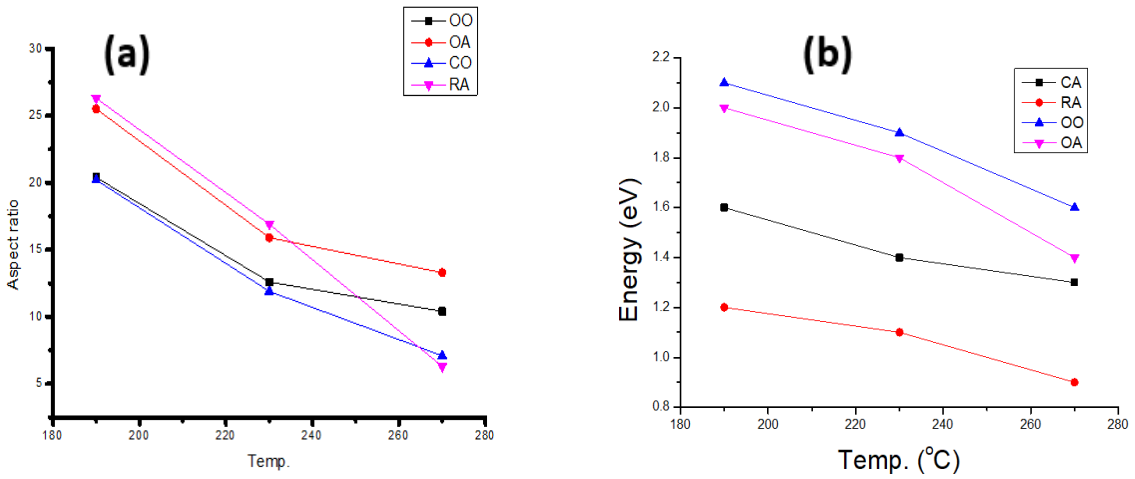

Figure 79. Variation of (a) aspect ratio (b) band gap energy with temperature for green capped Bi_2S_3 nanoparticles.

There was a general decrease in aspect ratio as temperature increase with the same capping agent (Figure79 a). However, at low temperature the aspect ratio increased from CO to OO passing through OA and finally RA. At 270 RA had the lowest aspect ratio followed by CO and finally OA. The quality of the TEM images showed that despite the additional components in castor oil and olive oil, they offer no additional advantage in tuning the morphology of the synthesized Bi_2S_3 nanorods compared to RA and OA. However, the band gap energy of the rods prepared from CA and OO are more blue-shifted compared to those obtained from RA and OA at the same temperature (Figure 79b). This shows that the additional components in CO and OA play a role in enhancing the electronic properties of the nanorods.

3.4. Solvent-free syntheses of Bi_2S_3 (melt reactions)

TEM analysis on the particles obtained from melt reactions revealed irregularly shaped rods when $[Bi(S_2CPip)_2NO_3]$ was used (Figure 80). The rods at 350 ^oC were 349.13 nm by 115.95 nm, much longer than those obtained from hot injection thermolysis. At 400 ^oC the rods were 521.08 nm by 86.76 nm and at 450 ^oC, the rods were averagely 1037.35 nm by 299.89 nm. When $[Bi(S_2CThq)_2NO_3]$ was used(Figure 81), irregularly shaped particles were obtained at 350 ^oC . at 400 irregularly shaped elongated rod-like particles were obtained

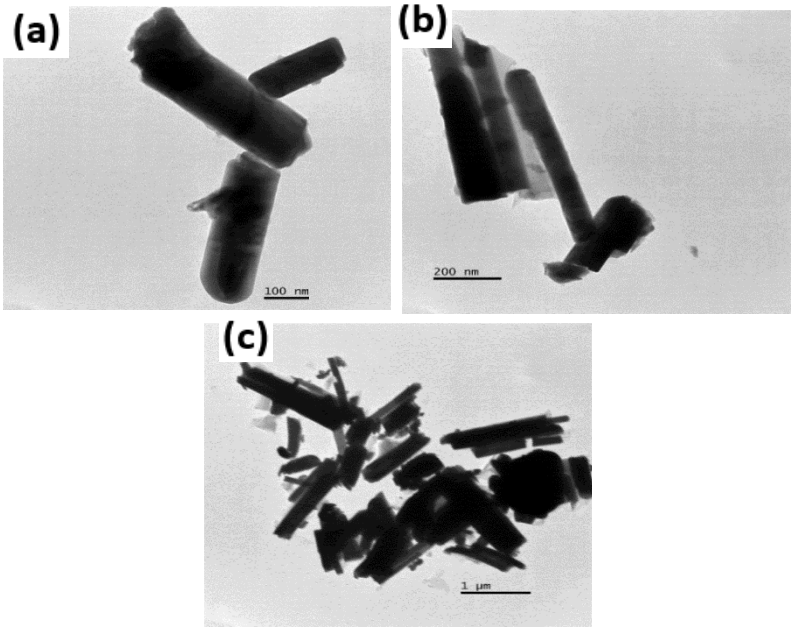

Figure 80. TEM images of Bi_2S_3 rods synthesized from $[Bi(S_2CPip)_2NO_3]$ by melt method at (a) 190 °C, (b) 230 °C and (c) 270 °C.

while at 450 °C a mixture of irregularly shaped particles and elongated rod were formed. Bi_2S_3 has a lamella structure with a tendency to grow along the c-axis in the (001) direction. However, the irregularity in the morphology of the particles obtained compared to those from hot injection thermolysis in shape directing solvents, shed more light on the role played by capping groups in tailoring the final morphology of the particles. Also, since there is no sequestrating agent to limit the growth of the particles, very elongated and large particles out of the nano range are obtained.

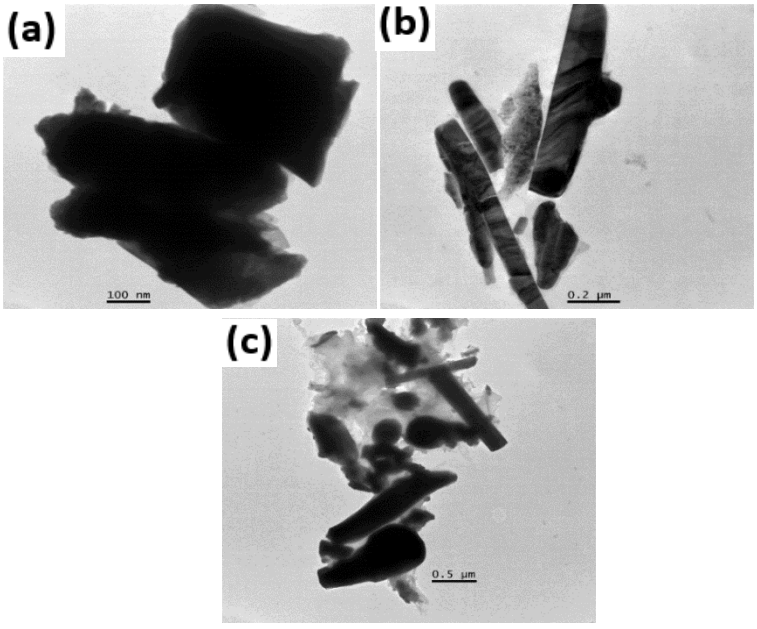

Figure 81. TEM images of Bi_2S_3 rods synthesized from $[Bi(S_2CThq)_2NO_3]$ by melt method at (a) 190 °C, (b) 230 °C and (c) 270 °C.

Figure 82 shows the p-XRD of the particles prepared from $[Bi(S_2CPip)_2NO_3]$ at 350, 400 and 450 ^oC. The peaks are indexed to the orthorhombic bismuthinite lattice ICCD 03-265-2435. The presence of some unindexed peaks shows the limitation of this synthetic method for the preparation of pure Bi_2S_3 compared to the hot injection thermolysis method.

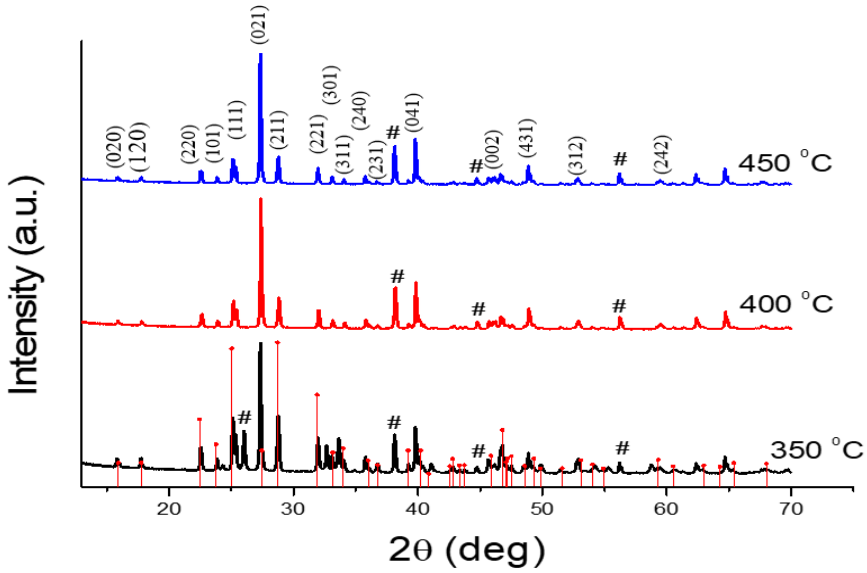

Figure 82. p-XRD of Bi_2S_3 rods synthesized from $[Bi(S_2CPip)_2NO_3]$ by melt method.

3.5. Syntheses and characterization of Sb_2S_3 Nanoparticles

A search through literature shows that, the hot injection thermolysis of single source precursors for the synthesis of Sb_2S_3 nanoparticles has not yet been reported. This section couples the advantages of single source precursors with that of hot injection thermolysis to synthesize Sb_2S_3.

The Sb_2S_3 particles were synthesized as reported in section 2.2.4.

3.5.1. OLA capped Sb_2S_3

The morphologies of the products synthesized from $[Sb(S_2CPip)_3]$, $[Sb(S_2CMor)_3]$ and $[Sb(S_2CDed)_3]$ at 230 ^oC in OLA were examined by TEM. Sb_2S_3 crystalizes into the orthorhombic system which has a lamella structure and shows a strong propensity for anisotropic growth along the (001) crystal plane forming a 1-dimensional structure like rods[167]. Thermolysis of all three complexes in oleyamine at 230 °C gave sub-micrometre sized peg-like rods staged to each other (Figure 83).

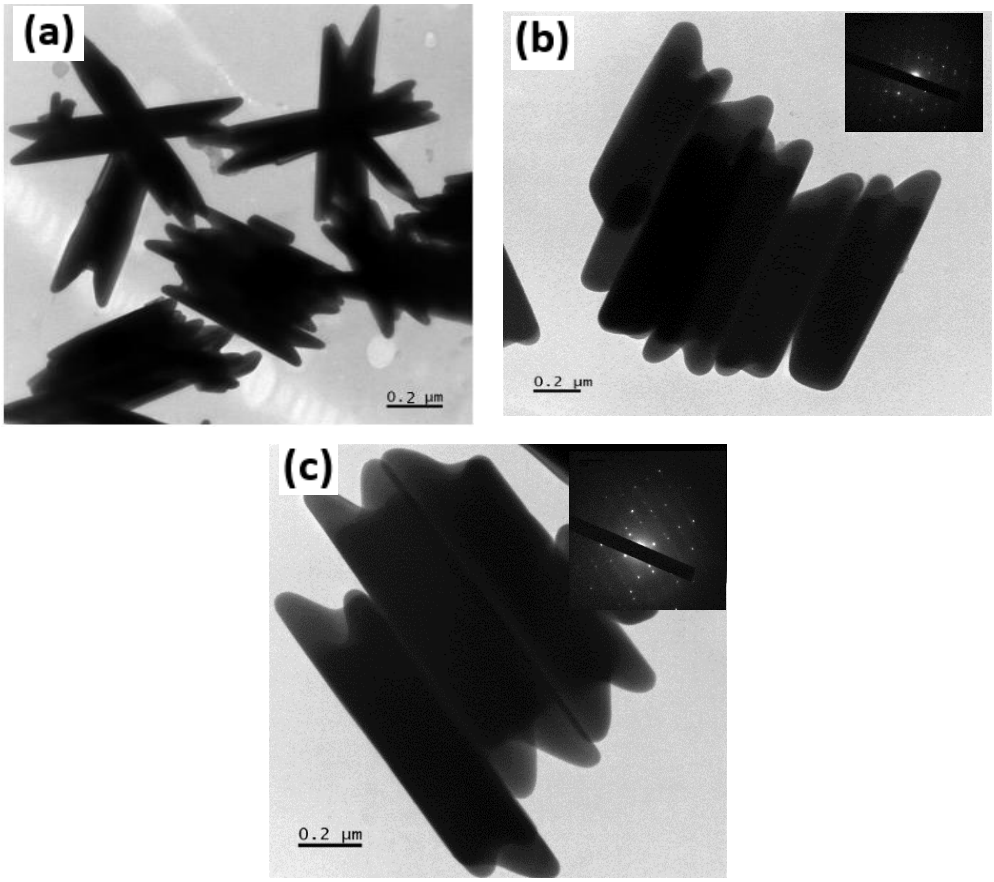

Figure 83. TEM images of Sb_2S_3 rods synthesized in OLA from (a) [$Sb(S_2CPip)_3$] (b) [$Sb(S_2CMor)_3$] and (c) [$Sb(S_2CDed)_3$] at) 230 °C .

The rods are of length between 764.48 ±111.79 and 911.67 ±228.90 width between 168.87 ±33.96 and 228.287 ±62.53 as shown in Table 27. The table also shows a very slight variation in the aspect ratios 4.53, 4.12 and 3.99 when complexes [$Sb(S_2CPip)_3$], [$Sb(S_2CMor)_3$] and [$Sb(S_2CDed)_3$] were thermolyzed. This slight variation coupled with the similarity in shape indicates that the alkyl chain has very little influence on the growth of the particles. The uniformness of the morphologies of the particles show the appropriateness of our experimental environment to grow stibnite crystals. SAED patterns of the particles prepared from complex [$Sb(S_2CMor)_3$] and [$Sb(S_2CDed)_3$] shown in the inset in Figure 83 b and c, reveal sharp sports typical of single crystalline Sb_2S_3.

The p-XRD patterns of the particles obtained from all the precursors under the various experimental conditions were indexed to pure orthorhombic stibnite phase of space group *P*nma and typical calculated lattice parameters, a =11.2942, b = 3.8263, c = 11.2261 close to the reported data (amcsd 0008825 parameters a =11.2990, b = 3.8313, c = 11.2270 and cell volume V = 483.7) (Figure 84). The absence of unindexed peaks shows that pure Stibnite was obtained under the experimental conditions, and the sharpness of the peaks shows the highly crystalline nature of the samples.

Table 27. Synthetic parameters, length, width and aspect ratio of as-synthesized Sb_2S_3 particles

Compound	Solvent		Temp (°C)	Time (min)	Length (nm)		Width (nm)		Aspect ratio
$[Sb(S_2CPip)_3].3H_2O$	OLA	-	230	30	764.48	±111.79	168.87	±33.96	4.53
	OLA	DDT	230	30	1589.68	±250.18	220.39	±58.98	7.31
$[Sb(S_2CMor)_3]$	OLA	-	230	30	688.97	±237.30	167.317	±46.71	4.12
	OLA	DDT	230	30	1783.70	±444.90	239.837	±54.00	7.44
$[Sb(S_2CDed)_3]$	OLA	-	230	30	911.67	±228.90	228.287	±62.53	3.99
	OLA	DDT	230	30	1244.15	±97.76	157.147	±53.38	7.92

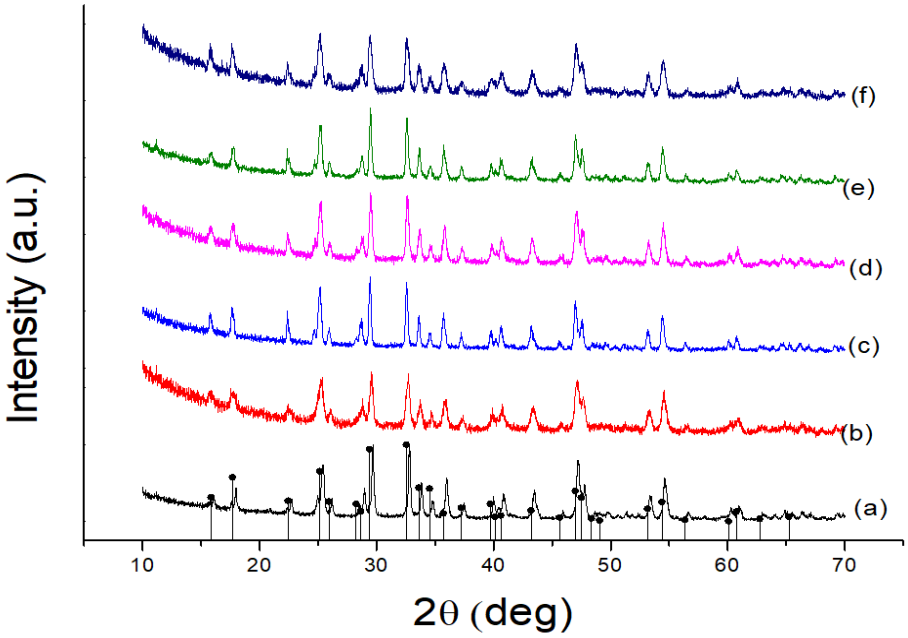

Figure 84. p-XRD pattern of as synthesized Sb_2S_3 nanorods prepared from (a) $[Sb(S_2CPip)_3]$ (b) $[Sb(S_2CPip)_3]$ in DT $[Sb(S_2CPip)_3]$ (c) $[Sb(S_2CMor)_3]$ (d) $[Sb(S_2CMor)_3]$ in DT $[Sb(S_2CPip)_3]$ (e) $[Sb(S_2CDed)_3]$ and (f) $[Sb(S_2CDed)_3]$ in DT $[Sb(S_2CPip)_3]$.

3.5.2. Sb_2S_3 from OLA and DT

In order to control the growth of the nanorods, 0.2 mL of dodecanethiol was added to the precursor prior to interjection into hot oleylamine at 230 °C.

When we added DT in our experiment the yellow solution turned black almost immediately after injection. The TEM images(Figure 85 a-c) show more define sub-micrometre sized nanorods twice as long with higher aspect ratios of 7.31, 7.44, and 7.92 compared to those obtained without dodecanethiol (Table 27). Figure 85 d shows the HRTEM image of a single nanorod prepared from $[Sb(S_2CDed)_3]$ OLA/DT with a calculated interplanar spacing of 3.08 Å, identical to the 3.08 Å inter-planar spacing of the of (112) plane of the orthorhombic stibnite lattice.

The ease of formation of rods is favoured by the intrinsic anisotropic structure of Sb_2S_3 and the chemical potential of the starting mixture.

In the absence of dodecanethiol, the reaction mixture took a longer time to decompose, resulting in agglomerated peg-like rods. The use of dodecanethiol enhances the reactivity of the starting materials by increasing the chemical potential of the reaction mixture leading to more defined and highly crystalline rods.

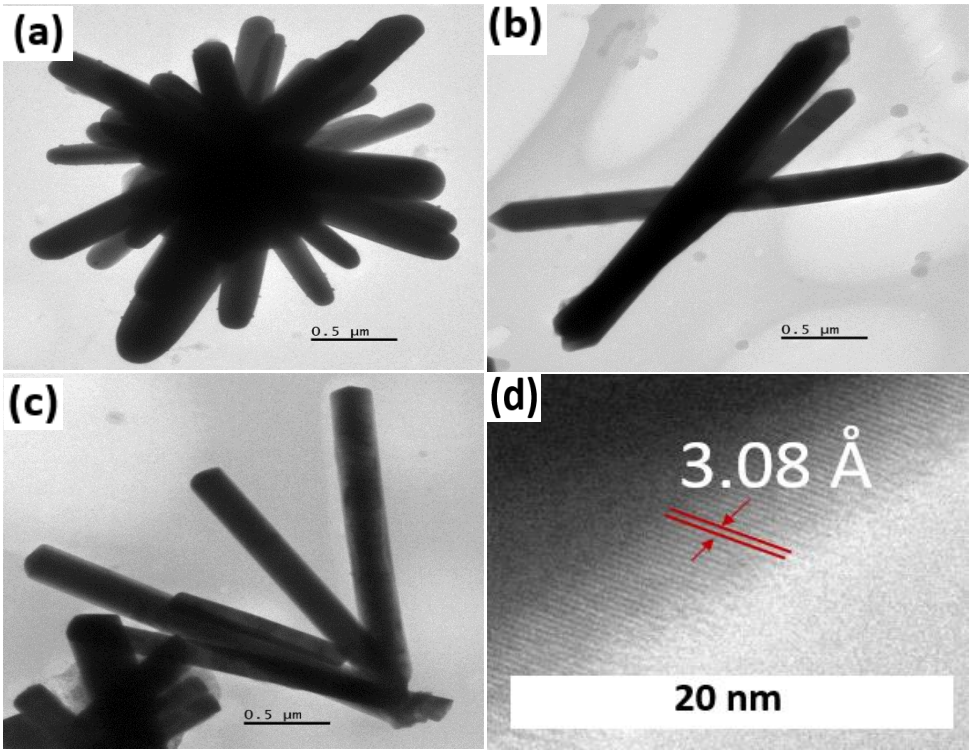

Figure 85. TEM images of Sb_2S_3 rods synthesized in OLA/DT from (a) $[Sb(S_2CPip)_3]$ (b) $[Sb(S_2CMor)_3$ and (c) $[Sb(S_2CDed)_3]$ at 230 °C.

The formation of Sb_2S_3 rods can be further explained by the kinetically controlled anisotropic growth mechanism[290]. Immediately after injection, there is rapid formation of Sb_2S_3 seed. In oleylamine, these seeds may cluster but with oleylamine acting as a surfactant, selectively caps the (100) and (110) faces more strongly than others in the presence of more monomer, the clusters grow anisotropically giving agglomerated peg-like rods. The increase in the chemical potential when dodecanethiol is added to the reaction mixture also has the

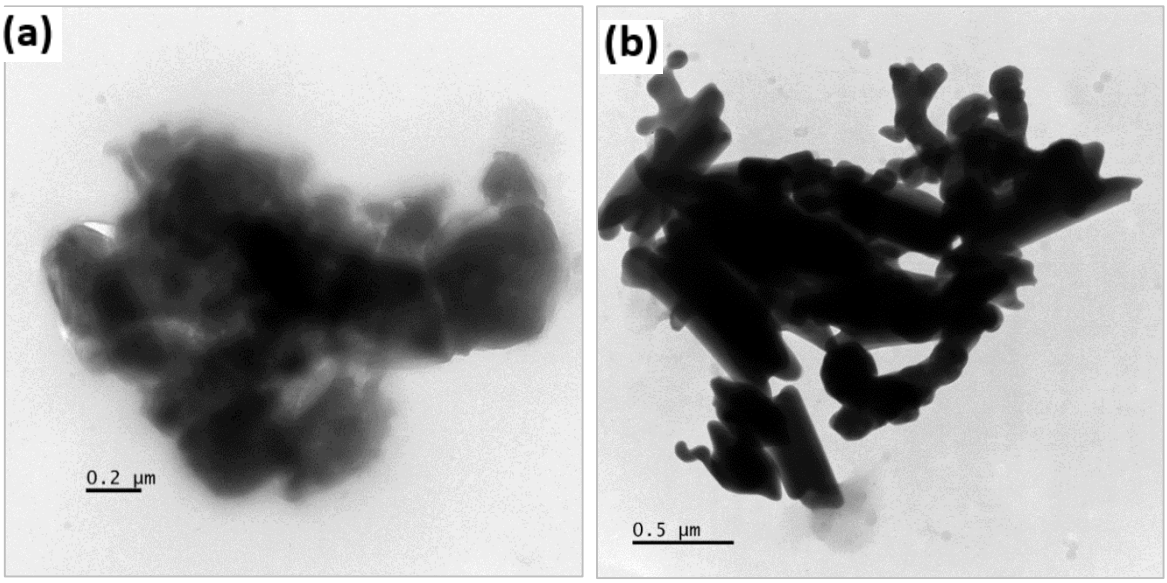

Figure 86. TEM images of showing poorly formed Sb_2S_3 rods synthesized from [$Sb(S_2CMor)_3$] in (a) OLA (b) OLA/DT at 190 °C.

effect of faster capping during nucleation preventing agglomeration of the seeds which grow into isolated rods.

The solvent, precursor and reaction temperature were all important parameter for the formation of Sb_2S_3. At 190 °C, the colour of the solution changed from yellow to reddish brown and did not change any further. The precursor did not decompose completely leading to amorphous Sb_2S_3 (Figure 86).

3.6. Syntheses and characterization of $(Bi_{1-x}Sb_x)_2S_3$ ternary nanoparticles

3.6.1. $(Bi_{1-x}Sb_x)_2S_3$ ternary nanoparticles

$(Bi_{1-x}Sb_x)_2S_3$ solid solution was prepared by varying the mole ratio of the two single source precursors [$Bi(S_2CPip)_3$] and [$Sb(S_2CPip)_3$] dispersed in OLA and injected into a solution of hot OLA/DT at 230 °C as described in section 2.2.4. Full range $(Bi_{1-x}Sb_x)_2S_3$ solid solution was prepared, starting with pure Bi_2S_3, and gradually increasing the mole fraction of Sb until pure Sb_2S_3, and the result presented below.

Bi_2S_3 and Sb_2S_3 are semiconductor materials with a direct band gap of about 1.3 and 1.7 eV respectively, corresponding to 954 and 729 nm in wavelength. The band gap energy of the ternary $(Bi_{1-x}Sb_x)_2S_3$ solid solutions made by different ratios of Bi/Sb should be a linear interpolation of the two endmembers.

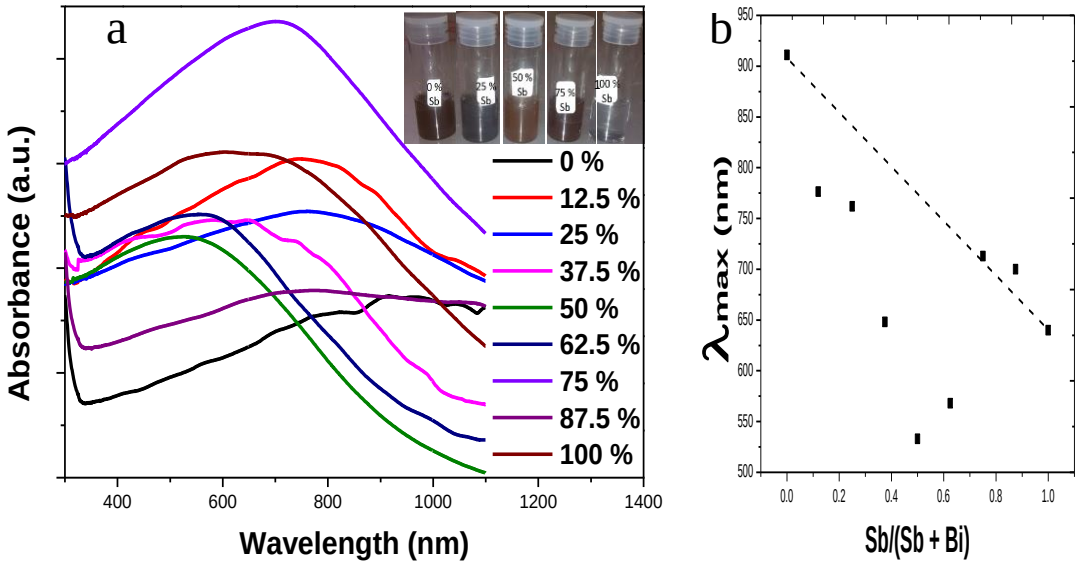

Figure 87. (a) UV/visible absorption spectrum of Bi_2S_3, Sb_2S_3 and $(Bi_{1-x}Sb_x)_2S_3$ solid solutions. (b) plot of absorption maximum against mole fraction of Sb, showing deviation from ideal behaviour.

Figure 87 a, shows the UV−visible absorption spectra of the as-prepared ternary $(Bi_{1-x}Sb_x)_2S_3$ nanorods in which a strong broad-spectrum absorption was seen within the wavelength range of 300−1100 nm. In general, the absorption edge of $(Bi_{1-x}Sb_x)_2S_3$ nanorods is blue-shifted with the increase of Sb ratio. However, a plot of the absorption maximum against the antimony mole fraction shows that there is a serious deviation from the expected linear behaviour of the band gap of ternary semiconductor materials (Figure 87 b). This phenomenon known as band gap bowing is often ascribed to local compositional fluctuations which occur on substitution. The extent of such local atom displacements usually brings about nonlinear dependence on optical properties in ternary materials[291,292].

The Raman spectra of the particles are shown in Figure 88. The spectra of Bi_2S_3 and Sb_2S_3 show two peaks each at 236, 256 cm^{-1} and 272, 294 cm^{-1} respectively. The solid solutions consisting of 25 % antimony show mainly one broad band around 240 cm^{-1} which shift to higher frequencies of 253 and 260 cm^{-1} when the percentage of antimony is increased to 50 and 75 % respectively. These results are consistent with what is reported in literature[293,294].

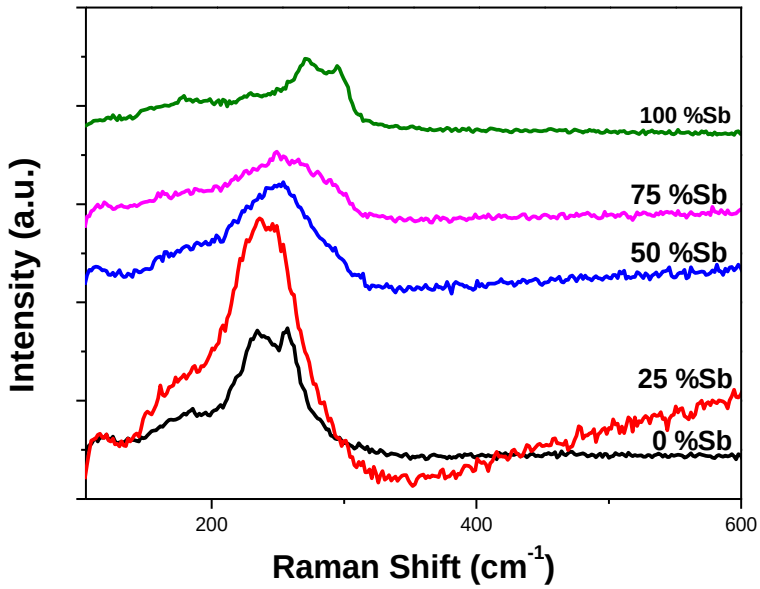

Figure 88. Raman spectra of nanorods of Sb_2S_3, Bi_2S_3 and $(Bi_{1-x}Sb_x)_2S_3$ solid solutions.

Chemical composition and homogeneity were determined by means of Energy-dispersive X-ray spectroscopy (EDX) analysis using an Oxford instrument X-max 50 EDX detector attached to the FEI TEM. Bi_2S_3, Sb_2S_3 and $(Bi_{1-x}Sb_x)_2S_3$ solid solutions were prepared by varying the mole ratio of Bi and Sb in the reaction mixture.

Figure 89 a, clearly represent the difference in the Bi/Sb proportions in the as-prepared nanorods. The result shows that the measured Bi and Sb ratios are proportional to the added amounts. Plotting the measured Sb mole fraction against the added amount gave an almost straight line (Figure 89 b), indicating the incorporation of Sb in the Bi_2S_3 matrix under the

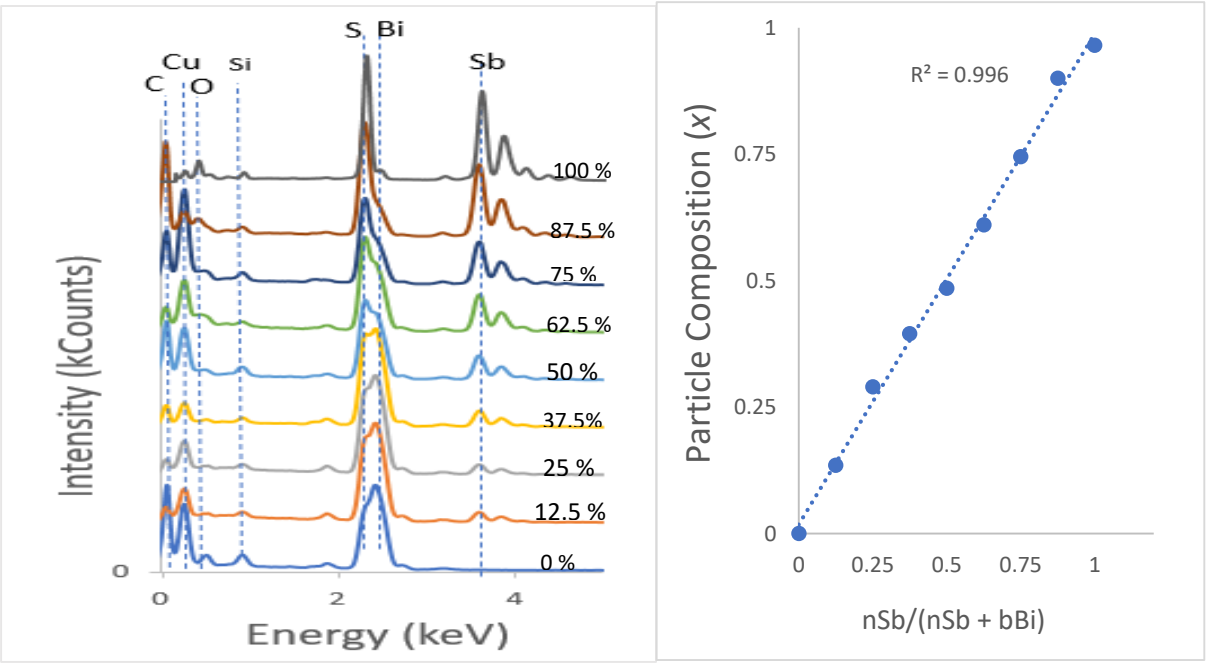

Figure 89. EDX spectra of Sb_2S_3, Bi_2S_3 and $(Bi_{1-x}Sb_x)_2S_3$ nanorods at different Bi:Sb mole ratios (b) Theoretical Sb metal content vs experimental observed value.

given experimental conditions. Based on EDX values, the empirical formula for the various samples prepared by varying Bi/Sb ratios was calculated without any correction for $(B_{1-x}Sb_x)_2S_3$, $(0 < x < 1)$ and the results presented in Table 28. Many of the samples were sulfur rich which is possibly due to the relatively low reaction temperature (230 °C) which avoids evaporation of sulfur, a situation commonly encountered in samples prepared at a much higher temperature[295,296].

Table 28. Structural data for Sb_2S_3, Bi_2S_3 and $(Bi_{1-x}Sb_x)_2S_3$ solid solution

X_{Bi} (%)	X_{Sb} (%)	Chemical composition (EDX)	Crystal system	Space group	a (Å)	b (Å)	c (Å)	V (Å)^3
1.00	0.00	$Sb_0Bi_{1.82}S_{3.18}$	orthorhombic	*P*nma	11.24	3.97	11.13	496.68
0.94	0.06	$Sb_{0.14}Bi_{1.66}S_{3.20}$	orthorhombic	*P*nma	11.23	3.96	11.14	495.40
0.88	0.13	$Sb_{0.27}Bi_{1.58}S_{3.15}$	orthorhombic	*P*nma	11.24	3.95	11.14	494.32
0.81	0.19	$Sb_{0.40}Bi_{1.48}S_{3.13}$	orthorhombic	*P*nma	11.24	3.94	11.14	493.03
0.75	0.25	$Sb_{1.49}Bi_{0.95}S_{3.08}$	orthorhombic	*P*nma	11.24	3.93	11.14	492.90
0.69	0.31	$Sb_{0.56}Bi_{1.23}S_{3.21}$	orthorhombic	*P*nma	11.25	3.92	11.15	492.13
0.63	0.38	$Sb_{0.79}Bi_{1.15}S_{3.06}$	orthorhombic	*P*nma	11.25	3.92	11.16	491.88
0.56	0.44	$Sb_{0.72}Bi_{1.15}S_{3.13}$	orthorhombic	*P*nma	11.25	3.90	11.15	488.88
0.50	0.50	$Sb_{0.97}Bi_{0.95}S_{3.08}$	orthorhombic	*P*nma	11.26	3.91	11.19	492.00
0.44	0.56	$Sb_{0.97}$ $Bi_{1.0}$ $S_{2.99}$	orthorhombic	*P*nma	11.26	3.90	11.19	491.44
0.38	0.63	$Sb_{1.22}Bi_{0.75}S_{3.04}$	orthorhombic	*P*nma	11.26	3.87	11.19	487.13
0.31	0.69	$Sb_{1.24}Bi_{0.71}S_{3.06}$	orthorhombic	*P*nma	11.26	3.87	11.19	487.50
0.25	0.75	$Sb_{1.49}Bi_{0.50}S_{3.00}$	orthorhombic	*P*nma	11.26	3.87	11.21	489.03
0.19	0.81	$Sb_{1.51}Bi_{0.39}S_{3.11}$	orthorhombic	*P*nma	11.26	3.85	11.21	485.52
0.13	0.88	$Sb_{1.80}Bi_{0.24}S_{2.96}$	orthorhombic	*P*nma	11.27	3.86	11.22	487.23
0.06	0.94	$Sb_{1.81}Bi_{0.15}S_{3.04}$	orthorhombic	*P*nma	11.27	3.83	11.22	484.57
0.00	1.00	$Sb_{1.93}Bi_{0.00}S_{3.07}$	orthorhombic	*P*nma	11.27	3.82	11.22	483.22

X-ray photoelectron spectroscopy (XPS) is much more surface sensitive than EDX, with sampling depths varying 6.3 – 9.0 nm for Sb, Bi and S[297], which is much less than the nanorod diameter. Bi *4f* coincides with the S *2p* region, and Sb *3d* coincides with O *1s*. Figure 90 shows a pile-up of the Bi *4f*/ S *2p* and Sb *3d*/ O *1s* regions for Bi_2S_3, Sb_2S_3 and $(Bi_xSb_{1-x})_2S_3$. In all cases, the Bi *4f* doublet required two chemical species (two sets of spin-orbit-split doublets) in order to obtain an adequate fit, with positions for the Bi $4f_{7/2}$ photoelectron peaks at 158.1 eV (associated with Bi_2S_3 [298] and 158.8 eV (associated with oxidized Bi_2O_3[299]. Likewise, the Sb *3d* doublet required two chemical species for adequate fitting, with peak positions for $3d_{5/2}$ at 259.1 eV (associated with Sb_2S_3[300] and 530.1 eV (associated with oxidized Sb_2O_3 [301]. Note that O *1s* photoelectron peaks are close to the Sb $3d_{5/2}$ signal (typically with binding energy positions at ~ 530.5 eV associated with metal

oxides (*i.e.*, BiO_x, SbO_x), ~ 532 eV associated with C-O contamination, and ~ 533 eV associated with C=O contamination). A variety of $(Bi_{1-x}Sb_x)_2S_3$ samples was measured, and consistently, a peak-fitting model including sulfide and oxide species was required for both Bi and Sb.

However, no oxidation was seen for S; only one species for the S *2p* doublet was observed for all the samples measured, with the peak position for $2p_{3/2}$ at ~ 161.0 eV associated with sulfide [298,300], and in the spectra there is a clear absence of any signal associated with sulfate which is expected in the binding energy region 168-170 eV[302]. Also, when calculating the atomic ratios of Bi:Sb:S, there is consistently an absence of S as expected for $(Bi_{1-x}Sb_x)_2S_3$; in Figure 90 the $(Bi_{1-x}Sb_x)_2S_3$ sample exhibits a Bi:Sb:S ratio of 3:3:4 (or 1:1:1.3, short of the expected 1:1:1.5). This indicates that there is an absence of sulfur atoms at the surface

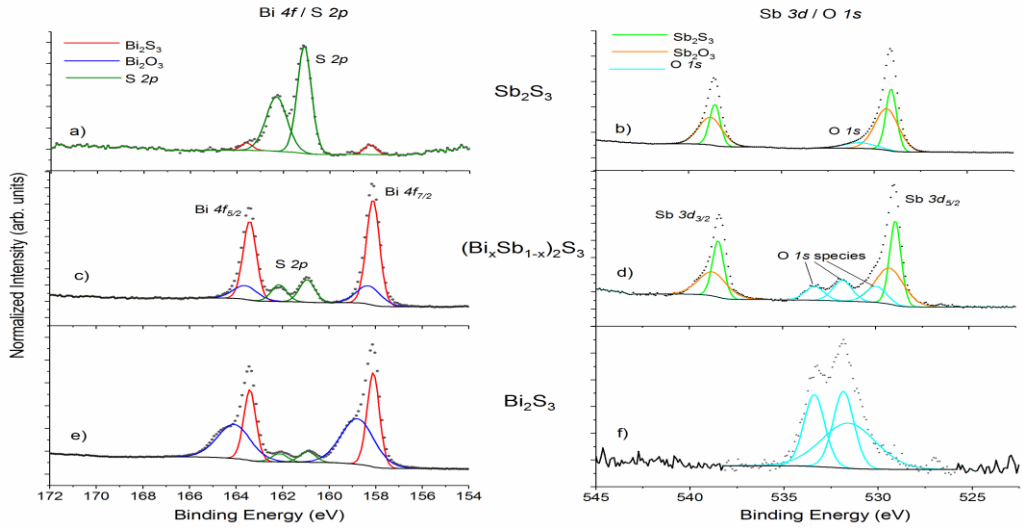

Figure 90. XPS spectra for Sb_2S_3 (top panels (a) and (b)), Bi_2S_3 (bottom panels (e) and (f)), and $(Bi_{1-x}Sb_x)_2S_3$ (middle panels (c) and (d)). The Bi $_{4f}$ and S $_{2p}$ spectral regions overlap ((a), (c), (e)), and the Sb 3d region overlaps with O 1s ((b), (d), (f)). Bi.

of the nanorods (hence the atomic concentrations are skewed from the bulk measurement by EDX analysis, and this also explains the lack of sulfur oxidation), and a small amount of Bi and Sb atoms at the surface of the nanorods are susceptible to oxidation. For the range of $(Bi_{1-x}Sb_x)_2S_3$ nanorod materials measured, the amount of oxidation of Bi and Sb observed varied between 10-40% (with an average value of 20% for Bi and 26% for Sb).

Table 29. Relative percentage concentrations of Bi, Sb and S for Sb_2S_3, Bi_2S_3 and $(Bi_{1-x}Sb_x)_2S_3$ obtained from XPS.

Sb/(Sb+Bi)	Bi-S %	Bi-O %	Total Bi %	Sb-S %	Sb-O%	Total Sb %	S %
0	49.79	18.69	68.49	0.00	0.00	0.00	31.51
0.125	49.11	9.33	58.43	4.44	0.49	4.93	36.64
0.25	45.20	8.61	53.81	7.86	1.56	9.43	36.76
0.375	37.32	8.25	45.57	17.53	1.76	19.29	35.14
0.5	34.86	5.81	40.67	15.55	6.17	21.72	37.60
0.625	27.85	5.32	33.17	20.94	7.39	28.34	38.49
0.75	27.45	3.40	30.85	23.36	6.67	30.03	39.13
0.875	17.09	1.66	18.74	29.75	11.16	40.91	40.35
1	3.56	0.00	3.56	38.20	12.14	50.34	46.10

The XRD peaks at all ratios correspond well to the orthorhombic crystals, with the peaks for Bi-Sb-S system falling in between those of orthorhombic bismuthinite (a = 11.2690 Å, b = 3.9717 Å and c = 11.1290 Å, accsd 0009004 bottom) and orthorhombic stibnite (a = 11.2990 Å, b = 3.8313 Å and c = 11.2270 Å, amscd 0008825 top) in Figure 91 a. Refinement was also performed to determine unit cell parameters and investigate the Vegard's law

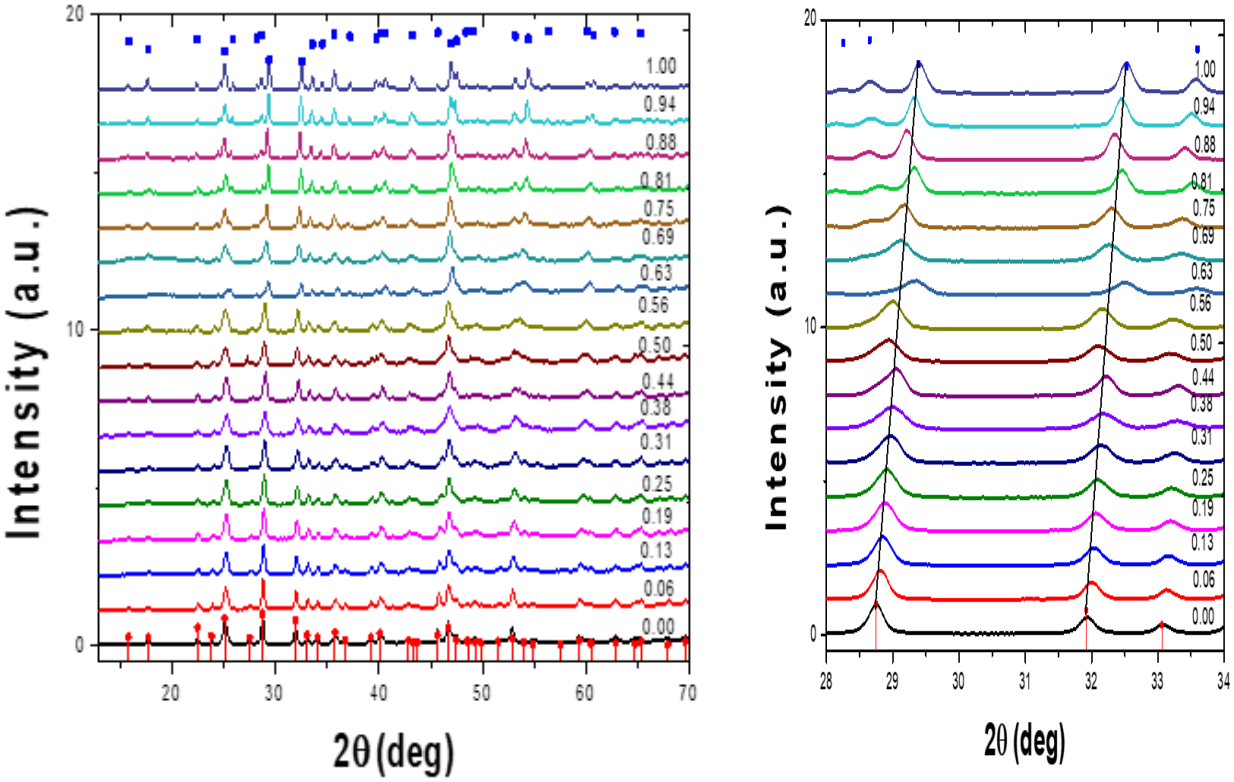

Figure 91. (a) Powder XRD pattern of Bi_2S_3 (bottom), $((Bi_{1-x}Sbx)_2S_3$ and Sb_2S_3 (top), Samples synthesized from different Sb mole fraction (b) p-XRD pattern of 2ϑ range 28-34 degree showing shift in peaks.

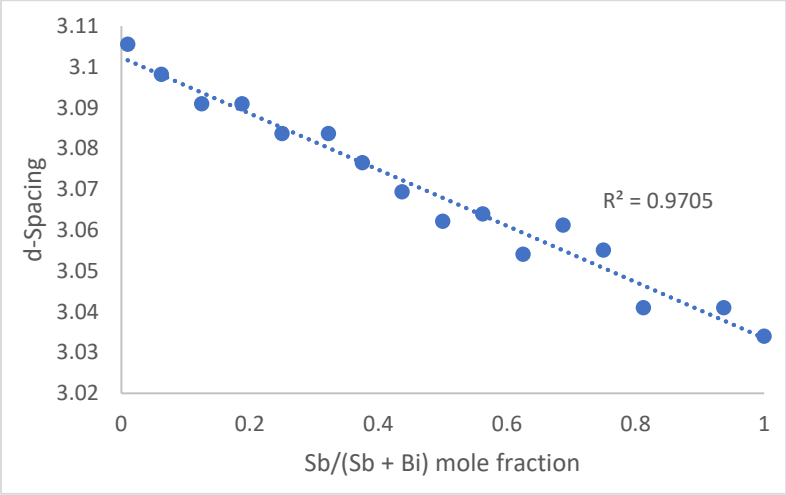

Figure 92. Plot of d-spacing against Sb/(Sb+Bi) mole fraction.

behaviour of the $(Bi_{1-x}\,Sb_x)_2S_3$ solid solution. For a crystal whose lattice reacts as an elastic medium Vegard's law requires the change of the lattice constant to be proportional to the concentration of the dopant and to the difference between ionic radii of the dopant and substituted host atom. Sb_2S_3 and B_2S_3 both crystalize into the same orthorhombic lattice with a difference in cell volume of 3.5 %. Substituting Sb^{3+} of smaller ionic radius for Bi^{3+}

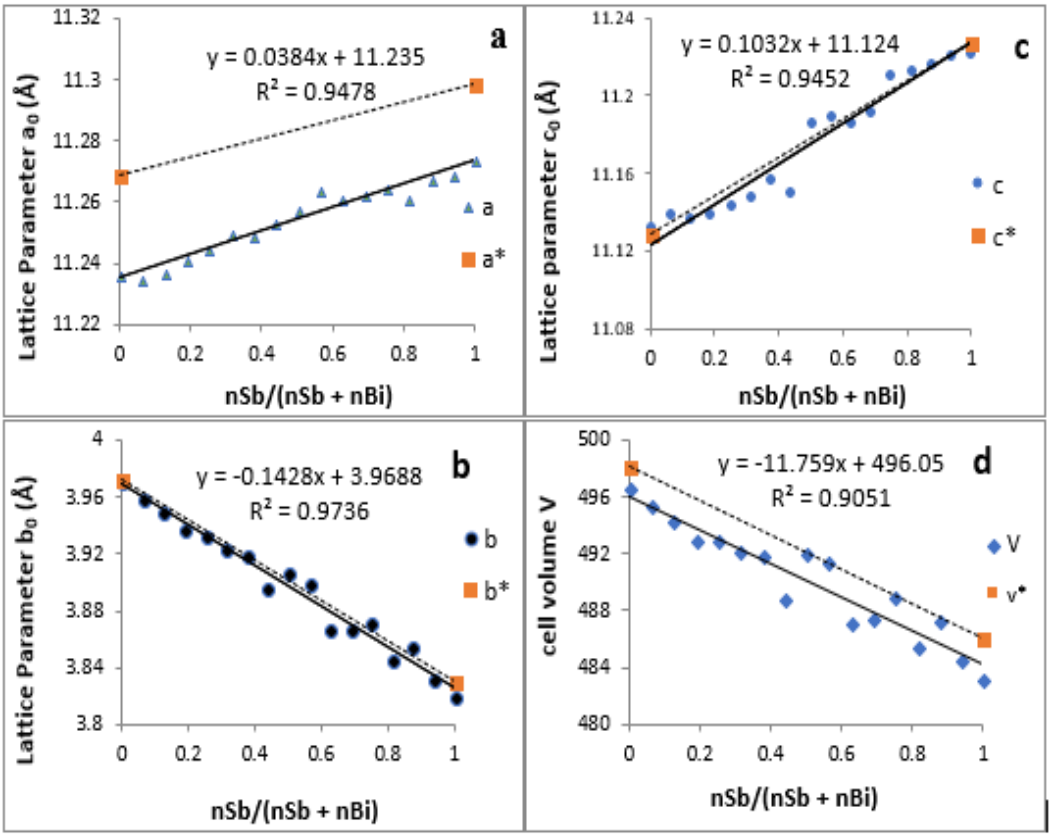

*Figure 93. Variation of lattice constants with increasing mole fraction of Sb. (a) lattice parameter a, (b) lattice parameter b, (c) lattice parameter c and (d) cell volume. * values represent the reported standard value (dotted lines) for Bi_2S_3 and Sb_2S_3.*

should cause the lattice to contract with a reduction in unit cell volume. Figure 91 b shows an enlarge potion of the XRD pattern of the samples from 27 -33°. The gradual splitting and shift in the peaks positions confirm the incorporation of Sb into the Bi_2S_3 lattice and formation of a solid solution of $(Bi_{1-x}Sb_x)_2S_3$.

A plot of the d-spacing for the (112) plane shows a gradual decrease from Bi_2S_3 to the Sb_2S_3 end with a percentage difference of 2.31% (Figure 92).

Refinement of p-XRD data shows the dependence of each lattice parameter on substitution. Figure 93 a-c, shows the b axis shrinks almost monotonously but the a and c axes elongate. They all show a linear dependence on Vegard's law but slight deviations are seen for the a and c axes. The slight deviation from ideal behaviour may be due to the influence of two factors namely, The size effect of substituting Bi with Sb of smaller radius which should bring about contraction in the lattice, and secondly the more influential and contrasting effect of the steoreochemical active lone pair of $5S^2$ and $6S^2$ electrons on antimony and bismuth atoms, which is positioned in the a-c plane of the lattice[192,291].

On increasing dilution with Sb, there is an expansion of the inter-rod space due to increase expression of the activity of the lone electron pair which is larger for antimony, with a resulting expansion of the a and c parameters[189]. However, the b axis which is least affected by the stereochemical active lone pair experiences a continuous contraction on Sb substitution, probably due to a decrease in the shortest M-S bond as we move from the Bi_2S_3 to the Sb_2S_3 end . There is a general shrinkage of the overall cell volume of $(Bi_{1-x}Sb_x)_2S_3$ as Bi is replaced by Sb (Figure 93 d).

Table 30. Dimensions of synthesized nanorods of Bi_2S_3, Sb_2S_3 and $(Bi_{1-x}Sb_x)_2S_3$ solid solution

Sb/(Sb + Bi)	Length (nm)		width (nm)		Aspect ratio
0.00	474.4	± 92.62	28.61	± 12.90	16.58
0.06	169.25	±48.15	26.69	±23.79	6.34
0.13	104.99	± 46.38	19.79	± 9.13	5.31
0.19	161.60	±71.87	42.96	±24.84	3.76
0.25	65.13	± 13.52	23.69	± 6.50	2.75
0.31	77.61	±15.00	23.19	±5.21	3.35
0.38	57.00	± 11.12	15.55	± 4.07	3.66
0.44	81.39	±26.94	30.66	±8.02	2.65
0.50	60.38	± 12.60	23.38	± 4.38	2.58
0.56	80.93	±23.76	19.09	±3.27	4.24
0.63	25.04	± 7.37	5.56	± 1.09	4.51
0.69	115.17	±34.89	21.54	±3.37	5.35
0.75	142.81	± 56.58	28.56	± 5.01	5.00
0.81	245.18	±101.09	32.92	±13.01	7.45
0.88	386.32	± 137.43	40.05	± 11.08	9.65
0.94	474.14	±137.23	32.62	±5.54	14.53
1.00	2880.47	± 550.22	137.09	± 44.82	21.01

TEM analysis on the samples showed that they all consist of 1-d rods Figure 94 a-q. With no Sb present, we obtained elongated uniform cylindrical nanorods of Bi_2S_3 (Figure 115a). Without any Bi, elongated sheaf-like rods of Sb_2S_3 in the sub-micrometre range were obtained(Figure 94 q). There was a conspicuous change in aspect ratio and morphology of the rods as the ratio of Bi/Sb was varied as summarized in Table 30. With a Bi:Sb mole ratio of 7:1 (0.06 Sb), there was a considerable reduction in both the length and aspect ratio of the nanorods compared to pure Bi_2S_3. This decrease continued till a mole ratio of 1:1, where the aspect ratio is smallest. At higher mole ratios of Sb, the aspect ratio starts increasing again with an increase in the length of the rods. At 1:7 Bi:Sb mole ratio (0.94 Sb) the longest rods of the Bi-Sb-S ternary system were obtained. Figure 95 shows the variation of aspect ratio with mole fraction of Sb. Addition of Bi into Sb_2S_3 lattice tuned morphology as there was a shift from very long sheaf-like sub-micrometre rods to shorter separate nanorods. Figure 96 shows the particle size distribution of some of the nanorods.

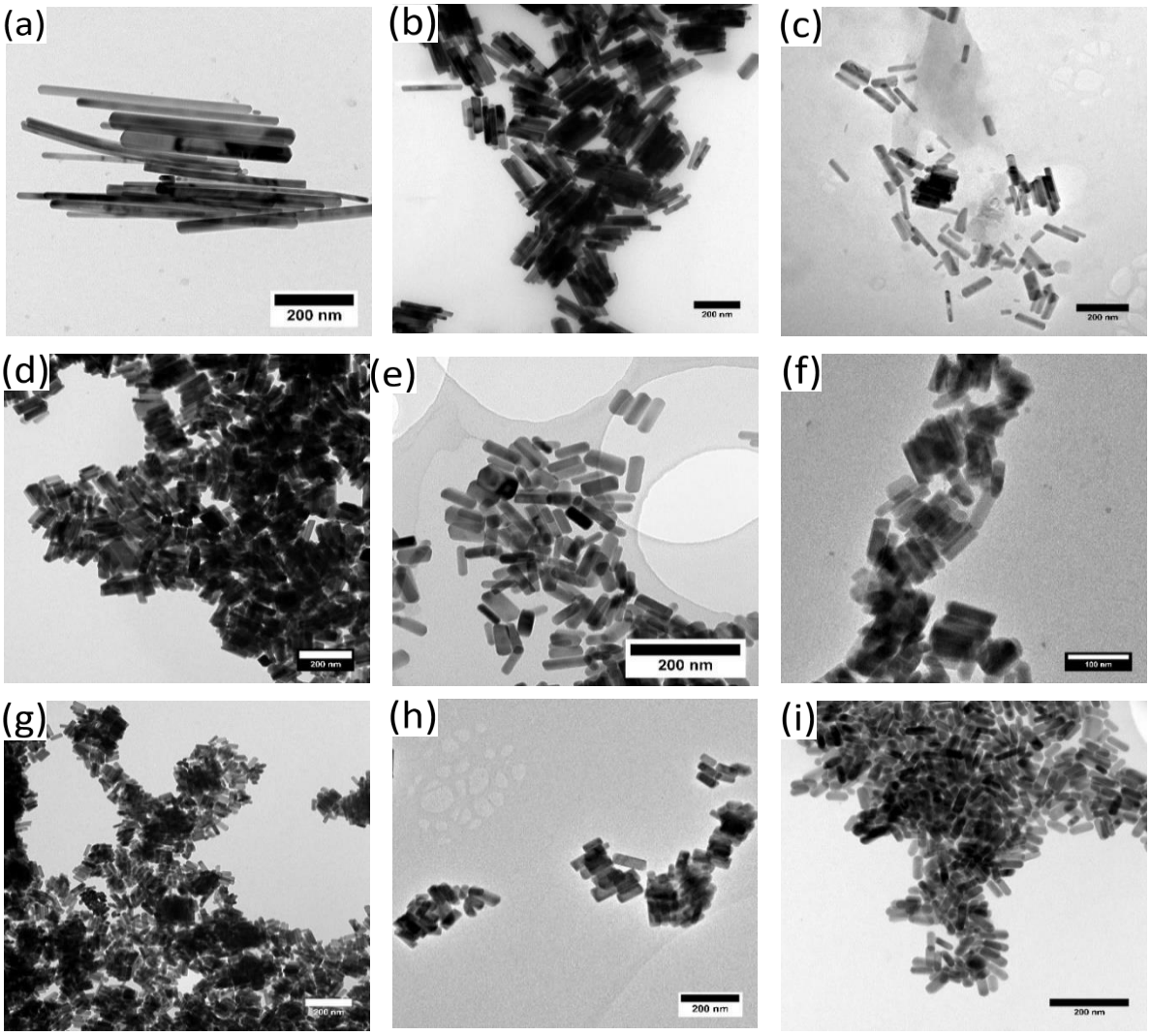

Figure 94. (i). TEM images showing the as synthesized nanorods with Sb/(Sb + Bi) mole fraction of (a) 0, (b) 0.06 (c) 0.13 (d) 0.19 (e) 0.25 (f) 0.32 (g) 0.38 (h) 0.44 (i) 0.50.

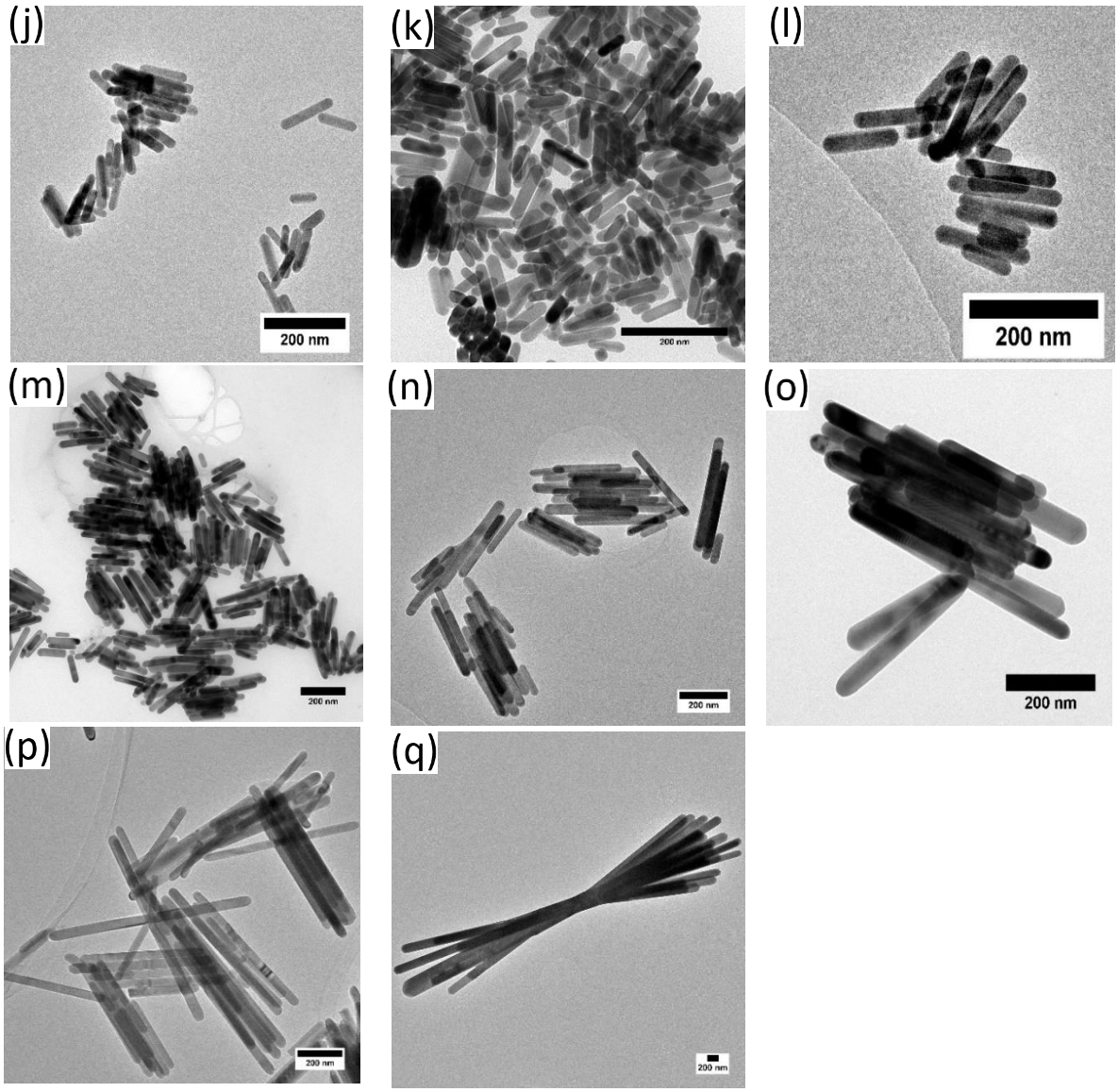

(ii). TEM images showing the as synthesized nanorods with Sb/(Sb + Bi) mole fraction of of 0.56, (k) 0.63 (l) 0.69 (m) 0.75 (n) 81 (o) 0.88 (p) 0.94) (q) 1.

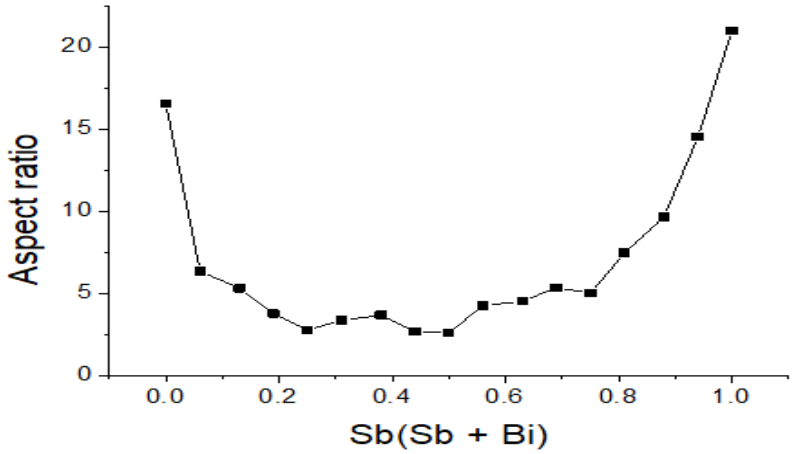

Figure 95. Variation of aspect ratio with Sb/(Sb + Bi) mole fraction.

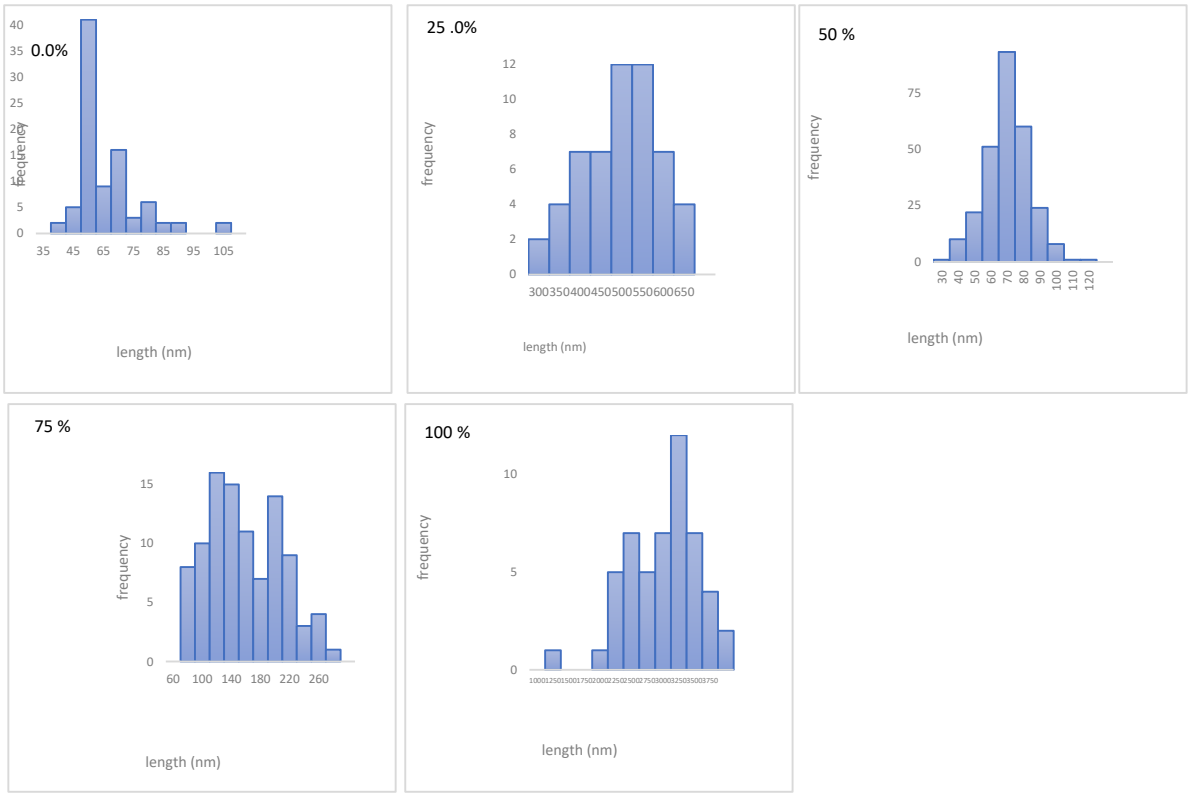

Figure 96. particle size distribution of the as synthesized nanorods against % Sb in nanorods.

Figure 97 a-q shows the High-resolution transmission electron microscopy (HRTEM) images of the samples together with their selected area electron diffraction (SAED) patterns. The patterns reveal highly polycrystalline powders showing two-dimensional lattice fringes. d-spacings of 3.69 and 4.98 Å were measured for pure Bi_2S_3 (Figure 97 a, corresponding to the (011) and (102) planes (SG *P*nma with a= 11.2690 Å, b =3.9717 Å and c= 11.1290 Å) while for pure Sb_2S_3 (Figure 97 q, a d-spacings of 3.50 Å corresponding to the (111) (SG *P*nma with a = 11.2990 Å, b = 3.8313 Å and c = 11.2270 Å) plane was recorded. The micrographs of the solid solutions prepared by varying Bi:Sb mole ratios (Figure 97 b,-p), shows measured lattice spacing values close to those expected for the pure end members. The measured d-spacings together with their respective reflections are shown in Table 31.

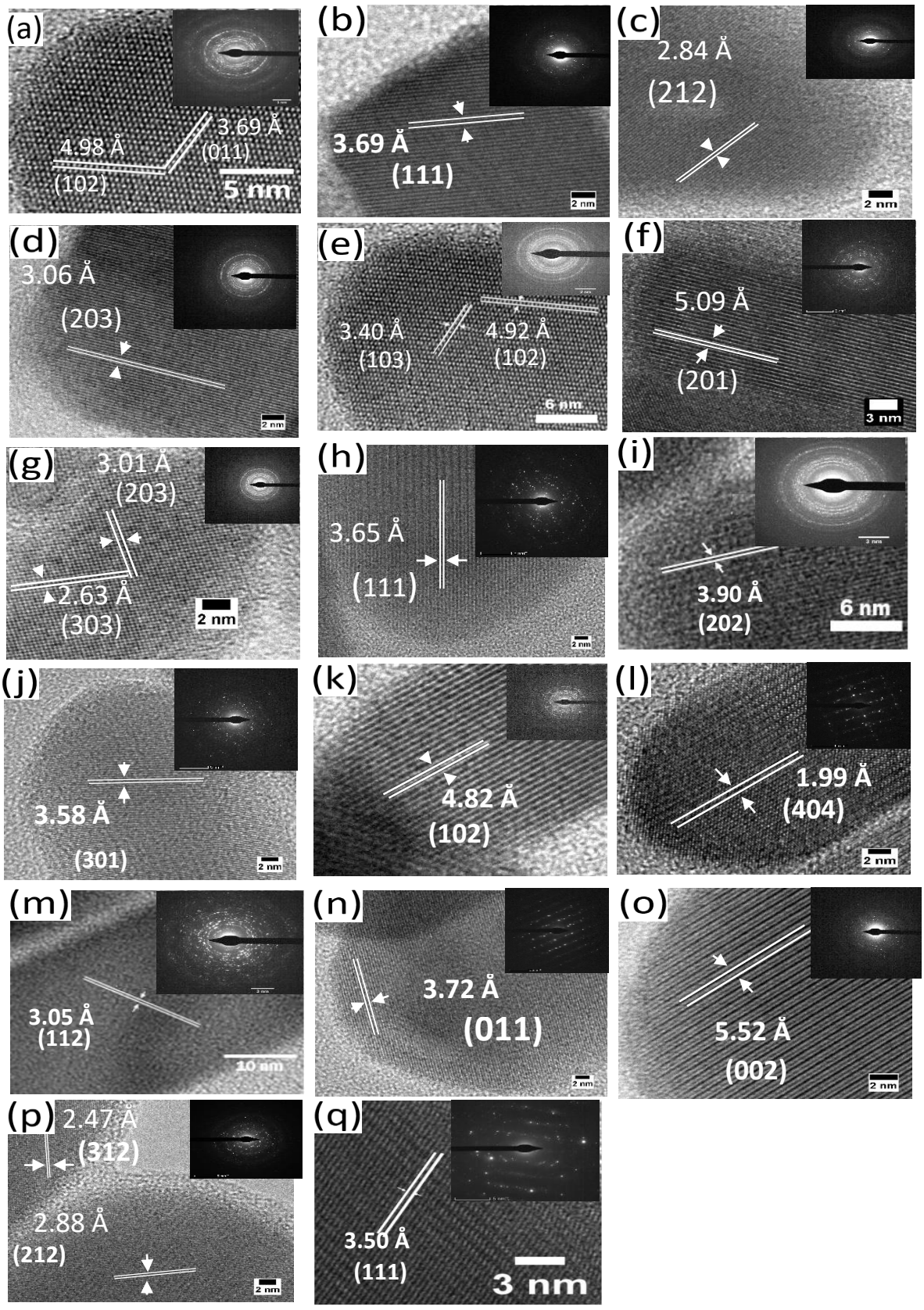

Figure 97. HRTEM images of synthesized nanorods with Sb/(Sb + Bi) mole fraction of 0, (b) 0.06 (c) 0.13 (d) 0.19 (e) 0.25 (f) 0.31 (g) 0.38 (h) 0.44 (i) 0.50 j) 0.56, (k) 0.63 (l) 0.69 (m) 0.75 (n) 81 (o) 0.88 (p) 0.94) (q) 1. Inset in each image shows the SAED pattern.

Table 31. observed d-spacing for Bi_2S_3, Sb_2S_3 and $(Bi_{1-x}Sb_x)_2S_3$ solid solution

Sb/(Sb + Bi)	Measured d-spacing (Å)	Bismuthinite, stibnite ref. d-spacing (Å)	hkl
0.00	3.69	3.63	011
	4.98	4.99	102
0.06	3.69	3.56	111
0.13	2.84	2.80	212
0.19	3.06	3.09	203
0.25	3.40	3.52	103
	4.92	4.99	102
0.31	5.09	5.03	201
0.38	3.01	3.09	203
	2.63	2.64	303
0.44	3.65	3.55	111
0.50	3.90	3.96	202
0.56	3.58	3.57	301
0.63	4.82	5.03	102
0.69	1.99	1.99	404
0.75	3.72	3.63	011
0.81	3.05	3.05	112
0.88	5.52	5.61	002
0.94	2.47	2.42	312
	2.88	2.76	212
1.00	3.50	3.45	111

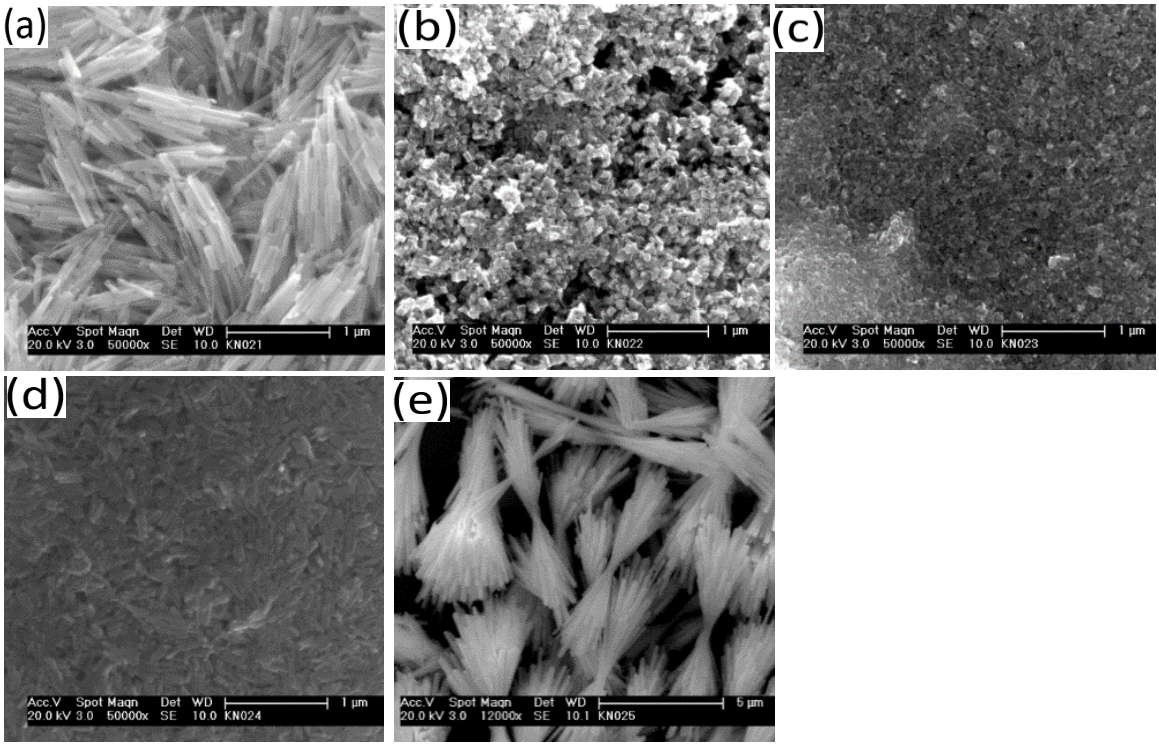

Figure 98. SEM images showing surface scan of films with Bi:Sb mole ratios of (a) 1:0, (b) 3:1 (c) 1:1 (d) 1:3 (e) 0:1.

Figure 98 a-e. shows a representative SEM micrograph of as synthesized particles. The images presented uniform microstructure, and the rod morphology reported by TEM. The composition driven growth evolution was very evident as the shape and size of the particles changed with changes in Bi/Sb mole ratio. Figure 99 shows the elemental mappings of Bi, Sb and S respectively in the 1: 1 Bi/Sb mole ratio indicating uniform distribution of the elements, confirming that we obtained a pure crystal phase under synthetic conditions.

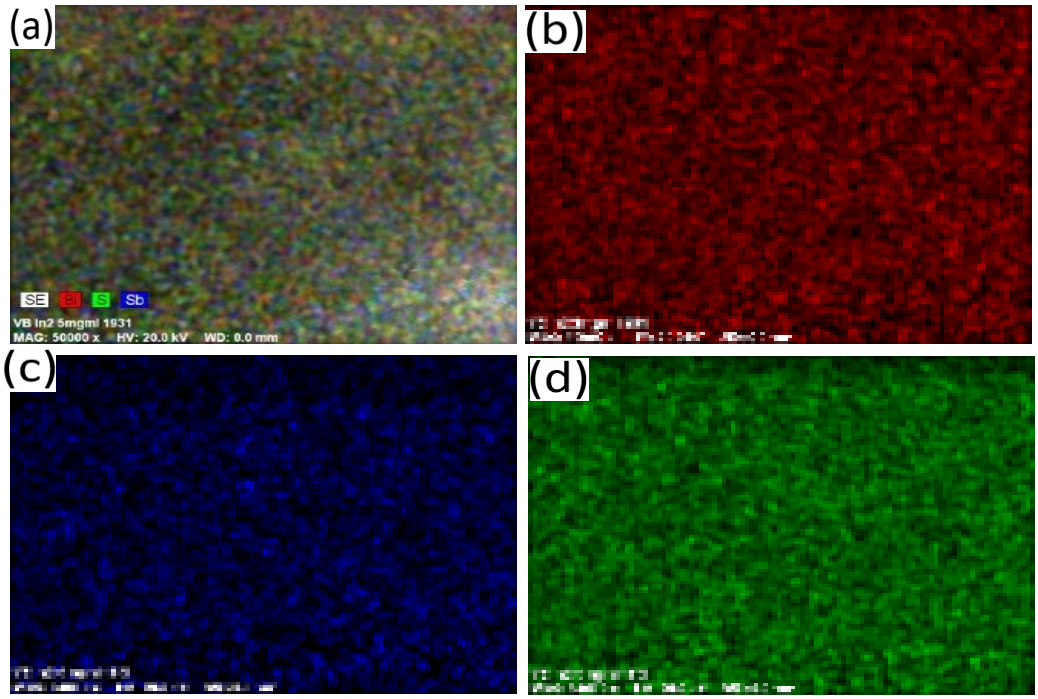

Figure 99. Figure elemental mapping of the particle synthesized at Bi:Sb mole ratio of 1:1 showing distribution of atoms.

3.7. Deposition of Bi_2S_3 thin films on glass substrate

Several studies on the deposition of Bi_2S_3 thin films using DSPs have been reported. Ahire *et al* deposited Bi_2S_3 thin films by a modified chemical bath deposition technique from $Bi(NO_3)_3$ and thioacetanamide and improved the crystallinity of the films after annealing[303]. Killedar *et al* deposited Bi_2S_3 thin films by spraying a non-aqueous solution of $Bi(NO_3)_3$ in acetic acid and thiourea in formaldehyde on to a hot glass substrate. The films were found to consist of non-crystalline grains of Bi_2S_3[304]. Wang *et al* deposited 'nanoleaf-like' Bi_2S_3 thin films on indium tin oxide (ITO) glass using $Bi(NO_3)_3$ and $Na_2S_2O_3$ as precursors by a cathodic electrodeposition process and found that the crystallization of the films increased with increase in $Bi(NO_3)_3$: $Na_2S_2O_3$ concentration ratio[305]. Monteiro and co-workers

reported the low-pressure metal-organic chemical vapour deposition of Bi_2S_3 thin films on glass substrates using bismuth(III) dithiocarbamate complexes[28].

This section reports on the deposition of crystalline Bi_2S_3 thin films using bismuth dithiocarbamate complexes as single source precursors by aerosol assisted chemical vapour deposition (AACVD) and spin coating techniques. Thin films of Bi_2S_3 were deposited on glass substrate, by varying the solvent mixture and substrate temperature as reported in section 2.3.6 page 49.

3.7.1. Deposition of Bi_2S_3 thin films from chloroform/methanol 3:1 by AACVD

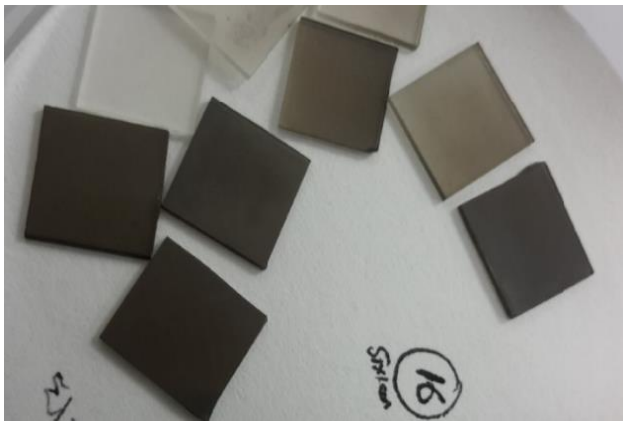

Figure 100. Images of Bi_2S_3 thin films deposited from $[Bi(S_2CPip)_3]$ in $CHCl_3/CH_3OH$ on glass substrate 400 °C.

The complexes $[Bi(S_2CPip)_3]$ and $[Bi(S_2CThq)_3]$ were dissolved in $CHCl_3/CH_3OH$ 3:1 mixture and used to deposit Bi_2S_3 thin films on glass substrate by AACVD at substrate temperatures of 350 °C, 400 °C and 450 °C. The films where either silver grey or specular, when both complexes were used depending on the temperature. Dark brown and slightly powdery films were obtained at 350 °C whilst silver grey films were obtained at 400 and 450 °C (Figure 100).

Optoelectronic properties for semiconducting materials are essential since most of their applications depend on both the nature and the magnitude of their optical band structure. Figure 101 shows the room temperature optical absorption spectra of the thin films deposited by AACVD from $[Bi(S_2CPip)_3]$ in $CHCl_3/CH_3OH$ mixture 3:1 at 350-450 °C. The bandgap for the various transitions was estimated by plotting a graph of $(\alpha h\nu)2$ versus $h\nu$ and read from the intercept of the extrapolated linear fit to the experimental data of the Tauc plot (inset of Figure 101). The estimated band gap was found to be 1.68 eV for the films at 350,

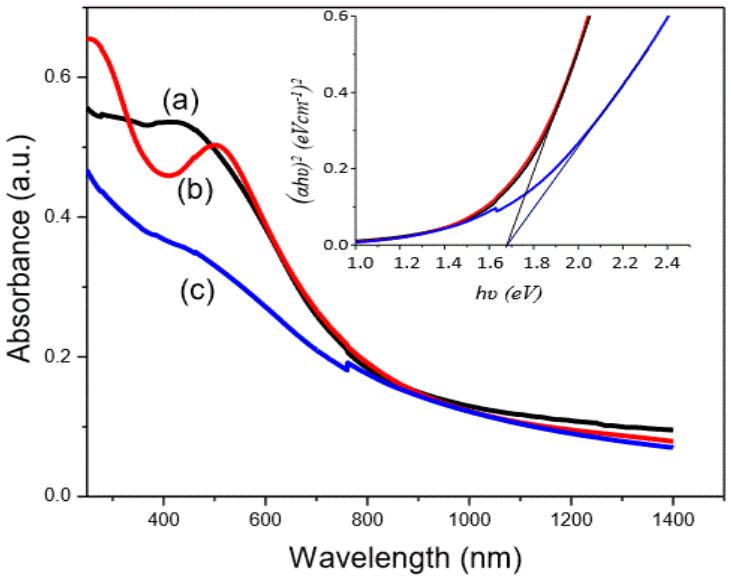

Figure 101. UV/Visible spectra of Bi_2S_3 thin films prepared from [$Bi(S_2CPip)_3$] by AACVD in $CHCl_3$/ CH_3OH mixture at (a) 350 °C (b) 400 °C and (c) 450 °C.

400 and 450 °C. This value corroborates with that reported for bulk bismuth sulfide, which has an energy band gap of 1.2-1.7 eV.

The p-XRD patterns for Bi_2S_3 films prepared from [$Bi(S_2CPip)_3$] in $CHCl_3$/CH_3OH mixture 3:1 at 350-450 °C is shown in Figure 102. The XRD patterns clearly show the polycrystalline nature of the films deposited at all reaction temperatures. The diffraction planes were indexed to the standard orthorhombic Bi_2S_3 (ICCD 00-02-0391) phase with no significant deviation of the peak intensity from that of bulk bismuthinite.

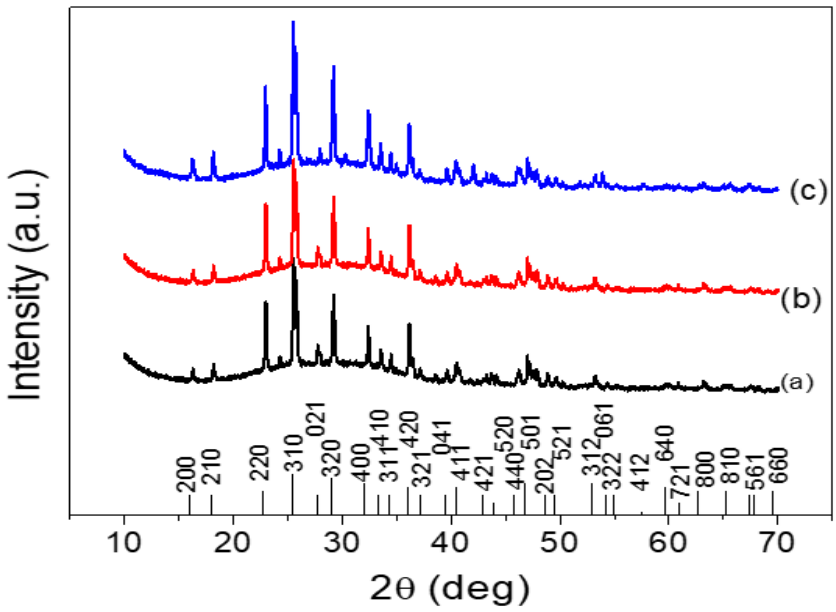

Figure 102 p-XRD of Bi_2S_3 thin films prepared from [$Bi(S_2CPip)_3$] by AACVD in $CHCl_3$/ CH_3OH mixture at (a) 350 °C (b) 400 °C and (c) 450 °C.

Table 32. EDX results for Bi_2S_3 thin films deposited on glass substrate

Complex	Solvent	Synthetic method	Substrate Temp. °C	Bi:S Atomic % from EDX	
				Bi %	S %
$[Bi(S_2CPip)_3]$	$CHCl_3/CH_3OH$ 3:1	AACVD	350	53.80	46.20
			400	50.90	49.10
			450	70.40	29.60
$[Bi(S_2CThq)_3]$			350	81.00	19.00
			400	55.10	44.90
			450	67.60	32.40
$[Bi(S_2CPip)_3]$	$CHCl_3/CH_3CN$ 3:1	AACVD	350	34.90	65.10
			400	35.30	64.70
			450	30.20	69.80
$[Bi(S_2CThq)_3]$			350	29.20	70.80
			400	45.60	54.40
			450	47.70	52.30
$[Bi(S_2CPip)_3]$	$CHCl_3/CH_3OH$ 3:1	Spin Coating	350	41.20	58.80
			400	40.20	59.80
			450	44.30	55.70
$[Bi(S_2CThq)_3]$			350	41.80	58.20
			400	43.00	57.00
			450	43.50	56.50

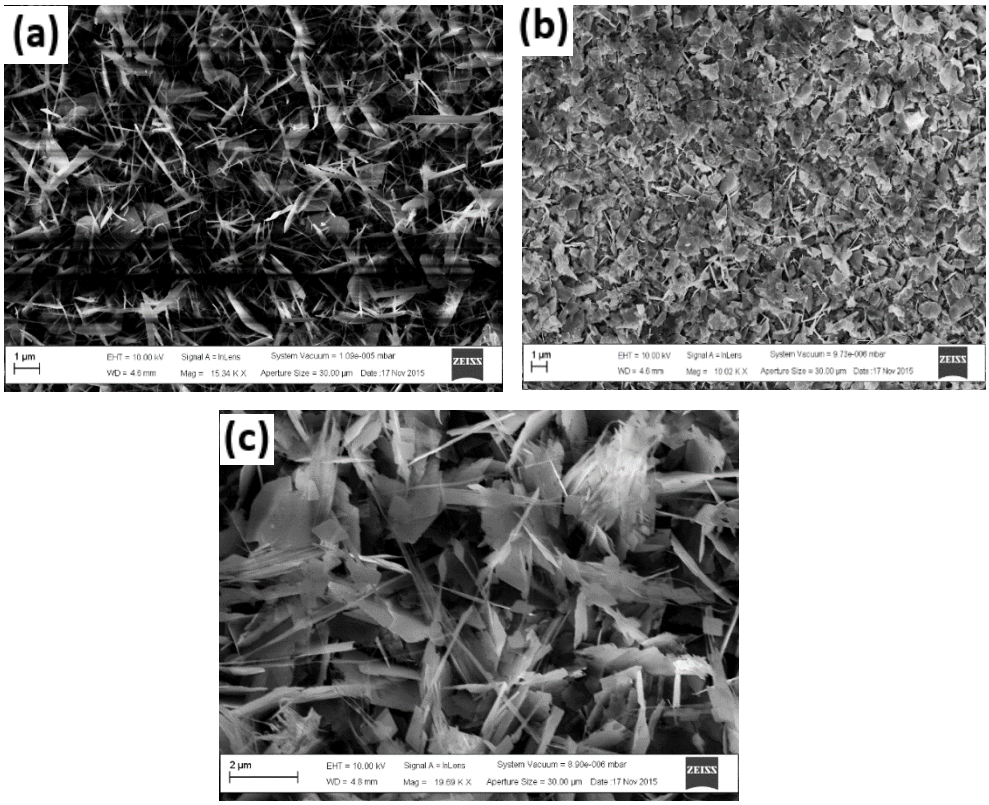

Figure 103. SEM of Bi_2S_3 thin films deposited from $[Bi(S_2CPip)_3]$ by AACVD at (a) 350 °C (b) 400 °C and (c) 450 °C in $CHCl_3$/MeOH mixture.

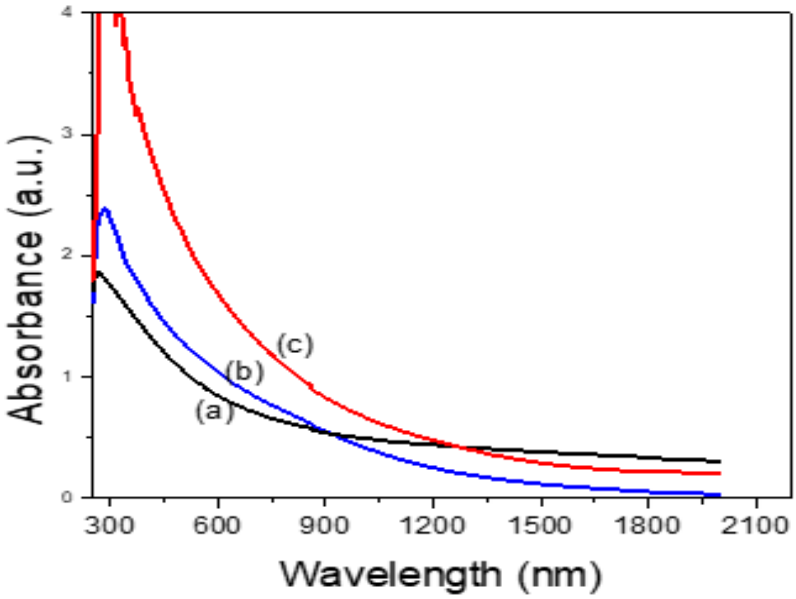

Figure 104. UV/Visible spectra of Bi_2S_3 thin films prepared by AACVD from $Bi(S_2CThq)_3$ at (a) 350 °C (b) 400 °C and (c) 450 °C in $CHCl_3$/MeOH mixture.

The SEM micrographs of the films revealed a mixture of randomly oriented nanoplatelets and nanofibers for films deposited at all reaction temperatures (Figure 103). At 350 °C randomly oriented hexagonal plates grow alongside ribbon-like fibers while at 400 °C irregularly shaped plates with a wide size distribution grow parallel to the axis of the substrate. At 450 °C, leaf-like plates are formed with needle-like fibers. EDX analysis was performed on the films in order to determine their composition. The results show some sulfur

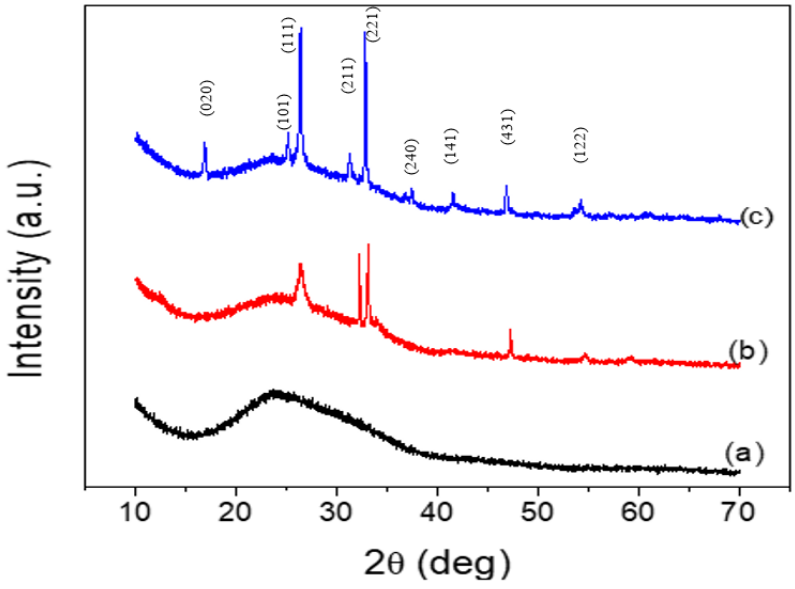

Figure 105. p-XRD patterns of the films deposited using $[Bi(S_2CThq)_3]$ at 350, 400 and 450 °C consist of orthorhombic Bi_2S_3 (ICDD number 00-02-0391).

deficiency in the films deposited at all three temperatures with the highest percentage of sulfur deposited at 400 °C compared to 350 °C and 450 °C (Table 32) .

Figure 104 shows the UV/Visible spectra of Bi_2S_3 thin films prepared by AACVD from $Bi(S_2CThq)_3$ at a) 350 °C b) 400 °C and c) 450 °C in $CHCl_3$/MeOH solvent mixture. The spectra show a broad absorption in the near infra-red region.

p-XRD patterns of the films deposited at 350, 400 and 450 °C (Figure 105) consist of orthorhombic Bi_2S_3 (ICDD number 00-02-0391). The morphology of the films was similar to those obtained from $[Bi(S_2CPip)_3]$. However, they had more compact grains with more defined leaf-like shapes at 400 and 450 °C (Figure 106 a-c). A cross section of the film deposited from $[Bi(S_2CThq)_3]$ at 450 °C revealed the formation of rectangular plates of about 1.49 x 0.86 µm and wire of about 0.20 x 3.40 µm growing obliquely from the edges of the plates (Figure 106 d).

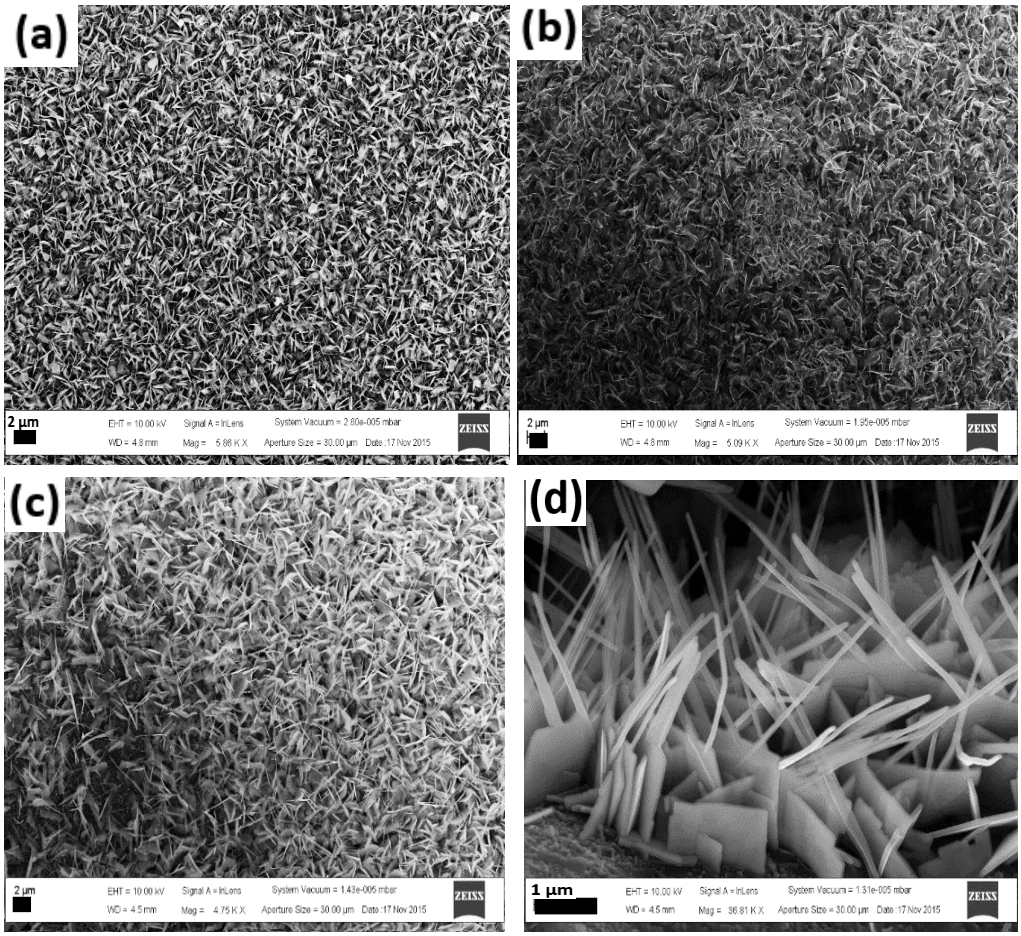

Figure 106. SEM images of Bi_2S_3 thin films deposited from $[Bi(S_2CThq)_3]$ by AACVD at (a) 350 °C (b) 400 °C and (c) 450 °C in $CHCl_3$/MeOH mixture d) side view of film at 450 °C.

3.7.2. Deposition of Bi_2S_3 thin films from chloroform/acetonitrile 3:1 by AACVD

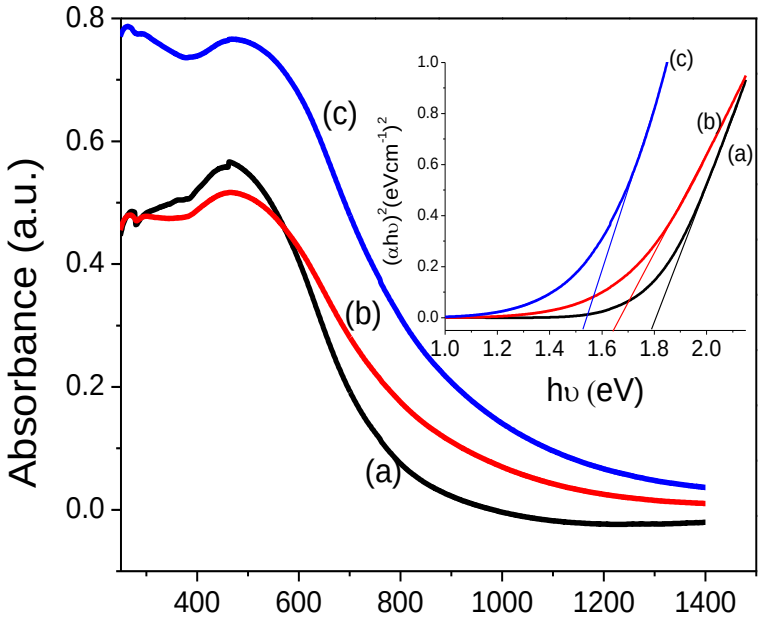

Figure 108. UV/Visible spectra of Bi_2S_3 thin films prepared by AACVD from $[Bi(S_2CPip)_3]$ at (a) 350 °C (b) 400 °C and (c) 450 °C in $CHCl_3/CH_3CN$ solvent mixture.

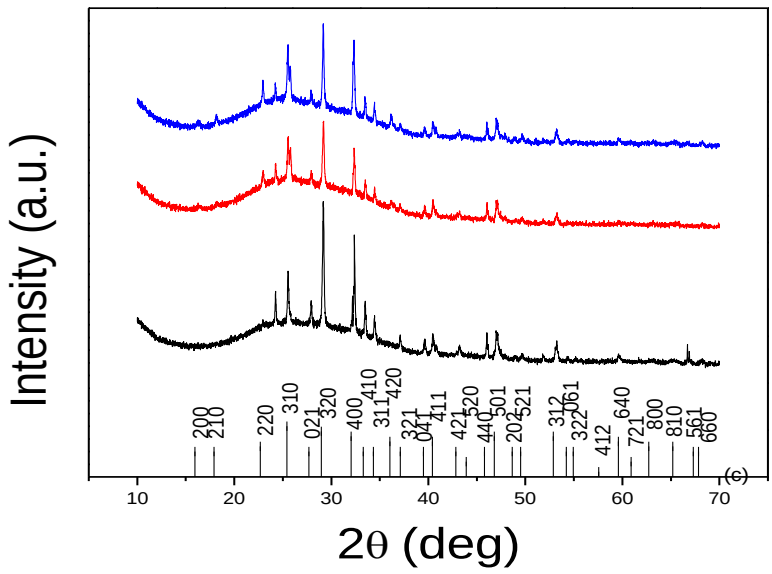

Figure 107. p-XRD of Bi_2S_3 thin films prepared by AACVD from $[Bi(S_2CPip)_3]$ at (a) 350 °C (b) 400 °C and (c) 450 °C in $CHCl_3/CH_3CN$ solvent mixture.

The films deposited from $CHCl_3/CH_3CN$ 3:1 were grey at 350 °C and silvery at 400 and 450 °C. UV/Visible spectra of the films deposited using $[Bi(S_2CPip)_3]$ at 350, 400 and 450 °C (Figure 107) showed a decreasing red shift in the absorption band edge from 1.79, 1.69 to

1.54 eV as the deposition temperature was increased from 350 to 400 °C, then to 450 °C respectively. This decrease in energy band gap is due to increase in mean particle size as the temperature increases.

The p-XRD patterns of films deposited from [$Bi(S_2CPip)_3$] in $CHCl_3/CH_3CN$ solvent mixture at 350 ^oC , 400 ^oC and 450 ^oC are shown in Figure 108. The samples were polycrystalline and consisted of orthorhombic Bi_2S_3 (ICDD number 00-02-0391) with a preferred orientation in the (320) direction as well as a significant reduction in the intensity of the (310) peak when compared to those deposited from $CHCl_3/CH_3OH$.

Figure 109 shows the SEM analysis of the films deposited from [$Bi(S_2CPip)_3$]. Long cylindrical fibers were formed at 350 and 450 °C. At 400 °C the film consisted of a mixture of fibers and underlying plates. The breadth of the fibers was found to increase with increase

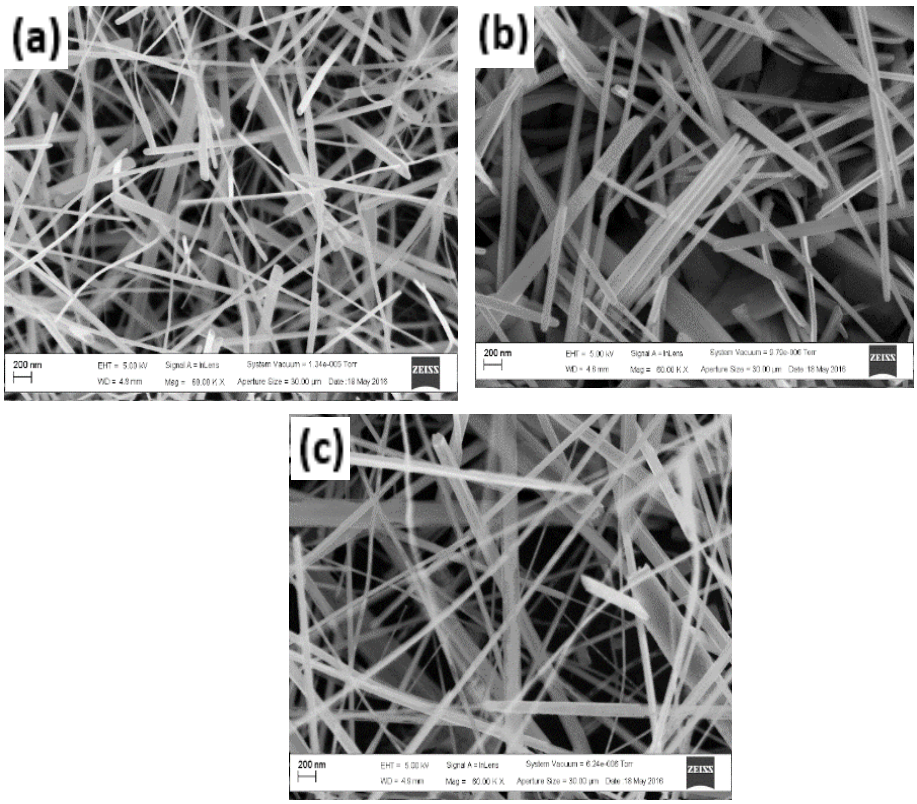

Figure 109. SEM images of Bi_2S_3 thin films from [$Bi(S_2CPip)_3$] deposited by AACVD at (a) 350 °C (b) 400 °C, (c) 450 °C in $CHCl_3$/ CH_3CN mixture.

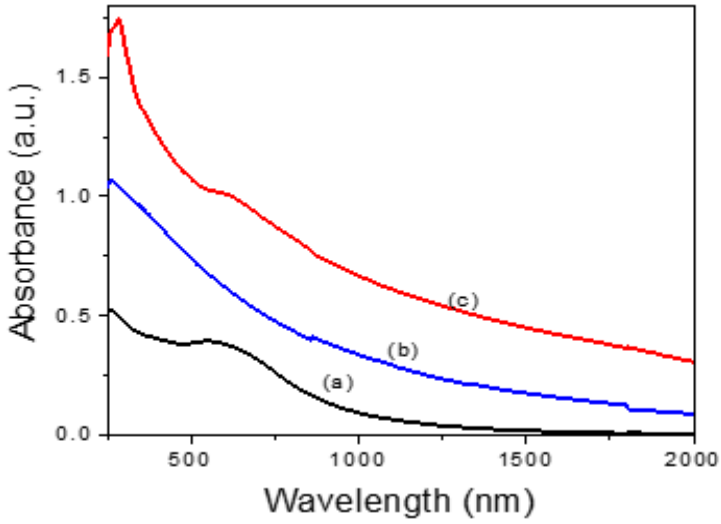

Figure 110. UV/Visible spectra of Bi_2S_3 thin films prepared by AACVD from $[Bi(S_2CThq)_3]$ at (a) 350 °C (b) 400 °C, (c) 450 °C in $CHCl_3/CH_3CN$ solvent mixture.

in temperature of deposition. At 350 °C, the average breadth of the fibers was found to be 67.53 ± 0.20 nm. At 400 °C the breadth increased to 105.05 ± 0.15 nm and to 123.22 ± 0.31 nm at 450 °C.

The UV/Visible spectra films deposited from $[Bi(S_2CThq)_3]$ are shown in Figure 110. The adsorptions were all broad and red shifted compared to bulk Bi_2S_3 which absorbs at about 980 nm. EDX analysis on the films showed a sulfur rich face when $[Bi(S_2CPip)_3]$ was used and a slight deficiency in sulfur when $[Bi(S_2CThq)_3]$ was decomposed at 400 and 450 °C

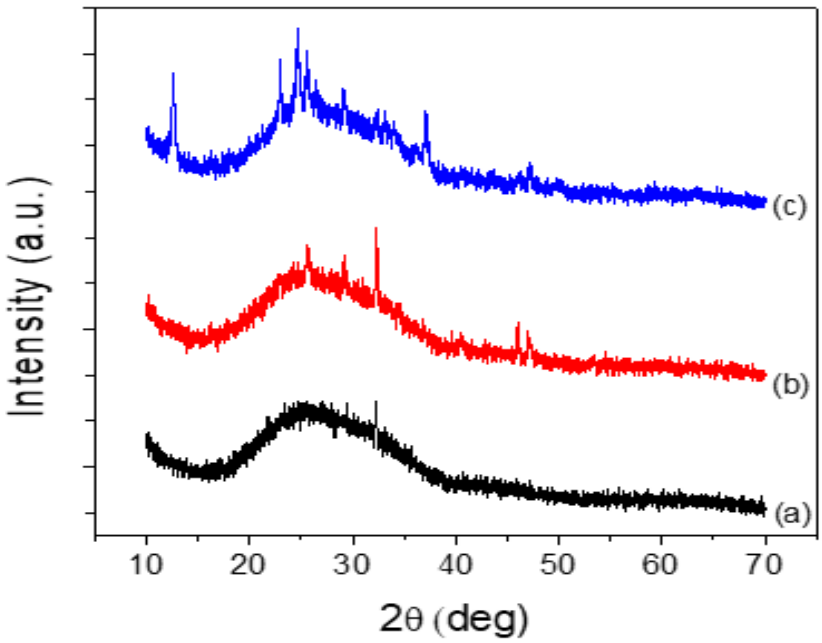

Figure 111. p-XRD of Bi_2S_3 thin films prepared by AACVD from $[Bi(S_2CThq)_3]$ (a) 350 °C (b) 400 °C and (c) 450 °C in $CHCl_3/CH_3CN$ solvent mixture.

(Table 32 page 142). Formation of sulfur deficient films is known to occur at elevated temperatures, possibly due to sublimation of the metal sulfide to gaseous forms of sulfur[142]. However, the p-XRD diffraction studies showed some peaks corresponding to the formation of bismuth sulfide films at at 400 and 450 °C (Figure 111)

TEM analysis showed a change in the morphology of the films when $[Bi(S_2CThq)_3]$ was used (Figure 112). This is due to the different decomposition patterns of $[Bi(S_2CPip)_3]$ and $[Bi(S_2CThq)_3]$ (Figure 30, section 3.1.3. on page 72). $[Bi(S_2CPip)_3]$ decomposed at a higher temperature (322 °C) compared to $[Bi(S_2CThq)_3]$ (300 °C), suggesting that $[Bi(S_2CPip)_3]$ is more stable. At 350 °C a mixture of fibers, nanocubes and plates were obtained (Figure 112 a). The increase in deposition temperature from 350 °C to 400 °C seemed to favour the growth of the cubes into fibers which were found to be mixed with leaf-like platelets orientating vertically on the substrate surface (Figure 112 b). At 450 °C, only nanoplatelets were formed (Figure 112 c).

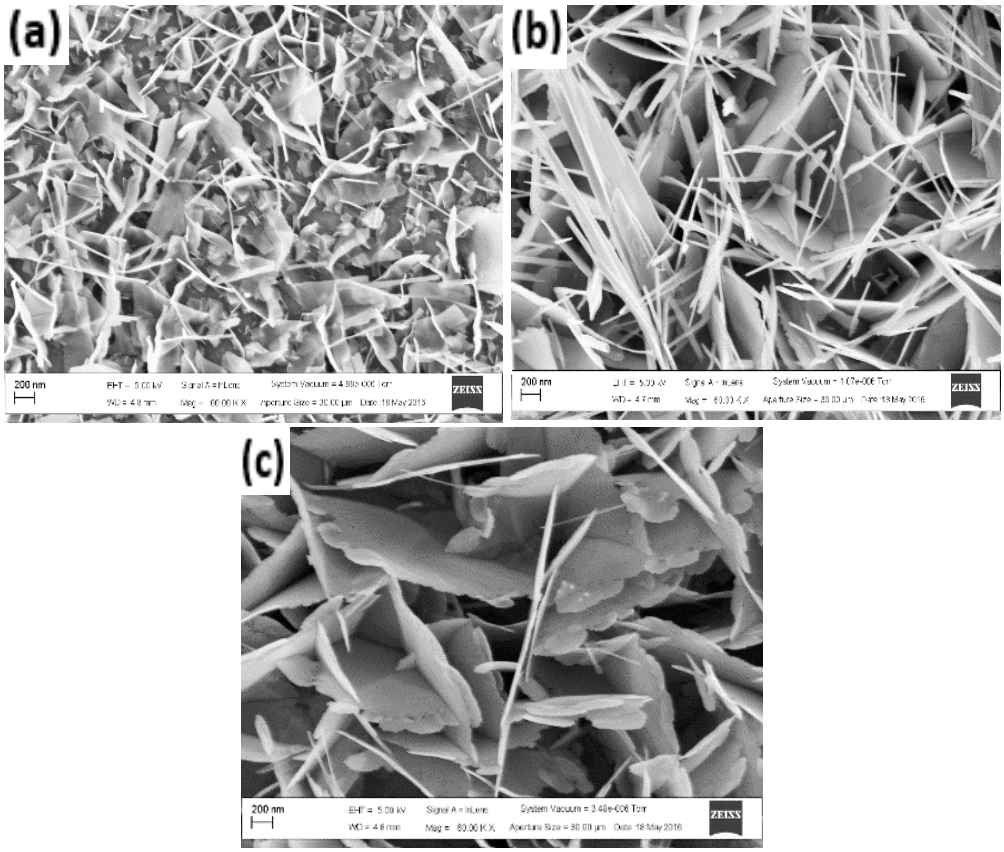

Figure 112. SEM images of Bi_2S_3 thin films from $[Bi(S_2CThq)_3]$ deposited by AACVD at (a) 350 °C (b) 400 °C and (c) 450 °C in $CHCl_3$/ CH_3CN mixture.

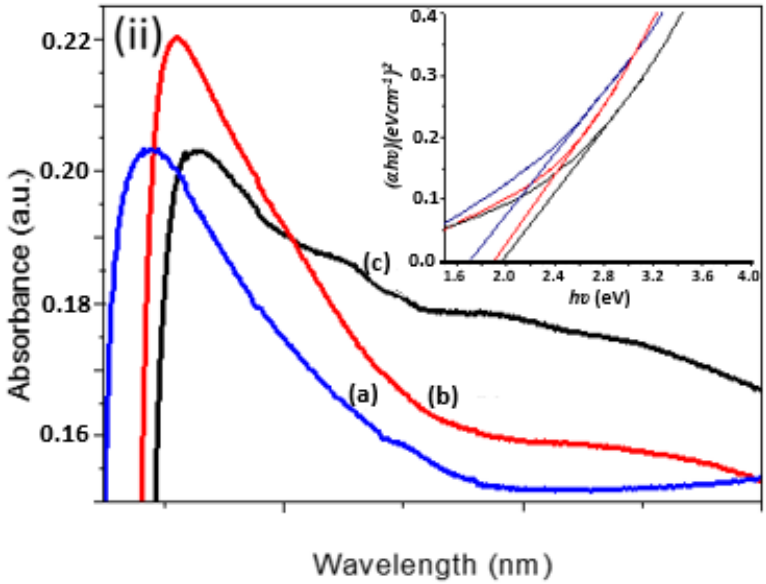

Figure 113. UV/Visible spectra of Bi_2S_3 thin films from $[Bi(S_2CPip)_3]$ at (a) 350 °C (b) 400 °C and (c) 450 °C deposited by spin coating.

3.7.3. Thin films deposited from chloroform/methanol by spin coating

The films obtained by spin coating a solution of the complexes in $CHCl_3$/MeOH were dark grey and non-specular. The samples were prepared by spin coating 10 µL of a 0.15 mmol solution of $[Bi(S_2CPip)_3]$ in a 3:1 mixture of $CHCl_3/CH_3OH$ at 1420 RPM for 25 s under atmospheric pressure. After drying on a preheated hot plat at 70 °C, the films were annealed at 350 °C, 400 °C and 450 °C respectively.

Figure 113 shows the UV/Visible spectra for the films deposited from $[Bi(S_2CPip)_3]$ at 350, 400 and 450 °C. A plot of hν vs $(\alpha h\nu)^2$ (inset of Figure 113) shows an increasing blue shift in the optical band gap from 1.70 eV at 350 °C, 1.90 eV at 400 °C to 1.99 eV at 450 °C. This blue shift compared to the value of 1.20 eV of bulk Bi_2S_3 is a result of quantum confinement suggesting that at least one of the dimensions of the particles are in the nano-range. The shift to higher energy as we increase the annealing temperature also suggests a decrease in particle size with temperature. Figure 114 shows the p-XRD patterns of the samples. The peaks were indexed to the orthorhombic unit cell of Bi_2S_3 corresponding to the ICDD card number 00-02-0391. Some additional peaks indexed to metallic Bi were also present in the diffraction pattern. The pattern also shows a preferred orientation along the (021) plane. The SEM images of the films obtained at all the three temperatures showed rods (Figure 115). At 350 °C, the rods were obtained with an average length of 557.67 ± 150 nm and breadth of 53.00 ± 20 nm. At 400 °C, the average length decreased to 550.21 ± 130

nm and breadth 52.76 ± 22 nm while at 450 °C, an average length of 512.54 ± 113 and breadth 51.09 ± 25 nm were obtained.

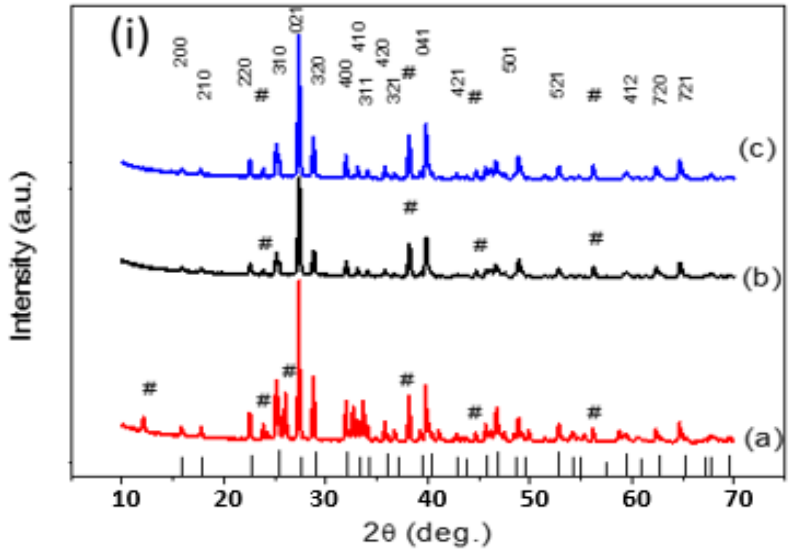

Figure 114. p-XRD of Bi_2S_3 thin films from [$Bi(S_2CPip)_3$] a) 350 °C (b) 400 °C and (c) 450 °C deposited by spin coating.

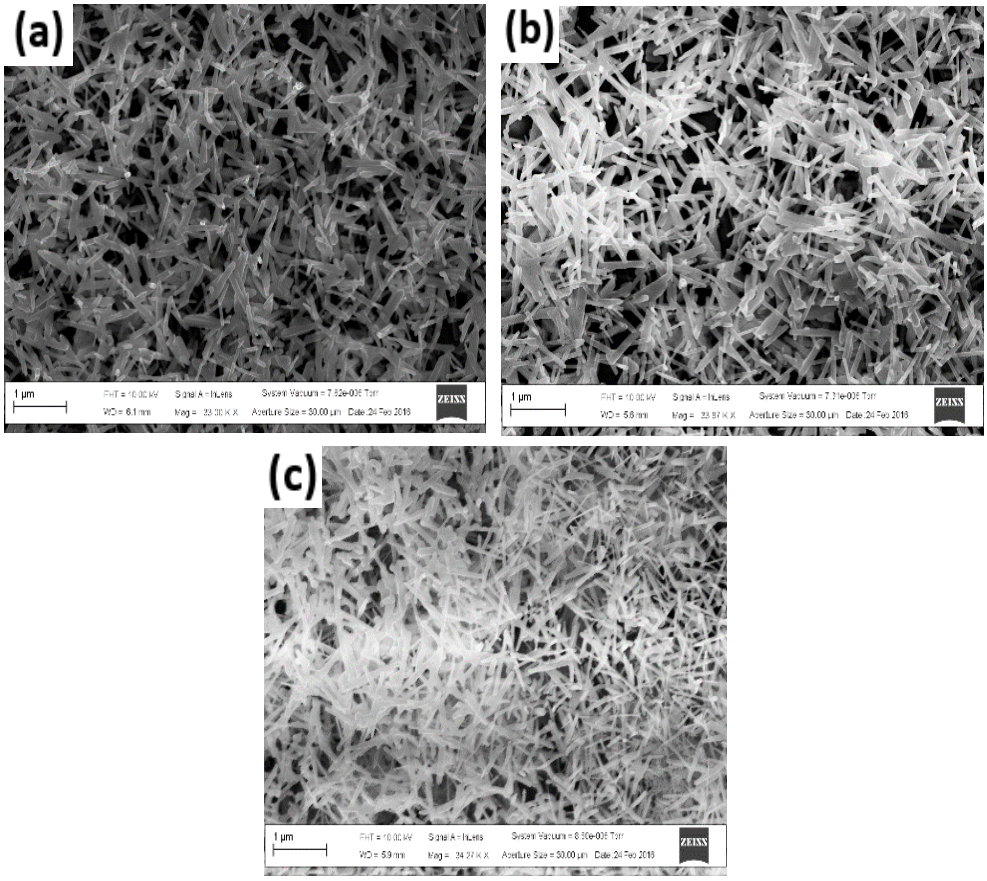

Figure 115. SEM images Bi_2S_3 thin films deposited by spin coating [$Bi(S_2CPip)_3$] in $CHCl_3$/MeOH and annealing at (a) 350 °C (b) 400 °C and (c) 450 °C.

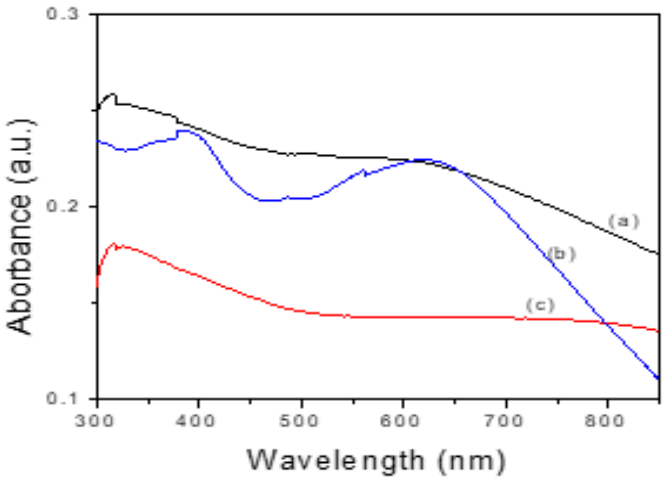

Figure 116. UV/Visible spectra of Bi_2S_3 thin films from $[Bi(S_2CThq)_3]$ 3 at (a) 350 °C (b) 400 °C, (c) 450 °C deposited by spin coating.

The UV/Visible spectra of the films deposited from $[Bi(S_2CThq)_3]$ are shown in Figure 116. The spectra show broad absorption bands for films deposited at 350 °C with an absorption maximum at 630 nm for the film deposited at 350 and 400 °C. A secondary absorption at 400 °C appears at 360 nm. At 450 °C, the UV/Visible adsorption is blueshifted to 35 nm.

TEM images revealed long interwoven nanowires at all three temperatures (Figure 117). These results suggest that the precursor used may have played a role in the nature of the deposited films.

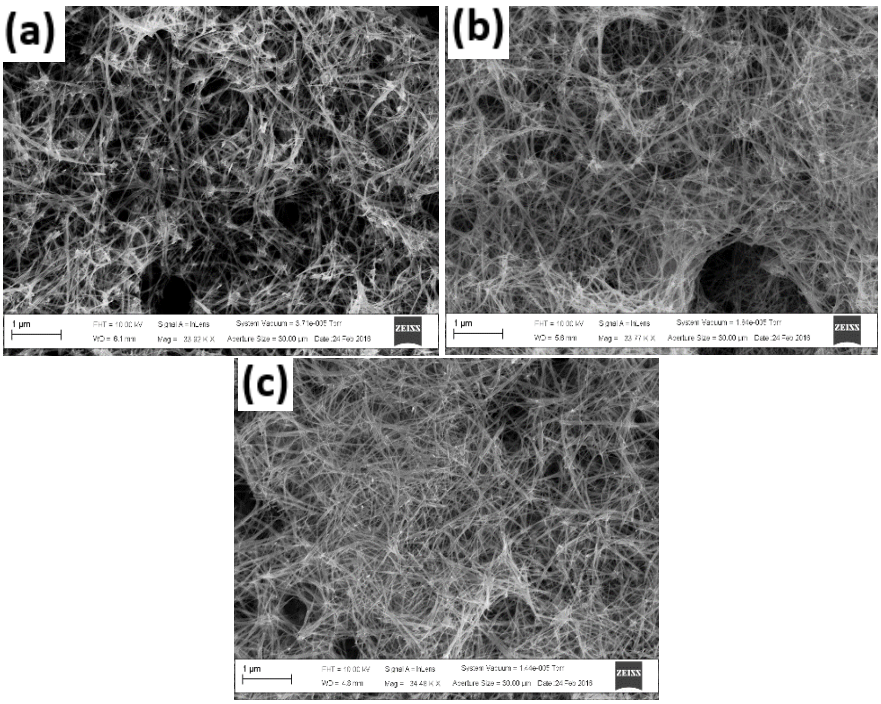

Figure 117. SEM Images Bi_2S_3 thin films deposited by spin coating $[Bi(S_2CThq)_3]$ in $CHCl_3$/MeOH and annealing at (a) 350 °C (b) 400 °C and (c) 450 °C.

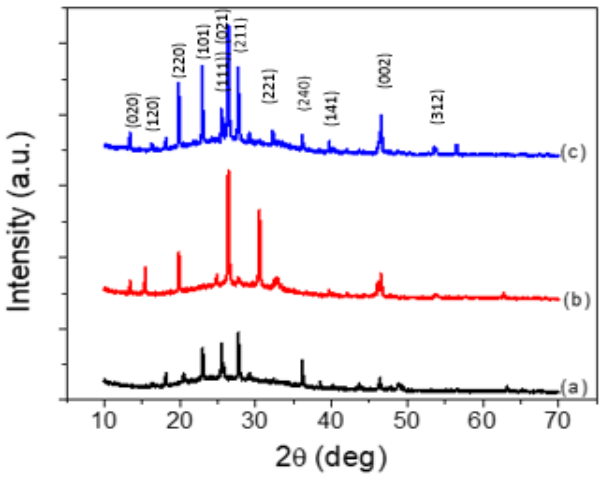

Figure 118. p-XRD of Bi_2S_3 thin films from [$Bi(S_2CThq)_3$] at (a) 350 °C (b) 400 °C and (c) 450 °C deposited by spin coating.

p-XRD analysis gave peaks indexed to bismuthinite lattice(Figure 118). EDX analysis reveals that all the samples were slightly sulfur deficient (Table 32 page 142). There is a close agreement in the Bi:S ratio for the samples annealed at 350 and 400 °C for both [$Bi(S_2CPip)_3$] and [$Bi(S_2CThq)_3$].

Film thicknesses for both spin coated and AACVD synthesized films were calculated by weighing the glass substrate before deposition and after deposition using the equation[306].

$$t = \frac{m}{A\rho} \quad (5)$$

Where 't' is the thickness of the film, 'm' is the weight gain, A is the area of the coated film and ρ is the density of Bi_2S_3.

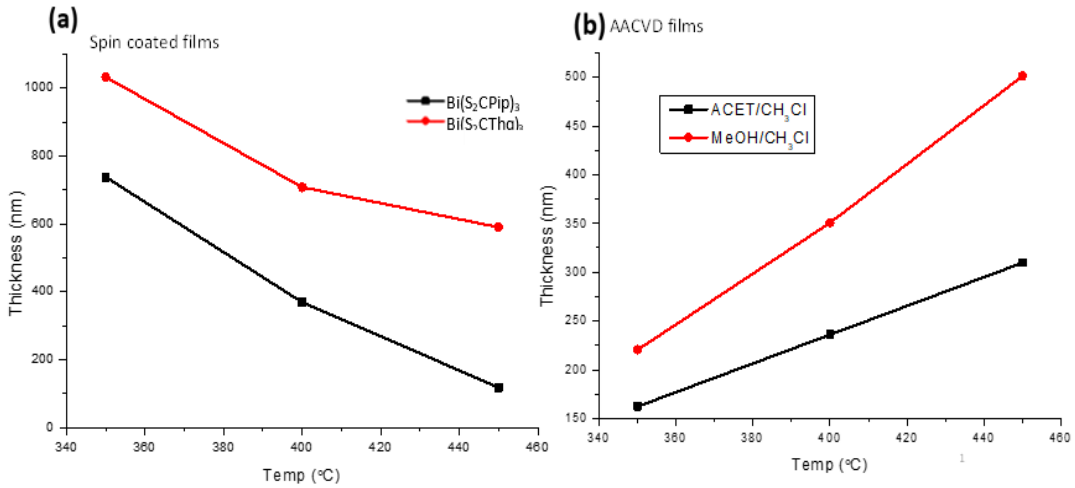

Figure 119. A graph of film thickness growth versus temperature of deposition (a) Spin coated films and (b) AACVD films from [$Bi(S_2CPipq)_3$].

A plot of thickness versus temperature of the films for the spin coated samples for both [$Bi(S_2CPip)_3$] and [$Bi(S_2CThq)_3$]. Figure 119 a, shows a decreasing trend of thickness as temperature increases. Interestingly, the calculated thicknesses for AACVD deposited films from [$Bi(S_2CPip)_3$] for chloroform/acetonitrile and chloroform/methanol (Figure 119 b) was found to increase as temperature increased.

A similar trend of increasing thickness with temperature was observed when the film thickness was measured from the Cross-sectional SEM images of the Bi2S3 thin films deposited from [$Bi(S_2CThq)_3$] by AACVD in $CHCl_3$/MeOH mixture(Figure 120). An observed mean thickness of 241.16 ± 16.14 nm at 350 °C, 311.67 ± 20.63 nm at 400 °C and 463.45 ± 10.30 nm at 450 °C was obtained.

Variation in the morphology of the films observed can be explained by the difference in the heat of combustion and evaporation of the solvents which can lead to either homogeneous or heterogeneous deposition reactions[307]. During CVD, decomposition of the precursor in the gas phase is termed 'homogeneous' whilst decomposition on the heated substrate is

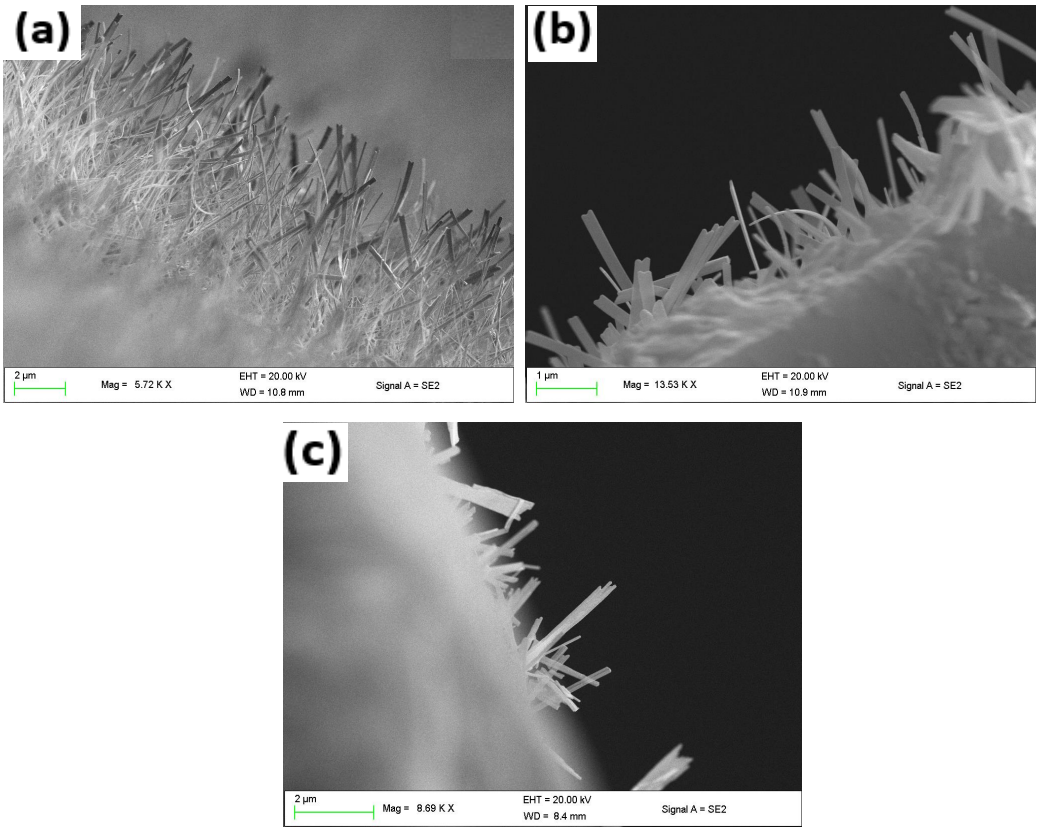

Figure 120. Cross-sectional SEM images of Bi_2S_3 thin films deposited from [$Bi(S_2CThq)_3$] by AACVD at a) 350 °C (b) 400 °C and (c) 450 °C in $CHCl_3$/MeOH mixture showing relative film thickness variation with temperature.

'heterogeneous', the ratio between these two processes are directly responsible for a number of characteristics.

3.7.4. Influence of solvent on growth mechanism of films

Chloroform facilitates the homogeneous reaction during deposition by evaporating and leaving the precursor molecule to vaporize in the heated zone as it is a low combustion heat solvent (473.21 $KJmol^{-1}$). The homogeneous reaction results in decomposition of the precursor starting in the gaseous phase after vaporization, which is followed by nucleation to form Bi_2S_3 particles. However, with the addition of methanol, a higher combustion heat solvent (715.00 $KJmol^{-1}$) compared to chloroform, the vaporization temperature of the aerosol droplets is increased, and the heterogeneous reaction is promoted. Thus, the formation of a mixture of Bi_2S_3 nanoplates and nanofibers from $[Bi(S_2CPip)_3]$ in chloroform/methanol mixture (Figure 103 page 142) is due to a combination of homogeneous nucleation in the gas phase and heterogeneous growth on the substrates. When the chloroform/acetonitrile mixture was used to deposit Bi_2S_3 thin films from $[Bi(S_2CPip)_3]$, nanofibers only (Figure 109 page 146) were formed due to the heterogeneous growth that was predominant since acetonitrile has a higher heat of combustion (1256.33 $KJmol^{-1}$).

3.8. Hydrogen/oxygen evolution and supercapacitance studies

The effect of change in capping agent on electrochemical performance was investigated. The activity of Sb_2S_3 samples was studied as OER electrocatalyst in 1.0 M KOH electrolyte using linear sweep voltammetry (LSV). The polarization curves for Sb_2S_3 samples in OER potential range were given in Figure 121(a). The DT/OLA-capped Sb_2S_3 had a lower overpotential (482 mV) to generate a current density of 10 mA/cm2 than OLA-capped Sb_2S_3 (634 mV) Figure 121(b). The Tafel slopes were further used to measure the OER kinetics of Sb_2S_3 samples. OLA-capped Sb_2S_3 and DT/OLA-capped Sb_2S_3 showed the Tafel slopes of 223 and 180 mV/dec, respectively (Figure 121 (c) and (d)). The lower Tafel slope of DT/OLA-capped Sb2S3 suggested faster electron transfer and OER kinetics, which confirmed to the lower overpotential and better electrocatalyst performance compared to OLA-capped Sb_2S_3.

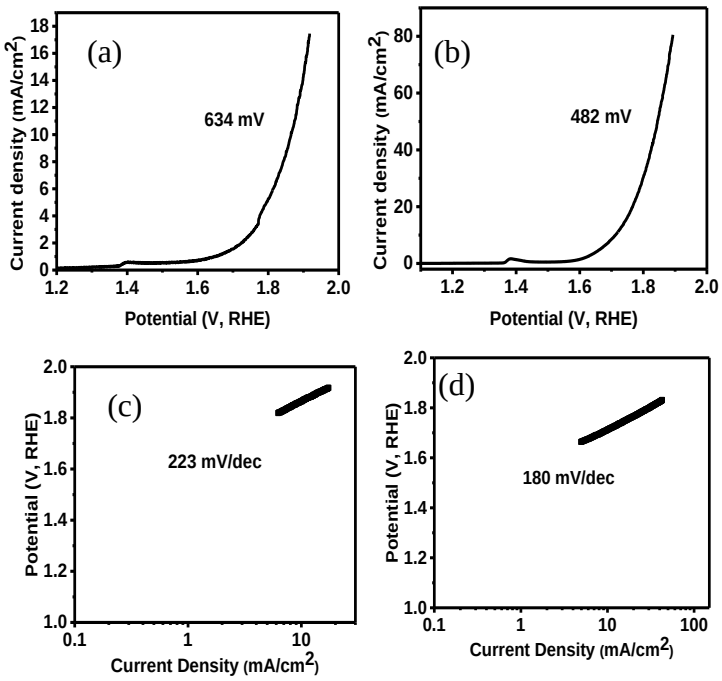

Figure 121. Polarization curves for (a) OLA-capped Sb_2S_3 (b)) DT/OLA-capped Sb_2S_3 (c)Tafel slopes for DT/OLA-capped Sb_2S_3 and (d) Tafel slopes for DT/OLA-capped Sb_2S_3 for OER.

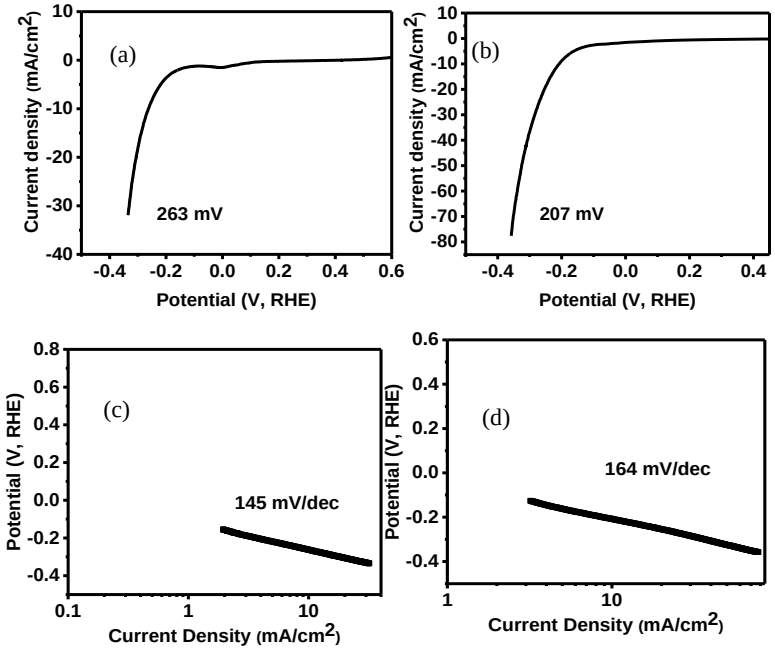

Figure 122. (a) Polarization curves for (a) OLA-capped Sb_2S_3 (b) DT/OLA-capped Sb_2S_3 (c)Tafel slopes for OLA-capped Sb_2S_3(c and (d) Tafel slopes for DT/OLA-capped Sb_2S_3 for HER.

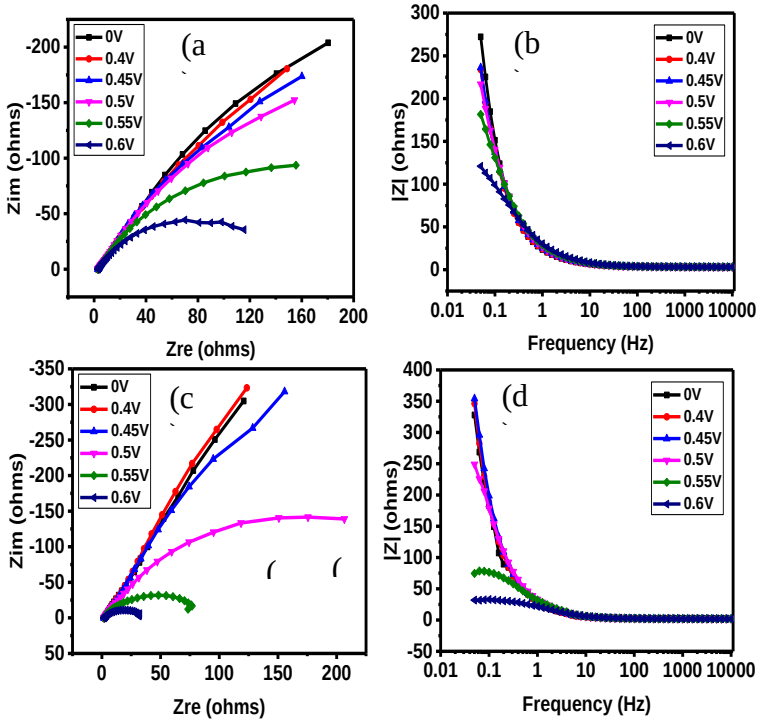

Figure 123. (a) Nyquist plots for OLA-Sb_2S_3 and (b) IZI vs frequency plots for OLA-Sb_2S_3 at various HER overpotentials. (c) Nyquist plots for DT/OLA-Sb_2S_3 and (d) IZI vs frequency plots for DT/OLA-Sb_2S_3 at various OER overpotentials.

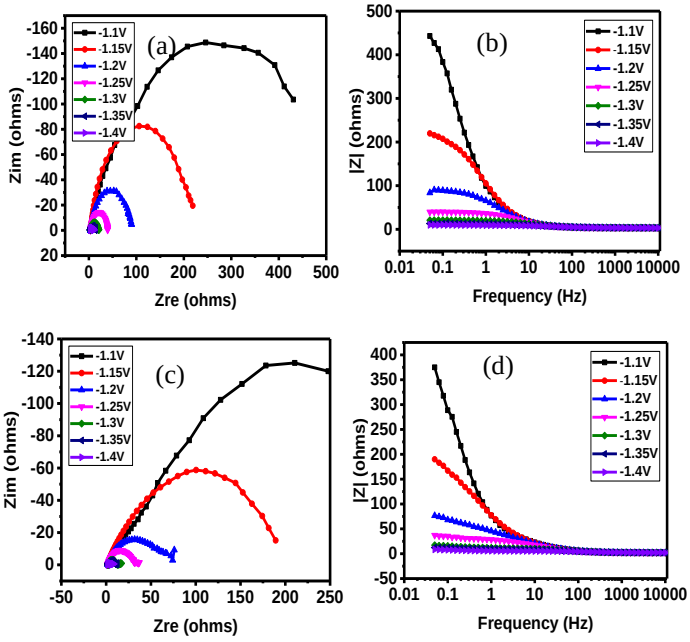

Figure 124. (a) Nyquist plots for OLA- Sb_2S_3 and (b) IZI vs frequency plots for OLA- Sb_2S_3 at various HER overpotentials. (c) Nyquist plots for DT/OLA- Sb_2S_3 and (d) IZI vs frequency plots for DT/OLA- Sb_2S_3 at various HER overpotential.

The HER activity of the Sb_2S_3 samples was also studied. The polarization curve in HER region is given in figure 122 (a) and (b). DT/OLA-capped Sb_2S_3 required an overpotential of 207 mV while OLA-capped Sb_2S_3 required an overpotential of 263 mV. OLA-capped Sb_2S_3 showed a significant improvement in the HER performance compared to DT/OLA-capped Sb_2S_3. It can be observed in Figure 122 (c) and (d), the Tafel slope for OLA-capped Sb_2S_3 and DT/OLA-capped Sb_2S_3 was calculated to be 145 and 164 mV/dec respectively. The lower Tafel slope for OLA-capped Sb_2S_3 showed faster HER kinetics for electrocatalysts, which confirmed the better HER performance.

Electrochemical impedance spectroscopy (EIS) measurements were used to study the electrocatalytic properties. Figure 123 (a) and Figure 123(c) showed the Nyquist plots (Zreal vs Zim) of OLA-capped Sb_2S_3 and DT/OLA-capped Sb_2S_3 at various potentials. It was clear that for both Sb_2S_3 samples, the curves from Nyquist plots start to convert to a small semicircle from a straight line with the increase in the potential. This was because the increase in the potential offered faster reaction which leads to the reduction of the smaller radius of semicircle at the low-frequency region, indicating better activity of Sb_2S_3 electrodes at higher potential. From further comparison of Nyquist plots of DT/OLA-capped Sb_2S_3 and OLA-capped Sb_2S_3 at 0 V (at open circuit potential) and 0.45 V (vs SCE, most close to the overpotential at 10 mA/cm2), it can be observed that the OLA-capped Sb_2S_3 had shorter length at 0 V . This can be further confirmed by the lower total impedance IZI as a function of the frequency of OLA-capped Sb_2S_3 than DT/OLA-capped from Figure 123(b) and (d).

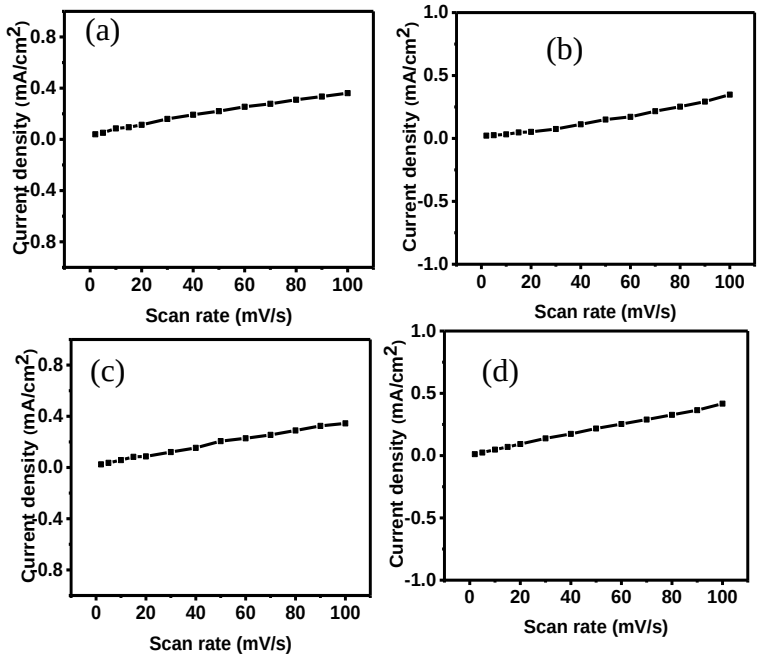

Figure 125. The CV curves in (a) OLA and (b) DT/OLA in OER (c) OLA and (d) DT/OLA in HER.

Figure 124 shows the Nyquist plots at various HER overpotentials of OLA-capped Sb_2S_3 Figure 124(a) and DT/OLA-capped Sb_2S_3 in Figure 124(c). The same phenomenon with the Nyquist plots at OER overpotentials was observed. The curves showed semicircles from straight lines and the radius of semicircles decreasing. This phenomenon was consistent with the reduction of total impedance IZI with the increase of negative potential for both Sb_2S_3 samples in Figure 124 (b) and (d) indicating lower charge transfer resistance.

To further understand the differences in electro-catalytic properties the electrochemical active surface area of OLA-capped Sb_2S_3 and DT/OLA-capped Sb_2S_3 was determined using cyclic voltammograms in the non-faradic region. The CV curves were recorded as shown in (Figure 125 (a) and (b) for OLA-capped Sb_2S_3 and DT/OLA-capped Sb_2S_3 OER respectively and in Figure 125 (c) and (d) for OLA-capped Sb_2S_3 and DT/OLA-capped Sb_2S_3 HER respectively at various scan rates to determine the electrochemical double layer capacitance (Cdl), which is directly proportional to the electro-chemical active surface area of the sample. The Cdl value of the OLA-capped Sb_2S_3 and DT/OLA-capped Sb_2S_3 was calculated to be 0.4 and 0.45 mA/cm^2, respectively for the OER, and 0.25 and 0.49 mA/cm ^{2}, respectively for the HER. The higher HER and OER activity of DT/OLA-capped Sb_2S_3 can be attributed to a higher electrochemical surface area of DT/OLA-capped Sb_2S_3 compared to that of OLA-capped Sb_2S_3.

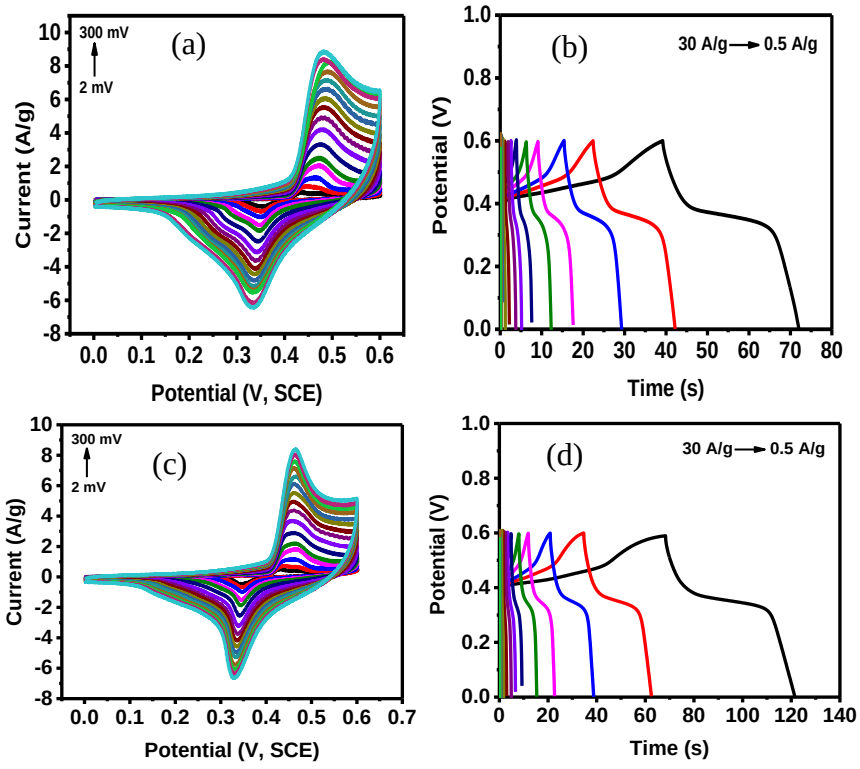

Figure 126. Galvanostatic charge-discharge curves of (a) OLA-Sb_2S_3 and (c) DT/OLA-Sb_2S_3 at various current densities in 3M KOH electrolyte. CV curves of (b) OLA-Sb_2S_3 and (d) DT/OLA-Sb_2S_3 at various scan rates in 3M KOH electrolyte.

The supercapacitor performances of Sb_2S_3 samples were also studied in a 3 M KOH solution. The galvanostatic charge-discharge curves of OLA-capped Sb_2S_3 and DT/OLA-capped Sb_2S_3 at various current densities were given in Figure 126(a) and (d). A non-linear curve shows typical pseudo-capacitance behaviours attributed to Faradaic redox reactions at the Sb_2S_3 samples surface. With the decrease of current density, both samples need more time to complete a charge-discharge cycle. The longer charge and discharge time of DT/OLA-capped Sb_2S_3 than OLA-capped Sb_2S_3 at the same current density showed a larger charge storage capacity.

Figure 127(a-d) showed the specific capacitance of Sb_2S_3 samples calculated from the GCD data and CV data as a function of current densities and scan rates, respectively. A lower scan rate and lower current density, higher specific capacitances were observed, which was due to more time being provided to the redox reactions. The maximum specific capacitance for OLA-capped Sb_2S_3 than DT/OLA-capped Sb_2S_3 samples was 47 F g−1 and 28 F g−1 which were calculated from the GCD curve and CV curve of Sb_2S_3 samples at a current density of 1 A g-1 and a scan rate of 1 mV s−1, respectively. The results for OLA-capped Sb_2S_3 exhibited better specific capacitance than DT/OLA-capped Sb_2S_3.

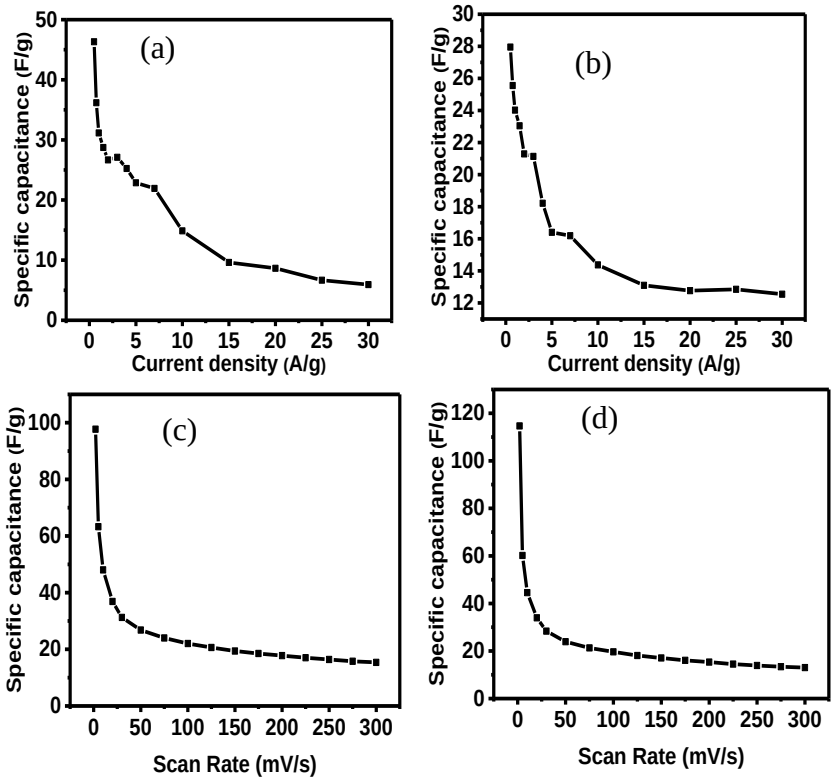

Figure 127. Variation of specific capacitance as a function of current density and scan rate for (a), (c) OLA-Sb_2S_3 and (b), (d) DT/OLA-Sb_2S_3 samples respectively.

GENERAL CONCLUSION

Heterocyclic bismuth and antimony dithiocarbamate ligands were effectively synthesized from the reaction of carbon disulfide with heterocyclic amines such as piperidine, tetrahydroquinoline, and morpholine. These ligands together with the commercially obtained diethyl dithiocarbamate ligand were used to synthesize bismuth and antimony dithiocarbamate complexes. Analysis showed that the ligands were all air stable and obtained in appreciable yield. FT-IR analysis on the ligand and complexes showed the bidentate coordination nature of the complexes. Structural elucidation of the ligand and complexes by ^{1}H and ^{13}C NMR analysis showed the various chemical shift of the protons and carbons in the respective molecules. The TGA of the complexes showed single and two steps decompositions, typical of dithiocarbamates complexes. Elemental analysis showed good agreement between the expected and the actual elemental compositions of the complexes.

The crystal structure of all the complexes was determined by x-ray single crystal analysis. The bismuth complex $[Bi(S_2CPip)_2NO_3]2H_2O$ (catena-(μ_2-nitrato-O,O')bis(piperidinedithiocarbamato)bismuth(III)) crystallized in the monoclinic crystal system, spece group *P*21/c. The structure is polymeric with an asymmetric unit made of a bismuth(III) ion, two chelating dithiocarbamate ions, and a bridging nitrate ion. The structure of the complex $[Bi(S_2CThq)_2]NO_3$ (tetrakis(μ-nitrato)tetrakis[bis(tetrahydroquinolinedithiocarbamato) bismuth(III) shows a distorted octahedral coordination geometry and crystalises in a monoclinic crystal structure of space group *P*21/c. The structure consisting of a centrosymmetric tetranuclear Bi(III) cluster with bridging nitrate groups.

The $[Bi(S_2CPip)_3]$ complex (tris- (piperidinedithiocarbamato)bismuth(III)) shows a distorted octahedral coordination geometry and crystalizes in an orthorhombic crystal system with space group *P*bca. The structure has two enantiomorph molecules in the asymmetric unit.

The $[Bi(S_2CPip)_3]2CHCl_3$ formed a bis-chloroform solvate of tris(piperidinedithiocarbamato)bismuth(III) of space group P21/c. The bismuth(III) ions are bound to six sulfur donor atoms, each from three chelating dithiocarbamate ligands. The overall structure is stabilized by two chloroform molecules.

In $[Sb(S_2CDed)_3]$ (tris(N,N-diethyldithiocarbamato)antimony(III)), the Sb atom is coordinated by three diethyldithiocarbamato groups, two groups in an almost planar fashion coordinated in a bidentate manner, the third group is perpendicular to the plane and coordinated only through 1 S atom, forming a five coordinate structure of a monoclinic crystal system of space group $P2_1/c$.

$[Sb(S_2CMor)_3]$ (tris(morpholinedithiocarbamato)antimony(III)) also crystalizes into a monoclinic crystal system of space group $P2_1/c$. The SbIII ion is coordinated by the six S atoms belonging to three morpholinedithiocarboxylate ligands. The resulting SbS6 coordination polyhedron approximates to a pentagonal pyramid with atoms Sb1 and S1, S2—S6 at the base of the pyramid and S3 in the apical position.

$[Sb(S_2CPip)_3]$, (tris(piperidinedithiocarbamato)antimony(III)) forms a four coordinate Sb complex surrounded by three piperidinedithiocarbate groups. One group is coordinated to the central Sb in a bidentate manner while the other two are coordinated through single s-atoms forming a distorted octahedral structure of a monoclinic crystal system and space group $P2_1/c$.

Bi_2S_3 nanorods were synthesized from these single source precursors (Heterocyclic bismuth dithiocarbamate complexes catena-(μ2-nitrato-O,O')bis(piperidinedithiocarbamato)bismuth(III) and tetrakis(μ-nitrato)tetrakis[bis(tetrahydroquinolinedithiocarbamato)bismuth(III)]), by hot injection thermolysis in long chains amines such as oleylamin (OLA), hexadecylamine (HDA), dodecylamine (DDA), Decylamine (DA) and and trioctylphospine oxide (TOPO). Green capping solvents such as olive oil, oleic acid, castor oil and ricinoleic acid were also used. There was no noticeable change in the morphology of the rods obtained with change in precursor, but an average increase in the size and change in optical properties was observed when the length of the carbon chain of the capping solvent was increased. This result is similar to that obtained by Trindade and co[24] who also observed that the coordianting solvent played a signifant role in the final morphology of the Bi_2S_3 nanoparticles single source precursors. The effect of change in reaction temperature on the growth of the nanoparticles was evaluated, by varying the reaction temperature from 190 , 230 and 270 ^oC. The reaction was controlled by two temperature regime. At higher temperatue, there is improper capping due to the dynamic nature of the surface ligand. As a result, the morphology tends to more thermodynamically stable spherical particles. At lower tmperature, rods were obtained. The aspect ratio of the rods decreased with increase in the reaction temperature. This trend is similar to that reported by Xie *et al*[308]. The optical properties of the nanorods obtained under all reaction conditions revealed quantum-confinement in the particles, with a slight red shift

in the optical absorption as temperature is increased. The use of duodecanethiol was essential in obtaining good quality naanorods. Addition of small quantity of DT controlled the chemical potential of the solution leading to the formation of less thermodynamically stable particles. With no dodecane thiol, poorly formed rods were obtained. Using green capping agents effectively produced Bi_2S_3 nanorods as revealed by p-XRD, though the rods were less crystalline than those obtained from the non-green capping agents. The absorption band edge of the rods was red shifted compared to those synthesized from the non-green capping agents at the same temperature.

Bi_2S_3 submicrometer range particles were also prepared by solvent-free process in which the precursors were pyrolyzed in an inert atmosphere at 350, 400, and 450 ^oC. The rods were poorly formed compared to those obtained by hot injection thermolysis, indicating that the capping agents play a crucial role in directing the morphology of the rods. The p-XRD of the rods formed through this method revealed some unindexed peaks due to the residues formed during the decomposition of the precursor, showing the limitations of this method in forming pure nanoparticles.

Sb_2S_3 was prepared by thermolyzing $[Sb(S_2CPip)_3]$, $[Sb(S_2CMor)_3]$ and $[Sb(S_2CDed)_3]$ at 230 ^oC in hot oleylamine, with and without dodecanethiol. Thermolysis of all three complexes in oleyamine at 230 °C gave sub-micrometre sized peg-like Sb_2S_3 rod which were staged in a sheaf-like manner staged. Addition of small amount of dodecanethiol gave elongated sub-micrometre sized nanorods with higher aspect ratio than those obtained without dodecanethiol.

The entire range of $(Bi_{1-x}Sb_x)_2S_3$ Solid solution was prepared by the thermal decomposition of bismuth and antimony piperidinedithiocarbamates in oleylamine and small quantity of dodecanethiol by varying the bismuth and antimony precursor mole fraction. There was a good control over stoichiometry compared to the result obtained by Kyono *et al*[189]. who obtained a full range solid solution series of $(BiSb)S_3$ with an almost statistical substituion but with no stochiometric control. The morphologies of the nanorods depended on their compositions, and aspect ratios that decreased to a minimum of 2.58 with maxima of 16.58 when using just the bismuth precursor and 21.01 when using the antimony precursor. Wang *et al*[309] otained a similar variation in mophology from a dual precursor approach. The XRD peaks at all ratios correspond to the orthorhombic crystals system and fall in between those of orthorhombic Bi_2S_3 and orthorhombic Sb_2S_3. The gradual shift in the peaks position in combination with compositional data from EDX confirms the successful incorporation of antimony into bismuth sulfide with almost adheres to Vegard's law.

A solution of the precursors (tris-(piperidinedithiocarbamato) complex of bismuth(III) and tris-(tetrahydroquinolinedithiocarbamato) bismuth(III)) in chloroform/acetonitrile and chloroform/ethanol was used to deposit Bi_2S_3 thin films on glass substrate by aerosol assisted chemical vapour deposition and spin coating technique at substrate temperatures of 350, 400, and 450 ^oC. Both deposition methods, gave sulfur deficient polycrystalline films of bismuthinite. AACVD gave films of hexagonal nanoplatelets, leaf-like platelet, ribbon-like fibre, needle-like fibre morphologies depending on the precursor, solvent and substrate temperature. Films in the form of rods and interwoven nanowires were obtained from spin coating.

The effect of addition of small quantity of dodecane thiol on the morphology of the Sb_2S_3 rods was evaluated for energy generation and energy storage studies. DT/OLA-capped Sb_2S_3 displayed better electrochemical and electrocatalytic performances than OLA-capped Sb_2S_3. Furthermore, DT/OLA-capped Sb_2S_3 had a lower overpotential (482 mV) to generate a current density of 10 mA/cm2 than OLA-capped Sb_2S_3 (634 mV), indicative of the superiority of DT/OLA-capped Sb_2S_3 in terms of electrocatalytic performance. The maximum specific capacitance for OLA-capped Sb_2S_3 than DT/OLA-capped Sb_2S_3 samples was 47 F g−1 and 28 F g−1 which were calculated from the GCD curve and CV curve of Sb_2S_3 samples at a current density of 1 A g-1 and a scan rate of 1 mV s−1, respectively. The results for OLA-capped Sb_2S_3 exhibited better specific capacitance than DT/OLA-capped Sb_2S_3.

PERSPECTIVE

For the completion of this work, we envisage to;

- Carry out studies on the mechanism of decomposition of precursors in capping agents in order to fully understand the mechanism of shape evolution and influence of specific capping agents on the nature of the material produced.
- Investigate the use of other class of compounds as ligands for preparation of single source precursors.
- Study the possible use of local oils as potential capping agents.
- Extend the study of solid solutions of Bi and Sb to systems containing Mn, Fe, Pb, S as well as Se.
- Design a purification stage in order to obtain highly pure nanomaterials for opto electronic applications.
- Apply the synthesized materials in photocatalysis for water purification, and in solar device fabrication.

REFERENCES

(1) Jeevanandam, J., Barhoum, A., Chan, Y. S., Dufresne, A., and Danquah, M. K. (2018) Review on nanoparticles and nanostructured materials: history, sources, toxicity and regulations. *Beilstein J. Nanotechnol. 9*, 1050–1074.

(2) Parab, H. J., Chen, H. M., Bagkar, N. C., Liu, R.-S., Hwu, Y.-K., and Tsai, D. P. (2010) Approaches to the Synthesis and Characterization of Spherical and Anisotropic Noble Metal Nanomaterials, in *Nanotechnologies for the Life Sciences* (Kumar, C. S. S. R., Ed.). Wiley-VCH Verlag GmbH & Co. KGaA, Weinheim, Germany.

(3) Saallah, S., and Lenggoro, I. W. (2018) Nanoparticles Carrying Biological Molecules: Recent Advances and Applications. *KONA Powder Part. J. 35*, 89–111.

(4) Chang, T.-P., Shih, J.-Y., Yang, K.-M., and Hsiao, T.-C. (2007) Material properties of portland cement paste with nano-montmorillonite. *J. Mater. Sci. 42*, 7478–7487.

(5) Buzea, C., Pacheco, I. I., and Robbie, K. (2007) Nanomaterials and nanoparticles: Sources and toxicity. *Biointerphases 2*, 17–71.

(6) Gatoo, M. A., Naseem, S., Arfat, M. Y., Mahmood Dar, A., Qasim, K., and Zubair, S. (2014) Physicochemical Properties of Nanomaterials: Implication in Associated Toxic Manifestations. *BioMed Res. Int. 2014*, 1–8.

(7) Vitalie Stavila, Enton H. Whitmire, and Irene Rusakova. (2009) Synthesis of Bi2S3 Nanostructures from Bismuth (III) Thiourea and Thiosemicarbazed Complexes. *Chem. Mater. 21*, 5456–5465.

(8) Nigel L. Pickett, and Paul O'Brien. (2001) Synthesis of Semiconductor Nanoparticles Using Single-Molecular Precursors. *Chem. Rec. 1*, 647–679.

(9) Roduner, E. (2006) Size matters: why nanomaterials are different. *Chem. Soc. Rev. 35*, 583.

(10) Bohidar, H. B., and Rawat, K. (2017) Design of Nanostructures: Self-Assembly of Nanomaterials. Wiley-VCH Verlag GmbH & Co. KGaA, Weinheim, Germany.

(11) Tao, A. R., Habas, S., and Yang, P. (2008) Shape Control of Colloidal Metal Nanocrystals. *Small 4*, 310–325.

(12) Kelly, K. L., Coronado, E., Zhao, L. L., and Schatz, G. C. (2003) The Optical Properties of Metal Nanoparticles: The Influence of Size, Shape, and Dielectric Environment. *J. Phys. Chem. B 107*, 668–677.

(13) Sosa, I. O., Noguez, C., and Barrera, R. G. (2003) Optical Properties of Metal Nanoparticles with Arbitrary Shapes. *J. Phys. Chem. B 107*, 6269–6275.

(14) Noguez, C. (2007) Surface Plasmons on Metal Nanoparticles: The Influence of Shape and Physical Environment. *J. Phys. Chem. C 111*, 3806–3819.

(15) Rao, C. N. R., Kulkarni, G. U., Thomas, P. J., and Edwards, P. P. (2002) Size-Dependent Chemistry: Properties of Nanocrystals. *Chem. - Eur. J. 8*, 28–35.

(16) Salavati-Niasari, M., Ghanbari, D., and Davar, F. (2009) Synthesis of different morphologies of bismuth sulfide nanostructures via hydrothermal process in the presence of thioglycolic acid. *J. Alloys Compd. 488*, 442–447.

(17) Yang, X., Wang, X., and Zhang, Z. (2006) Facile solvothermal synthesis of single-crystalline Bi2S3 nanorods on a large scale. *Mater. Chem. Phys. 95*, 154–157.

(18) Zhang, H., and Wang, L. (2007) Synthesis and characterization of Bi2S3 nanorods by solvothermal method in polyol media. *Mater. Lett. 61*, 1667–1670.

(19) Xie, G., Qiao, Z.-P., Zeng, M.-H., Chen, X.-M., and Gao, S.-L. (2004) A Single-Source Approach to Bi_2S_3 and Sb_2S_3 Nanorods via a Hydrothermal Treatment. *Cryst. Growth Des. 4*, 513–516.

(20) Wu, J., Qin, F., Cheng, G., Li, H., Zhang, J., Xie, Y., Yang, H.-J., Lu, Z., Yu, X., and Chen, R. (2011) Large-scale synthesis of bismuth sulfide nanorods by microwave irradiation. *J. Alloys Compd. 509*, 2116–2126.

(21) Wang, D., Shao, M., Yu, D., Li, G., and Qian, Y. (2002) Polyol-mediated preparation of Bi2S3 nanorods. *J. Cryst. Growth 243*, 331–335.

(22) Geng, J., Jefferson, D., and Johnson, B. F. G. (2005) Direct conversion of nickel stearate into carbon nanotubes or pure-phase metallic Ni nanoparticles encapsulated in polyhedral graphite cages. *J. Mater. Chem. 15*, 844.

(23) Seinberg, L., Yamamoto, S., Gallage, R., Tsujimoto, M., Kobayashi, Y., Isoda, S., Takano, M., and Kageyama, H. (2012) Low temperature solventless synthesis and characterization of Ni and Fe magnetic nanoparticles. *Chem. Commun. 48*, 8237.

(24) Monteiro, O. C., Nogueira, H. I. S., Trindade, T., and Motevalli, M. (2001) Use of Dialkyldithiocarbamato Complexes of Bismuth(III) for the Preparation of Nano- and Microsized Bi_2S_3 Particles and the X-ray Crystal Structures of $[Bi\{S_2CN(CH_3)(C_6H_{13})\}_3]$ and $[Bi\{S_2CN(CH_3)(C_6H_{13})\}_3(C_{12}H_8N_2)]$. *Chem. Mater. 13*, 2103–2111.

(25) Shen, X.-P., Yin, G., Zhang, W.-L., and Xu, Z. (2006) Synthesis and characterization of Bi2S3 faceted nanotube bundles. *Solid State Commun. 140*, 116–119.

(26) Tahir, A. A., Ehsan, M. A., Mazhar, M., Wijayantha, K. G. U., Zeller, M., and Hunter, A. D. (2010) Photoelectrochemical and Photoresponsive Properties of Bi_2S_3 Nanotube and Nanoparticle Thin Films. *Chem. Mater. 22*, 5084–5092.

(27) Biswal, J. B., Garje, S. S., Nuwad, J., and Pillai, C. G. S. (2013) Bismuth(III) dialkyldithiophosphates: Facile single source precursors for the preparation of bismuth sulfide nanorods and bismuth phosphate thin films. *J. Solid State Chem. 204*, 348–355.

(28) Monteiro, O. C., Trindade, T., Park, J.-H., and O'Brien, P. (2000) The Use of Bismuth(III) Dithiocarbamato Complexes as Precursors for the Low-Pressure MOCVD of Bi2S3. *Chem. Vap. Depos. 6*, 230–232.

(29) Bonnet, G., Lachkar, M., Colson, J. C., and Larpin, J. P. (1995) Characterization of thin solid films of rare earth oxides formed by the metallo-organic chemical vapour deposition technique, for high temperature corrosion applications. *Thin Solid Films 261*, 31–36.

(30) Edwards, D. A., Harker, R. M., Mahon, M. F., and Molloy, K. C. (1999) Aerosol-assisted chemical vapour deposition (AACVD) of silver films from triphenylphosphine adducts of silver β-diketonates and β-diketoiminates, including the structure of [Ag(hfac)(PPh_3)]. *J. Mater. Chem. 9*, 1771–1780.

(31) Chang, C.-H., and Lee, Y.-L. (2007) Chemical bath deposition of CdS quantum dots onto mesoscopic TiO2 films for application in quantum-dot-sensitized solar cells. *Appl. Phys. Lett. 91*, 053503.

(32) Nair, P. S., Radhakrishnan, T., Revaprasadu, N., Kolawole, G. A., and O'Brien, P. (2002) A single-source route to CdS nanorods. *Chem. Commun.* 564–565.

(33) Okuyama, K., and Wuled Lenggoro, I. (2003) Preparation of nanoparticles via spray route. *Chem. Eng. Sci. 58*, 537–547.

(34) Li, Y., Wu, Y., and Ong, B. S. (2005) Facile Synthesis of Silver Nanoparticles Useful for Fabrication of High-Conductivity Elements for Printed Electronics. *J. Am. Chem. Soc. 127*, 3266–3267.

(35) Suh, S. K., Yuet, K., Hwang, D. K., Bong, K. W., Doyle, P. S., and Hatton, T. A. (2012) Synthesis of Nonspherical Superparamagnetic Particles: *In Situ* Coprecipitation of Magnetic Nanoparticles in Microgels Prepared by Stop-Flow Lithography. *J. Am. Chem. Soc. 134*, 7337–7343.

(36) Tsuzuki, T., and McCormick, P. G. (2004) Mechanochemical synthesis of nanoparticles. *J. Mater. Sci. 39*, 5143–5146.

(37) Lam, C., Zhang, Y. F., Tang, Y. H., Lee, C. S., Bello, I., and Lee, S. T. (2000) Large-scale synthesis of ultrafine Si nanoparticles by ball milling. *J. Cryst. Growth 220*, 466–470.

(38) Lal, S., Verma, J., and Van Noorden, C. J. F. (2014) Nanoparticles for hyperthermic therapy: synthesis strategies and applications in glioblastoma. *Int. J. Nanomedicine* 2863.

(39) Uschakov, A. V., Karpov, I. V., Lepeshev, A. A., and Petrov, M. I. (2016) Plasma-chemical synthesis of copper oxide nanoparticles in a low-pressure arc discharge. *Vacuum 133*, 25–30.

(40) Revaprasadu, N., and Mlondo, S. N. (2006) Use of metal complexes to synthesize semiconductor nanoparticles. *Pure Appl. Chem. 78*, 1691–1702.

(41) An, K., and Somorjai, G. A. (2012) Size and Shape Control of Metal Nanoparticles for Reaction Selectivity in Catalysis. *ChemCatChem 4*, 1512–1524.

(42) Trindade, T., O'Brien, P., Zhang, X., and Motevalli, M. (1997) Synthesis of PbS nanocrystallites using a novel single molecule precursors approach: X-ray single-crystal structure of $Pb(S_2CNEtPri)_2$. *J. Mater. Chem. 7*, 1011–1016.

(43) Lewis, D. J., Kevin, P., Bakr, O., Muryn, C. A., Malik, M. A., and O'Brien, P. (2014) Routes to tin chalcogenide materials as thin films or nanoparticles: a potentially important class of semiconductor for sustainable solar energy conversion. *Inorg Chem Front 1*, 577–598.

(44) Faller, J. W., and Parr, J. (2016) A convenient synthesis of cadmium chalcogenide quantum dots from cadmium acetate and bis(diphenylphosphino)methane monosulfide and –selenide or 1,4-bis(diphenylphosphino)butane monoselenide. *Phosphorus Sulfur Silicon Relat. Elem. 191*, 800–802.

(45) Lou, W., Chen, M., Wang, X., and Liu, W. (2007) Synthesis of high-luminescent cadmium sulfide nanocrystallites by a novel single-source precursor route. *Mater. Lett. 61*, 3612–3615.

(46) Stavila, V., Whitmire, K. H., and Rusakova, I. (2009) Synthesis of Bi_2S_3 Nanostructures from Bismuth(III) Thiourea and Thiosemicarbazide Complexes. *Chem. Mater. 21*, 5456–5465.

(47) Pawar, A. S., Masikane, S. C., Mlowe, S., Garje, S. S., and Revaprasadu, N. (2016) Preparation of CdS Nanoparticles from Thiosemicarbazone Complexes: Morphological Influence of Chlorido and Iodido Ligands: Preparation of CdS Nanoparticles. *Eur. J. Inorg. Chem. 2016*, 366–372.

(48) Pawar, A. S., Mlowe, S., Garje, S. S., Akerman, M. P., and Revaprasadu, N. (2017) Zinc thiosemicarbazone complexes: Single source precursors for alkylamine capped ZnS nanoparticles. *Inorganica Chim. Acta 463*, 7–13.

(49) Bruce, J. C., Revaprasadu, N., and Koch, K. R. (2007) Cadmium(ii) complexes of N,N-diethyl-N′-benzoylthio(seleno)urea as single-source precursors for the preparation of CdS and CdSe nanoparticles. *New J. Chem. 31*, 1647.

(50) Moloto, M. J., Malik, M. A., O'Brien, P., Motevalli, M., and Kolawole, G. A. (2003) Synthesis and characterisation of some N-alkyl/aryl and N,N′-dialkyl/aryl thiourea cadmium(II) complexes: the single crystal X-ray structures of $[CdCl_2(CS(NH_2)NHCH_3)_2]n$ and $[CdCl_2(CS(NH_2)NHCH_2CH_3)_2]$. *Polyhedron 22*, 595–603.

(51) Nair, P. S., Radhakrishnan, T., Revaprasadu, N., Kolawole, G., and O'Brien, P. (2002) Cadmium ethylxanthate: A novel single-source precursor for the preparation of CdS nanoparticles. *J. Mater. Chem. 12*, 2722–2725.

(52) Nyamen, L. D., Rajasekhar Pullabhotla, V. S., Nejo, A. A., Ndifon, P., and Revaprasadu, N. (2011) Heterocyclic dithiocarbamates: precursors for shape controlled growth of CdS nanoparticles. *New J. Chem. 35*, 1133.

(53) Nyamen, L. D., Rajasekhar Pullabhotla, V. S. R., Nejo, A. A., Ndifon, P. T., Warner, J. H., and Revaprasadu, N. (2012) Synthesis of anisotropic PbS nanoparticles using heterocyclic dithiocarbamate complexes. *Dalton Trans. 41*, 8297.

(54) Nyamen, L. D., Revaprasadu, N., Pullabhotla, R. V. S. R., Nejo, A. A., Ndifon, P. T., Malik, M. A., and O'Brien, P. (2013) Synthesis of multi-podal CdS nanostructures using heterocyclic dithiocarbamato complexes as precursors. *Polyhedron 56*, 62–70.

(55) Nyamen, L. D., Nejo, A. A., Pullabhotla, V. S. R., Ndifon, P. T., Malik, M. A., Akhtar, J., O'Brien, P., and Revaprasadu, N. (2014) The syntheses and structures of Zn(II) heterocyclic piperidine and tetrahydroquinoline dithiocarbamates and their use as single source precursors for ZnS nanoparticles. *Polyhedron 67*, 129–135.

(56) Lewis, E. A., McNaughter, P. D., Yin, Z., Chen, Y., Brent, J. R., Saah, S. A., Raftery, J., Awudza, J. A. M., Malik, M. A., O'Brien, P., and Haigh, S. J. (2015) In Situ Synthesis of PbS Nanocrystals in Polymer Thin Films from Lead(II) Xanthate and Dithiocarbamate Complexes: Evidence for Size and Morphology Control. *Chem. Mater. 27*, 2127–2136.

(57) Mthethwa, T., Pullabhotla, V. S. R. R., Mdluli, P. S., Wesley-Smith, J., and Revaprasadu, N. (2009) Synthesis of hexadecylamine capped CdS nanoparticles using heterocyclic cadmium dithiocarbamates as single source precursors. *Polyhedron 28*, 2977–2982.

(58) Khandel, P., and Shahi, S. K. (2018) Mycogenic nanoparticles and their bio-prospective applications: current status and future challenges. *J. Nanostructure Chem. 8*, 369–391.

(59) Sagadevan Suresh. (2013) Semiconductor Nanomaterials, Methods and Applications: A Review. *Nanosci. Nanotechnol. 3*, 62–74.

(60) Gubin, S. P., Kataeva, N. A., and Khomutov, G. B. (2005) Promising avenues of research in nanoscience: chemistry of semiconductor nanoparticles. *Russ. Chem. Bull. 54*, 827–852.

(61) Colvin, V. L., Goldstein, A. N., and Alivisatos, A. P. (1992) Semiconductor nanocrystals covalently bound to metal surfaces with self-assembled monolayers. *J. Am. Chem. Soc. 114*, 5221–5230.

(62) Labrenz, M. (2000) Formation of Sphalerite (ZnS) Deposits in Natural Biofilms of Sulfate-Reducing Bacteria. *Science 290*, 1744–1747.

(63) Tanori, J., and Paule Pileni, M. (1995) Change in the shape of copper nanoparticles in ordered phases. *Adv. Mater. 7*, 862–864.

(64) Guzelian, A. A., Banin, U., Kadavanich, A. V., Peng, X., and Alivisatos, A. P. (1996) Colloidal chemical synthesis and characterization of InAs nanocrystal quantum dots. *Appl. Phys. Lett. 69*, 1432–1434.

(65) Banin, U., Lee, C. J., Guzelian, A. A., Kadavanich, A. V., Alivisatos, A. P., Jaskolski, W., Bryant, G. W., Efros, Al. L., and Rosen, M. (1998) Size-dependent electronic

level structure of InAs nanocrystal quantum dots: Test of multiband effective mass theory. *J. Chem. Phys. 109*, 2306–2309.

(66) Norris, D. J., Efros, Al. L., Rosen, M., and Bawendi, M. G. (1996) Size dependence of exciton fine structure in CdSe quantum dots. *Phys. Rev. B 53*, 16347–16354.

(67) McKittrick, J., and Shea-Rohwer, L. E. (2014) Review: Down Conversion Materials for Solid-State Lighting. *J. Am. Ceram. Soc.* (Green, D. J., Ed.) *97*, 1327–1352.

(68) Edwards, P. P., Lodge, M. T. J., Hensel, F., and Redmer, R. (2010) '… a metal conducts and a non-metal doesn't.' *Philos. Trans. R. Soc. Math. Phys. Eng. Sci. 368*, 941–965.

(69) Xu, Y., and Schoonen, M. A. A. (2000) The absolute energy positions of conduction and valence bands of selected semiconducting minerals. *Am. Mineral. 85*, 543–556.

(70) Darling, R. B. (1991) Defect-state occupation, Fermi-level pinning, and illumination effects on free semiconductor surfaces. *Phys. Rev. B 43*, 4071–4083.

(71) Bard, A. J., Bocarsly, A. B., Fan, F.-R. F., Walton, E. G., and Wrighton, M. S. (1980) The Concept of Fermi Level Pinning at Semiconductor/Liquid Junctions. Consequences for Energy Conversion Efficiency and Selection of Useful Solution Redox Couples in Solar Device. *J. Am. Chem. Soc. 102*, 3671–3677.

(72) Taoka, N., Yokoyama, M., Hyeon Kim, S., Suzuki, R., Lee, S., Iida, R., Hoshii, T., Jevasuwan, W., Maeda, T., Yasuda, T., Ichikawa, O., Fukuhara, N., Hata, M., Takenaka, M., and Takagi, S. (2013) Impact of Fermi level pinning inside conduction band on electron mobility in InGaAs metal-oxide-semiconductor field-effect transistors. *Appl. Phys. Lett. 103*, 143509.

(73) Schirripa Spagnolo, G., Leccese, F., and Leccisi, M. (2019) LED as Transmitter and Receiver of Light: A Simple Tool to Demonstration Photoelectric Effect. *Crystals 9*, 531.

(74) Brus, L. E. (1984) Electron–electron and electron-hole interactions in small semiconductor crystallites: The size dependence of the lowest excited electronic state. *J. Chem. Phys. 80*, 4403–4409.

(75) Abbasi, E., Aval, S., Akbarzadeh, A., Milani, M., Nasrabadi, H., Joo, S., Hanifehpour, Y., Nejati-Koshki, K., and Pashaei-Asl, R. (2014) Dendrimers: synthesis, applications, and properties. *Nanoscale Res. Lett. 9*, 247.

(76) Camargo, P. H. C., Satyanarayana, K. G., and Wypych, F. (2009) Nanocomposites: synthesis, structure, properties and new application opportunities. *Mater. Res. 12*, 1–39.

(77) Pokropivny, V. V., and Skorokhod, V. V. (2007) Classification of nanostructures by dimensionality and concept of surface forms engineering in nanomaterial science. *Mater. Sci. Eng. C 27*, 990–993.

(78) Tiwari, J. N., Tiwari, R. N., and Kim, K. S. (2012) Zero-dimensional, one-dimensional, two-dimensional and three-dimensional nanostructured materials for advanced electrochemical energy devices. *Prog. Mater. Sci. 57*, 724–803.

(79) Norris, D. J., and Bawendi, M. G. (1996) Measurement and assignment of the size-dependent optical spectrum in CdSe quantum dots. *Phys. Rev. B 53*, 16338–16346.

(80) Schon, G., and Simon, U. (1995) A fascinating new field in colloid science: small ligand-stabilized metal clusters and possible application in microelectronics: Part I: State of the art. *Colloid Polym. Sci. 273*, 101–117.

(81) Martinez-Manez, R., and Rurack, K. (2010) The Supramolecular Chemistry of Organic – Inorganic Hybrid Materials. John Wiley & Sons, Inc., Hoboke, New Jersey.

(82) Chen, W., Wang, Z., Lin, Z., and Lin, L. (1997) Absorption and luminescence of the surface states in ZnS nanoparticles. *J. Appl. Phys. 82*, 3111–3115.

(83) Albrecht, C. Joseph R. Lakowicz: (2008) Principles of fluorescence spectroscopy, *Anal. Bioanal. Chem. 390*, 1223–1224.

(84) Ellis, B., and Moss, T. S. (1970) Calculated efficiencies of practical GaAs and Si solar cells including the effect of built-in electric fields. *Solid-State Electron. 13*, 1–24.

(85) Lang, D. V., and Kimerling, L. C. (1974) Observation of Recombination-Enhanced Defect Reactions in Semiconductors. *Phys. Rev. Lett. 33*, 489–492.

(86) Zhang, Y., Dai, R., and Hu, S. (2017) Study of the role of oxygen vacancies as active sites in reduced graphene oxide-modified TiO_2. *Phys. Chem. Chem. Phys. 19*, 7307–7315.

(87) Murray, C. B., Norris, D. J., and Bawendi, M. G. (1993) Synthesis and characterization of nearly monodisperse CdE (E = sulfur, selenium, tellurium) semiconductor nanocrystallites. *J. Am. Chem. Soc. 115*, 8706–8715.

(88) Roussignol, P., Ricard, D., Lukasik, J., and Flytzanis, C. (1987) New results on optical phase conjugation in semiconductor-doped glasses. *J. Opt. Soc. Am. B 4*, 5.

(89) Jung, D.-R., Kim, J., Nahm, C., Choi, H., Nam, S., and Park, B. (2011) Review paper: Semiconductor nanoparticles with surface passivation and surface plasmon. *Electron. Mater. Lett. 7*, 185–194.

(90) Jung, D.-R., Son, D., Kim, J., Kim, C., and Park, B. (2008) Highly luminescent surface-passivated ZnS:Mn nanoparticles by a simple one-step synthesis. *Appl. Phys. Lett. 93*, 163118.

(91) Murray, C. B., Kagan, C. R., and Bawendi, M. G. (2000) Synthesis and Characterization of Monodisperse Nanocrystals and Close-Packed Nanocrystal Assemblies. *Annu. Rev. Mater. Sci. 30*, 545–610.

(92) Kitchens, C. L., McLeod, M. C., and Roberts, C. B. (2003) Solvent Effects on the Growth and Steric Stabilization of Copper Metallic Nanoparticles in AOT Reverse Micelle Systems. *J. Phys. Chem. B 107*, 11331–11338.

(93) Steigerwald, M. L., Alivisatos, A. P., Gibson, J. M., Harris, T. D., Kortan, R., Muller, A. J., Thayer, A. M., Duncan, T. M., Douglass, D. C., and Brus, L. E. (1988) Surface derivatization and isolation of semiconductor cluster molecules. *J. Am. Chem. Soc. 110*, 3046–3050.

(94) Stark, A., and Seddon, K. R. (2007) Ionic Liquids, in *Kirk-Othmer Encyclopedia of Chemical Technology* (John Wiley & Sons, Inc., Ed.). John Wiley & Sons, Inc., Hoboken, NJ, USA.

(95) Bonnemann, H., and Brijoux, W. (1995) Catalytically Active Metal Powders and Colloids, in *Active Metals* (Frstner, A., Ed.), pp 339–379. Wiley-VCH Verlag GmbH, Weinheim, Germany.

(96) Carey, G. H., Abdelhady, A. L., Ning, Z., Thon, S. M., Bakr, O. M., and Sargent, E. H. (2015) Colloidal Quantum Dot Solar Cells. *Chem. Rev. 115*, 12732–12763.

(97) Boles, M. A., Ling, D., Hyeon, T., and Talapin, D. V. (2016) The surface science of nanocrystals. *Nat. Mater. 15*, 141–153.

(98) Kumar, S., and Nann, T. (2006) Shape Control of II–VI Semiconductor Nanomaterials. *Small 2*, 316–329.

(99) Oxtoby, D. W. (1998) Nucleation of First-Order Phase Transitions. *Acc. Chem. Res. 31*, 91–97.

(100) Kwon, S. G., and Hyeon, T. (2011) Formation Mechanisms of Uniform Nanocrystals via Hot-Injection and Heat-Up Methods. *Small 7*, 2685–2702.

(101) LaMer, V. K., and Dinegar, R. H. (1950) Theory, Production and Mechanism of Formation of Monodispersed Hydrosols. *J. Am. Chem. Soc. 72*, 4847–4854.

(102) Liebig, F., Thünemann, A. F., and Koetz, J. (2016) Ostwald Ripening Growth Mechanism of Gold Nanotriangles in Vesicular Template Phases. *Langmuir 32*, 10928–10935.

(103) Green, M., and O'Brien, P. (1999) Recent advances in the preparation of semiconductors as isolated nanometric particles: new routes to quantum dots. *Chem. Commun.* 2235–2241.

(104) Pickett, N. L., and O'Brien, P. (2001) Syntheses of semiconductor nanoparticles using single-molecular precursors. *Chem. Rec. 1*, 467–479.

(105) Kumar, A., Gaurav, Malik, A. K., Tewary, D. K., and Singh, B. (2008) A review on development of solid phase microextraction fibers by sol–gel methods and their applications. *Anal. Chim. Acta 610*, 1–14.

(106) Abbas Oudh, A.-J., Al-Mashhadani, A. H., and Twej, W. A. A. (2019) The Effect of Ce-doping Molar Concentration with Silica Xerogel on the Materials Optical Properties. *J. Phys. Conf. Ser. 1279*, 012043.

(107) Fievet, F., Lagier, J., Blin, B., Beaudoin, B., and Figlarz, M. (1989) Homogeneous and heterogeneous nucleations in the polyol process for the preparation of micron and submicron size metal particles. *Solid State Ion. 32–33*, 198–205.

(108) Carroll, K. J., Reveles, J. U., Shultz, M. D., Khanna, S. N., and Carpenter, E. E. (2011) Preparation of Elemental Cu and Ni Nanoparticles by the Polyol Method: An Experimental and Theoretical Approach. *J. Phys. Chem. C 115*, 2656–2664.

(109) Kotoulas, Dendrinou-Samara, Angelakeris, and Kalogirou. (2019) The Effect of Polyol Composition on the Structural and Magnetic Properties of Magnetite Nanoparticles for Magnetic Particle Hyperthermia. *Materials 12*, 2663.

(110) Demazeau, G. (2008) Solvothermal reactions: an original route for the synthesis of novel materials. *J. Mater. Sci. 43*, 2104–2114.

(111) Anandan, K., and Rajendran, V. (2017) Chromia (Cr2O3) Nanoparticles Synthesized By Using Cro3 Via The Facile Solvothermal Process And Their Optical Properties. *Int. J. Eng. Sci. Res. Technol. 6*, 916–921.

(112) de Mello Donegá, C., Liljeroth, P., and Vanmaekelbergh, D. (2005) Physicochemical Evaluation of the Hot-Injection Method, a Synthesis Route for Monodisperse Nanocrystals. *Small 1*, 1152–1162.

(113) Scher, E. C., Manna, L., and Alivisatos, A. P. (2003) Shape control and applications of nanocrystals. *Philos. Trans. R. Soc. Math. Phys. Eng. Sci. 361*, 241–257.

(114) Xia, Y., Xiong, Y., Lim, B., and Skrabalak, S. E. (2009) Shape-Controlled Synthesis of Metal Nanocrystals: Simple Chemistry Meets Complex Physics? *Angew. Chem. Int. Ed. 48*, 60–103.

(115) Kruszynska, M., Borchert, H., Bachmatiuk, A., Rümmeli, M. H., Büchner, B., Parisi, J., and Kolny-Olesiak, J. (2012) Size and Shape Control of Colloidal Copper(I) Sulfide Nanorods. *ACS Nano 6*, 5889–5896.

(116) Uehara, M., Watanabe, K., Tajiri, Y., Nakamura, H., and Maeda, H. (2008) Synthesis of CuInS2 fluorescent nanocrystals and enhancement of fluorescence by controlling crystal defect. *J. Chem. Phys. 129*, 134709.

(117) Connor, S. T., Hsu, C.-M., Weil, B. D., Aloni, S., and Cui, Y. (2009) Phase Transformation of Biphasic Cu_2S−$CuInS_2$ to Monophasic $CuInS_2$ Nanorods. *J. Am. Chem. Soc. 131*, 4962–4966.

(118) Choi, S.-H., Kim, E.-G., and Hyeon, T. (2006) One-Pot Synthesis of Copper−Indium Sulfide Nanocrystal Heterostructures with Acorn, Bottle, and Larva Shapes. *J. Am. Chem. Soc. 128*, 2520–2521.

(119) Zhong, H., Zhou, Y., Ye, M., He, Y., Ye, J., He, C., Yang, C., and Li, Y. (2008) Controlled Synthesis and Optical Properties of Colloidal Ternary Chalcogenide $CuInS_2$ Nanocrystals. *Chem. Mater. 20*, 6434–6443.

(120) Koo, B., Patel, R. N., and Korgel, B. A. (2009) Wurtzite−Chalcopyrite Polytypism in $CuInS_2$ Nanodisks. *Chem. Mater. 21*, 1962–1966.

(121) Marchand, P., and Carmalt, C. J. (2013) Molecular precursor approach to metal oxide and pnictide thin films. *Coord. Chem. Rev. 257*, 3202–3221.

(122) Sun, J., and Buhro, W. E. (2008) The Use of Single-Source Precursors for the Solution–Liquid–Solid Growth of Metal Sulfide Semiconductor Nanowires. *Angew. Chem. 120*, 3259–3262.

(123) Yu, K., Liu, X., Zeng, Q., Yang, M., Ouyang, J., Wang, X., and Tao, Y. (2013) The Formation Mechanism of Binary Semiconductor Nanomaterials: Shared by Single-Source and Dual-Source Precursor Approaches. *Angew. Chem. Int. Ed. 52*, 11034–11039.

(124) Bendt, G., Weber, A., Heimann, S., Assenmacher, W., Prymak, O., and Schulz, S. (2015) Wet-chemical synthesis of different bismuth telluride nanoparticles using metal organic precursors – single source vs. dual source approach. *Dalton Trans. 44*, 14272–14280.

(125) Cumberland, S. L., Hanif, K. M., Javier, A., Khitrov, G. A., Strouse, G. F., Woessner, S. M., and Yun, C. S. (2002) Inorganic Clusters as Single-Source Precursors for Preparation of CdSe, ZnSe, and CdSe/ZnS Nanomaterials. *Chem. Mater. 14*, 1576–1584.

(126) Disale, S. D., and Garje, S. S. (2010) Deposition of copper-doped iron sulfide (CuxFe1−xS) thin films using aerosol-assisted chemical vapor deposition technique. *Appl. Organomet. Chem. 24*, 734–740.

(127) Liu, K., Zhao, N., and Kumacheva, E. (2011) Self-assembly of inorganic nanorods. *Chem. Soc. Rev. 40*, 656.

(128) Anastas, P. T., and Warner, J. C. (1998) Green Chemistry: Theory and Practice, Oxford University Press:, New York.

(129) Dahl, J. A., Maddux, B. L. S., and Hutchison, J. E. (2007) Toward Greener Nanosynthesis. *Chem. Rev. 107*, 2228–2269.

(130) Parveen, K., Banse, V., and Ledwani, L. (2016) Green synthesis of nanoparticles: Their advantages and disadvantages, in *AIP Conference Proceedings*, p 020048. AIP Conference Proceedings.

(131) Ahmed, S., Saifullah, Ahmad, M., Swami, B. L., and Ikram, S. (2016) Green synthesis of silver nanoparticles using Azadirachta indica aqueous leaf extract. *J. Radiat. Res. Appl. Sci. 9*, 1–7.

(132) Green, M. (2010) The nature of quantum dot capping ligands. *J. Mater. Chem. 20*, 5797.

(133) Xue, B., Sun, T., Mao, F., and Xie, J. (2014) Gelatin-assisted green synthesis of bismuth sulfide nanorods under microwave irradiation. *Mater. Lett. 122*, 106–109.

(134) Shombe, G. B., Mubofu, E. B., Mlowe, S., and Revaprasadu, N. (2016) Synthesis and characterization of castor oil and ricinoleic acid capped CdS nanoparticles using single source precursors. *Mater. Sci. Semicond. Process. 43*, 230–237.

(135) Nyamen, L. D., Revaprasadu, N., and Teke Ndifon, P. (2014) Low temperature synthesis of PbS and CdS nanoparticles in olive oil. *Mater. Sci. Semicond. Process. 27*, 191–196.

(136) Hassan, E. A., and Zayed, S. E. (2014) Dithiocarbamates as Precursors in Organic Chemistry; Synthesis and Uses. *Phosphorus Sulfur Silicon Relat. Elem. 189*, 300–323.

(137) Halls, D. J. (1969) The properties of dithiocarbamates A Review. *Mikrochim. Acta 57*, 62–77.

(138) Kanchi, S., Singh, P., and Bisetty, K. (2014) Dithiocarbamates as hazardous remediation agent: A critical review on progress in environmental chemistry for inorganic species studies of 20th century. *Arab. J. Chem. 7*, 11–25.

(139) Baggio, R., Frigerio, A., Halac, E. B., Vega, D., and Perec, M. (1992) Synthesis and characterization of dithiocarbonate derivatives of zinc and cadmium bis(dithiocarbamates). *J. Chem. Soc. Dalton Trans.* 1887.

(140) Ferreira, I. P., de Lima, G. M., Paniago, E. B., Takahashi, J. A., Krambrock, K., Pinheiro, C. B., Wardell, J. L., and Visentin, L. C. (2013) Synthesis, characterization, structural and biological aspects of copper(II) dithiocarbamate complexes. *J. Mol. Struct. 1048*, 357–366.

(141) Kellner, R., St. Nikolov, G., and Trendafilova, N. (1984) Detecting the bonding type of dithiocarbamate ligands in their complexes as inferred from the asymmetric CS mode. *Inorganica Chim. Acta 84*, 233–239.

(142) Mlowe, S., Lewis, D. J., Malik, M. A., Raftery, J., Mubofu, E. B., O'Brien, P., and Revaprasadu, N. (2016) Heterocyclic dithiocarbamato-iron(III) complexes: single-source precursors for aerosol-assisted chemical vapour deposition (AACVD) of iron sulfide thin films. *Dalton Trans. 45*, 2647–2655.

(143) Arndt, D., Zielasek, V., Dreher, W., and Bäumer, M. (2014) Ethylene diamine-assisted synthesis of iron oxide nanoparticles in high-boiling polyolys. *J. Colloid Interface Sci. 417*, 188–198.

(144) Liu, J., Ruffini, N., Pollet, P., Llopis-Mestre, V., Dilek, C., Eckert, C. A., Liotta, C. L., and Roberts, C. B. (2010) More Benign Synthesis of Palladium Nanoparticles in Dimethyl Sulfoxide and Their Extraction into an Organic Phase. *Ind. Eng. Chem. Res. 49*, 8174–8179.

(145) García-Peña, N. G., Redón, R., Herrera-Gomez, A., Fernández-Osorio, A. L., Bravo-Sanchez, M., and Gomez-Sosa, G. (2015) Solventless synthesis of ruthenium nanoparticles. *Appl. Surf. Sci. 340*, 25–34.

(146) Thathagar, M. B., Kooyman, P. J., Boerleider, R., Jansen, E., Elsevier, C. J., and Rothenberg, G. (2005) Palladium Nanoclusters in Sonogashira Cross-Coupling: A True Catalytic Species? *Adv. Synth. Catal. 347*, 1965–1968.

(147) Debnath, D., Kim, S. H., and Geckeler, K. E. (2009) The first solid-phase route to fabricate and size-tune gold nanoparticles at room temperature. *J. Mater. Chem. 19*, 8810.

(148) Rak, M. J., Saadé, N. K., Friščić, T., and Moores, A. (2014) Mechanosynthesis of ultra-small monodisperse amine-stabilized gold nanoparticles with controllable size. *Green Chem 16*, 86–89.

(149) Mohadesi, A., Ranjbar, M., and Hosseinpour-Mashkani, S. M. (2014) Solvent-free synthesis of mercury oxide nanoparticles by a simple thermal decomposition method. *Superlattices Microstruct. 66*, 48–53.

(150) Kantevari, S., Chary, M. V., Rudra Das, A. P., Vuppalapati, S. V. N., and Lingaiah, N. (2008) Catalysis by an ionic liquid: Highly efficient solvent-free synthesis of aryl-14H-dibenzo[a.j]xanthenes by molten tetrabutylammonium bromide under conventional and microwave heating. *Catal. Commun. 9*, 1575–1578.

(151) Ghosh, C., and Varma, B. P. (1979) Optical properties of amorphous and crystalline Sb2S3 thin films. *Thin Solid Films 60*, 61–65.

(152) Arivuoli, D., Gnanam, F. D., and Ramasamy, P. (1988) Growth and microhardness studies of chalcogneides of arsenic, antimony and bismuth. *J. Mater. Sci. Lett. 7*, 711–713.

(153) Huang, L., Nair, P. K., Nair, M. T. S., Zingaro, R. A., and Meyers, E. A. (1995) Chemical deposition of Bi2S3 thin films on glass substrates pretreated with organosilanes. *Thin Solid Films 268*, 49–56.

(154) Rincón, M. E., and Nair, P. K. (1996) Kinetics of electrical conductivity enhancement in bismuth sulphide thin films. Part I: Argon and hydrogen annealing. *J. Phys. Chem. Solids 57*, 1937–1945.

(155) Nayak, B. B., Acharya, H. N., Mitra, G. B., and Mathur, B. K. (1983) Structural characterization of $Bi_{2-x}Sb_xS_3$ films prepared by the dip-dry method. *Thin Solid Films 105*, 17–24.

(156) Trindade, T., O'Brien, P., and Pickett, N. L. (2001) Nanocrystalline Semiconductors: Synthesis, Properties, and Perspectives. *Chem. Mater. 13*, 3843–3858.

(157) Deshmukh, L. P. (1994) Preparation and Properties of Sb_2S_3] Thin Films for Photoelectrochemical Applications. *J. Electrochem. Soc. 141*, 1779.

(158) Biswal, J. B., Sawant, N. V., and Garje, S. S. (2010) Deposition of rod-shaped antimony sulfide thin films from single-source antimony thiosemicarbazone precursors. *Thin Solid Films 518*, 3164–3168.

(159) Xiong, X., Wang, G., Lin, Y., Wang, Y., Ou, X., Zheng, F., Yang, C., Wang, J.-H., and Liu, M. (2016) Enhancing Sodium Ion Battery Performance by Strongly Binding

Nanostructured Sb_2S_3 on Sulfur-Doped Graphene Sheets. *ACS Nano 10*, 10953–10959.

(160) Yu, D. Y. W., Prikhodchenko, P. V., Mason, C. W., Batabyal, S. K., Gun, J., Sladkevich, S., Medvedev, A. G., and Lev, O. (2013) High-capacity antimony sulphide nanoparticle-decorated graphene composite as anode for sodium-ion batteries. *Nat. Commun. 4*, 2299.

(161) Ramasamy, K., Sims, H., Butler, W. H., and Gupta, A. (2014) Mono-, Few-, and Multiple Layers of Copper Antimony Sulfide ($CuSbS_2$): A Ternary Layered Sulfide. *J. Am. Chem. Soc. 136*, 1587–1598.

(162) Sarkar, S., Guria, A. K., Patra, B. K., and Pradhan, N. (2014) Chemical Sealing of Nanotubes: A Case Study on Sb_2S_3. *Angew. Chem. Int. Ed.* 12566–12570.

(163) Manna, G., Bose, R., and Pradhan, N. (2014) Photocatalytic Au-Bi_2S_3 Heteronanostructures. *Angew. Chem. Int. Ed. 53*, 6743–6746.

(164) Ma, J., Wang, Y., Wang, Y., Chen, Q., Lian, J., and Zheng, W. (2009) Controlled Synthesis of One-Dimensional Sb_2Se_3 Nanostructures and Their Electrochemical Properties. *J. Phys. Chem. C 113*, 13588–13592.

(165) Yao, S., Cui, J., Lu, Z., Xu, Z.-L., Qin, L., Huang, J., Sadighi, Z., Ciucci, F., and Kim, J.-K. (2017) Unveiling the Unique Phase Transformation Behavior and Sodiation Kinetics of 1D van der Waals Sb_2S_3 Anodes for Sodium Ion Batteries. *Adv. Energy Mater. 7*, 1602149.

(166) Zhang, R., Chen, X., Mo, M., Wang, Z., Zhang, M., Liu, X., and Qian, Y. (2004) Morphology-controlled growth of crystalline antimony sulfide via a refluxing polyol process. *J. Cryst. Growth 262*, 449–455.

(167) Park, K. H., Choi, J., Kim, H. J., Lee, J. B., and Son, S. U. (2007) Synthesis of Antimony Sulfide Nanotubes with Ultrathin Walls via Gradual Aspect Ratio Control of Nanoribbons. *Chem. Mater. 19*, 3861–3863.

(168) Biswal, J. B., Garje, S. S., and Revaprasadu, N. (2014) A convenient synthesis of antimony sulfide and antimony phosphate nanorods using single source dithiolatoantimony(III) dialkyldithiophosphate precursors. *Polyhedron 80*, 216–222.

(169) Lou, W., Chen, M., Wang, X., and Liu, W. (2007) Novel Single-Source Precursors Approach to Prepare Highly Uniform Bi_2S_3 and Sb_2S_3 Nanorods via a Solvothermal Treatment. *Chem. Mater. 19*, 872–878.

(170) Wang, J., Yu, H., Wang, T., Qiao, Y., Feng, Y., and Chen, K. (2018) Composition-Dependent Aspect Ratio and Photoconductivity of Ternary (BiSb)S Nanorods. *ACS Appl. Mater. Interfaces 10*, 7334–7343.

(171) Zhang, K., Luo, T., Chen, H., Lou, Z., and Shen, G. (2017) Au-nanoparticles-decorated Sb_2S_3 nanowire-based flexible ultraviolet/visible photodetectors. *J. Mater. Chem. C 5*, 3330–3335.

(172) Huang, R., Zhang, J., Wei, F., Shi, L., Kong, T., and Cheng, G. (2014) Ultrahigh Responsivity of Ternary Sb-Bi-Se Nanowire Photodetectors. *Adv. Funct. Mater. 24*, 3581–3586.

(173) Martinez, L., Bernechea, M., de Arquer, F. P. G., and Konstantatos, G. (2011) Near IR-Sensitive, Non-toxic, Polymer/Nanocrystal Solar Cells Employing Bi_2S_3 as the Electron Acceptor. *Adv. Energy Mater. 1*, 1029–1035.

(174) Gödel, K. C., Choi, Y. C., Roose, B., Sadhanala, A., Snaith, H. J., Seok, S. I., Steiner, U., and Pathak, S. K. (2015) Efficient room temperature aqueous Sb_2S_3 synthesis for inorganic–organic sensitized solar cells with 5.1% efficiencies. *Chem. Commun. 51*, 8640–8643.

(175) Christians, J. A., and Kamat, P. V. (2013) Trap and Transfer. Two-Step Hole Injection Across the Sb_2S_3 /CuSCN Interface in Solid-State Solar Cells. *ACS Nano 7*, 7967–7974.

(176) Hor, Y. S., Williams, A. J., Checkelsky, J. G., Roushan, P., Seo, J., Xu, Q., Zandbergen, H. W., Yazdani, A., Ong, N. P., and Cava, R. J. (2010) Superconductivity in $Cu_xBi_2Se_3$ and its Implications for Pairing in the Undoped Topological Insulator. *Phys. Rev. Lett. 104*.

(177) Shang, M.-H., Zhang, J., Wei, S., Zhu, Y., Wang, L., Hou, H., Wu, Y., Fujikawa, T., and Ueno, N. (2016) Bi-doped Sb_2S_3 for low effective mass and optimized optical properties. *J. Mater. Chem. C 4*, 5081–5090.

(178) Deng, Z., Mansuripur, M., and Muscat, A. J. (2009) Simple Colloidal Synthesis of Single-Crystal Sb−Se−S Nanotubes with Composition Dependent Band-Gap Energy in the Near-Infrared. *Nano Lett. 9*, 2015–2020.

(179) Patra, B. K., Khilari, S., Bera, A., Mehetor, S. K., Pradhan, D., and Pradhan, N. (2017) Chemically Filled and Au-Coupled $BiSbS_3$ Nanorod Heterostructures for Photoelectrocatalysis. *Chem. Mater. 29*, 1116–1126.

(180) Zhao, Y., and Manthiram, A. (2015) $Bi_{0.94}Sb_{1.06}S_3$ Nanorod Cluster Anodes for Sodium-Ion Batteries: Enhanced Reversibility by the Synergistic Effect of the Bi_2S_3–Sb_2S_3 Solid Solution. *Chem. Mater. 27*, 6139–6145.

(181) Rockett, A. (2008) The materials science of semiconductors. Springer, New York.

(182) Mocatta, D., Cohen, G., Schattner, J., Millo, O., Rabani, E., and Banin, U. (2011) Heavily Doped Semiconductor Nanocrystal Quantum Dots. *Science 332*, 77–81.

(183) Chen, H.-Y., Maiti, S., and Son, D. H. (2012) Doping Location-Dependent Energy Transfer Dynamics in Mn-Doped CdS/ZnS Nanocrystals. *ACS Nano 6*, 583–591.

(184) Virgil W. Lueth, Philip C. Goodell, and Nicholas E. Pngitore. (1990) Encoding the Evolution of an Ore System in Bismuthinite-Stibnite CompositionsJ. ulcani,P eru. *Econ. Geol. 85*, 1462–1472.

(185) Poleti, D., Karanović, L., Balić-Žunić, T., and Gržetić, I. (2012) Crystal structure of $(Bi_{0.94}Sb_{1.06})S_3$ and reconsideration of cation distribution over mixed sites in the

bismuthinitestibnite solid-solution series. *Neues Jahrb. Für Mineral. - Abh. J. Mineral. Geochem. 189*, 177–187.

(186) Lundegaard, L. F., Miletich, R., Balic-Zunic, T., and Makovicky, E. (2003) Equation of state and crystal structure of Sb 2 S 3 between 0 and 10 GPa. *Phys. Chem. Miner. 30*, 463–468.

(187) Lundegaard, L. F., Makovicky, E., Boffa-Ballaran, T., and Balic-Zunic, T. (2005) Crystal structure and cation lone electron pair activity of Bi2S3 between 0 and 10 GPa. *Phys. Chem. Miner. 32*, 578–584.

(188) Filip, M. R., Patrick, C. E., and Giustino, F. (2013) G W quasiparticle band structures of stibnite, antimonselite, bismuthinite, and guanajuatite. *Phys. Rev. B 87*.

(189) Atsushi Kyono, and Mitsuyoshi Kimata. (2004) Structural variations induced by difference of the inert pair efect i the stibnite-bismuthinite solid solution series $(Sb,Bi)_2S_3$. *Am. Mineral. 89*, 932–940.

(190) Liu, J., Liu, J., Li, J., Xie, H., Wang, J., Deng, J., Feng, C., Qi, F., and Zhang, N. (2008) Experimental Synthesis of the Stibnite-Antimonselite Solid Solution Series. *Int. Geol. Rev. 50*, 163–176.

(191) Springer G. (1969) Naturally occurring compositions in the solid-solution series Bi_2S_3-Sb_2S_3. *Miniralogical Mag. 37*, 294.

(192) Leszczynski M., Litwin-Staszewska E, and Suski T. (1995) Lattice Constant of Doped Semiconductor. *Acta Phys. Pol. A 88*, 837–840.

(193) Jilani, A., Abdel-wahab, M. S., and Hammad, A. H. (2017) Advance Deposition Techniques for Thin Film and Coating, in *Modern Technologies for Creating the Thin-film Systems and Coatings* (Nikitenkov, N. N., Ed.). InTech.

(194) Rao, M. C., and Shekhawat, M. S. (2013) A Brief Survey on Basic Properties of Thin Films for Device Apllication. *Int. J. Mod. Phys. Conf. Ser. 22*, 576–582.

(195) West, A. R. (2014) Solid State Chemistry and Its Applications, Second edition, s John Wiley & Sons, Inc, Chichester, West Sussex.

(196) Nancheva, N., Docheva, P., Djourelov, N., and Balcheva, M. (2002) Positron and X-ray diffraction study of Cu–Se, In–Se and $CuInSe_2$ thin films. *Mater. Lett. 54*, 169–174.

(197) Powell, M. J., and Carmalt, C. J. (2017) Aerosols: A Sustainable Route to Functional Materials. *Chem. - Eur. J. 23*, 15543–15552.

(198) Powell, M. J., Potter, D. B., Wilson, R. L., Darr, J. A., Parkin, I. P., and Carmalt, C. J. (2017) Scaling aerosol assisted chemical vapour deposition: Exploring the relationship between growth rate and film properties. *Mater. Des. 129*, 116–124.

(199) Salazar, K. V., Ott, K. C., Dye, R. C., Hubbard, K. M., Peterson, E. J., Coulter, J. Y., and Kodas, T. T. (1992) Aerosol assisted chemical vapor deposition of superconducting $YBa_2Cu_3O_{7-\chi}$. *Phys. C Supercond. 198*, 303–308.

(200) Dixon, S. C., Peveler, W. J., Noor, N., Bear, J. C., and Parkin, I. P. (2016) Superhydrophobic Au/polymer nanocomposite films via AACVD/swell encapsulation tandem synthesis procedure. *RSC Adv. 6*, 31146–31152.

(201) Ramasamy, K., Kuznetsov, V. L., Gopal, K., Malik, M. A., Raftery, J., Edwards, P. P., and O'Brien, P. (2013) Organotin Dithiocarbamates: Single-Source Precursors for Tin Sulfide Thin Films by Aerosol-Assisted Chemical Vapor Deposition (AACVD). *Chem. Mater. 25*, 266–276.

(202) Shahid, M., Mazhar, M., Hamid, M., Zeller, M., O'Brien, P., Malik, M. A., Raftery, J., and Hunter, A. D. (2009) Isostructural cage complexes of copper with cadmium or zinc for single source deposition of composite materials. *New J. Chem. 33*, 2241.

(203) Marchand, P., Hassan, I. A., Parkin, I. P., and Carmalt, C. J. (2013) Aerosol-assisted delivery of precursors for chemical vapour deposition: expanding the scope of CVD for materials fabrication. *Dalton Trans. 42*, 9406.

(204) Birnie, D. P. (2004) Spin Coating Technique, in *Sol-Gel Technologies for Glass Producers and Users* (Aegerter, M. A., and Mennig, M., Eds.), pp 49–55. Springer US, Boston, MA.

(205) Taylor, J. F. (2001) Spin coating: An overview. *Met. Finish. 99*, 16–21.

(206) Hou, Y., Lohe, M. R., Zhang, J., Liu, S., Zhuang, X., and Feng, X. (2016) Vertically oriented cobalt selenide/NiFe layered-double-hydroxide nanosheets supported on exfoliated graphene foil: an efficient 3D electrode for overall water splitting. *Energy Environ. Sci. 9*, 478–483.

(207) Shi, J., Hu, J., Luo, Y., Sun, X., and Asiri, A. M. (2015) Ni_3Se_2 film as a non-precious metal bifunctional electrocatalyst for efficient water splitting. *Catal. Sci. Technol. 5*, 4954–4958.

(208) Wang, Z., Li, J., Tian, X., Wang, X., Yu, Y., Owusu, K. A., He, L., and Mai, L. (2016) Porous Nickel–Iron Selenide Nanosheets as Highly Efficient Electrocatalysts for Oxygen Evolution Reaction. *ACS Appl. Mater. Interfaces 8*, 19386–19392.

(209) Duan, H., Li, D., Tang, Y., He, Y., Ji, S., Wang, R., Lv, H., Lopes, P. P., Paulikas, A. P., Li, H., Mao, S. X., Wang, C., Markovic, N. M., Li, J., Stamenkovic, V. R., and Li, Y. (2017) High-Performance Rh_2P Electrocatalyst for Efficient Water Splitting. *J. Am. Chem. Soc. 139*, 5494–5502.

(210) Pu, Z., Zhao, J., Amiinu, I. S., Li, W., Wang, M., He, D., and Mu, S. (2019) A universal synthesis strategy for P-rich noble metal diphosphide-based electrocatalysts for the hydrogen evolution reaction. *Energy Environ. Sci. 12*, 952–957.

(211) Guo, Y., Park, T., Yi, J. W., Henzie, J., Kim, J., Wang, Z., Jiang, B., Bando, Y., Sugahara, Y., Tang, J., and Yamauchi, Y. (2019) Nanoarchitectonics for Transition-Metal-Sulfide-Based Electrocatalysts for Water Splitting. *Adv. Mater. 31*, 1807134.

(212) Menezes, P. W., Indra, A., Zaharieva, I., Walter, C., Loos, S., Hoffmann, S., Schlögl, R., Dau, H., and Driess, M. (2019) Helical cobalt borophosphates to master durable overall water-splitting. *Energy Environ. Sci. 12*, 988–999.

(213) Karade, S. S., Banerjee, K., Majumder, S., and Sankapal, B. R. (2016) Novel application of non-aqueous chemical bath deposited Sb2S3 thin films as supercapacitive electrode. *Int. J. Hydrog. Energy 41*, 21278–21285.

(214) Xu, Y., Ding, L., Zhong, T., Han, X., Jiao, L., Yuan, H., and Wang, Y. (2015) Novel application of LiCoO2 as a high-performance candidate material for supercapacitor. *J. Energy Chem. 24*, 193–198.

(215) Pujari, R. B., Lokhande, A. C., Kim, J. H., and Lokhande, C. D. (2016) Bath temperature controlled phase stability of hierarchical nanoflakes CoS_2 thin films for supercapacitor application. *RSC Adv. 6*, 40593–40601.

(216) Qian, J., Chen, Y., Wu, L., Cao, Y., Ai, X., and Yang, H. (2012) High capacity Na-storage and superior cyclability of nanocomposite Sb/C anode for Na-ion batteries. *Chem. Commun. 48*, 7070.

(217) Thompson, S. E., and Parthasarathy, S. (2006) Moore's law: the future of Si microelectronics. *Mater. Today 9*, 20–25.

(218) Hahn, H., Sidorenko, A., and Tiginyanu, I. (2009) Nanoscale Phenomena. Springer Berlin Heidelberg, Berlin, Heidelberg.

(219) Buzea, C., and Robbie, K. (2005) Assembling the puzzle of superconducting elements: a review. *Supercond. Sci. Technol. 18*, R1–R8.

(220) Visakh, P. M., and Martínez Morlanes, M. J. (2016) Nanomaterials and nanocomposites: zero- to three-dimensional materials and their composites. Wiley-VCH Verlag GmbH & Co. KGaA, Weinheim.

(221) Guo, B., Li, C., and Yuan, Z.-Y. (2010) Nanostructured Co_3O_4 Materials: Synthesis, Characterization, and Electrochemical Behaviors as Anode Reactants in Rechargeable Lithium Ion Batteries. *J. Phys. Chem. C 114*, 12805–12817.

(222) Carey, J. D. (2003) Engineering the next generation of large-area displays: prospects and pitfalls. *Philos. Trans. R. Soc. Math. Phys. Eng. Sci. 361*, 2891–2907.

(223) Menard-Moyon, C., Kostarelos, K., Prato, M., and Bianco, A. (2010) Functionalized Carbon Nanotubes for Probing and Modulating Molecular Functions. *Chem. Biol. 17*, 107–115.

(224) Caballero-George, C., Marin, and Briceño. (2013) Critical evaluation of biodegradable polymers used in nanodrugs. *Int. J. Nanomedicine* 3071.

(225) Kneuer, C., Sameti, M., Bakowsky, U., Schiestel, T., Schirra, H., Schmidt, H., and Lehr, C.-M. (2000) A Nonviral DNA Delivery System Based on Surface Modified Silica-Nanoparticles Can Efficiently Transfect Cells in Vitro. *Bioconjug. Chem. 11*, 926–932.

(226) Joshi, A. W. (2009) Emerging physics. Pearson : Dorling Kindersley (India), Delhi.

(227) Weinberg, G. (2003) Lipid emulsion infusion rescues dogs from bupivacaine-induced cardiac toxicity. *Reg. Anesth. Pain Med. 28,* 198–202.

(228) Wang, M. L., Tuli, R., Manner, P. A., Sharkey, P. F., Hall, D. J., and Tuan, R. S. (2003) Direct and indirect induction of apoptosis in human mesenchymal stem cells in response to titanium particles. *J. Orthop. Res. 21,* 697–707.

(229) Sidorenko, D., Loginov, P., Mishnaevsky, L., and Levashov, E. (2017) Nanocomposites for Machining Tools. *Materials 10,* 1171.

(230) Lanone, S., and Boczkowski, J. (2006) Biomedical Applications and Potential Health Risks of Nanomaterials: Molecular Mechanisms. *Curr. Mol. Med. 6,* 651–663.

(231) Bahadar, H., Maqbool, F., Niaz, K., and Abdollahi, M. (2016) Toxicity of Nanoparticles and an Overview of Current Experimental Models. *Iran. Biomed. J. 20,* 1–11.

(232) Soto, K. F., Carrasco, A., Powell, T. G., Garza, K. M., and Murr, L. E. (2005) Comparative in vitro cytotoxicity assessment of some manufacturednanoparticulate materials characterized by transmissionelectron microscopy. *J. Nanoparticle Res. 7,* 145–169.

(233) Kumar, N., and Kumbhat, S. (2016) Essentials in nanoscience and nanotechnology. Wiley, Hoboken, New Jersey.

(234) Akpan, U. G., Jimoh, A., and Mohammed, A. D. (2006) Extraction, Characterization and Modification of Castor Seed Oil. *Leonardo J. Sci. 5,* 43–52.

(235) Vaisman, B., Shikanov, A., and Domb, A. J. (2008) The Isolation of Ricinoleic Acid from Castor Oil by Salt-solubility-based Fractionation for the Biopharmaceutical Applications. *J. Am. Oil Chem. Soc. 85,* 169–184.

(236) Skoog, D. A., Holler, F. J., and Crouch, S. R. (2007) Principles of instrumental analysis 6th ed. Thomson Brooks/Cole, Belmont, CA.

(237) Kenkel, J. (2003) Analytical chemistry for technicians 3rd ed. Lewis Publishers, Boca Raton.

(238) Thompson, M. (2008, April) CHNS Elemental Analysers. The Royal Society of Chemistry.

(239) Haines, P. J. (2002) Principles of thermal analysis and calorimetry (Royal Society of Chemistry (Great Britain), Ed.). Royal Society of Chemistry, Cambridge.

(240) Coats, A. W., and Redfern, J. P. (1963) Thermogravimetric analysis. A review. *The Analyst 88,* 906.

(241) Speyer, R. F. (1994) Thermal analysis of materials. Marcel Dekker, New York.

(242) Lambert, J. B., and Mazzola, E. P. (2004) Nuclear Magnetic Resonnace Spectroscopy. An Introduction to Principles, Applications, and Experimental Methods. Pearson Education Inc., New Jersey 07458.

(243) Bruice, P. Y. (2011) Organic chemistry 6th ed. Prentice Hall, Boston.

(244) Baryshevskiĭ, V. G., Feranchuk, I. D., and Ulyanenkov, A. P. (2005) Parametric X-ray radiation in crystals: theory, experiment, and applications. Springer, Berlin ; New York.

(245) Saravanan, R., and Prema Rani, M. (2012) Charge Density Analysis from X-Ray Diffraction, in *Metal and Alloy Bonding - An Experimental Analysis*, pp 31–64. Springer London, London.

(246) Kalantar-zadeh, K., and Fry, B. N. (2008) Nanotechnology-enabled sensors. Springer, New York.

(247) Rani, A., and Shukla, G. (2017) Applications of nanotechnology an introduction. Horion Books.

(248) Carter, M., and Shieh, J. (2015) Microscopy, in *Guide to Research Techniques in Neuroscience*, pp 117–144. Elsevier.

(249) Goldstein, J. I., Newbury, D. E., Echlin, P., Joy, D. C., Lyman, C. E., Lifshin, E., Sawyer, L., and Michael, J. R. (2003) The SEM and Its Modes of Operation, in *Scanning Electron Microscopy and X-ray Microanalysis*, pp 21–60. Springer US, Boston, MA.

(250) Martin, J. W. (2003) The local chemical analysis of materials. Elsevier, Amsterdam ; Boston.

(251) Cullity, B. D., and Stock, S. R. (2014) Elements of X-Ray Diffraction. Pearson, Harlow.

(252) Spence, J. C. H. (1999) The future of atomic resolution electron microscopy for materials science. *Mater. Sci. Eng. R Rep. 26*, 1–49.

(253) Zhang, S., Li, L., and Kumar, A. (2009) Materials characterization techniques. CRC Press, Boca Raton.

(254) Watts, J. F., and Wolstenholme, J. (2003) An introduction to surface analysis by XPS and AES. J. Wiley, Chichester, West Sussex, England ; New York.

(255) Kelsall, R. W., Hamley, I. W., Geoghegan, M., and John Wiley & Sons. (2005) Nanoscale science and technology. John Wiley, Chichester, England.

(256) Wartewig, S. (2003) IR and Raman spectroscopy: fundamental processing. Wiley-VCH, Weinheim.

(257) McCreery, R. L. (2000) Raman spectroscopy for chemical analysis. John Wiley & Sons, New York.

(258) Saravanan, R., and Rani, M. P. (2012) Metal and alloy bonding: an experimental analysis: charge density in metals and alloys. Springer, London.

(259) Birkholz, M., Fewster, P. F., and Genzel, C. (2006) Thin film analysis by X-ray scattering. Wiley-VCH, Weinheim.

(260) Monshi, A., Foroughi, M. R., and Monshi, M. R. (2012) Modified Scherrer Equation to Estimate More Accurately Nano-Crystallite Size Using XRD. *World J. Nano Sci. Eng. 02*, 154–160.

(261) Muniz, F. T. L., Miranda, M. A. R., Morilla dos Santos, C., and Sasaki, J. M. (2016) The Scherrer equation and the dynamical theory of X-ray diffraction. *Acta Crystallogr. Sect. Found. Adv. 72*, 385–390.

(262) Ronconi, L., Giovagnini, L., Marzano, C., Bettìo, F., Graziani, R., Pilloni, G., and Fregona, D. (2005) Gold Dithiocarbamate Derivatives as Potential Antineoplastic Agents: Design, Spectroscopic Properties, and in Vitro Antitumor Activity. *Inorg. Chem. 44*, 1867–1881.

(263) Nami, S. A. A., Husain, A., and Ullah, I. (2014) Self assembled homodinuclear dithiocarbamates: One pot synthesis and spectral characterization. *Spectrochim. Acta. A. Mol. Biomol. Spectrosc. 118*, 380–388.

(264) Rodarte de Moura, C. V., de Sousa, A. P. G., Silva, R. M., Abras, A., Hörner, M., Bortoluzzi, A. J., Filgueiras, C. A. L., and Wardell, J. L. (1999) Syntheses and spectra of triphenyltin heteroarenethiolates. *Polyhedron 18*, 2961–2969.

(265) Sheldrick, G. M. (1990) Phase annealing in SHELX-90: direct methods for larger structures. *Acta Crystallogr. A 46*, 467–473.

(266) Yin, H., Li, F., Li, F., and Wang, D. (2007) Synthesis and Characterization of Bismuth Complexes $[BiI_2(4,4'\text{-bpy})(S_2CNR_2)]\infty$ and $[BiI(S_2CNR_2)_2]\infty$ and Crystal Structure of $[BiI_2(4,4'\text{-bpy})(S_2CNC_4H_8O)]\infty$ and $[BiI(S_2CNC_5H_{10})_2]\infty$. *J. Inorg. Organomet. Polym. Mater. 17*, 331–331.

(267) Yin, H., Li, F., and Wang, D. (2007) Synthesis and crystal structure of two new Bi(III) complexes $\{(Me_2NCS_2)_3\ Bi\}_2$ and $\{[(CH_2)_5NCS_2]_2BiI\}_2$. *J. Coord. Chem. 60*, 1133–1141.

(268) Yin, H., and Wang, C. (2004) Crystallographic report: $Bi(S_2CNC_5H_{10})_2(NO_3)$(1,10-phenanthroline). *Appl. Organomet. Chem. 18*, 195–196.

(269) Li, F., Yin, H., and Wu, G. (2014) Iodidobis(morpholine-4-carbodithioato-κ^2 *S,S′*)(1,10-phenanthroline-κ^2 *N,N′*)bismuth(III). *Acta Crystallogr. Sect. E Struct. 70*, 20–20.

(270) Chauhan, R., Chaturvedi, J., Trivedi, M., Singh, J., Molloy, K. C., Kociok-Köhn, G., Amalnerkar, D. P., and Kumar, A. (2015) New single-source precursor for bismuth sulfide and its use as low-cost counter electrode material for dye-sensitized solar cells. *Inorganica Chim. Acta 430*, 168–175.

(271) Li, M.-X., Zhang, L.-Z., Yang, M., Niu, J.-Y., and Zhou, J. (2012) Synthesis, crystal structures, in vitro biological evaluation of zinc(II) and bismuth(III) complexes of 2-acetylpyrazine N(4)-phenylthiosemicarbazone. *Bioorg. Med. Chem. Lett. 22*, 2418–2423.

(272) Alvarez, S. (2013) A cartography of the van der Waals territories. *Dalton Trans. 42*, 8617.

(273) Dodds, C. A., Reglinski, J., and Spicer, M. D. (2006) Lower Main-Group Element Complexes with a Soft Scorpionate Ligand: The Structural Influence of Stereochemically Active Lone Pairs. *Chem. - Eur. J. 12*, 931–939.

(274) Garcia-Montalvo, V., Cea-Olivares, R., Williams, D. J., and Espinosa-Perez, G. (1996) Stereochemical Consequences of the Bismuth Atom Electron Lone Pair, a Comparison between MX_6 E and MX_6 Systems. Crystal and Molecular Structures of Tris[*N* -(*P* , *P* -diphenylphosphinoyl)- *P* , *P* -diphenylphosphinimidato]bismuth(III), $[Bi\{(OPPh_2)_2N\}_3]$, -indium(III), $[In\{(OPPh_2)_2N\}_3]\cdot C_6H_6$, and -gallium(III), $[Ga\{(OPPh_2)_2 N\}_3]\cdot CH_2Cl_2$. *Inorg. Chem. 35*, 3948–3953.

(275) Summers, S. P., Abboud, K. A., Farrah, S. R., and Palenik, G. J. (1994) Syntheses and structures of bismuth(III) complexes with nitrilotriacetic acid, ethylenediaminetetraacetic acid, and diethylenetriaminepentaacetic acid. *Inorg. Chem. 33*, 88–92.

(276) Breunig, H. J., Nema, M. G., Silvestru, C., Soran, A. P., and Varga, R. A. (2010) Organobismuth compounds with the pincer ligand 2,6-(Me2NCH2)2C6H3: Monoorganobismuth(iii) carbonate, sulfate, nitrate, and a diorganobismuthenium(iii) salt. *Dalton Trans. 39*, 11277.

(277) Allen, F. H. (2002) The Cambridge Structural Database: a quarter of a million crystal structures and rising. *Acta Crystallogr. B 58*, 380–388.

(278) Groom, C. R., Bruno, I. J., Lightfoot, M. P., and Ward, S. C. (2016) The Cambridge Structural Database. *Acta Crystallogr. Sect. B Struct. Sci. Cryst. Eng. Mater. 72*, 171–179.

(279) Li, F., Yin, H.-D., Zhai, J., and Wang, D.-Q. (2006) (Morpholine-1-dithiocarboxylato-κ^2 *S* , *S* ′)bis(piperidine-1-dithiocarboxylato-κ^2 *S* , *S* ′)bismuth(III). *Acta Crystallogr. Sect. E Struct. Rep. Online 62*, m1083–m1085.

(280) Liu, Y., and Tiekink, E. R. T. (2005) Supramolecular associations in binary antimony(iii) dithiocarbamates: influence of ligand steric bulk, influence on coordination geometry, and competition with hydrogen-bonding. *CrystEngComm 7*, 20.

(281) Que, M., Zhang, Y. C., Liu, Z. D., and Zhou, H. P. (2009) Redetermination of tris(*N* , *N* -diethyldithiocarbamato)antimony(III). *Acta Crystallogr. Sect. E Struct. Rep. Online 65*, 311–312.

(282) Zhai, J., Yin, H., and Wang, D. (2007) Tris(morpholine-4-dithiocarboxylato-κ^2 *S* , *S* ′)antimony(III). *Acta Crystallogr. Sect. E Struct. Rep. Online 63*, m2989–m2989.

(283) Bakshi, M. S. (2016) How Surfactants Control Crystal Growth of Nanomaterials. *Cryst. Growth Des. 16*, 1104–1133.

(284) Sigman, M. B., and Korgel, B. A. (2005) Solventless Synthesis of Bi $_2$ S $_3$ (Bismuthinite) Nanorods, Nanowires, and Nanofabric. *Chem. Mater. 17*, 1655–1660.

(285) Penn, R. L., and Banfield, J. F. (1999) Morphology development and crystal growth in nanocrystalline aggregates under hydrothermal conditions: insights from titania. *Geochim. Cosmochim. Acta 63*, 1549–1557.

(286) Campbell, C. T. (2002) The Effect of Size-Dependent Nanoparticle Energetics on Catalyst Sintering. *Science 298*, 811–814.

(287) Peng, X. (2003) Mechanisms for the Shape-Control and Shape-Evolution of Colloidal Semiconductor Nanocrystals. *Adv. Mater. 15*, 459–463.

(288) Peng, Z. A., and Peng, X. (2002) Nearly Monodisperse and Shape-Controlled CdSe Nanocrystals via Alternative Routes: Nucleation and Growth. *J. Am. Chem. Soc. 124*, 3343–3353.

(289) Thambidurai, M., Muthukumarasamy, N., Velauthapillai, D., and Lee, C. (2013) Quantum confinement effects in Gd-doped CdS nanoparticles prepared by chemical precipitation technique. *J. Mater. Sci. Mater. Electron. 24*, 4535–4541.

(290) Jun, Y., Choi, J., and Cheon, J. (2006) Shape Control of Semiconductor and Metal Oxide Nanocrystals through Nonhydrolytic Colloidal Routes. *Angew. Chem. Int. Ed. 45*, 3414–3439.

(291) Groom, R. A., Jacobs, A., Cepeda, M., Drummey, R., and Latturner, S. E. (2017) Structural and Optical Properties of Sb-Substituted BiSI Grown from Sulfur/Iodine Flux. *Inorg. Chem. 56*, 12362–12368.

(292) Seong, M. J., Alawadhi, H., Miotkowski, I., Ramdas, A. K., and Miotkowska, S. (1999) The anomalous variation of band gap with alloy composition: cation vs anion substitution in ZnTe. *Solid State Commun. 112*, 329–334.

(293) Zumeta-Dubé, I., Ortiz-Quiñonez, J.-L., Díaz, D., Trallero-Giner, C., and Ruiz-Ruiz, V.-F. (2014) First Order Raman Scattering in Bulk Bi_2S_3 and Quantum Dots: Reconsidering Controversial Interpretations. *J. Phys. Chem. C 118*, 30244–30252.

(294) Minceva-Sukarova, B., Najdoski, M., Grozdanov, I., and Chunnilall, C. J. (1997) Raman spectra of thin solid films of some metal sulfides. *J. Mol. Struct. 410–411*, 267–270.

(295) Chen, L., Deng, H., Cui, J., Tao, J., Zhou, W., Cao, H., Sun, L., Yang, P., and Chu, J. (2015) Composition dependence of the structure and optical properties of Cu2MnxZn1−xSnS4 thin films. *J. Alloys Compd. 627*, 388–392.

(296) He, J., Sun, L., Zhang, K., Wang, W., Jiang, J., Chen, Y., Yang, P., and Chu, J. (2013) Effect of post-sulfurization on the composition, structure and optical properties of Cu_2ZnSnS_4 thin films deposited by sputtering from a single quaternary target. *Appl. Surf. Sci. 264*, 133–138.

(297) Tanuma, S., Powell, C. J., and Penn, D. R. (1994) Calculations of electron inelastic mean free paths. V. Data for 14 organic compounds over the 50-2000 eV range. *Surf. Interface Anal. 21*, 165–176.

(298) Grigas, J., Talik, E., and Lazauskas, V. (2002) X-ray Photoelectron Spectra and Electronic Structure of Bi2S3 Crystals. *Phys. Status Solidi B 232*, 220–230.

(299) Uchida, K., and Ayame, A. (1996) Dynamic XPS measurements on bismuth molybdate surfaces. *Surf. Sci. 357–358*, 170–175.

(300) Zakaznova-Herzog, V. P., Harmer, S. L., Nesbitt, H. W., Bancroft, G. M., Flemming, R., and Pratt, A. R. (2006) High resolution XPS study of the large-band-gap semiconductor stibnite (Sb_2S_3): Structural contributions and surface reconstruction. *Surf. Sci. 600*, 348–356.

(301) Wagner, C. D. (1975) Chemical shifts of Auger lines, and the Auger parameter. *Faraday Discuss. Chem. Soc. 60*, 291.

(302) Audi, A. A., and Sherwood, P. M. A. (2000) X-ray photoelectron spectroscopic studies of sulfates and bisulfates interpreted by X? and band structure calculations. *Surf. Interface Anal. 29*, 265–275.

(303) Ahire, R. R., and Sharma, R. P. (2006) Photoelectrochemical characterization of Bi_2S_3 thin films deposited by modified chemical bath deposition. *CSIR* 140–144.

(304) Killedar, V. V., Lokhande, C. D., and Bhosale, C. H. (1996) Preparation and characterization of Bi2S3 thin films spray deposited from non-aqueous media. *Thin Solid Films 289*, 14–16.

(305) Wang, Y., Huang, J., Cao, L., Zhu, H., He, H., and Wu, J. (2009) Preparation of Bi_2S_3 thin films with a nanoleaf structure by electrodeposition method. *Appl. Surf. Sci. 255*, 7749–7752.

(306) Beevi, M. M., Anusuya, M., and Saravanan, V. (2010) Characterization of CdO Thin Films Prepared By SILAR Deposition Technique. *Int. J. Chem. Eng. Appl. 1*, 151–154.

(307) Chaudhari, K. R., Yadav, N., Wadawale, A., Jain, V. K., and Bohra, R. (2010) Monoorganobismuth(III) dithiocarboxylates: Synthesis, structures and their utility as molecular precursors for the preparation of Bi_2S_3 films and nanocrystals. *Inorganica Chim. Acta 363*, 375–380.

(308) Xie, G., Qiao, Z.-P., Zeng, M.-H., Chen, X.-M., and Gao, S.-L. (2004) A Single-Source Approach to Bi_2S_3 and Sb_2S_3 Nanorods via a Hydrothermal Treatment. *Cryst. Growth Des. 4*, 513–516.

(309) Wang, J., Yu, H., Wang, T., Qiao, Y., Feng, Y., and Chen, K. (2018) Composition-Dependent Aspect Ratio and Photoconductivity of Ternary (BiSb)S Nanorods. *ACS Appl. Mater. Interfaces 10*, 7334–7343.

APPENDIX

1. List of publications

Kun W.N., Mlowe S., Nyamen L.D., Peter T. Ndifon P.T., Malik M.A., Munro O.Q., and Revaprasadu N., Heterocyclic Bismuth(III) Dithiocarbamato Complexes as Single-Source Precursors for the Synthesis of Anisotropic Bi_2S_3 Nanoparticles, *Chem. Eur. J.* **2016**, 22, 1 – 10

Kun W.N., Mlowe S., Nyamen L.D., Akerman M.P., O'Brien P., Ndifon P.T., Revaprasadu N., Deposition of Bi_2S_3 thin films from heterocyclic bismuth(III) dithiocarbamato complexes, *Polyhedron*, **2018**, 154, 173-1811

Kun W. N., McNaughter P. D., Nyamen L. D., Spencer B. F., O' Brien P., Ndifon P. T., and Revaprasadu N., Synthesis of $(Bi_{1-x}Sb_x)_2S_3$ solid solutions via thermal decomposition of bismuth and antimony piperidinedithiocarbamtes, *RSC Adv*., **2019**, 9 15836

2. Other publications

Francis K. Ngounoue, Evans N. Mainsah, Aseng M. Conde, 'Awawou G. Paboudam, Sally-Judith E Ntum, **Walter K. Ndamukong**, Choumkeu Mbakop Vanessa and Peter T Ndifon 'Antimicrobial and antioxidant studies on some transition metal complexes derived from the Schiff base ligand, 4-hydroxypent-3-en-2-ylideneaminophenol', Der Pharma Chemica, 2015, 7(5) :101-106

ChemPubSoc Europe

CHEMISTRY A European Journal

DOI: 10.1002/chem.201602106 Full Paper

Nanoparticles

Heterocyclic Bismuth(III) Dithiocarbamato Complexes as Single-Source Precursors for the Synthesis of Anisotropic Bi_2S_3 Nanoparticles

Walter N. Kun,[a, b] Sixberth Mlowe,[a] Linda D. Nyamen,[b] Peter T. Ndifon,[b] Mohammad A. Malik,[a, c] Orde Q. Munro,[d] and Neerish Revaprasadu*[a]

Abstract: New complexes catena-(μ2-nitrato-O,O')bis(piperidinedithiocarbamato)bismuth(III) (1) and tetrakis(μ-nitrato)tetrakis[bis(tetrahydroquinolinedithiocarbamato)bismuth(III)] (2) were synthesized and characterised by elemental analysis, FTIR spectroscopy and thermogravimetric analysis. The single-crystal X-ray structures of 1 and 2 were determined. The coordination numbers of the Bi^{III} ion are 8 for 1 and 6 for 2 when the experimental electron density for the nominal $6s^2$ lone pair of electrons is included. Both complexes phosphine oxide-capped Bi_2S_3 nanoparticles at different temperatures. UV/Vis spectra showed a blueshift in the absorbance band edge characteristic of a quantum size effect. High-quality, crystalline, long and short Bi_2S_3 nanorods were obtained depending on the thermolysis temperature, which was varied from 190 to 270 8C. A general trend of increasing particle breadth with increasing reaction temperature and increasing length of the carbon chain of the amine (capping agent) was observed. Powder XRD patterns revealed the or-thorhombic crystal structure of Bi_2S_3.

Introduction

Semiconductor materials of type V–VI have recently attracted attention due to their photoconductive, photosensitive, thermoelectric and fluorescence properties.[1–5] Among these materials, bismuth sulfide (Bi_2S_3), owing to its high figure of merit (ZT value) with a large absorption coefficient and high energy conversion efficiency, is widely used as a thermoelectric-cool-ing material. It has a direct energy bandgap between 1.3 and 1.7 eV and finds applications in photovoltaic converters[6] and photodiode arrays.[7]

The morphology, size and phase of nanostructured materials are influenced by reaction parameters such as passivating groups, monomer concentration, thermolysis temperature and precursor type. Many approaches have been proposed for fab-ricating one-dimensional Bi_2S_3 nanostructures, including micro-wave irradiation,[8] the polyol method,[9] solvo(hydro)thermal routes,[10–12] and molecular-precursor routes.[7, 13–16] As a simple, easily controlled, low-cost and effective heating method, ther-mal decomposition of single-source precursors (SSPs) in coor-dinating solvents has been widely used in the synthesis of high-quality nanomaterials.[17]

Trindade et al. reported the synthesis of Bi_2S_3 nanoparticulates from bismuth dithiocarbamato complexes by chemical vapour deposition or by thermal decomposition in an organic solvent at 400 8C.[7, 14] The coordinating solvent used in the hot-injection route had a strong influence on the final properties and morphology of the Bi_2S_3 particles. Shen et al. used bismuth tris(diethyldithiocarbamate) as SSP to prepare Bi_2S_3 nanotubes by pyrolysis at 530 8C.[13] Xie et al. synthesized Bi_2S_3 nanorods using the same bismuth complex and observed that varying the temperature from 115 to 170 8C did not alter the phase of the products.[15] Garje and co-workers synthesized Bi_2S_3 nano-rods with a small aspect ratio by the thermal decomposition of bismuth(III) dialkyldithiophosphate complexes in ethylene glycol at 197 8C.[16b]

The mechanism of the preferential growth of Bi_2S_3 nanorods with variation of reaction parameters has been studied in some detail. Many studies have concluded that the type of sol-vent used, for example, ethylene glycol, diethylene glycol or thioglycolic acid, favoured the formation of Bi_2S_3 nano-rods.[8, 11, 12, 16] Stavila et al. reported the decomposition of bis-muth(III) thiourea and thiosemicarbazide complexes in differ-

a W. N. Kun, Dr. S. Mlowe, Dr. M. A. Malik, Prof. N. Revaprasadu
Department of Chemistry, University of Zululand
Private Bag X1001, Kwa-Dlangezwa, 3886 (South Africa) Fax : (+27) 35 902 65681
E-mail : RevaprasaduN@unizulu.ac.za

a W. N. Kun, Dr. L. D. Nyamen, Prof. P. T. Ndifon
Department of Inorganic Chemistry, University of Yaound I P.O. Box 812, Yaound (Cameroon)

a Dr. M. A. Malik
School of Materials, University of Manchester
Oxford Road, Manchester, M13 9PL (UK)

a Prof. O. Q. Munro
Molecular Sciences Institute, School of Chemistry
University of Witwatersrand, P.O. WITS 2050 Johannesburg, (South Africa)

Supporting information for this article can be found under http ://dx.doi.org/10.1002/chem.201602106.

ent solvents at 120 8C. The addition of a small amount of dodecanethiol or octadecanethiol resulted in the formation of Bi_2S_3 nanorods up to several nanometres in length, with better crystallinity.[18]

Recently, we have reported the use of heterocyclic dithiocarbamates as SSPs for the preparation of nanocrystalline materials.[19–25] These dithiocarbamate complexes containing bulky alkyl groups have been particularly effective in producing high-quality CdS, ZnS and PbS nanomaterials.[19, 21, 22] Herein we describe the synthesis of Bi_2S_3 nanorods at different temperatures and with different capping agents from newly synthes-ised complexes catena-(m2-nitrato-O,O')bis(piperidinedithiocarbamato)bismuth(III) (1) and the tetranuclear cluster tetrakis(m-nitrato)tetrakis[bis(tetrahydroquinolinedithiocarbamato)bismuth(III)] (2). The single-crystal X-ray structures of both complexes are also reported. Compared with former methods and SSPs, the present technique is more convenient, environmental friendly and scalable.

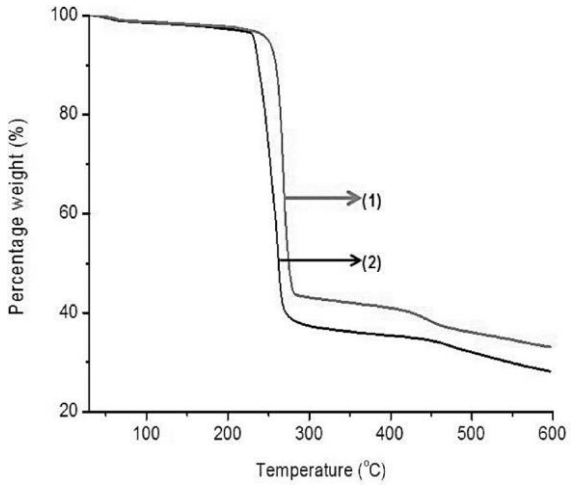

Figure 1. TGA plots of 1 and 2.

Results and Discussion

Characterisation of the ligand and the complexes

The bismuth dithiocarbamato complexes used in this work are easily synthesized with cost-effective starting materials and reaction protocols ; they are stable to air and moisture. The li-gands and the complexes were obtained in good yields, and microanalysis confirmed their purity. The complexes are yellow microcrystalline powders soluble in most organic solvents. IR spectroscopic analysis revealed a very broad band around 3324–3367 cm 1 in the spectra of the ligands due to n(O H) of water (Supporting Information, Figures S1 and S2). This band was absent in the spectra of the complexes. Both the ligands and complexes showed bands in the 1466–1485 cm 1 region, corresponding to n(C=N) and n(C N). The n(C=S) band was observed in the 999–975 cm 1 region in the spectra of the li-gands. The upward shift of this band in the complexes com-pared to the free ligand, together with a strong band (or very close bands) attributed to n(C S) was indicative of a bidentate or slightly anisobidentate dithiocarbamate ligand.

The TGA plots of both complexes showed a two-step decomposition pattern. The first step with weight losses of 57.5 and 65.0 % (calcd : 55.6 and 63.5 %) at 248.4 and 221.6 8C for complexes 1 and 2, respectively (Figure 1), corresponds to the loss of the organic moiety and sulfur atom. The second decomposition step at 436.9 and 436.4 8C corresponds to the loss of more sulfur atoms with mass losses of 7.5 and 6.0 % (calcd: 7.3 and 5.8 %). The final residues of 35.0 and 29.0 % were close to the calculated values of 37.1 and 30.7 % for Bi_2S_3 from com-plexes 1 and 2, respectively.

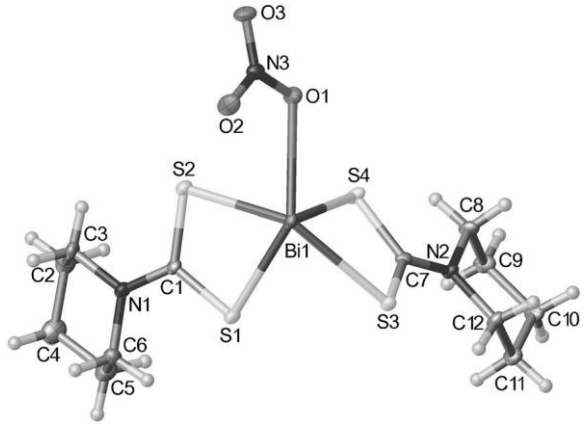

Figure 2. Thermal ellipsoid plot (50 % probability surfaces) of the ASU of the single-crystal X-ray structure of 1, determined at 100 K. Labels for all non-H atoms are shown.

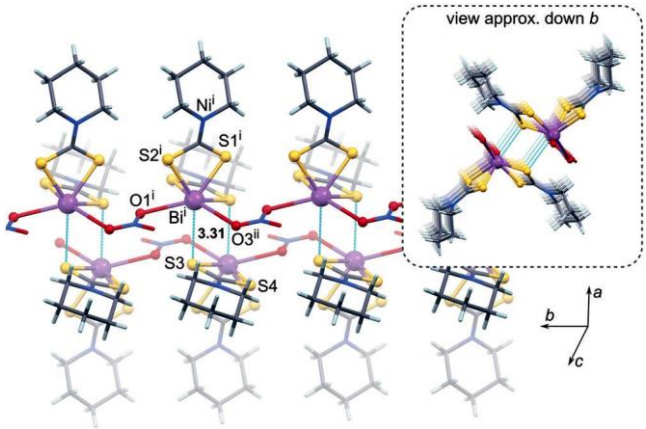

Figure 3. Illustration of the 1D coordination polymer formed by 1 and the interaction between adjacent inversion-related chains in the lattice. Selected atoms are rendered as spheres and labelled (others are depicted as cylin-ders) ; the Bi···S3 interaction distance is 3.310(2) &. Atom symmetry operator codes : i) 1 x, y, 1 z; ii) 1 x, 1 y, 1 z.

Single-crystal X-ray structures

Thermal ellipsoid plots of the crystal structures of 1 and 2 are shown in Figures 2, 3 and 4. Crystal data, data collection and structure refinement details for compounds 1 and 2 are summarised in Table 1, and selected bond lengths and angles are

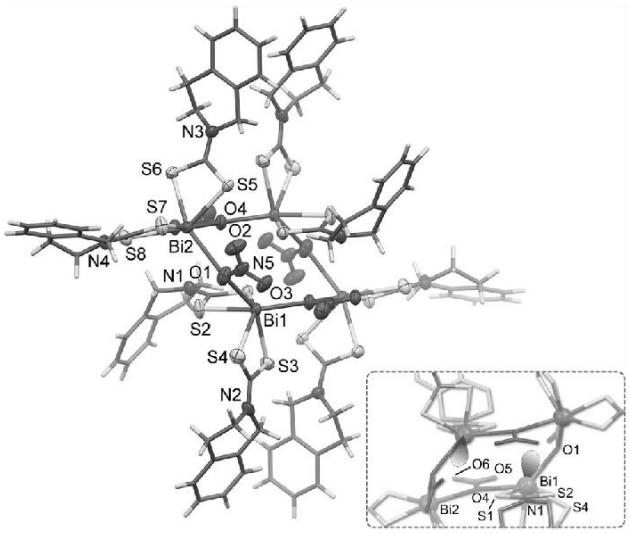

Figure 4. Partially labelled thermal ellipsoid plot (35 % probability surfaces) and cylinder model of the X-ray structure of 2. Labels are shown for selected atoms belonging to the symmetry-unique portion of the molecule. The inset depicts the possible orientations of the stereochemically active $6s^2$ lone pairs on two of the symmetry-related Bi^{III} ions Bi1. The difference electron-density map of 2 confirming the lone pair orientations is given in the Sup-porting Information (Figure S4).

Table 2. Selected bond lengths [&] and angles [8] for 1.

Bi(1) S(1)	2.6480(14)	S(1)-Bi(1)-S(2)	66.25(5)
Bi(1) S(2)	2.7937(16)	S(1)-Bi(1)-S(3)	78.32(5)
Bi(1) S(3)	2.7980(14)	S(1)-Bi(1)-O(1)	137.69(9)
Bi(1) S(4)	2.6169(14)	S(2)-Bi(1)-S(3)	134.65(4)
Bi(1) O(1)	2.723(4)	S(4)-Bi(1)-S(1)	94.64(5)
S(1) C(1)	1.744(5)	S(4)-Bi(1)-S(2)	88.27(5)
S(2) C(1)	1.727(5)	S(4)-Bi(1)-S(3)	66.63(4)
S(3) C(7)	1.736(5)	S(4)-Bi(1)-O(1)	72.54(8)

Table 3. Selected bond lengths [&] and angles [8] for 2.

Bi(1) S(1)	2.7734(14)	Bi(1) O(1)	2.694(5)
Bi(1) S(3)	2.6343(15)	Bi(2) S(5)	2.7313(14)
Bi(1) S(4)	2.7745(16)	Bi(2) S(7)	2.6174(16)
Bi(1) S(2)	2.6456(14)	Bi(2) S(6)	2.6026(15)
Bi(1) O(4)	2.725(4)	Bi(2) S(8)	2.8105(15)
S(1)-Bi(1)-S(4)	137.35(5)	O(1)-Bi(1)-S(1)	112.28(11)
S(3)-Bi(1)-S(1)	86.28(4)	O(1)-Bi(1)-S(4)	83.23(12)
S(3)-Bi(1)-S(4)	66.27(5)	S(5)-Bi(2)-O(4)	81.50(9)
S(3)-Bi(1)-S(2)	95.02(6)	S(7)-Bi(2)-O(4)	170.49(9)
S(3)-Bi(1)-O(4)	76.40(9)	O(4)-Bi(1)-S(1)	69.31(9)
S(2)-Bi(1)-O(4)	134.67(9)	O(4)-Bi(1)-S(4)	128.64(9)
S(2)-Bi(1)-O(1)	71.53(11)	Bi(1)-O(4)-Bi(2)	150.95(15)

listed in Tables 2 and 3. Both compounds crystallise in the monoclinic crystal system (space group $P2_1/c$).

The low-temperature X-ray structure of 1 is novel[26] and reveals that the complex forms a 1D coordination polymer in the crystalline solid state. The asymmetric unit (ASU) shown in Figure 2, which is also the polymer repeat unit, comprises a bis-muth(III) ion, the two chelating dithiocarbamate ions, and the bridging nitrate ion. The mean Bi S coordination bond length is 2.71(8) & (Table 2) and compares favourably with the mean distance of 2.75(10) & for the eight known X-ray structures of Bi^{III} coordinated to dithiocarbamate ions of a similar struc-ture.[27] The Bi O bond lengths average 2.79(7) & and are longer than those reported for the monodentate nitrato li-gands (h^1-NO_3), for example, bis(nitrato)(methanol){N-phenyl-N'-[1-(pyrazin-2-yl)ethylidene]carbamohydrazonothioato}bismu-th(III), which are distinctly non-bridging (Bi O, 2.45(6) &).[28] Bi-dentate coordination of nitrate ions (h^2-NO_3) tends to be the most common binding mode in Bi^{III} complexes (presumably the large ionic radius of Bi^{3+} facilitates increased donor atom density at the metal centre), whereas monodentate polymeric or multinuclear nitrato-bridged species are infrequently ob-served. More specifically, only three crystallographically charac-terised examples of complexes with linking m_2-nitrato-O,O' li-gands, Bi O(NO)O' Bi, are known : the room-temperature structure of 1,[26] catena-{(m_2-nitrato-O,O')-bis[(h^5-cyclopentadie-nyl)dicarbonyliron(II)]bismuth(III)}[29] and the Bi^{III}–Nd^{III} heterome-

Table 1. Crystal system, selected data collection parameters, and X-ray structure refinement details for 1 and 2.

Chemical formula	$C_{12}H_{20}BiN_3O_3S_4$	$2(C_{40}H_{40}Bi_2N_6O_6S_8)$
M_r	591.53	2750.44
Crystal system, space group	monoclinic, $P2_1/c$	monoclinic, $P2_1/c$
T [K]	100	296
a, b, c [&]	13.712 (7), 6.172 (3), 22.415 (11)	14.1529 (16), 12.8531 (15), 26.270 (3)
b [8]	102.351 (7)	90.773 (2)
V [&^{3}]	1853.0 (16)	4778.3 (9)
Z	4	2
radiation	Mo_{Ka}	Mo_{Ka}
m [mm ^{1}]	9.98	7.76
crystal size [mm]	0.35 0 0.2 0 0.15	0.4 0 0.16 0 0.12
I_{min}, I_{max}	0.421, 0.746	0.226, 0.746
no. of measured, independent, and observed [I > 2s(I)] reflections	67 445, 5396, 5276	114 395, 12 667, 9423
R_{int}	0.040	0.044
$(\sin q/l)_{max}$ [& ^{1}]	0.717	0.697
R[F^2 >2s(F^2)], wR(F^2), S	0.033, 0.073, 1.15	0.035, 0.096, 1.09
no. of reflections, parameters	5396, 208	12 667, 560
$D1_{max}$, $D1_{min}$ [e & ^{3}]	3.10, 2.81	1.69, 1.24

tallic coordination polymer {[(NO3)Nd(H2O)4(m3-cydta)Bi-(m-ONO2)]·2.5 H2O}n, where cydta is trans-cyclohexylene-1,2-diami-netetraacetate.[30]

The intrachelate S-Bi-S bond angles of 1 average 66.4(2)8, consistent with the mean of 65(2)8 for related structures in the literature.[27] The coordination group of each BiS_4 unit is completed by one O atom of a nitrate ion (Bi O1 2.723(4) &). However, the coordination geometry around Bi^{III} in 1 is distinctly irregular, and defies typical classification. Each nitrate ion functions as a bridging ligand in the 1D chain by virtue of coordi-nation of its second oxygen atom to the adjacent Bi^{III} ion in the lattice (Figure 3). The extended structure may thus be de-scribed as a 1D coordination polymer comprising alternating BiS_4 repeat units and bridging nitrate ions. Interestingly, the in-version-related 1D polymer chain interacts significantly with its counterpart through weaker (longer) Bi···S interactions (3.31 &). Note that the sum of the van der Waals radii[31] of Bi (2.54 &) and S (1.89 &) far exceeds the Bi···S interaction distance in 1, consistent with the interaction being effectively a dative cova-lent bond. This results in the formation of columns comprising symmetry-related pairs of 1D chains whose axes run parallel to one another but in opposite directions. The obtuse $O1^{i}$-Bi-$O3^{ii}$ bond angle of 125.28 (Figure 3) suggests, furthermore, that the Bi^{III} valence lone pair ($6s^2$) may be stereochemically active in 1, as in soft scorpionate[32] and tetraphenylimidodiphosphinate[33] chelates of Bi^{III}, and is most likely positioned midway between the two nitrate ion O donors (projecting approximately out of the plane of Figure 3 towards the reader). This electron-density projection is in fact clearly supported by the difference Fourier map for 1 shown in the Supporting Information (Figure S3). It is common to count the lone pair as occupying one coordina-tion site at the metal centre for Bi^{III} coordination com-pounds.[34] Applying this principle here suggests that the Bi^{III} ions of 1 are in fact eight-coordinate. Interestingly, there are some well-characterised Bi^{III} coordination complexes in the lit-erature with geometries that clearly indicate the presence of the stereochemically active $6s^2$ lone pair of Bi^{III} ; however, its contribution to the irregular coordination geometry around the metal ion is apparently not always recognised.[35] A sound theoretical basis (s–p mixing of metal-cation and oxide-ligand atomic orbitals) exists to account for the variable appearance of the lone pair in Sb_2O_3 and other $6s^2$ metal oxides (e.g., PbO),[36] but has seemingly not yet been extended to a molecu-lar orbital treatment of lone-pair effects in large coordination complexes of Bi^{III} with complex ligands such as those described in this work.

Complex 2 is a centrosymmetric tetranuclear Bi^{III} cluster with bridging nitrate groups (m_1,h^1-NO_3 , Figure 4). Because the geometry about the centre of gravity of the cluster is opened out by the bridging nitrate ions, no acutely short Bi···S intra-molecular interactions are evident. The shortest of these, $Bi1\cdots S1^{i}$ (3.650(1) &, symmetry code i: x, y, z), is probably too long to be considered even a weak dative covalent bond, despite the contact distance lying within the sum of the van der Waals radii of the bonded elements. Consistent with 1, the obtuse O1-Bi1-O4 bond angle of 133.7(1)8 probably signals the presence of the stereochemically active nominally $6s^2$ lone pair of the Bi^{III} ion, which evidently projects in a direction that roughly bisects the O1-Bi1-O4 bond angle (inset to Figure 4). If the $6s^2$ lone pair is treated as occupying one coordination site, each symmetry-unique Bi^{III} ion labelled Bi1 in 2 should be re-garded as seven-coordinate with the remaining coordination sites occupied by the four sulfur atoms of the bidentate 3,4-di-hydroisoquinoline-2(1H)-carbodithioate ions and the two ni-trate ion oxygen atoms O1 and O4.

The coordination geometry around the second symmetry-unique Bi^{III} ion, Bi2, is markedly different to that of Bi1. For example, the O1-Bi2-$O4^{i}$ bond angle is 85.8(1)8 and the structural distortion around Bi2 appears to be less severe. Since we cannot be certain of the existence of a stereochemically active $6s^2$ electron pair for Bi2 (as suggested by the more diffuse elec-tron density distribution about Bi2, see Figure S4 of the Sup-porting Information), the coordination number around Bi2 is best regarded as being definitively six. The Bi S bond lengths for 2 range from 2.603(1) to 2.810(2) & (av 2.70(8) &), in agree-ment with those of 1 and other similar Bi^{III} chelate complexes in the literature.[27] The Bi O bond lengths average 2.74(4) &, consistent with the bridging nature of the NO_3 ions in the structure, as noted for 1. The S-Bi-S bond angles for 2 average 66.3(5)8, are similar to those of 1 and in close agreement with S-Bi-S intrachelate angles observed for related compounds in the CSD.[27, 37] For both 1 and 2, the C S bond lengths are stat-istically equivalent, averaging 1.74(1) and 1.72(1) &, respective-ly, consistent with the expected resonance-delocalised elec-tronic structure of the dithiocarbamate ions in both com-pounds.

The crystal packing in 2 is somewhat loose, presumably because of the inherent difficulty of efficiently packing the large tetranuclear cluster. The total solvent-accessible volume per unit cell is 227.5 $&^3$ (4.8 %), and the total electron count within the void space is 19.9 electrons ; this equates to two water molecules per unit cell. Due to their disorder, the water molecules occupying the two larger void spaces (2 0 51.4 $&^3$; Figure 5) were not discretely modelled during structure refinement. The smaller void spaces (2 0 25.7 $&^3$, 4 0 10.1 $&^3$, and 4 0 8.2 $&^3$) are vacant.

The reaction between $Bi(NO_3)_3$·4 H_2O and piperidinedithiocarbamate in water followed by recrystallisation from chloroform/methanol afforded complex 3. A thermal ellipsoid view of the crystal structure of the bis-chloroform solvate of tris(piperidine-dithiocarbamato)bismuth(III) (3; space group $P2_1/c$), is shown in the Supporting Information (Figure S5). Crystal data, data collection and structure refinement details for complex 3 (two independent molecules per ASU) are summarised in the Sup-porting Information (Table S1). The independent bismuth(III) ions are bound to six sulfur donor atoms, each from three che-lating dithiocarbamate ligands. The coordination geometry about each Bi^{III} ion reflects an uneven distribution of the three chelate rings due to formation of a dimer comprising the two crystallographically independent molecules in the lattice (Sup-porting Information, Figure S6). The dimer is stabilised by intra-molecular Sb···S interactions with distances of 3.367(1) & (Bi2···S4) and 3.402(1) & (Bi1···S8) ; the B1-S4···Bi2-S8 and S4-Bi1···S8-Bi2 dihedral angles of 45.53(3) and 45.46(3)8, respec-

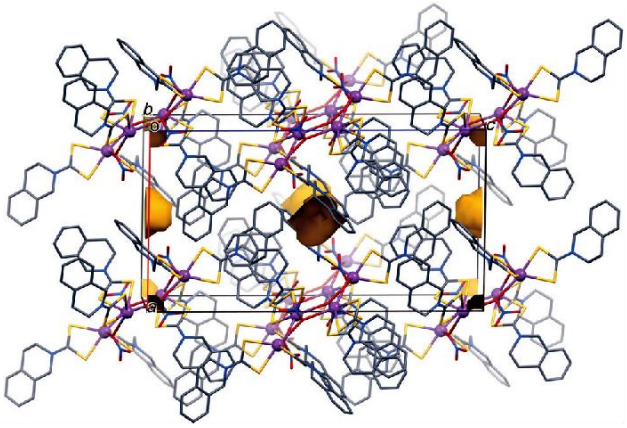

Figure 5. Void locations (gold surfaces) in the lattice of complex 2 (unit cell oriented approximately along the b axis). The larger voids (51.4 &) are occupied by a single disordered water molecule ; the smaller voids are vacant. The voids were calculated with a probe radius of 1.2 &. H atoms have been omitted for clarity, Bi^{III} ions are rendered as spheres (arbitrary radii), and all other bonds and atoms are shown as cylinders.

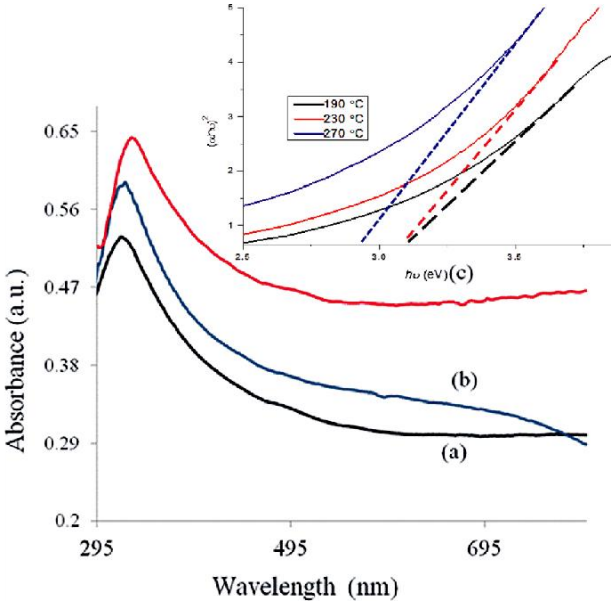

Figure 6. UV/Vis absorption spectra of OLA-capped Bi_2S_3 nanorods obtained from 1 at a) 190, b) 230 and c) 270.

tively, reflect considerable twisting of the Bi_2S_2 core of the dimer. Interestingly, the Bi_2S_2 core of the centrosymmetric dimer observed for the analogous morpholinodithiocarbamate derivative[38] is planar (Supporting Information, Figure S7). This leaves substantial room in the morpholinodithiocarbamate complex for a stereochemically active, nominally $6s^2$, lone pair, which clearly culminates in a coordination number of eight for this complex. The twisted Bi_2S_2 dimer core of 3, in contrast, ap-pears to exclude space for the $6s^2$ lone pair, such that the Bi^{III} ions are seven-coordinate. The Bi S and S-Bi-S bond lengths and angles of 3 average 2.81(12) & and 63.9(7)8, respectively, which are normal for this class of compounds (as discussed above).

Bi_2S_3 nanoparticles

The thermolysis of precursors in high-boiling point solvents is a well-reported route to high-quality nanoparticles. The size of the nanoparticles depends on the reaction time and tempera-ture, precursor/capping agent ratio and alkyl groups. Long-chain amines were found to be suitable surfactants for II–VI semiconductor nanomaterials. In this work we explored the use of long-chain amines, such as hexadecylamine (HDA), do-decylamine (DDA) and oleylamine (OLA), as well as traditional tri-n-octylphosphine oxide (TOPO), as capping agents for Bi_2S_3 nanoparticles. Bismuth complexes 1 and 2 were thermolysed in coordinating solvents at temperatures of 190, 230, and [270] 8C for 2 h. The choice of reaction temperatures was based on our previous work on PbS.[22]

Optical properties

The absorption spectra of the Bi_2S_3 particles synthesized from precursor 1 in 3.0 g of OLA at 190, 230, and 270 8C are shown in Figure 6. A strong blueshift with absorption band edges of 3.1, 3.09 and 2.9 eV were observed for particles synthesized at 190, 230 and 270 8C, respectively, compared to that of 1.3 eV (950 nm) for bulk Bi_2S_3, characteristic of the quantum confine-ment. This shift can be explained by the presence of Bi_2S_3 nanocrystals in which at least one linear dimension is in the nanosize regime. A slight shift in the optical absorption associ-ated with increasing reaction temperature is also observed, and indicates an increase in mean particle size with increasing temperature. A similar trend was observed when precursor 1 was thermolysed in HDA, DDA, and TOPO. No significant changes in the optical properties of the Bi_2S_3 particles were ob-served when precursor 2 was thermolysed in DDA, HDA, and TOPO with corresponding reaction parameters.

Structural and morphological characterisation

Powder X-ray diffraction (P-XRD) studies on the powders ob-tained from precursor 1 in HDA at 190, 230, and 270 8C are shown in Figure 7. The (020), (120), (220), (101), (111), (021), (211), (002) and (240) peaks correspond to the pure ortho-rhombic phase of Bi_2S_3 (ICCD 03-065-2435). The strong and sharp peaks in the XRD patterns are an indication that the Bi_2S_3 particles are highly crystalline. The XRD data are in agree-ment with reported data for Bi_2S_3 nanostructures synthesized from dithiocarbamate precursors by other methods.[13, 14, 16] We compared the P-XRD patterns of the Bi_2S_3 particles prepared from precursor 1 at 270 8C in DDA, HDA, OLA and TOPO (Figure 8). All the particles were crystalline, except for OLA-capped Bi_2S_3, which exhibited broad peaks, typical of poorly crystalline particles. The broadening of the peaks in Figure 6 c also implies a smaller grain size of the Bi_2S_3 crystals prepared in OLA compared to the other capping agents. This was con-firmed by their average crystallite sizes estimated by applying the Scherrer formula to the (111) peak, which were 15.7 (OLA), 21.5 (TOPO); 21.9 (HDA) and 21.5 nm (DDA). A representative

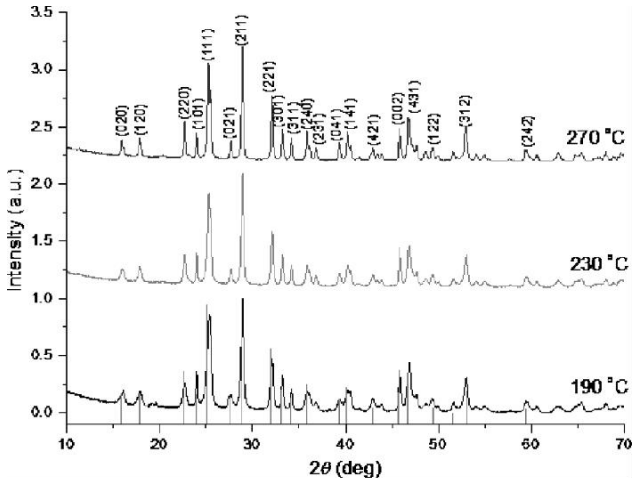

Figure 7. P-XRD patterns of Bi_2S_3 nanorods synthesized in HDA from 1 at 190, 230 and 270 8C.

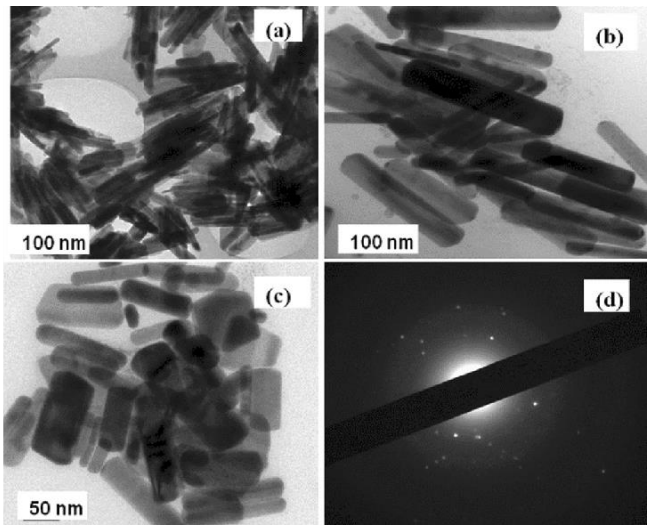

Figure 9. TEM images of Bi_2S_3 nanoparticles synthesized from 1 in DDA at a) 190, b) 230 and c) 270 8C. d) Corresponding SAED pattern

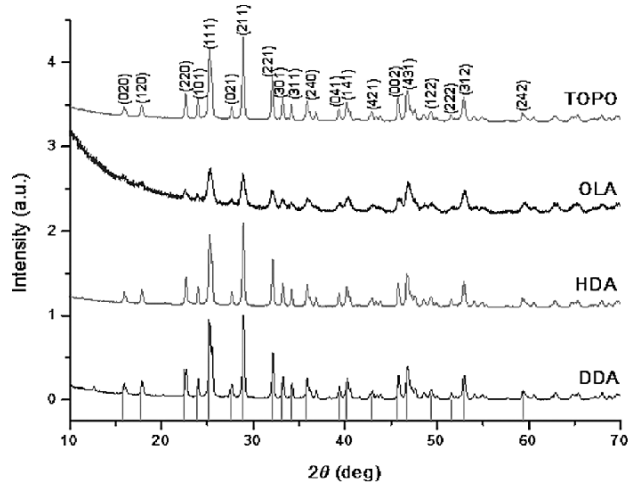

Figure 8. P-XRD patterns of Bi_2S_3 nanorods synthesized from 1 at 270 8C in DDA, HDA, OLA and TOPO.

Table 4. Lengths L and widths W of the Bi_2S_3 nanorods synthesized from 1 with various reaction parameters.

Capping agent	T [8C]	L [nm]	W [nm]	Aspect ratio (0.1)
DDA	190	161.9 0.3	16.5 0.1	9.8
DDA	230	154.7 0.4	22.7 0.1	6.8
DDA	270	76.1 0.5	23.9 0.1	3.2
HDA	190	236.9 0.2	20.3 0.1	11.7
HDA	230	217.2 0.1	24.4 0.1	8.9
HDA	270	193.5 0.3	49.9 0.2	3.9
OLA	190	252.6 0.2	31.2 0.1	8.1
OLA	230	221.5 0.2	36.4 0.2	6.1
OLA	270	194.2 0.4	38.3 0.2	5.1
TOPO	190	182.3 0.2	29.2 0.2	6.2
TOPO	230	106.6 0.1	42.8 0.2	2.4
TOPO	270	95.4 0.3	44.1 0.2	2.1

P-XRD pattern for the material prepared from precursor 2 at a reaction temperature 230 8C is shown in the Supporting Information (Figure S8).

The morphology of the Bi_2S_3 nanostructures was studied by TEM. Figure 9 shows the images of Bi_2S_3 nanocrystals prepared from precursor 1 in DDA (C_{10}) at 190, 230 and 270 8C. It has been reported that at high temperatures the influence of the surface ligands is minimised through the dynamic bonding nature of the ligands, and as a result particles revert to ther-modynamically stable morphologies such as spheres. Low-tem-perature routes offer more flexibility in shape control, and ani-sotropic-shaped particles such as rods are formed through ju-dicious use of surfactants.[22] We obtained Bi_2S_3 nanorods at the three different reaction temperatures (Figure 9 a–c) using DDA as capping group. Similar results were obtained by Xie et al. by thermolysing bismuth tris(diethyldithiocarbamate) complexes at temperatures ranging from 115 to 170 8C. The formation of nanorods at all the temperatures could be attributed to bonding to metal ions.[15] The dimensions of the Bi_2S_3 nanostructures obtained under different reaction conditions with a variety of capping groups are summarised in Table 4.

The DDA-capped Bi_2S_3 nanostructures obtained at 190 8C are rods with average length of 161.9 0.3 nm and average breadth of 16.5 0.1 nm (Figure 9 a). When the temperature was raised to 230 8C, a slight increase in the breadth (22.7 0.1 nm) and decrease in the length (154.7 0.4 nm) of the rods was observed (Figure 9 b). At 270 8C, the aspect ratio of the rods decreased further (Figure 9 c). The darker, opaque regions of the rods observed in the TEM images indicate overlap or stacking of rods. The selected-area electron diffraction (SAED) pattern confirmed the formation of a highly crystalline single Bi_2S_3 nanorod (Figure 9 d), and energy-dispersive X-ray analysis revealed a Bi :S molar ratio of 30.88:48, close to the expected 2:3 molar ratio of Bi_2S_3 (Supporting Information, Figure 9).

The carbon chain length of the amine was increased from C_{10} (DDA) to C_{16} (HDA). When complex 1 was thermolysed in HDA at the same reaction temperatures (190–270 8C), no signif-icant change in the Bi_2S_3 morphology was revealed by TEM

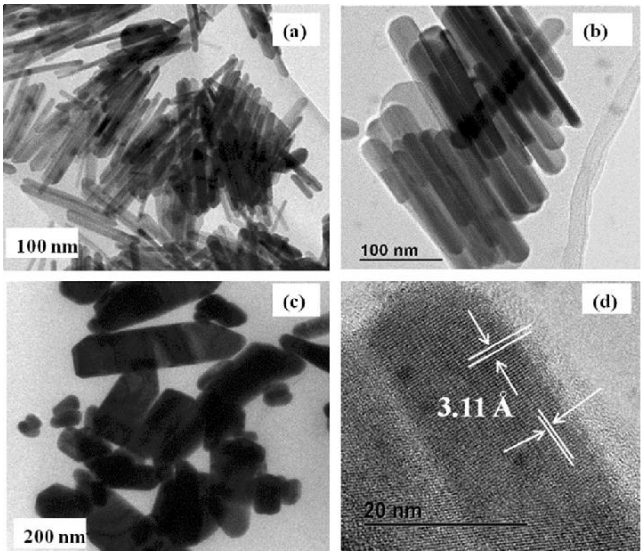

Figure 10. TEM images of Bi_2S_3 nanorods synthesized from 1 in HDA at a) 190, b) 230 and c) 270 °C. d) Corresponding HRTEM image.

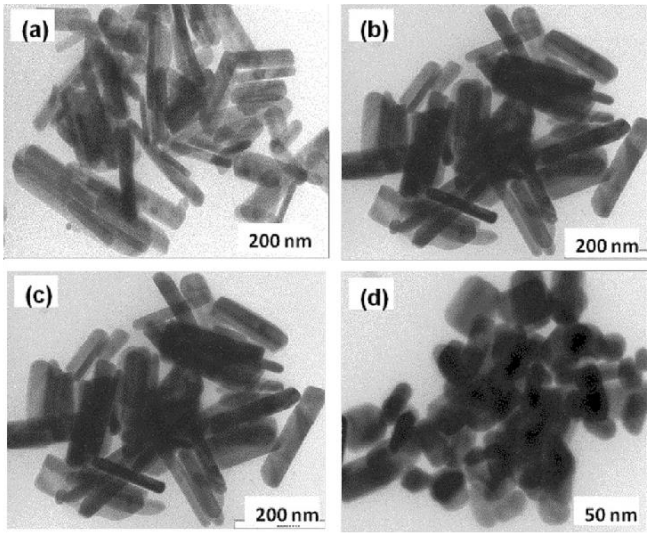

Figure 11. TEM images of a) DDA-, b) HDA-, c) OLA- and d) TOPO-capped Bi_2S_3 nanoparticles synthesized from 2 at 230 °C.

(Figure 10). Overall the average breadth of the rods increased with increasing length of the carbon chain. The HDA-capped Bi_2S_3 nanorods obtained at 190 °C appeared to be agglomerated, and stacking was also observed. The aspect ratio also increased compared to the DDA-capped Bi_2S_3 rods. When synthesised at 230 °C the distinct nanorods have equal lengths with some degree of alignment (Figure 10 b). Larger and more irregularly shaped particles were obtained at 270 °C (Figure 10 c). The HRTEM image of a single nanorod synthesized at 230 °C (Figure 10 d) shows distinct lattice fringes with a lattice spacing of 0.311 nm, assigned to the (211) lattice plane.

When precursor 1 was thermolysed in TOPO, spherical Bi_2S_3 particles were expected at high temperature according to the thermodynamic growth regime. Monteiro et al. reported the synthesis of spherical Bi_2S_3 when a bismuth tris(alkyldithiocarbamate) complex was thermolysed in TOPO at 150 °C.[7] However rod-like morphologies were obtained at 190 and 230 °C when thermolysis of 1 was carried out in TOPO (Supporting Information, Figure S10). The higher temperature of 270 °C gave less anisotropic morphologies with higher degrees of agglomeration. Similar results were obtained when precursor 2 was thermolysed in DDA, HDA, OLA and TOPO, and the representative images for samples prepared at 230 °C are shown in Figure 11.

The role of dodecanethiol (DT) in the formation of rod-shaped nanostructures has been reported previously for Bi_2S_3 and $Cu_{2-x}S$.[18, 41, 42] In our work, decomposition of the bismuth complexes at high temperatures allowed the sulfur atoms of DT to react with the Bi^{3+} ions. This coordination of sulfur to the metal can control the reaction chemical potential of the solution. High chemical potentials result in thermodynamically less stable elongated structures. We thermolysed both complexes in HDA at 230 °C without the addition of DT. The absence of DT resulted in the formation of poorly crystalline bismuth sulfide nanoparticles, as observed by TEM (Supporting Information, Figure 11).

Trindade and co-workers also observed that the coordinating solvent plays a significant role in the final morphology of the Bi_2S_3 nanoparticles.[7] They obtained Bi_2S_3 nanofibers when bismuth (III) dithiocarbamate complexes were thermolysed in ethylene glycol. The use of p-xylene, 2-ethoxyethanol and 4-ethylpyridine also gave fibre-type Bi_2S_3 particles. The high quality of the Bi_2S_3 nanostructures shows that the use of SSPs is effective. The synthetic route allows for the manipulation of shape and properties. We have done extensive work on the use of heterocyclic metal dithiocarbamate complexes in various coordinating solvents.[19, 21, 22] Our experience has shown that long-chain alkyl amine ligands are effective in producing anisotropic nanostructures. We have used hexadecylamine (HDA), dodecylamine (DDA) and oleylamine (OLA) to synthesise elongated CdS[19] and PbS[22] nanostructures. In this work we have shown that the judicious choice of capping groups in combination with DT is essential to obtain good-quality nanorods. We have also shown that the bulky nature of the heterocyclic precursor is also important in the decomposition pathway to the nanostructures. In general, SSPs behave better than the multisource precursors, partly due to the absence of pre-reactions, built-in stoichiometry, high purity and decomposition at a single temperature, because most of the SSPs are solid crystalline materials.

Conclusion

Heterocyclic bismuth dithiocarbamate complexes catena-(μ2-nitrato-O,O')bis(piperidinedithiocarbamato)bismuth(III) (1) and tetrakis(μ-nitrato)tetrakis[bis(tetrahydroquinolinedithiocarbamato)bismuth(III)] (2) have been synthesized and characterised. The single-crystal X-ray structures of both complexes were determined; that of 1 is based on a 1D coordination polymer, whereas 2 is a cyclic tetramer. High-quality Bi_2S_3 nanorods were obtained by thermolysis of 1 and 2 with variation of the temperature and the capping agent. The optical properties of

the materials obtained under all reaction conditions confirmed the quantum-confined nature of the particles. The length of the carbon chain of the amine used as capping agent affects the optical properties and size of the Bi_2S_3 nanorods. The or-thorhombic phase and the crystalline nature of the synthesized particles were confirmed by P-XRD. We envisage further investi-gating the use of these precursors for the deposition of Bi_2S_3 thin films by aerosol-assisted chemical vapour deposition.

Experimental Section

Chemicals

Hexadecylamine (HDA), dodecylamine (DDA), oleylamine (OLA), tri-n-octylphosphine oxide (TOPO), acetonitrile, 1,2,3,4-tetrahydroquinoline (98 %), piperidine (99 %), bismuth nitrate tetrahydrate, and 1-dodecanethiol were purchased from Sigma-Aldrich. Petroleum ether, methanol (99.5 %), dichloromethane, carbon disulfide (99.5 %), chloroform, sodium hydroxide (98 %) and acetone were purchased from Merck and used without any further purification.

Instrumentation

Microanalysis was performed with a PerkinElmer automated model 2400 series II CHNS/O analyser. IR spectra were recorded with a Bruker FTIR Tensor 27 spectrophotometer directly on small sam-ples of the compounds in the range 200–4000 cm^{-1}. TGA was car-ried out at a heating rate of 20 8C min^{-1} with a PerkinElmer Pyris 6 instrument up to 600 8C in a closed perforated aluminium pan under N_2 gas flow.

Optical absorption measurements were carried out with a Perki-nElmer Lambda 1050 UV/Visible NIR spectrophotometer. The sam-ples were placed in silica cuvettes (1 cm path length), and hexane was used as reference solvent. TEM and HRTEM were performed with JEOL 1010 TEM and JEOL 2100 HRTEM microscopes. Samples were prepared by placing a drop of dilute solution of nanoparticles on Formvar-coated Cu grids (150 mesh) for TEM and holey carbon grids for HRTEM. The samples were allowed to dry completely at room temperature and viewed at accelerating voltages of 100 kV (TEM) and 200 kV (HRTEM), and images were captured digitally with a Megaview III camera and stored and measured by using Soft Imaging Systems iTEM software (TEM) and a Gatan camera and Gatan software (HRTEM). P-XRD patterns were recorded in the high-angle 2q range of 20–608 by using a Bruker AXS D8 Advance X-Ray diffractometer, equipped with nickel-filtered Cu_{K_a} radiation (l =1.5406 &) at 40 kV, 40 mA, and at room temperature.

Single-crystal X-ray structure analysis

Flat, yellow, needle-like single crystals measuring about 0.35 0 0.20 0 0.15 mm for 1 and 0.40 0 0.16 0 0.12 mm for 2 were mounted on the goniometer of a Bruker Apex II Duo CCD diffractometer by using a 500 mm-long needle mount and a 200 mm-diameter cryo-loop (MiTeGen), respectively, after initial suspension and selection in Paratone oil. Intensity data were collected with Mo_{K_a} radiation from an Incoatec microsource (IuS, Quazar mirror optics) at 100 K for complex 1 and 296 K for complex 2. The structures were solved by direct methods with SHELXS[39] running in Olex2.[40] The struc-tures were refined by least-squares methods (SHELXL).[39] All non-H atoms were refined anisotropically ; H atoms were included in cal-culated positions, assigned isotropic thermal parameters (U_{iso} for H atoms =1.2 U_{iso} for the attached C atom) and allowed to ride on their parent carbon atoms by using the standard HFIX parameters in SHELXL. In the case of 2, the tetrahydroisoquinoline ring containing atoms N1 and C1 C9 was slightly disordered with two puckered half-chair conformations. The disorder was resolved by using two positions for C8 and C9 (C8A and C8B ; C9A and C9B) with standard SHELXL restraints (79 in total). Solvent-accessible voids exist in the structure of 2 and the total solvent-accessible volume per cell is 220.9 $&^3$ (4.6 %). The largest voids located at the special positions (0.500,0.000,0.500) and (0.500,0.500, 0.000) have volumes of 51.4 $&^3$ and contain a disordered water molecule (9.9 electrons). The electron density, however, was not allocated to the solvent in the final structural model. Crystal data and structure re-finement parameters are presented in Table 1. CCDC 1425649 (1) and 418494 (2) contain the supplementary crystallographic data for this paper. These data can be obtained free of charge from The Cambridge Crystallographic Data Centre.

Preparation of the ligands

Carbon disulfide (0.1 mol, 6.0 mL) was added in small portions to an equimolar mixture of sodium hydroxide (4.0 g, 0.1 mol) and the corresponding amine (piperidine, tetrahydroquinoline, 0.1 mol) cooled in an ice bath. After 15 min, a precipitate was formed and was then dried in air and recrystallised from acetone/petroleum ether. The final product was collected, washed with chloroform and suction-dried.

Na(S2CPip): Yield: 92 %. Significant IR bands: $\tilde{n}$ =3377 (O H), 967 (C=S), 1468 cm^{-1} (C=N); elemental analysis (%) calcd for $C_6H_{14}NS_2O_2Na$: C 32.86, H 6.43, N 6.39; found: C 32.91, H 6.53, N 6.20.

Na(S2CThq): Yield: 66 %. Significant IR bands: $\tilde{n}$ =3324 (O H), 967 (C=S),: 1485 $\tilde{n}$(C=N); elemental analysis (%) calcd for $C_{10}H_{18}NS_2O_4Na$: C 39.59 H 5.98 N 4.62; found: C 40.00, H 5.38, N 4.38.

Preparation of bismuth complexes

$Bi(NO_3)_3{\cdot}4\,H_2O$ (2.43 g, 5 mmol) was suspended in deionised water (15 mL), and the suspension added dropwise to a solution of the corresponding dithiocarbamate ligand (10 mmol) in deionised water (25 mL). The mixture was stirred at room temperature for 1 h. The yellow precipitate that formed was collected by filtration and recrystallised from chloroform/methanol (3:1).

Complex 1: Yield : 62 %. Significant IR bands: $\tilde{n}$ =964 cm^{-1} (C=S), 1473 (C=N),: 365 cm^{-1} (Bi S); elemental analysis (%) calcd for $Bi(C_6H_{10}NS_2)_2NO_3{\cdot}2H_2O$: C 24.36, H 3.41, N 7.10; found: C 24.37, H 3.24, N 6.95; m.p. 279 8C.

Complex 2: Yield: 68 %. Significant IR bands: $\tilde{n}$ =960 (C=S), 1475 (C=N), 388 cm^{-1} (Bi S); elemental analysis (%) calcd for $Bi(C_{10}H_{10}NS_2)_2{\cdot}NO_3$: C 34.93, H 2.93, N 6.11; found: C 34.8, H 2.86, N 6.06; m.p. 270 8C.

Preparation of HDA-capped Bi_2S_3 nanoparticles

Complex 1 or complex 2 (0.3 g) was dissolved in OLA (3.0 mL) and the solution injected into HDA (3.0 g) and DT (0.2 mL) in a three-necked flask at 190 8C. The mixture turned to a blackish liquid and a drop in temperature of 25–30 8C was observed. The reaction was allowed to stabilise at 190 8C. After 2 h of reaction, heating was stopped and methanol was added, resulting in the formation of a flocculent precipitate. The precipitate was separated by centrifu-gation, washed several times with acetone/methanol and dis-persed in toluene to give dark gray HDA-capped Bi_2S_3 nanoparti-cles. The reaction was repeated at 230 8C and 270 8C. The above re-

action procedure was repeated with DDA, OLA and TOPO as capping agents.

Acknowledgements

The authors thank the National Research Foundation (NRF), South Africa through the South African Research Chair initiative (SARChI) and the Royal Society-DFID program for financial support. L.D.N. also acknowledges the Organization for Women Scientists for the Developing World (OWSDW) formerly TWOWS for a Sandwich Postgraduate Fellowship. The authors also acknowledge the Centre for Electron Microscopy, Universi-ty of Kwa-Zulu Natal for the TEM and National Centre for Nano-structured Materials (NCNSM), CSIR, and Pretoria for HRTEM measurements.

Keywords: bismuth · chain structures · nanoparticles · S ligands · sulfur

[1] G. Ghosh, B. P. Varma, Thin Solid Films 1979, 60, 61.
[2] D. Arivuoli, F. D. Gnanam, P. Ramasamy, J. Mater. Sci. Lett. 1988, 7, 711.
[3] L. Huang, P. K. Nair, M. T. S. Nair, R. A. Zingaro, E. A. Meyers, Thin Solid Films 1995, 268, 49.
[4] M. E. Rinc_n, P. K. Nair, J. Phys. Chem. Solids 1996, 57, 1937.
[5] E. R. Swy, A. S. Schwartz-Duval, D. D. Shuboni, M. T. Latourette, C. L. Mallet, M. Parys, D. P. Cormoded, E. M. Shapiro, Nanoscale 2014, 6, 13104.
[6] B. B. Nayak, H. N. Acharya, G. B. Mitra, B. K. Mathur, Thin Solid Films 1983, 105, 17.
[7] O. C. Monteiro, H. I. S. Nogueira, T. Trindade, M. Motevalli, Chem. Mater. 2001, 13, 2103.
[8] J. Wu, F. Qin, G. Cheng, H. Li, J. Zhang, Y. Xie, H.-J. Yang, Z. Lu, X. Yu, R. Chen, J. Alloys Compd. 2011, 509, 2116.
[9] D. Wang, M. Shao, D. Yu, G. Li, Y. Qian, J. Cryst. Growth 2002, 243, 331.
[10] X. Yang, X. Wang, Z. Zhang, Mater. Chem. Phys. 2006, 95, 154.
[11] M. Salavati-Niasari, D. Ghanbari, F. Davar, J. Alloys Compd. 2009, 488, 442.
[11] H. Zhang, L. Wang, Mater. Lett. 2007, 61, 1667.
[12] X.-P. Shen, G. Yin, W.-L. Zhang, Z. Xu, Solid State Commun. 2006, 140, 116.
[13] O. C. Monteiro, T. Trindade, J.-H. Park, P. O'Brien, Chem. Vap. Deposition 2000, 6, 230.
[14] G. Xie, Z.-P. Qiao, M.-H. Zeng, X.-M. Chen, S.-L. Gao, Cryst. Growth Des. 2004, 4, 513.
[15] a) A. A. Tahir, M. A. Ehsan, M. Mazhar, K. G. U. Wijayantha, M. Zeller, A. D. Hunter, Chem. Mater. 2010, 22, 5084; b) B. Biswal, S. S. Garje, J. Nuwad, C. G. S. Pillai, J. Solid State Chem. 2013, 204, 348.
[16] a) J. N. Revaprasadu, M. A. Malik, P. O'Brien, J. Mater. Res. 1999, 14, 3237; b) M. A. Malik, M. Motevalli, P. O'Brien, Inorg. Chem. 1995, 34, 6223; c) M. A. Malik, M. Motevalli, P. O'Brien, J. R. Walsh, Organometallics 1992, 11, 3136; d) A. A. M. Memon, M. Afzaal, M. A. Malik, C. Nguyen, P. O'Brien, J. Raftery, Dalton Trans. 2006, 4499; e) D. J. Binks, S. P. Bants, D. P. West, M. A. Malik, P. O'Brien, J. Mod. Opt. 2003, 50, 299 ; f) C. Q. Nguyen, A. E. Adeogun, M. Afzaal, M. A. Malik, P. O'Brien, Chem. Commun. 2006, 2182; g) M. A. Malik, M. Motevalli, T. Saeed, P. O'Brien, Adv. Mater. 1993, 5, 653 ; h) A. Panneerselvam, C. Q. Nguyen, M. A. Malik, P. O'Brien, J. Raftery, J. Mater. Chem. 2009, 19, 419.
[18] V. Stavila, K. H. Whitmire, I. Rusakova, Chem. Mater. 2009, 21, 5456.
[19] L. D. Nyamen, V. S. R. Pullabhota, A. A. Nejo, P. T. Ndifon, N. Revaprasadu, New J. Chem. 2011, 35, 1133.
[20] L. D. Nyamen, N. Revaprasadu, A. A. Nejo, V. S. R. Pullabhota, P. T. Ndifon, M. A. Malik, P. O'Brien, Polyhedron 2013, 56, 62.
[21] L. D. Nyamen, A. A. Nejo, V. S. R. Pullabhota, P. T. Ndifon, M. A. Malik, J. Akhtar, P. O'Brien, N. Revaprasadu, Polyhedron 2014, 67, 129.
[22] L. D. Nyamen, V. S. R. Pullabhotla, A. A. Nejo, P. T. Ndifon, J. H. Warner, N. Revaprasadu, Dalton Trans. 2012, 41, 8297.
[23] S. Mlowe, D. Lewis, A. M. Malik, J. Raftery, E. B. Mubofu, P. O'Brien, N. Re-vaprasadu, New J. Chem. 2014, 38, 6073.
[24] S. Mlowe, D. Lewis, A. M. Malik, J. Raftery, E. B. Mubofu, P. O'Brien, N. Re-vaprasadu, Dalton Trans. 2016, 45, 2647.
[25] S. Mlowe, L. D. Nyamen, P. T. Ndifon, A. M. Malik, J. Raftery, P. O'Brien, N. Revaprasadu, Inorg. Chim. Acta 2015, 434, 181.
[26] X-ray structure of 1 at room temperature has been reported elsewhere: H. D. Yin, C. H. Wang, L. Wang, Chin. J. Struct. Chem. 2004, 23, 1201.
[27] a) F. Li, H.-D. Yin, J. Zhai, d.-Q. Wang, Acta Crystallogr. E 2006, 62, m1083 ; b) H. Yin, F. Li, F. Li, D. Wang, J. Inorg. Organomet. Polym. 2006, 16, 161; c) H. Yin, F. Li, D. Wang, J. Coord. Chem. 2007, 60, 1133 ; d) H. Yin, C. Wang, Appl. Organomet. Chem. 2004, 18, 195 ; e) F. Li, H. Yin, G. Wu, Acta Crystallogr. E 2014, 70, m20 ; f) R. Chauhan, J. Chaturvedi, M. Trivedi, J. Singh, K. C. Molloy, G. Kociok-Kçhn, A. Kumar, Inorg. Chim. Acta 2015, 430, 168.
[28] M. X. Li, L. Z. Zhang, M. Yang, J. Y. Niu, J. Zhou, Bioorg. Med. Chem. Lett. 2012, 22, 2418.
[29] R. J. Errington, L. J. Farrugia, G. A. Fisher, A. Niklaus, N. C. Norman, J. Chem. Soc. Dalton Trans. 1993, 1201.
[30] Q. Y. Jiang, H. Q. Deng, Y. M. Hu, J. Shen, G. Q. Hong, N. H. Hu, Huaxue Xuebao (Acta Chim. Sinica) 2008, 66, 1429.
[31] S. Alvarez, Dalton Trans. 2013, 42, 8617.
[32] C. A. Dodds, J. Reglinski, M. D. Spicer, Chem. Eur. J. 2006, 12, 931.
[33] V. Garc%a-Montalvo, R. Cea-Olivares, D. J. Williams, G. Espinosa-Perez, Inorg. Chem. 1996, 35, 3948.
[34] S. P. Summers, K. A. Abboud, S. R. Farrah, G. J. Palenik, Inorg. Chem. 1994, 33, 88.
[35] H. J. Breunig, M. G. Nema, C. Silvestru, A. P. Soran, R. A. Varga, Dalton Trans. 2010, 39, 11277.
[36] A. Walsh, D. J. Payne, R. G. Egdell, G. W. Watson, Chem. Soc. Rev. 2011, 40, 4455.
[37] F. H. Allen, Acta Crystallogr. Sect. B 2002, 58, 380.
[38] H. D. Yin, C. H. Wang, Appl. Organomet. Chem. 2004, 18, 420.
[39] G. M. Sheldrick, Acta Crystallogr. Sect. A 2008, 64, 112.
[40] O. V. Dolomanov, L. J. Bourhis, R. J. Gildea, J. A. K. Howard, H. Pusch-mann, J. Appl. Crystallogr. 2009, 42, 339.
[41] M. Kruszynska, H. Borchert, A. Bachmatiuk, M. H. Rummeli, B. Buchner, J. Parisi, J. Kolny-Olesiak, ACS Nano 2012, 6, 5889.
[42] M. B. Sigman, B. A. Korgel, Chem. Mater. 2005, 17, 1655.

Received: May 4, 2016

Published online on && &&, 0000

FULL PAPER

&Nanoparticles

W. N. Kun, S. Mlowe, L. D. Nyamen, P. T. Ndifon, M. A. Malik, O. Q. Munro, N. Revaprasadu*

&&– &&

Heterocyclic Bismuth(III) Dithiocarbamato Complexes as Single-Source Precursors for the Synthesis of Anisotropic Bi2S3 Nanoparticles

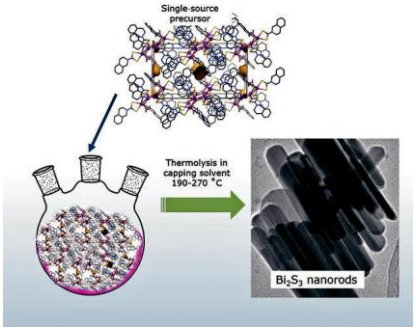

Bismuth sulfide nanorods: Two bismuth(III) dithiocarbamato complexes were synthesized and characterised by elemental analysis, FTIR spectroscopy, thermogravimetric analysis and single-crys-tal XRD. Both complexes were used as single-source precursors for the synthe-sis of capped Bi2S3 nanoparticles at dif-ferent temperatures. High-quality, crys-talline, long and short Bi2S3 nanorods were obtained (see figure) depending on the thermolysis temperature, which was varied from 190 to 270 8C.

Polyhedron 154 (2018) 173–181

Contents lists available at ScienceDirect

Polyhedron

journal homepage: www.elsevier.com/locate/poly

Deposition of Bi_2S_3 thin films from heterocyclic bismuth(III) dithiocarbamato complexes

Walter N. Kun [a,b], Sixberth Mlowe [a], Linda D. Nyamen [b], Matthew P. Akerman [c], Paul O'Brien [d], Peter T. Ndifon [b,*], Neerish Revaprasadu [a,*]

[a] Department of Chemistry, University of Zululand, Private Bag X1001, Kwa-Dlangezwa, 3886, South Africa
[b] Department of Inorganic Chemistry, University of Yaoundé I, P.O. Box 812, Yaoundé, Cameroon
[c] Department of Chemistry, University of KwaZulu-Natal, Private Bag X01, Scottsville, Pietermaritzburg 3209, South Africa
[d] Schools of Chemistry and Materials, University of Manchester, Oxford Road, Manchester M13 9PL, UK

ARTICLE INFO

Article history:
Received 13 June 2018
Accepted 26 July 2018
Available online 4 August 2018

Keywords:
Single source precursors
Spin coating
AACVD
Bismuth sulfide
Tin films

ABSTRACT

Two heterocyclic dithiocarbamate complexes, *tris*-(piperidinedithiocarbamato)bismuth(III) (**1**) and *tris*-(tetrahydroquinolinedithiocarbamato)bismuth(III) (**2**) were synthesized and characterized by elemental analysis and thermogravimetric analysis. The structure of complex (**1**) was confirmed by single-crystal X-ray analysis. Both complexes were used as single source precursors for the deposition of bismuth sulfide thin films by aerosol assisted chemical vapour deposition (AACVD) at 350, 400, 450 °C and spin coating followed by thermal treatment at 350 °C, 400 °C and 450 °C. Both deposition methods, gave sulfur deficient polycrystalline films of bismuthinite. Scanning electron microscopy (SEM) images of the films showed morphology was dependent on the solvent mixture, temperature, precursor type and method of deposition. AACVD gave films with hexagonal nanoplatelets, leaf-like platelet, ribbon-like fibre, needle-like fibre morphologies. Films in the form of rods and interwoven nanowires were obtained from spin coating.

1. Introduction

Binary V–VI metal chalcogenides have drawn considerable attention as they are an important class of semiconductors which have properties important for: photoconducting targets, electronic and optoelectronic devices, thermoelectric devices, hydrogen storage materials and sensors [1–4]. Amongst these materials, Bi_2S_3 is an interesting material with a direct band gap of 1.7 eV close to optimal for terrestrial PV solar cells. The band gap can be tuned by varying the size of the crystallite with a high optical absorption coefficient ($\geq 10^5$ cm^{-1}) [5,6]. The structure of bismuthinite (Fig. 1) is quite complex involving two different bismuth centres with differing coordination number. It is orthorhombic (*Pnma*), in which Bi_2S_3 units form infinite chains parallel to the *c* axis connected via weaker van der Waals interactions between the unit cells [7]. Conventionally these structures of bismuth have been described in terms of a stereochemically active lone pair based on a VSREPR approach. Pyykkö [8] suggested many years ago that relativistic effects on the energy of the p-orbital provide a more plausible picture of the electron density. Bismuthinite is an n-type crystalline semiconductor with coordinated polyhedral composition of Bi–S bond length increasing with increasing Bi concentration (ESI Table S1) [9].

Due to its size-dependent band Bi_2S_3 has exhaustively been investigated for possible applications in photodiode arrays, photovoltaic converters and potential applications in thermoelectric cooling devices based on the Peltier effect [10,11]. Photoeletrochemical devices based on Bi_2S_3 have demonstrated potential in rechargeable electrical septum storage cells and redox couple storage devices [12,13]. Recently a new application of Bi_2S_3 as an imaging agent in X-ray computed tomography application has led to renewed interest in Bi_2S_3 nanomaterials and thin films [2]. Crystallinity and electrical resistivity are both important properties of thin films in their use in electronic applications [14]. Highly crystalline and low electrical resistant films have been obtained by vapour disposal based techniques such as chemical vapour deposition (CVD), spray pyrolysis, electrodeposition [13–18]. However, these methods employ the use of specialized equipment which are expensive. Conventional CVD relies on volatile precursors to form the thin film [19]. The nature of precursors, toxicity and sustainability are issues to consider. Therefore, alternative thin film deposition techniques have been developed to find routes

* Corresponding authors.
E-mail addresses: pndifon@yahoo.com (P.T. Ndifon), RevaprasaduN@unizulu.ac.za (N. Revaprasadu).

https://doi.org/10.1016/j.poly.2018.07.055
0277-5387/

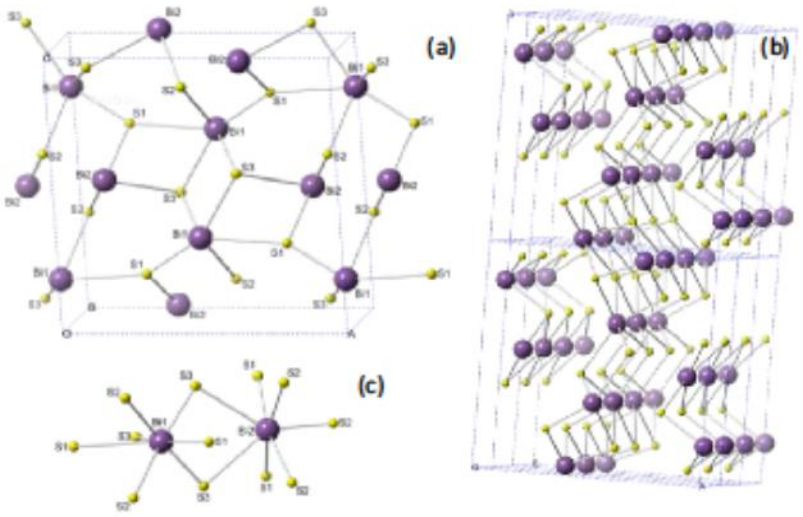

Fig. 1. (a) Bismuthinite unit cell with Bi–S separations up to 4 Å, (b) with shorter Bi–S contacts to emphasise layers and (c) coordination sphere at Bi(1) and Bi(2).

with higher sustainability [19,20]. Aerosol-assisted chemical vapour deposition (AACVD) offers improved versatility and flexibility as compared to conventional CVD processes. AACVD involves solution based precursor delivery using solvents from which an aerosol can be generated [3,20]. The aerosol is then transported to the reaction chamber where the formation of films takes place by a heterogeneous or homogeneous decomposition mechanism under reaction temperature. The method often enables the use of less expensive and environmental friendly chemicals as precursors, which is important for mass production [21]. High quality thin films can be obtained as the homogeneity of the aerosol is easily controlled by the size of the aerosol droplets. The morphology of the films can be controlled by varying experimental parameters such as solution concentration, solvent, deposition time, carrier gas flow rate, and substrate temperature [3,22,23]. The process is easy, allowing the formation of a multicomponent material using a single source precursor with high reproducibility, while the simplification of the delivery stage reduces the cost of the deposition process. The use of single-source precursors provide additional potential intrinsic advantages, such as improved air moisture stability of the precursor, excluding pre-reactions and lower toxicity [24]. Waters and co-workers have detailed the deposition of rods and rectangular platelets of bismuth sulfide films by AACVD and LP-MOCVD methods using $Bi[(SPiPr_2)_2N]_3$ complex as a single source precursor [16].

The solvent can significantly influence the morphologies of the films deposited by AACVD [25]. Peters et al. reported the influence of hexane and dichloromethane on TaS_2 thin films by AACVD. More uniform TaS_2 clusters were formed by decomposition from dichloromethane and clusters formed by the deposition from hexane were found to be larger than those deposited from dichloromethane [26]. Also, in addition to the influence on film microstructure, the solvent can also affect the composition of the growing film. The deposition of TiO_2 films using chlorinated solvents (dichloromethane and chloroform) did not show any evidence of chlorine contamination [27].

Several studies on the chemical deposition of Bi_2S_3 thin films have been reported. Ahire et al. deposited Bi_2S_3 thin films by a modified chemical bath deposition technique from $Bi(NO_3)_3$ and thioacetanamide and improved the crystallinity of the films after annealing [13]. Killedar et al. deposited Bi_2S_3 thin films by spraying a non-aqueous solution of $Bi(NO_3)_3$ in acetic acid and thiourea in formaldehyde on to a hot glass substrate. They found out that the films consisted of non-crystalline grains of Bi_2S_3 [28]. Wang et al. deposited 'nanoleaf-like' Bi_2S_3 thin films on indium tin oxide (ITO) glass using $Bi(NO_3)_3$ and $Na_2S_2O_3$ as precursors by a cathodic electrodeposition process and found that the crystallization of the films increased with increase in $Bi(NO_3)_3$: $Na_2S_2O_3$ concentration ratio [4]. Monteiro and co-workers reported the low-pressure metal–organic chemical vapour deposition of Bi_2S_3 thin films on glass substrates using bismuth(III) dithiocarbamate complexes [29].

We have recently reported the synthesis of Bi_2S_3 nanoparticles using *tris*-(piperidinyldithiocarbamato)bismuth(III) (**1**) and *tris*-(tetrahydroquinolinedithiocarbamato)bismuth(III) (**2**) as single source precursors, in which the effect of temperature and coordinating solvents were studied [30]. Herein, we report the deposition of crystalline Bi_2S_3 thin films using these bismuth complexes as single source precursors by aerosol assisted chemical vapour deposition (AACVD) and spin coating techniques. The single X-ray crystal structure of complex (**1**) is also reported.

2. Experimental

2.1. Chemicals

Bismuth acetate was purchased from Sigma Aldrich. Methanol, 99.5%; dichloromethane, acetonitrile, ethanol, chloroform and acetone were purchased from Merck and used without any further purification. The ligands were prepared using the method reported previously [30].

2.2. Preparation of bismuth complexes

$Bi(OAc)_3$ (1.93 g, 5.0 mmol) was suspended in 15.0 mL of deionized water, and added drop wise to a 25.0 mL solution of the corresponding dithiocarbamate ligand (15.0 mmol). The mixture was stirred at room temperature for 1 h, and the yellow precipitate

The thermogravimetric analysis (TGA) of both complexes are shown in Fig. 2. Complex (**1**) showed a two steps decomposition with the first step occurring at 184 °C and second decomposition step at 322 °C. The residue obtained after complete decomposition of complex (**1**) was black in colour, typical of bismuth sulfide inorganic materials. The mechanism of decomposition of *tris*-(piperidinyldithiocarbamato)iron(III) complex was studied by Mlowe et al. using TGA and GC–MS spectroscopy [37]. They proposed that the first decomposition step corresponded to a loss of one of the three dithiocarbamate ligands forming an intermediate four coordinate complex, whilst the final step corresponded to the elimination/rearrangement of the four coordinate complex to form the final product. The decomposition of complex (**2**) proceeded through a single step, with a mass loss at 300 °C. The thermogravimetric study was conducted solely to confirm the thermal stability of the complexes and their stability under ambient conditions and thus, the scope of our study did not involve a comprehensive investigation of the thermogravimetric data. These complexes were however more thermally stable compared to those reported in our previous work when, $Bi(NO_3)_3{\cdot}4H_2O$ was used as the metal salt [30].

3.2. Single crystal X-ray structure determination

The *tris*-(piperidinyldithiocarbamato) complex of bismuth(III) has not apparently been reported (Cambridge Structural Database (CSD) [38], though a different polymorph of this molecule has been briefly mentioned by Kun et al. [30]. Herein, we report the structure of the *tris*-(piperidinyldithiocarbamato)bismuth(III) complex of (**1**). The structure is orthorhombic, (*Pbca*) with two enantiomorph molecules in the asymmetric unit and $Z = 16$ (Fig. 3). Key bond parameters describing the coordination sphere of complex (**1**) are summarized in Table 1. The data in Table 1 shows a few interesting trends. Firstly, for each coordinating ligand one bond is extended and the other is compressed. This is surprising as measurement of the C–S bonds show they are all approximately equal ranging from 1.709 to 1.745 Å with a median of 1.727 Å.

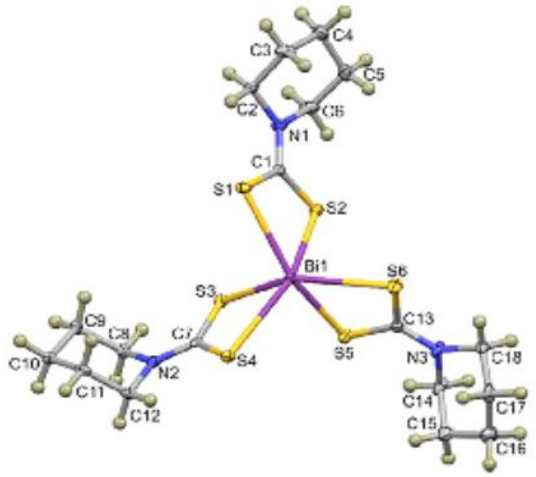

Fig. 3. Thermal ellipsoid plot of a single molecule from the asymmetric unit of **B** ($S_2CPip)_3$ showing the distorted octahedral coordination geometry. The molecule is one of two in the asymmetric unit. Each of these molecules exhibit a similar distorted octahedron. Hydrogen atoms have been rendered as spheres of arbitrary radius, all other atoms are shown at the 50% probability level (CCDC 153180).

Table 1
Selected bond parameters describing the coordination sphere of complex (**1**).

Bond	Length (Å)	Bond	Angle (°)
Bi1A–S1A	2.673(1)	S1A–Bi1A–S2A	63.77(3)
Bi1A–S2A	2.946(1)	S3A–Bi1A–S4A	63.37(3)
Bi1A–S3A	2.707(1)	S5A–Bi1A–S6A	64.12(3)
Bi1A–S4A	2.987(1)	S1A–Bi1A–S5A	150.87(4)
Bi1A–S5A	2.921(1)	S2A–Bi1A–S3A	146.53(4)
Bi1A–S6A	2.680(1)	S4A–Bi1A–S6A	149.80(4)
Bi1B–S1B	2.951(1)	S1B–Bi1B–S2B	63.69(3)
Bi1B–S2B	2.674(1)	S3B–Bi1B–S4B	63.16(3)
Bi1B–S3B	2.657(1)	S5B–Bi1B–S6B	63.35(3)
Bi1B–S4B	2.986(1)	S1B–Bi1B–S5B	148.66(4)
Bi1B–S5B	2.664(1)	S2B–Bi1B–S4B	147.76(4)
Bi1B–S6B	2.984(1)	S3B–Bi1B–S6B	147.79(4)

These data suggest that neither sulfur atom carry a formal negative charge with there being genuine delocalization. It would therefore be expected that the two coordinative bonds would be similar in length. A similar result is noted for related structures in the CSD [39,40]. The intraligand S–Bi–S bond angles are notably acute measuring ca. 63°. This is a consequence of the small ligand bite and the resulting four-atom coordination sphere. These bond lengths and bond angles are comparable to those of related structures [30,39,40]. Although the molecule is formally six-coordinate with three bidentate ligands forming the coordination sphere, it does not show octahedral symmetry. The *trans* S1–Bi–S5 bond angles which measure 150.87(4)° and 148.66(4)° for molecules A and B of the asymmetric unit, respectively (indeed all of the trans S–Bi–S bond lengths measure <151°), this deviation from an ideal octahedral geometry is conventionally attributed to a stereochemically active lone pair on the Bi(III) ion. A similar coordination geometry is noted in related structures [30,39,40] (see Fig. 4).

The two molecules in the asymmetric unit form a dimeric motif (shown in Fig. 5). These dimers are stabilised by Bi···S interactions. The mean Bi···S distance for the dimer is 3.323(2)Å, this is approximately 0.48 Å shorter than the sum of the van der Waals radii of the interacting atoms. Although the length of an interaction does not necessarily correlate with strength (due to packing constraints in the lattice), this separation is notably shorter than the sum of the van der Waals radii, suggesting an interaction. This notion is

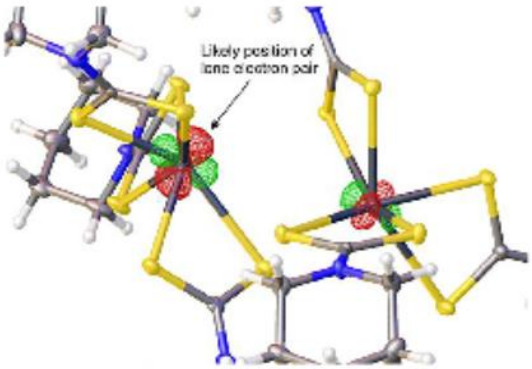

Fig. 4. The Difference Fourier map of complex (**1**) showing the probable location of the lone pair of electrons which reside on the bismuth(III) ion. To allow for visualization of the electron density corresponding to the lone pair of electrons, the bismuth ions were refined isotropically in this model. The remaining non-hydrogen atoms were refined anisotropically. The contour has been rendered with $p = -1.8$ e, the red and green grids indicate electron density maxima and minima, respectively. The plot was rendered using OLEX2 [41].

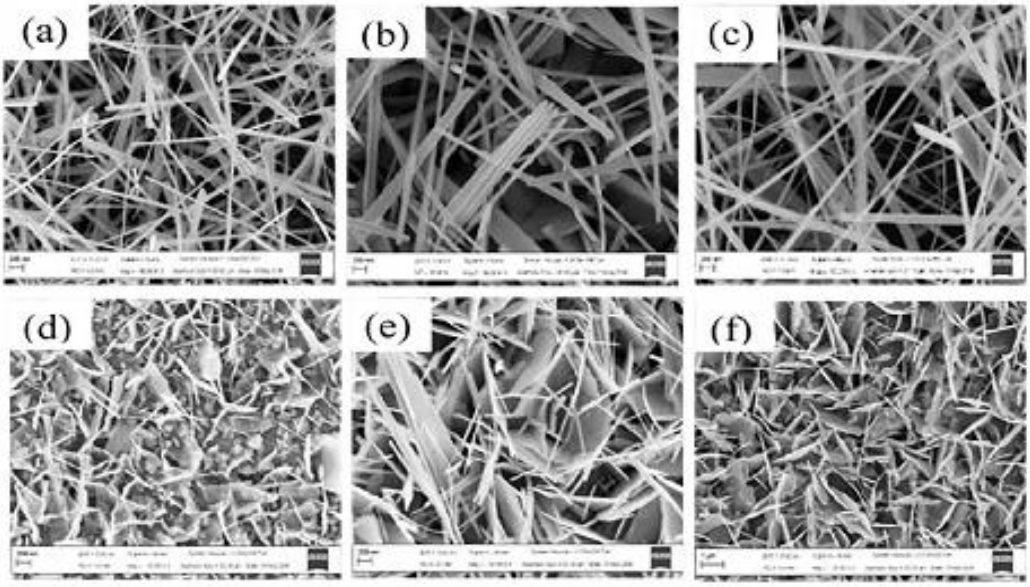

Fig. 8. SEM images of Bi_2S_3 thin films from complex (**1**) deposited by AACVD at (a) 350 °C, (b) 400 °C, (c) 450 °C and from complex (**2**) at (d) 350 °C, (e) 400 °C and (f) 450 °C in $CHCl_3/CH_3CN$ mixture.

average length of 557.67 ± 150 nm and breadth of 53.00 ± 20 nm. At 400 °C, the average length decreased to 550.21 ± 130 nm and breadth 52.76 ± 22 nm while at 450 °C, an average length of 512.54 ± 113 and breadth 51.09 ± 25 nm was obtained. When complex (**2**) was used, long interwoven nanowires at all three temperatures were obtained. These results suggest that the precursor used may have played a role in the nature of the deposited films. The p-XRD and UV/Visible spectra of the films deposited from complex (**2**) are shown in ESI Fig. S7i and 7ii. EDX analysis reveals that all the samples are slightly sulfur deficient. There is a close agreement in the Bi:S ratio for the samples annealed at 350 and 400 °C or both complexes (**1**) and (**2**). Film thicknesses for both spin coated and AACVD were calculated by weighing the glass substrate before deposition and after deposition using equation reported elsewhere [44]. A plot of thickness versus temperature of the films for the spin coated for both complexes (**1**) and (**2**) (ESI Fig. S8) shows a trend of thickness decreasing as temperature increases. Interestingly, the calculated thicknesses for AACVD deposited films from complex (**1**) for acetonitrile/chloform and methanol/chloform (ESI Fig. S9) were found to increase as temperature increased. A similar trend of increasing thickness with temperature was observed when we measured the film thickness from the cross-sectional SEM images of the Bi_2S_3 thin films deposited from complex (**2**) by AACVD in the $CHCl_3$/MeOH mixture. We observed a mean thickness of 241.16 ± 16.14 nm at 350 °C, 311.67 ± 20.63 nm at 400 °C and 463.45 ± 10.30 nm at 450 °C (ESI Fig. S9).

Variation in the morphology of the films observed can be explained by the difference in the heat of combustion and evaporation of the solvents which can lead to either homogeneous or heterogeneous deposition reactions [45]. During CVD, decomposition of the precursor in the gas phase is termed 'homogeneous' whilst decomposition on the heated substrate is 'heterogeneous', the ratio between these two processes are directly responsible for a number of characteristics. Chloroform facilitates the homogeneous reaction during deposition by evaporating and leaving the precursor molecule to vaporize in the heated zone as it is a low

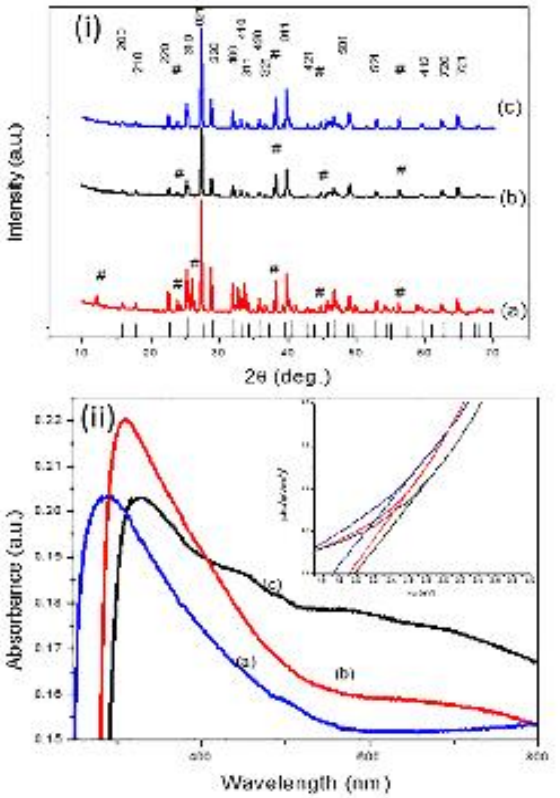

Fig. 9. (i) p-XRD and (ii) UV/Visible spectra of Bi_2S_3 thin films from complex (**1**) at (a) 350, (b) 400 and (c) 450 °C deposited by spin coating.

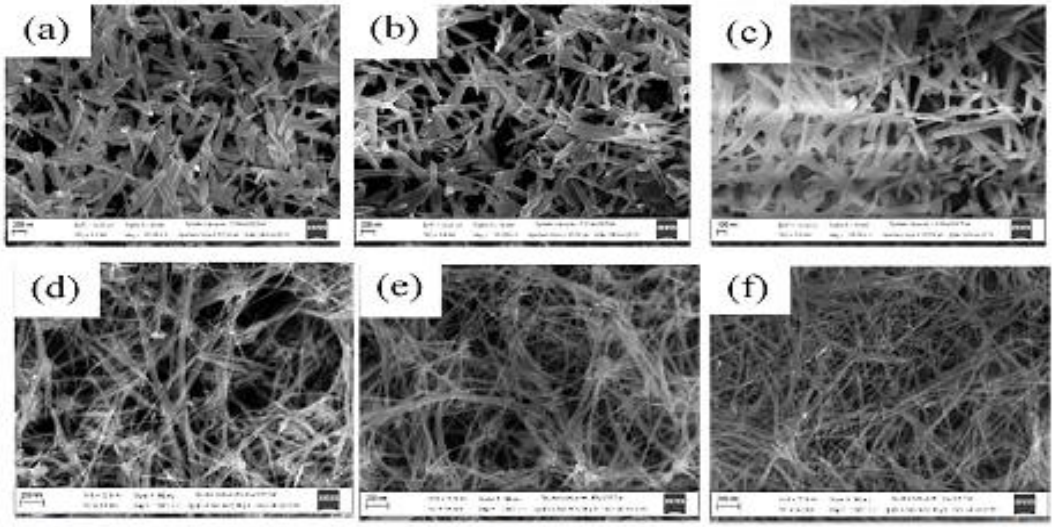

Fig. 10. SEM images Bi_2S_3 thin films deposited by spin coating complex (**1**) in $CHCl_3$/MeOH and annealing at (a) 350 °C, (b) 400 °C, (c) 450 °C and from complex (**2**) at (d) 350 °C, (e) 400 °C and (f) 450 °C.

combustion heat solvent (473.21 kJ mol^{-1}). The homogeneous reaction results in decomposition of the precursor starting in the gaseous phase after vaporization, which is followed by nucleation to form Bi_2S_3 partides. However, with addition of methanol, a higher combustion heat solvent (715.00 kJ mol^{-1}) compared to chloroform, the vaporization temperature of the aerosol droplets is increased and heterogeneous reaction is promoted. Thus, the formation of mixture of Bi_2S_3 nanoplates and nanofibers from complex (**1**) in chloroform/methanol mixture (ESI Fig. S4) is due to a combination of homogeneous nucleation in the gas phase and heterogeneous growth on the substrates. When the chloroform/acetonitrile mixture was used to deposit Bi_2S_3 thin films from complex (**1**), only nanofibers (Fig. 8(a–c)) were formed due to the heterogeneous growth that was predominant since acetonitrile has a higher heat of combustion (1256.33 kJ mol^{-1}).

4. Conclusions

Complexes (**1**) and (**2**) have been used as precursors at temperatures between 350 and 450 °C by AACVD. The p-XRD of all the films were of polycrystalline orthorhombic bismuthinite with various preferred growth directions. SEM showed that the morphology of the films changed with changes in solvent mixture and precursor, but only slight changes were observed with temperature. A more uniform morphology was obtained when the films were deposited by spin coating. EDX analysis revealed, in most cases, that the elemental composition was close to 2:3, most of the films were however somewhat sulfur deficient. Exceptions were from the AACVD of complex (**1**) using $CHCl_3/CH_3CN$ 3:1 which at all three temperatures with complex (**2**) at 350 °C which showed a slight deficiency in bismuth. In future work, we will further investigate on the mechanism of how the precursor type interacts on the final morphology of the films.

Acknowledgements

The authors thank the Royal Society/Department for International Development (RS-DFID) programme and the National Research Foundation (NRF) (NRF Grant number 64820), South Africa through the South African Research Chair Initiative (SARChi) for their financial support.

Appendix A. Supplementary data

Supplementary data associated with this article can be found, in the online version, at https://doi.org/10.1016/j.poly.2018.07.055.

References

[1] D.-B. Li, L. Hu, Y. Xie, G.N.T. Liu, Y. Zhou, L. Gao, B. Yang, J. Tang, ACS Photon. 3 (2016) 2122.
[2] L. Tian, H. Yao Tan, J.J. Vittal, Cryst. Growth Des. 8 (2007) 734.
[3] A.A. Tahir, M.A. Ehsan, M. Mazhar, K.G.U. Wijayantha, M. Zeller, A.D. Hunter, Chem. Mater. 22 (2010) 5084.
[4] Y. Wang, J. Huang, L. Cao, H. Zhu, H. He, J. Wu, Appl. Surf. Sci. 255 (2009) 7749.
[5] C. Lokhande, Mater. Chem. Phys. 27 (1991) 1.
[6] H. He, T. Liu, JOM-US 66 (2014) 979.
[7] D.B. Wang, M.W. Shao, D.B. Yu, G.P. Li, Y.T. Qian, J. Cryst. Growth 243 (2002) 331.
[8] P. Pyykkö, Chem. Rev. 88 (1988) 563.
[9] K. Łukaszewicz, J. Stępień-Damm, A. Pietraszko, A. Kajokas, J. Grigas, Polym. J. Chem. 73 (1999) 541.
[10] C.H. Ye, G.W. Meng, Z. Jiang, Y.H. Wang, G.Z. Wang, L.D. Zhang, J. Am. Chem. Soc. 124 (2002) 15180.
[11] R. Suarez, P.K. Nair, P.V. Kamat, Langmuir 14 (1998) 3236.
[12] S. Liufu, L. Chen, Q. Yao, C. Wang, J. Phys. Chem. B 110 (2006) 24054.
[13] R. Ahire, R. Sharma, Indian J. Eng. Mater. Sci. 13 (2006) 140.
[14] A. Mihi, M. Ocaña, H. Míguez, Adv. Mater. 18 (2006) 2244.
[15] K. Ramasamy, M.A. Malik, M. Helliwell, J. Raftery, P. O'Brien, Chem. Mater. 23 (2011) 1471.
[16] J. Waters, D. Crouch, J. Raftery, P. O'Brien, Chem. Mater. 16 (2004) 3289.
[17] D.B. Mitzi, L.L. Kosbar, C.E. Murray, M. Copel, A. Afzali, Nature 428 (2004) 299.
[18] N. Kamoun, H. Bouzouita, B. Rezig, Thin Solid Films 515 (2007) 5949.
[19] (a) M.A. Malik, M. Afzaal, P. O'Brien, Chem. Rev. 110 (2010) 4417;
(b) M.J. Powell, C.J. Carmalt, Chem. Eur. J. 23 (2017) 15543;
(c) M.J. Powell, D.B. Potter, R.L. Wilson, J.A. Darr, I.P. Parkin, C.J. Carmalt, Mater. Des. 129 (2017) 116.
[20] K. Salazar, K. Ort, R. Dye, K. Hubbard, E. Peterson, J. Goulter, T. Kodas, Physica C 198 (1992) 303.
[21] K. Ramasamy, V.L. Kuznetsov, K. Gopal, M.A. Malik, J. Raftery, P.P. Edwards, P. O'Brien, Chem. Mater. 25 (2013) 266.
[22] A.F. Hepp, J.S. McNatt, J.E. Dickman, M.H.-C. Jin, K.K. Banger, C.V. Kelly, A.R.A. González, A.A. Rockett, 4th International Energy Conversion Engineering Conference and Exhibit (IECEC), (2006). doi.org/10.2514/6.2006.

[23] M. Shahid, M. Mazhar, M. Hamid, M. Zeller, P. O'Brien, M.A. Malik, J. Raftery, A. D. Hunter, New J. Chem. 33 (2009) 2341.
[24] P. O'Brien, R. Nomura, J. Mater. Chem. 5 (1995) 1761.
[25] P. Marchand, I.A. Hassan, I.P. Parkin, C.J. Carmalt, Dalton Trans. 42 (2013) 9406.
[26] E.S. Peters, C.J. Carmalt, I.P. Parkin, D.A. Tocher, Eur. J. Inorg. Chem. 2005 (2005) 4179.
[27] C. Edusi, G. Sankar, I.P. Parkin, Chem. Vap. Depos. 18 (2012) 126.
[28] V. Killedar, C. Lokhande, C. Bhosale, Thin Solid Films 289 (1996) 14.
[29] O.C. Monteiro, T. Trindade, J.H. Park, P. O'Brien, Chem. Vap. Depos. 6 (2000) 230.
[30] W.N. Kun, S. Mlowe, I.D. Nyamen, P.T. Ndifon, M.A. Malik, O.Q. Munro, N. Revaprasadu, Chem. Eur. J. 22 (2016) 13127.
[31] S. Mlowe, D.J. Lewis, A.M. Malik, J. Raftery, E.B. Mubofu, P. O'Brien, N. Revaprasadu, New J. Chem. 38 (2014) 6073.
[32] Bruker. APEX2, SAINT and SADABS. Bruker AXS Inc., Madison, Wisconsin, USA (2012).
[33] G.M. Sheldrick, Acta Crystallogr., Sect. C 71 (2015) 3.
[34] L.J. Farrugia, J. Appl. Crystallogr. 45 (2012) 849.
[35] A.L. Spek, Acta Crystallogr., Sect. D. 65 (2009) 148.
[36] R. Kellner, G.S. Nikolov, N. Trendafilova, Inorg. Chim. Acta 84 (1984) 233.
[37] S. Mlowe, D.J. Lewis, M.A. Malik, J. Raftery, E.B. Mubofu, P. O'Brien, N. Revaprasadu, Dalton Trans. 45 (2016) 2647.
[38] C.R. Groom, I.J. Bruno, M.P. Lightfoot, S.C. Ward, Acta Crystallogr., Sect. B 72 (2016) 171.
[39] F. Li, H.-D. Yin, J. Zhai, D.-Q. Wang, Acta Crystallogr., Sect. E 62 (2006) 1083.
[40] R. Chauhan, J. Chaturvedi, M. Trivedi, J. Singh, K.C. Molloy, G. Kociok-Kohn, D.P. Amalnerkar, A. Kumar, Inorg. Chim. Acta 430 (2015) 168.
[41] O.V. Dolomanov, L.J. Bourhis, R.J. Gildea, J.A.K. Howard, H. Puschmann, J. Appl. Crystallogr. 42 (2009) 339.
[42] C. Li, J. Zhao, Q. Hu, Z. Liu, Z. Yu, H. Yan, J. Alloys Compd. 688 (2016) 329.
[43] A.A. Tahir, M.A. Ehsan, M. Mazhar, K.G. Upul Wijayantha, M. Zeller, A.D. Hunter, Chem. Mater. 22 (2010) 5084.
[44] M.M. Beevi, M. Anusuya, V. Saravanan, I. Member, Int. J. Chem. Eng. Appl. 1 (2010) 151.
[45] K.R. Chaudhari, N. Yadav, A. Wadawale, V.K. Jain, R. Bohra, Inorg. Chim. Acta 363 (2010) 375.

RSC Advances

PAPER

Cite this: *RSC Adv.*, 2019, 9, 15836

Synthesis of $(Bi_{1-x}Sb_x)_2S_3$ solid solutions *via* thermal decomposition of bismuth and antimony piperidinedithiocarbamates†

Walter N. Kun,[ab] Paul D. McNaughter,[b] Linda D. Nyamen,[a] Ben F. Spencer,[c] Paul O'Brien,[bc] Peter T. Ndifon*[a] and Neerish Revaprasadu *[d]

Received 13th February 2019
Accepted 9th May 2019

DOI: 10.1039/c9ra01127g

rsc.li/rsc-advances

The synthesis of the complete range of $(Bi_{1-x}Sb_x)_2S_3$ solid solutions, where $0 \# x \# 1$, by the variation of the mole ratio of bismuth and antimony piperidine dithiocarbamate complexes is reported. There was a near linear expansion of *a* and *c* lattice parameters as the mole ratio of the antimony precursor was increased. The composition of the particles directionally followed the amount of precursor ratio used. When the composition of particles was compared to cell parameters, a slight deviation from Vegard's law was observed with a corresponding contraction of the *b* parameter and an approximately 3.5% reduction of the lattice volume. The nanorods obtained showed aspect ratios that depend on the composition of the material. The Bi and Sb rich materials had high aspect ratios of 16.58 and 16.58 respectively with a minimum aspect ratio of 2.58 observed for x ¼ 0.50.

Introduction

The composition, size, shape and surface topography play important roles in the performance of electronic, optoelectronic, and energy devices.[1] The incorporation of a foreign atom or ion into a host crystal lattice of a semiconductor material can introduce new functional properties.[2–4] Group V–VI compounds have attracted much attention due to their earth abundance and environmentally friendly nature. They display many important properties suitable for optoelectronic applications.[1,5–8] Bi_2S_3 has a direct band gap between 1.30 eV and 1.70 eV close to the optimal band gap for terrestrial solar cell energy conversion and a high energy conversion efficiency (10^5 cm^{-1}) and as such, is widely used for photovoltaic materials and photodiode arrays.[9–13] Sb_2S_3 has an energy band gap between 1.78 eV and 2.50 eV covering the visible and the near infrared region of the electromagnetic spectrum and shows good photovoltaic properties.[14,15] It has found use in thermoelectric devices, write once and read many (WORM) optical storage devices, IR region television cameras, infrared spectroscopy and in lithium/sodium ion batteries.[16–22] solar cells based on Sb_2S_3 □lms have been fabricated with power conversion efficiency of 4.3%.[23,24]

Despite the signi□cant difference in their sizes Bi and Sb form a full range solid solution series between stibnite and bismuthinite.[25,26] The formation of a solid solution between the two compounds is due to their similarity in charge, ability to crystallize in the same orthorhombic lattice with space group *Pnma*, having typical lattice parameters of *a* ¼ 11.2690 Å, *b* ¼ 3.9717 Å and *c* ¼ 11.1290 Å for bismuthinite and *a* ¼ 11.2990 Å, *b* ¼ 3.8313 Å and *c* ¼ 11.2270 Å for stibnite.[27,28] Their orthorhombic unit cell volume differs by 3.5%.[29–32] Analysis on various stibnite and bismuthinite samples from various localities show that replacement of Sb with Bi goes up to 55 moles% giving a limiting mixability range of $(Bi_{0.45}Sb_{0.55})_2S_3$ in naturally occurring Bi_2S_3–Sb_2S_3 solid solution.[25,32,33] This paucity of representation covering the whole solid solution range in natural samples is attributed to the different geological condi- tions under which bismuthinite and stibnite are deposited in nature.[25,34] Kyono *et al.* synthesised a full range $(BiSb)_2S_3$ solid solution series with a nearly statistical substitution of Sb for bismuth by heating Bi_2S_3 and Sb_2S_3 at 800 to 1000 °C.[30] However, their method provided no control over stoichiometry as four samples with the same composition range were obtained from a starting mixture with the same Bi_2S_3 : Sb_2S_3 molar ratio. This observation of large deviations from linear trends in the lattice constants was in contradiction to earlier work by Nayak *et al.* that showed good agreement with Vegard's law on the entire solid solution range by depositing thin □lms of the solid solution by a dip-dry method.[10] Colloidal synthesis of nanostructures in surface passivating agents has proven to be an efficient route as it provides easy control over size and

[a]*Department of Inorganic Chemistry, University of Yaoundé, I. P. O. Box 812, Yaoundé, Cameroon*

[b]*School of Materials, University of Manchester, Oxford Road, Manchester, M13 9PL, UK*

[c]*Schools of Chemistry and Materials, University of Manchester, Oxford Road, Manchester, M13 9PL, UK*

[d]*Department of Chemistry, University of Zululand, Private Bag X1001, Kwa- Dlangezwa, 3886 South Africa. E-mail: RevaprasaduN@unizulu.ac.za*

† Electronic supplementary information (ESI) available. CCDC 1889653. For ESI and crystallographic data in CIF or other electronic format see DOI: 10.1039/c9ra01127g

shape.[35,36] Wang *et al.* used a dual precursor source route to synthesize a full range solid solution of $(Bi_{1-x}Sb_x)_2S_3$ with aspect ratios that depended on their compositions.[1] Patra *et al.* did similar work using diethyldithiocarbamate complexes in oleylamine and thiol.[4] However, they did not investigate the influence of the Sb substitution on the lattice constant.[37] Khan *et al.* prepared the entire range of $(SnS_{1-x}Se_x)$ from bis(selonobenzoato)dibutyltin(IV) and bis(thiobenzoato)-dibutyltin(IV) complexes by colloidal and melt methods and showed that the colloidal method provided superior control over composition, though both methods showed compositional dependence in the variation of the lattice parameters.[38] In our earlier work, we showed that addition of a small amount of dodecanethiol was efficient in directing the shapes of Bi_2S_3 rods from single source precursors by thermal decomposition of bismuth dithiocarbamate complexes in high boiling point coordination solvents.[39]

This paper examines the effect of substituting antimony for bismuth on the structure of the bismuthinite–stibnite solid solution prepared by bismuth piperidine and antimony piperidine dithiocarbamate complexes.

Experimental section

Bismuth trichloride (98%, Sigma-Aldrich), antimony trichloride (99%, Sigma-Aldrich), carbon disulphide (99.9%, Sigma-Aldrich), piperidine (99.5% Sigma-Aldrich), oleylamine (98% Sigma-Aldrich), 1-dodecanethiol (98% Sigma-Aldrich), ethanol (99.8% Sigma-Aldrich), chloroform (99.8% Sigma-Aldrich), chloroform-d (99.8% Sigma-Aldrich), and sodium hydroxide (97% Fisher Scientific) were used as supplied without further purification.

Synthesis of the precursors

Preparation sodium piperidine dithiocarbamate (1). The synthesis of (1) followed previously reported procedure with modifications.[39] In a typical synthesis, carbon disulfide (0.1 mol, 6.0 mL) was added to an equimolar mixture of sodium hydroxide (0.1 mol, 4.0 g) and piperidine (0.1 mol, 9.9 mL) cooled to 0 °C. After 15 min, the white precipitate formed was filtered, dried in air and recrystallised from acetone/petroleum ether. Na(S_2CPip): yield: 92%/mp 295 °C. Significant IR bands: n ¼ 3377 (O–H), 964 (C]S), 1468 cm^{-1} (C]N); elemental analysis (%) for $C_6H_{14}NS_2O_2Na$: C 32.86, H 6.43, N 6.39, Na 10.48, S 29.24; found: C 33.05, H 6.34, N 6.6.33, Na 10.66, S 28.88.

Preparation of tris(piperidindithiocarbamato)bismuth(III) (2). The synthesis of (2) followed our previous procedure with modifications.[37] $BiCl_3$ (5.0 mmol, 1.58 g) was suspended in ethanol (15.0 mL), and added dropwise to a solution of the piperidine dithiocarbamate ligand (15.0 mmol, 2.75 g) in ethanol (25.0 mL) followed by stirring for 1 h. The yellow precipitate formed was collected by filtration and recrystallized from chloroform. $Bi(PipDtc)_3\$H_2O$: yield 89% mp 230 °C. Significant IR bands: n ¼ 3477 (O–H), 967 (C]S), 1468 cm^{-1} (C]N); elemental analysis (%) for $C_{18}H_{32}N_3OS_6Bi$; calc; C 30.54, H 4.56, N 5.94, S 27.18, Bi 29.52. Found; C 30.99, H 4.28, N 5.98, S 26.80, Bi 29.39.

Preparation of tris(piperidindithiocarbamato)antimony(III) (3). The procedure for (3) was the same as (2) with some modifications. $SbCl_3$ (5.0 mmol, 1.14 g) was suspended in ethanol (15.0 mL) and added dropwise to a solution of the piperidine dithiocarbamate ligand (15.0 mmol, 2.75 g) in ethanol (25.0 mL). The resultant solution was stirred for 1 h. The pale-yellow precipitate formed was collected by filtration and recrystallized from chloroform.

$Sb(PipDtc)_3\$3H_2O$: yield 82% mp 239 °C. Significant IR bands: n ¼ 3377 (O–H), 967 (C]S), 1476 cm^{-1} (C]N); elemental analysis (%) for $C_{18}H_{36}N_3O_3S_6Sb$; calc; C 32.92, H 5.53, N 6.40, S 29.30, Sb 18.54. Found; C 32.72, H 5.84, N 6.47, S 30.14, Sb 19.15.

Synthesis of $(Bi_xSb_{1-x})_2S_3$ solid solutions

$(Bi_xSb_{1-x})_2S_3$ solid solutions were prepared by variation of the mole ratio of (2) and (3). In a typical experiment, a mixture of (2) and (3) totalling 0.29 mmol was dispersed in a mixture of oleylamine (4.0 mL) and 1-dodecanethiol (0.2 mL). This was injected into 8.0 mL of hot oleylamine (230 °C) under N_2. After 30 min the reaction was quenched, and the ensuing black precipitate washed three times with ethanol (12.0 mL), centrifuged (11 000 rpm) and dispersed in toluene (5.0 mL).

Instrumentation

Fourier transform infrared spectroscopy was performed using a Thermo Scientific Nicolet iS5 instrument (4000–400 cm^{-1}, resolution 4 cm^{-1}). Optical measurements were performed on a Shimadzu UV-1800 spectrophotometer. Elemental analysis was performed with a Thermo Flash 2000 and Carlo Erba EA 1108 elemental analysers (Department of Chemistry University of Manchester). Melting points were recorded on a Stuart SMP10 Melting point apparatus. Thermogravimetric analysis was performed on a Seiko SSC5200/S220TG/DTA model, at a heating rate of 10 °C min^{-1} from 30 °C to 600 °C, under nitrogen.

XRD patterns of the thin films were collected on a PANalytical X'Pert PRO powder diffractometer (Material Science University of Manchester) with a Cu Ka radiation source (l ¼ 1.5406 Å). The samples were mounted flat and scanned over the 2q range of 10–70° in a step size of 0.05.

X-ray photoelectron spectroscopy (XPS) was performed using an Axis Ultra Hybrid (Kratos Analytical, United Kingdom) using 10 mA emission (150 W) of monochromated Al Ka radiation (1486.6 eV). Samples were pressed onto carbon tape, and a charge neutraliser was used to replenish electrons at the surface and remove the effects of differential charging under the X-ray beam. High resolution spectra were collected using an electron energy analyser pass energy of 20 eV and survey spectra with 80 eV pass energy.

X-ray photoelectron spectroscopy (XPS) data were analysed using CASAXPS (www.casaxps.com): the binding energy scales were calibrated using the principle C 1s peak associated with hydrocarbon at 284.8 eV, Shirley backgrounds were fitted where appropriate, and atomic concentrations were calculated using relative sensitivity factors incorporating the photoionization

cross section for each core electron orbital, as well as the transmission function of the electron energy analyser. Peak □tting using Voigt-approximation Gaussian–Lorentzian products was performed to obtain binding energy positions for chemical species determination.

Transmission electron microscope (TEM) images, high resolution transmission electron microscope (HRTEM) images, selected area electron diffraction (SAED) patterns and energy dispersive X-ray spectroscopy (EDS) spectra were obtained with an FEI Talos F200A microscope (PSI, University of Manchester) equipped with an X-FEG electron source and Super-X SDD EDS detectors. The experiment was performed using an acceleration voltage of 200 kV and a beam current of approximately 5 nA. Images were recorded with a FEI CETA 4k × 4k CMOS camera. Single crystal X-ray data were collected on a dual source Rigaku FR-X rotating anode diffractometer using Cu Kα wavelength at 150 K and reduced using CrysAlisPro 171.39.30c. Absorption correction was performed using empirical methods (SCALE3 ABSPACK) based upon symmetry-equivalent re□ections combined with measurements at different azimuthal angles. The structure was solved and re□ned using Shelx-2016 implemented through Olex2 v1.2.9.2,3.

Results and discussion

Characterization of the precursors

The reaction of piperidine dithiocarbamate with $BiCl_3$ and $SbCl_3$ gave tris(piperidinedithiocarbamato)bismuth(III) ($Bi(S_2CPip)_3$) (2) and tris(piperidinedithiocarbamato)antimony(III) ($Sb(S_2CPip)_3$) (3) respectively. The presence of the dithiocarbamate moiety in the two complexes was shown by the characteristic thioureide band ν(C–N) around the 1450–1500 cm^{-1} region and the ν(C–S) band around the 960–1000 cm^{-1}. These bands appeared shi□ed to higher frequencies in the spectrum of the corresponding free ligand. The bidentate nature of the coordination of the dithiocarbamate ligand was shown by the band around 960–1000 cm^{-1} which appeared unsplit.[40] Broad bands around 3300–3500 cm^{-1} in the spectra of the ligands as well as the antimony piperidine complex is due to the presence of moisture in the compounds.

Single crystals of complex (3) were grown in chloroform/ethanol mixture, and their X-ray crystal structure was determined at 150 K. The low temperature structure of tris(piperidinedithiocarbamato)antimony(III) ($Sb(S_2CPip)_3$), crystallizes into a six coordinate Sb complex surrounded by three piperidinedithiocarbamato groups bonded through S donor atoms. There are three short Sb–S distances of ~2.53 Å and three long Sb–S distances of ~2.9–3.0 Å. There is a stereochemically active lone pair on the Sb atom such that the (seven) steric groups (6 S donors and 1 lone pair) occupy the vertices of an 'elongated triangular pyramid' in which there are parallel triangular sets of S donors with the lone pair pointed normal to the planes of 3 S atoms (the short Sb–S and the long Sb–S). A similar structure was reported by Liu and Tiekink[41] at a much higher temperature of 223 K. The three short Sb–S bond length was found to be ~2.52 Å and that of the three long Sb–S bonds were 2.86 Å, which favourably compares to those of complex (3). The mean interchelate S–Sb–S bond angles of 93.60 of complex (3) is also comparable to 92.32 of the reported structure. The crystal structure, some selected bond lengths together with the crystallographic data and structural re□nement parameters for complex (3) are shown in ESI 2, 3 and 4 respectively.†

The thermogram of complex (2) shows a three-step decomposition pattern. The □rst mass loss of 3.05% (2.56% calculated) at 128 °C corresponds to the loss of H_2O molecules. The second mass loss of 59.47% (58.56% calculated) at 281 °C corresponds to the loss of the organic moiety and sulfur, while the third mass loss of 10.41% (11.09% calculated) at 464 °C is attributed to the additional loss of sulfur with the formation of a □nal residue of 33.67% (35.9% calculated) corresponding to Bi_2S_3. Complex (3) shows a two-step decomposition pattern, with the □rst mass loses of 8.68% (8.14% calculated) at 100 °C corresponding to the loss of the three water molecules and a second mass loss of 70.49% (72.44% calculated) attributed to the loss of the organic moiety and sulfur with the formation of a residue of 26.16% (25.56% calculated) which corresponds to Sb_2S_3 (Fig. 1).

Compositional characterization

The EDX data (Fig. 2) (where the sampling depth is ▮ the nanorod diameter) shows that the composition of the particles synthesised is in close agreement with the mole fraction of precursors used. This result is unusual with single source precursors as the difference in metal–sulfur bond strengths normally governs the rate of decomposition and consequen- tially skews the composition to the more reactive metal–sulfur bond. A plot of Sb precursor mole fraction against the propor- tion of antimony in the particles gave a close to straight line (Fig. 2b) with full details in Table 1. Many of the samples were sulfur rich which is possibly due to the relatively low reaction temperature which prevented evaporation of sulfur, a situation commonly observed in samples prepared at a much higher temperature.[42,43]

The X-ray diffraction patterns obtained for all the Bi/Sb ratios correspond well to the orthorhombic crystal system, with peaks for the Bi–Sb–S system falling between previously reported patterns of orthorhombic bismuthinite[26] (*a* ¼ 11.2690 Å, *b* ¼ 3.9717 Å and *c* ¼ 11.1290 Å) and orthorhombic stibnite[27] (*a* ¼ 11.2990 Å, *b* ¼ 3.8313 Å and *c* ¼ 11.2270 Å), Fig. 3a. Sb_2S_3 and

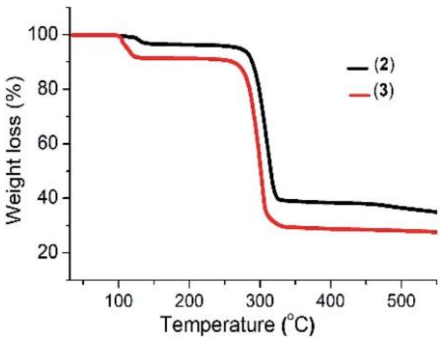

Fig. 1 Thermogram of complexes (2) and (3).

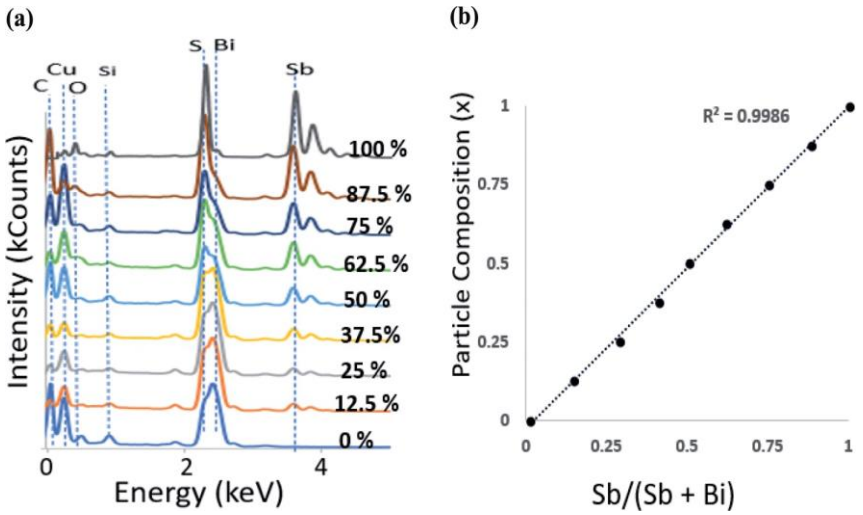

Fig. 2 (a) EDS spectra of $(Bi_{1-x}Sb_x)_2S_3$ nanorods at different Bi : Sb mole ratios (b) particle composition *x* obtained from EDS against precursor mole fraction.

Table 1 Structural data for Bi_2S_3, Sb_2S_3 and $(Bi_xSb_{1-x})_2S_3$ solid solution

X_{Bi} (%)	X_{Sb} (%)	Chemical composition (EDX)	*a* (Å)	*b* (Å)	*c* (Å)	*V* (Å)^3
100.0	0.0	$Bi_{1.95}S_{3.05}$	11.24	3.97	11.13	496.68
87.5	12.5	$Sb_{0.27}Bi_{1.68}S_{3.05}$	11.24	3.95	11.14	494.32
75.0	25.0	$Sb_{0.58}Bi_{1.34}S_{3.08}$	11.24	3.93	11.14	492.90
62.5	37.5	$Sb_{0.79}Bi_{1.15}S_{3.06}$	11.25	3.92	11.16	491.88
50.0	50.0	$Sb_{0.97}Bi_{0.95}S_{3.08}$	11.26	3.91	11.19	492.00
37.5	67.5	$Sb_{1.22}Bi_{0.75}S_{3.04}$	11.26	3.87	11.19	487.13
25.0	75.0	$Sb_{1.49}Bi_{0.51}S_{3.00}$	11.26	3.87	11.21	489.03
12.5	87.5	$Sb_{1.80}Bi_{0.24}S_{2.96}$	11.27	3.86	11.22	487.23
0.0	100.0	$Sb_{1.93}S_{3.07}$	11.27	3.82	11.22	483.22

Bi_2S_3 both crystallize in the same orthorhombic lattice system with a difference in cell volume of 3.5% due to Sb^{3+} possessing a smaller ionic radius than Bi^{3+}. The enlarged portion of the XRD pattern of the samples show a shi in the peak position con rming the successful incorporation of Sb into the Bi_2S_3 lattice and the movement through the entire compositional range of the $(Bi_{1-x}Sb_x)_2S_3$ solid solution, Fig. 3b. A plot of the d- spacing for the (112) plane shows a gradual decrease from Bi_2S_3 to the Sb_2S_3 end with a percentage difference of 2.26% (ESI 5†). Re nement of the powder XRD data shows that all three axis of the unit cell vary linearly (Fig. 4). Upon increased incorporation of antimony, *a* and *c* increase whereas *b* decreases which is the expected behaviour when moving between Bi_2S_3 and Sb_2S_3. All three cell parameters show a linear dependency on the amount of antimony in the solid solution which agrees with Vegard's law. The subtle deviations in *a* and *c* from ideal behaviour may be due to the contrasting effect of the stereochemical active lone pair of the $5s^2$ and $6s^2$ electrons of the antimony and bismuth atoms, which is positioned in the *a*–*c* plane of the lattice.[37,44] With an increased concentration of antimony, there is expansion of the inter-rod space due to the expression of the stereochemically active lone electron pair with a resulting expansion of the *a* and *c* parameters.[30] However, the *b* axis which is least affected by the stereochemical active lone pair experiences a continuous contraction on Sb substitution, probably due to decrease in the shortest M–S bond as we move from the Bi_2S_3 to the Sb_2S_3 end.[26] There is a general shrinkage of the overall cell volume of $(Bi_{1-x}Sb_x)_2S_3$ as Bi is replaced by Sb (Fig. 4d).

The high-resolution transmission electron microscopy (HRTEM) images of the samples together with their selected area electron diffraction (SAED) patterns reveal the formation of highly polycrystalline powders showing two-dimensional lattice fringes (Fig. 4). Measured *d*-spacings of 3.69 and 4.98 Å were obtained for pure Bi_2S_3 (Fig. 5a) corresponding to the (011) and (102) planes (SG *Pnma* with *a* ¼ 11.2690 Å, *b* ¼ 3.9717 Å and *c* ¼ 11.1290 Å) while for pure Sb_2S_3 (Fig. 5i) a *d*-spacings of 3.50 Å corresponding to the (111) (SG *Pnma* with *a* ¼ 11.2990 Å, *b* ¼ 3.8313 Å and *c* ¼ 11.2270 Å) plane was recorded.

XPS is a much more surface sensitive technique than EDX, with sampling depths varying 6.3–9.0 nm for Sb, Bi and S,[45] which is much less than the nanorod diameter. Bi 4f coincides with the S 2p region, and Sb 3d coincides with O 1s. Fig. 6 shows a pile-up of the Bi 4f/S 2p and Sb 3d/O 1s regions for Bi_2S_3, Sb_2S_3 and $(Bi_{1-x}Sb_x)_2S_3$.

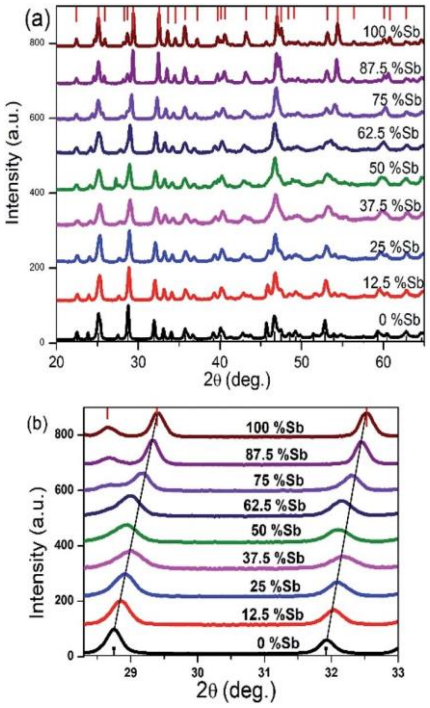

Fig. 3 (a) Powder XRD pattern of Bi_2S_3 bottom, $(Bi_{1-x}Sb_x)_2S_3$ and Sb_2S_3 top, samples synthesized from different Bi/Sb ratios (b) p-XRD pattern of 2q range 27–33 degree showing shift in peaks.

In all cases the Bi 4f doublet required two chemical species (two sets of spin–orbit–split doublets) in order to obtain an adequate □t, with positions for the Bi $4f_{7/2}$ photoelectron peaks at 158.1 eV (associated with Bi_2S_3 [46] and 158.8 eV (associated with oxidized Bi_2O_3.[47] Likewise, the Sb 3d doublet required two chemical species for adequate □tting, with peak positions for $3d_{5/2}$ at 259.1 eV (associated with Sb_2S_3 [48] and 530.1 eV (associated with oxidized Sb O).[49] Note that O 1s photoelectron peaks are

2 3

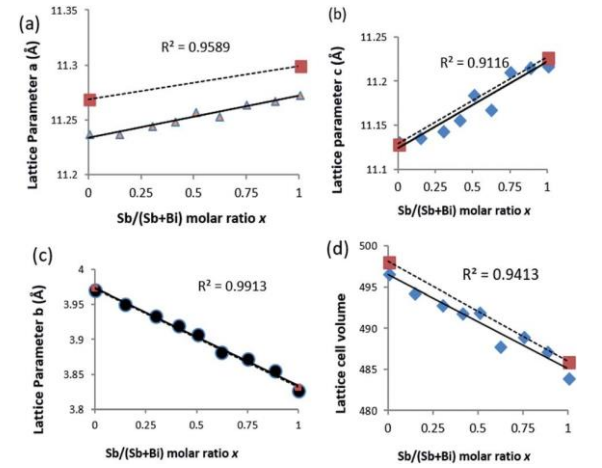

Fig. 4 Variation of lattice constants with increasing mole fraction of Sb obtained from EDS. (a) Lattice parameter *a*, (b) lattice parameter *b*, (c) lattice parameter *c* and (d) cell volume. * values represent the reported standard value (dotted lines) for Bi_2S_3 and Sb_2S_3.

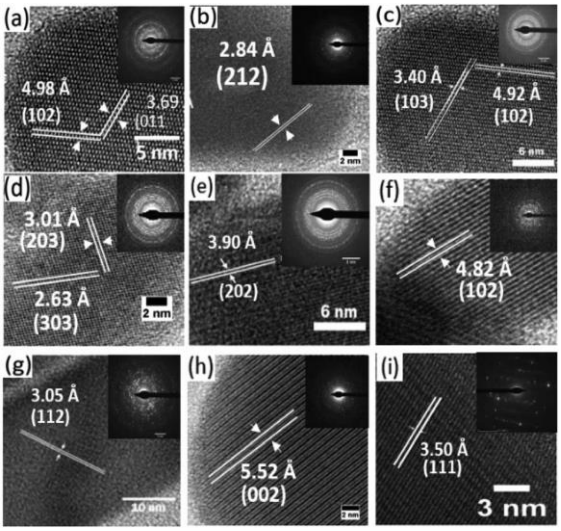

Fig. 5 HRTEM images of synthesized nanorods with Sb/(Sb + Bi) mole fraction of (a) 1 : 0, (b) 7 : 1, (c) 3 : 1, (d) 5 : 3, (e) 1 : 1, (f) 3 : 5, (g) 1 : 3, (h) 1 : 7 and (i) 0 : 1. Inset in each image shows the SAED pattern.

close to the Sb $3d_{5/2}$ signal, typically with binding energy positions at ~530.5 eV associated with metal oxides (*i.e.*, BiO_x, SbO_x), ~532 eV associated with C–O contamination, and ~533 eV associated with C▌O contamination. A variety of $(Bi_xSb_{1-x})_2S_3$ samples were measured, and consistently a peak-□tting model including sul□de and oxide species was required for both Bi and Sb. However, no oxidation was seen for S, only one species for the S 2p doublet was observed for all the samples measured, with the peak position for $2p_{3/2}$ at ~161.0 eV associated with sul□de,[46,48] and in the spectra there is a clear absence of any signal associated with sulfate which is expected in the binding energy region 168– 170 eV.[50] Also, when calculating the atomic ratios of Bi : Sb : S, there is consistently an absence of S as expected for $(Bi_{1-x}Sb_x)_2S_3$.

In Fig. 6 the $(Bi_xSb_{1-x})_2S_3$ sample exhibits a Bi : Sb : S ratio of 3 : 3 : 4 (or 1 : 1 : 1.3, short of the expected 1 : 1 : 1.5). This indicates that there is an absence of sulfur atoms at the surface of

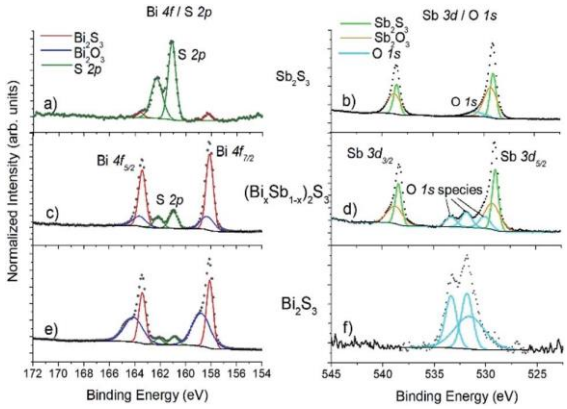

Fig. 6 XPS spectra for Sb_2S_3 (top panels (a) and (b)), Bi_2S_3 (bottom panels (e) and (f)), and $(Bi_xSb_{1-x})_2S_3$ (middle panels (c) and (d)). The Bi 4f and S 2p spectral regions overlap ((a), (c), (e)), and the Sb 3d region overlaps with O 1s ((b), (d), (f)).

the nanorods hence the atomic concentrations (Table 2) are skewed from the bulk measurement by EDX analysis. This also explains the lack of sulfur oxidation while a small amount of Bi and Sb atoms at the surface of the nanorods are susceptible to oxidation. For the range of $(Bi_{1-x}Sb_x)_2S_3$ nanorod materials measured, the amount of oxidation of Bi and Sb observed varied between 10–40% (with an average value of 20% for Bi and 26% for Sb).

Morphological characterization

TEM analysis on the samples showed the presence of particles with a rod-shaped morphology, Fig. 7a–i. When the bismuth precursor was exclusively used, uniform elongated cylindrical nanorods of Bi_2S_3 were obtained however the antimony precursor gave long sheaf-like collections of Sb_2S_3 rods in the sub-micrometre range (Fig. 7i and 8e).

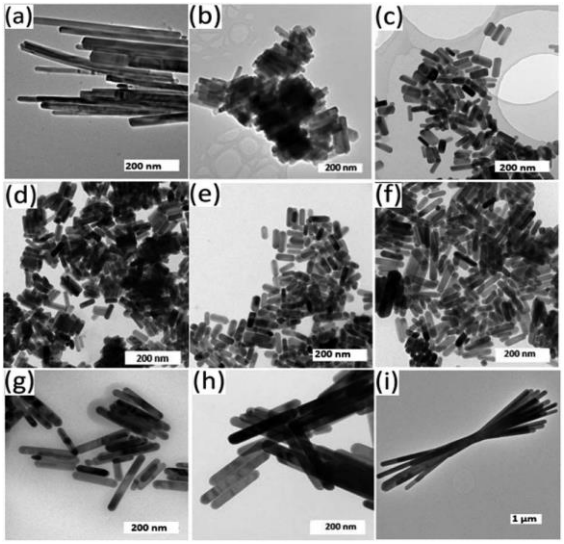

Fig. 7 TEM images showing the as synthesized nanorods with Bi : Sb mole ratios of (a) 1 : 0, (b) 7 : 1, (c) 3 : 1, (d) 5 : 3, (e) 1 : 1, (f) 3 : 5, (g) 1 : 3, (h) 1 : 7 and (i) 0 : 1.

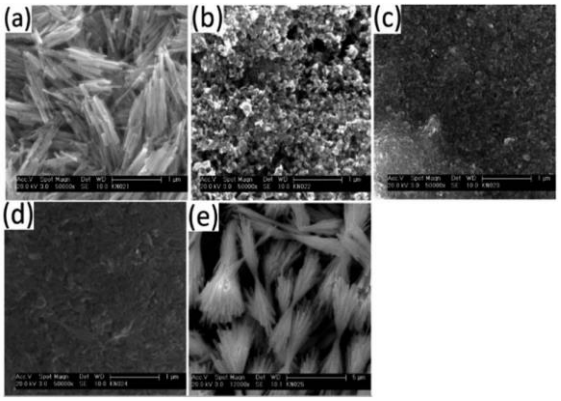

Fig. 8 SEM images showing surface scan of films with Bi : Sb mole ratios of (a) 1 : 0, (b) 3 : 1, (c) 1 : 1, (d) 1 : 3, (e) 0 : 1.

There was a conspicuous change in the aspect ratio of the rods as the Bi : Sb precursor mole ratio was varied, Table 3. With a Bi : Sb precursor mole ratio of 7 : 1, there was a considerable reduction in both the length and aspect ratio of the nanorods compared to pure Bi_2S_3 until a mole ratio of 1 : 1, which gave an aspect ratio of 2.58 (Table 3). Wang *et al.* prepared $(Bi_{1-x}Sb_x)_2S_3$ 1-d rods, by reacting bismuth chloride, antimony chloride, sulphur powder, oleylamine and thiols and observed composition dependant aspect ratios.[1] Sun *et al.* synthesized □ower-like architectures $Sb_{2-x}Bi_xS_3$ by solvothermal treatment of bismuth and antimony diethyldithiocarbamate complexes. They proposed a mechanism in which 3-d □owers grow through an epitaxial growth on $Sb_{2-x}Bi_xS_3$ core.[51] When we increased the precursor mole ratio of Sb beyond 1 : 1, the aspect ratio increased along with the length of the rods. At a mole ratio of 1 : 7 the longest rods of the solid solution were observed. Sb_2S_3 has a partial fractal splitting growth habit which o□en lead to the formation of sheaf-like morphologies.[52] However, the inclusion of Bi ions alters the growth dynamics by inducing complete splitting growth and consequently changes morphology from very long sheaf-like sub-micrometre Sb_2S_3 rods to shorter separate nanorods. The particle size distribution of the as synthesized nanorods are shown in ESI 6.† TEM images of intermediate Bi : Sb ratio to those reported are shown in ESI 7.†

Table 2 Relative percentage concentrations of Bi, Sb and S for Bi_2S_3, Sb_2S_3 and $(Bi_{1-x}Sb_x)_2S_3$. Bi and Sb are further delineated into sulfide and oxide species, where oxidation occurs between 10–40% of the time (with an average of 20% for Bi and 26% for Sb)

Sb/(Sb + Bi)	Bi–S%	Bi–O%	Total Bi%	Sb–S%	Sb–O%	Total Sb%	S%
0	49.79	18.69	68.49	0.00	0.00	0.00	31.51
0.125	49.11	9.33	58.43	4.44	0.49	4.93	36.64
0.25	45.20	8.61	53.81	7.86	1.56	9.43	36.76
0.375	37.32	8.25	45.57	17.53	1.76	19.29	35.14
0.5	34.86	5.81	40.67	15.55	6.17	21.72	37.60
0.625	27.85	5.32	33.17	20.94	7.39	28.34	38.49
0.75	27.45	3.40	30.85	23.36	6.67	30.03	39.13
0.875	17.09	1.66	18.74	29.75	11.16	40.91	40.35
1	3.56	0.00	3.56	38.20	12.14	50.34	46.10

Table 3 Dimensions of synthesised nanorods of Bi_2S_3, Sb_2S_3 and $(Bi_{1-x}Sb_x)_2S_3$ solid solution

Sb/(Sb + Bi)	Length (nm)	Width (nm)	Aspect ratio
0	474.4 T 92.62	28.61 T 12.90	16.58
0.125	104.99 T 46.38	19.79 T 9.13	5.31
0.25	65.13 T 13.52	23.69 T 6.50	2.75
0.375	57.00 T 11.12	15.55 T 4.07	3.66
0.5	60.38 T 12.60	23.38 T 4.38	2.58
0.625	25.04 T 7.37	5.56 T 1.09	4.51
0.75	142.81 T 56.58	28.56 T 5.01	5.00
0.875	386.32 T 137.43	40.05 T 11.08	9.65
1	2880.47 T 550.22	137.09 T 44.82	21.01

Optical properties

Bi_2S_3 and Sb_2S_3 possess direct band gaps of approximately 1.3 and 1.7 eV respectively, corresponding to 954 and 729 nm. The band gap of the ternary $(Bi_{1-x}Sb_x)_2S_3$ solid solutions made using different ratios of Bi and Sb should be a linear interpolation of the two parent materials. Fig. 9a shows the UV-visible absorption spectra of the as-prepared ternary $(Bi_{1-x}Sb_x)_2S_3$ in which a strong broad absorption was seen within the wavelength range of 300–1100 nm. In general, the absorption edge of $(Bi_{1-x}Sb_x)_2S_3$ nanorods is blue-shi□ed with the increase of Sb ratio.

However, a plot of the absorption maximum against the antimony mole fraction shows a marked deviation from the expected linear behaviour of the band gap of ternary semiconductor materials (Fig. 10). This phenomenon known as band gap bowing is o□en ascribed to local compositional □uctuations which occur on substitution. The extent of such local atom displacements usually brings about nonlinear dependence on optical properties in ternary materials.[44,53] O'Brien *et al.* synthesize $Bi_{2-2x}Sb_{2x}S_3$ solid solutions from solvent less thermolysis of metal xanthate precursors and showed a slight deviation from linearity in the energy band gap on Sb substitution due to stoichiometric variations in the synthesized solid solution.[54]

The Raman spectra of the particles are shown in Fig. 11. In case of pure Bi_2S_3 sample, a minor peak was observed at 184 cm^{-1} and two prominent peaks at 236 and 256 cm^{-1}, which is in agreement with the previously reported Raman data for Bi_2S_3. The minor peak is assigned as A_g symmetric bending mode, whereas the dominant peaks (236 and 256 cm^{-1}) are A_g and B_{1g} anti-symmetric stretching modes, respectively.[55,56] Similarly, one minor and two major peaks at 186, 272 and 294 cm^{-1} were observed for pure Sb_2S_3, which are in good agreement with the previous reports.[57–59] The peak at 186 cm^{-1} can be assigned to the B_{1g} anti-symmetric S–Sb–S bending modes, whereas the peaks at 272 and 294 cm^{-1} are assigned to the A_g and B_{1g} anti-symmetric Sb–S stretching modes, respectively.[56,57] The solid solutions consisting of 25% antimony show mainly one broad band around 240 cm^{-1}, which shi□ to higher frequencies of 253 and 260 cm^{-1} when the percentage of antimony is increased to 50 and 75% respectively. The shi□ towards the higher wavenumber is due to lower mass of Sb as compare to Bi and shorter Sb–S bond respectively.[60,61]

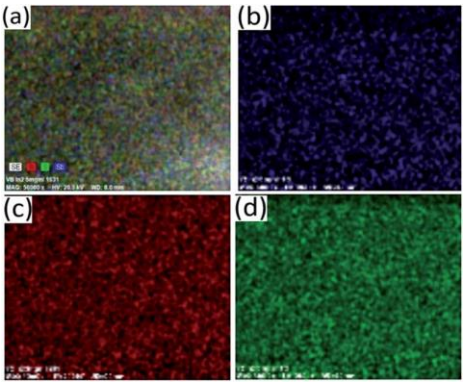

Fig. 9 Elemental mapping of the particles synthesized at Bi : Sb mole ratio of 1 : 1 showing distribution of atoms (a) SE, (b) Sb, (c) Bi and (d) S.

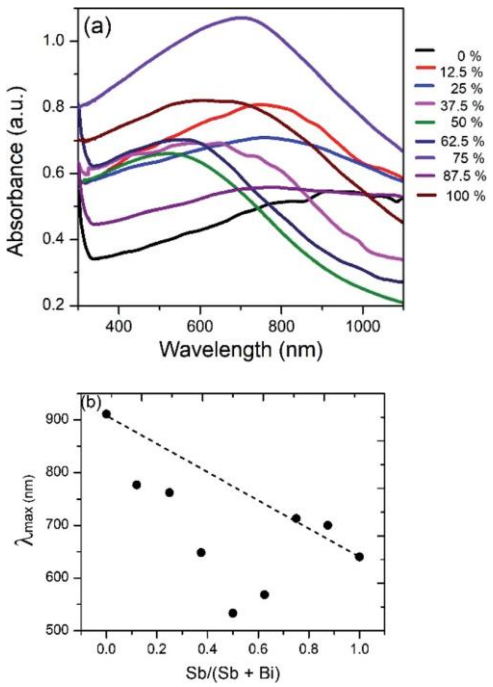

Fig. 10 (a) UV/visible absorption spectrum of Bi_2S_3, Sb_2S_3 and $(Bi_{1-x}Sb_x)_2S_3$ solid solutions. (b) Plot of absorption maximum against mole fraction of Sb, showing deviation from ideal behaviour.

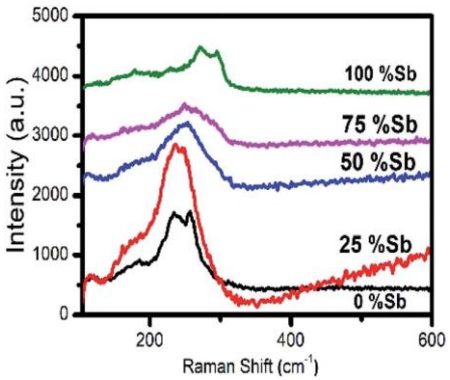

Fig. 11 Raman spectra of nanorods of Sb_2S_3, Bi_2S_3 and $(Bi_{1-x}Sb_x)_2S_3$ solid solutions.

Conclusions

By the thermal decomposition of bismuth and antimony piperidinedithiocarbamates in oleylamine nanorods of the entire compositional range of $(Bi_{1-x}Sb_x)_2S_3$ of solid solutions have been produced by varying the bismuth and antimony precursor mole fraction. The morphologies of the nanorods

decreased to a minimum of 2.58 with maxima of 16.58 when using just the bismuth precursor and 21.01 when using the antimony precursor.

The XRD peaks at all ratios correspond to the orthorhombic crystals system and fall between those of orthorhombic Bi_2S_3 and orthorhombic Sb_2S_3. The gradual shi in the peaks position in combination with compositional data from EDX con rms the successful incorporation of antimony into bismuth sulphide which almost adheres to Vegard's law.

Conflicts of interest

There are no con icts to declare.

Acknowledgements

The authors thank the Royal Society-Department for International Development (RS-DFID) for their nancial support. NR acknowledges the National Research Foundation (NRF), South Africa through the South African Research Chair Initiative (SARChI) for nancial support. We thank Dr George Whiteheard of the X-ray crystallography unit, School of Chemistry of the University of Manchester for the X-ray crystal structure of complex (3).

References

1 J. Wang, H. Yu, T. Wang, Y. Qiao, Y. Feng and K. Chen, *ACS Appl. Mater. Interfaces*, 2018, 10, 7334–7343.
2 D. Mocatta, G. Cohen, J. Schattner, O. Millo, E. Rabani and U. Banin, *Science*, 2011, 332, 77–81.
3 H.-Y. Chen, S. Maiti and D. H. Son, *ACS Nano*, 2012, 6, 583–591.
4 B. K. Patra, S. Khilari, A. Bera, S. K. Mehetor, D. Pradhan and N. Pradhan, *Chem. Mater.*, 2017, 29, 1116–1126.
5 V. V. Killedar, C. D. Lokhande and C. H. Bhosale, *Thin Solid Films*, 1996, 289, 14–16.
6 B. Yang, D.-J. Xue, M. Leng, J. Zhong, L. Wang, H. Song, Y. Zhou and J. Tang, *Sci. Rep.*, 2015, 5, DOI: 10.1038/srep10978.
7 F. Caruso, M. R. Filip and F. Giustino, *Phys. Rev. B: Condens. Matter Mater. Phys.*, 2015, 92, DOI: 10.1103/PhysRevB.92.125134.
8 A. Hussain, A. Begum and A. Rahman, *Mater. Sci. Semicond. Process.*, 2014, 21, 74–81.
9 O. C. Monteiro, H. I. S. Nogueira, T. Trindade and M. Motevalli, *Chem. Mater.*, 2001, 13, 2103–2111.
10 B. B. Nayak, H. N. Acharya, G. B. Mitra and B. K. Mathur, *Thin Solid Films*, 1983, 105, 17–24.
11 G. Konstantatos, L. Levina, J. Tang and E. H. Sargent, *Nano Lett.*, 2008, 8, 4002–4006.
12 M. Bernechea, Y. Cao and G. Konstantatos, *J. Mater. Chem. A*, 2015, 3, 20642–20648.
13 W. Lou, M. Chen, X. Wang and W. Liu, *Chem. Mater.*, 2007, 19, 872–878.
14 J. B. Biswal, N. V. Sawant and S. S. Garje, *Thin Solid Films*, 2010, 518, 3164–3168.
15 L. P. Deshmukh, *J. Electrochem. Soc.*, 1994, 141, 1779.
16 X. Xiong, G. Wang, Y. Lin, Y. Wang, X. Ou, F. Zheng, C. Yang, J.-H. Wang and M. Liu, *ACS Nano*, 2016, 10, 10953–10959.
17 D. Y. W. Yu, P. V. Prikhodchenko, C. W. Mason, S. K. Batabyal, J. Gun, S. Sladkevich, A. G. Medvedev and O. Lev, *Nat. Commun.*, 2013, 4, DOI: 10.1038/ncomms3922.
18 K. Ramasamy, H. Sims, W. H. Butler and A. Gupta, *J. Am. Chem. Soc.*, 2014, 136, 1587–1598.
19 S. Sarkar, A. K. Guria, B. K. Patra and N. Pradhan, *Angew. Chem., Int. Ed.*, 2014, 12566–12570.
20 G. Manna, R. Bose and N. Pradhan, *Angew. Chem., Int. Ed.*, 2014, 53, 6743–6746.
21 J. Ma, Y. Wang, Y. Wang, Q. Chen, J. Lian and W. Zheng, *J. Phys. Chem. C*, 2009, 113, 13588–13592.
22 S. Yao, J. Cui, Z. Lu, Z.-L. Xu, L. Qin, J. Huang, Z. Sadighi, F. Ciucci and J.-K. Kim, *Adv. Energy Mater.*, 2017, 7, 1602149.
23 K. Zhang, T. Luo, H. Chen, Z. Lou and G. Shen, *J. Mater. Chem. C*, 2017, 5, 3330–3335.
24 X. Wang, R. Tang, C. Wu, C. Zhu and T. Chen, *J. Energy Chem.*, 2018, 27, 713–721.
25 V. W. Lueth, P. C. Goodell and N. E. Pngitore, *Econ. Geol.*, 1990, 85, 1462–1472.
26 D. Poleti, L. Karanović, T. Balić-Žunić and I. Gržetić, *Neues Jahrb. Mineral., Abh.*, 2012, 189, 177–187.
27 L. F. Lundegaard, R. Miletich, T. Balic-Zunic and E. Makovicky, *Phys. Chem. Miner.*, 2003, 30, 463–468.
28 L. F. Lundegaard, E. Makovicky, T. Boffa-Ballaran and T. Balic-Zunic, *Phys. Chem. Miner.*, 2005, 32, 578–584.
29 M. R. Filip, C. E. Patrick and F. Giustino, *Phys. Rev. B: Condens. Matter Mater. Phys.*, 2013, 87, DOI: 10.1103/PhysRevB.87.205125.
30 A. Kyono and M. Kimata, *Am. Mineral.*, 2004, 89, 932–940.
31 J. Liu, J. Liu, J. Li, H. Xie, J. Wang, J. Deng, C. Feng, F. Qi and N. Zhang, *Int. Geol. Rev.*, 2008, 50, 163–176.
32 G. Springer, *Mineral. Mag.*, 1969, 37, 294.
33 P. S. Nair, T. Radhakrishnan, N. Revaprasadu, G. A. Kolawole and P. O'Brien, *Chem. Commun.*, 2002, 564–565.
34 S. Ghosal and R. O. Sack, *Mineral. Mag.*, 1999, 63, 723–733.
35 J. Chang and E. R. Waclawik, *RSC Adv.*, 2014, 4, 23505–23527.
36 A. V. Nikam, B. L. V. Prasad and A. A. Kulkarni, *CrystEngComm*, 2018, 20, 5091–5107.
37 M. Leszczynski, E. Litwin-Staszewska and T. Suski, *Acta Phys. Pol., A*, 1995, 88, 837–840.
38 M. D. Khan, M. Aamir, G. Murtaza, M. A. Malik and N. Revaprasadu, *Dalton Trans.*, 2018, 47, 10025–10034.
39 W. N. Kun, S. Mlowe, L. D. Nyamen, P. T. Ndifon, M. A. Malik, O. Q. Munro and N. Revaprasadu, *Chem.–Eur. J.*, 2016, 22, 13127–13135.
40 R. Kellner, G. St. Nikolov and N. Trenda lova, *Inorg. Chim. Acta*, 1984, 84, 233–239.
41 Y. Liu and E. R. T. Tiekink, *CrystEngComm*, 2005, 7, 20.
42 L. Chen, H. Deng, J. Cui, J. Tao, W. Zhou, H. Cao, L. Sun, P. Yang and J. Chu, *J. Alloys Compd.*, 2015, 627, 388–392.

24 J. He, L. Sun, K. Zhang, W. Wang, J. Jiang, Y. Chen, P. Yang and J. Chu, *Appl. Surf. Sci.*, 2013, 264, 133–138.
25 R. A. Groom, A. Jacobs, M. Cepeda, R. Drummey and S. E. Latturner, *Inorg. Chem.*, 2017, 56, 12362–12368.
26 S. Tanuma, C. J. Powell and D. R. Penn, *Surf. Interface Anal.*, 1994, 21, 165–176.
27 J. Grigas, E. Talik and V. Lazauskas, *Phys. Status Solidi B*, 2002, 232, 220–230.
47 K. Uchida and A. Ayame, *Surf. Sci.*, 1996, 357–358, 170–175.
48 V. P. Zakaznova-Herzog, S. L. Harmer, H. W. Nesbitt, G. M. Bancro□, R. Flemming and A. R. Pratt, *Surf. Sci.*, 2006, 600, 348–356.
49 C. D. Wagner, *Faraday Discuss. Chem. Soc.*, 1975, 60, 291.
50 A. A. Audi and P. M. A. Sherwood, *Surf. Interface Anal.*, 2000, 29, 265–275.
51 J. Sun, X. Shen, L. Guo, G. Wang, J. Park and K. Wang, *Nanoscale Res. Lett.*, 2010, 5, 364–369.
52 J. Wang, Y. Qiao, T. Wang, H. Yu, Y. Feng and J. Zhang, *CrystEngComm*, 2019, 21, 554–562.
53 M. J. Seong, H. Alawadhi, I. Miotkowski, A. K. Ramdas and S. Miotkowska, *Solid State Commun.*, 1999, 112, 329–334.
54 T. Alqahtani, M. D. Khan, D. J. Kelly, S. J. Haigh, D. J. Lewis and P. O'Brien, *J. Mater. Chem. C*, 2018, 6, 12652–12659.
55 V. Kaltenhauser, T. Rath, W. Haas, A. Torvisco, S. K. Müller, B. Friedel, B. Kunert, R. Saf, F. Hofer and G. Trimmel, *J. Mater. Chem. C*, 2013, 1, 7825.
56 S. Kharbish, E. Libowitzky and A. Beran, *Eur. J. Mineral.*, 2009, 21, 325–333.
57 M. Medles, N. Benramdane, A. Bouzidi, K. Sahraou, R. Miloua, R. Desfeux and C. Mathie, *J. Optoelectron. Adv. Mater.*, 2014, 16, 726–731.
58 G. Wang and C. L. Cheung, *Mater. Lett.*, 2012, 67, 222–225.
59 J. Ota, P. Roy, S. K. Srivastava, B. B. Nayak and A. K. Saxena, *Cryst. Growth Des.*, 2008, 8, 2019–2023.
60 I. Zumeta-Dubé, J.-L. Ortiz-Quiñonez, D. Díaz, C. Trallero-Giner and V.-F. Ruiz-Ruiz, *J. Phys. Chem. C*, 2014, 118, 30244–30252.
61 B. Minceva-Sukarova, M. Najdoski, I. Grozdanov and C. J. Chunnilall, *J. Mol. Struct.*, 1997, 410–411, 267–270.

Available online at www.derpharmachemica.com

Scholars Research Library

Der Pharma Chemica, 2015, 7(5):101-106
(http://derpharmachemica.com/archive.html)

ISSN 0975-413X
CODEN (USA): PCHHAX

Antimicrobial and antioxidant studies on some transition metal complexes derived from the Schiff base ligand, 4-hydroxypent-3-en-2-ylideneaminophenol

Francis K. Ngounoue[1], Evans N. Mainsah[2], Aseng M. Conde[3], Awawou G. Paboudam[1], Sally-Judith E. Ntum[1], Walter K. Ndamukong[1], Choumkeu Mbakop Vanessa[1] and Peter T Ndifon[1*]

[1]Department of Inorganic Chemistry, Faculty of Science, University of Yaoundé1, Yaoundé, Cameroon
[2]Department of Chemistry, University of Buea, Buea, Cameroon
[3]Department of Inorganic Chemistry, Faculty of Science, University of Douala, Cameroon

---

ABSTRACT

A series of metal complexes have been synthesised using the Schiff base ligand, 4-hydroxypent-3-en-2-ylideneaminophenol, (L_1) derived from the condensation reaction of 2-aminophenol with acetyl acetone in ethanol. This series of M-L_1 complexes (M=Fe(III),Co(II),Mn(II), Cu(II) and Zn(II)) were characterized by spectroscopic techniques (IR, UV-visible), elemental analysis, and conductivity measurement. The analytical results reveal that the Schiff base acted as a tridentate ligand and coordinated to the metal ion in a 1:1 M: L stoichiometric ratio. The Fe(III), Mn(II) and Co(II) complexes showed octahedral geometry, while the Zn(II) and Cu(II) complexes showed tetrahedral geometry. Invitro antibacterial activity of the Schiff base ligand and its metal complexes carried out on four bacterial strains (E. coli, P. aeruginosa, S. typhi, S. aureus) and four fungal strains (C. albicans ATCC 12C, C. albicans ATCC P37037, C. albicans ATCC P37039, C. neoformans) showed higher activity of the complexes compared to the ligand. The Schiff base and its metal complexes showed antioxidant (free radical scavenging) activities when compared to garlic acid.

Keywords: Schiff base ligand, Metal complexes, antimicrobial, antioxidant activity.

INTRODUCTION

Schiff's bases are an important class of organic compounds due to their excellent coordination chemistry and their wide range of industrial and biological applications [1-3]. They are excellent coordinating compounds forming stable complexes with transition metal ions. Schiff's bases and their metal complexes have been used as catalysts for the epoxydation of olefins, photo-stabilisation of polymers [2, 3] and for the polymerisation of metals complexes. They have also been shown to exhibit a broad range of antifungal, anti-inflammatory, and antituberculosis properties [1, 4-6].

The common structural feature of Schiff's base ligands is the azomethine group, RHC=NR' where R and R' are alkyl or aryl groups. The presence of the imine group in Schiff's bases has been shown to account for the observed biological activities [7- 9]. Coordination of the Schiff bases to different metal atoms has shown to enhance the observed biological activity [9].

In recent decades, the incidence of bacterial resistance to existing drugs has become a major worldwide concern and necessitating the development of new molecules to fight this drug resistance by pathogens.

In this paper we report the synthesis of some metal complexes of the Schiff base ligand, 4-hydroxypent-3-en-2-ylideneaminophenol, (L_1) derived from 2-aminophenol and acetyl acetone as well as their antimicrobial properties. The free radical scavenging activity of the Schiff base ligand L_1 and that of the transition metal complexes is evaluated and compared to that of Garlic Acid (GA).

MATERIALS AND METHODS

All chemicals are of reagent grade and were used without further purification. The solvents were purified by standard methods. Elemental analysis for C, H, N were carried out on a Fisons instrument 1108 CHNS/O analyser while quantitative estimation of metals was done using the atomic absorption technique on the Perkins-Elmer model 2400 series II instrument. Infrared spectra were recorded on an Alpha-Bruke and Perkins Elmer spectrometer while UV-visible spectra were recorded on a HACH DR 3900 spectrophotometer. Conductivity measurements were made on 10^{-3}M solutions of the complexes in water at 25°C using the HANNA, Hi9811-5. Melting points were determined using Stuart Melting point Apparatus. Thermogravimetric analysis was carried out using Perkin-Elmer Pyris 6 TGA up to 900°C in a closed perforated aluminium pan.

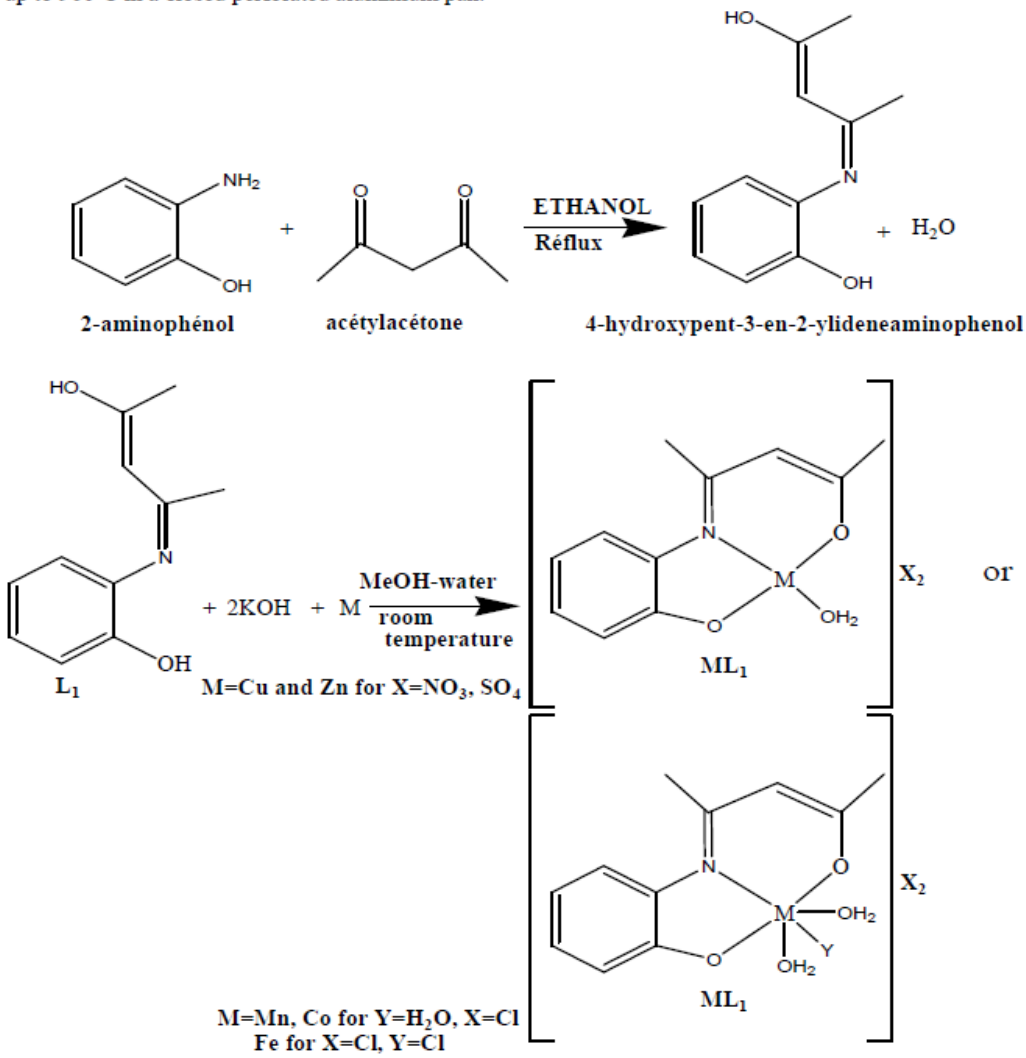

Figure 1: Schematic representation of the synthesis of the ligand, L_1 and its complexes

Synthesis

Synthesis of Schiff base

2-aminophenol (4. 4 g; 40 mmol) was dissolved in 20 mL of ethanol in a 100 mL beaker at 50-60°C. A solution of acetylacetone (4.12 mL; 40 mmol) predissolved in 5 mL of ethanol was added drop wise to the 2-aminophenol solution while stirring. The mixture was heated under reflux for 5 hours in a water bath at a temperature of 80°C and

allowed to cool. A yellow precipitate was obtained, which was filtered, dried and weighed (m = 5.54 g representing a yield of 72 %).

Synthesis of metal Complexes

All complexes were prepared by gradually adding a methanol solution of the ligand to an aqueous solution of the corresponding metal salt. The preparation of the Cobalt(II) complex will illustrate this synthesis. A solution of 4-hydroxypent-3-èn-2-ylidèneaminophénol (L_1) (0.78 g; 2.8 mmol) and KOH (0.11 g; 5.6 mmol) in 20 mL methanol was added gradually with stirring to a 10 mL aqueous solution of cobalt (II) nitrate (2.8 mmol). The mixture was stirred for (3-4) hrs at 25°C. The resulting solution was allowed to stand at room temperature until the solvent evapoprated to half its volume. The coloured complexes separated out and the product was filtered, washed several times with ethanol and recrystallized from hot ethanol and air dried at room temperature (yield 58-80 %). Figure 1 represents the scheme for the synthesis of the ligand and its complexes.

Antimicrobial activities

Antibacterial activities of ligand (L_1) and complexes were carried out against *E. coli, P. aeruginosa, S. typhi, S. aureu* and antifungal activities against *C. albicans* ATCC 12C, *C. albicans* ATCC P37037, *C. albicans ATCC P37039, C. neoformans* using Mueller Hilton agar solidified medium for bacterial strains and Sabouraud dextrose agar for the fungal strains. The disks impregnated test products were deposited on the surface of petri dishes seeded and incubated aerobically at 37°C for bacterial strains and at 25°C for fungal strains for 24 hours. The diameter (mm) of the area of inhibition around each disc was measured after 24 hours.

Antioxidant activity by DPPH radical scavenging activity

The 1, 1-Diphenyl-2-picryl hydrazyl (DPPH) radical scavenging activity was measured by spectrophotometric method at 517 nm. To a methanolic solution of DPPH (0.01 mmol) and garlic acid (GA), ligand(L_1) and complexes were added separately at different concentrations (0.5, 1.5, 2, 2.5 mg/mL) and an equal amount of methanol (2 mL) was added as control. After 30 min at 30°C, absorbance was measured. The activity was compared with that of garlic acid which was used as a standard antioxidant. The percentage of free radical scavenging was calculated by using the following equation.

$$Percentage\ of\ scavenging\ activity = \frac{A_o - A_e}{A_o} \times 100$$

Where A_o *corresponds to the absorbance of DPPH without sample and* A_e *corresponds to the absorbance of sample with complex or ligand.* A_o *is the absorbance of sample containing only DPPH (blank).* The % inhibitions were plotted against the respective concentrations used and from the graph, the the concentration causing 50% inhibitionIC_{50} values were calculated [10-12].

RESULTS AND DISCUSSION

Complexes obtained by reaction of the some metals ions with 4-hydroxypent-3-en-2-ylideneaminophenol show different melting points than the ligand indicating that new compounds are formed. They are all coloured, non-hygroscopic and thermally stable suggesting a strong metal-ligand bond. The complexes are soluble in common polar solvents such as water, ethanol, methanol and acetone. The molar conductance values of complexes measured in water range from 121.2-277.1 $\Omega^{-1}cm^2\ mol^{-1}$ suggesting that they are either 1:1 or 1:2 type electrolytes [13]. All analytical and physical data are shown in Table 1.

The azomethine IR band of the free ligand occurs at 1650 cm^{-1}. This band is shifted to 1610-1637 cm^{-1} on coordination, indicating the involvement of the azomethine nitrogen in coordination.

This is also confirmed by the presence of new bands around 491-409 cm^{-1} assigned to metal-Nitrogen bond [14]. The absence of the phenolic (-OH) band in all the spectra of the metal complexes suggests the involvement of the phenolic oxygen in bonding through deprotonation of the OH group. The band at 1250 cm^{-1} in the free ligand attributed to the =C-O stretch is shifted to about 1200 cm^{-1} in the complexes while new bands are observed at 528-580 cm^{-1} which could be assigned to the metal-oxygen bond.

The electronic absorption spectra of Mn(II) and Fe(III) complexes revealed bands at 23,809 cm^{-1} and 22,936 cm^{-1} respectively which can be attributed to the $^6A_{1g} \rightarrow {}^4T_{2g}$ (G) transition suggesting octahedral environment[15]. The spectrum of cobalt revealed two bands at 22,471 cm^{-1} and 19,230 cm^{-1} attributed for the$^4T_{1g}(F) \rightarrow {}^4T_{1g}(P)$ transition also suggesting the octahedral geometry [15]. The electronic spectrum of Cu(II) complex shows bands at 22,727 cm^{-1} assigned $^2B_{1g} \rightarrow {}^2A_{1g}$ transition indicated the square-planar geometry. The absence of any band below 10000 cm^{-1} excludes the possibility of tetrahedral geometry [16].

Table 1: Physical Properties and Elemental analytical data for L_1 and its Metal Complexes

Compound	Colour	Melting point °C	Molar conductance ($ohm^{-1} cm^2 mol^{-1}$)	Elemental analyses Expt. (Calc.)		
				C	H	N
$L_1 = C_{11}H_{13}NO_2$	Yellow	192 °C	—	69.21.(69.09)	6.75.(6.85)	7.35(7.32)
$[MnL_1(H_2O)_2]Cl_2$ (MnL_1)	Reddish brown	>260 °C	131.7	37.52.(37.63)	4.13(4.31)	4.42(3.99)
$[Fe\ L_1Cl(H_2O)_2]Cl_2.H_2O$ (FeL_1)	Rust brown	>260 °C	277.1	32.85(32.58)	3.92(4.23)	3.95(3.45)
$[ZnL_1H_2O]SO_4.5H_2O$ (ZnL_1)	Pale yellow	>260 °C	121.2	28.96(28.80)	4.35(5.05)	3.02(3.05)
$[Co\ L_1(H_2O)_3]\ Cl_2$ (CoL_1)	Dark brown	160°C	138.4	35.48(35.41)	4.46(4.59)	3.72(3.75)
$[Cu\ L_1\ H_2O](NO_2)_2$ (CuL_1)	Green	> 360 °C	134.7	34.85(33.47)	2.88(3.32)	10.85(10.64)

Thermo gravimetric analysis

The Thermogravimetric analysis of Fe(III) complex is used to exemplify the decomposition of these metal complexes and shows a mass loss at 78°C corresponding to the loss of lattice water molecule . The second mass loss obtained at 210°C (80 %) corresponds to the loss of Schiff base ligand which is probably decomposed into gases. At 465°C, the thermogram shows a residue representing 4% mass corresponding to the metal oxide residue [17-20].

The differential thermal analysis (DTA) curve shows endothermic processes at 75-110°C consistent with the loss of lattice water molecule and the endothermic processes at 150-250°C corresponding to the decomposition of Schiff base ligand and the formation of iron oxide residue.

Antimicrobial activity

The antimicrobial activities of the ligand L_1 and the transition metal complexes were evaluated for their *in vitro* antibacterial activities against *E. coli, P. aeruginosa, S. typhi, S. aureus,*and antifungal activities against *C. albicans* ATCC 12C, *C. albicans* ATCC P37037, *C. albicans ATCC P37039 and C. Neoformans.*

Antimicrobial activity was evaluated by measuring the diameter of the inhibition zones (mm) observed with respect to each microbial strain, using a calliper. Each test was performed three times and the results are shown on Table 2.

The ligand L_1 shows moderate activity on the bacteria *E. coli*, *P. aeruginosa,S. aureus*, and on the fungi strains, *C. albicans ATCC12C* because the DZI range between 10-24 mm.

The MnL_1 complex (L_1 =4-hydroxypent-3-en-2-ylideneaminophenol) showed low activity on both bacterial and fungal strains while CoL_1 and CuL_1 complexes exhibited moderate activity on most of the bacterial strains. FeL_1, CoL_1 and ZnL_1 complexes also showed moderate activity on some of the fungal strains. CuL_1 complex exhibited antifungal activities which were higher than the reference antibiotic.

The DZI values of show that most of the metal complexes with 4-hydroxypent-3-en-2-ylideneaminophenol as ligand are active on the bacteria and yeast strains used for this study. It is clear from this study that coordination of the Schiff base affects the biological activity of the ligand. Coordination enhances the activity for CuL_1 while CoL_1, ZnL_1, FeL_1 and MnL_1 complexes showed less activity compared to the reference antibiotics and the ligand.

Table 2: Growth Inhibition Zone of Microbes in mm.

Compound	Bacteria				Fungi			
	Escherichia coli	*Pseudomonas aeruginosa*	*Salmonella typhi*	*Staphylococcus aureus*	*Candida albicans ATCC 12C*	*Candida albicans ATCC P37037*	*Candida albicans ATCC P37039*	*Cryptococcus neoformans*
L_1	17,5±0,70	12±0	0±0	11,5±0,70	24±0	5±7,07	0±0	6±0
MnL_1	6±0	6±0	10,33±0,57	7±0	6±0	6±0	6±0	6±0
FeL_1	7,66±1,15	6±0	11,33±0,57	6±0	12,66±1,15	13,66±1,15	6,66±0,57	6±0
CoL_1	20±0	14±0	10±0	12,5±0,70	10,5±0,70	15,5±2,12	14±1,41	12,5±0,70
CuL_1	12±1,41	12±0	0±0	11,5±0,70	30±5,65	22,5±2,12	26±0	10±0
ZnL_1	7,33±0,57	6±0	6±0	8,66±1,15	9±0	13,33±0,57	7±0	6±0
Ciprofloxacine	14±0	28±1,73	30±0	29±1,73	/	/	/	/
Doxycycline	12±0	28,5±2,12	29±1,73	13,33±1,52	/	/	/	/
Fuconazole	/	/	/	/	19±3,46	19,66±0,57	29,66±0,57	12,66±1,15
Nystatine	/	/	/	/	28,33±1,52	12,33±0,57	19±1	15±0

The antioxidant (radical scavenging) activity of 1, 1- Diphenyl-2-picryl hydrazyl (DPPH)

Figures 1(a) and 1(b) show the free radical scavenging activity of Garlic Acid (GA), the Schiff base) ligand L_1 and the transition metal complexes. At a concentration of 5 mg /mL, the scavenging activities of the CuL_1, L_1, ZnL_1, CoL_1 and MnL_1 are 92.58, 86.44, 82.30, 66.02, 27.75% respectively, while at the same concentration, the activity of garlic acid (reference antioxidant) is 91.13 %. This means that CuL_1, L_1 and ZnL_1 exhibited significant free radical scavenging activity. The scavenging activities of CoL1 and MnL_1 were less significant. The IC_{50} of CuL_1, L_1, ZnL_1, and CoL_1 are 0.21, 0.37, 0.45 and 1.16 mg/mL respectively. The IC_{50} of CuL_1 is less than the IC_{50} of GA which is 0.26 mg/mL suggesting that CuL_1 complex is more active. The order of the IC_{50} is thus, CuL_1>AG> L_1>ZnL_1>CoL_1 with CoL_1 exhibiting the least antioxidant activity.

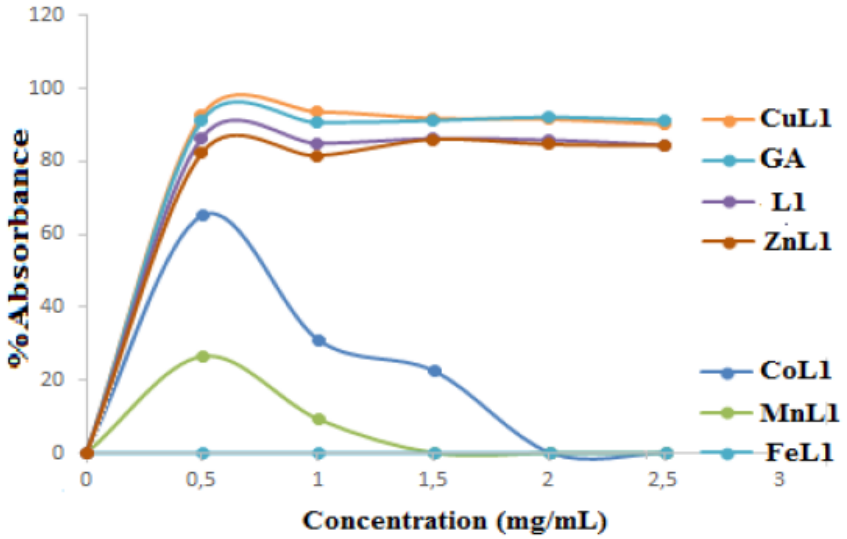

4a) The scavenging activity of the DPPH radical

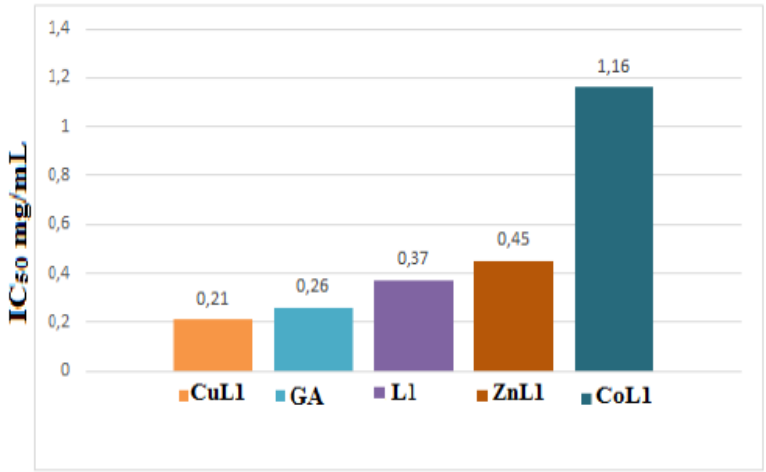

4b) IC_{50} for GA, L_1 and M-L_1 complexes

Figure 4: Free radical scavenging activity of the Garlic Acid (GA), the Schiff base ligand L_1 and the transition metal complexes

CONCLUSION

The metal complexes of 4-hydroxypent-3-en-2-ylidèneaminophenol have tetrahedral and octahedral geometry and exhibited strong to moderate antibacterial activities. Cu(II) and Co(II) complexes are more effective as antibacterial agents than their precursor ligand. These compounds can serve as good targets for the design of antimicrobial

agents. All the compounds showed varying antioxidant (free radical scavenging) activities when compared to garlic acid.

Acknowledgement
The authors thank the University of Zululand in South Africa and the University of Reims Champagne-Ardenne, France for assisting with some of the analysis and the microbiology laboratory of the University of Dschang for the biological tests.

REFERENCES

[1] Gupta C., Satur K. *Coord. Chem. Rev.* (**2008**), **52**, 1420-1450.
[2] Sivasan M., Theodore david S. *J. Indian Chem. SOC*, (**2000**), 77, 220.
[3] Yousif E., Salih N., Salimon J. *J. Appl. Polym. Sci*, **120**, 2207-2214.
[4] Nejo A., Kolawole G., Ayorinde O., Muller J. *Inter. J. Drug. For. Res, (***2011**), **2(4)**, 196-209.
[5] Evans N Mainsah, Peter T Ndifon, Emmanuel N Nfor and Julius N Njapba. *Bull. Chem. Soc3. Eth.* (**2013**), **27(3)**, 1-10.
[6] Salomon J., Salih N., Ibrahim H., Yousif E. *Asian. J. Chem*, **22(7)**, 5289-5296.
[7] Guo Z., Xing R., Liu S., Zhong Z., Ji X., wang L. *Carbohydr. Res*, (**2007**), **342(10)**, 1329-1332.
[8] Li Y., Yang ZS., Zhang H., Cao BJ., Wang FD. *Bioorg. Med. Chem*, (**2003**), **11**, 4363-4368.
[9] Usharani M., Akila E., Rajavel R. *J. Chem. Pharm. Res,* (**2012**), **4(1)**, 726-731.
[10] Sreejayan N., Rao M. *J. Pharm. Pharmacology,* (**1990**), **58**, 237.
[11] Molyneux P., klanakarin S. *J. Sci. Technol,* (**2004**), **26**,211-219.
[12] Topcu G., Ertas A., Kolak U., Ulubelen M. *Arkivoc,* (**2007**), 7, 195-208.
[13] Manjula B., Arulantony S. *Asian. J. Bio. Pharm. Res*, (**2013**), **3**,4.
[14] Shamsipur M., Sadeghi S., Naeimi H., Sharghi H. *Polish pjc*, (**2000**), **74**, 231–238.
[15] Lappert M, (**1968**), Physical Inorganique Chemistry, ED :A. B. P LEVEL, *elsever plublishing company*, Toronto, p 362.
[16] Sunitha M., Jogi P., Gyanakumari C. *J. Chem. Pharm. Res,* (**2012**), **4(3),** 1553-1561.
[17] alkanes with transition metal ions and their thermokinetic and biological studies. *J. Coord. Chem*, (**2005**), **58**, 1145.
[18] Modi C., Patel S., Patel M. *J. Therm. Anal. Cal,* (**2007**), **87**, 441.
[19] Mohamed G., Abd El-Wahab Z. *J. Therm. Anal. Cal.*, (**2003**), **73**, 347.
[20] Mohamed G., Nour El-Dien F., Nadia El-Gamel A. *J. Therm. Anal. Cal,* (**2002**), **67**, 135.

3. Spectroscopic information

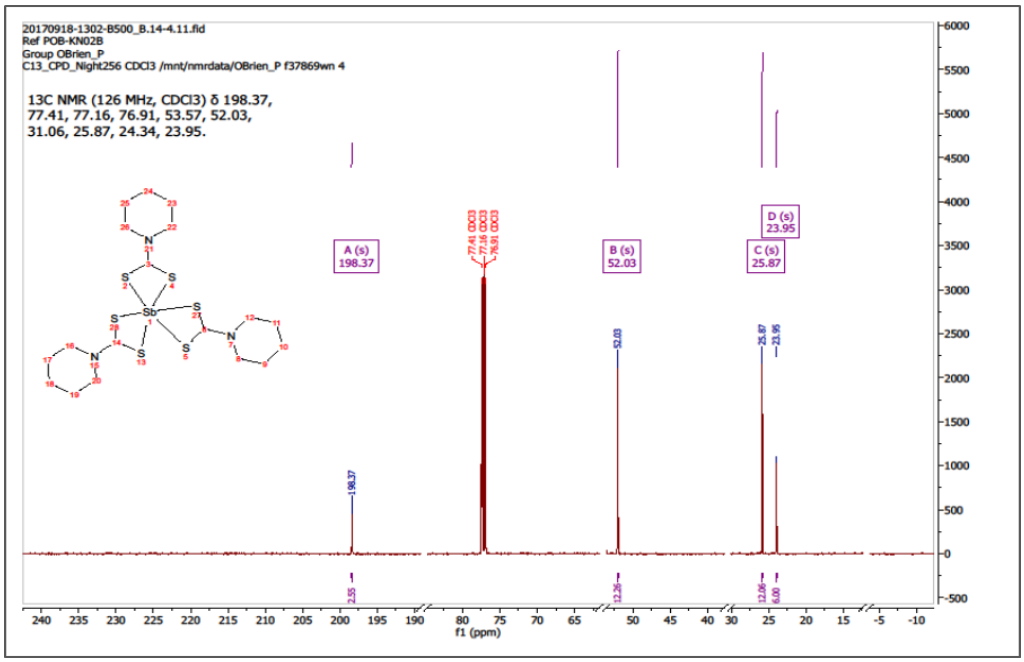

^{13}C NMR spectrum for [Sb(S_2CPip)$_3$]

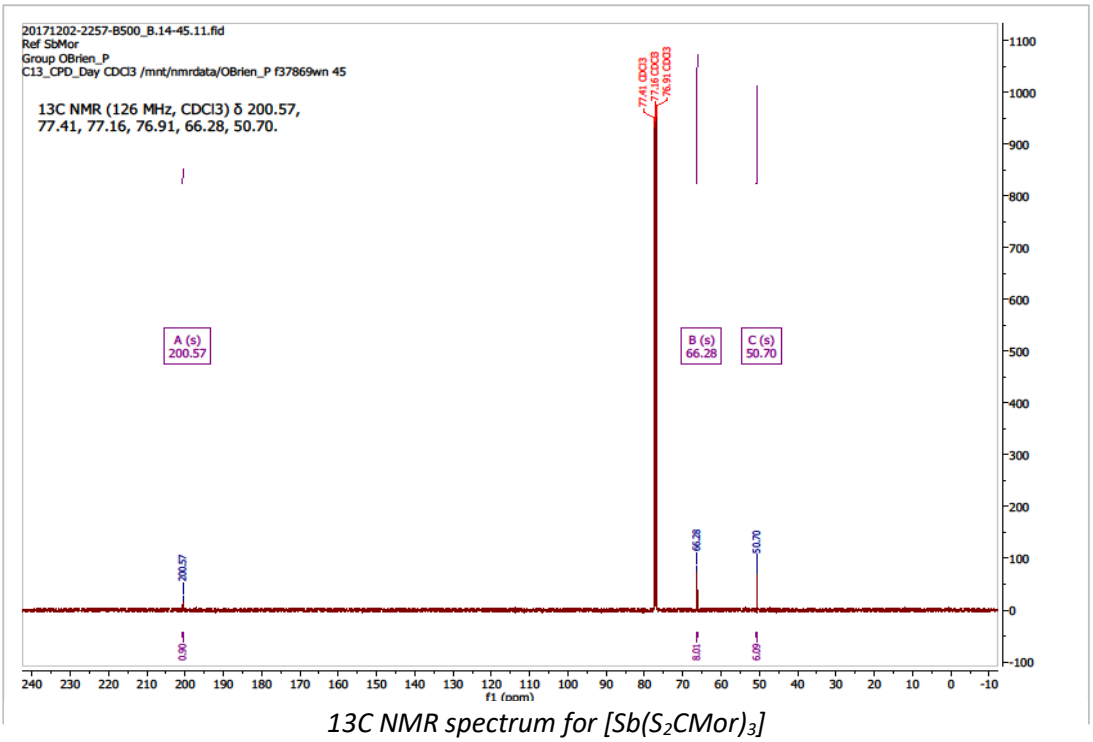

13C NMR spectrum for [Sb(S_2CMor)$_3$]

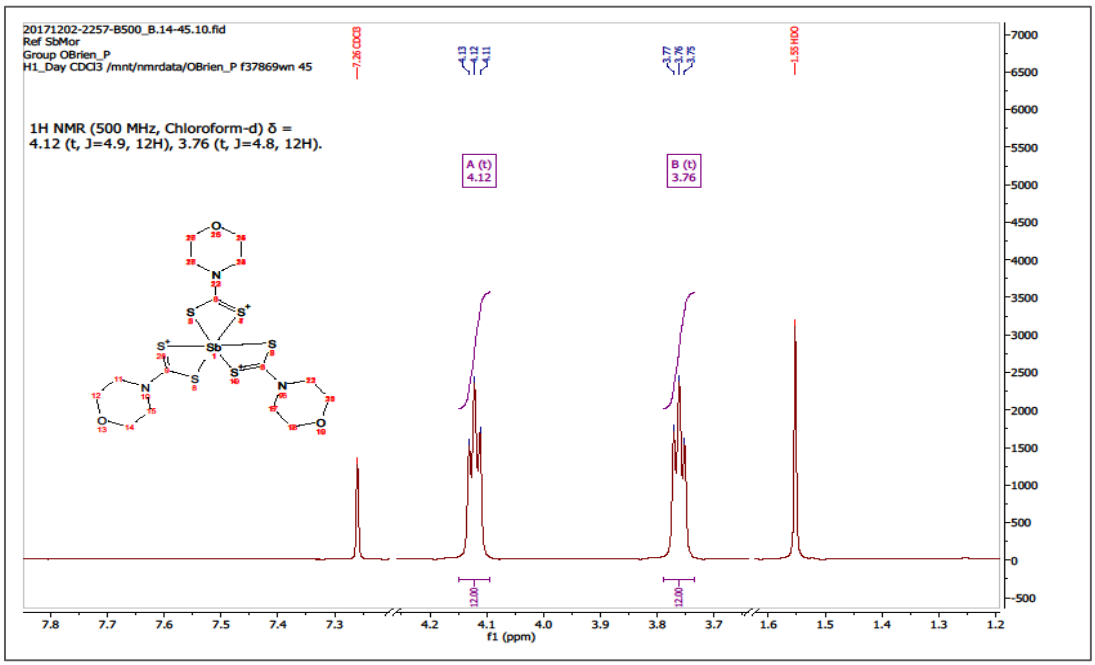

1H NMR spectrum for [Sb(S_2CMor)$_3$]

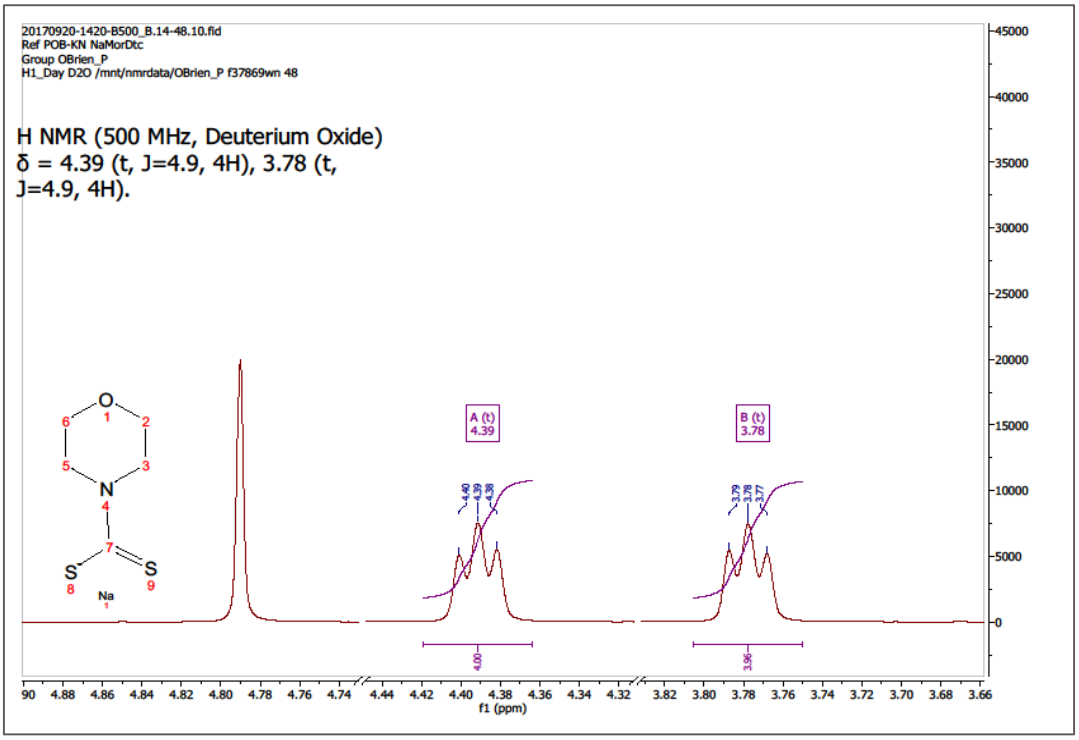

1H NMR spectrum for Na(S_2CMor)

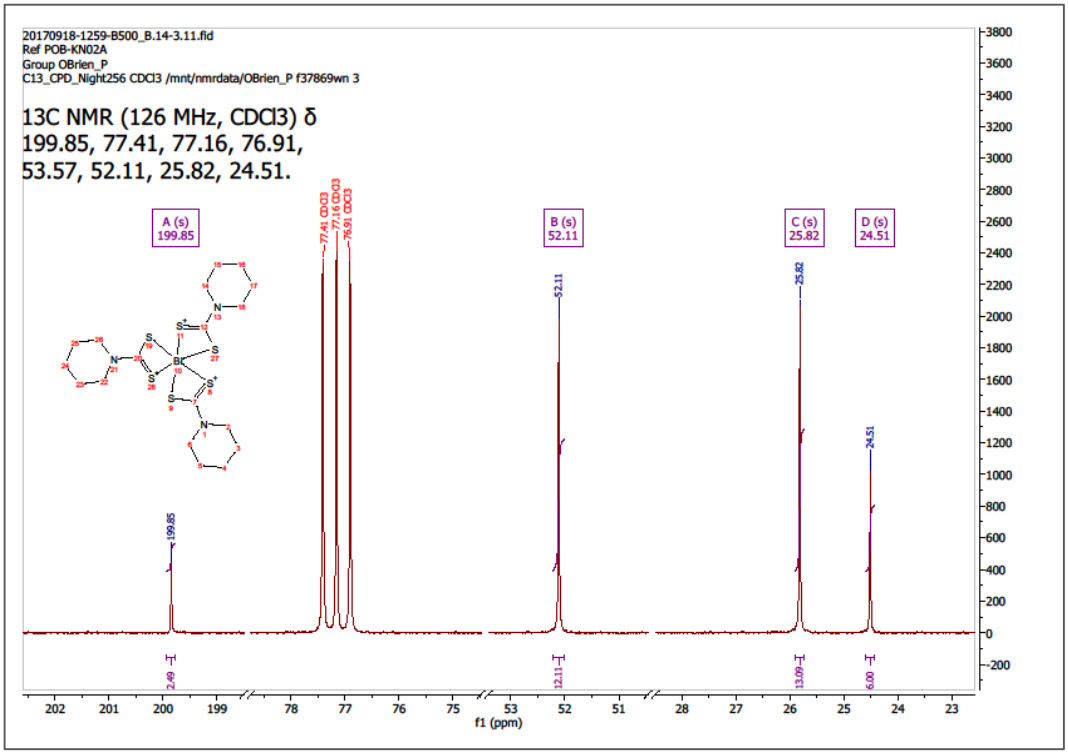

[1]H NMR spectrum for [Bi(S_2CPip)$_3$]

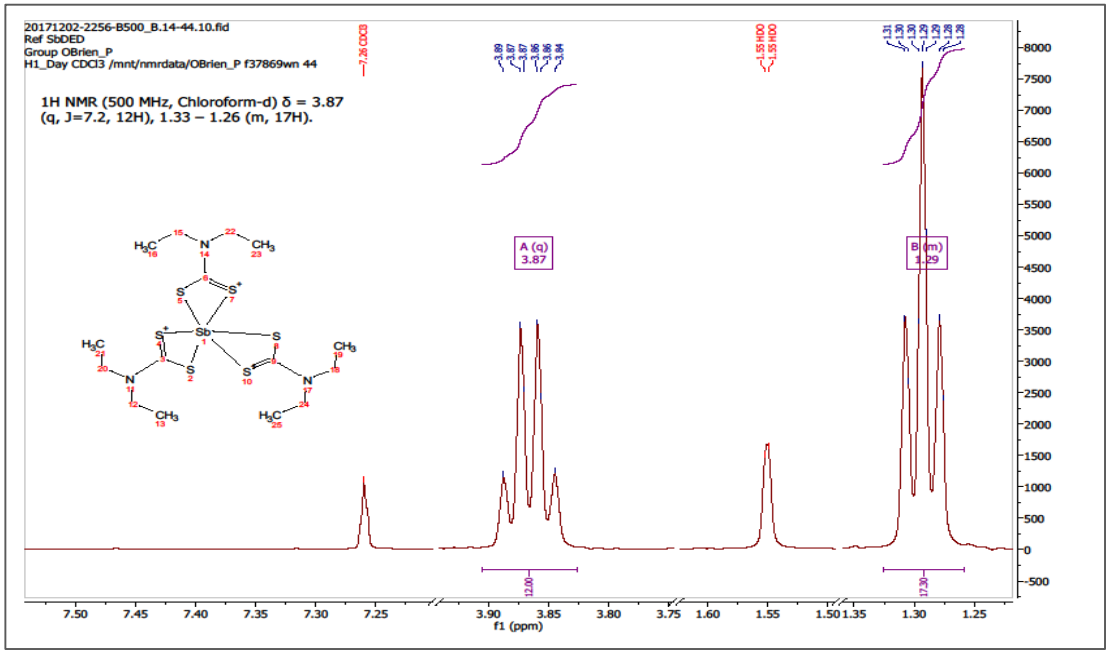

1H NMR spectrum for [Sb(S_2CDed)$_3$]

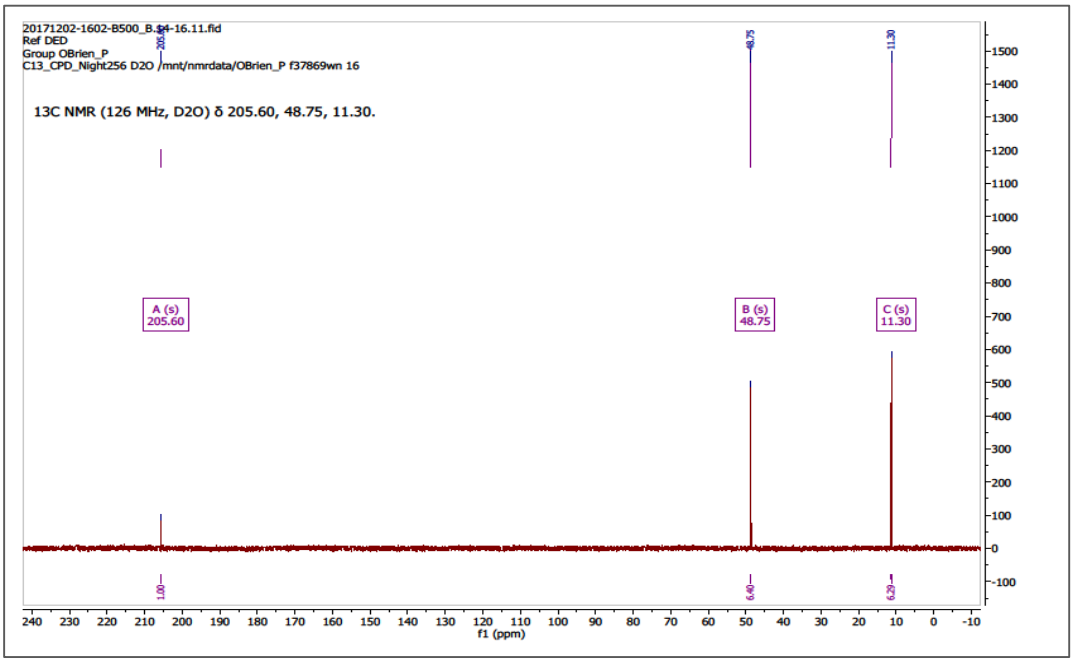

^{13}C NMR spectrum for Na(S_2CDed)

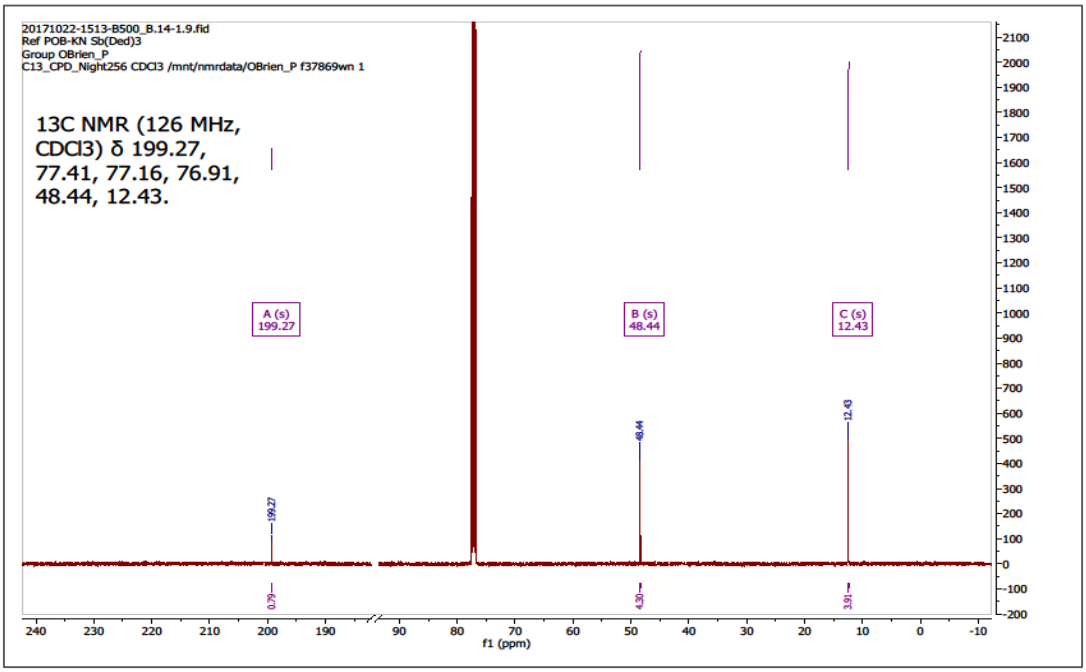

^{13}C NMR spectrum for [Sb(S$_2$CDed)$_3$]

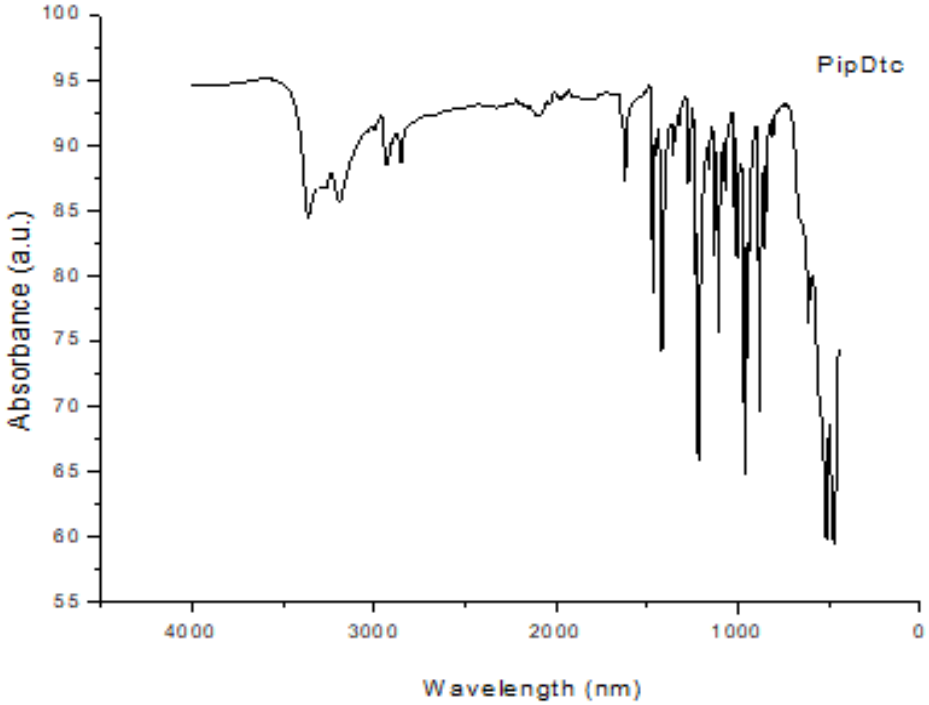

FT-IR spectrum of $Na(S_2CPip)$

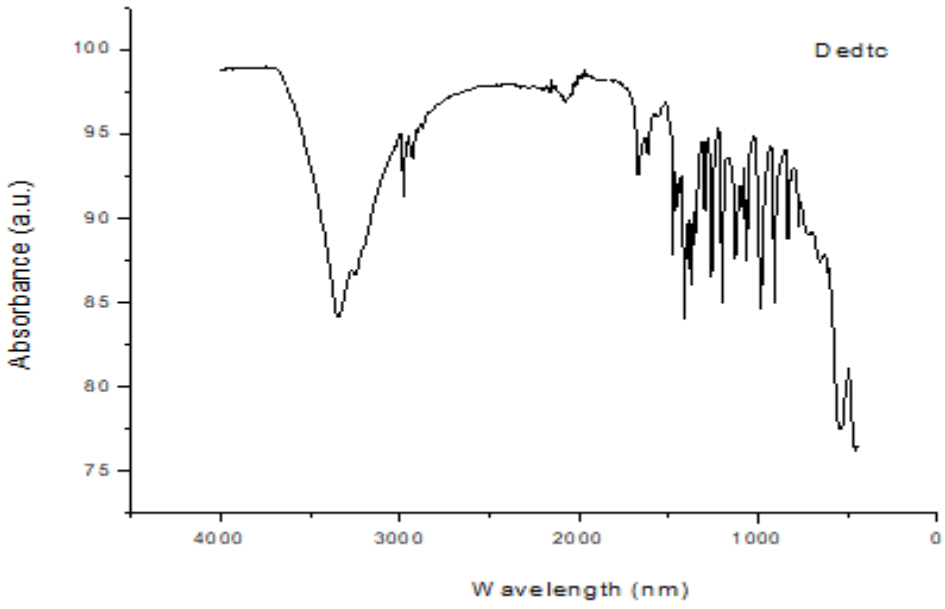

FT-IR spectrum of $Na(S_2CDed) \cdot 3H_2O$

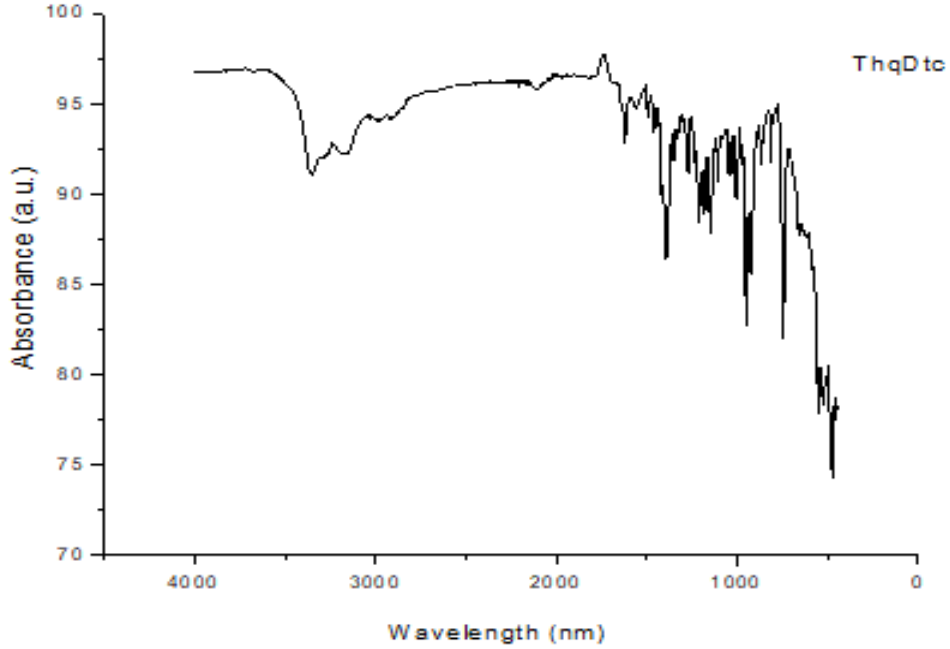

FT-IR spectrum of $Na(S_2CThq) \cdot 4H_2O$

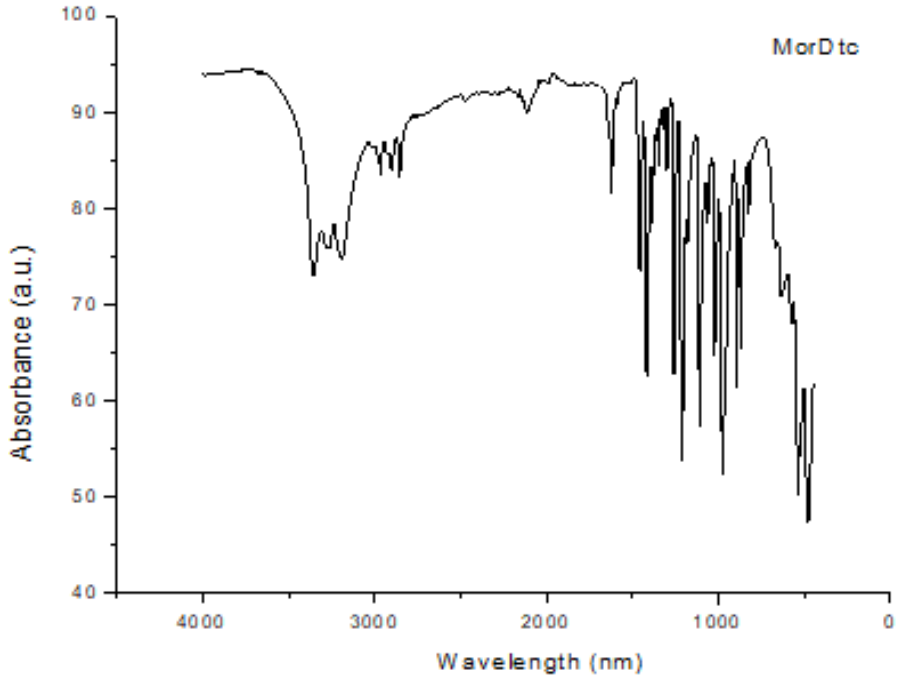

FT-IR spectrum of $Na(S_2CMor) \cdot 2H_2O$

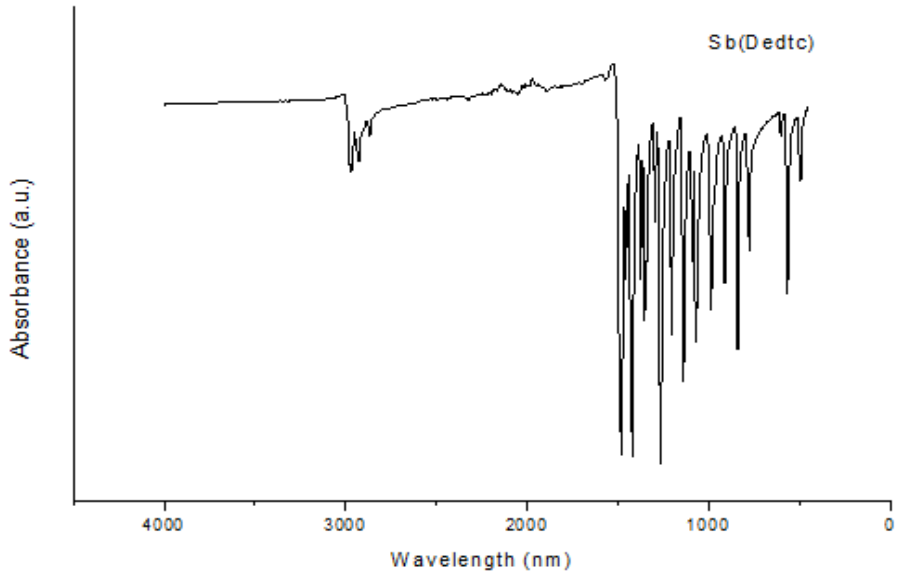

FT-IR spectrum of [Sb(S_2CDed)$_3$]

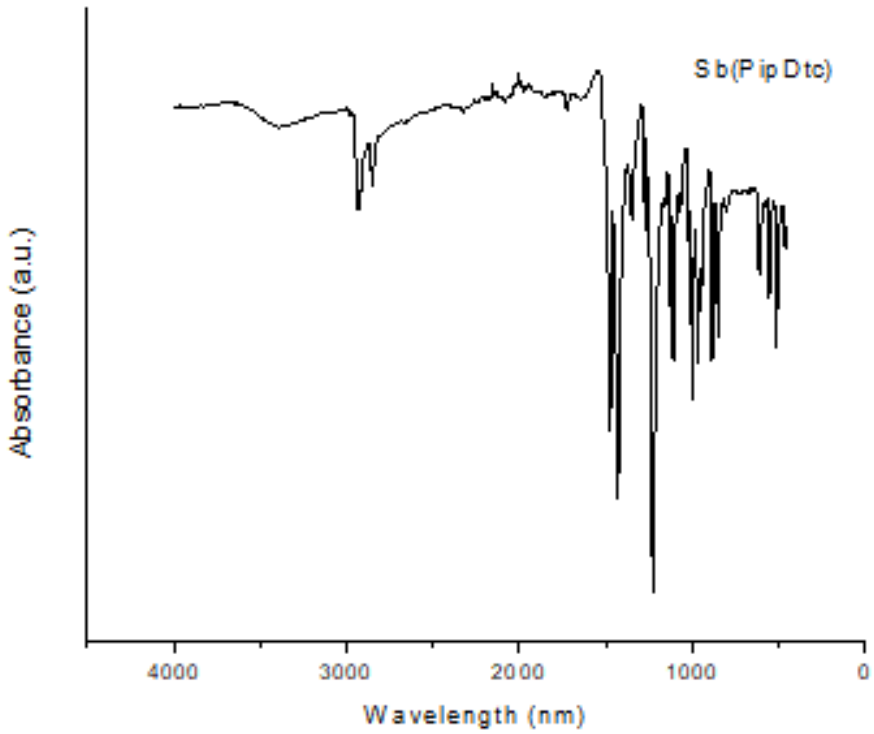

FT-IR spectrum of Sb(S2CPip)3 ·3H2O

4. Crystallographic information

Crystallographic data for catena-(m2-nitrato-O,O')bis(piperi-dinedithiocarbam/ato)bismuth(III)

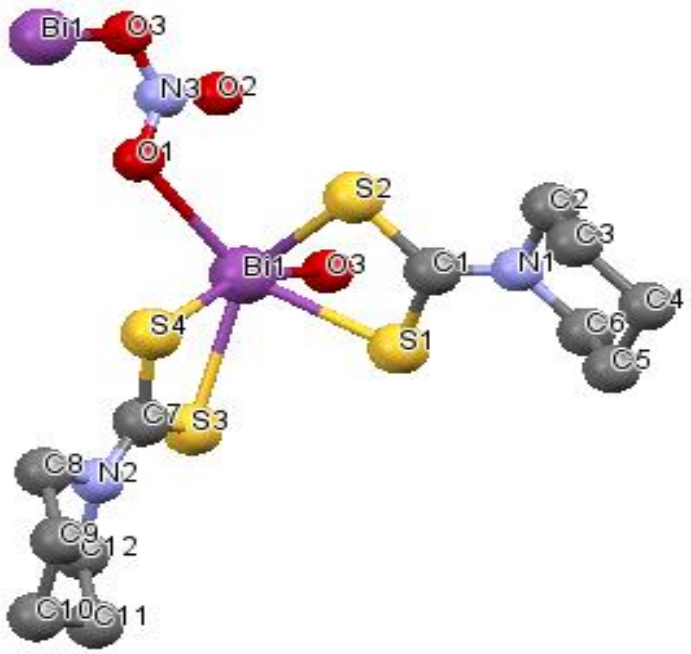

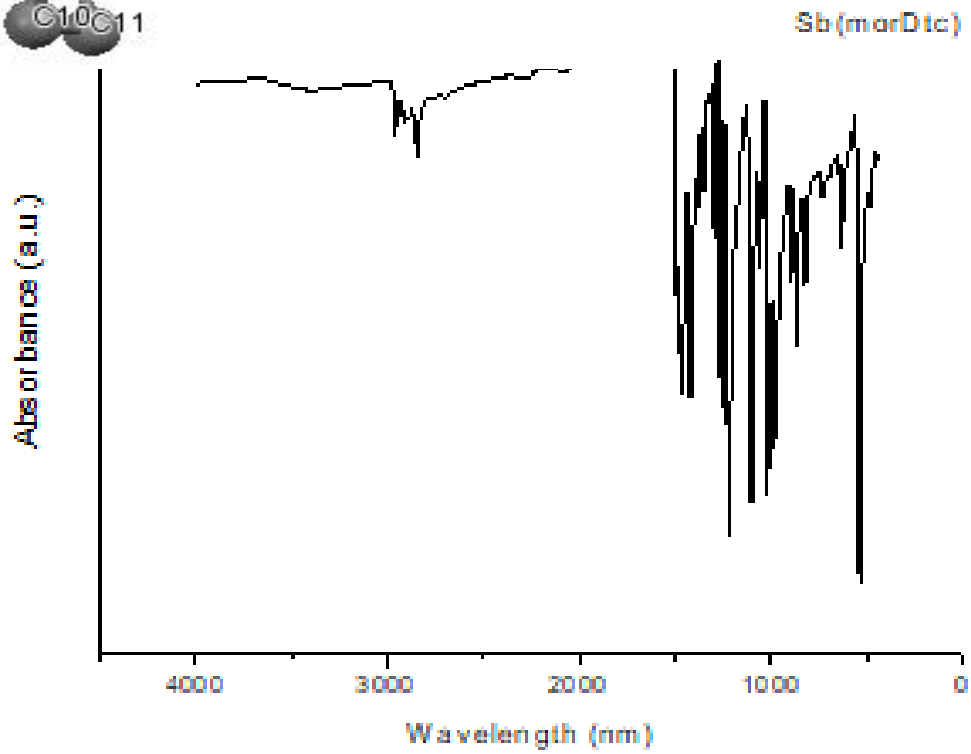

FT-IR spectrum of [Sb(S_2CMor)$_3$]

Experimental details

Crystal data	
Chemical formula	$C_{12}H_{20}BiN_3O_3S_4$
M_r	591.53
Crystal system, space group	Monoclinic, $P2_1/c$
Temperature (K)	100
a, b, c (Å)	13.712 (7), 6.172 (3), 22.415 (11)
β (°)	102.351 (7)
V (Å^3)	1853.0 (16)
Z	4
Radiation type	Mo $K\alpha$
μ (mm^{-1})	9.98
Crystal size (mm)	0.35 × 0.2 × 0.15
Data collection	Bruker *SMART APEX2* area detector
Diffractometer	
Absorption correction	Multi-scan
T_{min}, T_{max}	0.421, 0.746
No. of measured, independent and observed [$I > 2\sigma(I)$] reflections	67445, 5396, 5276
R_{int}	0.040
$(\sin\theta/\lambda)_{max}$ (Å^{-1})	0.717
Refinement	
$R[F^2 > 2\sigma(F^2)]$, $wR(F^2)$,	S 0.033, 0.073, 1.15
No. of reflections	5396
No. of parameters	208
H-atom treatment	H-atom parameters constrained
$w = 1/[\sigma^2(F_o^2) + (0.010P)^2 + 23.0841P]$ where $P = (F_o^2 + 2F_c^2)/3$	
$\Delta\rho_{max}$, $\Delta\rho_{min}$ (e Å^{-3})	3.10, −2.81

Fractional atomic coordinates and isotropic or equivalent isotropic displacement parameters (Å^2) for (catena-(m$_2$-nitrato-O,O')bis(piperi-dinedithiocarbamato)bismuth(III))

	x	*y*	*z*	U_{iso}*/U_{eq}
Bi1	0.33570 (2)	0.38279 (3)	0.50704 (2)	0.01091 (5)
S1	0.23371 (8)	0.63786 (19)	0.56656 (5)	0.0145 (2)
S2	0.16603 (9)	0.18712 (19)	0.53333 (6)	0.0149 (2)
S3	0.48622 (8)	0.65165 (17)	0.57158 (5)	0.01143 (19)
S4	0.44067 (9)	0.20245 (19)	0.60580 (5)	0.0158 (2)
C1	0.1433 (3)	0.4365 (7)	0.5625 (2)	0.0123 (8)
N1	0.0587 (3)	0.4789 (7)	0.5811 (2)	0.0165 (8)
C2	−0.0196 (4)	0.3132 (9)	0.5818 (2)	0.0191 (10)

H2A	−0.0010	0.1781	0.5651	0.023*
H2B	−0.0825	0.3613	0.5566	0.023*
C3	−0.0316 (4)	0.2774 (9)	0.6475 (3)	0.0230 (11)
H3A	−0.0847	0.1739	0.6477	0.028*
H3B	0.0297	0.2185	0.6718	0.028*
C4	−0.0562 (5)	0.4918 (10)	0.6752 (3)	0.0276 (12)
H4A	−0.0611	0.4687	0.7173	0.033*
H4B	−0.1202	0.5449	0.6528	0.033*
C5	0.0254 (4)	0.6609 (9)	0.6727 (3)	0.0240 (11)
H5A	0.0074	0.7983	0.6884	0.029*
H5B	0.0882	0.6138	0.6982	0.029*
C6	0.0373 (4)	0.6896 (8)	0.6069 (2)	0.0187 (9)
H6A	−0.0235	0.7501	0.5824	0.022*
H6B	0.0915	0.7897	0.6059	0.022*
C7	0.5140 (3)	0.4350 (7)	0.6217 (2)	0.0121 (8)
N2	0.5877 (3)	0.4429 (6)	0.67123 (17)	0.0122 (7)
C12	0.6574 (4)	0.6289 (8)	0.6835 (2)	0.0166 (9)
H12A	0.6279	0.7529	0.6597	0.020*
H12B	0.7188	0.5925	0.6709	0.020*
C11	0.6812 (4)	0.6884 (8)	0.7513 (2)	0.0171 (9)
H11A	0.6216	0.7450	0.7625	0.021*
H11B	0.7317	0.8010	0.7586	0.021*
C10	0.7188 (4)	0.4916 (8)	0.7912 (2)	0.0185 (9)
H10A	0.7292	0.5312	0.8340	0.022*
H10B	0.7821	0.4435	0.7832	0.022*
C9	0.6421 (4)	0.3079 (8)	0.7772 (2)	0.0179 (9)
H9A	0.6675	0.1812	0.8012	0.022*
H9B	0.5808	0.3522	0.7887	0.022*
C8	0.6204 (4)	0.2503 (8)	0.7095 (2)	0.0167 (9)
H8A	0.6802	0.1907	0.6991	0.020*
H8B	0.5687	0.1404	0.7013	0.020*
O1	0.3485 (3)	−0.0481 (6)	0.48383 (16)	0.0188 (7)
O3	0.2784 (3)	−0.2891 (6)	0.41649 (17)	0.0195 (7)
O2	0.2456 (3)	0.0555 (6)	0.40011 (17)	0.0216 (8)
N3	0.2908 (3)	−0.0933 (7)	0.43313 (18)	0.0145 (7)

Atomic displacement parameters (Å^2) for (mo_om_unizul_bip2_0m)

	U_{11}	U_{22}	U_{33}	U_{12}	U_{13}	U_{23}
Bi1	0.01101 (8)	0.01190 (8)	0.00865 (8)	−0.00085 (6)	−0.00052 (5)	0.00057 (6)
S1	0.0141 (5)	0.0125 (5)	0.0167 (5)	−0.0028 (4)	0.0031 (4)	−0.0020 (4)
S2	0.0145 (5)	0.0126 (5)	0.0172 (5)	−0.0023 (4)	0.0028 (4)	−0.0017 (4)
S3	0.0130 (5)	0.0091 (4)	0.0113 (5)	−0.0006 (4)	0.0005 (4)	0.0019 (4)
S4	0.0205 (5)	0.0113 (5)	0.0124 (5)	−0.0039 (4)	−0.0035 (4)	0.0025 (4)
C1	0.0121 (19)	0.0133 (19)	0.0100 (19)	−0.0015 (15)	−0.0008 (15)	−0.0015 (15)
N1	0.0138 (18)	0.0129 (18)	0.023 (2)	−0.0031 (15)	0.0038 (15)	−0.0023 (15)

C2	0.011 (2)	0.019 (2)	0.027 (3)	−0.0041 (17)	0.0026 (18)	−0.0007 (19)
C3	0.022 (2)	0.022 (2)	0.023 (3)	−0.003 (2)	0.000 (2)	0.009 (2)
C4	0.033 (3)	0.032 (3)	0.021 (3)	−0.006 (2)	0.010 (2)	0.001 (2)
C5	0.025 (3)	0.024 (3)	0.021 (3)	−0.004 (2)	0.002 (2)	−0.002 (2)
C6	0.017 (2)	0.014 (2)	0.025 (3)	0.0014 (17)	0.0044 (19)	0.0014 (18)
C7	0.016 (2)	0.0103 (18)	0.0107 (19)	0.0002 (15)	0.0033 (16)	−0.0022 (15)
N2	0.0147 (17)	0.0103 (16)	0.0101 (17)	−0.0016 (14)	−0.0010 (14)	0.0004 (13)
C12	0.018 (2)	0.014 (2)	0.016 (2)	−0.0048 (18)	−0.0008 (17)	0.0010 (17)
C11	0.019 (2)	0.017 (2)	0.013 (2)	0.0001 (18)	−0.0023 (17)	−0.0022 (17)
C10	0.021 (2)	0.020 (2)	0.012 (2)	0.0021 (19)	−0.0038 (17)	−0.0025 (18)
C9	0.026 (2)	0.017 (2)	0.009 (2)	0.0018 (18)	−0.0011 (18)	0.0013 (16)
C8	0.022 (2)	0.010 (2)	0.015 (2)	0.0014 (17)	−0.0015 (17)	0.0016 (16)
O1	0.0186 (17)	0.0178 (17)	0.0168 (17)	0.0017 (13)	−0.0036 (13)	−0.0023 (13)
O3	0.0274 (19)	0.0135 (16)	0.0173 (17)	−0.0015 (14)	0.0041 (14)	−0.0038 (13)
O2	0.0271 (19)	0.0188 (17)	0.0149 (17)	−0.0007 (15)	−0.0041 (14)	0.0068 (14)
N3	0.0174 (18)	0.0137 (18)	0.0132 (18)	−0.0010 (15)	0.0051 (14) −	0.0002 (14)

Geometric parameters (Å, º) for (catena-(m$_2$-nitrato-O,O')bis(piperi-dinedithiocarbamato)bismuth(III))

Bi1—S1	2.6480 (14)	C5—C6	1.530 (8)
Bi1—S2	2.7937 (16)	C6—H6A	0.9700
Bi1—S3	2.7980 (14)	C6—H6B	0.9700
Bi1—S4	2.6169 (14)	C7—N2	1.332 (6)
Bi1—O1	2.723 (4)	N2—C12	1.482 (6)
S1—C1	1.744 (5)	N2—C8	1.479 (6)
S2—C1	1.727 (5)	C12—H12A	0.9700
S3—C7	1.736 (5)	C12—H12B	0.9700
S4—C7	1.745 (5)	C12—C11	1.529 (7)
C1—N1	1.340 (6)	C11—H11A	0.9700
N1—C2	1.485 (6)	C11—H11B	0.9700
N1—C6	1.477 (6)	C11—C10	1.531 (7)
C2—H2A	0.9700	C10—H10A	0.9700
C2—H2B	0.9700	C10—H10B	0.9700
C2—C3	1.533 (8)	C10—C9	1.533 (7)
C3—H3A	0.9700	C9—H9A	0.9700
C3—H3B	0.9700	C9—H9B	0.9700
C3—C4	1.530 (9)	C9—C8	1.525 (7)
C4—H4A	0.9700	C8—H8A	0.9700
C4—H4B	0.9700	C8—H8B	0.9700
C4—C5	1.540(8)	O1—N3	1.269 (5)
C5—H5A	0.9700	O3—N3	1.265 (5)
C5—H5B	0.9700	O2—N3	1.257 (5)
S1—Bi1—S2	66.25 (5)	N1—C6—H6A	109.6
S1—Bi1—S3	78.32 (5)	N1—C6—H6B	109.6
S1—Bi1—O1	137.69 (9)	C5—C6—H6A	109.6
S2—Bi1—S3	134.65 (4)	C5—C6—H6B	109.6
S4—Bi1—S1	94.64 (5)	H6A—C6—H6B	108.1
S4—Bi1—S2	88.27 (5)	S3—C7—S4	117.6 (3)

S4—Bi1—S3	66.63 (4)	N2—C7—S3	122.2 (3)
S4—Bi1—O1	72.54 (8)	N2—C7—S4	120.1 (3)
O1—Bi1—S2	73.07 (9)	C7—N2—C12	121.8 (4)
O1—Bi1—S3	127.41 (8)	C7—N2—C8	122.4 (4)
C1—S1—Bi1	89.80 (16)	C8—N2—C12	114.3 (4)
C1—S2—Bi1	85.45 (16)	N2—C12—H12A	109.4
C7—S3—Bi1	85.04 (16)	N2—C12—H12B	109.4
C7—S4—Bi1	90.69 (16)	N2—C12—C11	111.2 (4)
S2—C1—S1	118.1 (3)	H12A—C12—H12B	108.0
N1—C1—S1	119.9 (4)	C11—C12—H12A	109.4
N1—C1—S2	122.1 (4)	C11—C12—H12B	109.4
C1—N1—C2	123.0 (4)	C12—C11—H11A	109.4
C1—N1—C6	123.4 (4)	C12—C11—H11B	109.4
C6—N1—C2	113.5 (4)	C12—C11—C10	111.4 (4)
N1—C2—H2A	109.8	H11A—C11—H11B	108.0
N1—C2—H2B	109.8	C10—C11—H11A	109.4
N1—C2—C3	109.6 (4)	C10—C11—H11B	109.4
H2A—C2—H2B	108.2	C11—C10—H10A	109.7
C3—C2—H2A	109.8	C11—C10—H10B	109.7
C3—C2—H2B	109.8	C11—C10—C9	109.7 (4)
C2—C3—H3A	109.6	H10A—C10—H10B	108.2
C2—C3—H3B	109.6	C9—C10—H10A	109.7
H3A—C3—H3B	108.1	C9—C10—H10B	109.7
C4—C3—C2	110.1 (4)	C10—C9—H9A	109.5
C4—C3—H3A	109.6	C10—C9—H9B	109.5
C4—C3—H3B	109.6	H9A—C9—H9B	108.1
C3—C4—H4A	109.6	C8—C9—C10	110.8 (4)
C3—C4—H4B	109.6	C8—C9—H9A	109.5
C3—C4—C5	110.3 (5)	C8—C9—H9B	109.5
H4A—C4—H4B	108.1	N2—C8—C9	111.1 (4)
C5—C4—H4A	109.6	N2—C8—H8A	109.4
C5—C4—H4B	109.6	N2—C8—H8B	109.4
C4—C5—H5A	109.7	C9—C8—H8A	109.4
C4—C5—H5B	109.7	C9—C8—H8B	109.4
H5A—C5—H5B	108.2	H8A—C8—H8B	108.0
C6—C5—C4	110.0 (4)	N3—O1—Bi1	109.4 (3)
C6—C5—H5A	109.7	O3—N3—O1	119.5 (4)
C6—C5—H5B	109.7	O2—N3—O1	120.1 (4)
N1—C6—C5 1	10.3 (4)	O2—N3—O3	120.4 (4)
Bi1—S1—C1—S2	6.3 (3)	S4—C7—N2—C8	9.0 (6)
Bi1—S1—C1—N1	−172.8 (4)	C1—N1—C2—C3	117.6 (5)
Bi1—S2—C1—S1	−6.0 (2)	C1—N1—C6—C5	−117.8 (5)
Bi1—S2—C1—N1	173.1 (4)	N1—C2—C3—C4	56.8 (6)
Bi1—S3—C7—S4	−0.5 (2)	C2—N1—C6—C5	58.2 (6)
Bi1—S3—C7—N2	−179.9 (4)	C2—C3—C4—C5	−57.0 (6)
Bi1—S4—C7—S3	0.6 (3)	C3—C4—C5—C6	56.3 (6)
Bi1—S4—C7—N2	179.9 (4)	C4—C5—C6—N1	−55.9 (6)
Bi1—O1—N3—O3	−173.4 (3)	C6—N1—C2—C3	−58.4 (5)
Bi1—O1—N3—O2	5.9 (5)	C7—N2—C12—C11	140.2 (4)

S1—C1—N1—C2	−177.1 (4)	C7—N2—C8—C9	−139.2 (5)
S1—C1—N1—C6	−1.6 (6)	N2—C12—C11—C10	53.6 (5)
S2—C1—N1—C2	3.8 (7)	C12—N2—C8—C9	54.4 (6)
S2—C1—N1—C6	179.3 (4)	C12—C11—C10—C9	−55.7 (6)
S3—C7—N2—C12	−6.3 (6)	C11—C10—C9—C8	56.5 (5)
S3—C7—N2—C8	−171.6 (4)	C10—C9—C8—N2	−55.5 (5)
S4—C7—N2—C12	174.4 (3)	C8—N2—C12—C11	−53.4 (5)

Crystal data for tetrakis(m-nitrato)te-trakis[bis(tetrahydroquinolinedithiocarbamato)bismuth(III)

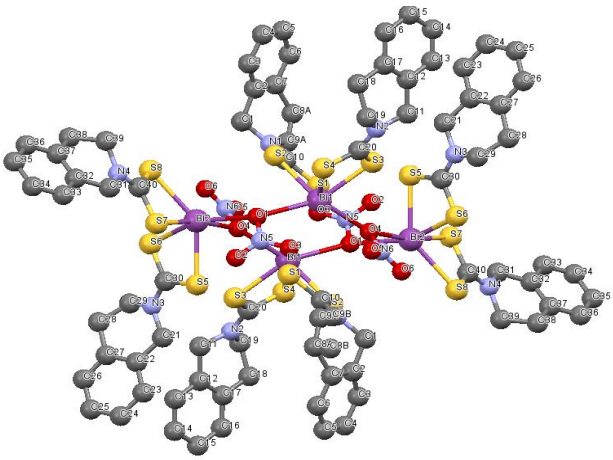

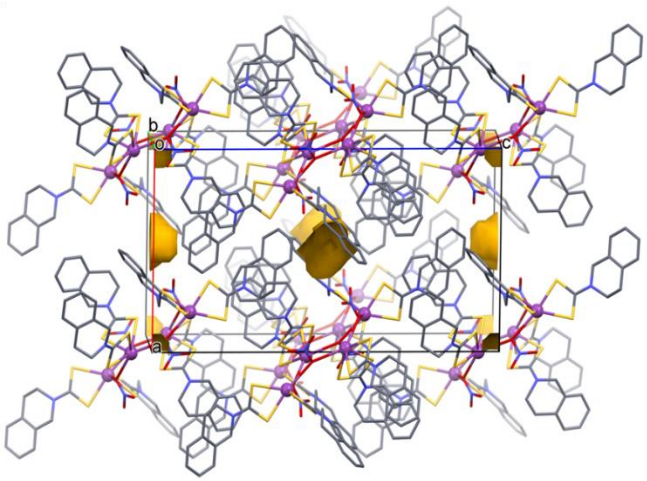

Void locations (gold surfaces) in the lattice of [Bi(S_2CThq)$_2$$NO_3$], (unit cell oriented approximately down the b-axis). The larger voids (51.4 Å3) are occupied by a single disordered water molecule; the smaller voids are vacant. The voids were calculated using a probe readus of 1.2 Å. H atoms have been omitted for clarity; Bi(III) ion sare rendered as spheres (arbitrary radii) while all othrer bonds and atems are rendered as cylinders

Experimental details

Crystal data	
Chemical formula	2($C_{40}H_{40}Bi_2N_6O_6S_8$)
M_r	2750.44
Crystal system, space group	Monoclinic, $P2_1/c$
Temperature (K)	296
a, *b*, *c* (Å)	14.1529 (16), 12.8531 (15), 26.270 (3)
β (°)	90.773 (2)
V (Å3)	4778.3 (9)
Z	2
Radiation type	Mo *K*α
μ (mm−1)	7.76
Crystal size (mm)	0.4 × 0.16 × 0.12
Data collection	
Diffractometer	Bruker *SMART APEX2* area detector
Absorption correction	Multi-scan

	SADABS2012/1 (Bruker,2012) was used for absorption correction. wR2(int) was 0.1398 before and 0.0497 after correction. The Ratio of minimum to maximum transmission is 0.3023. The λ/2 correction factor is 0.0015.
T_{min}, T_{max}	0.226, 0.746
No. of measured, independent and observed [$I > 2\sigma(I)$] reflections	114395, 12667, 9423
R_{int}	0.044
$(\sin \theta/\lambda)_{max}$ (Å^{-1})	0.697
Refinement	
$R[F^2 > 2\sigma(F^2)]$, $wR(F^2)$,	S 0.035, 0.096, 1.09
No. of reflections	12667
No. of parameters	560
No. of restraints	79
H-atom treatment	H-atom parameters constrained
$\Delta\rho_{max}$, $\Delta\rho_{min}$ (e Å^{-3})	1.69, −1.24

Fractional atomic coordinates and isotropic or equivalent isotropic displacement parameters (Å^2) for tetrakis(m-nitrato)te-trakis[bis(tetrahydroquinolinedithiocarbamato)bismuth(III)

	x	*y*	*z*	U_{iso}*/U_{eq}	Occ. (<1)
Bi1	1.03285 (2)	0.15304 (2)	0.44588 (2)	0.04877 (6)	
Bi2	0.83013 (2)	0.17580 (2)	0.61346 (2)	0.05288 (7	
S1	0.87167 (10)	0.03655 (10)	0.46365 (5)	0.0526 (3)	
S5	0.72042 (11)	0.22575 (10)	0.53069 (5)	0.0550 (3)	
S3	0.91858 (11)	0.31371 (11)	0.43570 (5)	0.0586 (3)	
S4	1.09279 (11)	0.29824 (14)	0.37515 (6)	0.0690 (4)	
S7	0.67801 (11)	0.17453 (15)	0.66903 (6)	0.0714 (4)	
S6	0.82154 (12)	0.37523 (11)	0.59686 (6)	0.0683 (4)	
S8	0.86220 (11)	0.23733 (14)	0.71489 (6)	0.0649 (4)	
S2	0.96637 (12)	0.05318 (15)	0.36495 (5)	0.0707 (4)	
O4	0.9698 (3)	0.1858 (3)	0.54210 (14)	0.0597 (9)	
O5	1.1008 (3)	0.2691 (4)	0.54099 (18)	0.0762 (12)	
O3	1.2527 (3)	0.1418 (3)	0.45549 (19)	0.0788 (13)	
O1	1.1733 (4)	0.0375 (4)	0.40688 (19)	0.0853 (14)	
O6	1.0269 (3)	0.2502 (3)	0.61153 (14)	0.0670 (11)	
N6	1.0338 (3)	0.2361 (3)	0.56492 (17)	0.0538 (10)	
N5	1.2475 (4)	0.0602 (4)	0.4309 (2)	0.0668 (13)	
O2	1.3131 (4)	−0.0029 (4)	0.4313 (2)	0.1042 (18)	
N3	0.7245 (3)	0.4286 (3)	0.51384 (17)	0.0549 (11)	
N4	0.7050 (3)	0.2078 (4)	0.76759 (16)	0.0567 (11)	
N1	0.8204 (3)	−0.0697 (4)	0.38144 (16)	0.0568 (11)	
C30	0.7522 (4)	0.3511 (4)	0.5433 (2)	0.0485 (11)	
N2	0.9669 (3)	0.4513 (4)	0.36550 (16)	0.0558 (11)	
C10	0.8790 (4)	−0.0028 (4)	0.40134 (18)	0.0480 (11)	
C40	0.7460 (4)	0.2079 (4)	0.72226 (19)	0.0519 (12)	
C20	0.9904 (4)	0.3643 (4)	0.38860 (19)	0.0530 (12)	
C31	0.6070 (4)	0.1791 (5)	0.7735 (2)	0.0689 (16)	

H31A	0.6031	0.1039	0.7759	0.083*	
H31B	0.5724	0.2000	0.7431	0.083*	
C11	0.8820 (4)	0.5114 (4)	0.37699 (19)	0.0584 (14)	
H11A	0.8994	0.5706	0.3980	0.070*	
H11B	0.8390	0.4683	0.3963	0.070*	
C21	0.6613 (4)	0.4110 (4)	0.4704 (2)	0.0569 (13)	
H21A	0.6172	0.3562	0.4789	0.068*	
H21B	0.6982	0.3872	0.4418	0.068*	
C1	0.8241 (4)	−0.1058 (5)	0.3280 (2)	0.0654 (15)	
H1A	0.8243	−0.1812	0.3269	0.078*	
H1B	0.8814	−0.0808	0.3122	0.078*	
C29	0.7662 (5)	0.5345 (4)	0.5174 (3)	0.0689 (16)	
H29A	0.8062	0.5393	0.5476	0.083*	
H29B	0.8051	0.5474	0.4879	0.083*	
C28	0.6909 (5)	0.6127 (4)	0.5198 (3)	0.0727 (17)	
H28A	0.7188	0.6816	0.5186	0.087*	
H28B	0.6585	0.6060	0.5519	0.087*	
C39	0.7587 (5)	0.2178 (6)	0.8159 (2)	0.0727 (11)	
H39A	0.7637	0.1499	0.8318	0.087*	
H39B	0.8222	0.2416	0.8086	0.087*	
C19	1.0235 (4)	0.5004 (6)	0.3260 (2)	0.0727 (18)	
H19A	1.0821	0.4622	0.3220	0.087*	
H19B	1.0391	0.5710	0.3360	0.087*	
C8A	0.6516 (12)	−0.078 (3)	0.3849 (8)	0.072 (6)	0.39 (3)
H8AA	0.6215	−0.0162	0.3986	0.086*	0.39 (3)
H8AB	0.6096	−0.1357	0.3916	0.086*	0.39 (3)
C22	0.6069 (4)	0.5055 (4)	0.45465 (18)	0.0491 (11)	
C27	0.6208 (4)	0.6017 (4)	0.4770 (2)	0.0557 (13)	
C23	0.5407 (4)	0.4962 (5)	0.4156 (2)	0.0682 (16)	
H23	0.5314	0.4319	0.4001	0.082*	
C26	0.5691 (5)	0.6867 (5)	0.4598 (3)	0.0756 (18)	
H26	0.5793	0.7520	0.4741	0.091*	
C24	0.4888 (5)	0.5794 (6)	0.3995 (3)	0.081 (2)	
H24	0.4442	0.5715	0.3735	0.097*	
C25	0.5023 (5)	0.6740 (6)	0.4214 (3)	0.080 (2)	
H25	0.4665	0.7306	0.4104	0.096*	
C32	0.5595 (4)	0.2253 (5)	0.8187 (2)	0.0572 (13)	
C12	0.8324 (4)	0.5495 (4)	0.3298 (2)	0.0550 (13)	
C2	0.7381 (4)	−0.0639 (5)	0.2997 (2)	0.0619 (14)	
C37	0.6112 (4)	0.2742 (4)	0.8567 (2)	0.0594 (14)	
C17	0.8733 (5)	0.5447 (5)	0.2827 (2)	0.0674 (16)	
C7	0.6536 (4)	−0.0635 (5)	0.3253 (2)	0.0646 (15)	
C38	0.7148 (5)	0.2903 (6)	0.8514 (2)	0.0727 (11)	
H38A	0.7259	0.3609	0.8398	0.087*	
H38B	0.7450	0.2827	0.8846	0.087*	
C18	0.9706 (5)	0.5018 (6)	0.2770 (2	) 0.0760 (18)	
H18A	0.9665	0.4315	0.2637	0.091*	
H18B	1.0047	0.5437	0.2527	0.091*	
C13	0.7412 (5)	0.5902 (5)	0.3345 (3)	0.0740 (17)	

H13	0.7137	0.5946	0.3664	0.089*	
C6	0.5731 (5)	−0.0190 (6)	0.3011 (3)	0.082 (2)	
H6	0.5155	−0.0184	0.3178	0.098*	
C14	0.6922 (6)	0.6236 (7)	0.2922 (4)	0.098 (2)	
H14	0.6317	0.6506	0.2957	0.118*	
C3	0.7425 (6)	−0.0196 (8)	0.2520 (3)	0.103 (3)	
H3	0.7998	−0.0191	0.2350	0.123*	
C36	0.5634 (5)	0.3116 (5)	0.8995 (2)	0.0726 (17)	
H36	0.5972	0.3424	0.9260	0.087*	
C33	0.4625 (5)	0.2167 (6)	0.8220 (2)	0.0747 (18)	
H33	0.4280	0.1849	0.7959	0.090*	
C35	0.4675 (6)	0.3031 (6)	0.9022 (3)	0.083 (2)	
H35	0.4362	0.3297	0.9303	0.100*	
C34	0.4168 (5)	0.2555 (6)	0.8640 (3)	0.083 (2)	
H34	0.3516	0.2494	0.8664	0.100*	
C5	0.5795 (6)	0.0225 (6)	0.2542 (3)	0.096 (3)	
H5	0.5259	0.0507	0.2386	0.115*	
C16	0.8211 (6)	0.5787 (8)	0.2401 (3)	0.101 (3)	
H16	0.8478	0.5747	0.2080	0.121*	
C4	0.6646 (7)	0.0237 (8)	0.2288 (3)	0.121 (4)	
H4	0.6689	0.0534	0.1967	0.145*	
C15	0.7317 (7)	0.6175 (8)	0.2448 (4)	0.119 (3)	
H15	0.6979	0.6395	0.2162	0.143*	
C9A	0.7277 (11)	−0.0934 (17)	0.4121 (6)	0.049 (4)	0.39 (3)
H9AA	0.7290	−0.1652	0.4234	0.059*	0.39 (3)
H9AB	0.7262	−0.0493	0.4420	0.059*	0.39 (3)
C8B	0.6535 (11)	−0.1240 (16)	0.3742 (5)	0.0727 (11)	0.61 (3)
H8BA	0.6382	−0.1959	0.3665	0.087*	0.61 (3)
H8BB	0.6039	−0.0969	0.3956	0.087*	0.61 (3)
C9B	0.7457 (13)	−0.1216 (15)	0.4042 (6)	0.0727 (11)	0.61 (3)
H9BA	0.7341	−0.0892	0.4368	0.087*	0.61 (3)
H9BB	0.7652	−0.1928	0.4108	0.087*	0.61 (3)

*Atomic displacement parameters (Å^2) for (*tetrakis(m-nitrato)te-trakis[bis(tetrahydroquinolinedithiocarbamato)bismuth(III)*)*

	U_{11}	U_{22}	U_{33}	U_{12}	U_{13}	U_{23}
Bi1	0.05688 (12)	0.04752 (11)	0.04200 (10)	−0.00711 (8)	0.00428 (8)	−0.00586 (7)
Bi2	0.06543 (14)	0.04353 (10)	0.04989 (11)	0.00580 (9)	0.00856 (9)	0.00080 (8)
S1	0.0638 (8)	0.0518 (7)	0.0425 (6)	−0.0067 (6)	0.0071 (6)	−0.0036 (5)
S5	0.0690 (9)	0.0369 (6)	0.0590 (7)	−0.0048 (6)	−0.0030 (6)	−0.0072 (5)
S3	0.0646 (9)	0.0588 (8)	0.0528 (7)	0.0000 (6)	0.0132 (6)	0.0127 (6)
S4	0.0611 (9)	0.0781 (10)	0.0681 (9)	−0.0052 (8)	0.0159 (7)	0.0117 (8)
S7	0.0587 (9)	0.1084 (13)	0.0471 (7)	−0.0105 (8)	0.0011 (6)	−0.0122 (8)
S6	0.0908 (11)	0.0435 (7)	0.0699 (9)	0.0033 (7)	−0.0298 (8)	−0.0081 (6)
S8	0.0559 (8)	0.0805 (10)	0.0584 (8)	−0.0008 (7)	−0.0010 (6)	−0.0004 (7)

S2	0.0751 (10)	0.0960 (12)	0.0413 (7)	−0.0307 (9)	0.0107 (6)	−0.0161 (7)
O4	0.069 (2)	0.064 (2)	0.0468 (19)	−0.0086 (19)	0.0010 (18)	−0.0120 (17)
O5	0.064 (3)	0.080 (3)	0.085 (3)	−0.017 (2)	0.011 (2)	−0.011 (2)
O3	0.079 (3)	0.053 (2)	0.105 (3)	−0.016 (2)	0.014 (3)	−0.022 (2)
O1	0.085 (3)	0.083 (3)	0.088 (3)	−0.010 (3)	0.006 (3)	−0.034 (3)
O6	0.074 (3)	0.077 (3)	0.051 (2)	0.009 (2)	−0.0105 (19)	−0.0172 (19)
N6	0.057 (3)	0.049 (2)	0.055 (3)	0.004 (2)	−0.005 (2)	−0.009 (2)
N5	0.074 (3)	0.044 (3)	0.084 (4)	−0.011 (2)	0.028 (3)	−0.005 (2)
O2	0.096 (4)	0.060 (3)	0.158 (5)	0.012 (3)	0.024 (4)	−0.006 (3)
N3	0.061 (3)	0.040 (2)	0.064 (3)	−0.0067 (19)	−0.017 (2)	−0.0009 (19)
N4	0.052 (3)	0.074 (3)	0.044 (2)	0.007 (2)	0.0008 (19)	−0.010 (2)
N1	0.058 (3)	0.064 (3)	0.048 (2)	−0.012 (2)	−0.003 (2)	−0.004 (2)
C30	0.052 (3)	0.039 (2)	0.055 (3)	−0.001 (2)	0.000 (2)	−0.005 (2)
N2	0.060 (3)	0.063 (3)	0.044 (2)	−0.019 (2)	−0.004 (2)	0.013 (2)
C10	0.051 (3)	0.048 (3)	0.045 (2)	0.000 (2)	−0.002 (2)	−0.001 (2)
C40	0.053 (3)	0.053 (3)	0.050 (3)	0.007 (2)	−0.002 (2)	−0.005 (2)
C20	0.057 (3)	0.060 (3)	0.042 (2)	−0.017 (2)	0.000 (2)	0.002 (2)
C31	0.063 (4)	0.087 (4)	0.057 (3)	−0.004 (3)	0.014 (3)	−0.015 (3)
C11	0.080 (4)	0.050 (3)	0.044 (3)	−0.010 (3)	0.001 (3)	0.000 (2)
C21	0.067 (3)	0.048 (3)	0.056 (3)	−0.010 (2)	−0.009 (3)	−0.004 (2)
C1	0.067 (4)	0.072 (4)	0.057 (3)	−0.007 (3)	−0.005 (3)	−0.020 (3)
C29	0.082 (4)	0.047 (3)	0.078 (4)	−0.014 (3)	−0.022 (3)	0.003 (3)
C28	0.096 (5)	0.043 (3)	0.079 (4)	0.000 (3)	−0.016 (4)	−0.009 (3)
C39	0.074 (3)	0.085 (3)	0.059 (2)	0.006 (2)	−0.0014 (19)	−0.010 (2)
C19	0.065 (4)	0.089 (5)	0.064 (4)	−0.020 (3)	0.002 (3)	0.027 (3)
C8A	0.060 (9)	0.084 (14)	0.073 (11)	0.024 (9)	0.032 (8)	0.015 (10)
C22	0.049 (3)	0.053 (3)	0.045 (2)	−0.007 (2)	0.003 (2)	0.004 (2)
C27	0.065 (3)	0.052 (3)	0.051 (3)	0.001 (3)	0.002 (2)	0.001 (2)
C23	0.064 (4)	0.079 (4)	0.061 (3)	−0.005 (3)	−0.013 (3)	−0.002 (3)
C26	0.086 (5)	0.059 (4)	0.082 (4)	0.017 (3)	0.003 (4)	0.003 (3)
C24	0.068 (4)	0.103 (6)	0.072 (4)	0.004 (4)	−0.021 (3)	0.014 (4)
C25	0.066 (4)	0.086 (5)	0.089 (5)	0.018 (4)	−0.003 (4)	0.022 (4)
C32	0.059 (3)	0.061 (3)	0.052 (3)	0.007 (3)	0.007 (2)	0.005 (2)
C12	0.067 (4)	0.047 (3)	0.051 (3)	−0.014 (2)	−0.001 (2)	0.001 (2)
C2	0.064 (4)	0.067 (3)	0.055 (3)	−0.016 (3)	−0.006 (3)	−0.011 (3)
C37	0.074 (4)	0.056 (3)	0.048 (3)	0.012 (3)	0.007 (3)	0.002 (2)
C17	0.078 (4)	0.074 (4)	0.050 (3)	−0.003 (3)	−0.006 (3)	0.008 (3)
C7	0.060 (4)	0.062 (3)	0.072 (4)	−0.008 (3)	−0.007 (3)	0.000 (3)
C38	0.074 (3)	0.085 (3)	0.059 (2)	0.006 (2)	−0.0014 (19)	−0.010 (2)
C18	0.079 (4)	0.098 (5)	0.051 (3)	−0.009 (4)	0.009 (3)	0.010 (3)
C13	0.077 (4)	0.066 (4)	0.079 (4)	−0.004 (3)	0.007 (3)	0.006 (3)
C6	0.071 (4)	0.080 (5)	0.095 (5)	−0.010 (4)	−0.020 (4)	−0.006 (4)
C14	0.086 (5)	0.100 (6)	0.108 (7)	0.003 (5)	−0.014 (5)	0.009 (5)
C3	0.085 (5)	0.165 (9)	0.058 (4)	−0.039 (5)	−0.010 (4)	0.002 (5)
C36	0.093 (5)	0.074 (4)	0.051 (3)	0.016 (4)	0.008 (3)	−0.004 (3)
C33	0.064 (4)	0.101 (5)	0.059 (3)	0.012 (4)	0.006 (3)	0.003 (3)
C35	0.093 (5)	0.090 (5)	0.068 (4)	0.034 (4)	0.026 (4)	0.005 (4)
C34	0.064 (4)	0.108 (6)	0.078 (4)	0.024 (4)	0.014 (3)	0.015 (4)
C5	0.096 (6)	0.090 (5)	0.099 (6)	−0.011 (4)	−0.054 (5)	0.012 (4)

C16	0.098 (6)	0.146 (8)	0.058 (4)	0.012 (5)	−0.013 (4)	0.021 (4)
C4	0.122 (8)	0.158 (9)	0.081 (5)	−0.045 (7)	−0.039 (5)	0.028 (6)
C15	0.119 (8)	0.140 (8)	0.096 (6)	0.030 (7)	−0.037 (6)	0.024 (6)
C9A	0.041 (8)	0.063 (10)	0.043 (7)	−0.013 (7)	0.020 (6)	−0.013 (6)
C8B	0.074 (3)	0.085 (3)	0.059 (2)	0.006 (2)	−0.0014 (19)	−0.010 (2)
C9B	0.074 (3)	0.085 (3)	0.059 (2)	0.006 (2)	−0.0014 (19)	−0.010 (2)

*Geometric parameters (Å, º) for (*tetrakis(m-nitrato)te-trakis[bis(tetrahydroquinolinedithiocarbamato)bismuth(III)*)*

Bi1—S1	2.7734 (14)	C19—H	19B 0.9700
Bi1—S3	2.6343 (15)	C19—C18	1.480 (8)
Bi1—S4	2.7745 (16)	C8A—H8AA	0.9700
Bi1—S2	2.6456 (14)	C8A—H8AB	0.9700
Bi1—O4	2.725 (4)	C8A—C7	1.58 (2)
Bi1—O1	2.694 (5)	C8A—C9A	1.299 (17)
Bi2—S5	2.7313 (14)	C22—C27	1.381 (7)
Bi2—S7	2.6174 (16)	C22—C23	1.386 (7)
Bi2—S6	2.6026 (15)	C27—C26	1.388 (8)
Bi2—S8	2.8105 (15)	C23—H23	0.9300
Bi2—O4	2.745 (4)	C23—C24	1.361 (9)
S1—C10	1.718 (5)	C26—H26	0.9300
S5—C30	1.703 (5)	C26—C25	1.383 (10)
S3—C20	1.739 (5)	C24—H24	0.9300
S4—C20	1.720 (6)	C24—C25	1.357 (10)
S7—C40	1.741 (5)	C25—H25	0.9300
S6—C30	1.733 (5)	C32—C37	1.380 (8)
S8—C40	1.701 (6)	C32—C33	1.382 (8)
S2—C10	1.730 (5)	C12—C17	1.375 (8)
O4—N6	1.259 (5)	C12—C13	1.400 (9)
O5—N6	1.221 (6)	C2—C7	1.380 (8)
O3—N5	1.234 (6)	C2—C3	1.380 (9)
O1—N5	1.253 (7)	C37—C38	1.489 (9)
O6—N6	1.243 (5)	C37—C36	1.405 (8)
N5—O2	1.233 (7)	C17—C18	1.493 (9)
N3—C30	1.318 (6)	C17—C16	1.401 (8)
N3—C21	1.458 (6)	C7—C6	1.416 (9)
N3—C29	1.485 (7)	C7—C8B	1.503 (15)
N4—C40	1.332 (7)	C38—H38A	0.9700
N4—C31	1.444 (7)	C38—H38B	0.9700
N4—C39	1.475 (7)	C18—H18A	0.9700
N1—C10	1.300 (6)	C18—H18B	0.9700
N1—C1	1.480 (7)	C13—H13	0.9300
N1—C9A	1.578 (16)	C13—C14	1.370 (10)
N1—C9B	1.391 (18)	C6—H6	0.9300
N2—C20	1.313 (7)	C6—C5	1.348 (10)
N2—C11	1.464 (7)	C14—H14	0.9300
N2—C19	1.463 (7)	C14—C15	1.375 (13)
C31—H31A	0.9700	C3—H3	0.9300
C31—H31B	0.9700	C3—C4	1.369 (12)

C31—C32	1.497 (8)	C36—H36	0.9300
C11—H11A	0.9700	C36—C35	1.365 (10)
C11—H11B	0.9700	C33—H33	0.9300
C11—C12	1.497 (7)	C33—C34	1.381 (9)
C21—H21A	0.9700	C35—H35	0.9300
C21—H21B	0.9700	C35—C34	1.369 (11)
C21—C22	1.494 (7)	C34—H34	0.9300
C1—H1A	0.9700	C5—H5	0.9300
C1—H1B	0.9700	C5—C4	1.384 (13)
C1—C2	1.517 (8)	C16—H16	0.9300
C29—H29A	0.9700	C16—C15	1.367 (12)
C29—H29B	0.9700	C4—H4	0.9300
C29—C28	1.468 (9)	C15—H15	0.9300
C28—H28A	0.9700	C9A—H9AA	0.9700
C28—H28B	0.9700	C9A—H9AB	0.9700
C28—C27	1.496 (8)	C8B—H8BA	0.9700
C39—H39A	0.9700	C8B—H8BB	0.9700
C39—H39B	0.9700	C8B—C9B	1.516 (19)
C39—C38	1.463 (8)	C9B—H9BA	0.9700
C19—H19A	0.9700	C9B—H9BB	0.9700
S1—Bi1—S4	137.35 (5)	H19A—C19—H19B	108.1
S3—Bi1—S1	86.28 (4)	C18—C19—H19A	109.6
S3—Bi1—S4	66.27 (5)	C18—C19—H19B	109.6
S3—Bi1—S2	95.02 (6)	H8AA—C8A—H8AB	106.6
S3—Bi1—O4	76.40 (9)	C7—C8A—H8AA	106.7
S3—Bi1—O1	148.03 (12)	C7—C8A—H8AB	106.7
S2—Bi1—S1	65.73 (4)	C9A—C8A—H8AA	106.7
S2—Bi1—S4	84.07 (5)	C9A—C8A—H8AB	106.7
S2—Bi1—O4	134.67 (9)	C9A—C8A—C7	122.5 (12)
S2—Bi1—O1	71.53 (11)	C27—C22—C21	122.7 (5)
O4—Bi1—S1	69.31 (9)	C27—C22—C23	118.9 (5)
O4—Bi1—S4	128.64 (9)	C23—C22—C21	118.4 (5)
O1—Bi1—S1	112.28 (11)	C22—C27—C28	119.6 (5)
O1—Bi1—S4	83.23 (12)	C22—C27—C26	119.7 (5)
O1—Bi1—O4	133.67 (14)	C26—C27—C28	120.7 (5)
S5—Bi2—S8	140.49 (4)	C22—C23—H23	119.4
S5—Bi2—O4	81.50 (9)	C24—C23—C22	121.2 (6)
S7—Bi2—S5	89.00 (5)	C24—C23—H23	119.4
S7—Bi2—S8	66.21 (5)	C27—C26—H26	120.1
S7—Bi2—O4	170.49 (9)	C25—C26—C27	119.8 (6)
S6—Bi2—S5	67.07 (4)	C25—C26—H26	120.1
S6—Bi2—S7	93.60 (6)	C23—C24—H24	120.0
S6—Bi2—S8	83.59 (5)	C25—C24—C23	120.0 (6)
S6—Bi2—O4	82.65 (9)	C25—C24—H24	120.0
O4—Bi2—S8	121.72 (8)	C26—C25—H25	119.8
C10—S1—Bi1	86.45 (18)	C24—C25—C26	120.4 (6)
C30—S5—Bi2	85.51 (18)	C24—C25—H25	119.8
C20—S3—Bi1	90.1 (2)	C37—C32—C31	121.0 (5)
C20—S4—Bi1	85.91 (18)	C37—C32—C33	120.7 (6)

C40—S7—Bi2	89.79 (19)	C33—C32—C31	118.3 (6)
C30—S6—Bi2	89.09 (17)	C17—C12—C11	122.2 (6)
C40—S8—Bi2	84.33 (18)	C17—C12—C13	119.7 (6)
C10—S2—Bi1	90.39 (17)	C13—C12—C11	118.2 (5)
Bi1—O4—Bi2	150.95 (15)	C7—C2—C1	117.3 (5)
N6—O4—Bi1	106.1 (3)	C3—C2—C1	123.2 (6)
N6—O4—Bi2	102.7 (3)	C3—C2—C7	119.4 (6)
N5—O1—Bi1	107.4 (3)	C32—C37—C38	120.6 (5)
O5—N6—O4	119.5 (5)	C32—C37—C36	118.5 (6)
O5—N6—O6	121.9 (5)	C36—C37—C38	120.8 (6)
O6—N6—O4	118.5 (5)	C12—C17—C18	120.4 (5)
O3—N5—O1	120.4 (6)	C12—C17—C16	118.8 (7)
O2—N5—O3	121.0 (6)	C16—C17—C18	120.8 (6)
O2—N5—O1	118.5 (5)	C2—C7—C8A	120.6 (7)
C30—N3—C21	121.1 (4)	C2—C7—C6	118.7 (6)
C30—N3—C29	122.8 (4)	C2—C7—C8B	115.1 (8)
C21—N3—C29	115.5 (4)	C6—C7—C8A	117.8 (8)
C40—N4—C31	121.8 (5)	C6—C7—C8B	125.6 (8)
C40—N4—C39	122.8 (5)	C39—C38—C37	113.4 (6)
C31—N4—C39	114.5 (5)	C39—C38—H38A	108.9
C10—N1—C1	123.9 (5)	C39—C38—H38B	108.9
C10—N1—C9A	116.9 (8)	C37—C38—H38A	108.9
C10—N1—C9B	129.0 (8)	C37—C38—H38B	108.9
C1—N1—C9A	117.6 (8)	H38A—C38—H38B	107.7
C9B—N1—C1	107.1 (8)	C19—C18—C17	112.0 (5)
S5—C30—S6	118.2 (3)	C19—C18—H18A	109.2
N3—C30—S5	121.7 (4)	C19—C18—H18B	109.2
N3—C30—S6	120.1 (4)	C17—C18—H18A	109.2
C20—N2—C11	123.9 (5)	C17—C18—H18B	109.2
C20—N2—C19	123.9 (5)	H18A—C18—H18B	107.9
C19—N2—C11	112.2 (5)	C12—C13—H13	119.9
S1—C10—S2	117.2 (3)	C14—C13—C12	120.2 (7)
N1—C10—S1	122.1 (4)	C14—C13—H13	119.9
N1—C10—S2	120.7 (4)	C7—C6—H6	119.8
S8—C40—S7	119.2 (3)	C5—C6—C7	120.4 (7)
N4—C40—S7	118.3 (4)	C5—C6—H6	119.8
N4—C40—S8	122.4 (4)	C13—C14—H14	119.7
S4—C20—S3	117.6 (3)	C13—C14—C15	120.6 (8)
N2—C20—S3	120.0 (5)	C15—C14—H14	119.7
N2—C20—S4	122.3 (4)	C2—C3—H3	119.2
N4—C31—H31A	108.5	C4—C3—C2	121.7 (8)
N4—C31—H31B	108.5	C4—C3—H3	119.2
N4—C31—C32	115.2 (5)	C37—C36—H36	119.8
H31A—C31—H31B	107.5	C35—C36—C37	120.3 (7)
C32—C31—H31A	108.5	C35—C36—H36	119.8
C32—C31—H31B	108.5	C32—C33—H33	120.1
N2—C11—H11A	109.2	C34—C33—C32	119.7 (7)
N2—C11—H11B	109.2	C34—C33—H33	120.1
N2—C11—C12	112.3 (4)	C36—C35—H35	119.7

H11A—C11—H11B	107.9	C36—C35—C34	120.5 (6)
C12—C11—H11A	109.2	C34—C35—H35	119.7
C12—C11—H11B	109.2	C33—C34—H34	119.9
N3—C21—H21A	108.9	C35—C34—C33	120.1 (7)
N3—C21—H21B	108.9	C35—C34—H34	119.9
N3—C21—C22	113.5 (4)	C6—C5—H5	119.6
H21A—C21—H21B	107.7	C6—C5—C4	120.9 (7)
C22—C21—H21A	108.9	C4—C5—H5	119.6
C22—C21—H21B	108.9	C17—C16—H16	119.3
N1—C1—H1A	110.0	C15—C16—C17	121.4 (8)
N1—C1—H1B	110.0	C15—C16—H16	119.3
N1—C1—C2	108.4 (5)	C3—C4—C5	118.9 (8)
H1A—C1—H1B	108.4	C3—C4—H4	120.6
C2—C1—H1A	110.0	C5—C4—H4	120.6
C2—C1—H1B	110.0	C14—C15—H15	120.3
N3—C29—H29A	109.7	C16—C15—C14	119.3 (8)
N3—C29—H29B	109.7	C16—C15—H15	120.3
H29A—C29—H29B	108.2	N1—C9A—H9AA	109.2
C28—C29—N3	110.0 (5)	N1—C9A—H9AB	109.2
C28—C29—H29A	109.7	C8A—C9A—N1	112.2 (13)
C28—C29—H29B	109.7	C8A—C9A—H9AA	109.2
C29—C28—H28A	109.2	C8A—C9A—H9AB	109.2
C29—C28—H28B	109.2	H9AA—C9A—H9AB	107.9
C29—C28—C27	112.1 (5)	C7—C8B—H8BA	108.5
H28A—C28—H28B	107.9	C7—C8B—H8BB	108.5
C27—C28—H28A	109.2	C7—C8B—C9B	115.1 (12)
C27—C28—H28B	109.2	H8BA—C8B—H8BB	107.5
N4—C39—H39A	109.1	C9B—C8B—H8BA	108.5
N4—C39—H39B	109.1	C9B—C8B—H8BB	108.5
H39A—C39—H39B	107.8	N1—C9B—C8B	116.1 (12)
C38—C39—N4	112.7 (5)	N1—C9B—H9BA	108.3
C38—C39—H39A	109.1	N1—C9B—H9BB	108.3
C38—C39—H39B	109.1	C8B—C9B—H9BA	108.3
N2—C19—H19A	109.6	C8B—C9B—H9BB	108.3
N2—C19—H19B	109.6	H9BA—C9B—H9BB	107.4
N2—C19—C18	110.3 (5)		
Bi1—S1—C10—S2	−4.6 (3)	C1—C2—C7—C6	176.1 (5)
Bi1—S1—C10—N1	177.2 (5)	C1—C2—C7—C8B	−11.6 (11)
Bi1—S3—C20—S4	−3.3 (3)	C1—C2—C3—C4	−175.6 (8)
Bi1—S3—C20—N2	178.2 (4)	C29—N3—C30—S5	−167.1 (5)
Bi1—S4—C20—S3	3.2 (3)	C29—N3—C30—S6	13.7 (8)
Bi1—S4—C20—N2	−178.4 (4)	C29—N3—C21—C22	−32.7 (7)
Bi1—S2—C10—S1	4.8 (3)	C29—C28—C27—C22	26.9 (8)
Bi1—S2—C10—N1	−177.0 (4)	C29—C28—C27—C26	−153.7 (6)
Bi1—O4—N6—O5	8.1 (6)	C28—C27—C26—C25	−177.8 (7)
Bi1—O4—N6—O6	−171.6 (4)	C39—N4—C40—S7	169.7 (5)
Bi1—O1—N5—O3	−18.8 (6)	C39—N4—C40—S8	−9.3 (8)
Bi1—O1—N5—O2	157.7 (5)	C39—N4—C31—C32	36.5 (8)
Bi2—S5—C30—S6	−3.4 (3)	C19—N2—C20—S3	179.1 (4)

Bi2—S5—C30—N3	177.4 (5)	C19—N2—C20—S4	0.7 (7)
Bi2—S7—C40—S8	6.6 (3)	C19—N2—C11—C12	44.1 (6)
Bi2—S7—C40—N4	−172.4 (4)	C8A—C7—C6—C5	160.9 (15)
Bi2—S6—C30—S5	3.6 (3)	C22—C27—C26—C25	1.6 (10)
Bi2—S6—C30—N3	−177.2 (5)	C22—C23—C24—C25	0.8 (11)
Bi2—S8—C40—S7	−6.2 (3)	C27—C22—C23—C24	−0.8 (9)
Bi2—S8—C40—N4	172.8 (5)	C27—C26—C25—C24	−1.7 (11)
Bi2—O4—N6—O5	−168.2 (4)	C23—C22—C27—C28	179.0 (6)
Bi2—O4—N6—O6	12.1 (5)	C23—C22—C27—C26	−0.4 (9)
N3—C21—C22—C27	4.4 (8)	C23—C24—C25—C26	0.5 (12)
N3—C21—C22—C23	−176.4 (5)	C32—C37—C38—C39	−22.8 (9)
N3—C29—C28—C27	−53.1 (7)	C32—C37—C36—C35	−2.4 (9)
N4—C31—C32—C37	−12.1 (9)	C32—C33—C34—C35	0.5 (11)
N4—C31—C32—C33	168.7 (6)	C12—C17—C18—C19	−18.7 (9)
N4—C39—C38—C37	46.6 (8)	C12—C17—C16—C15	1.0 (13)
N1—C1—C2—C7	−39.6 (7)	C12—C13—C14—C15	0.1 (13)
N1—C1—C2—C3	135.1 (7)	C2—C7—C6—C5	−0.3 (10)
C30—N3—C21—C22	156.4 (5)	C2—C7—C8B—C9B	34.9 (14)
C30—N3—C29—C28	−131.0 (6)	C2—C3—C4—C5	−0.2 (14)
N2—C11—C12—C17	−11.7 (7)	C37—C32—C33—C34	−1.3 (10)
N2—C11—C12—C13	167.7 (5)	C37—C36—C35—C34	1.7 (11)
N2—C19—C18—C17	50.3 (8)	C17—C12—C13—C14	1.1 (10)
C10—N1—C1—C2	−111.6 (6)	C17—C16—C15—C14	0.1 (16)
C10—N1—C9A—C8A	124.5 (14)	C7—C8A—C9A—N1	14 (3)
C10—N1—C9B—C8B	134.2 (10)	C7—C2—C3—C4	−1.0 (12)
C40—N4—C31—C32	−154.1 (5)	C7—C6—C5—C4	−0.8 (12)
C40—N4—C39—C38	135.7 (6)	C7—C8B—C9B—N1	−4.0 (17)
C20—N2—C11—C12	−137.1 (5)	C38—C37—C36—C35	175.2 (6)
C20—N2—C19—C18	116.0 (6)	C18—C17—C16—C15	179.6 (9)
C31—N4—C40—S7	1.2 (8)	C13—C12—C17—C18	179.8 (6)
C31—N4—C40—S8	−177.8 (5)	C13—C12—C17—C16	−1.6 (10)
C31—N4—C39—C38	−55.0 (8)	C13—C14—C15—C16	−0.7 (15)
C31—C32—C37—C38	5.3 (9)	C6—C7—C8B—C9B	−153.5 (9)
C31—C32—C37—C36	−177.0 (6)	C6—C5—C4—C3	1.0 (14)
C31—C32—C33—C34	177.9 (6)	C3—C2—C7—C8A	−159.5 (16)
C11—N2—C20—S3	0.4 (7)	C3—C2—C7—C6 1	.2 (9)
C11—N2—C20—S4	−178.0 (4)	C3—C2—C7—C8B	173.4 (10)
C11—N2—C19—C18	−65.1 (7)	C36—C37—C38—C39	159.5 (6)
C11—C12—C17—C18	−0.7 (9)	C36—C35—C34—C33	−0.7 (11)
C11—C12—C17—C16	177.9 (6)	C33—C32—C37—C38	−175.4 (6)
C11—C12—C13—C14	−178.4 (6)	C33—C32—C37—C36	2.2 (9)
C21—N3—C30—S5	3.1 (8)	C16—C17—C18—C19	162.8 (7)
C21—N3—C30—S6	−176.1 (4)	C9A—N1—C10—S1	14.3 (10)
C21—N3—C29—C28	58.3 (7)	C9A—N1—C10—S2	−163.8 (8)
C21—C22—C27—C28	−1.9 (9)	C9A—N1—C1—C2	54.0 (10)
C21—C22—C27—C26	178.7 (6)	C9A—C8A—C7—C2	−2 (3)
C21—C22—C23—C24	−180.0 (6)	C9A—C8A—C7—C6	−162.9 (17)
C1—N1—C10—S1	−180.0 (4)	C8B—C7—C6—C5	−171.7 (11)
C1—N1—C10—S2	1.9 (8)	C9B—N1—C10—S1	−1.1 (13)

C1—N1—C9A—C8A	−42.2 (17)	C9B—N1—C10—S2	−179.2 (11)
C1—N1—C9B—C8B	−46.8 (13)	C9B—N1—C1—C2	69.3 (10)
C1—C2—C7—C8A	15.5 (17)		

Crystallographic data for tris(piperidinedithiocarbamato)bismuth(III) chloroform solvate

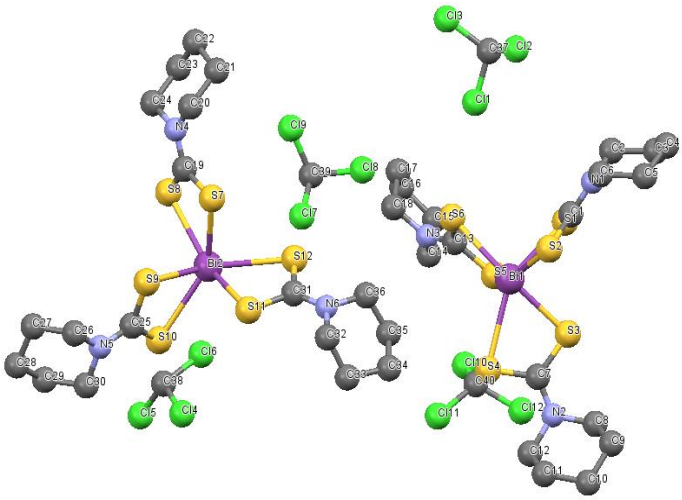

Experimental details

Crystal data	
Chemical formula	$C_{20}H_{32}BiCl_6N_3S_6$
M_r 928.53	
Crystal system, space group	Monoclinic, $P2_1/c$
Temperature (K)	100
a, *b*, *c* (Å)	11.0038 (3), 21.5260 (5), 28.1836 (7)
β (°)	94.047 (2)
V (Å^3)	6659.1 (3)
Z	8
Radiation type	Cu $K\alpha$
μ (mm^{-1})	18.49
Crystal size (mm)	0.14 × 0.11 × 0.05
Data collection	
Diffractometer	Bruker *APEX*-II CCD

Absorption correction	Multi-scan *SADABS*
T_{min}, T_{max}	0.345, 0.458
No. of measured, independent and observed [$I > 2\sigma(I)$] reflections	39017, 12577, 10574
R_{int}	0.058
$(\sin \theta/\lambda)_{max}$ (Å^{-1})	0.617
Refinement	
$R[F^2 > 2\sigma(F^2)]$, $wR(F^2)$, S	0.031, 0.066, 1.01
No. of reflections	12577
No. of parameters	649
H-atom treatment	H-atom parameters constrained
$\Delta\rho_{max}$, $\Delta\rho_{min}$ (e Å^{-3})	0.77, −0.81

*Fractional atomic coordinates and isotropic or equivalent isotropic displacement parameters (Å^2) for (*of tris(piperidinedithiocarbamato)bismuth(III) chloroform solvate *)*

	x	*y*	*z*	U_{iso}*/U_{eq}
Bi1	0.065331 (14)	0.299929 (7)	0.296089 (6)	0.01156 (4)
Bi2	0.950522 (13)	0.187677 (7)	0.420937 (6)	0.01039 (4)
C1	−0.1040 (4)	0.2576 (2)	0.20513 (17)	0.0155 (9)
C2	−0.1487 (5)	0.2718 (3)	0.11786 (17)	0.0240 (11)
H2A	−0.1100	0.2447	0.0949	0.029*
H2B	−0.0969	0.3092	0.1232	0.029*
C3	−0.2734 (5)	0.2911 (3)	0.09740 (19)	0.0274 (12)
H3A	−0.2664	0.3096	0.0656	0.033*
H3B	−0.3067	0.3231	0.1181	0.033*
C4	−0.3604 (5)	0.2362 (3)	0.0931 (2)	0.0321 (13)
H4A	−0.3359	0.2081	0.0677	0.038*
H4B	−0.4437	0.2514	0.0840	0.038*
C5	−0.3612 (4)	0.2003 (2)	0.13961 (19)	0.0240 (11)
H5A	−0.3990	0.2261	0.1636	0.029*
H5B	−0.4108	0.1622	0.1345	0.029*
C6	−0.2334 (5)	0.1827 (2)	0.1579 (2)	0.0255 (11)
H6A	−0.2359	0.1616	0.1891	0.031*
H6B	−0.1983	0.1535	0.1355	0.031*
C7	−0.0606 (4)	0.3754 (2)	0.38167 (17)	0.0155 (9)
C8	−0.2347 (4)	0.4414 (2)	0.4012 (2)	0.0216 (11)
H8A	−0.2459	0.4463	0.3662	0.026*
H8B	−0.2263	0.4832	0.4157	0.026*
C9	−0.3452 (4)	0.4081 (2)	0.4195 (2)	0.0251 (11)
H9A	−0.4188	0.4340	0.4130	0.030*
H9B	−0.3583	0.3682	0.4024	0.030*
C10	−0.3267 (5)	0.3957 (3)	0.4729 (2)	0.0293 (12)

H10A	−0.3272	0.4357	0.4903	0.035*
H10B	−0.3951	0.3702	0.4831	0.035*
C11	−0.2079 (5)	0.3623 (3)	0.48567 (18)	0.0272 (12)
H11A	−0.2123	0.3196	0.4727	0.033*
H11B	−0.1943	0.3595	0.5207	0.033*
C12	−0.1016 (5)	0.3970 (3)	0.46548 (18)	0.0250 (11)
H12A	−0.0923	0.4384	0.4807	0.030*
H12B	−0.0252	0.3735	0.4725	0.030*
C13	0.3347 (4)	0.3441 (2)	0.27359 (17)	0.0143 (9)
C14	0.4902 (4)	0.4267 (2)	0.28857 (17)	0.0169 (9)
H14A	0.5527	0.4261	0.3156	0.020*
H14B	0.4198	0.4512	0.2980	0.020*
C15	0.5427 (4)	0.4564 (2)	0.24515 (18)	0.0199 (10)
H15A	0.4778	0.4604	0.2192	0.024*
H15B	0.5731	0.4986	0.2535	0.024*
C16	0.6468 (4)	0.4170 (2)	0.22822 (19)	0.0217 (11)
H16A	0.6736	0.4344	0.1982	0.026*
H16B	0.7168	0.4185	0.2523	0.026*
C17	0.6072 (4)	0.3505 (2)	0.22032 (19)	0.0216 (11)
H17A	0.6781	0.3252	0.2125	0.026*
H17B	0.5457	0.3485	0.1929	0.026*
C18	0.5532 (4)	0.3237 (2)	0.2640 (2)	0.0220 (11)
H18A	0.5241	0.2808	0.2573	0.026*
H18B	0.6163	0.3221	0.2908	0.026*
C19	1.0602 (4)	0.1103 (2)	0.33393 (16)	0.0117 (8)
C20	1.0265 (4)	0.0279 (2)	0.27319 (17)	0.0155 (9)
H20A	0.9485	0.0223	0.2881	0.019*
H20B	1.0713	−0.0120	0.2752	0.019*
C21	1.0013 (4)	0.0461 (2)	0.22136 (17)	0.0193 (10)
H21A	0.9485	0.0834	0.2193	0.023*
H21B	0.9572	0.0119	0.2041	0.023*
C22	1.1188 (4)	0.0598 (2)	0.19788 (18)	0.0233 (11)
H22A	1.0994	0.0754	0.1652	0.028*
H22B	1.1667	0.0211	0.1958	0.028*
C23	1.1945 (4)	0.1085 (2)	0.22687 (17)	0.0191 (10)
H23A	1.2735	0.1145	0.2128	0.023*
H23B	1.1507	0.1488	0.2255	0.023*
C24	1.2167 (4)	0.0881 (2)	0.27835 (17)	0.0173 (10)
H24A	1.2666	0.0498	0.2800	0.021*
H24B	1.2618	0.1209	0.2968	0.021*
C25	1.0811 (4)	0.1393 (2)	0.52236 (16)	0.0120 (8)
C26	1.1630 (4)	0.0460 (2)	0.56519 (19)	0.0206 (10)
H26A	1.1377	0.0251	0.5348	0.025*
H26B	1.1186	0.0266	0.5907	0.025*
C27	1.2986 (5)	0.0382 (3)	0.5760 (2)	0.0298 (13)
H27A	1.3420	0.0539	0.5489	0.036*
H27B	1.3177	−0.0065	0.5800	0.036*
C28	1.3432 (5)	0.0729 (3)	0.6209 (2)	0.0383 (16)
H28A	1.4330	0.0697	0.6256	0.046*

H28B	1.3079	0.0539	0.6488	0.046*
C29	1.3064 (5)	0.1411 (3)	0.6172 (2)	0.0283 (12)
H29A	1.3287	0.1623	0.6478	0.034*
H29B	1.3509	0.1616	0.5922	0.034*
C30	1.1696 (4)	0.1472 (2)	0.60519 (18)	0.0209 (10)
H30A	1.1251	0.1310	0.6319	0.025*
H30B	1.1481	0.1916	0.6007	0.025*
C31	0.6565 (4)	0.2037 (2)	0.41253 (17)	0.0135 (9)
C32	0.4659 (4)	0.1759 (2)	0.44938 (19)	0.0198 (10)
H32A	0.5208	0.1499	0.4704	0.024*
H32B	0.4027	0.1487	0.4336	0.024*
C33	0.4060 (4)	0.2252 (2)	0.47871 (18)	0.0208 (10)
H33A	0.4697	0.2508	0.4959	0.025*
H33B	0.3575	0.2049	0.5026	0.025*
C34	0.3233 (4)	0.2669 (2)	0.44662 (17)	0.0181 (10)
H34A	0.2920	0.3013	0.4657	0.022*
H34B	0.2528	0.2425	0.4332	0.022*
C35	0.3927 (4)	0.2939 (2)	0.40597 (19)	0.0190 (10)
H35A	0.3349	0.3158	0.3833	0.023*
H35B	0.4533	0.3245	0.4191	0.023*
C36	0.4575 (4)	0.2434 (2)	0.37980 (17)	0.0172 (10)
H36A	0.3965	0.2161	0.3628	0.021*
H36B	0.5078	0.2626	0.3560	0.021*
C37	0.2578 (5)	0.1666 (3)	0.0728 (2)	0.0278 (12)
H37	0.2514	0.2022	0.0499	0.033*
C38	0.7724 (5)	0.0067 (2)	0.58694 (18)	0.0236 (11)
H38	0.8238	−0.0293	0.5781	0.028*
C39	0.6417 (4)	0.1140 (2)	0.28763 (19)	0.0205 (10)
H39	0.7075	0.1446	0.2967	0.025*
C40	0.2391 (5)	0.4772 (2)	0.40386 (19)	0.0229 (11)
H40	0.2235	0.4429	0.3803	0.027*
Cl1	0.27525 (15)	0.19667 (7)	0.13078 (5)	0.0380 (3)
Cl2	0.12421 (13)	0.12117 (7)	0.06448 (6)	0.0396 (3)
Cl3	0.38652 (13)	0.12160 (8)	0.06093 (6)	0.0419 (4)
Cl4	0.64699 (12)	−0.02200 (6)	0.61511 (5)	0.0299 (3)
Cl5	0.86149 (11)	0.05557 (6)	0.62579 (5)	0.0289 (3)
Cl6	0.72543 (16)	0.04734 (7)	0.53481 (5)	0.0399 (3)
Cl7	0.59037 (12)	0.08100 (6)	0.33947 (5)	0.0277 (3)
Cl8	0.52081 (11)	0.15290 (6)	0.25591 (6)	0.0374 (3)
Cl9	0.70145 (10)	0.05570 (6)	0.25168 (5)	0.0250 (3)
Cl10	0.34932 (13)	0.52754 (7)	0.38247 (6)	0.0382 (3)
Cl11	0.29312 (14)	0.44449 (6)	0.45802 (5)	0.0365 (3)
Cl12	0.10170 (12)	0.51762 (7)	0.40935 (5)	0.0339 (3)
N1	−0.1567 (4)	0.23830 (19)	0.16329 (15)	0.0190 (8)
N2	−0.1245 (3)	0.40437 (19)	0.41379 (15)	0.0169 (8)
N3	0.4512 (3)	0.36293 (18)	0.27676 (15)	0.0160 (8)
N4	1.0992 (3)	0.07641 (18)	0.29885 (14)	0.0150 (8)
N5	1.1328 (3)	0.11261 (18)	0.56181 (14)	0.0158 (8)
N6	0.5356 (3)	0.20622 (18)	0.41341 (14)	0.0145 (8)

S1	−0.02205 (10)	0.32662 (5)	0.20779 (4)	0.0181 (2)
S2	−0.11661 (10)	0.21587 (5)	0.25634 (4)	0.0197 (2)
S3	−0.10102 (10)	0.38360 (5)	0.32173 (4)	0.0166 (2)
S4	0.06262 (9)	0.32978 (5)	0.39986 (4)	0.0154 (2)
S5	0.22112 (9)	0.39647 (5)	0.28737 (4)	0.0154 (2)
S6	0.29445 (10)	0.27030 (5)	0.25675 (5)	0.0196 (2)
S7	0.92007 (9)	0.09498 (5)	0.35621 (4)	0.0126 (2)
S8	1.14770 (9)	0.17004 (5)	0.35917 (4)	0.0149 (2)
S9	1.03365 (10)	0.09204 (5)	0.47441 (4)	0.0153 (2)
S10	1.05759 (10)	0.21769 (5)	0.51792 (4)	0.0164 (2)
S11	0.73742 (9)	0.15781 (5)	0.45477 (4)	0.0170 (2)
S12	0.73326 (9)	0.24225 (5)	0.37068 (4)	0.0137 (2)

*Atomic displacement parameters (Å²) for (*tris(piperidinedithiocarbamato)bismuth(III) chloroform solvate*)*

	U_{11}	U_{22}	U_{33}	U_{12}	U_{13}	U_{23}
Bi1	0.00988 (7)	0.01155 (8)	0.01327 (9)	−0.00147 (5)	0.00092 (6)	0.00068 (6)
Bi2	0.00858 (7)	0.01146 (8)	0.01115 (9)	0.00146 (5)	0.00078 (6)	−0.00043 (6)
C1	0.0129 (19)	0.016 (2)	0.018 (3)	0.0007 (16)	0.0015 (18)	−0.0011 (18)
C2	0.028 (3)	0.037 (3)	0.007 (2)	−0.006 (2)	0.001 (2)	−0.002 (2)
C3	0.031 (3)	0.034 (3)	0.016 (3)	−0.006 (2)	−0.004 (2)	0.007 (2)
C4	0.031 (3)	0.036 (3)	0.027 (3)	−0.004 (2)	−0.012 (2)	−0.001 (2)
C5	0.024 (2)	0.021 (2)	0.026 (3)	−0.0071 (19)	−0.005 (2)	0.003 (2)
C6	0.028 (3)	0.017 (2)	0.031 (3)	−0.0059 (19)	−0.005 (2)	−0.005 (2)
C7	0.0138 (19)	0.013 (2)	0.019 (3)	−0.0056 (16)	0.0021 (19)	0.0008 (18)
C8	0.019 (2)	0.017 (2)	0.030 (3)	0.0007 (18)	0.007 (2)	−0.004 (2)
C9	0.015 (2)	0.026 (3)	0.035 (3)	0.0017 (19)	0.006 (2)	−0.002 (2)
C10	0.028 (3)	0.030 (3)	0.031 (3)	−0.007 (2)	0.012 (3)	−0.002 (2)
C11	0.038 (3)	0.035 (3)	0.009 (2)	−0.001 (2)	0.007 (2)	−0.001 (2)
C12	0.027 (2)	0.034 (3)	0.015 (3)	0.000 (2)	0.002 (2)	−0.007 (2)
C13	0.014 (2)	0.017 (2)	0.012 (2)	0.0014 (16)	0.0025 (18)	0.0030 (18)
C14	0.0111 (19)	0.022 (2)	0.018 (3)	−0.0055 (17)	0.0012 (18)	0.0029 (19)
C15	0.020 (2)	0.016 (2)	0.023 (3)	−0.0048 (18)	0.000 (2)	0.005 (2)
C16	0.015 (2)	0.028 (3)	0.022 (3)	0.0001 (19)	0.006 (2)	0.011 (2)
C17	0.013 (2)	0.025 (3)	0.026 (3)	0.0079 (18)	0.001 (2)	−0.002 (2)
C18	0.0103 (19)	0.019 (2)	0.037 (3)	0.0038 (17)	0.003 (2)	0.005 (2)
C19	0.0091 (18)	0.014 (2)	0.012 (2)	0.0020 (15)	−0.0001 (17)	0.0037 (17)
C20	0.015 (2)	0.015 (2)	0.017 (3)	0.0000 (16)	0.0053 (19)	−0.0011 (18)
C21	0.021 (2)	0.022 (2)	0.015 (3)	−0.0060 (18)	0.000 (2)	−0.0040 (19)
C22	0.023 (2)	0.032 (3)	0.016 (3)	−0.005 (2)	0.003 (2)	−0.004 (2)
C23	0.020 (2)	0.022 (2)	0.016 (3)	−0.0048 (18)	0.003 (2)	−0.0018 (19)
C24	0.0077 (18)	0.028 (3)	0.016 (2)	−0.0010 (17)	0.0001 (18)	−0.002 (2)
C25	0.0076 (17)	0.019 (2)	0.010 (2)	0.0014 (15)	0.0026 (17)	0.0032 (17)
C26	0.026 (2)	0.017 (2)	0.018 (3)	0.0013 (18)	−0.004 (2)	0.0036 (19)
C27	0.031 (3)	0.027 (3)	0.029 (3)	0.011 (2)	−0.015 (2)	−0.005 (2)
C28	0.038 (3)	0.032 (3)	0.040 (4)	0.019 (3)	−0.025 (3)	−0.016 (3)
C29	0.026 (3)	0.030 (3)	0.027 (3)	0.008 (2)	−0.011 (2)	−0.013 (2)

C30	0.025 (2)	0.023 (3)	0.014 (3)	0.0073 (19)	−0.003 (2)	−0.001 (2)
C31	0.0121 (19)	0.014 (2)	0.014 (2)	−0.0010 (16)	0.0012 (18)	−0.0036 (17)
C32	0.0122 (19)	0.022 (2)	0.026 (3)	0.0018 (17)	0.005 (2)	0.007 (2)
C33	0.018 (2)	0.028 (3)	0.017 (3)	0.0020 (19)	0.002 (2)	0.002 (2)
C34	0.0093 (19)	0.024 (2)	0.021 (3)	−0.0023 (17)	0.0020 (19)	−0.007 (2)
C35	0.0099 (19)	0.022 (2)	0.026 (3)	0.0029 (17)	0.0013 (19)	0.006 (2)
C36	0.0079 (18)	0.029 (3)	0.014 (2)	0.0039 (17)	−0.0035 (18)	0.001 (2)
C37	0.029 (3)	0.028 (3)	0.026 (3)	−0.004 (2)	−0.005 (2)	0.006 (2)
C38	0.034 (3)	0.022 (3)	0.016 (3)	0.007 (2)	0.011 (2)	0.004 (2)
C39	0.015 (2)	0.018 (2)	0.029 (3)	−0.0001 (17)	0.001 (2)	−0.004 (2)
C40	0.032 (3)	0.018 (2)	0.018 (3)	−0.003 (2)	0.001 (2)	−0.003 (2)
Cl1	0.0571 (9)	0.0306 (7)	0.0254 (7)	−0.0016 (6)	−0.0037 (7)	0.0032 (6)
Cl2	0.0346 (7)	0.0399 (8)	0.0428 (9)	−0.0125 (6)	−0.0088 (6)	0.0138 (7)
Cl3	0.0327 (7)	0.0496 (9)	0.0413 (9)	0.0033 (6)	−0.0125 (6)	−0.0133 (7)
Cl4	0.0301 (6)	0.0305 (7)	0.0298 (7)	−0.0047 (5)	0.0062 (6)	0.0002 (5)
Cl5	0.0225 (5)	0.0305 (7)	0.0336 (8)	0.0009 (5)	0.0011 (5)	0.0054 (5)
Cl6	0.0660 (10)	0.0340 (8)	0.0195 (7)	0.0061 (7)	0.0029 (7)	0.0067 (6)
Cl7	0.0347 (6)	0.0267 (6)	0.0228 (6)	−0.0105 (5)	0.0094 (5)	−0.0037 (5)
Cl8	0.0218 (6)	0.0284 (7)	0.0604 (10)	0.0026 (5)	−0.0085 (6)	0.0146 (6)
Cl9	0.0187 (5)	0.0263 (6)	0.0307 (7)	−0.0047 (4)	0.0071 (5)	−0.0104 (5)
Cl10	0.0397 (7)	0.0288 (7)	0.0478 (9)	−0.0031 (5)	0.0158 (7)	0.0035 (6)
Cl11	0.0563 (8)	0.0210 (6)	0.0298 (7)	−0.0027 (6)	−0.0140 (7)	0.0037 (5)
Cl12	0.0272 (6)	0.0332 (7)	0.0411 (8)	0.0016 (5)	0.0003 (6)	−0.0048 (6)
N1	0.0196 (19)	0.020 (2)	0.017 (2)	−0.0007 (15)	0.0029 (17)	−0.0034 (17)
N2	0.0148 (17)	0.019 (2)	0.017 (2)	0.0004 (15)	−0.0001 (16)	−0.0024 (16)
N3	0.0115 (17)	0.0160 (19)	0.021 (2)	−0.0018 (14)	0.0040 (16)	0.0043 (16)
N4	0.0116 (16)	0.0153 (19)	0.018 (2)	0.0018 (14)	0.0008 (16)	−0.0004 (16)
N5	0.0171 (18)	0.017 (2)	0.013 (2)	0.0027 (14)	−0.0004 (16)	0.0041 (15)
N6	0.0109 (16)	0.0173 (19)	0.015 (2)	0.0014 (14)	0.0009 (16)	0.0045 (16)
S1	0.0190 (5)	0.0197 (6)	0.0156 (6)	−0.0080 (4)	0.0006 (5)	0.0030 (4)
S2	0.0216 (5)	0.0176 (5)	0.0191 (6)	−0.0080 (4)	−0.0055 (5)	0.0068 (5)
S3	0.0163 (5)	0.0193 (5)	0.0139 (6)	0.0040 (4)	−0.0002 (4)	0.0032 (4)
S4	0.0132 (4)	0.0178 (5)	0.0148 (6)	0.0019 (4)	−0.0015 (4)	0.0012 (4)
S5	0.0122 (4)	0.0128 (5)	0.0217 (6)	−0.0005 (4)	0.0039 (4)	−0.0011 (4)
S6	0.0152 (5)	0.0138 (5)	0.0305 (7)	−0.0005 (4)	0.0063 (5)	−0.0033 (5)
S7	0.0096 (4)	0.0142 (5)	0.0144 (5)	−0.0016 (3)	0.0027 (4)	−0.0030 (4)
S8	0.0107 (4)	0.0169 (5)	0.0170 (6)	−0.0032 (4)	0.0017 (4)	−0.0044 (4)
S9	0.0180 (5)	0.0122 (5)	0.0149 (6)	0.0038 (4)	−0.0032 (4)	−0.0008 (4)
S10	0.0200 (5)	0.0131 (5)	0.0155 (6)	0.0029 (4)	−0.0027 (4)	−0.0032 (4)
S11	0.0132 (5)	0.0215 (6)	0.0166 (6)	0.0025 (4)	0.0027 (4)	0.0086 (4)
S12	0.0109 (4)	0.0155 (5)	0.0147 (6)	0.0020 (4)	0.0019 (4)	0.0043 (4)

*Geometric parameters (Å, º) for (*tris(piperidinedithiocarbamato)bismuth(III) chloroform solvate*)*

Bi1—S1	2.6666 (12)	C19—S7	1.737 (4)
Bi1—S3	2.7024 (11)	C20—N4	1.473 (6)
Bi1—S5	2.7160 (11)	C20—C21	1.519 (6)
Bi1—S2	2.8671 (11)	C20—H20A	0.9900
Bi1—S6	2.8960 (11)	C20—H20B	0.9900

Bi1—S4	2.9966 (12)	C21—C22	1.522 (6)
Bi2—S11	2.6715 (11)	C21—H21A	0.9900
Bi2—S9	2.6743 (11)	C21—H21B	0.9900
Bi2—S7	2.7083 (11)	C22—C23	1.539 (6)
Bi2—S8	2.9010 (11)	C22—H22A	0.9900
Bi2—S12	2.9366 (10)	C22—H22B	0.9900
Bi2—S10	2.9703 (11)	C23—C24	1.519 (6)
C1—N1	1.342 (6)	C23—H23A	0.9900
C1—S2	1.713 (5)	C23—H23B	0.9900
C1—S1	1.737 (5)	C24—N4	1.475 (6)
C2—N1	1.478 (6)	C24—H24A	0.9900
C2—C3	1.509 (7)	C24—H24B	0.9900
C2—H2A	0.9900	C25—N5	1.342 (6)
C2—H2B	0.9900	C25—S10	1.711 (4)
C3—C4	1.520 (7)	C25—S9	1.741 (5)
C3—H3A	0.9900	C26—N5	1.473 (6)
C3—H3B	0.9900	C26—C27	1.511 (7)
C4—C5	1.521 (7)	C26—H26A	0.9900
C4—H4A	0.9900	C26—H26B	0.9900
C4—H4B	0.9900	C27—C28	1.522 (7)
C5—C6	1.511 (7)	C27—H27A	0.9900
C5—H5A	0.9900	C27—H27B	0.9900
C5—H5B	0.9900	C28—C29	1.525 (7)
C6—N1	1.466 (6)	C28—H28A	0.9900
C6—H6A	0.9900	C28—H28B	0.9900
C6—H6B	0.9900	C29—C30	1.525 (6)
C7—N2	1.339 (6)	C29—H29A	0.9900
C7—S4	1.723 (5)	C29—H29B	0.9900
C7—S3	1.725 (5)	C30—N5	1.464 (6)
C8—N2	1.473 (6)	C30—H30A	0.9900
C8—C9	1.532 (6)	C30—H30B	0.9900
C8—H8A	0.9900	C31—N6	1.333 (6)
C8—H8B	0.9900	C31—S12	1.713 (5)
C9—C10	1.528 (8)	C31—S11	1.742 (5)
C9—H9A	0.9900	C32—N6	1.467 (6)
C9—H9B	0.9900	C32—C33	1.524 (7)
C10—C11	1.512 (7)	C32—H32A	0.9900
C10—H10A	0.9900	C32—H32B	0.9900
C10—H10B	0.9900	C33—C34	1.528 (6)
C11—C12	1.531 (7)	C33—H33A	0.9900
C11—H11A	0.9900	C33—H33B	0.9900
C11—H11B	0.9900	C34—C35	1.535 (7)
C12—N2	1.469 (6)	C34—H34A	0.9900
C12—H12A	0.9900	C34—H34B	0.9900
C12—H12B	0.9900	C35—C36	1.519 (6)
C13—N3	1.342 (6)	C35—H35A	0.9900
C13—S6	1.708 (5)	C35—H35B	0.9900
C13—S5	1.746 (5)	C36—N6	1.470 (6)
C14—N3	1.468 (6)	C36—H36A	0.9900

C14—C15	1.531 (6)	C36—H36B	0.9900
C14—H14A	0.9900	C37—Cl1	1.755 (6)
C14—H14B	0.9900	C37—Cl3	1.768 (6)
C15—C16	1.528 (6)	C37—Cl2	1.768 (5)
C15—H15A	0.9900	C37—H37	1.0000
C15—H15B	0.9900	C38—Cl4	1.752 (5)
C16—C17	1.509 (7)	C38—Cl6	1.757 (5)
C16—H16A	0.9900	C38—Cl5	1.765 (6)
C16—H16B	0.9900	C38—H38	1.0000
C17—C18	1.518 (7)	C39—Cl7	1.753 (5)
C17—H17A	0.9900	C39—Cl8	1.761 (5)
C17—H17B	0.9900	C39—Cl9	1.768 (5)
C18—N3	1.470 (6)	C39—H39	1.0000
C18—H18A	0.9900	C40—Cl11	1.747 (5)
C18—H18B	0.9900	C40—Cl12	1.761 (5)
C19—N4	1.325 (6)	C40—Cl10	1.765 (5)
C19—S8	1.729 (4)	C40—H40	1.0000
S1—Bi1—S3	84.23 (4)	C20—C21—H21B	109.4
S1—Bi1—S5	86.50 (3)	C22—C21—H21B	109.4
S3—Bi1—S5	87.59 (3)	H21A—C21—H21B	108.0
S1—Bi1—S2	64.88 (3)	C21—C22—C23	110.2 (4)
S3—Bi1—S2	93.30 (3)	C21—C22—H22A	109.6
S5—Bi1—S2	151.08 (4)	C23—C22—H22A	109.6
S1—Bi1—S6	87.50 (4)	C21—C22—H22B	109.6
S3—Bi1—S6	150.87 (3)	C23—C22—H22B	109.6
S5—Bi1—S6	64.01 (3)	H22A—C22—H22B	108.1
S2—Bi1—S6	108.31 (3)	C24—C23—C22	110.8 (4)
S1—Bi1—S4	146.82 (3)	C24—C23—H23A	109.5
S3—Bi1—S4	62.78 (3)	C22—C23—H23A	109.5
S5—Bi1—S4	88.51 (3)	C24—C23—H23B	109.5
S2—Bi1—S4	117.51 (3)	C22—C23—H23B	109.5
S6—Bi1—S4	119.33 (3)	H23A—C23—H23B	108.1
S11—Bi2—S9	83.54 (3)	N4—C24—C23	109.7 (4)
S11—Bi2—S7	89.61 (3)	N4—C24—H24A	109.7
S9—Bi2—S7	80.42 (3)	C23—C24—H24A	109.7
S11—Bi2—S8	153.54 (3)	N4—C24—H24B	109.7
S9—Bi2—S8	89.82 (3)	C23—C24—H24B	109.7
S7—Bi2—S8	64.00 (3)	H24A—C24—H24B	108.2
S11—Bi2—S12	64.10 (3)	N5—C25—S10	122.4 (4)
S9—Bi2—S12	144.51 (3)	N5—C25—S9	118.7 (3)
S7—Bi2—S12	84.95 (3)	S10—C25—S9	118.9 (3)
S8—Bi2—S12	112.38 (3)	N5—C26—C27	109.7 (4)
S11—Bi2—S10	91.43 (3)	N5—C26—H26A	109.7
S9—Bi2—S10	63.33 (3)	C27—C26—H26A	109.7
S7—Bi2—S10	143.35 (3)	N5—C26—H26B	109.7
S8—Bi2—S10	108.41 (3)	C27—C26—H26B	109.7
S12—Bi2—S10	127.83 (3)	H26A—C26—H26B	108.2
N1—C1—S2	121.5 (4)	C26—C27—C28	111.7 (5)
N1—C1—S1	119.5 (4)	C26—C27—H27A	109.3

S2—C1—S1	119.0 (3)	C28—C27—H27A	109.3
N1—C2—C3	110.9 (4)	C26—C27—H27B	109.3
N1—C2—H2A	109.5	C28—C27—H27B	109.3
C3—C2—H2A	109.5	H27A—C27—H27B	107.9
N1—C2—H2B	109.5	C27—C28—C29	110.3 (5)
C3—C2—H2B	109.5	C27—C28—H28A	109.6
H2A—C2—H2B	108.0	C29—C28—H28A	109.6
C2—C3—C4	111.6 (5)	C27—C28—H28B	109.6
C2—C3—H3A	109.3	C29—C28—H28B	109.6
C4—C3—H3A	109.3	H28A—C28—H28B	108.1
C2—C3—H3B	109.3	C30—C29—C28	110.6 (5)
C4—C3—H3B	109.3	C30—C29—H29A	109.5
H3A—C3—H3B	108.0	C28—C29—H29A	109.5
C3—C4—C5	111.6 (4)	C30—C29—H29B	109.5
C3—C4—H4A	109.3	C28—C29—H29B	109.5
C5—C4—H4A	109.3	H29A—C29—H29B	108.1
C3—C4—H4B	109.3	N5—C30—C29	110.6 (4)
C5—C4—H4B	109.3	N5—C30—H30A	109.5
H4A—C4—H4B	108.0	C29—C30—H30A	109.5
C6—C5—C4	111.1 (5)	N5—C30—H30B	109.5
C6—C5—H5A	109.4	C29—C30—H30B	109.5
C4—C5—H5A	109.4	H30A—C30—H30B	108.1
C6—C5—H5B	109.4	N6—C31—S12	122.3 (4)
C4—C5—H5B	109.4	N6—C31—S11	118.2 (4)
H5A—C5—H5B	108.0	S12—C31—S11	119.5 (2)
N1—C6—C5	110.2 (4)	N6—C32—C33	109.4 (4)
N1—C6—H6A	109.6	N6—C32—H32A	109.8
C5—C6—H6A	109.6	C33—C32—H32A	109.8
N1—C6—H6B	109.6	N6—C32—H32B	109.8
C5—C6—H6B	109.6	C33—C32—H32B	109.8
H6A—C6—H6B	108.1	H32A—C32—H32B	108.2
N2—C7—S4	120.3 (4)	C32—C33—C34	110.5 (4)
N2—C7—S3	120.2 (4)	C32—C33—H33A	109.5
S4—C7—S3	119.5 (3)	C34—C33—H33A	109.5
N2—C8—C9	109.0 (4)	C32—C33—H33B	109.5
N2—C8—H8A	109.9	C34—C33—H33B	109.5
C9—C8—H8A	109.9	H33A—C33—H33B	108.1
N2—C8—H8B	109.9	C33—C34—C35	110.9 (4)
C9—C8—H8B	109.9	C33—C34—H34A	109.5
H8A—C8—H8B	108.3	C35—C34—H34A	109.5
C10—C9—C8	111.1 (4)	C33—C34—H34B	109.5
C10—C9—H9A	109.4	C35—C34—H34B	109.5
C8—C9—H9A	109.4	H34A—C34—H34B	108.0
C10—C9—H9B	109.4	C36—C35—C34	111.5 (4)
C8—C9—H9B	109.4	C36—C35—H35A	109.3
H9A—C9—H9B	108.0	C34—C35—H35A	109.3
C11—C10—C9	111.7 (4)	C36—C35—H35B	109.3
C11—C10—H10A	109.3	C34—C35—H35B	109.3
C9—C10—H10A	109.3	H35A—C35—H35B	108.0

C11—C10—H10B	109.3	N6—C36—C35	110.5 (4)
C9—C10—H10B	109.3	N6—C36—H36A	109.6
H10A—C10—H10B	107.9	C35—C36—H36A	109.6
C10—C11—C12	110.5 (4)	N6—C36—H36B	109.6
C10—C11—H11A	109.6	C35—C36—H36B	109.6
C12—C11—H11A	109.6	H36A—C36—H36B	108.1
C10—C11—H11B	109.6	Cl1—C37—Cl3	110.0 (3)
C12—C11—H11B	109.6	Cl1—C37—Cl2	111.3 (3)
H11A—C11—H11B	108.1	Cl3—C37—Cl2	109.9 (3)
N2—C12—C11	109.8 (4)	Cl1—C37—H37	108.5
N2—C12—H12A	109.7	Cl3—C37—H37	108.5
C11—C12—H12A	109.7	Cl2—C37—H37	108.5
N2—C12—H12B	109.7	Cl4—C38—Cl6	111.1 (3)
C11—C12—H12B	109.7	Cl4—C38—Cl5	110.5 (3)
H12A—C12—H12B	108.2	Cl6—C38—Cl5	109.8 (3)
N3—C13—S6	121.8 (4)	Cl4—C38—H38	108.5
N3—C13—S5	119.1 (4)	Cl6—C38—H38	108.5
S6—C13—S5	119.1 (3)	Cl5—C38—H38	108.5
N3—C14—C15	109.3 (4)	Cl7—C39—Cl8	109.8 (3)
N3—C14—H14A	109.8	Cl7—C39—Cl9	110.2 (3)
C15—C14—H14A	109.8	Cl8—C39—Cl9	110.2 (3)
N3—C14—H14B	109.8	Cl7—C39—H39	108.9
C15—C14—H14B	109.8	Cl8—C39—H39	108.9
H14A—C14—H14B	108.3	Cl9—C39—H39	108.9
C16—C15—C14	110.6 (4)	Cl11—C40—Cl12	111.3 (3)
C16—C15—H15A	109.5	Cl11—C40—Cl10	110.3 (3)
C14—C15—H15A	109.5	Cl12—C40—Cl10	110.0 (3)
C16—C15—H15B	109.5	Cl11—C40—H40	108.4
C14—C15—H15B	109.5	Cl12—C40—H40	108.4
H15A—C15—H15B	108.1	Cl10—C40—H40	108.4
C17—C16—C15	110.9 (4)	C1—N1—C6	123.5 (4)
C17—C16—H16A	109.4	—N1—C2	124.2 (4)
C15—C16—H16A	109.4	C6—N1—C2	112.3 (4)
C17—C16—H16B	109.5	C7—N2—C12	124.0 (4)
C15—C16—H16B	109.4	C7—N2—C8	123.5 (4)
H16A—C16—H16B	108.0	C12—N2—C8	112.2 (4)
C16—C17—C18	111.5 (4)	C13—N3—C14	124.0 (4)
C16—C17—H17A	109.3	C13—N3—C18	123.6 (4)
C18—C17—H17A	109.3	C14—N3—C18	112.2 (4)
C16—C17—H17B	109.3	C19—N4—C20	124.3 (4)
C18—C17—H17B	109.3	C19—N4—C24	122.5 (4)
H17A—C17—H17B	108.0	C20—N4—C24	112.9 (4)
N3—C18—C17	109.2 (4)	C25—N5—C30	123.4 (4)
N3—C18—H18A	109.8	C25—N5—C26	123.4 (4)
C17—C18—H18A	109.8	C30—N5—C26	113.1 (4)
N3—C18—H18B	109.8	C31—N6—C32	124.4 (4)
C17—C18—H18B	109.8	C31—N6—C36	123.3 (4)
H18A—C18—H18B	108.3	C32—N6—C36	112.1 (4)
N4—C19—S8	121.1 (3)	C1—S1—Bi1	90.45 (16)

N4—C19—S7	120.5 (3)	C1—S2—Bi1	84.42 (16)
S8—C19—S7	118.4 (3)	C7—S3—Bi1	93.50 (16)
N4—C20—C21	110.2 (4)	C7—S4—Bi1	83.90 (17)
N4—C20—H20A	109.6	C13—S5—Bi1	89.58 (15)
C21—C20—H20A	109.6	C13—S6—Bi1	84.51 (15)
N4—C20—H20B	109.6	C19—S7—Bi2	91.87 (15)
C21—C20—H20B	109.6	C19—S8—Bi2	85.74 (15)
H20A—C20—H20B	108.1	C25—S9—Bi2	93.43 (15)
C20—C21—C22	111.4 (4)	C25—S10—Bi2	84.30 (15)
C20—C21—H21A	109.4	C31—S11—Bi2	92.23 (15)
C22—C21—H21A	109.4	C31—S12—Bi2	84.16 (15)
N1—C2—C3—C4	−53.4 (6)	S4—Bi1—S1—C1	−108.99 (16)
C2—C3—C4—C5	51.0 (7)	N1—C1—S2—Bi1	169.8 (4)
C3—C4—C5—C6	−52.3 (6)	S1—C1—S2—Bi1	−10.7 (2)
C4—C5—C6—N1	56.1 (6)	S1—Bi1—S2—C1	6.69 (15)
N2—C8—C9—C10	55.5 (6)	S3—Bi1—S2—C1	88.74 (15)
C8—C9—C10—C11	−52.8 (6)	S5—Bi1—S2—C1	−2.26 (18)
C9—C10—C11—C12	52.6 (6)	S6—Bi1—S2—C1	−71.43 (16)
C10—C11—C12—N2	−56.2 (6)	S4—Bi1—S2—C1	149.62 (15)
N3—C14—C15—C16	−56.2 (5)	N2—C7—S3—Bi1	−174.4 (3)
C14—C15—C16—C17	53.0 (5)	S4—C7—S3—Bi1	5.8 (3)
C15—C16—C17—C18	−53.4 (5)	S1—Bi1—S3—C7	−179.55 (15)
C16—C17—C18—N3	56.5 (5)	S5—Bi1—S3—C7	−92.82 (15)
N4—C20—C21—C22	55.3 (5)	S2—Bi1—S3—C7	116.13 (15)
C20—C21—C22—C23	−53.8 (6)	S6—Bi1—S3—C7	−105.28 (16)
C21—C22—C23—C24	54.6 (5)	S4—Bi1—S3—C7	−3.26 (14)
C22—C23—C24—N4	−56.6 (5)	N2—C7—S4—Bi1	174.9 (4)
N5—C26—C27—C28	55.9 (6)	S3—C7—S4—Bi1	−5.2 (2)
C26—C27—C28—C29	−54.7 (7)	S1—Bi1—S4—C7	10.03 (16)
C27—C28—C29—C30	53.7 (7)	S3—Bi1—S4—C7	3.27 (15)
C28—C29—C30—N5	−55.3 (6)	S5—Bi1—S4—C7	91.33 (15)
N6—C32—C33—C34	58.0 (5)	S2—Bi1—S4—C7	−75.49 (15)
C32—C33—C34—C35	−53.3 (5)	S6—Bi1—S4—C7	150.18 (15)
C33—C34—C35—C36	51.3 (5)	N3—C13—S5—Bi1	−162.8 (4)
C34—C35—C36—N6	−53.7 (5)	S6—C13—S5—Bi1	16.9 (3)
S2—C1—N1—C6	3.2 (6)	S1—Bi1—S5—C13	−98.50 (16)
S1—C1—N1—C6	−176.3 (4)	S3—Bi1—S5—C13	177.14 (16)
S2—C1—N1—C2	−179.6 (4)	S2—Bi1—S5—C13	−90.39 (17)
S1—C1—N1—C2	0.9 (6)	S6—Bi1—S5—C13	−9.57 (16)
C5—C6—N1—C1	117.9 (5)	S4—Bi1—S5—C13	114.33 (16)
C5—C6—N1—C2	−59.7 (6)	N3—C13—S6—Bi1	163.8 (4)
C3—C2—N1—C1	−119.1 (5)	S5—C13—S6—Bi1	−15.9 (3)
C3—C2—N1—C6	58.5 (6)	S1—Bi1—S6—C13	97.16 (16)
S4—C7—N2—C12	−4.1 (6)	S3—Bi1—S6—C13	23.72 (18)
S3—C7—N2—C12	176.1 (4)	S5—Bi1—S6—C13	9.84 (16)
S4—C7—N2—C8	−176.6 (3)	S2—Bi1—S6—C13	159.64 (16)
S3—C7—N2—C8	3.6 (6)	S4—Bi1—S6—C13	−62.29 (16)
C11—C12—N2—C7	−111.5 (5)	N4—C19—S7—Bi2	179.2 (4)
C11—C12—N2—C8	61.8 (5)	S8—C19—S7—Bi2	0.1 (2)

C9—C8—N2—C7	112.2 (5)	S11—Bi2—S7—C19	−178.09 (14)
C9—C8—N2—C12	−61.1 (5)	S9—Bi2—S7—C19	−94.58 (15)
S6—C13—N3—C14	176.6 (3)	S8—Bi2—S7—C19	−0.06 (14)
S5—C13—N3—C14	−3.8 (6)	S12—Bi2—S7—C19	117.88 (14)
S6—C13—N3—C18	3.2 (7)	S10—Bi2—S7—C19	−86.22 (15)
S5—C13—N3—C18	−177.2 (4)	N4—C19—S8—Bi2	−179.2 (4)
C15—C14—N3—C13	−112.7 (5)	S7—C19—S8—Bi2	−0.1 (2)
C15—C14—N3—C18	61.4 (5)	S11—Bi2—S8—C19	4.47 (17)
C17—C18—N3—C13	112.8 (5)	S9—Bi2—S8—C19	79.47 (15)
C17—C18—N3—C14	−61.3 (5)	S7—Bi2—S8—C19	0.06 (14)
S8—C19—N4—C20	−175.3 (3)	S12—Bi2—S8—C19	−72.08 (15)
S7—C19—N4—C20	5.6 (6)	S10—Bi2—S8—C19	141.17 (14)
S8—C19—N4—C24	−1.7 (6)	N5—C25—S9—Bi2	179.7 (3)
S7—C19—N4—C24	179.2 (3)	S10—C25—S9—Bi2	0.9 (2)
C21—C20—N4—C19	115.5 (5)	S11—Bi2—S9—C25	−95.37 (14)
C21—C20—N4—C24	−58.6 (5)	S7—Bi2—S9—C25	173.94 (14)
C23—C24—N4—C19	−114.8 (5)	S8—Bi2—S9—C25	110.30 (14)
C23—C24—N4—C20	59.5 (5)	S12—Bi2—S9—C25	−119.04 (14)
S10—C25—N5—C30	2.5 (6)	S10—Bi2—S9—C25	−0.49 (14)
S9—C25—N5—C30	−176.3 (3)	N5—C25—S10—Bi2	−179.5 (4)
S10—C25—N5—C26	−174.9 (3)	S9—C25—S10—Bi2	−0.8 (2)
S9—C25—N5—C26	6.3 (6)	S11—Bi2—S10—C25	82.54 (14)
C29—C30—N5—C25	−119.2 (5)	S9—Bi2—S10—C25	0.50 (14)
C29—C30—N5—C26	58.4 (6)	S7—Bi2—S10—C25	−8.72 (15)
C27—C26—N5—C25	119.3 (5)	S8—Bi2—S10—C25	−79.66 (14)
C27—C26—N5—C30	−58.3 (6)	S12—Bi2—S10—C25	140.28 (14)
S12—C31—N6—C32	−177.8 (4)	N6—C31—S11—Bi2	−179.6 (4)
S11—C31—N6—C32	3.8 (6)	S12—C31—S11—Bi2	1.9 (3)
S12—C31—N6—C36	−1.8 (7)	S9—Bi2—S11—C31	−166.07 (15)
S11—C31—N6—C36	179.8 (3)	S7—Bi2—S11—C31	−85.67 (15)
C33—C32—N6—C31	114.4 (5)	S8—Bi2—S11—C31	−89.63 (17)
C33—C32—N6—C36	−62.0 (5)	S12—Bi2—S11—C31	−1.09 (15)
C35—C36—N6—C31	−116.5 (5)	S10—Bi2—S11—C31	130.97 (15)
C35—C36—N6—C32	59.9 (5)	N6—C31—S12—Bi2	179.9 (4)
N1—C1—S1—Bi1	−169.1 (4)	S11—C31—S12—Bi2	−1.8 (2)
S2—C1—S1—Bi1	11.4 (3)	S11—Bi2—S12—C31	1.11 (15)
S3—Bi1—S1—C1	−102.95 (15)	S9—Bi2—S12—C31	27.44 (17)
S5—Bi1—S1—C1	169.12 (15)	S7—Bi2—S12—C31	93.13 (15)
S2—Bi1—S1—C1	−6.56 (15)	S8—Bi2—S12—C31	152.31 (15)
S6—Bi1—S1—C1	105.01 (15)	S10—Bi2—S12—C31	−68.90 (16)

Crystallographic data for (tris-(jpiperidinedithiocarbamato)bismuth(III))

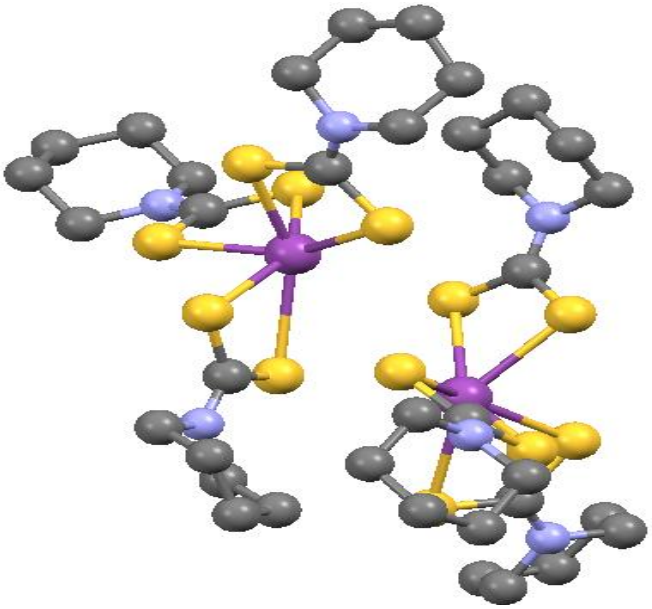

Experimental details
Crystal data

Chemical formula	C18H30BiN3S6
Mr	689.79
Crystal system, space group=	Orthorhombic, Pbca
a =	11.011 (5) Å
b =	27.789 (5) Å
c =	35.120 (5) Å
V =	10746 (5) Å3
Z =	16
F(000) =	5408

Data collection

diffractometer	Bruker APEXII CCD
Absorption correction:	multi-scan
Tmin =	0.546,
Tmax =	0.745

Refinement
Refinement on F2
Least-squares matrix: full

R[F2 > 2σ(F2)] =	0.024

Dx =	1.705 Mg m−3
Mo Kα radiation, λ =	0.71073 Å

Cell parameters from 10639 reflections

θ =	1.5–26.1°
μ =	7.04 mm−1
T =	100 K

Needle, yellow
0.45 × 0.02 × 0.02 mm

Fractional atomic coordinates and isotropic or equivalent isotropic displacement parameters ($Å^2$) for

(tris-(jpiperidinedithiocarbamato)bismuth(III))

	x	y	z	U_{iso}*/U_{eq}
Bi01	0.40459 (2)	0.38678 (2)	0.09056 (2)	0.01221 (5)
Bi02	0.53380 (2)	0.24319 (2)	0.13380 (2)	0.01364 (5)
S003	0.18566 (9)	0.42294 (4)	0.07342 (3)	0.0177
S004	0.36647 (10)	0.25524 (4)	0.18817 (3)	0.0169 (2)
S005	0.50028 (10)	0.45807 (4)	0.04920 (3)	0.0172 (2)
S006	0.39462 (9)	0.34176 (4)	0.02229 (3)	0.0144 (2)
S007	0.46234 (10)	0.15161 (4)	0.13360 (3)	0.0175 (2)
S008	0.61300 (9)	0.32598 (4)	0.07036 (3)	0.0136 (2)
S009	0.52266 (9)	0.33936 (4)	0.16925 (3)	0.0165 (2)
S010	0.19620 (9)	0.32980 (4)	0.11535 (3)	0.0162 (2)
S011	0.31846 (10)	0.21933 (4)	0.08581 (3)	0.0191 (2)
S012	0.67860 (10)	0.21825 (4)	0.19101 (3)	0.0212 (2)
S013	0.78970 (10)	0.21796 (4)	0.11400 (3)	0.0179 (2)
S014	0.45891 (11)	0.47665 (4)	0.13167 (3)	0.0223 (2)
C20	0.5282 (3)	0.30995 (14)	0.03127 (11)	0.0118 (8)
N016	0.3354 (3)	0.34248 (13)	0.21724 (10)	0.0182 (8)
N017	−0.0088 (3)	0.37667 (13)	0.09965 (10)	0.0161 (7)
N018	0.9161 (3)	0.21364 (15)	0.17867 (10)	0.0204 (8)
N019	0.5629 (4)	0.53900 (13)	0.08386 (10)	0.0187 (8)
N020	0.2921 (3)	0.12395 (14)	0.08489 (10)	0.0209 (8)
N021	0.5622 (3)	0.27443 (13)	0.00845 (10)	0.0136 (7)
C4	−0.0797 (4)	0.34019 (16)	0.12033 (13)	0.0182 (9)
H4A	−0.024867	0.314441	0.129518	0.022*
H4B	−0.139899	0.325478	0.102935	0.022*
C7	0.9969 (4)	0.16635 (19)	0.23180 (13)	0.0268(11)
H7A	1.007840	0.165582	0.259775	0.032*
H7B	0.946743	0.138301	0.224416	0.032*
C3	0.2307 (4)	0.10596 (16)	0.01894 (14)	0.0234 (10)
H3A	0.296318	0.125500	0.007447	0.028*
H3B	0.160450	0.106451	0.001340	0.028*
C6	0.9325 (4)	0.21234 (19)	0.22053 (12)	0.0250 (11)
H6A	0.852357	0.213935	0.233234	0.030*
H6B	0.980940	0.240472	0.228801	0.030*
C21	0.8080 (4)	0.21621 (15)	0.16230 (12)	0.0168 (9)
C5	−0.2226 (4)	0.40547 (18)	0.14140 (14)	0.0264 (10)
H5A	−0.255466	0.422062	0.164106	0.032*
H5B	−0.291900	0.393632	0.126094	0.032*
C2	0.5120 (4)	0.49570 (16)	0.08842 (12)	0.0157 (9)
C029	0.4930 (4)	0.25820 (15)	−0.02514 (12)	0.0148 (8)
H02A	0.545551	0.258902	−0.047995	0.018*
H02B	0.423211	0.279967	−0.029578	0.018*
C030	1.1034 (4)	0.16652 (19)	0.16914 (13)	0.0280 (11)
H03A	1.184197	0.167318	0.156813	0.034*
H03B	1.059872	0.137618	0.159867	0.034*
C032	−0.1486 (5)	0.44078 (18)	0.11789 (16)	0.0312 (12)
H03C	−0.202719	0.466222	0.107800	0.037*
H03D	−0.086900	0.456321	0.134295	0.037*
C033	0.2369 (4)	0.41981 (17)	0.20405 (15)	0.0261 (10)
H03E	0.244866	0.455100	0.207018	0.031*
H03F	0.230385	0.412568	0.176524	0.031*
C035	0.2295 (4)	0.32446 (17)	0.23853 (12)	0.0204 (9)
H03G	0.238706	0.332280	0.265878	0.025*
H03H	0.224441	0.289034	0.235974	0.025*
C036	0.5895 (4)	0.57184 (16)	0.11570 (12)	0.0202 (10)
H03I	0.549745	0.560009	0.139174	0.024*
H03J	0.557215	0.604289	0.109960	0.024*
C037	0.4479 (4)	0.20740 (16)	−0.01819 (12)	0.0175 (9)
H03K	0.405198	0.195678	−0.041204	0.021*
H03L	0.389036	0.207605	0.003118	0.021*
C038	−0.0859 (4)	0.41527 (17)	0.08495 (13)	0.0216 (10)
H03M	−0.147484	0.401698	0.067460	0.026*

H03N	−0.035818	0.438563	0.070499	0.026*
C040	0.7265 (4)	0.57458 (17)	0.12174 (13)	0.0244 (10)
H04A	0.744534	0.598561	0.141805	0.029*
H04B	0.756673	0.542922	0.130543	0.029*
C042	0.2744 (5)	0.05456 (17)	0.02376 (15)	0.0302 (11)
H04C	0.307083	0.042615	−0.000735	0.036*
H04D	0.205180	0.033783	0.031092	0.036*
C043	0.7922 (5)	0.5886 (2)	0.08536 (14)	0.0331 (12)
H04E	0.880871	0.585668	0.089352	0.040*
H04F	0.774039	0.622635	0.079308	0.040*
C044	0.7544 (4)	0.55684 (18)	0.05170 (13)	0.0248 (10)
H04G	0.790610	0.569662	0.027978	0.030*
H04H	0.785701	0.523811	0.055594	0.030*
C045	1.0328 (4)	0.21107 (19)	0.15819 (13)	0.0226 (10)
H04I	1.081754	0.239989	0.164167	0.027*
H04J	1.017436	0.210765	0.130421	0.027*
C046	0.5521 (4)	0.17321 (17)	−0.00870 (13)	0.0208 (9)
H04K	0.606698	0.170020	−0.030960	0.025*
H04L	0.519562	0.140948	−0.002468	0.025*
C047	0.3508 (4)	0.16166 (16)	0.09921 (11)	0.0165 (9)
C049	0.6230 (4)	0.19305 (16)	0.02527 (12)	0.0176 (9)
H04M	0.569977	0.193629	0.048042	0.021*
H04N	0.693065	0.171858	0.030780	0.021*
C050	0.3497 (4)	0.39494 (17)	0.22051 (14)	0.0236 (10)
H05A	0.422916	0.405390	0.206415	0.028*
H05B	0.359836	0.403997	0.247582	0.028*
C051	0.3273 (5)	0.07362 (17)	0.09140 (13)	0.0277 (11)
H05C	0.256681	0.055132	0.100887	0.033*
H05D	0.392249	0.072108	0.110873	0.033*
C052	0.3727 (5)	0.05174 (17)	0.05420 (15)	0.0296 (11)
H05E	0.395480	0.017702	0.058446	0.036*
H05F	0.445779	0.069293	0.045475	0.036*
C053	1.1193 (5)	0.1632 (2)	0.21255 (14)	0.0305 (11)
H05G	1.158855	0.132342	0.219225	0.037*
H05H	1.171947	0.189749	0.221505	0.037*
C055	0.4018 (4)	0.31565 (16)	0.19391 (11)	0.0151 (9)
C058	0.1120 (4)	0.37600 (15)	0.09707 (11)	0.0128 (8)
C059	0.1937 (4)	0.12803 (19)	0.05665 (13)	0.0261 (10)
H05I	0.173348	0.162392	0.052818	0.031*
H05J	0.120340	0.111503	0.066359	0.031*
C062	0.6170 (4)	0.55527 (16)	0.04767 (12)	0.0214 (10)
H06A	0.585968	0.587673	0.041140	0.026
H06B	0.594206	0.532897	0.026929	0.026*
C065	0.1136 (4)	0.34743 (17)	0.22316 (13)	0.0208 (10)
H06C	0.043410	0.336775	0.238611	0.025*
H06D	0.100149	0.336802	0.196587	0.025*
C068	0.1228 (4)	0.40262 (18)	0.22439 (15)	0.0273 (11)
H06E	0.050351	0.416864	0.212052	0.033*
H06F	0.124562	0.413539	0.251218	0.033*
C069	−0.1449 (4)	0.36297 (18)	0.15398 (12)	0.0228 (10)
H06G	−0.084241	0.374040	0.172865	0.027*
H06H	−0.197095	0.338591	0.166401	0.027*
C1	0.6674 (4)	0.24325 (15)	0.01680 (13)	0.0174 (9)
H1A	0.712574	0.256037	0.038985	0.021*
H1B	0.723057	0.242635	−0.005339	0.021*

Atomic displacement parameters ($Å^2$) for (tris-(jpiperidinedithiocarbamato)bismuth(III))

	U^{11}	U^{22}	U^{33}	U^{12}	U^{13}	U^{23}
Bi01	0.01017 (8)	0.01409 (8)	0.01237 (8)	−0.00111 (6)	0.00024 (6)	−0.00008 (6)
Bi02	0.01293 (9)	0.01786 (9)	0.01012 (8)	0.00178 (6)	0.00089 (6)	0.00101 (6)
S003	0.0135 (5)	0.0144 (5)	0.0251 (6)	−0.0008 (4)	−0.0005 (4)	0.0050 (4)
S004	0.0163 (5)	0.0211 (5)	0.0134 (5)	−0.0002 (4)	0.0024 (4)	0.0019 (4)
S005	0.0216 (5)	0.0183 (5)	0.0116 (5)	−0.0057 (4)	0.0011 (4)	−0.0011 (4)
S006	0.0123 (5)	0.0158 (5)	0.0150 (5)	0.0007 (4)	−0.0046 (4)	−0.0005 (4)
S007	0.0177 (5)	0.0188 (5)	0.0160 (5)	0.0020 (4)	−0.0034 (4)	0.0024 (4)
S008	0.0116 (5)	0.0186 (5)	0.0107 (5)	−0.0001 (4)	−0.0026 (4)	−0.0011 (4)
S009	0.0131 (5)	0.0227 (5)	0.0138 (5)	−0.0014 (4)	0.0010 (4)	0.0001 (4)
S010	0.0125 (5)	0.0179 (5)	0.0182 (5)	0.0018 (4)	0.0014 (4)	0.0056 (4)
S011	0.0209 (5)	0.0219 (6)	0.0144 (5)	0.0081 (5)	−0.0029 (4)	−0.0005 (4)
S012	0.0155 (5)	0.0373 (7)	0.0109 (5)	0.0046 (5)	0.0026 (4)	0.0029 (4)
S013	0.0162 (5)	0.0270 (6)	0.0104 (5)	−0.0004 (4)	0.0008 (4)	0.0008 (4)
S014	0.0307 (6)	0.0221 (6)	0.0142 (5)	0.0091 (5)	0.0071 (4)	−0.0027 (4)
C20	0.0115 (19)	0.014 (2)	0.0101 (19)	−0.0034 (16)	0.0026 (15)	0.0024 (15)
N016	0.0158 (18)	0.025 (2)	0.0140 (18)	0.0018 (16)	0.0005 (14)	−0.0012 (15)
N017	0.0126 (17)	0.0173 (18)	0.0185 (18)	0.0012 (15)	0.0011 (14)	0.0039 (15)
N018	0.0132 (18)	0.037 (2)	0.0115 (18)	0.0047 (16)	0.0007 (14)	−0.0040 (16)
N019	0.0256 (19)	0.0179 (19)	0.0125 (18)	−0.0093 (16)	0.0006 (15)	0.0005 (15)
N020	0.0189 (19)	0.028 (2)	0.0163 (19)	0.0002 (17)	−0.0040 (15)	0.0001 (16)
N021	0.0114 (16)	0.0173 (18)	0.0123 (17)	−0.0021 (14)	−0.0017 (13)	−0.0010 (14)
C4	0.011 (2)	0.019 (2)	0.024 (2)	−0.0016 (17)	0.0016 (17)	0.0026 (19)
C7	0.026 (2)	0.039 (3)	0.016 (2)	−0.008 (2)	−0.0063 (19)	0.003 (2)
C3	0.024 (2)	0.021 (2)	0.026 (2)	−0.0076 (19)	−0.007 (2)	−0.0005 (19)
C6	0.018 (2)	0.046 (3)	0.012 (2)	0.000 (2)	−0.0018 (17)	−0.004 (2)
C21	0.018 (2)	0.017 (2)	0.016 (2)	0.0024 (17)	0.0006 (17)	0.0008 (17)
C5	0.019 (2)	0.029 (3)	0.031 (3)	0.004 (2)	0.002 (2)	−0.009 (2)
C2	0.015 (2)	0.017 (2)	0.015 (2)	−0.0019 (17)	0.0013 (16)	−0.0012 (17)
C029	0.016 (2)	0.018 (2)	0.010 (2)	0.0009 (17)	−0.0049 (16)	−0.0030 (16)
C030	0.024 (2)	0.041 (3)	0.019 (2)	0.006 (2)	0.0034 (19)	−0.008 (2)
C032	0.024 (3)	0.019 (2)	0.051 (3)	0.003 (2)	0.000 (2)	−0.004 (2)
C033	0.023 (2)	0.020 (2)	0.035 (3)	0.002 (2)	0.001 (2)	−0.002 (2)
C035	0.017 (2)	0.032 (3)	0.013 (2)	0.004 (2)	0.0047 (17)	−0.0012 (18)
C036	0.028 (2)	0.015 (2)	0.018 (2)	−0.0039 (19)	0.0049 (18)	−0.0038 (17)
C037	0.015 (2)	0.022 (2)	0.016 (2)	−0.0001 (18)	−0.0017 (17)	−0.0084 (18)
C038	0.014 (2)	0.025 (2)	0.027 (2)	0.0029 (19)	0.0005 (18)	0.0104 (19)
C040	0.029 (3)	0.021 (2)	0.023 (2)	−0.003 (2)	−0.008 (2)	−0.0094 (19)
C042	0.040 (3)	0.020 (2)	0.030 (3)	−0.005 (2)	−0.006 (2)	−0.001 (2)
C043	0.027 (3)	0.042 (3)	0.030 (3)	−0.011 (2)	0.003 (2)	−0.015 (2)
C044	0.026 (2)	0.026 (2)	0.023 (2)	−0.007 (2)	0.004 (2)	−0.0019 (19)
C045	0.013 (2)	0.042 (3)	0.012 (2)	0.000 (2)	−0.0001 (17)	0.002 (2)
C046	0.016 (2)	0.020 (2)	0.026 (2)	−0.0002 (18)	0.0042 (18)	−0.0019 (19)
C047	0.015 (2)	0.027 (2)	0.0072 (19)	0.0024 (18)	0.0042 (16)	0.0005 (17)
C049	0.014 (2)	0.021 (2)	0.018 (2)	0.0052 (18)	0.0055 (17)	0.0032 (17)
C050	0.020 (2)	0.028 (2)	0.023 (2)	0.000 (2)	−0.0016 (19)	−0.0103 (19)
C051	0.034 (3)	0.023 (2)	0.026 (3)	−0.010 (2)	−0.010 (2)	0.006 (2)
C052	0.036 (3)	0.016 (2)	0.036 (3)	0.002 (2)	−0.008 (2)	−0.001 (2)
C053	0.029 (3)	0.037 (3)	0.025 (3)	0.009 (2)	−0.003 (2)	0.002 (2)
C055	0.0118 (19)	0.024 (2)	0.0097 (19)	0.0006 (17)	−0.0052 (15)	0.0027 (17)
C058	0.014 (2)	0.014 (2)	0.0112 (19)	−0.0011 (16)	0.0025 (15)	−0.0015 (16)
C059	0.019 (2)	0.032 (3)	0.027 (3)	0.003 (2)	−0.008 (2)	−0.003 (2)
C062	0.031 (2)	0.019 (2)	0.014 (2)	−0.010 (2)	−0.0006 (19)	0.0029 (17)
C065	0.013 (2)	0.033 (3)	0.017 (2)	0.0033 (19)	0.0005 (17)	−0.0006 (19)
C068	0.019 (2)	0.032 (3)	0.031 (3)	0.003 (2)	−0.002 (2)	−0.008 (2)
C069	0.015 (2)	0.038 (3)	0.015 (2)	−0.001 (2)	−0.0006 (18)	−0.001 (2)
C1	0.011 (2)	0.024 (2)	0.017 (2)	0.0016 (18)	0.0007 (17)	0.0002 (18)

Geometric parameters (Å, º) for (tris-(jpiperidinedithiocarbamato)bismuth(III))

Bi01—S005	2.6729 (11)	C030—C053	1.537
(7) Bi01—S003	2.6801 (14)	C030—H03A	0.9900
Bi01—S006	2.7063 (11)	C030—H03B	0.9900
Bi01—S010	2.9206 (13)	C032—C038	1.523
(7) Bi01—S008	2.9366 (13)	C032—H03C	0.9900
Bi01—S014	2.9462 (12)	C032—H03D	0.9900
Bi02—S012	2.6571 (12)	C033—C068	1.522 (7)
Bi02—S007	2.6638 (12)	C033—C050	1.534 (6)
Bi02—S004	2.6746 (12)	C033—H03E	0.9900
Bi02—S009	2.9508 (12)	C033—H03F	0.9900
Bi02—S011	2.9838 (14)	C035—C065	1.526
(6) Bi02—S013	2.9856 (16)	C035—H03G	0.9900
S003—C058	1.746 (4)	C035—H03H	0.9900
S004—C055	1.735 (5)	C036—C040	1.525
(7) S005—C2	1.734 (4)	C036—H03I	0.9900
S006—C20	1.745 (4)	C036—H03J	0.9900
S007—C047	1.745 (4)	C037—C046	1.527
(6) S008—C20	1.719 (4)	C037—H03K	0.9900
S009—C055	1.719 (4)	C037—H03L	0.9900
S010—C058	1.709 (4)	C038—H03M	0.9900
S011—C047	1.708 (5)	C038—H03N	0.9900
S012—C21	1.746 (4)	C040—C043	1.519
(7) S013—C21	1.709 (4)	C040—H04A	0.9900
S014—C2	1.711 (4)	C040—H04B	0.9900
C20—N021	1.325 (5)	C042—C052	1.523
(7) N016—C055	1.328 (6)	C042—H04C	0.9900
N016—C035	1.472 (5)	C042—H04D	0.9900
N016—C050	1.471 (6)	C043—C044	1.533
(6) N017—C058	1.333 (5)	C043—H04E	0.9900
N017—C038	1.462 (6)	C043—H04F	0.9900
N017—C4	1.471 (5)	C044—C062	1.520
(7) N018—C21	1.324 (5)	C044—H04G	0.9900
N018—C045	1.474 (5)	C044—H04H	0.9900
N018—C6	1.482 (5)	C045—H04I	0.9900
N019—C2	1.337 (6)	C045—H04J	0.9900
N019—C036	1.473 (5)	C046—C049	1.528
(6) N019—C062	1.475 (5)	C046—H04K	0.9900
N020—C047	1.330 (6)	C046—H04L	0.9900
N020—C051	1.470 (6)	C049—C1	1.508
(6) N020—C059	1.473 (6)	C049—H04M	0.9900
N021—C1	1.476 (5)	C049—H04N	0.9900
N021—C029	1.475 (5)	C050—H05A	0.9900
C4—C069	1.521 (6)	C050—H05B	0.9900
C4—H4A	0.9900	C051—C052	1.525
(7) C4—H4B	0.9900	C051—H05C	0.9900
C7—C053	1.510 (7)	C051—H05D	0.9900
C7—C6	1.514 (7)	C052—H05E	0.9900
C7—H7A	0.9900	C052—H05F	0.9900
C7—H7B	0.9900	C053—H05G	0.9900
C3—C059	1.515 (7)	C053—H05H	0.9900
C3—C042	1.517 (7)	C059—H05I	0.9900
C3—H3A	0.9900	C059—H05J	0.9900
C3—H3B	0.9900	C062—H06A	0.9900
C6—H6A	0.9900	C062—H06B	0.9900
C6—H6B	0.9900	C065—C068	1.537
(7) C5—C069	1.524 (7)	C065—H06C	0.9900
C5—C032	1.519 (7)	C065—H06D	0.9900
C5—H5A	0.9900	C068—H06E	0.9900
C5—H5B	0.9900	C068—H06F	0.9900
C029—C037	1.516 (6)	C069—H06G	0.9900
C029—H02A	0.9900	C069—H06H	0.9900
C029—H02B	0.9900	C1—H1A	0.9900
C030—C045	1.511 (7)	C1—H1B	0.9900

S005—Bi01—S003 87.40 (4)
(4) S005—Bi01—S006 82.95 (3)
S003—Bi01—S006 86.44 (3)
S005—Bi01—S010 150.87 (3)
S003—Bi01—S010 64.12 (4)
S006—Bi01—S010 88.95 (3)
S005—Bi01—S008 89.26 (4)
(4) S003—Bi01—S008 149.81 (3)
S006—Bi01—S008 63.37 (3)
S010—Bi01—S008 111.96 (4)
S005—Bi01—S014 63.77 (3)
S003—Bi01—S014 88.56 (4)
S006—Bi01—S014 146.53 (3)
S010—Bi01—S014 118.23 (3)
S008—Bi01—S014 116.58 (4)
S012—Bi02—S007 85.99 (4)
S012—Bi02—S004 84.61 (4)
S007—Bi02—S004 85.30 (3)
S012—Bi02—S009 86.68 (3)
111.5 (4) S007—Bi02—S009 148.66 (3)
S004—Bi02—S009 63.69 (3)
S012—Bi02—S011 147.78 (4)
S007—Bi02—S011 63.35 (3)
S004—Bi02—S011 83.32 (4)
S009—Bi02—S011 113.99 (3)
110.6 (4) S012—Bi02—S013 63.17 (4)
S007—Bi02—S013 93.09 (4)
S004—Bi02—S013 147.76 (3)
S009—Bi02—S013 110.50 (3)
S011—Bi02—S013 124.49 (4)
C058—S003—Bi01 91.76 (14)
111.8 (4) C055—S004—Bi02 92.85 (14)
C2—S005—Bi01 92.56 (15)
C20—S006—Bi01 92.29 (14)
C047—S007—Bi02 93.26 (16)
C20—S008—Bi01 85.27 (14)
C055—S009—Bi02 84.13 (15)
(4) C058—S010—Bi01 84.65 (14)
C047—S011—Bi02 83.53 (15)
C21—S012—Bi02 93.51 (15)
C21—S013—Bi02 83.49 (15)
C2—S014—Bi01 84.06 (15)
N021—C20—S008 121.5 (3)
(4) N021—C20—S006 120.4 (3)
S008—C20—S006 118.1 (2)
C055—N016—C035 123.9 (4)
C055—N016—C050 123.1 (4)
C035—N016—C050 112.5 (4)
C058—N017—C038 124.4 (4)
(4) C058—N017—C4 123.6 (4)
C038—N017—C4 111.8 (3)
C21—N018—C045 125.1 (4)
C21—N018—C6 122.8 (4)
C045—N018—C6 112.1 (3)
C2—N019—C036 123.4 (4)
C2—N019—C062 123.3 (4)
C036—N019—C062 112.6 (3)
C047—N020—C051 124.2 (4)
C047—N020—C059 123.5 (4)
C051—N020—C059 111.9 (4)
C20—N021—C1 122.6 (3)
C20—N021—C029 124.4 (3)
C1—N021—C029 112.6 (3)
N017—C4—C069 110.3 (4)
N019—C036—C040 109.5
N019—C036—H03I 109.8
C040—C036—H03I 109.8
N019—C036—H03J 109.8
C040—C036—H03J 109.8
H03I—C036—H03J 108.2
C029—C037—C046 111.6
C029—C037—H03K 109.3
C046—C037—H03K 109.3
C029—C037—H03L 109.3
C046—C037—H03L 109.3
H03K—C037—H03L 108.0
N017—C038—C032 109.7 (4)
N017—C038—H03M 109.7
C032—C038—H03M 109.7
N017—C038—H03N 109.7
C032—C038—H03N 109.7
H03M—C038—H03N 108.2
C043—C040—C036
C043—C040—H04A 109.3
C036—C040—H04A 109.3
C043—C040—H04B 109.3
C036—C040—H04B 109.3
H04A—C040—H04B 108.0
C3—C042—C052
C3—C042—H04C 109.5
C052—C042—H04C 109.5
C3—C042—H04D 109.5
C052—C042—H04D 109.5
H04C—C042—H04D 108.1
C040—C043—C044
C040—C043—H04E 109.2
C044—C043—H04E 109.2
C040—C043—H04F 109.2
C044—C043—H04F 109.2
H04E—C043—H04F 107.9
C062—C044—C043 111.0
C062—C044—H04G 109.4
C043—C044—H04G 109.4
C062—C044—H04H 109.4
C043—C044—H04H 109.4
H04G—C044—H04H 108.0
N018—C045—C030 111.3
N018—C045—H04I 109.4
C030—C045—H04I 109.4
N018—C045—H04J 109.4
C030—C045—H04J 109.4
H04I—C045—H04J 108.0
C037—C046—C049 109.2
C037—C046—H04K 109.8
C049—C046—H04K 109.8
C037—C046—H04L 109.8
C049—C046—H04L 109.8
H04K—C046—H04L 108.3
N020—C047—S011 122.3 (3)
N020—C047—S007 118.5 (3)
S011—C047—S007 119.2 (3)
C1—C049—C046 110.2 (4)
C1—C049—H04M 109.6
C046—C049—H04M 109.6
C1—C049—H04N 109.6
C046—C049—H04N 109.6
H04M—C049—H04N 108.1
N016—C050—C033 109.3 (4)

N017—C4—H4A 109.6
C069—C4—H4A 109.6
N017—C4—H4B 109.6
C069—C4—H4B 109.6
H4A—C4—H4B 108.1
C053—C7—C6 110.5 (4)
(4) C053—C7—H7A 109.6
C6—C7—H7A 109.6
C053—C7—H7B 109.6
C6—C7—H7B 109.6
H7A—C7—H7B 108.1
C059—C3—C042 111.6 (4)
(4) C059—C3—H3A 109.3
C042—C3—H3A 109.3
C059—C3—H3B 109.3
C042—C3—H3B 109.3
H3A—C3—H3B 108.0
N018—C6—C7 109.7 (4)
(4) N018—C6—H6A 109.7
C7—C6—H6A 109.7
N018—C6—H6B 109.7
C7—C6—H6B 109.7
H6A—C6—H6B 108.2
N018—C21—S013 122.6 (3)
N018—C21—S012 119.0 (3)
S013—C21—S012 118.4 (2)
C069—C5—C032 110.9 (4)
C069—C5—H5A 109.5
C032—C5—H5A 109.5
C069—C5—H5B 109.4
C032—C5—H5B 109.5
H5A—C5—H5B 108.0
N019—C2—S014 121.9 (3)
N019—C2—S005 118.6 (3)
S014—C2—S005 119.5 (3)
N021—C029—C037 109.0 (3)
(4) N021—C029—H02A 109.9
C037—C029—H02A 109.9
N021—C029—H02B 109.9
C037—C029—H02B 109.9
H02A—C029—H02B 108.3
C045—C030—C053 111.1 (4)
110.7 (4) C045—C030—H03A 109.4
C053—C030—H03A 109.4
C045—C030—H03B 109.4
C053—C030—H03B 109.4
H03A—C030—H03B 108.0
C038—C032—C5 110.8 (4)
(4) C038—C032—H03C 109.5
C5—C032—H03C 109.5
C038—C032—H03D 109.5
C5—C032—H03D 109.5
H03C—C032—H03D 108.1
C068—C033—C050 110.5 (4)
111.2 (4) C068—C033—H03E 109.6
C050—C033—H03E 109.6
C068—C033—H03F 109.6
C050—C033—H03F 109.6
H03E—C033—H03F 108.1
N016—C035—C065 109.9 (4)
109.1 (3) N016—C035—H03G 109.7
C065—C035—H03G 109.7
N016—C035—H03H 109.7
C065—C035—H03H 109.7
N016—C050—H05A 109.8
C033—C050—H05A 109.8
N016—C050—H05B 109.8
C033—C050—H05B 109.8
H05A—C050—H05B 108.3
N020—C051—C052 109.4
N020—C051—H05C 109.8
C052—C051—H05C 109.8
N020—C051—H05D 109.8
C052—C051—H05D 109.8
H05C—C051—H05D 108.2
C051—C052—C042 110.4
C051—C052—H05E 109.6
C042—C052—H05E 109.6
C051—C052—H05F 109.6
C042—C052—H05F 109.6
H05E—C052—H05F 108.1
C7—C053—C030 109.8
C7—C053—H05G 109.7
C030—C053—H05G 109.7
C7—C053—H05H 109.7
C030—C053—H05H 109.7
H05G—C053—H05H 108.2
N016—C055—S009 121.5 (3)
N016—C055—S004 119.5 (3)
S009—C055—S004 119.1 (2)
N017—C058—S010 121.7 (3)
N017—C058—S003 119.0 (3)
S010—C058—S003 119.2 (2)
N020—C059—C3 111.1 (4)
N020—C059—H05I 109.4
C3—C059—H05I 109.4
N020—C059—H05J 109.4
C3—C059—H05J 109.4
H05I—C059—H05J 108.0
N019—C062—C044 109.3
N019—C062—H06A 109.8
C044—C062—H06A 109.8
N019—C062—H06B 109.8
C044—C062—H06B 109.8
H06A—C062—H06B 108.3
C035—C065—C068
C035—C065—H06C 109.5
C068—C065—H06C 109.5
C035—C065—H06D 109.5
C068—C065—H06D 109.5
H06C—C065—H06D 108.1
C033—C068—C065 110.7
C033—C068—H06E 109.5
C065—C068—H06E 109.5
C033—C068—H06F 109.5
C065—C068—H06F 109.5
H06E—C068—H06F 108.1
C4—C069—C5
C4—C069—H06G 109.4
C5—C069—H06G 109.4
C4—C069—H06H 109.4
C5—C069—H06H 109.4
H06G—C069—H06H 108.0
N021—C1—C049
N021—C1—H1A 109.9
C049—C1—H1A 109.9
N021—C1—H1B 109.9
C049—C1—H1B 109.9

H03G—C035—H03H	108.2	H1A—C1—H1B	108.3

Crystallographic data for (tris(N,N-diethyldithiocarbamato)antimony(III))

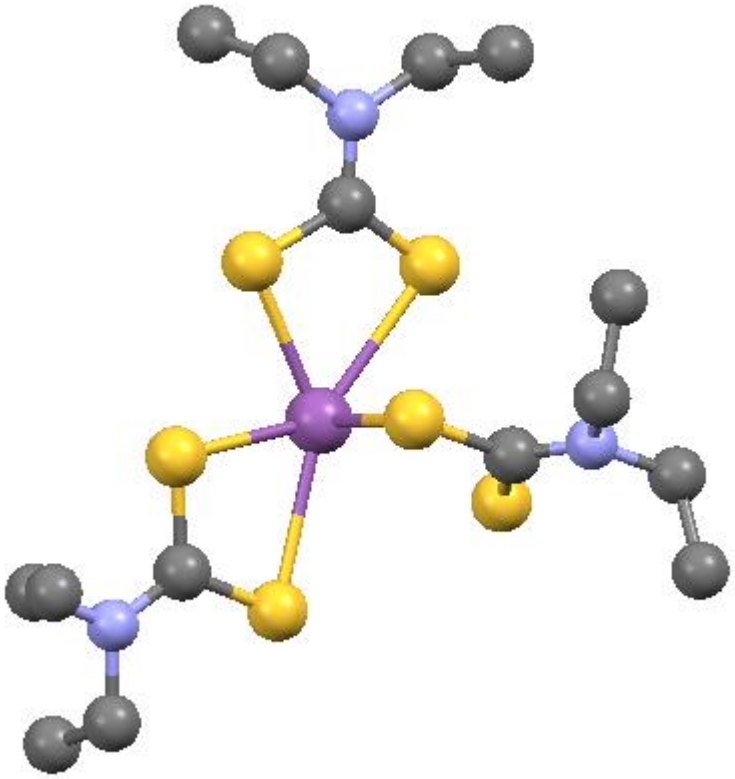

Experimental details

Crystal data	
Chemical formula	$C_{15}H_{30}N_3S_6Sb$
M_r	566.53
CCDC	1889651
Crystal system, space group	Monoclinic, $P2_1/c$
Temperature (K)	150
a, *b*, *c* (Å)	12.4427 (2), 13.5147 (2), 14.6373 (2)
β (°)	99.915 (1)

V (Å$_3$)	2424.64 (6)
Z	4
Radiation type	Mo $K\alpha$
μ (mm^{-1})	1.66
Crystal size (mm)	0.22 × 0.2 × 0.2

Data collection
Diffractometer XtaLAB AFC11 (RINC): quarter-chi single
Absorption correction Multi-scan
CrysAlis PRO 1.171.39.30c (Rigaku Oxford Diffraction, 2017) Empirical absorption correction using spherical harmonics, implemented in SCALE3 ABSPACK scaling algorithm.

T_{min}, T_{max}	0.638, 1.000
No. of measured, independent and observed [$I > 2\sigma(I)$] reflections	25360, 5750, 5316
R_{int}	0.018
$(\sin \theta/\lambda)_{max}$ (Å^{-1})	0.674

Refinement
$R[F^2 > 2\sigma(F^2)]$, $wR(F^2)$, S 0.015, 0.036, 1.04
No. of reflections 5750
No. of parameters 232
H-atom treatment H-atom parameters constrained
$\Delta\rho_{max}$, $\Delta\rho_{min}$ (e Å^{-3}) 0.27, −0.30
Computer programs: *CrysAlis PRO* 1.171.39.30c (Rigaku OD, 2017), ShelXT (Sheldrick, 2015), *SHELXL* (Sheldrick, 2015), Olex2 (Dolomanov *et al.*, 2009).

Fractional atomic coordinates and isotropic or equivalent isotropic displacement parameters (Å^2) for ((tris(N,N-diethyldithiocarbamato)antimony(III))*)*

	X	*y*	*z*	U_{iso}*/U_{eq}
Sb1	0.33691 (2)	0.00974 (2)	−0.04458 (2)	0.01794 (3)
S5	0.17071 (3)	0.02552 (2)	0.02704 (2)	0.02141 (7)
S1	0.41044 (3)	0.17465 (2)	0.03939 (2)	0.02328 (7)
S2	0.44099 (3)	−0.01225 (2)	0.14575 (2)	0.02307 (7)
S3	0.21151 (3)	−0.05229 (2)	−0.21896 (2)	0.02626 (7)
S4	0.26420 (3)	0.15304 (2)	−0.15907 (2)	0.02310 (7)
S6	0.24839 (3)	−0.18060 (2)	0.00897 (2)	0.02741 (8)
N3	0.11343 (8)	−0.12592 (8)	0.12277 (7)	0.0196 (2)
N1	0.49708 (9)	0.16532 (8)	0.21760 (7)	0.0235 (2)
N2	0.18262 (10)	0.10455 (9)	−0.33234 (8)	0.0272 (2)
C12	0.05264 (11)	−0.05505 (10)	0.17046 (9)	0.0236 (3)
H12A	−0.0143	−0.0871	0.1842	0.028*
H12B	0.0304	0.0021	0.1292	0.028*
C1	0.45427 (10)	0.11357 (9)	0.14342 (9)	0.0195 (2)
C14	0.10554 (11)	−0.22951 (10)	0.15071 (9)	0.0236 (3)
H14A	0.0995	−0.2325	0.2172	0.028*

H14B	0.1726	−0.2653	0.1424	0.028*
C11	0.17255 (10)	−0.09978 (9)	0.05919 (8)	0.0192 (2)
C2	0.53838 (12)	0.11731 (11)	0.30727 (9)	0.0308 (3)
H2A	0.6008	0.1558	0.3405	0.037*
H2B	0.5649	0.0501	0.2959	0.037*
C7	0.17810 (12)	0.21101 (11)	−0.35402 (10)	0.0287 (3)
H7A	0.1838	0.2204	−0.4201	0.034*
H7B	0.2411	0.2446	−0.3160	0.034*
C4	0.51041 (12)	0.27355 (10)	0.21523 (10)	0.0281 (3)
H4A	0.5093	0.3009	0.2778	0.034*
H4B	0.4484	0.3026	0.1721	0.034*
C6	0.21579 (10)	0.06958 (10)	−0.24706 (9)	0.0222 (3)
C8	0.07320 (13)	0.25779 (11)	−0.33543 (10)	0.0336 (3)
H8A	0.0108	0.2190	−0.3662 0.050*	
H8B	0.0677	0.3255	−0.3596	0.050*
H8C	0.0734	0.2591	−0.2685	0.050*
C15	0.00719 (12)	−0.27932 (11)	0.09365 (10)	0.0323 (3)
H15A	0.0175	−0.2840	0.0289	0.048*
H15B	−0.0584	−0.2403	0.0971	0.048*
H15C	−0.0012	−0.3459	0.1181	0.048*
C13	0.12069 (15)	−0.01895 (12)	0.25977 (11)	0.0391 (4)
H13A	0.1844	0.0169	0.2459	0.059*
H13B	0.1449	−0.0757	0.2998	0.059*
H13C	0.0768	0.0253	0.2916	0.059*
C5	0.61635 (12)	0.30257 (12)	0.18443 (12)	0.0371 (3)
H5A	0.6155	0.2796	0.1208	0.056*
H5B	0.6778	0.2721	0.2258	0.056*
H5C	0.6242	0.3747	0.1868	0.056*
C9	0.14201 (16)	0.03929 (13)	−0.41055 (11)	0.0461 (4)
H9A	0.0765	0.0694	−0.4483	0.055*
H9B	0.1202	−0.0248	−0.3866	0.055*
C3	0.45112 (15)	0.10989 (13)	0.36753 (11)	0.0421 (4)
H3A	0.4816	0.0780	0.4264	0.063*
H3B	0.3899	0.0705	0.3355	0.063*
H3C	0.4254	0.1764	0.3796	0.063*
C10	0.2266 (2)	0.0213 (2)	−0.47135 (14)	0.0843 (9)
H10A	0.1973	−0.0246	−0.5213	0.126*
H10B	0.2922	−0.0074	−0.4341	0.126*
H10C	0.2454	0.0841	−0.4981	0.126*

Atomic displacement parameters (Å²) for ((tris(N,N-diethyldithiocarbamato)antimony(III))*)*

	U_{11}	U_{22}	U_{33}	U_{12}	U_{13}	U_{23}
Sb1	0.01864 (5)	0.01733 (5)	0.01920 (5)	−0.00097 (3)	0.00708 (3)	−0.00049 (3)
S5	0.02209 (16)	0.01785 (15)	0.02671 (16)	0.00125 (12)	0.01100 (12)	0.00127 (12)
S1	0.02939 (17)	0.01751 (14)	0.02244 (15)	−0.00293 (12)	0.00306 (13)	0.00171 (12)
S2	0.02826 (17)	0.01720 (15)	0.02437 (16)	0.00040 (12)	0.00628 (13)	0.00201 (12)

S3	0.03193 (18)	0.02047 (16)	0.02579 (16)	−0.00056 (13)	0.00325 (13)	−0.00257 (13)
S4	0.02666 (17)	0.02015 (15)	0.02215 (15)	−0.00273 (12)	0.00319 (12)	0.00057 (12)
S6	0.03384 (19)	0.01848 (15)	0.03475 (18)	0.00077 (13)	0.01955 (15)	−0.00223 (13)
N3	0.0190 (5)	0.0199 (5)	0.0210 (5)	0.0002 (4)	0.0061 (4)	0.0008 (4)
N1	0.0257 (6)	0.0223 (6)	0.0227 (5)	−0.0007 (4)	0.0045 (4)	−0.0029 (4)
N2	0.0329 (6)	0.0278 (6)	0.0206 (5)	0.0006 (5)	0.0033 (5)	0.0006 (5)
C12	0.0214 (6)	0.0264 (7)	0.0254 (6)	0.0021 (5)	0.0108 (5)	0.0001 (5)
C1	0.0179 (6)	0.0198 (6)	0.0219 (6)	0.0011 (5)	0.0069 (5)	−0.0004 (5)
C14	0.0263 (7)	0.0215 (6)	0.0244 (6)	−0.0004 (5)	0.0085 (5)	0.0046 (5)
C11	0.0191 (6)	0.0184 (6)	0.0204 (6)	−0.0017 (5)	0.0042 (5)	−0.0014 (5)
C2	0.0322 (8)	0.0353 (8)	0.0228 (7)	0.0023 (6)	−0.0014 (6)	−0.0017 (6)
C7	0.0325 (8)	0.0305 (7)	0.0242 (7)	−0.0030 (6)	0.0079 (6)	0.0074 (6)
C4	0.0326 (8)	0.0216 (7)	0.0313 (7)	−0.0030 (6)	0.0084 (6)	−0.0086 (5)
C6	0.0211 (6)	0.0249 (6)	0.0219 (6)	0.0001 (5)	0.0072 (5)	−0.0006 (5)
C8	0.0414 (9)	0.0291 (7)	0.0325 (8)	0.0010 (6)	0.0127 (6)	0.0059 (6)
C15	0.0367 (8)	0.0284 (7)	0.0323 (7)	−0.0101 (6)	0.0077 (6)	−0.0003 (6)
C13	0.0476 (10)	0.0418 (9)	0.0274 (8)	0.0100 (7)	0.0052 (7)	−0.0090 (7)
C5	0.0323 (8)	0.0312 (8)	0.0490 (9)	−0.0085 (6)	0.0097 (7)	−0.0080 (7)
C9	0.0697 (12)	0.0366 (9)	0.0256 (8)	0.0062 (8)	−0.0099 (8)	−0.0043 (7)
C3	0.0577 (11)	0.0440 (9)	0.0275 (8)	0.0126 (8)	0.0155 (7)	0.0022 (7)
C10	0.108 (2)	0.109 (2)	0.0313 (10)	0.0604 (17)	−0.0030 (11)	−0.0216 (11)

Geometric parameters (Å, º) for ((tris(N,N-diethyldithiocarbamato)antimony(III))*)*

Sb1—S5	2.4835 (3)	C2—C3	1.515 (2)
Sb1—S1	2.6321 (3)	C7—H7A	0.9900
Sb1—S2	2.8783 (3)	C7—H7B	0.9900
Sb1—S3	2.8777 (3)	C7—C8	1.516 (2)
Sb1—S4	2.6183 (3)	C4—H4A	0.9900
S5—C11	1.7566 (13)	C4—H4B	0.9900
S1—C1	1.7354 (13)	C4—C5	1.516 (2)
S2—C1	1.7092 (13)	C8—H8A	0.9800
S3—C6	1.7007 (14)	C8—H8B	0.9800
S4—C6	1.7398 (13)	C8—H8C	0.9800
S6—C11	1.6920 (13)	C15—H15A	0.9800
N3—C12	1.4693 (16)	C15—H15B	0.9800
N3—C14	1.4666 (16)	C15—H15C	0.9800
N3—C11	1.3295 (15)	C13—H13A	0.9800
N1—C1	1.3239 (16)	C13—H13B	0.9800
N1—C2	1.4751 (17)	C13—H13C	0.9800
N1—C4	1.4731 (17)	C5—H5A	0.9800
N2—C7	1.4723 (18)	C5—H5B	0.9800
N2—C6	1.3321 (17)	C5—H5C	0.9800
N2—C9	1.4644 (19)	C9—H9A	0.9900
C12—H12A	0.9900	C9—H9B	0.9900

C12—H12B	0.9900	C9—C10	1.511 (3)
C12—C13	1.511 (2)	C3—H3A	0.9800
C14—H14A	0.9900	C3—H3B	0.9800
C14—H14B	0.9900	C3—H3C	0.9800
C14—C15	1.5153 (19)	C10—H10A	0.9800
C2—H2A	0.9900	C10—H10B	0.9800
C2—H2B	0.9900	C10—H10C	0.9800
S5—Sb1—S1	88.735 (11)	C8—C7—H7B	109.3
S5—Sb1—S2	82.463 (10)	N1—C4—H4A	109.3
S5—Sb1—S3	92.048 (11)	N1—C4—H4B	109.3
S5—Sb1—S4	89.174 (11)	N1—C4—C5	111.78 (12)
S1—Sb1—S2	64.732 (10)	H4A—C4—H4B	107.9
S1—Sb1—S3	138.821 (10)	C5—C4—H4A	109.3
S3—Sb1—S2	155.972 (10)	C5—C4—H4B	109.3
S4—Sb1—S1	74.129 (10)	S3—C6—S4	118.04 (7)
S4—Sb1—S2	138.086 (10)	N2—C6—S3	123.55 (10)
S4—Sb1—S3	64.720 (10)	N2—C6—S4	118.40 (10)
C11—S5—Sb1	93.26 (4)	C7—C8—H8A	109.5
C1—S1—Sb1	92.20 (4)	C7—C8—H8B	109.5
C1—S2—Sb1	84.66 (4)	C7—C8—H8C	109.5
C6—S3—Sb1	84.12 (5)	H8A—C8—H8B	109.5
C6—S4—Sb1	91.81 (5)	H8A—C8—H8C	109.5
C14—N3—C12	115.16 (10)	H8B—C8—H8C	109.5
C11—N3—C12	123.47 (11)	C14—C15—H15A	109.5
C11—N3—C14	121.37 (11)	C14—C15—H15B	109.5
C1—N1—C2	121.79 (11)	C14—C15—H15C	109.5
C1—N1—C4	122.44 (11)	H15A—C15—H15B	109.5
C4—N1—C2	115.74 (11)	H15A—C15—H15C	109.5
C6—N2—C7	122.88 (12)	H15B—C15—H15C	109.5
C6—N2—C9	121.90 (12)	C12—C13—H13A	109.5
C9—N2—C7	115.14 (12)	C12—C13—H13B	109.5
N3—C12—H12A	109.4	C12—C13—H13C	109.5
N3—C12—H12B	109.4	H13A—C13—H13B	109.5
N3—C12—C13	111.34 (11)	H13A—C13—H13C	109.5
H12A—C12—H12B	108.0	H13B—C13—H13C	109.5
C13—C12—H12A	109.4	C4—C5—H5A	109.5
C13—C12—H12B	109.4	C4—C5—H5B	109.5
S2—C1—S1	118.29 (7)	C4—C5—H5C	109.5
N1—C1—S1	119.31 (10)	H5A—C5—H5B	109.5
N1—C1—S2	122.40 (10)	H5A—C5—H5C	109.5
N3—C14—H14A	109.5	H5B—C5—H5C	109.5
N3—C14—H14B	109.5	N2—C9—H9A	109.2
N3—C14—C15	110.90	(11) N2—C9—H9B	109.2
H14A—C14—H14B	108.0	N2—C9—C10	112.08 (17)
C15—C14—H14A	109.5	H9A—C9—H9B	107.9
C15—C14—H14B	109.5	C10—C9—H9A	109.2
S6—C11—S5	119.24 (7)	C10—C9—H9B	109.2
N3—C11—S5	117.41 (9)	C2—C3—H3A	109.5
N3—C11—S6	123.35 (10)	C2—C3—H3B	109.5

N1—C2—H2A	109.2	C2—C3—H3C	109.5
N1—C2—H2B	109.2	H3A—C3—H3B	109.5
N1—C2—C3	111.86 (12)	H3A—C3—H3C	109.5
H2A—C2—H2B	107.9	H3B—C3—H3C	109.5
C3—C2—H2A	109.2	C9—C10—H10A	109.5
C3—C2—H2B	109.2	C9—C10—H10B	109.5
N2—C7—H7A	109.3	C9—C10—H10C	109.5
N2—C7—H7B	109.3	H10A—C10—H10B	109.5
N2—C7—C8	111.77 (11)	H10A—C10—H10C	109.5
H7A—C7—H7B	107.9	H10B—C10—H10C	109.5
C8—C7—H7A	109.3		
Sb1—S5—C11—S6	−16.83 (7)	C14—N3—C11—S6	−3.18 (17)
Sb1—S5—C11—N3	163.04 (9)	C11—N3—C12—C13	−91.76 (15)
Sb1—S1—C1—S2	3.56 (7)	C11—N3—C14—C15	−92.74 (14)
Sb1—S1—C1—N1	−176.81 (10)	C2—N1—C1—S1	−178.38 (9)
Sb1—S2—C1—S1	−3.27 (6)	C2—N1—C1—S2	1.23 (17)
Sb1—S2—C1—N1	177.12 (11)	C2—N1—C4—C5	92.04 (14)
Sb1—S3—C6—S4	−10.56 (7)	C7—N2—C6—S3	174.65 (10)
Sb1—S3—C6—N2	170.49 (11)	C7—N2—C6—S4	−4.31 (17)
Sb1—S4—C6—S3	11.56 (7)	C7—N2—C9—C10	81.47 (18)
Sb1—S4—C6—N2	−169.43 (10)	C4—N1—C1—S1	−0.76 (17)
C12—N3—C14—C15	87.75 (13)	C4—N1—C1—S2	178.85 (10)
C12—N3—C11—S5	−3.58 (16)	C4—N1—C2—C3	90.86 (15)
C12—N3—C11—S6	176.28 (9)	C6—N2—C7—C8	−83.80 (16)
C1—N1—C2—C3	−91.37 (16)	C6—N2—C9—C10	−101.82 (18)
C1—N1—C4—C5	−85.71 (16)	C9—N2—C7—C8	92.87 (16)
C14—N3—C12—C13	87.74 (14)	C9—N2—C6—S3	−1.8 (2)
C14—N3—C11—S5	176.96 (9)	C9—N2—C6—S4	179.25 (12)

Crystallographic data for Tris(morpholinedithiocarbamato)antimony(III)

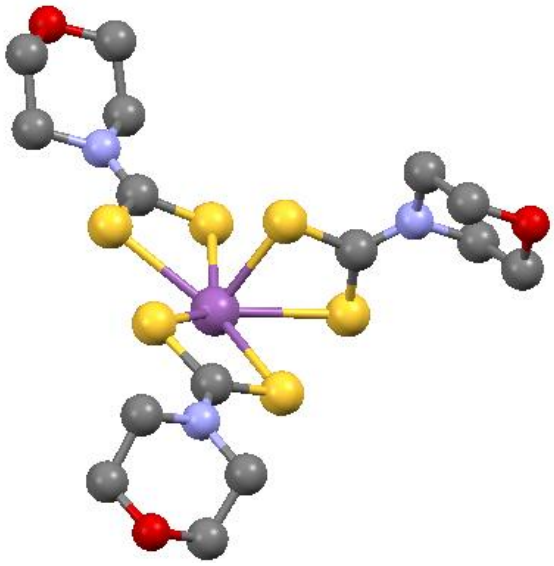

Experimental details

Crystal data

Chemical formula	C15H24N3O3S6Sb
Mr	608.48
CCDC	1889657
Crystal system, space group	Monoclinic, P21/c
Temperature (K)	150
a, b, c (Å)	12.7679 (3), 19.9695 (5), 8.9439 (2)
β (°)	93.858 (2)
V (Å3)	2275.27 (10)
Z	4
Radiation type	Mo Kα
μ (mm−1)	1.79
Crystal size (mm)	0.15 × 0.06 × 0.06

Data collection

Diffractometer	XtaLAB AFC11 (RINC): quarter-chi single
Absorption correction	Multi-scan
Tmin, Tmax	0.739, 0.748
No. of measured, independent and observed [I > 2σ(I)] reflections	13617, 5265, 4372
Rint	0.035
(sin θ/λ)max (Å−1)	0.682

Refinement

R[F2 > 2σ(F2)], wR(F2), S 0.027, 0.063, 1.02

No. of reflections 5265
No. of parameters 253
H-atom treatment H-atom parameters constrained
Δρmax, Δρmin (e Å−3) 0.75, −0.95

Fractional atomic coordinates and isotropic or equivalent isotropic displacement parameters (Å2) for (Tris(morpholinedithiocarbamato)antimony(III))

x	y	z	Uiso*/Ueq
Sb1	0.34995 (2)	0.45223 (2)	0.39913 (2) 0.01443 (6)
S1	0.34345 (5)	0.34839 (3)	0.58931 (6) 0.01825 (13)
S3	0.17856 (5)	0.48934 (3)	0.48314 (6) 0.01601 (13)
S2	0.42196 (5)	0.47951 (3)	0.69920 (6) 0.01651 (13)
S5	0.25900 (5)	0.48803 (3)	0.11731 (7) 0.02151 (14)
S4	0.33514 (5)	0.59278 (3)	0.41911 (6) 0.01822 (13)
S6	0.25227 (5)	0.35178 (3)	0.24464 (7) 0.02166 (14)
O1	0.60528 (15)	0.29786 (9)	1.0362 (2) 0.0303 (5)
O2	0.09696 (15)	0.69140 (8)	0.78561 (18) 0.0244 (4)
O3	0.01800	(16) 0.34266 (9)	−0.2493 (2) 0.0346 (5)
N1	0.44965	(17) 0.36521 (9)	0.8525 (2) 0.0184 (4)
N3	0.17544 (17)	0.38330 (10)	−0.0302 (2) 0.0220 (5)
N2	0.15185 (16)	0.61863 (10)	0.5327 (2) 0.0168 (4)
C7	0.17622 (19)	0.69040 (11)	0.5440 (3) 0.0187 (5)
H7A	0.1197	0.7168	0.4906 0.022*
H7B	0.2428	0.6999	0.4974 0.022*
C2	0.5096 (2)	0.40051 (12)	0.9746 (3) 0.0232 (6)
H2A	0.4708	0.3991	1.0667 0.028*
H2B	0.5193	0.4480	0.9468 0.028*
C10	0.05724 (19)	0.60251 (12)	0.6072 (3) 0.0214 (5)
H10A	0.0425	0.5539	0.5986 0.026*
H10B	−0.0034	0.6272	0.5593 0.026*
C4	0.5504 (2)	0.26456 (12)	0.9138 (3) 0.0263 (6)
H4A	0.5450	0.2162	0.9369 0.032*
H4B	0.5903	0.2692	0.8231 0.032*
C8	0.1860 (2)	0.70973 (12)	0.7082 (3) 0.0223 (5)
H8A	0.2490	0.6878	0.7569 0.027*
H8B	0.1963	0.7588	0.7164 0.027*
C6	0.21680 (19)	0.57334 (11)	0.4828 (2) 0.0148 (5)
C5	0.4420 (2)	0.29324 (11)	0.8831 (3) 0.0217 (6)
H5A	0.4061	0.2703	0.7958 0.026*
H5B	0.4001	0.2860	0.9709 0.026*
C3	0.6152 (2)	0.36721 (12)	1.0031 (3) 0.0273 (6)
H3A	0.6560	0.3724	0.9135 0.033*
H3B	0.6544	0.3897	1.0881 0.033*
C11	0.22424 (19)	0.40590 (12)	0.0966 (2) 0.0183 (5)
C12	0.1411 (2)	0.42700 (13) −	0.1553 (3) 0.0266 (6)
H12A	0.1870	0.4205	−0.2390 0.032*
H12B	0.1463	0.4744	−0.1232 0.032*
C1	0.41069 (18)	0.39512 (11)	0.7282 (2) 0.0156 (5)
C13	0.0292 (2)	0.41074 (14)	−0.2068 (3) 0.0314 (7)

H13A	−0.0170	0.4204	−0.1249	0.038*
H13B	0.0068	0.4396	−0.2931	0.038*
C15	0.1588 (2)	0.31220 (12)	−0.0665 (3)	0.0255 (6)
H15A	0.1743	0.2847	0.0244	0.031*
H15B	0.2072	0.2983	−0.1427	0.031*
C9	0.0734 (2)	0.62207 (12)	0.7703 (3)	0.0256 (6)
H9A	0.0091	0.6119	0.8219	0.031*
H9B	0.1317	0.5955	0.8186	0.031*
C14	0.0475 (2)	0.30064 (14)	−0.1254 (3)	0.0331 (7)
H14A	0.0391	0.2533	−0.1565	0.040*
H14B	0.0001	0.3090	−0.0443	0.040*

Atomic displacement parameters (Å2) for (Tris(morpholinedithiocarbamato)antimony(III))

U11	U22	U33	U12	U13	U23
Sb1	0.01612 (9)	0.01345 (9)	0.01373 (9)	−0.00010 (6)	0.00099 (6)	−0.00112 (6)
S1	0.0238 (3)	0.0137 (3)	0.0165 (3)	−0.0012 (2)	−0.0040 (2)	−0.0006 (2)
S3	0.0152 (3)	0.0137 (3)	0.0193 (3)	−0.0020 (2)	0.0021 (2)	0.0009 (2)
S2	0.0191 (3)	0.0134 (3)	0.0166 (3)	−0.0002 (2)	−0.0016 (2)	−0.0004 (2)
S5	0.0323 (4)	0.0140 (3)	0.0177 (3)	−0.0056 (3)	−0.0022 (3)	0.0019 (2)
S4	0.0186 (3)	0.0147 (3)	0.0220 (3)	−0.0026 (2)	0.0058 (2)	−0.0010 (2)
S6	0.0346 (4)	0.0136 (3)	0.0157 (3)	−0.0034 (3)	−0.0060 (3)	0.0018 (2)
O1	0.0302 (11)	0.0229 (10)	0.0355 (11)	−0.0006 (9)	−0.0154 (9)	0.0092 (8)
O2	0.0343 (11)	0.0206 (9)	0.0188 (9)	0.0012 (8)	0.0059 (8)	−0.0021 (7)
O3	0.0367 (12)	0.0350 (11)	0.0300 (10)	−0.0095 (10)	−0.0138 (9)	0.0006 (9)
N1	0.0221 (11)	0.0136 (10)	0.0186 (10)	−0.0012 (9)	−0.0053 (8)	0.0018 (8)
N3	0.0333 (13)	0.0164 (10)	0.0154 (10)	−0.0049 (10)	−0.0063 (9)	0.0025 (8)
N2	0.0165 (10)	0.0146 (10)	0.0195 (10)	−0.0005 (8)	0.0026 (8)	−0.0029 (8)
C7	0.0201 (12)	0.0144 (12)	0.0219 (12)	−0.0003 (10)	0.0018 (10)	0.0011 (10)
C2	0.0315 (15)	0.0210 (13)	0.0160 (12)	−0.0020 (12)	−0.0073 (11)	−0.0009 (10)
C10	0.0158 (12)	0.0210 (13)	0.0282 (13)	−0.0003 (11)	0.0066 (10)	−0.0026 (10)
C4	0.0309 (15)	0.0163 (13)	0.0308 (14)	0.0011 (11)	−0.0042 (12)	0.0037 (10)
C8	0.0256 (14)	0.0206 (13)	0.0203 (12)	0.0005 (11)	−0.0016 (10)	−0.0028 (10)
C6	0.0159 (12)	0.0166 (11)	0.0112 (11)	−0.0026 (10)	−0.0033 (9)	0.0004 (9)
C5	0.0254 (14)	0.0152 (12)	0.0232 (13)	−0.0039 (11)	−0.0070 (11)	0.0066 (10)
C3	0.0302 (15)	0.0193 (13)	0.0306 (14)	−0.0053 (12)	−0.0116 (12)	0.0045 (11)
C11	0.0201 (12)	0.0209 (12)	0.0139 (11)	−0.0023 (11)	0.0017 (9)	0.0000 (9)
C12	0.0381 (17)	0.0241 (14)	0.0165 (13)	−0.0042 (13)	−0.0054 (11)	0.0050 (11)
C1	0.0126 (11)	0.0176 (12)	0.0163 (11)	0.0022 (10)	−0.0004 (9)	−0.0013 (9)
C13	0.0320 (16)	0.0378 (17)	0.0237 (14)	0.0032 (14)	−0.0026 (12)	0.0039 (12)
C15	0.0371 (16)	0.0176 (12)	0.0204 (13)	−0.0043 (12)	−0.0077 (11)	−0.0026 (10)
C9	0.0297 (15)	0.0220 (13)	0.0258 (13)	0.0012 (12)	0.0077 (11)	0.0018 (11)
C14	0.0369 (17)	0.0307 (15)	0.0313 (15)	−0.0115 (14)	−0.0005 (13)	−0.0012 (12)

Geometric parameters (Å, º) for (Tris(morpholinedithiocarbamato)antimony(III))

Sb1—S1	2.6868 (6)	C7—C8	1.516 (3)

Sb1—S3	2.4746 (6)	C2—H2A	0.9900
Sb1—S2	2.8307 (6)	C2—H2B	0.9900
Sb1—S5	2.7962 (6)	C2—C3	1.509 (4)
Sb1—S4	2.8195 (6)	C10—H10A	0.9900
Sb1—S6	2.6937 (6)	C10—H10B	0.9900
S1—C1	1.734 (2)	C10—C9	1.511 (3)
S3—C6	1.747 (2)	C4—H4A	0.9900
S2—C1	1.713 (2)	C4—H4B	0.9900
S5—C11	1.706 (2)	C4—C5	1.507 (3)
S4—C6	1.695 (3)	C8—H8A	0.9900
S6—C11	1.728 (2)	C8—H8B	0.9900
O1—C4	1.424 (3)	C5—H5A	0.9900
O1—C3	1.424 (3)	C5—H5B	0.9900
O2—C8	1.418 (3)	C3—H3A	0.9900
O2—C9	1.421 (3)	C3—H3B	0.9900
O3—C13	1.416 (3)	C12—H12A	0.9900
O3—C14	1.420 (3)	C12—H12B	0.9900
N1—C2	1.471 (3)	C12—C13	1.507 (4)
N1—C5	1.468 (3)	C13—H13A	0.9900
N1—C1	1.329 (3)	C13—H13B	0.9900
N3—C11	1.335 (3)	C15—H15A	0.9900
N3—C12	1.463 (3)	C15—H15B	0.9900
N3—C15	1.469 (3)	C15—C14	1.499 (4)
N2—C7	1.469 (3)	C9—H9A	0.9900
N2—C10	1.454 (3)	C9—H9B	0.9900
N2—C6	1.325 (3)	C14—H14A	0.9900
C7—H7A	0.9900	C14—H14B	0.9900
C7—H7B	0.9900		
S1—Sb1—S2	64.544 (17)	O2—C8—C7	112.98 (19)
S1—Sb1—S5	137.675 (18)	O2—C8—H8A	109.0
S1—Sb1—S4	136.310 (18)	O2—C8—H8B	109.0
S1—Sb1—S6	73.566 (17)	C7—C8—H8A	109.0
S3—Sb1—S1	88.47 (2)	C7—C8—H8B	109.0
S3—Sb1—S2	83.797 (19)	H8A—C8—H8B	107.8
S3—Sb1—S5	82.82 (2)	S4—C6—S3	118.42 (14)
S3—Sb1—S4	67.554 (19)	N2—C6—S3	118.27 (19)
S3—Sb1—S6	89.45 (2)	N2—C6—S4	123.31 (18)
S5—Sb1—S2	153.399 (18)	N1—C5—C4	109.5 (2)
S5—Sb1—S4	77.118 (17)	N1—C5—H5A	109.8
S4—Sb1—S2	76.542 (17)	N1—C5—H5B	109.8
S6—Sb1—S2	137.668 (18)	C4—C5—H5A	109.8
S6—Sb1—S5	65.048 (17)	C4—C5—H5B	109.8
S6—Sb1—S4	137.991 (18)	H5A—C5—H5B	108.2
C1—S1—Sb1	90.19 (8)	O1—C3—C2	111.9 (2)
C6—S3—Sb1	91.95 (9)	O1—C3—H3A	109.2
C1—S2—Sb1	85.93 (7)	O1—C3—H3B	109.2
C11—S5—Sb1	86.64 (7)	C2—C3—H3A	109.2
C6—S4—Sb1	81.86 (8)	C2—C3—H3B	109.2
C11—S6—Sb1	89.56 (8)	H3A—C3—H3B	107.9

C3—O1—C4	109.91 (17)	S5—C11—S6	118.61 (12)
C8—O2—C9	112.1 (2)	N3—C11—S5	121.36 (17)
C13—O3—C14	109.95 (18)	N3—C11—S6	120.02 (18)
C5—N1—C2	111.64 (17)	N3—C12—H12A	109.8
C1—N1—C2	123.55 (19)	N3—C12—H12B	109.8
C1—N1—C5	124.78 (19)	N3—C12—C13	109.6 (2)
C11—N3—C12	123.1 (2)	H12A—C12—H12B	108.2
C11—N3—C15	124.54 (19)	C13—C12—H12A	109.8
C12—N3—C15	112.08 (18)	C13—C12—H12B	109.8
C10—N2—C7	111.3 (2)	S2—C1—S1	117.62 (12)
C6—N2—C7	123.7 (2)	N1—C1—S1	119.79 (17)
C6—N2—C10	124.2 (2)	N1—C1—S2	122.58 (16)
N2—C7—H7A	110.0	O3—C13—C12	111.4 (2)
N2—C7—H7B	110.0	O3—C13—H13A	109.3
N2—C7—C8	108.55 (19)	O3—C13—H13B	109.3
H7A—C7—H7B	108.4	C12—C13—H13A	109.3
C8—C7—H7A	110.0	C12—C13—H13B	109.3
C8—C7—H7B	110.0	H13A—C13—H13B	108.0
N1—C2—H2A	109.8	N3—C15—H15A	109.6
N1—C2—H2B	109.8	N3—C15—H15B	109.6
N1—C2—C3	109.2 (2)	N3—C15—C14	110.3 (2)
H2A—C2—H2B	108.3	H15A—C15—H15B	108.1
C3—C2—H2A	109.8	C14—C15—H15A	109.6
C3—C2—H2B	109.8	C14—C15—H15B	109.6
N2—C10—H10A	109.9	O2—C9—C10	111.0 (2)
N2—C10—H10B	109.9	O2—C9—H9A	109.4
N2—C10—C9	108.7 (2)	O2—C9—H9B	109.4
H10A—C10—H10B	108.3	C10—C9—H9A	109.4
C9—C10—H10A	109.9	C10—C9—H9B	109.4
C9—C10—H10B	109.9	H9A—C9—H9B	108.0
O1—C4—H4A	109.4	O3—C14—C15	112.3 (2)
O1—C4—H4B	109.4	O3—C14—H14A	109.2
O1—C4—C5	111.1 (2)	O3—C14—H14B	109.2
H4A—C4—H4B	108.0	C15—C14—H14A	109.2
C5—C4—H4A	109.4	C15—C14—H14B	109.2
C5—C4—H4B	109.4	H14A—C14—H14B	107.9
Sb1—S1—C1—S2	13.00 (14)	C10—N2—C7—C8	56.6 (2)
Sb1—S1—C1—N1	−168.1 (2)	C10—N2—C6—S3	8.9 (3)
Sb1—S3—C6—S4	4.71 (12)	C10—N2—C6—S4	−170.90 (16)
Sb1—S3—C6—N2	−175.15 (16)	C4—O1—C3—C2	59.8 (3)
Sb1—S2—C1—S1	−12.36 (13)	C8—O2—C9—C10	−56.5 (3)
Sb1—S2—C1—N1	168.8 (2)	C6—N2—C7—C8	−113.2 (2)
Sb1—S5—C11—S6	3.48 (14)	C6—N2—C10—C9	110.4 (2)
Sb1—S5—C11—N3	−177.2 (2)	C5—N1—C2—C3	54.2 (3)
Sb1—S4—C6—S3	−4.17 (10)	C5—N1—C1—S1	1.0 (4)
Sb1—S4—C6—N2	175.68 (19)	C5—N1—C1—S2	179.8 (2)
Sb1—S6—C11—S5	−3.60 (15)	C3—O1—C4—C5	−60.1 (3)
Sb1—S6—C11—N3	177.0 (2)	C11—N3—C12—C13	−132.1 (3)
O1—C4—C5—N1	57.7 (3)	C11—N3—C15—C14	133.4 (3)

N1—C2—C3—O1	−56.5 (3)	C12—N3—C11—S5	−4.7 (4)
N3—C12—C13—O3	−57.6 (3)	C12—N3—C11—S6	174.6 (2)
N3—C15—C14—O3	54.6 (3)	C12—N3—C15—C14	−52.0 (3)
N2—C7—C8—O2	−53.8 (3)	C1—N1—C2—C3	−123.8 (3)
N2—C10—C9—O2	58.4 (3)	C1—N1—C5—C4	122.9 (3)
C7—N2—C10—C9	−59.4 (2)	C13—O3—C14—C15	−59.1 (3)
C7—N2—C6—S3	177.49 (16)	C15—N3—C11—S5	169.2 (2)
C7—N2—C6—S4	−2.4 (3)	C15—N3—C11—S6	−11.4 (4)
C2—N1—C5—C4	−55.0 (3)	C15—N3—C12—C13	53.3 (3)
C2—N1—C1—S1	178.64 (19)	C9—O2—C8—C7	54.9 (3)
C2—N1—C1—S2	−2.5 (4)	C14—O3—C13—C12	60.4 (3)

Crystallographic data for tris(piperidinedithiocarbamato)antimony(III)

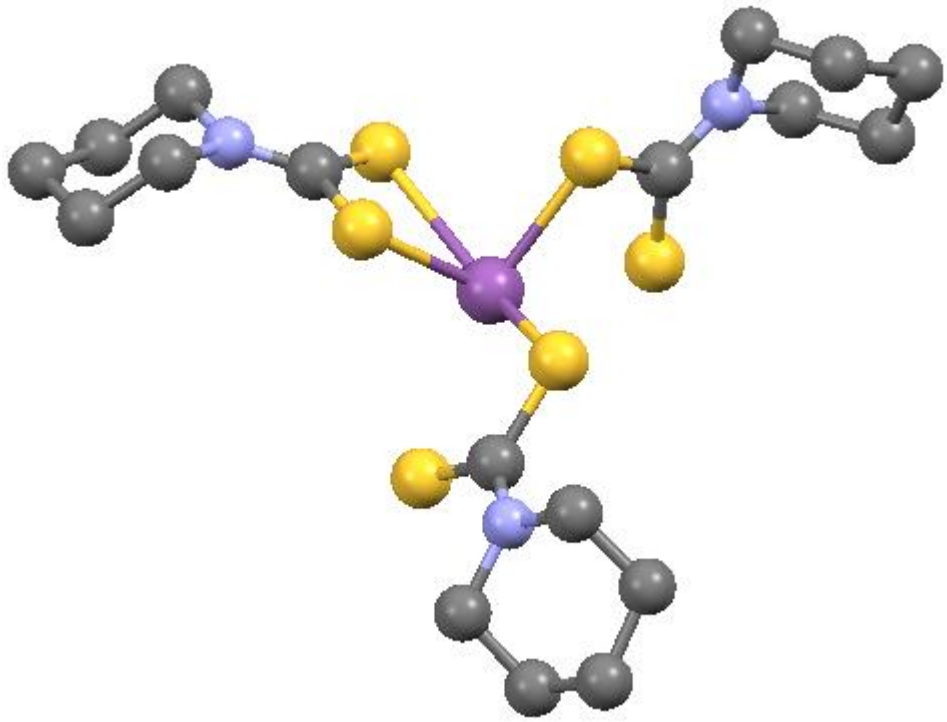

Crystal data	
Chemical formula	$C_{18}H_{30}N_3S_6Sb$
M_r	602.56
CCDC	1889653
Crystal system, space group	Monoclinic, $P2_1/c$

Temperature (K)	150
a, *b*, *c* (Å)	17.6331 (3), 11.84939 (19), 12.12535 (19)
β (°)	107.4771 (17)
V (Å3)	2416.54 (7)
Z	4
Radiation type	Cu *Kα*
μ (mm−1)	13.98
Crystal size (mm)	0.15 × 0.11 × 0.07
Data collection	
Diffractometer	XtaLAB AFC11 (RINC): Kappa single
Absorption correction	Multi-scan *CrysAlis PRO* 1.171.39.30c (Rigaku Oxford Diffraction, 2017) Empirical absorption correction using spherical harmonics, implemented in SCALE3 ABSPACK scaling algorithm.
*T*min, *T*max	0.705, 1.000
No. of measured, independent and observed [*I* > 2σ(*I*)] reflections	
*R*int	0.019
(sin θ/λ)max (Å−1)	0.602
Refinement	
R[*F*2 > 2σ(*F*2)], *wR*(*F*2), *S*	0.017, 0.043, 1.06
No. of reflections	4406
No. of parameters	254
H-atom treatment	H-atom parameters constrained
Δρmax, Δρmin (e Å−3)	0.31, −0.30

Fractional atomic coordinates and isotropic or equivalent isotropic displacement parameters (Å2) for (tris(piperidinedithiocarbamato)antimony(III))

X	*y*	*z*	*U*iso*/*U*eq
Sb00 (5)	0.26962 (2)	0.50363 (2)	0.69766 (2)	0.01971
S002 (10)	0.31060 (2)	0.37460 (4)	0.55900 (4)	0.02442
S003 (9)	0.25408 (2)	0.66051 (3)	0.55028 (3)	0.02231
S004 (10)	0.18442 (3)	0.69870 (4)	0.74152 (4)	0.02662
S005 (10)	0.20146 (3)	0.34058 (4)	0.82842 (3)	0.02738

S006	0.13281 (2)	0.42940 (4)	0.58906 (3)	0.02684 (10)
S007	0.44468 (3)	0.50547 (4)	0.71508 (4)	0.02623 (10)
N008	0.21797 (8)	0.86368 (12)	0.61447 (12)	0.0223 (3)
N009	0.05218 (8)	0.30691 (13)	0.69886 (12)	0.0244 (3)
N00A	0.45935 (8)	0.36226 (13)	0.55298 (12)	0.0242 (3)
C00B	0.21797 (9)	0.75381 (14)	0.63512 (13)	0.0200 (3)
C00C	0.25082 (10)	0.91558 (15)	0.52857 (14)	0.0233 (3)
H00A	0.208574	0.958024	0.471225	0.028*
H00B	0.270699	0.856013	0.487083	0.028*
C00D	0.12264 (10)	0.35301 (14)	0.70767 (14)	0.0210 (3)
C00E	0.41210 (10)	0.41008 (14)	0.60629 (14)	0.0218 (3)
C00F	0.31853 (12)	0.99516 (15)	0.58839 (17)	0.0300(4)
H00C	0.363304	0.950883	0.638540	0.036*
H00D	0.337593	1.033926	0.529395	0.036*
C00G	−0.01196 (11)	0.17233 (17)	0.54959 (15)	0.0294 (4)
H00E	0.039341	0.154709	0.535853	0.035*
H00F	−0.054810	0.161733	0.475871	0.035*
C00H	0.25500 (12)	1.02663 (17)	0.74512 (16)	0.0303 (4)
H00G	0.296102	0.983426	0.803482	0.036*
H00H	0.233663	1.085111	0.786037	0.036*
C00I	0.56480 (11)	0.17952 (16)	0.54191 (17)	0.0308 (4)
H00I	0.590449	0.107609	0.574601	0.037*
H00J	0.582916	0.199128	0.474538	0.037*
C00J	−0.02497 (11)	0.09182 (17)	0.64028 (16)	0.0310(4)
H00K	−0.019367	0.013054	0.616629	0.037*
H00L	−0.079668	0.101374	0.645087	0.037*
C00K	0.18846 (11)	0.94783 (16)	0.68132 (16)	0.0292(4)
H00M	0.166888	0.908777	0.737582	0.035*
H00N	0.144937	0.992091	0.628399	0.035*
C00L	0.58943 (10)	0.27207 (16)	0.63256 (16)	0.0278 (4)
H00O	0.577115	0.248335	0.703585	0.033*
H00P	0.647498	0.284539	0.652541	0.033*
C00M	0.03745 (11)	0.23778 (16)	0.79135 (15)	0.0286(4)
H00Q	−0.013640	0.260243	0.803125	0.034*
H00R	0.080302	0.250591	0.864622	0.034*
C00N	0.29224 (12)	1.08284 (17)	0.66120 (17)	0.0356 (4)
H00S	0.338740	1.128094	0.704974	0.043*
H00T	0.253171	1.134548	0.609852	0.043*
C00O	−0.01147 (10)	0.29432 (16)	0.58851 (16)	0.0294 (4)
H00U	−0.001719	0.345401	0.529584	0.035*
H00V	−0.063492	0.313938	0.598826	0.035*
C00P	0.47462 (12)	0.16488 (16)	0.50281 (16)	0.0307 (4)
H00W	0.459236	0.108685	0.439559	0.037*
H00X	0.457212	0.136355	0.568043	0.037*
C00Q	0.54592 (10)	0.38134 (15)	0.58771 (16)	0.0263(4)
H00Y	0.560613	0.439739	0.648850	0.032*
H	0.561641	0.408678	0.520574	0.032*

C00R	0.43374 (11)	0.27662 (16)	0.46089 (15)	0.0297(4)
H00Z	0.447419	0.302030	0.391441	0.036*
HA	0.375357	0.266827	0.439459	0.036*
C00S	0.03462 (11)	0.11349 (16)	0.75914 (15)	0.0300(4)
H00	0.019443	0.068513	0.818023	0.036*
HB	0.088135	0.088672	0.758683	0.036*

Atomic displacement parameters (Å²) for (Fractional atomic coordinates and isotropic or equivalent isotropic displacement parameters (Å²) for (tris(piperidinedithiocarbamato)antimony(III))

	U_{11}	U_{22}	U_{33}	U_{12}	U_{13}	U_{23}
Sb00	0.01906 (7)	0.02082 (8)	0.01856 (7)	−0.00209 (4)	0.00463 (5)	0.00162 (4)
S002	0.0208 (2)	0.0240 (2)	0.0261 (2)	−0.00199 (16)	0.00348 (16)	−0.00417 (16)
S003	0.0289 (2)	0.0206 (2)	0.02052 (19)	0.00078 (16)	0.01224 (16)	0.00056 (15)
S004	0.0272 (2)	0.0320 (2)	0.0257 (2)	−0.00219 (17)	0.01571 (17)	0.00138 (17)
S005	0.0264 (2)	0.0305 (2)	0.02064 (19)	−0.00702 (17)	0.00007 (16)	0.00409 (16)
S006	0.0231 (2)	0.0325 (2)	0.02113 (19)	−0.00623 (17)	0.00084 (16)	0.00564 (17)
S007	0.0236 (2)	0.0291 (2)	0.0246 (2)	−0.00369 (16)	0.00513 (18)	−0.00758 (16)
N008	0.0230 (7)	0.0214 (7)	0.0247 (7)	−0.0007 (6)	0.0105 (6)	−0.0015 (6)
N009	0.0222 (7)	0.0270 (8)	0.0238 (7)	−0.0030 (6)	0.0070 (6)	−0.0024 (6)
N00A	0.0217 (7)	0.0253 (8)	0.0239 (7)	0.0007 (6)	0.0041 (6)	−0.0030 (6)
C00B	0.0160 (7)	0.0241 (8)	0.0192 (7)	−0.0019 (6)	0.0043 (6)	−0.0019 (6)
C00C	0.0266 (8)	0.0225 (9)	0.0203 (8)	−0.0018 (7)	0.0064 (7)	0.0016 (7)
C00D	0.0213 (8)	0.0203 (8)	0.0217 (8)	−0.0003 (6)	0.0067 (6)	−0.0038 (6)
C00E	0.0228 (8)	0.0195 (8)	0.0205 (8)	0.0013 (7)	0.0028 (6)	0.0031 (6)
C00F	0.0291 (10)	0.0317 (11)	0.0277 (10)	−0.0089 (7)	0.0063 (8)	0.0007 (7)
C00G	0.0236 (9)	0.0401 (11)	0.0236 (8)	−0.0051 (8)	0.0057 (7)	−0.0055 (8)
C00H	0.0330 (10)	0.0280 (9)	0.0267 (9)	0.0040 (8)	0.0041 (8)	−0.0061 (8)
C00I	0.0311 (10)	0.0279 (10)	0.0358 (10)	0.0053 (8)	0.0139 (8)	0.0031 (8)
C00J	0.0309 (9)	0.0317 (10)	0.0340 (10)	−0.0072 (8)	0.0150 (8)	−0.0095 (8)
C00K	0.0291 (9)	0.0259 (10)	0.0358 (10)	0.0025 (8)	0.0145 (8)	−0.0061 (8)
C00L	0.0222 (8)	0.0291 (10)	0.0314 (9)	0.0009 (7)	0.0071 (7)	0.0034 (7)
C00M	0.0295 (9)	0.0363 (10)	0.0251 (8)	−0.0085 (8)	0.0159 (7)	−0.0058 (7)
C00N	0.0392 (11)	0.0275 (10)	0.0352 (10)	−0.0097 (8)	0.0038 (8)	−0.0072 (8)
C00O	0.0171 (8)	0.0354 (10)	0.0317 (9)	−0.0025 (7)	0.0015 (7)	0.0013 (8)
C00P	0.0336 (10)	0.0273 (10)	0.0325 (10)	−0.0030 (8)	0.0120 (8)	−0.0070 (8)
C00Q	0.0217 (8)	0.0267 (9)	0.0302 (9)	−0.0021 (7)	0.0072 (7)	−0.0008 (7)
C00R	0.0280 (9)	0.0348 (10)	0.0242 (8)	−0.0003 (8)	0.0046 (7)	−0.0081 (8)
C00S	0.0347 (10)	0.0316 (10)	0.0272 (9)	−0.0054 (8)	0.0144 (8)	−0.0008 (8)

Geometric parameters (Å, º) for (*Fractional atomic coordinates and isotropic or equivalent isotropic displacement parameters (Å^2) for (tris(piperidinedithiocarbamato)antimony(III))*

Sb00—S002	2.5330 (4)	N00A—C00E	1.326 (2)
Sb00—S003	2.5358 (4)	N00A—C00Q	1.474 (2)
Sb00—S004	2.8918 (5)	N00A—C00R	1.476 (2)
Sb00—S006	2.5337 (4)	C00C—C00F	1.523 (2)
S002—C00E	1.7584 (17)	C00F—C00N	1.523 (3)
S003—C00B	1.7549 (16)	C00G—C00J	1.524 (3)
S004—C00B	1.7027 (16)	C00G—C00O	1.520 (3)
S005—C00D	1.6955 (16)	C00H—C00K	1.517 (3)
S006—C00D	1.7535 (17)	C00H—C00N	1.520 (3)
S007—C00E	1.7007 (17)	C00I—C00L	1.521 (3)
N008—C00B	1.326 (2)	C00I—C00P	1.527 (3)
N008—C00C	1.470 (2)	C00J—C00S	1.529 (3)
N008—C00K	1.475 (2)	C00L—C00Q	1.520 (2)
N009—C00D	1.332 (2)	C00M—C00S	1.521 (3)
N009—C00M	1.474 (2)	C00P—C00R	1.520 (3)
N009—C00O	1.473 (2)		
S002—Sb00—S003	88.093 (14)	N008—C00C—C00F	109.93 (14)
S002—Sb00—S004	150.697 (13)	S005—C00D—S006	119.59 (10)
S002—Sb00—S006	82.089 (14)	N009—C00D—S005	122.46 (13)
S003—Sb00—S004	65.889 (12)	N009—C00D—S006	117.95 (12)
S006—Sb00—S003	90.215 (14)	S007—C00E—S002	119.05 (10)
S006—Sb00—S004	84.658 (14)	N00A—C00E—S002	117.78 (12)
C00E—S002—Sb00	96.00 (6)	N00A—C00E—S007	123.16 (13)
C00B—S003—Sb00	91.73 (6)	C00N—C00F—C00C	111.52 (16)
C00B—S004—Sb00	81.33 (6)	C00O—C00G—C00J	111.06 (15)
C00D—S006—Sb00	93.95 (6)	C00K—C00H—C00N	110.59 (16)
C00B—N008—C00C	124.54 (14)	C00L—C00I—C00P	110.56 (15)
C00B—N008—C00K	122.69 (14)	C00G—C00J—C00S	111.42 (15)
C00C—N008—C00K	112.68 (14)	N008—C00K—C00H	110.48 (15)
C00D—N009—C00M	122.71 (15)	C00Q—C00L—C00I	110.60 (15)
C00D—N009—C00O	123.53 (14)	N009—C00M—C00S	110.04 (14)
C00O—N009—C00M	112.00 (14)	C00H—C00N—C00F	110.91 (16)
C00E—N00A—C00Q	122.94 (14)	N009—C00O—C00G	108.06 (15)
C00E—N00A—C00R	124.66 (15)	C00R—C00P—C00I	110.48 (16)
C00Q—N00A—C00R	112.16 (14)	N00A—C00Q—C00L	109.86 (14)
S004—C00B—S003	118.19 (10)	N00A—C00R—C00P	109.84 (14)
N008—C00B—S003	119.16 (12)	C00M—C00S—C00J	111.41 (16)
N008—C00B—S004	122.65 (12)		

5. Electron microscopy images

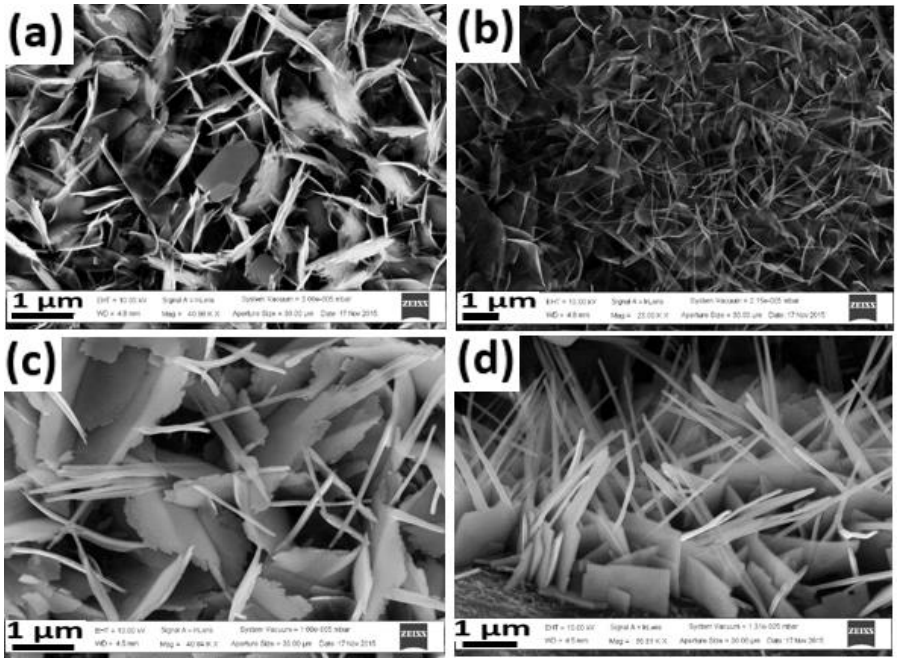

High magnification TEM images of Bi2S3 thin films deposited by AACVD

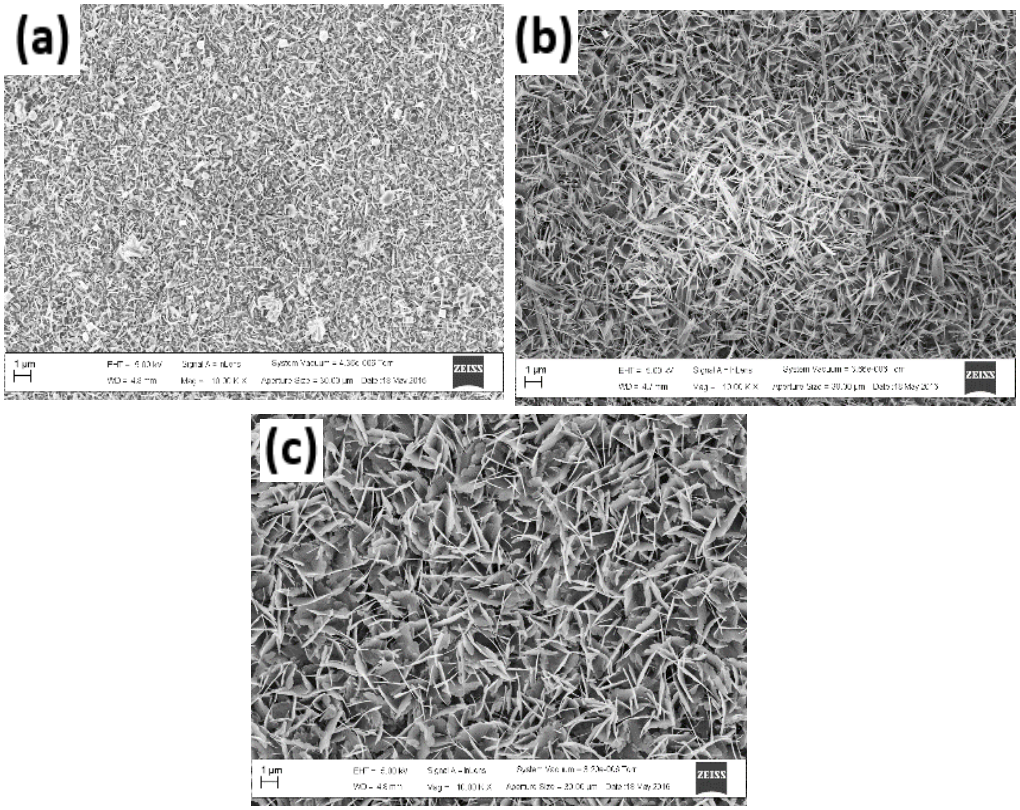

Low magnification SEM images of Bi_2S_3 thin films from $[Bi(S_2CThq)_3]$ deposited by AACVD at a) 350 °C b) 400 °C and c) 450 °C in $CHCl_3/CH_3CN$ mixture.

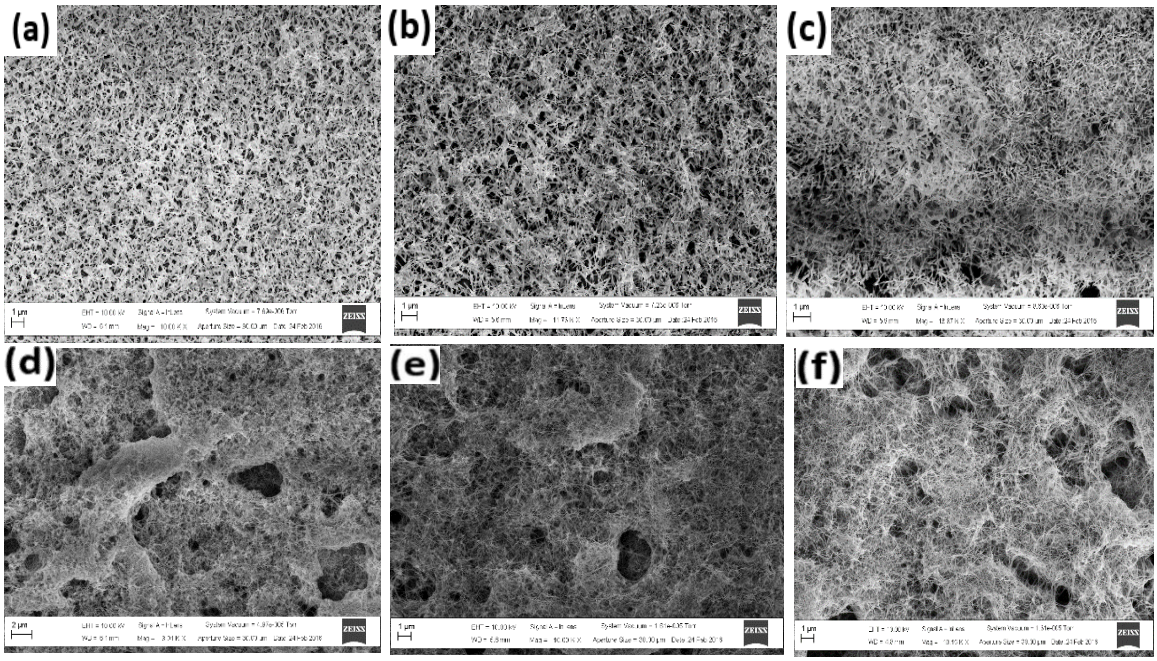

Low Magnification SEM images Bi_2S_3 thin films deposited by spin coating $[Bi(S_2CPip)_3]$ in $CHCl_3$/MeOH and annealing at a) 350 °C b) 400 °C, c) 450 °C and from $[Bi(S_2CThq)_3]$ at d) 350 °C e) 400 °C and f) 450 °C.